Design and Synthesis of Diarylethene Photoswitches: From Photochemical Properties to Switchable Fluorescence and Photopharmacology



Sili Qiu

Corpus Christi College, University of Oxford

A thesis submitted for the degree of

Doctor of Philosophy

Trinity Term 2024

Abstract

This thesis presents an investigation into diarylethene-based organic photoswitches, with emphasis on optimizing their photoswitching capabilities. The research then progresses to implement these enhanced photoswitches in practical applications, specifically focusing on switchable fluorescence systems and photopharmacology.

Chapter 1 provides a review of molecular photoswitch research, elucidating fundamental models, quantitative formalisms, and key photoswitching performance parameters. A comparative analysis of various photoswitch classes is presented, highlighting their structural and photochemical features. This analysis identifies diarylethenes as a promising class of photoswitch for further optimization.

Chapter 2 describes the synthesis and characterization of push-push, pull-pull, and push-pull diarylethenes with varying lengths of conjugation. A comprehensive examination of their photophysical and photochemical properties is presented, with observed trends rationalized through DFT and TD-DFT calculations, and conformational sampling. The chapter culminates in the identification of a water-soluble diarylethene, featuring two *N*-methylpyridinium groups with alkyne spacers, capable of bidirectional visible light photoswitching with quantitative photostationary state distribution.

Chapter 3 extends the findings of Chapter 2, utilizing the optimized diarylethene to develop two photoswitchable fluorophores based on a diarylethene-cyanine dyad design. The diarylethene functions as a photocontrollable switch for the fluorophore, enabling reversible transitions between fluorescent and non-fluorescent states. The chapter details the synthesis of these photoswitchable dyads and provides an in-depth characterization of their fluorescence switching properties and fatigue resistance.

Chapter 4 explores diarylethenes as photoswitchable ligands targeting G-quadruplexes. The synthesis of four diarylethene-based switchable ligands is outlined, followed by an examination of their binding interactions with G-quadruplexes. This chapter reveals that the open and closed isomers of the diarylethenes exhibit distinct affinities for G-quadruplexes and varying degrees of cytotoxicity.

Chapter 5 summarizes the key findings of the research and provides a critical outlook for future investigations in this field.

Acknowledgement

I would like to express my profound gratitude to my supervisor, Professor Harry L. Anderson, for his unwavering support, encouragement, and understanding throughout my DPhil journey, particularly during the challenging pandemic years. His guidance has been invaluable, consistently fostering my academic growth regardless of research outcomes.

I extend my heartfelt appreciation to my fellow Team RESOLFT members: Dr. Andrew Frawley, Dr. Kathryn Leslie, and Dr. Virginia Wycisk, for their exceptional mentorship and daily research guidance. I am equally grateful for the support from all other HLA group members: Dr. Arnau Rubio, Chiara Pigaiani, Dr. Connor Patrick, Edward Champness, Frederick Leslie, Dr. He Zhu, Dr. Henrik Gotfredsen, Dr. Igor Rončević, Isaac Ettedgui, Jack Pickering, Jake Holmes, Dr. Janko Hergenhahn, Dr. Jeff Van Raden, Dr. Jibin Sun, Dr. Jie-Ren Deng, Joshua Field, Dr. Kavita Rani, Dr. Keith Andrews, Lene Godde, Lidao Li, Dr. Lorel Scriven, Dr. Marcin Majewski, Dr. Marco Vitek, Owen Kanisius, Paramveer Kumar, Dr. Pernille Bols, Prakhar Gupta, Dr. Qiang Chen, Sara Borghi, Dr. Sebastian Kopp, Dr. Steffen Woltering, Dr. Stephen Marriott, Théa Toutoungy, Thomas Ebdon, Dr. Toby Johnson, Dr. Wenjun Xu, Dr. William Kendrick, Dr. Wojtek Stawski, and Dr. Yueze Gao. Their contributions have fostered a collaborative and enriching research environment.

I am grateful for the fruitful collaboration with Professor Matthew Fuchter and Dr. Marco Di Antonio's groups at Imperial College London, with particular thanks to Dr. Davia Prischich, Dr. Enrico Cadoni, and Dr. Ludovica Monti for their contributions to our study on photoswitchable G-quadruplex ligands.

My appreciation extends to the research facility staff in the Department of Chemistry, University of Oxford, especially Professor Tim Claridge, Dr. Nick Rees, Dr. Coral Mycroft, Dr. Victor Mikhailov, and Dr. John Walsby-Tickle, for their support with NMR and mass spectrometry experiments. I am also thankful for the often-overlooked heroes of the department: the facility maintenance, food supply, IT support, lab cleaning, safety, and store staff.

I am deeply indebted to the China Scholarship Council for granting me the CSC-Oxford Scholarship. A special note of gratitude goes to my dear friend Moheng Li and his father Jin Li, Chairman of the Board of Sichuan Chanhen Holding Group Co., Ltd. Their support was

instrumental in securing corporate funding from the Chanhen Group, for which I am profoundly grateful.

I also wish to extend my heartfelt thanks to my dear friends who have been pillars of support throughout my DPhil journey. Special thanks go to Gaoyu Du, whose initial groundwork in establishing Jinfanlinghang Educational Consulting Co. was pivotal in bringing our shared business vision to fruition. Additionally, I am deeply appreciative of Yilei Ding, whose constant encouragement has been a source of strength throughout my doctoral studies.

I would like to express my deepest gratitude to my parents and family for their unwavering support throughout this journey.

Last but not the least, I would like to acknowledge the inspiration I've drawn from Gareth Bale, my football idol. His diligence on the football pitch has been a constant source of motivation, helping me overcome setbacks and persevere in my academic pursuits.

To all these individuals and institutions, your contributions have not only advanced my research but have also enriched my personal and professional growth. Thank you for being an integral part of this transformative experience.

Supplement to Statement of Authorship

Chapter 2 presents the synthesis and characterization of eight dithienylethenes. In the computational rationalization section, the conformational sampling on the open DTEs with CREST was performed by Dr. Kathryn G. Leslie at the University of Oxford.

Chapter 4 presents the synthesis of four photoswitchable dithienylethene compounds and an investigation of their interactions with DNA G-quadruplexes. The fluorescence quenching assay measurements were performed at Imperial College London, jointly conducted by myself and Dr. Ludovica Monti, who additionally executed the cell viability assays. The circular dichroism titration experiments and the DNA FRET melting assays were conducted by Dr. Enrico Cadoni.

Contents

Chapter 1 – Introduction

1.1 Photochromism – From Historical Reference to Modern Discovery 3
1.2 Photoswitches – Definitions, Principles and the Quantitative Formalism 7
1.3 Photoswitch – Key Photoswitching Parameters 15
1.4 Main Families of Organic Photoswitches 17
1.4.1 Photoswitch Involving *Trans–Cis* Isomerization 18
1.4.1.1 Stilbenes 18
1.4.1.2 Azobenzenes 20
1.4.1.3 Indigoids 23
1.4.1.4 Hemiindigoids 24
1.4.1.5 Iminothioindigoids 28
1.4.1.6 Hydrazones 28
1.4.2 Photoswitch Involving Pericyclic Reactions 30
1.4.2.1 Diarylethenes 30
1.4.2.2 Dihydropyrene 34
1.4.3 Photoswitch Involving Mixed Switching Mechanisms 34
1.4.3.1 Spiropyrans 35
1.4.3.2 Fulgoids 36
1.4.4 Summary of Photoswitching Parameters for Different Families of Photoswitches 38
1.5 Project Aim 40

Chapter 2 - Dithienylethenes – A Systematic Structure-Property Relationship

2.1 Introduction 53
2.1.1 Discovery of Bistable Dithienylethenes 53
2.1.2 DAEs Responsive to Visible-Light Photoswitching 54
2.1.2.1 Extending π Conjugation 55
2.1.2.2 Triplet Sensitization 59
2.1.3 DAEs with Aqueous Solubility 61
2.1.4 Project Aim 63
2.2 Results and Discussion 64
2.2.1 Design and Synthesis of DTE Photoswitches 64

2.2.2 Photochromism 71
2.2.3 Structural Impact on UV-vis Absorption Spectra 76
2.2.4 Photostationary State Distribution 79
2.2.5 Quantum Yield of Photoswitching 83
2.2.6 Calculation of PSD Based on Molar Absorption Coefficient and Quantum Yield 87
2.2.7 Fatigue Resistance 88
2.2.8 Decomposition of **Dy-yD** 91
2.2.9 Solvatochromism of **D-A** 95
2.2.10 Computational Benchmarking for DFT and TD-DFT Calculations 98
2.2.11 Conformational Analysis on Open DTEs 104
2.3 Conclusions 106
2.4 Experimental 107
2.5 Appendix 135

Chapter 3 - DTE-Cyanine Dyads with Photoswitchable Fluorescence

3.1 Introduction 157
3.1.1 Fluorescence 157
3.1.2 Activatable, Convertible and Switchable Fluorescence 158
3.1.3 Switchable Fluorescent Probes for Super-Resolution Microscopy 161
3.1.4 Switchable Fluorescent Probes for Studying Cellular Dynamics 169
3.1.5 Project Aim 169
3.2 Results and Discussion 170
3.2.1 Molecular Design of Photoswitchable Dyads 170
3.2.2 Selection of the Fluorescent Dye 171
3.2.3 Modelling of FRET Quenching 175
3.2.4 Synthesis of Cy3 and Cy3B Dyes 179
3.2.5 Characterization of Cy3 and Cy3B Photophysics 181
3.2.6 Synthesis of Photoswitchable Fluorophores 184
3.2.7 Photoswitching of **DTE-Cy3** and **DTE-Cy3B** 187
3.2.8 Regulation of Cyanine Fluorescence by DTE 190
3.2.9 Fatigue Resistance of **DTE-Cy3** and **DTE-Cy3B** 193
3.2.10 Conclusion 194
3.3 Experimental 195
3.4 Appendix 211

Chapter 4 - Photoswitchable DNA G-Quadruplex Ligands

4.1 Introduction 225
4.1.1 Photopharmacology 225
4.1.2 Azobenzene-Based Agents 229
4.1.3 Agents Bearing Diarylethenes 230
4.1.4 Diarylethenes Targeting DNA G-Quadruplex 233
4.1.5 Project Aim 234
4.2 Results and Discussion 235
4.2.1 Synthesis of DTEs 235
4.2.2 UV-vis Absorption 237
4.2.3 Photostationary State Distribution 238
4.2.4 Photoswitching Quantum Yields 240
4.2.5 Fluorescence Quenching Assay 241
4.2.6 Circular Dichroism Titration 243
4.2.7 FRET Melting Assay 245
4.2.8 Cell Viability Assay 247
4.2.9 Conclusion 249
4.3 Experimental 250
4.4 Appendix 254

Chapter 5 – Conclusions and Outlook

5.1 Conclusions 261
5.2 Outlook 262

List of Publications

'How do donor and acceptor substituents change the photophysical and photochemical behavior of dithienylethenes? The search for a water-soluble visible-light photoswitch'
S. Qiu, A. T. Frawley, K. G. Leslie, H. L. Anderson, *Chem. Sci.*, 2023, **14**, 9123–9135.

'Light Up, Light Off: High-Contrast Photoswitchable Fluorophores Based on Dithienylethene-Cy3 Dyad'
S. Qiu, A. T. Frawley, K. G. Leslie, H. L. Anderson, manuscript in preparation.

'Dithienylethene Switches with Isomer-Specific DNA G-Quadruplex Affinity'
E. Cadoni, S. Qiu, L. Monti, A. T. Frawley, K. G. Leslie, M. J. Fuchter, H. L. Anderson, M. Di Antonio, manuscript in preparation.

Oral Presentations

'Syntheses and Properties of Push-Push, Pull-Pull, and Push-Pull Diarylethenes'
AstraZeneca Graduate Symposium, Chemistry Research Laboratory, Oxford, June 2022.

Poster Presentations

'Push-Push, Pull-Pull, and Push-Pull Diarylethenes'
28th IUPAC Symposium on Photochemistry, Amsterdam, Netherlands, July 2022.

List of Abbreviations

Abbreviations

abs.	absorption
Ac	acetate
ADME	absorption, distribution, metabolism, and excretion
aq.	aqueous
Ar	aromatic ring
Boc	*tert*-butoxycarbonyl
BODIPY	boron-dipyrromethene
br.	broad
Bu	butyl
CASPT2	complete active-space second order perturbation theory
CASSCF	complete active space self-consistent field
CB7	cucurbit[7]uril
CD	circular dichroism
CPD	cyclophanediene
CuAAc	copper(I)-catalyzed azide-alkyne cycloaddition
Cy	cyanine (fluorescent dye)
δ	chemical shift
d	doublet
Δ	difference
DAE	diarylethene
DCM	dichloromethane
dd	doublet of doublets
DFT	density functional theory
DHP	dimethyldihydropyrene
DIPEA	*N*,*N*-diisopropylethylamine
DMF	dimethylformamide
DMSO	dimethyl sulfoxide
DTE	dithienylethene
ε	molar absorption coefficient
EI	electron ionization
ESI	electrospray ionization
ESIPT	excited state intramolecular proton transfer
Et	ethyl
ex.	excitation
Φ	quantum yield
FAM	carboxy-fluorescein
FCS	fluorescence correlation spectroscopy
fl.	fluorescence
FLIM	fluorescence lifetime imaging
FMO	frontier molecular orbital
FRAP	fluorescence recovery after photobleaching
FRET	Förster resonance energy transfer
FWHM	full width at half maximum
G4	G-quadruplex
GFP	green fluorescent protein
GS	gramicidin S
HEK 293	human embryonic kidney 293 (cell line)
HER2	human epidermal growth factor receptor 2
HI	hemiindigo
HOMO	highest occupied molecular orbital
HPLC	high performance liquid chromatography
HR	high resolution
HTI	hemithioindigo
IC_{50}	half maximal inhibitory concentration
ICT	intramolecular charge transfer

ISC	intersystem crossing
ITI	iminothioindoxyl
KAT	Kamlet-Abboud-Taft (solvation model)
LSER	linear solvation energy relationship
LUMO	lowest unoccupied molecular orbital
m/*z*	mass/charge ratio
MC	merocyanine
Me	methyl
MMVB	molecular mechanics-valence bond
MNDO	modified neglect of diatomic overlap
MOF	metal-organic framework
MS	mass spectrometry
NA	numerical aperture
NHS	*N*-hydroxysuccinimide
NMR	nuclear magnetic resonance
PALM	photoactivated localization microscopy
PDI	perylenediimide
PDT	photodynamic therapy
PET	photoinduced electron transfer
PMI	perylenemonoimide
PPAR	peroxisome proliferator-activated receptors
ppm	parts per million
Pr	propyl
PSD	photostationary state distribution
PSF	point spread function
PSS	photostationary state
q	quartet
RESOLFT	reversible saturable optical fluorescence transitions
RMSD	root mean square deviation
ROS	reactive oxygen species
RP	reversed phase
s	singlet
SIM	structured illumination microscopy
SMD	solvation model based on density
SMLM	single-molecule localization microscopy
SP	spiropyran
SRM	super-resolution microscopy
STED	stimulated emission depletion
STORM	stochastic optical reconstruction microscopy
TAMRA	carboxy-tetramethylrhodamine
TCSPC	time-correlated single photon counting
TD-DFT	time dependent-density functional theory
TFA	trifluoroacetic acid
THF	tetrahydrofuran
TICT	twisted intramolecular charge transfer
TLC	thin layer chromatography
TMS	trimethylsilyl
ToF	time-of-flight
Tris	tris(hydroxymethyl) aminomethane
UV	ultraviolet light
UV-vis	ultraviolet-visible

1 Introduction

Contents

1.1 Photochromism – From Historical Reference to Modern Discovery 3

1.2 Photoswitches – Definitions, Principles and the Quantitative Formalism 7

1.3 Photoswitch – Key Photoswitching Parameters 15

1.4 Main Families of Organic Photoswitches 17

1.4.1 Photoswitch Involving *Trans–Cis* Isomerization 18

1.4.1.1 Stilbenes 18

1.4.1.2 Azobenzenes 20

1.4.1.3 Indigoids 23

1.4.1.4 Hemiindigoids 24

1.4.1.5 Iminothioindigoids 28

1.4.1.6 Hydrazones 28

1.4.2 Photoswitch Involving Pericyclic Reactions 30

1.4.2.1 Diarylethenes 30

1.4.2.2 Dihydropyrene 34

1.4.3 Photoswitch Involving Mixed Switching Mechanisms 34

1.4.3.1 Spiropyrans 35

1.4.3.2 Fulgoids 36

1.4.4 Summary of Photoswitching Parameters for Different Families of Photoswitches 38

1.5 Project Aim 40

Chapter 1 - Introduction

1.1 Photochromism – From Historical Reference to Modern Discovery

Numerous reviews have summarized the development of photochromic molecules.[1-6] Among these documentations, Jago's report provides a comprehensive overview of the discovery and development of different classes of photochromic systems.[3]

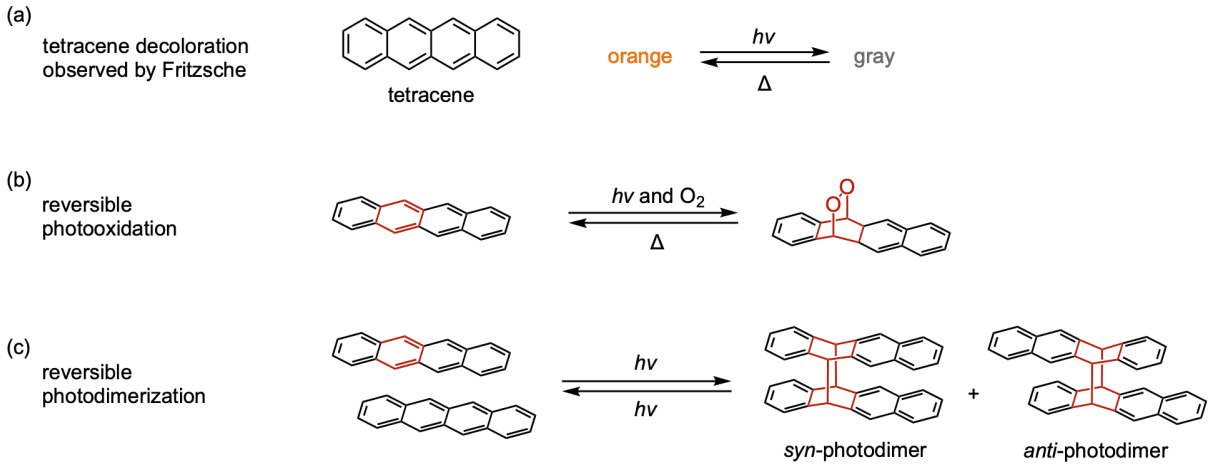
The phenomenon of photochromism, in which a material undergoes a reversible color change when exposed to light, dates to the time of Alexander the Great (356–323 BC). As the King of Macedonia, Alexander embarked on a campaign of global conquest that saw his empire stretch from Asia Minor to the far reaches of India and Egypt (Figure 1.1). His military triumphs were built on a foundation of meticulous strategic planning and well-coordinated attacks.



Figure 1.1 Alexander, depicted with his horse Bucephalus, fighting Persian king Darius III, from the Alexander Mosaic of Pompeii (Naples National Archaeological Museum, Italy). Reprint with permission.[7]

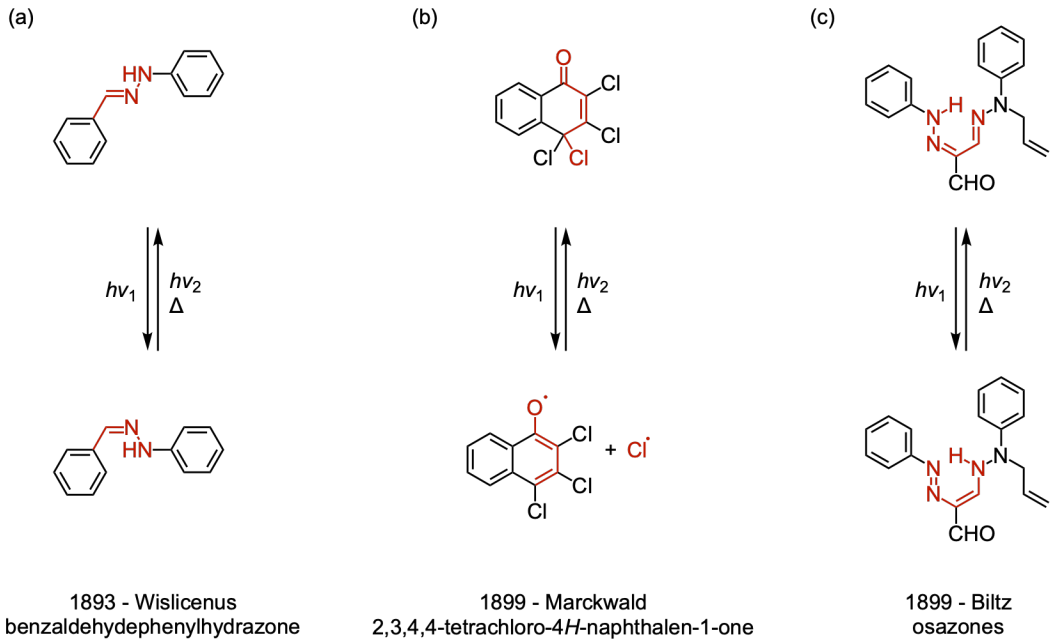
According to historical records, the soldiers of Macedonia were adorned with mysterious bracelets that possessed the remarkable ability to change color when exposed to sunlight. The composition of these photochromic accessories remains a mystery, but their purpose was clear: to serve as an advanced signaling mechanism that would alert the warriors to the ideal time to launch their assault.[1, 2]

More than two thousand years later in 1867, Johann Wilhelm Adolf Fritzsche made the first scientific discovery that would serve as the cornerstone for our current understanding of photochromism.[8] Fritzsche observed that a tetracene solution, initially a vibrant orange color, would gradually fade when exposed to sunlight (Scheme 1.1a). It slowly returned to its original orange color in dark. Gillet and colleagues later revealed that a photooxidation product forms during the decoloration process, which dissociates in the dark and upon heating.[9] One widely accepted mechanism for this photooxidation is that the photoexcited acene molecule sensitizes the formation of singlet oxygen,[10-12] which then reacts with ground-state acene to generate endoperoxide (Scheme 1.1b).[13-16] In addition to photooxidation, photo-induced dimerization also contributes to the decoloration observed by Fritzsche (Scheme 1.1c).[17, 18]



Scheme 1.1 (a) Light-induced decoloration of tetracene, a phenomenon that laid the foundation for the modern understanding of photochromism. (b) The reversible photooxidation of tetracene, leading to the formation of endoperoxide, a process that contributes to the observed decoloration. (c) The reversible photodimerization of tetracene, resulting in the generation of *syn*- and *anti*-photodimers. The red color highlights the photoactive unit.

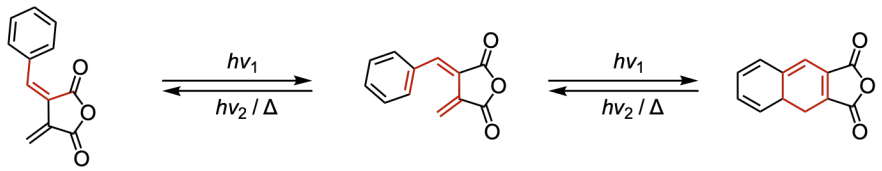
Since Fritzsche's groundbreaking discovery, numerous reports emerged describing solutions and solid materials that exhibit similar photochromic behavior (Scheme 1.2).[19-22] However, the early research primarily focused on the description of the phenomenon rather than providing a scientific understanding of the underlying mechanisms. In the last decade of the 19th century, Wislicenus noted the essential role that light had in turning benzaldehydephenylhydrazone red and its gradual reversal in the dark (Scheme 1.2a).[22] Marckwald noted the reversible color change of 2,3,4,4-tetrachloro-4*H*-naphthalen-1-one (Scheme 1.2b).[23] Marckwald coined the term "phototropie" (in German) to describe this light-induced reversible change in color. Biltz further observed the photochromism of osazones (Scheme 1.2c).[24]



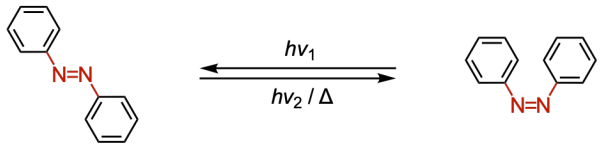
Scheme 1.2 Early descriptive reports on the photochromic phenomena in different classes of compounds including (a) benzaldehydephenylhydrazone, (b) 2,3,4,4-tetrachloro-4*H*-naphthalen-1-one, and (c) osazones. The red color highlights the photoactive unit.

Researchers in the early 20th century focused on synthesizing novel molecules and investigating their photochromic properties. A prime example is the fulgide family, whose initial synthesis and photochromic behavior were reported by Stobbe in 1905 (Scheme 1.3).[25] However, it was not until 1968 that the mechanism underlying fulgide photoswitching was fully elucidated,[26] when instruments such as UV-vis and NMR spectrometers became widely accessible. Even today, fulgides continue to captivate the interest of the scientific community, as evidenced by recent studies exploring their potential as universal chemical actinometers[27] and optical memory devices.[28]

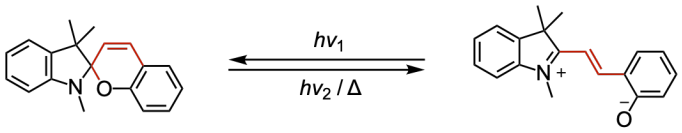
1905 - Stobbe - Fulgides



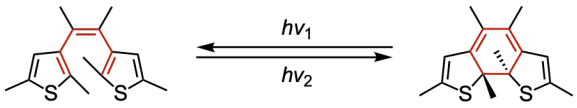
1937 - Hartley - Azobenzenes



1952 - Hirshberg and Fischer - Spiropyrans



1988 - Irie - Diarylethenes



Scheme 1.3 Timeline of the discovery of four major classes of photoswitches: fulgides, azobenzenes, spiropyrans, and diarylethenes. It showcases the historical progression and milestones achieved in the field of photoswitchable molecules. The red color highlights the photoactive unit.

Azobenzenes were first synthesized in 1834.[29] However, it was not until 1937 that Hartley made the groundbreaking discovery of azobenzene's photoswitching properties (Scheme 1.3).[30] Hartley discovered the change of azobenzene's solubility upon exposure to sunlight. He performed an experiment extracting the azobenzene molecule from an acetone-water mixture using light petroleum. The results showed a significant presence of azobenzene in the aqueous phase of samples exposed to sunlight, in contrast to the minimal amount found in samples kept in the dark. This finding indicated the formation of a more polar species upon light exposure, which was identified as the *cis* isomer.

The mid-20th century witnessed a significant expansion in the field of photochromic molecules. During this era, the term "photochromism" gained widespread acceptance. Hirschberg's discovery of spiropyrans marks as a milestone (Scheme 1.3).[31] In the next two decades, scientists sought to address the limitations of spiropyrans, such as poor fatigue resistance and the need for UV light for photoswitching. This led to the development of

spirooxazine and spironaphthoxazine derivatives,[32-34] enabling their use in variable transmission glasses.

The 1990s witnessed the emergence of diarylethenes as another major family of photoswitches (Scheme 1.3). Diarylethenes belong to P-type photoswitches, which undergo photoisomerization between two thermally stable isomers. This property renders them particularly attractive for applications in optical data storage.[5, 35, 36]

In the 21st century, research efforts have shifted from the synthesis and development of new classes of photoswitches to optimizing the photoswitching parameters of existing ones and translating these chemical tools to real-world applications. Molecular photoswitches have found applications in several areas, such as photopharmacology,[37] where they are used to control drug activity with light, energy storage,[38] where they can be employed in light-driven energy conversion and storage devices, optical data storage,[39] where they enable high-density and reversible data recording, and biological imaging, particularly in super-resolution microscopy,[40] where they allow for the visualization of biological structures and processes at the nanoscale level.

1.2 Photoswitches – Definitions, Principles and the Quantitative Formalism

In the preceding section, the terms "photochromic molecule" and "photochromism" were used to denote the color change linked to chemical reactions. Moving forward, the term "photoswitch" will be used synonymously with "photochromic molecule". However, it is crucial to distinguish between the terms "photoswitch" and "photochromic system". While "photoswitch" specifically refers to molecular entities, "photochromic system" encompasses both molecular photoswitches and systems that require multiple components to exhibit photochromic behavior. For example, the tetracene photochromism initially reported by Fritzsche (Scheme 1.1a) is considered a photochromic system rather than a photoswitch.[8]

A molecular photoswitch is defined as a chemical compound that can be transformed between two or more stable forms using light.[41, 42] This light-induced isomerization process results in changes to the molecular structure and electronic properties, which typically lead to distinct and well-characterized differences in the UV-vis absorption spectra of the isomeric states, causing the molecule to exhibit photochromic behavior.

The most basic model to describe the photoswitching process is a simple two-way reaction involving two molecular forms, A and B (Figure 1.2a). This reaction is assumed to be

unimolecular. While other photoreaction and decomposition pathways may potentially lead to the formation of by-products, these will be discussed later and are neglected in this basic model.

According to the Jablonski diagram (Figure 1.2b), photoswitching starts with the chromophore A absorbing light. The thermodynamically stable photoswitch A is elevated to the first or higher-order singlet excited state, undergoes vibrational relaxation, and then passes through a region containing a conical intersection before returning to the ground state of a different isomer (Figure 1.2c). The isomer B thermally reverts back to the stable state through a first-order process with a rate constant k. This isomer is further characterized by a thermal lifetime τ ($1/k$). If the thermal activation barrier separating the two states is low, a substantial amount of thermal back isomerization occurs at ambient conditions, classifying the photoswitch as a T-type. In contrast, when the thermal activation barriers are higher, the two photoisomers are considered bistable, and isomerization is almost exclusively triggered by photochemical processes (P-type). It is important to note that P-type and T-type photoswitches are not mutually exclusive. For most P-type photoswitches, thermal reverse reaction still occurs, but the rate constant k is extremely small, so that the thermal reversion is negligible over experimentally relevant time scales.

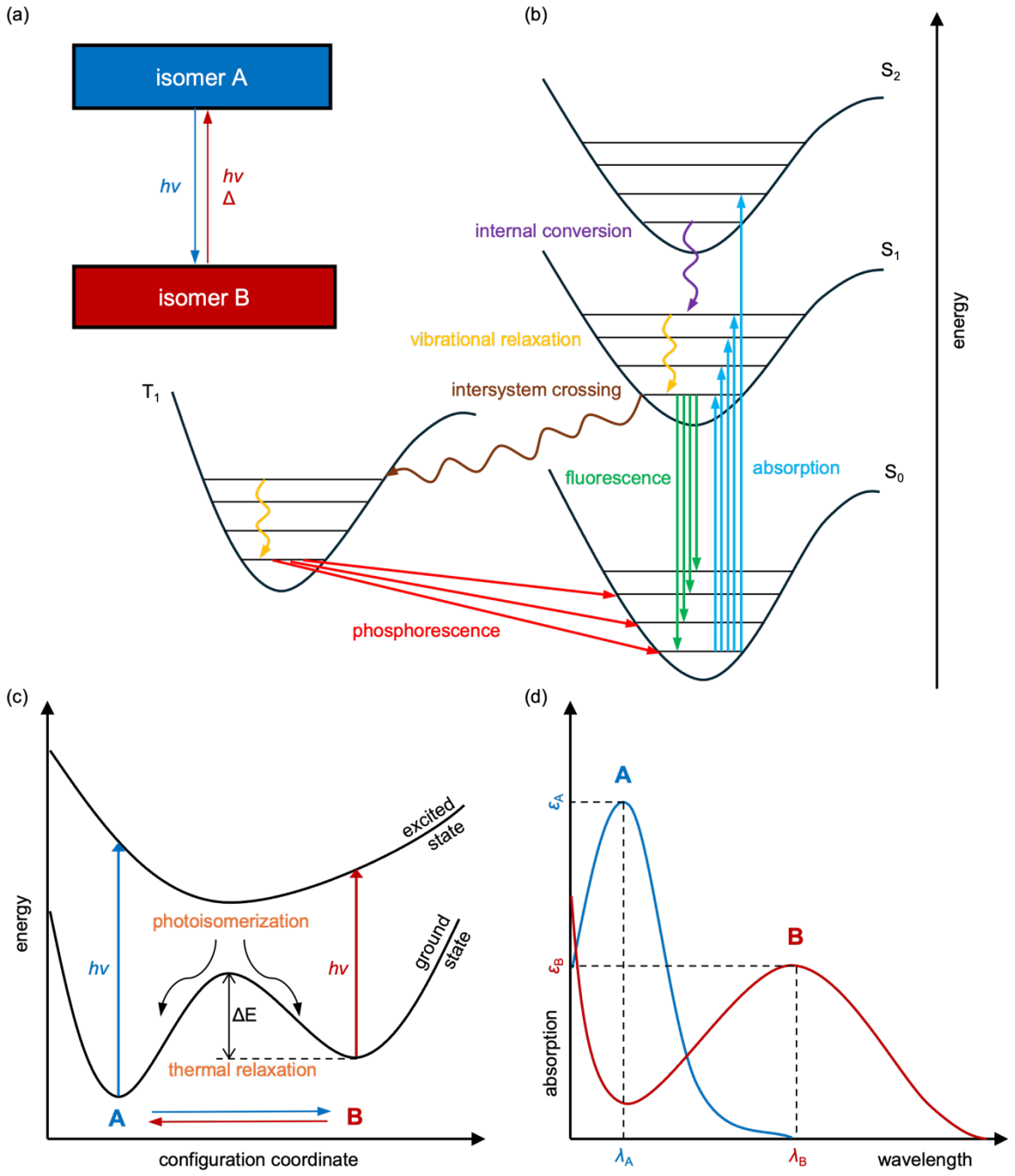


Figure 1.2 (a) Reversible isomerization of a photoswitch between isomer A and B; (b) the Jablonski diagram; (c) potential energy surfaces rationalizing photoisomerization; (d) schematic UV-vis absorption of isomers A and B.

The UV-vis absorption spectra of the isomers exhibit distinct features due to the difference in the energy gap when the molecule is in different isomers A and B (Figure 1.2d). Assuming that isomer A absorbs at a shorter wavelength than the isomer B, photoswitching occurs when isomer A absorbs at the wavelength λ_A. The molar absorption coefficient of A at this wavelength is ε_A. The excited-state A yields B with a probability of $\Phi_{A\rightarrow B}$, known as the forward photoswitching quantum yield. Conversely, B photochemically reverts to A, in an analogous way.

For such a two-way photoswitching system, a quantitative formalism can be established following a setup shown in Figure 1.3, involving a sample containing the photoswitch and an external light source providing irradiation.[2]

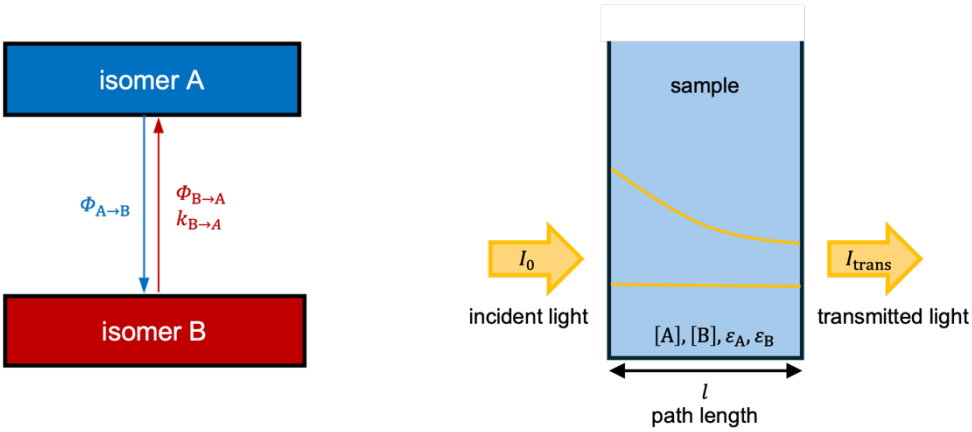


Figure 1.3 Schematic representation of the setup of a photoswitching system.

When a homogeneous sample (under constant stirring), containing a given photochromic species that exists in its two states A and B, is exposed to light irradiation at a certain wavelength, the composition of the mixture evolves with the following general differential Equation 1.1:

$$\frac{\mathrm{d[A]}(t)}{dt} = -\frac{\mathrm{d[B]}(t)}{dt} = -\Phi_{\mathrm{A}\to\mathrm{B}} \cdot I_{\mathrm{A}}(\lambda_{\mathrm{irr.}}, t) + \Phi_{\mathrm{B}\to\mathrm{A}} \cdot I_{\mathrm{B}}(\lambda_{\mathrm{irr.}}, t) + k_{\mathrm{B}\to\mathrm{A,thermal}} \cdot [\mathrm{B}](t) \quad (1.1)$$

where t is time; $[\mathrm{A}](t)$ and $[\mathrm{B}](t)$ are the concentration of A and B, respectively, at time t; $\Phi_{\mathrm{A}\to\mathrm{B}}$ and $\Phi_{\mathrm{B}\to\mathrm{A}}$ are the photoswitching quantum yields of the forward and reverse reactions; $k_{B\to\mathrm{A,thermal}}$ is the rate of thermal reverse reaction from B to A (assumed to be first-order kinetics); and $I_{\mathrm{A}}(\lambda_{\mathrm{irr.}}, t)$ and $I_{\mathrm{B}}(\lambda_{\mathrm{irr.}}, t)$ are intensities of the light absorbed by A and B at time t. The first, second and the third terms in the equation correspond to the forward photoswitching, the reverse photoswitching, and the thermal reverse reaction, respectively. The intensities of light absorbed by A and B can be derived from the Beer-Lamber Law (Equation 1.2):

$$\mathrm{Abs}(\lambda_{\mathrm{irr.}}, t) = \varepsilon(\lambda_{\mathrm{irr.}}, t) \cdot c(t) \cdot l = -\log_{10} \frac{I_{\mathrm{trans.}}(\lambda_{\mathrm{irr.}}, t)}{I_0(\lambda_{\mathrm{irr.}})} \quad (1.2)$$

where $\mathrm{Abs}(\lambda_{\mathrm{irr.}}, t)$ is the absorbance at the irradiation wavelength at time t; $\varepsilon(\lambda_{\mathrm{irr.}}, t)$ is the molar absorption coefficient at irradiation wavelength at time t; $c(t)$ is concentration at time t (as concentration of species change over time during photoswitching); and l is optical pathlength; $I_{\mathrm{trans.}}(\lambda_{\mathrm{irr.}}, t)$ is transmitted intensity at the irradiation wavelength at time t; and $I_0(\lambda_{\mathrm{irr.}})$ is incident intensity from the light source, which is independent of time. The intensity of light absorbed by the sample, $I_{\mathrm{abs.}}(\lambda_{\mathrm{irr.}}, t)$, is the difference between incident and transmitted intensity, and can be expressed as Equation 1.3.

$$I_{\mathrm{abs.}}(\lambda_{\mathrm{irr.}}, t) = I_0(\lambda_{\mathrm{irr.}}) - I_{\mathrm{trans.}}(\lambda_{\mathrm{irr.}}, t) \tag{1.3}$$

When a sample of interest contains two different chemical species, A and B, the total intensity of light being absorbed can be expressed as Equation 1.4, where $I_A(\lambda_{\mathrm{irr.}})$ and $I_B\ (\lambda_{\mathrm{irr.}})$ are the intensity of light be being absorbed by molecules A and B, respectively.

$$I_{\mathrm{abs.}}(\lambda_{\mathrm{irr.}}, t) = I_A(\lambda_{\mathrm{irr.}}, t) + I_B\ (\lambda_{\mathrm{irr.}}, t) \tag{1.4}$$

Combining Equation 1.2, Equation 1.3 and Equation 1.4, The light absorbed by compound A and B can be expressed as Equation 1.5 and Equation 1.6, respectively:

$$I_{\mathrm{A}}(\lambda_{\mathrm{irr.}}, t) = \frac{\left[1 - 10^{-\mathrm{Abs}(\lambda_{\mathrm{irr.}}, t)}\right]}{\mathrm{Abs}(\lambda_{\mathrm{irr.}}, t)} \cdot I_0(\lambda_{\mathrm{irr.}}) \cdot \varepsilon_{\mathrm{A}}(\lambda_{\mathrm{irr.}}) \cdot [\mathrm{A}](t) \cdot l \tag{1.5}$$

$$I_{\mathrm{B}}(\lambda_{\mathrm{irr.}}, t) = \frac{\left[1 - 10^{-\mathrm{Abs}(\lambda_{\mathrm{irr.}}, t)}\right]}{\mathrm{Abs}(\lambda_{\mathrm{irr.}}, t)} \cdot I_0(\lambda_{\mathrm{irr.}}) \cdot \varepsilon_{\mathrm{B}}(\lambda_{\mathrm{irr.}}) \cdot [\mathrm{B}](t) \cdot l \tag{1.6}$$

$$\text{Photokinetic Factor} = \frac{\left[1 - 10^{-\mathrm{Abs}(\lambda_{\mathrm{irr.}}, t)}\right]}{\mathrm{Abs}(\lambda_{\mathrm{irr.}}, t)} \tag{1.7}$$

where the photokinetic factor is employed to designate the nonlinear quantity; and $\varepsilon_{\mathrm{A}}(\lambda_{\mathrm{irr.}})$ and $\varepsilon_{\mathrm{B}}(\lambda_{\mathrm{irr.}})$ are the molar absorption coefficients of the A and B species at the irradiation wavelength.

In the general situation, in the absence of any approximation, the differential Equation 1.1 has no analytic solution. The "photokinetic factor," and thus $I_{\mathrm{A}}(\lambda_{\mathrm{irr.}}, t)$ and $I_{\mathrm{B}}(\lambda_{\mathrm{irr.}}, t)$, vary over time, according to Equation 1.5 and Equation 1.6.

The situation can be simplified by considering light irradiation at an isosbestic point of the photochemical system, where the molar absorption coefficients of A and B species are equal, and the absorption of the sample $\mathrm{Abs}(\lambda_{\mathrm{irr.}}, t)$ holds a constant value during the irradiation process, as well as the "photokinetic factor." Then, we can define the constant C as shown in Equation 1.8:

$$C = \frac{I_0(\lambda_{\mathrm{irr.}})}{[\mathrm{total}]}\left[1 - 10^{-\mathrm{Abs}(\lambda_{\mathrm{irr.}}, t)}\right] \tag{1.8}$$

where [total] represents the total concentration of species A and B. The generic differential Equation 1.1 then simplifies to:

$$\frac{\mathrm{d}[\mathrm{A}](t)}{dt} = \left(C \cdot \Phi_{\mathrm{B}\to\mathrm{A}} + k_{\mathrm{B}\to\mathrm{A,thermal}}\right) \cdot [\mathrm{Total}] - \left[C \cdot (\Phi_{\mathrm{A}\to\mathrm{B}} + \Phi_{\mathrm{B}\to\mathrm{A}}) + k_{\mathrm{B}\to\mathrm{A,thermal}}\right] \cdot [\mathrm{A}](t) \tag{1.9}$$

The time evolution of the molar fractions $x_{\mathrm{A}}(t)$ and $x_{\mathrm{B}}(t)$ of A and B, respectively, takes the expression of an exponential function:

$$x_{\mathrm{A}}(t) = \left(x_{\mathrm{A}}^0 - \frac{C \cdot \Phi_{\mathrm{B}\to\mathrm{A}} + k_{\mathrm{B}\to\mathrm{A,thermal}}}{C \cdot (\Phi_{\mathrm{A}\to\mathrm{B}} + \Phi_{\mathrm{B}\to\mathrm{A}}) + k_{\mathrm{B}\to\mathrm{A,thermal}}}\right) \cdot e^{\{-[C(\Phi_{\mathrm{A}\to\mathrm{B}} + \Phi_{\mathrm{B}\to\mathrm{A}}) + k_{\mathrm{B}\to\mathrm{A}}]t\}} + \frac{C \cdot \Phi_{\mathrm{A}\to\mathrm{B}}}{C \cdot (\Phi_{\mathrm{A}\to\mathrm{B}} + \Phi_{\mathrm{B}\to\mathrm{A}}) + k_{\mathrm{B}\to\mathrm{A,thermal}}} \tag{1.10}$$

$$x_{\mathrm{B}}(t) = -\left(\frac{C \cdot \Phi_{\mathrm{A}\to\mathrm{B}}}{C \cdot (\Phi_{\mathrm{A}\to\mathrm{B}} + \Phi_{\mathrm{B}\to\mathrm{A}}) + k_{\mathrm{B}\to\mathrm{A,thermal}}} - x_{\mathrm{B}}^{0}\right) \cdot e^{\{-[C(\Phi_{\mathrm{A}\to\mathrm{B}}+\Phi_{\mathrm{B}\to\mathrm{A}})+k_{\mathrm{B}\to\mathrm{A,thermal}}]t\}} + \frac{C \cdot \Phi_{\mathrm{A}\to\mathrm{B}}}{C \cdot (\Phi_{\mathrm{A}\to\mathrm{B}} + \Phi_{\mathrm{B}\to\mathrm{A}}) + k_{\mathrm{B}\to\mathrm{A,thermal}}} \tag{1.11}$$

where x_{A}^{0} and x_{B}^{0} are the initial molar fraction of species A and B, respectively.

Then, the conversion extent $\alpha_{\mathrm{B}}(\lambda_{\mathrm{irr.}})$ (from A to B) at the photostationary state (PSS), corresponding to the molar fraction of B isomer in the sample after an infinite time of irradiation, can be expressed as Equation 1.12.

$$\alpha_{\mathrm{B}}(\lambda_{\mathrm{irr.}}) = \frac{C \cdot \Phi_{\mathrm{A}\to\mathrm{B}}}{C \cdot (\Phi_{\mathrm{A}\to\mathrm{B}} + \Phi_{\mathrm{B}\to\mathrm{A}}) + k_{\mathrm{B}\to\mathrm{A,thermal}}} \tag{1.12}$$

The conversion extent of the B isomer at the PSS is called the photostationary state distribution (PSD). PSD can be further examined for both P-type and T-type photoswitches.

For a P-type photoswitch, where the thermal reverse reaction is negligible compared to the photochemical reaction due to high reaction activation energy barrier, the last thermal term of the generic kinetic Equation 1.1 is suppressed, and the PSD can be characterized by the following Equation 1.13, which can also be deduced from Equation 1.14 and 1.15 according to the definition of PSD.

$$\alpha_{\mathrm{B}}(\lambda_{\mathrm{irr.}}) = \mathrm{PSD}(\lambda_{\mathrm{irr.}}) = \frac{\varepsilon_{\mathrm{A}}(\lambda_{\mathrm{irr.}}) \cdot \Phi_{\mathrm{A}\to\mathrm{B}}}{\varepsilon_{\mathrm{A}}(\lambda_{\mathrm{irr.}}) \cdot \Phi_{\mathrm{A}\to\mathrm{B}} + \varepsilon_{\mathrm{B}}(\lambda_{\mathrm{irr.}}) \cdot \Phi_{\mathrm{B}\to\mathrm{A}}} \tag{1.13}$$

$$\mathrm{PSD}(\lambda_{\mathrm{irr.}}) = \frac{[B]}{[A] + [B]} = \frac{K}{1 + K} \tag{1.14}$$

$$K = \frac{k_{\mathrm{A}\to\mathrm{B,photo}}}{k_{\mathrm{B}\to\mathrm{A,photo}}} = \frac{\varepsilon_{\mathrm{A}}(\lambda_{\mathrm{irr.}}) \cdot \Phi_{\mathrm{A}\to\mathrm{B}}}{\varepsilon_{\mathrm{B}}(\lambda_{\mathrm{irr.}}) \cdot \Phi_{\mathrm{B}\to\mathrm{A}}} \tag{1.15}$$

According to Equation 1.13, the PSD at a given wavelength is commonly expressed as the mole fraction of one isomer.[42] PSD is always defined with respect to the product of the photochemical reaction. For example, the PSD ($\alpha_{\mathrm{B}}(\lambda_{\mathrm{irr.}})$)would be 100% if A can be fully converted to B at a given irradiation wavelength.[43] When considering the reverse photochemical reaction from B to A, the PSD equals to the conversion extent of A ($\alpha_{\mathrm{A}}(\lambda_{\mathrm{irr.}})$). Experimentally, a combination of high molar absorption coefficient (at the wavelength of irradiation), and a high photoswitching quantum yield, leads to a fast photoreaction. PSD is further related to the equilibrium constant by Equation 1.14. The photodynamic equilibrium constant, *K*, is given by Equation 1.15, where $k_{\mathrm{A\rightarrow B,photo}}$ and $k_{\mathrm{B\rightarrow A,photo}}$ are the effective first-order rate constants of the forward and the reverse photoswitching reaction; $\varepsilon_{\mathrm{A}}(\lambda_{\mathrm{irr.}})$ and $\varepsilon_{\mathrm{B}}(\lambda_{\mathrm{irr.}})$ are the molar absorption coefficients of the two isomers at the excitation wavelength; and $\Phi_{\mathrm{A\rightarrow B}}$ and $\Phi_{\mathrm{B\rightarrow A}}$ are the forward and reverse photoswitching quantum yields, respectively. Theoretically, the photoswitching quantum yields should be independent of the wavelength of excitation.

For thermally reversible photoswitches, assuming that the thermal reverse reaction is much more efficient than the photochemical reverse reaction, the photochemical reverse reaction term in differential Equation 1.1 is suppressed. To have a simple analytical solution of the equation, the case where the absorbance of the sample at the irradiation wavelength is low enough ($\mathrm{Abs}(\lambda_{\mathrm{irr.}}) \ll 1$) needs to be considered to allow the linearization of the differential equation with Equation 1.16. The initial kinetic differential Equation 1.1 then turns into the form shown in Equation 1.17. The PSD in terms of $\alpha_{\mathrm{B}}(\lambda_{\mathrm{irr.}})$ is dependent on the irradiation intensity $I_0(\lambda_{\mathrm{irr.}})$ and the relationship in shown in Equation 1.18.

$$1 - 10^{-\mathrm{Abs}(\lambda_{\mathrm{irr.}})} = \ln(10) \cdot \mathrm{Abs}(\lambda_{\mathrm{irr.}}) \tag{1.16}$$

$$\frac{\mathrm{d[A]}(t)}{dt} = -\ln(10) \cdot I_0(\lambda_{\mathrm{irr.}}) \cdot l \cdot \varepsilon_A(\lambda_{irr.}) \cdot \Phi_{\mathrm{A\rightarrow B}} \cdot [\mathrm{A}](t) + k_{B\rightarrow \mathrm{A,thermal}} \cdot [B](t) \tag{1.17}$$

$$\alpha_{\mathrm{B}}(\lambda_{\mathrm{irr.}}) = \frac{1}{1 + \frac{k_{\mathrm{B\rightarrow A,thermal}}}{\ln 10 \cdot I_0(\lambda_{\mathrm{irr.}}) \cdot l \cdot \varepsilon_{\mathrm{A}}(\lambda_{irr.}) \cdot \Phi_{\mathrm{A\rightarrow B}}}} \tag{1.18}$$

According to Equation 1.18, when the term $k_{B\rightarrow A}$ becomes high, i.e., the thermal reverse reaction takes place rapidly, the term $\alpha_B(\lambda_{irr.})$ approaches to 0. By measuring different variables within this photoswitching system, including the rate of thermal reverse reaction, the molar absorption coefficient of species A at the irradiation wavelength, the forward photochemical quantum yield, and the intensity of irradiation, the PSD of a T-type photoswitch can be calculated.

Although Equation 1.13 and Equation 1.18 allow the PSD of P-type and T-type photoswitches, respectively, to be calculated from measured experimental parameters, modern scientists tend to measure the PSD of P-type photoswitches directly using experimental methods such as quantitative NMR and HPLC. The prior relies on the difference in proton environments before and after photoswitching while the latter relies on physically separating the two species on a column. For T-type photoswitches, PSDs are not commonly reported due to quick reversion. Some literatures report the PSDs of T-type photoswitches with transient spectroscopy.[44] Overall, the quantitative formalism discussed here mainly serves as a secondary checkpoint for validating that the experimentally measured parameters are reliable.[45]

1.3 Photoswitch – Key Photoswitching Parameters

A good photoswitch generally possesses three essential characteristics. Firstly, it should have a high PSD in both directions, enabling the molecule to be quantitatively switched between the two states. Irrespective of the specific application, photoswitches are typically employed to alternate between different states to achieve contrast in the application. For instance, in optical memory devices, diarylethenes are toggled between open and closed states to simulate binary data storage, akin to magnetic disks.[46] Similarly, azobenzenes have been utilized in conjunction with medicines to switch the action of the drug on and off. [37] Such contrast in action can only be achieved with a high PSD. Secondly, fast photoswitching with minimal irradiation power is crucial, allowing the desired contrast to be achieved within a reasonable period of time. Certain fields of application have stringent requirements regarding the rate of photoswitching. For example, in super-resolution microscopy, the super-resolved image must be acquired within a reasonably short time period (minutes), particularly for live samples.[47] Thirdly, good fatigue resistance is essential to prevent the decomposition of the photoswitch during the switching process. Decomposition can result in reduced contrast over the lifecycle of the application.

From the definitions and the quantitative formalism discussed in Section 1.2, several photoswitching parameters are defined. Combinations of these parameters of a photoswitch

directly correlate with the three features mentioned above. According to Equation 1.13, for a P-type photoswitch, the PSD is related to the molar absorption coefficients of isomers A and B, as well as the photochemical quantum yields of forward and reverse photoswitching. Reversible photoswitching of any compound can be divided into two extreme scenarios (Figure 1.4). If there is a good separation between the absorption bands of the two isomers (Figure 1.4a), one isomer of the compound can be irradiated at a wavelength ($\lambda_{A,1}$ or $\lambda_{B,1}$) where the other isomer does not absorb significantly, leading to a clean conversion from one to the other. Alternatively, if there is a poor band separation (Figure 1.4b), forward and reverse reactions take place simultaneously under irradiation at $\lambda_{A,2}$ or $\lambda_{B,2}$. Assuming the same absorption coefficient for the two isomers at the irradiation wavelength, a quantitative (>99%) PSD can only be achieved if the quantum yield of the forward reaction is at least 100 times greater than that of the reverse reaction. Therefore, to design a molecular photoswitch with high PSD, contrast in either the position of UV-vis absorptions or the quantum yields of photoswitching is crucial. Generally, the prior is preferred, as low quantum yield in one direction results in slower photoswitching kinetics. However, this limitation can potentially be mitigated by employing a light source of higher intensity.

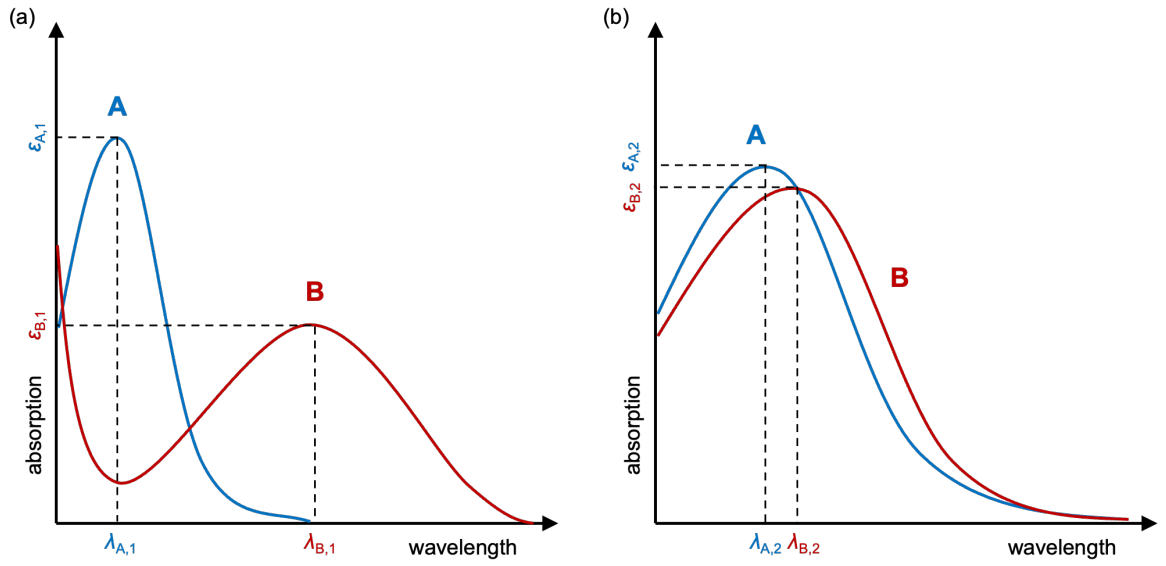


Figure 1.4 Schematic UV-vis absorption spectra of a photoswitch in (a) a good band separation scenario, where the absorption bands of the two isomers are well-separated, allowing for selective excitation of one isomer without affecting the other, and (b) a poor band separation scenario, where the absorption bands of the two isomers overlap significantly, leading to simultaneous excitation of both isomers and competing forward and reverse photoswitching processes.

The rate of photoswitching is influenced by several key parameters, including the molar absorption coefficient of the molecule at the irradiation wavelength, the intensity of the irradiating light, and the quantum yield of the reaction. The molar absorption coefficient determines the efficiency which the photoswitch absorbs photons at a specific wavelength. The

intensity of the irradiating light, typically expressed in terms of photon flux (photons per unit area per unit time), directly affects the number of photons available for absorption. Increasing the light intensity results in a higher rate of photon absorption and, thus, a faster photoswitching process. Finally, the photochemical quantum yield quantifies the efficiency of the photoswitching reaction itself. A higher quantum yield indicates that a larger fraction of the absorbed photons leads to successful isomerization events, thereby accelerating the overall photoswitching rate.

Fatigue resistance is the third feature of a high-performance photoswitch, ensuring its longevity and reliability in practical applications. While an ideal photoswitch is expected to toggle between two states, A and B, there are often additional pathways that lead to the decomposition of the molecule (Figure 1.5). A photoswitch with good fatigue resistance is characterized by high photoswitching quantum yields between states A and B, while exhibiting low quantum yields for decomposition pathways. For a fatigue resistant photoswitch, the ratio between the desired switching quantum yields and decomposition quantum yield determines the overall fatigue resistance of the photoswitch. A higher ratio indicates that the molecule undergoes numerous successful switching cycles before significant decomposition, resulting in a more robust and durable system. Researchers in the field of photoswitch design aim to minimize the quantum yield of non-switching processes while maximizing the quantum yield of the desired photoswitching reaction.

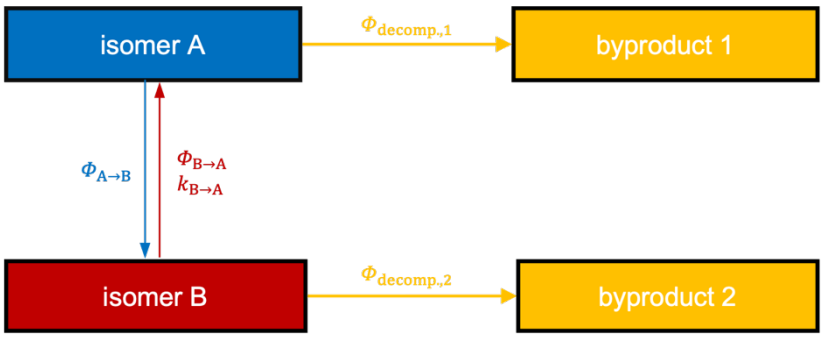


Figure 1.5 General scheme depicting isomerization of a photoswitch and the decomposition process upon light irradiation.

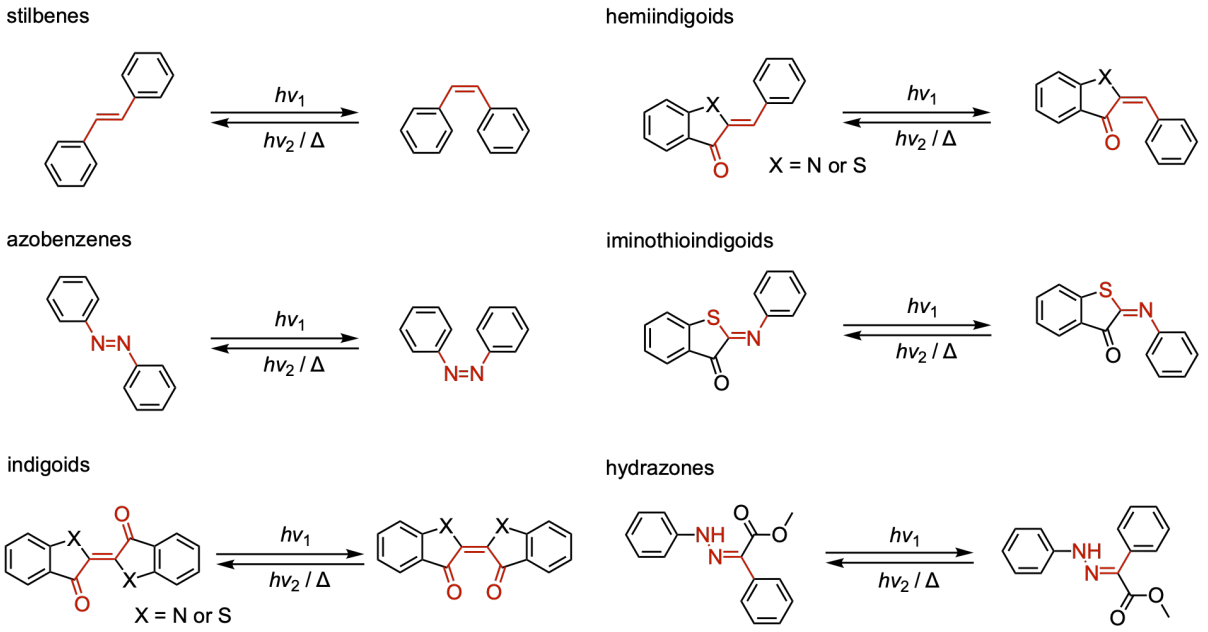
1.4 Main Families of Organic Photoswitches

In the last 30 years, research in organic photoswitch has focused on a handful of photoswitch families. The photoswitching mechanisms of various classes of photoswitches can be primarily divided into three categories: photoisomerization about a double bond, photoisomerization based on pericyclic reactions, and mixed reaction mechanisms.[42] This section considers the most promising photoswitches for practical applications in switchable fluorescence and

photopharmacology and examines the photophysical and photochemical properties, and synthetic procedures of well-studied parent compounds and closely-related analogues.

1.4.1 Photoswitch Involving *Trans–Cis* Isomerization

Trans–cis isomerization about a double bond is a fundamental process in organic chemistry. The *trans* isomer is generally more thermodynamically stable due to the minimization of steric repulsion between the substituents.[48] The energy barrier for thermal *trans–cis* isomerization in alkenes typically ranges from 100 to 600 kJ mol^{-1}. This high barrier is due to the requirement of breaking the carbon-carbon π bond.[49] Alternatively, *trans–cis* isomerization can be efficiently triggered by light. Upon absorption of a photon, the alkene is promoted to an excited state, where the π bond is weakened (or formally broken), and rotation can occur around the C–C bond. The excited state can then relax back to the ground state, forming either the *cis* or *trans* isomer. The photochemical *trans–cis* isomerization is typically much faster than the thermal process. In the following sections, we will investigate various types of photoswitches that undergo isomerization about C=C, C=N, or N=N double bonds (Scheme 1.4), including stilbenes, azobenzenes, indigoids, hemiindigoids, aryl iminoindigoids and hydrazones.

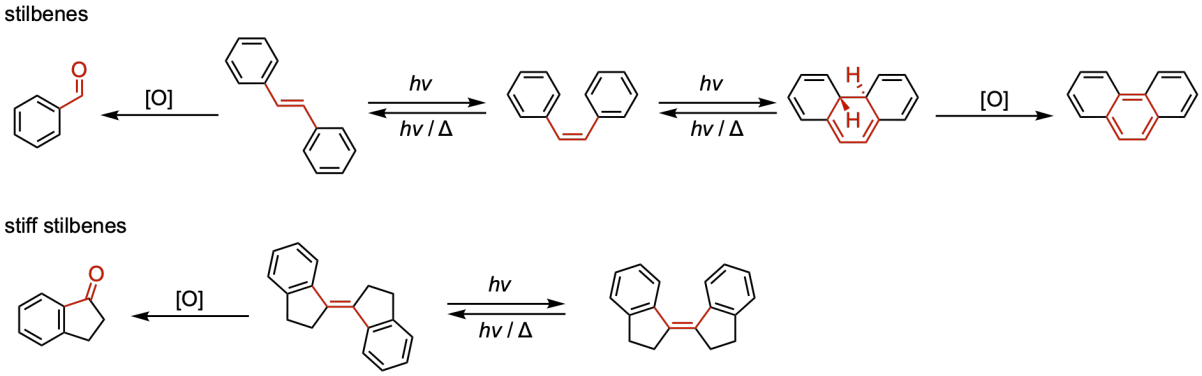


Scheme 1.4 Overview of various photoswitches relying on *trans–cis* isomerization about C=C, N=N, and C=N. The red color highlights the photoactive unit.

1.4.1.1 Stilbenes

Stilbenes, with the general formula Ar–CH=CH–Ar, exist in a thermodynamically stable *trans* isomer and a photochemically generated *cis* isomer (Scheme 1.5, top) with slow thermal reversion.[50] The *trans* isomer adopts a nearly planar conformation and displays an absorption

maximum around 290 nm with strong vibronic coupling.[51] Irradiation at this absorption band promotes the *trans* isomer to its excited state via a π–π* transition, from which it relaxes to the helical *cis* form with high photoswitching quantum yields ($\Phi_{trans \rightarrow cis}$) ranging from 0.40 to 0.60.[52] The absorption spectrum of the *cis* isomer is bathochromically shifted by around 10 nm. Due to the poor band separation, PSD of around 60% in the forward direction can be achieved under 313 nm irradiation.[53] Irradiation of the *cis* stilbene induces the photoreversion with quantum yields ($\Phi_{cis \rightarrow trans}$) ranging from 0.3 to 0.45.[52]



Scheme 1.5 Photochemical reactions of stilbene (top) and stiff stilbene (bottom). The red color highlights the photoactive unit.

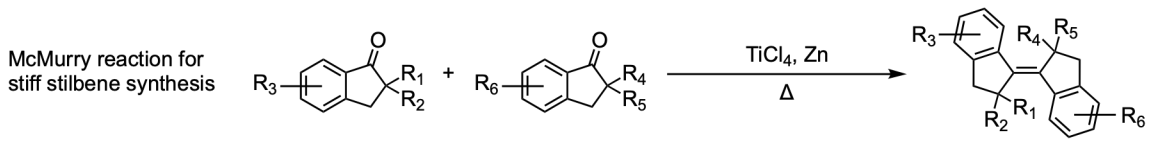
The *cis* isomer of the parent stilbene is not photostable. Photocyclization reactions can occur from the *cis* isomer, resulting in the formation of a cyclic product, and further oxidation yields phenanthrene (Scheme 1.5, top). To avoid photocyclization, 5-membered fused rings can be introduced to the parent stilbene, forming stiff stilbenes (Scheme 1.5, bottom). These molecules have been proven to be more photochemically robust.[50, 52]

Stiff stilbenes exhibit photochemical properties that are analogous to, yet simpler than, those of parent stilbenes.[53, 54] Their absorption maximum generally lies between 320 and 340 nm, depending on the ring size, and can be shifted up to approximately 360 nm with suitable substituents.[55-57] The UV-vis absorption of the *cis* isomer is red-shifted about 10 nm and broadened compared to the *trans* isomer.[58] The band separation is not strong enough to yield high PSD, with most stiff stilbenes reaching PSD of 65% in the forward direction and 80% in the reverse direction.[50]

Rather than being used explicitly as a molecular photoswitch, stiff-stilbene is widely recognized as a key structural component in Feringa-type molecular motors. The properties and applications of these molecular motors have been extensively covered in other reviews.[59, 60]

Stiff stilbenes are frequently prepared via the McMurry reaction (Scheme 1.6). McMurry reaction is particularly advantageous due to its ability to selectively form the thermodynamically

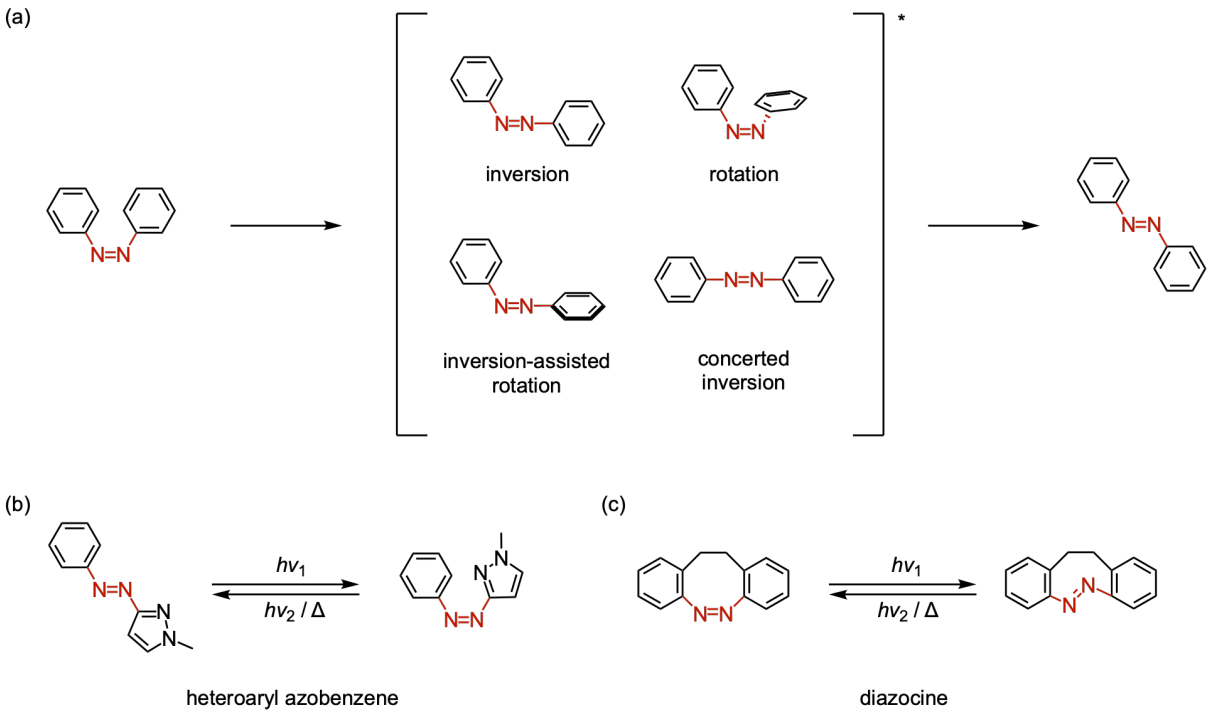
favored *trans* isomer of the stilbene product. This selectivity arises from the steric repulsion between the substituents on the aromatic rings. The McMurry reaction exhibits the highest efficiency when the two coupling partners are identical. However, the mixed McMurry reaction enables the synthesis of more complex asymmetrical stiff stilbenes by employing different carbonyl compounds as coupling partners. An alternative pathway for the synthesis of stiff stilbenes is the Barton-Kellogg reaction.[50]



Scheme 1.6 Synthesis of stiff stilbenes by McMurry reaction.

1.4.1.2 Azobenzenes

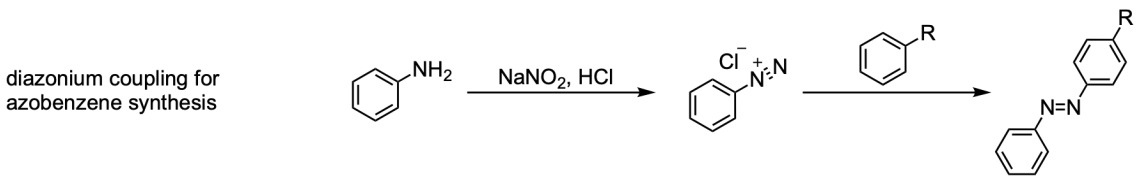
Azobenzenes, a family of T-type photoswitch with the general formula Ar–N=N–Ar,[61-63] have emerged as widely used photoswitches due to their compact size, reliable photochemical behavior, and the diverse range of methods available for their synthesis.[64, 65] Parent azobenzenes exist in a thermodynamically stable *trans* state and can be converted to the metastable *cis* form through irradiation. The reverse isomerization can be achieved through light irradiation or thermal relaxation.[61-63] Virtual screening studies have revealed that this thermal relaxation can occur through various pathways, including inversion, rotation, inversion-assisted rotation, or concerted inversion (Scheme 1.7a).



Scheme 1.7 (a) Possible thermal relaxation pathways of metastable azobenzenes.[66] Photoswitching (*cis*–*trans* isomerization) of (b) heteroaryl azobenzene[67] and (c) diaozcine.[68] The red color highlights the photoactive unit.

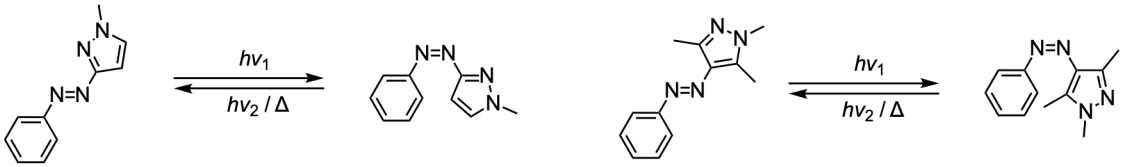
Compared to stilbene, the absorption maximum of parent azobenzene is bathochromically shifted to around 340 nm, allowing for operation with less harmful UV-A light.[52, 63] Special azobenzene designs, such as incorporating electron donor and acceptor groups at different ends of the azobenzene and substituting the ortho-position of the aryl rings with halogens, can further red-shift absorption into the visible region.[61] The main absorption band (π–π* transition) of the *trans* isomer generally absorbs at a longer wavelength (~20 nm) than the *cis* isomer. A satellite absorption band corresponding to the n–π* transition usually occurs in the 400–450 nm region.[69] Overall, the absorption spectra of the two isomeric forms of azobenzene do not exhibit massive difference, making it difficult to achieve quantitative PSD. Most azobenzenes achieve PSDs of 75–80% in the forward direction and 100% in the reverse direction.[70]

The most common method for synthesizing azobenzenes is through diazonium coupling (Scheme 1.8).[64] Other synthetic routes such as Mills reaction, Wallach reaction etc. are also commonly used.[64]



Scheme 1.8 General scheme for azobenzene synthesis by diazonium coupling.

Heteroaryl azobenzenes (Scheme 1.7b and Scheme 1.9) have one or both aryl rings substituted with heteroaromatic moieties (such as pyridine,[71-75] indole,[57, 76, 77] indazole,[78] purine,[79, 80] pyrimidine,[81, 82] pyrrole,[83] imidazole,[67, 83-85] pyrazole,[67, 86-92] oxazole,[93] thiazole,[83] or thiophene).[94-96] The incorporation of heteroatoms in these molecules introduces polarity in the *trans* isomer. While the *trans* isomer maintains a planar geometry, the *cis* isomer can adopt various conformations depending on the nature of the heteroaromatic ring. The presence of heteroatoms makes heteroaryl azobenzenes responsive to light of longer wavelengths than traditional azobenzenes.[67] The thermal half-lives vary significantly depending on the heteroaryl ring. In a systematic study on pyrazole-incorporated heteroaryl azobenzenes, the Fuchter group reported two molecules, **3pzH** and **4pzMe**, with outstanding photoswitching properties. Both molecules can achieve PSDs of >98% in both forward and reverse directions. Molecules **3pzH** and **4pzMe** have thermal half-lives of 72 days and 10 days, respectively, significantly longer than the parent azobenzene.[67]



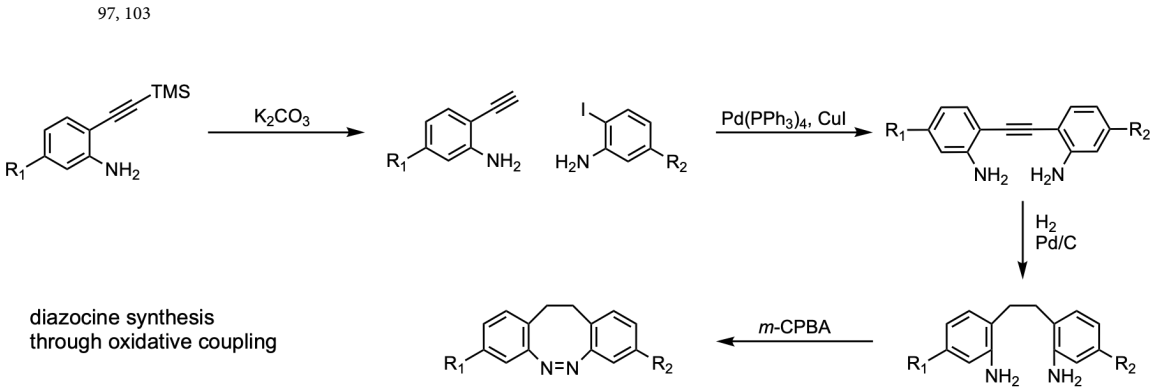
heteroaryl azobenzene **3pzH** heteroaryl azobenzene **4pzMe**

Scheme 1.9 Examples of heteroaryl azobenzenes with outstanding PSDs and thermal half-lives.

Diazocines are cyclic analogues of parent azobenzenes (Scheme 1.7c) responsive to visible light.[68, 97-99] The defining feature of diazocines is the presence of an 8-membered ring, which introduces strain into the molecular structure. Diazocines exhibit an inversion of stability, in which the *cis* isomer is thermodynamically stable. One of the most remarkable properties of diazocines is their ability to undergo bidirectional photoisomerization with visible light. Typically, the *cis* isomer absorbs at 300–420 nm and the *trans* isomer absorbs at a longer wavelength (480–600 nm).[100] The UV-vis absorption bands of the *cis* and the *trans* isomers are well separated (~80 nm vs. ~20 nm for traditional azobenzenes), allowing for selective excitation.[100] As for PSD, unsurprisingly, diazocine can achieve 88% in the forward direction (under 405 nm irradiation) and 100% in the reverse direction (under 525 nm irradiation).[101] Diazocines also have exceedingly high photoswitching quantum yields of 0.7 and 0.5 in the forward and reverse directions, respectively.[68]

The primary limitation of diazocine is the difficulty in its synthesis. While parent diazocine with aliphatic linkers can typically be prepared using an oxidative coupling route

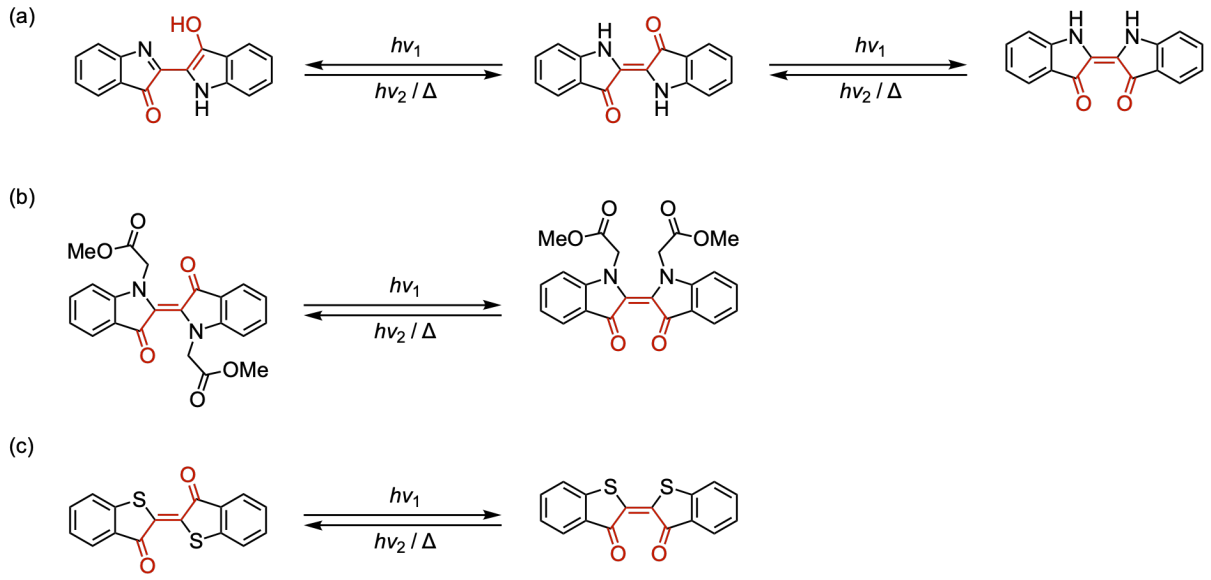
(Scheme 1.10),[101, 102] replacing one of the CH_2 groups with an oxygen or sulfur atom presents a more significant synthetic challenge. The oxidative coupling reaction itself can result in the formation of nitroso bridge due to over-oxidation.



Scheme 1.10 Synthesis of diazocine through oxidative coupling.

1.4.1.3 Indigoids

Indigoids involve two major classes of compounds: indigos and thioindigos. Indigo is a well-known natural dye with a long history of use in the textile industry. Its structure consists of two indole units connected by a central double bond (Scheme 1.11a). Thioindigo is obtained by replacing the nitrogen atoms with sulfur (Scheme 1.11c).[104-106]



Scheme 1.11 Photoswitching of indigo and thioindigo derivatives. (a) Competitive ESIPT pathway of parent indigo without *N*-substitution. Examples (b) indigo and (c) thioindigo with extended thermal half-lives. The red color highlights the photoactive unit.

Both indigos and thioindigos exhibit reversible *trans–cis* isomerization when exposed to visible light. The thermodynamically stable *trans* isomer typically absorbs at 550–650 nm, while the metastable *cis* isomer absorbs at 500–600 nm.[107, 108] When irradiated at 550–570 nm, the *trans* isomer converts to the *cis* isomer.[104, 109] The reverse process occurs either thermally or

photochemically. This *trans–cis* photoisomerization process is accompanied by a hypsochromic shift in the UV-vis absorption spectrum, known as negative photochromism.

The parent indigo is stable and does not photoswitch effectively due to an excited state intramolecular proton transfer (ESIPT) pathway (Scheme 1.11a). The ESIPT pathway can be suppressed by alkylating,[110] acetylating,[111-113] or arylating[107, 114] the indigo nitrogen center (Scheme 1.11b). Even after these substitutions, most metastable *cis* indigos have extremely short thermal half-lives of less than a few seconds and can only be studied using pump-probe experimental techniques.[110] For these indigo derivatives, accurate determination of the PSD is challenging.[107] PSDs have only been reported for analogues with sufficiently long thermal half-lives to allow for reliable measurements. Most of these indigo derivatives can achieve PSDs ranging from 60–80% in the forward direction and 70–90% in the reverse direction. The photoswitching quantum yield is strongly dependent on the *N*-substitution. For acylated indigos, the forward photoswitching quantum yield (~0.06) is lower than that of the reverse direction (~0.6). In contrast, arylated indigo derivatives exhibit comparable quantum yields (~0.1) for forward and reverse photoswitching.[107] Both the *trans* and *cis* isomers of indigos exhibit luminescence. The fluorescence quantum yields ($\Phi_{\text{fluo.}}$) of these compounds are lower than those observed in thioindigo derivatives.[112]

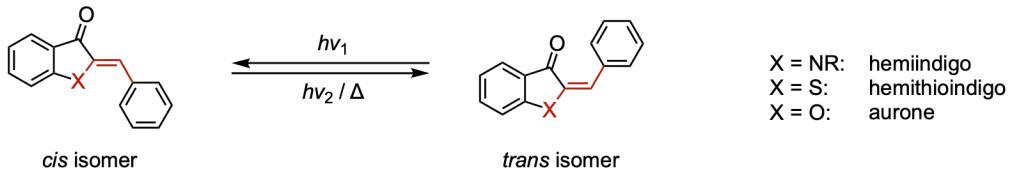
Indigo derivatives can be prepared using various synthetic methods, such as the Baeyer-Drewsen indigo synthesis, indole oxidative dimerization, and Heumann indigo synthesis. Huang and co-workers have reviewed these synthetic approaches.[109]

The effect of substitution of thioindigos have been the subject of numerous experimental and theoretical studies.[115-117] For 6,6'-di-isopropoxythioindigo in epoxy resin, PSDs of 63% and 74% can be reached in the forward and reverse directions, respectively. The forward and reverse photoswitching quantum yields are 0.20 and 0.38, respectively, in toluene.[118] Water-soluble thioindigos have been prepared by introducing solubilizing groups such as sulfonate, glycol, and phenol.[111, 119] The quantum yields for the forward and reverse isomerization processes were measured to be 0.19 and 0.05 in water.

1.4.1.4 Hemiindigoids

Hemiindigoids generally involve three classes of compounds including hemiindigos (HIs), hemithioindigos (HTIs), and aurones. These molecules are formally composed of half a indigoid and half a stilbene fragment, with a central C=C double bond acting as the photoactive motif (Scheme 1.12).[104] The key difference between HIs, HTIs, and aurones lies in the atom at

the X position, which follows the same naming convention as indigoids. When the atom at the X position is oxygen, the molecule is classified as an aurone. The UV-vis absorption these molecules falls between the absorption maxima of parent stilbene ($\lambda_{max} \approx 290$ nm) and indigoid (λ_{max} between 550 nm and 650 nm), at around 450 nm.[107, 119, 120]

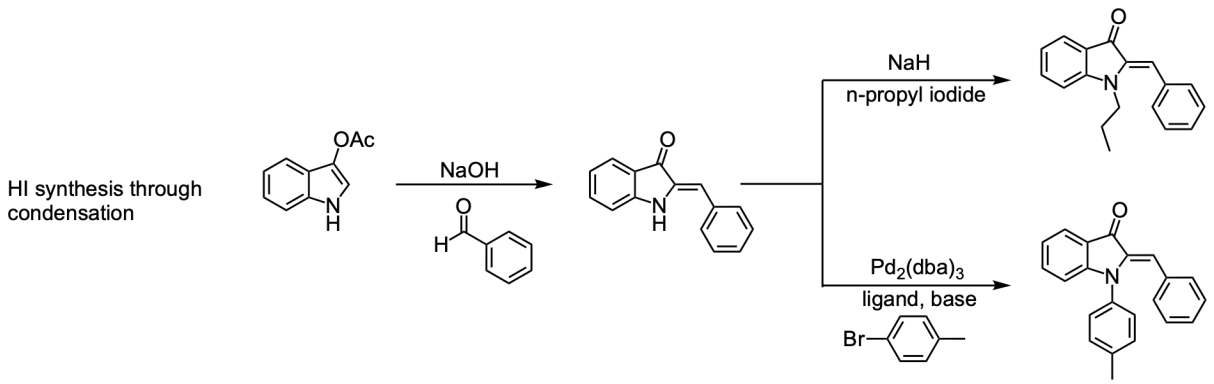


Scheme 1.12 Chemical structures and the photoswitching of hemiindigo, hemithioindigo, and aurone. The red color highlights the photoactive unit.

HI is a class of P-type photoswitch. Thermodynamically stable *cis* HI exhibits its absorption maximum around 450 nm.[104] Through substitutions with electron-donating aryl groups, such as aniline or julolidine, this absorption band can be red-shifted to up to 500 nm. Upon irradiation with blue light, the metastable *trans* isomer is formed, which has a red-shifted absorption maximum between 510 nm and 590 nm.[121] For most HIs, there is a desirable band separation of 50–80 nm, allowing for selective excitation of different isomers. Most HIs exhibit moderate photoswitching quantum yields and demonstrate minimal fatigue over 50 switching cycles. The forward photoswitching quantum yield usually ranges between 0.16 and 0.23 while the reverse photoswitching quantum yield ranges between 0.02 and 0.11. Regardless of the solvent (studied in toluene, THF, and DMSO), most HIs can achieve PSDs of over 95% in the forward direction and over 90% in the reverse reaction.[121]

In contrast to most molecular photoswitches that have a clearly defined stable and a metastable state, HIs with nitrogen substitutions exhibit a unique property: the two isomers are energetically similar. Experimental observations have shown that heating pure (photochemically generated) isomers results in a mixture of *cis* and *trans* isomers, regardless of the initial configuration.[104, 122, 123]

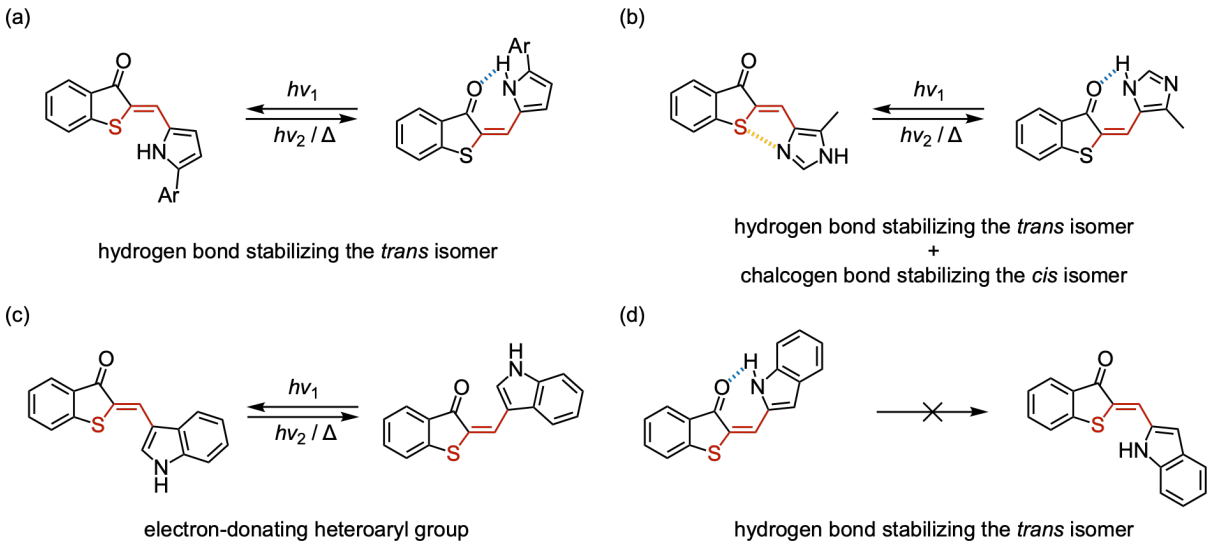
Synthesis of HIs is straightforward and usually commences with a condensation reaction between commercially available indoxyl acetate and a benzaldehyde (Scheme 1.13).[124] The nitrogen can be further functionalized by alkylation (with a strong base and an electrophile) or Hartwig palladium-catalyzed cross-coupling.[121]



Scheme 1.13 Synthesis of HI through condensation.

HTIs differ from HIs by replacing the nitrogen with sulfur and generally exhibit a smaller band separation (~30 nm). The stable *cis* HTI absorbs at 400–450 nm and the metastable *trans* isomer absorbs at 400–500 nm. Irradiating the HTI sample at 420 nm yields 94% of the *trans* isomer, while irradiating at 505 nm results in 100% of the *cis* isomer. However, introducing substituents such as methyl, julolidine, and thiol at the *para* or *ortho* positions of the aryl group can lead to a reduced forward PSD.[125]

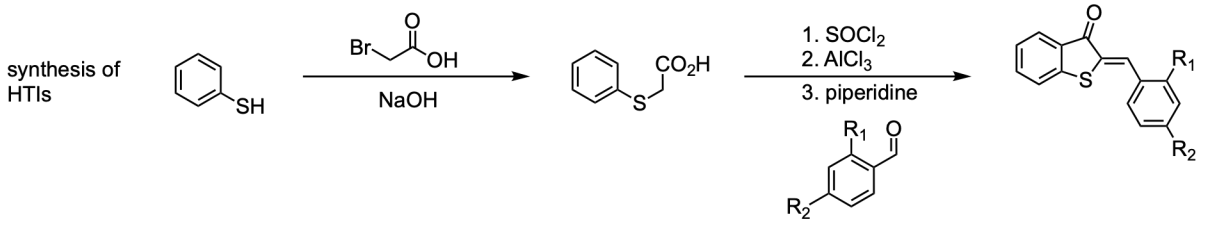
Newhouse and colleagues sought to address the challenge of reduced PSD in substituted HTIs through heterocyclic design.[126] Their approach involved the use of 2-pyrrole substituted with an Ar group (Scheme 1.14a). The pyrrole analogue demonstrated an improved band separation of 44 nm compared to the parent HTI. Most of these analogues exhibited nearly quantitative PSDs in both directions of photoswitching when irradiated with suitable wavelengths. However, the photoswitching behavior deteriorated when the Ar group in Scheme 1.14a represents an electron-donating aryl group such as julolidine or pyrrolidine.



Scheme 1.14 Examples of heteroaryl HTIs: (a) 2-pyrrole analogue with hydrogen bond stabilizing the *trans* isomer; (b) 4-imidazole analogue with chalcogen bond stabilizing the *cis* isomer and hydrogen bonding stabilizing the *trans* isomer; (c) HTI bearing electron-donating heteroaryl ring; (d) 2-indole derivative. The red color highlights the photoactive unit.

Dube and co-workers conducted a systematic investigation on heteroaryl HTIs and discovered that the 4-imidazole (Scheme 1.14b) and 3-indole (Scheme 1.14c) derivatives exhibit exceptional photoswitching properties.[127] Both molecules exhibit quantitative PSD in both directions of photoswitching.[127] The photoswitching behavior of these heteroaryl HTIs greatly depend on the molecular geometry, which is affected by intramolecular interactions. For example, the *cis* isomer of the imidazole derivative (Scheme 1.14b) adopts a conformation with chalcogen bonding interaction between the imidazole nitrogen and the sulfur while the *trans* isomer is stabilized by hydrogen bond. The exceptional photoswitching performance of this molecule can be ascribed to the precise geometry stabilization. Intramolecular interactions may also hinder photoswitching. For example, the 2-indole derivative (Scheme 1.14d) has diminished photoswitching behavior as the hydrogen bonding excessively stabilizes the *trans* isomer while the *cis* isomer is not stabilized by any intramolecular interaction.

The synthesis of HTIs follows a straightforward approach similar to that of HIs, utilizing the Friedländer synthesis. This method involves the condensation of a benzothiophenone and a benzaldehyde (Scheme 1.15). The benzothiophenone precursor is typically prepared through an intramolecular Friedel–Crafts acylation of 2-phenylthioacetic acid. Alternative synthetic routes for preparing HTIs have been reported in the literature by Dube and co-workers.[128]



Scheme 1.15 Synthesis of HTIs through condensation between benzothiophenone (generated in situ) and benzaldehyde.

Aurones (Scheme 1.12) are a class of compounds belonging to the flavonoid family. The *cis* isomer typically absorbs at 350–450 nm while the *trans* isomer absorbs at 380–490 nm.[129] In organic solvents such as chloroform and toluene, forward PSD of 55% can be achieved.[130, 131] However, according to Berdnikova's report, the forward PSD of various aurone analogues in aqueous environment does not exceed 40%.[129] The metastable *trans* isomer of aurones has a half-life of about 40 minutes. The reverse photoswitching process can be achieved by irradiating the sample with 480 nm light, resulting in a PSD of over 95%.

1.4.1.5 Iminothioindigoids

Iminothioindoxyl (ITI), also known as aryl iminoindigoids, is a recently reported class of photoswitch (Scheme 1.4).[123] ITI is formally composed of half thioindigo and half azobenzene, with the central photoactive C=N double bond. The *cis* isomer typically absorbs at 400–500 nm and the *trans* isomer absorb at 500–600 nm, with a band separation of approximately 100 nm. Upon irradiation with blue light at 455 nm ITI can achieve a PSD of 65%,[123] significantly lower than HIs and HTIs. Unfortunately, the metastable *trans* isomer of ITI typically has a half-life in the millisecond range at room temperature.

1.4.1.6 Hydrazones

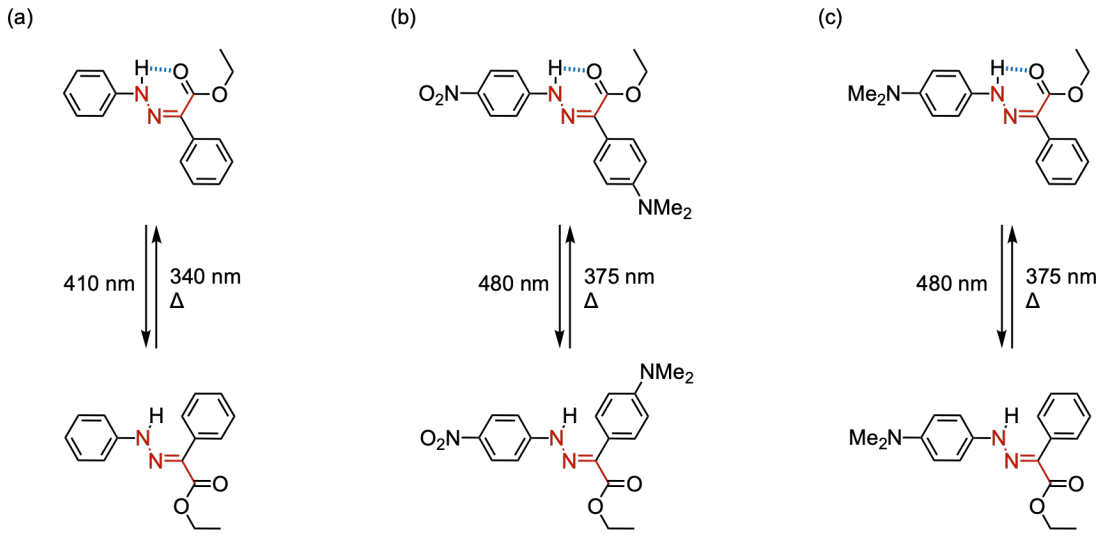
Hydrazones feature a photoactive C=N–N motif.[132-134] Acyl hydrazones have an additional acyl group adjacent to either the carbon center of C=N or the hydrazone NH (Scheme 1.16) and exhibit better switching properties than the parent hydrazones. Due to the presence of the NH group, acyl hydrazones can undergo *cis–trans* isomerization about the C=N double bond in response to pH,[135-139] metal ions,[140-142] or light.[132, 143]

The *cis* isomer of acyl hydrazones stabilized by intramolecular hydrogen bonding is typically the stable form (Scheme 1.16).[144] The parent acyl hydrazone exhibits negative photochromism, with the *cis* isomer absorbing at 350–450 nm and the *trans* isomer absorbing at 320–420 nm. The absorption of both isomers can be red shifted by introducing electron-donating groups at one end and electron-withdrawing groups at the other (Scheme 1.16b). Irradiation at 410 nm can result in a PSD of 95% in the forward direction. The

reverse reaction can be triggered at 340 nm, yielding a PSD of 80%. The photoswitching quantum yield varies depending on the substitution but typically ranges between 0.1 and 0.65 in the forward direction and between 5% and 10% in the reverse direction.

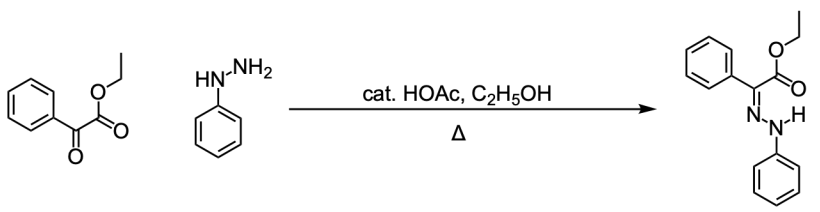
Aprahamian and co-workers prepared a family of acyl hydrazones with the terminal aryl rings bearing groups possessing different electronic properties.[144] These molecules manifest different photoswitching behaviors, depending on the substitution. Typically, introducing electron-withdrawing groups at the N–N end reduces leads to better photoswitching properties (Scheme 1.16b) while introducing electron-donating groups results in poor photoswitching (Scheme 1.16c).

The metastable isomer of acyl hydrazones without intramolecular stabilization thermally reverses quickly. However, functional groups such as pyridine and carbonyl in proximity can stabilize the metastable isomer through hydrogen bonding,[145, 146] increasing the thermal half-life of the metastable isomer to up to several thousand years.[147]



Scheme 1.16 Examples of Aprahamian-type acyl hydrazones bearing different substitution patterns. The red color highlights the photoactive unit.

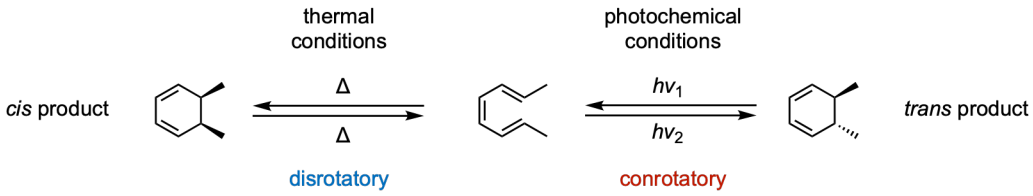
While the synthesis of acyl hydrazones is relatively concise, preparing the starting materials with specific aryl substitutions could be non-trivial. Aprahamian and co-workers have summarized the synthetic routes for these compounds (Scheme 1.17).[144]



Scheme 1.17 Synthetic route to Aprahamian-type hydrazones.

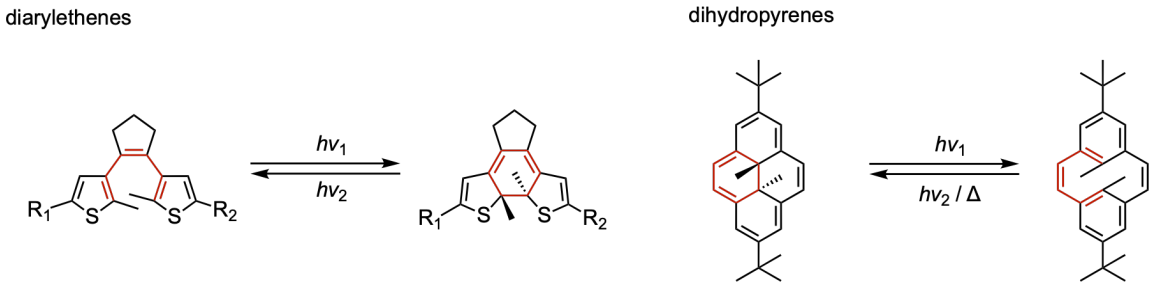
1.4.2 Photoswitch Involving Pericyclic Reactions

Pericyclic reactions are governed by the conservation of orbital symmetry, as described by the frontier molecular orbital (FMO) theory. According to FMO theory, the reactivity of a pericyclic reaction is determined by the interaction between the HOMO and the LUMO of the reactants. Most photoswitches involving pericyclic reactions rely on the 3,3'-electrocyclic reaction. For such a reaction, the stereochemical outcome is determined by the conrotation or disrotation of the terminal substituents during the cyclization process, with heat and light stimuli leading to different stereochemistry. The Woodward-Hoffmann rules predict that thermal 4n π-electron systems undergo conrotatory ring closure, while 4n+2 π-electron systems undergo disrotatory ring closure.[148] Conversely, photochemical electrocyclizations exhibit the opposite stereochemical outcome, with 4n π-electron systems undergoing disrotatory ring closure and 4n+2 π-electron systems undergoing conrotatory ring closure (Scheme 1.18).



Scheme 1.18 Schematic demonstration of the Woodward-Hoffmann rules for predicting the 3,3'-electrocyclic reactions.

This section focuses on molecules that rely exclusively on electrocyclization, including diarylethenes and dihydropyrenes (Scheme 1.19). Compounds that undergo isomerization through mixed mechanisms will be addressed in the subsequent Section 1.4.3.



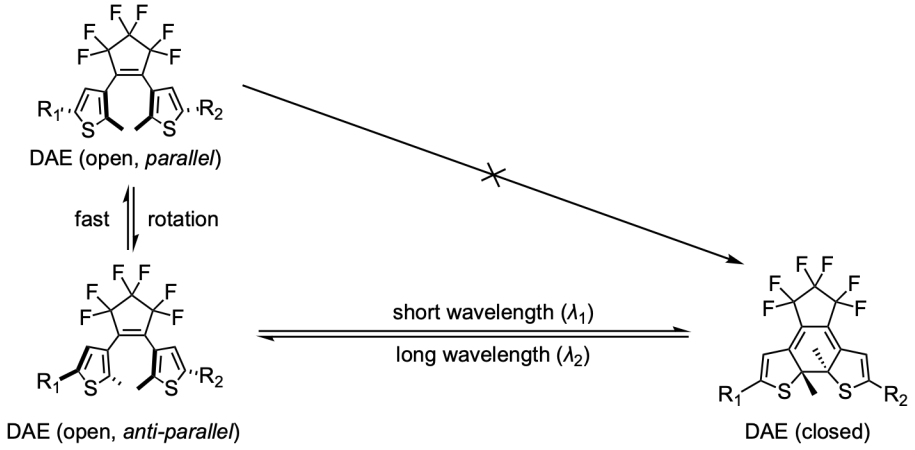
Scheme 1.19 Photoswitches relying on the pericyclic photocyclization reaction. The red color highlights the photoactive unit.

1.4.2.1 Diarylethenes

Diarylethenes (DAEs) consist of an ethene bridge substituted with two aryl (commonly heteroaryl) moieties, forming a photoactive hexatriene unit capable of undergoing 6π-electrocyclization reaction (Scheme 1.20). Open DAEs are highly flexible and can adopt many different conformations due to free rotation along the C–C bond adjacent to the central alkene (Scheme 1.20). In solution, there is a statistical distribution of DAEs in different

conformations that can interconvert thermally. However, only the anti-parallel conformation can lead to efficient photocyclization.

The electronic properties of DAEs change significantly before and after photocyclization. For open DAEs, the two aryl groups are twisted out of the plane of the ethene bridge, limiting conjugation to only half of the molecule. However, in the closed form, the π-conjugation extends throughout the entire backbone of the molecule. Such change in conjugation can lead to a difference in many properties like UV-vis absorption and conductance between the open and the closed isomers.[149]



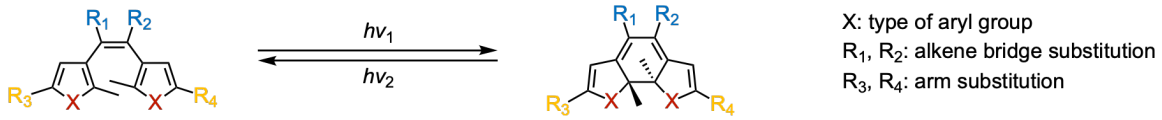
Scheme 1.20 Photoisomerization of a diarylethene from its anti-parallel conformer.

One of the strengths of DAEs lies in their extensive structural diversity.[36, 150] Different aryl groups can be incorporated into DAEs (Scheme 1.21, red) to achieve different thermal stability of the closed isomer. Thiophenes and benzothiophenes are the most employed aryl groups in DAEs due to their optimal photoswitching behavior and stability. DAEs featuring these specific aryl groups are referred to as dithienylethenes (DTEs, Scheme 1.22). Another common aryl group in DTEs is benzothiophene sulfone. These oxidized versions of DTEs generally exhibit strong fluorescence in the closed form. Researchers have also synthesized and studied DAEs with various other heteroaryl groups, such as pyridine,[151, 152] pyrimidine,[153] naphthalene,[154] indole,[155] benzofuran,[36, 150, 152] oxazole,[156] imidazole,[157] thiazole[158, 159] etc. These non-traditional aryl groups often (but not always) result in diminished photoswitching properties compared to their DTE counterparts.

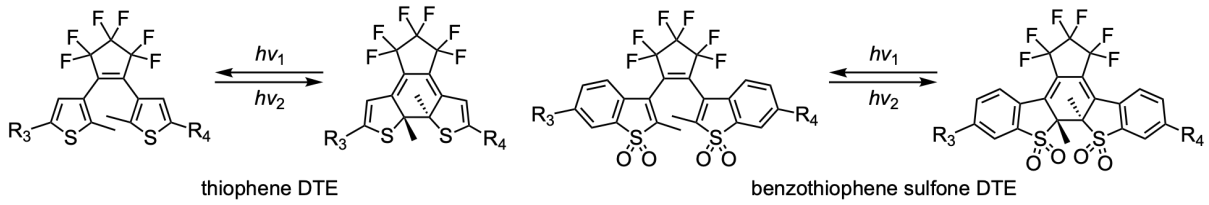
The central bridge of DAEs (R_1 and R_2) can be modified to incorporate sterically bulky or cyclic moieties (Scheme 1.21, blue), providing a means to modulate their photochromic behavior and stability. This C=C bond is commonly part of a cyclopentene or a perfluorinated cyclopentene ring (Scheme 1.21). The perfluorinated ring is particularly advantageous due to

its ease of synthesis and higher fatigue resistance compared to their perhydro-cyclopentene counterparts.[160] Nevertheless, the central alkene bridge can also be fused to more complex structures,[36] such as maleimide,[155, 161, 162] imidazole,[163] thiazole,[164] phenanthroline,[165] benzoquinone,[166, 167] triazolium,[168] benzo[*b*]germole,[169] helicene[170] etc. to tune the properties of the switch or enable additional function.[158, 171, 172]

The arms of DAEs (Scheme 1.21, yellow) are often the most synthetically accessible positions for functionalization. This is because the synthesis of DTEs bearing various reactive groups such as aryl chloride and alkyne is well-established. Many different starting thiophenes can be used in this DTE construction process. Thus, the arm of DTEs can be functionalized through a variety of cross-coupling reactions. Some recent and notable examples of arm functionalization include the incorporation of polyyne,[173] oligonucleotide,[174] metal-organic framework (MOF),[175, 176] aza-crown ring,[177, 178] hydrogen-bonding motifs,[179] microgel,[180] carbon dot,[181] rotaxane[182] etc.



Scheme 1.21 Structural variation of DAEs at various positions of the molecular structure.



Scheme 1.22 Examples DTEs bearing thiophene and benzothiophene as the aryl groups and their photoswitching.

DAEs generally exhibit shared photochemical properties despite their structural diversity. The open DAEs generally absorb at 250–400 nm. Under UV or blue light irradiation, DAEs undergo a ring-closure reaction that converts the more flexible and less intensely colored open isomer into a more rigid closed form (Figure 1.6).[36, 150] The closed form displays a vivid color due to its more extended π-system, with absorption maxima usually occurring between 500 and 750 nm (Figure 1.6).[183] The reverse ring-opening reaction can be induced by irradiating the closed form with a suitable wavelength of visible light. This process typically proceeds to completion, as the open isomer does not absorb light in the visible range.[45]

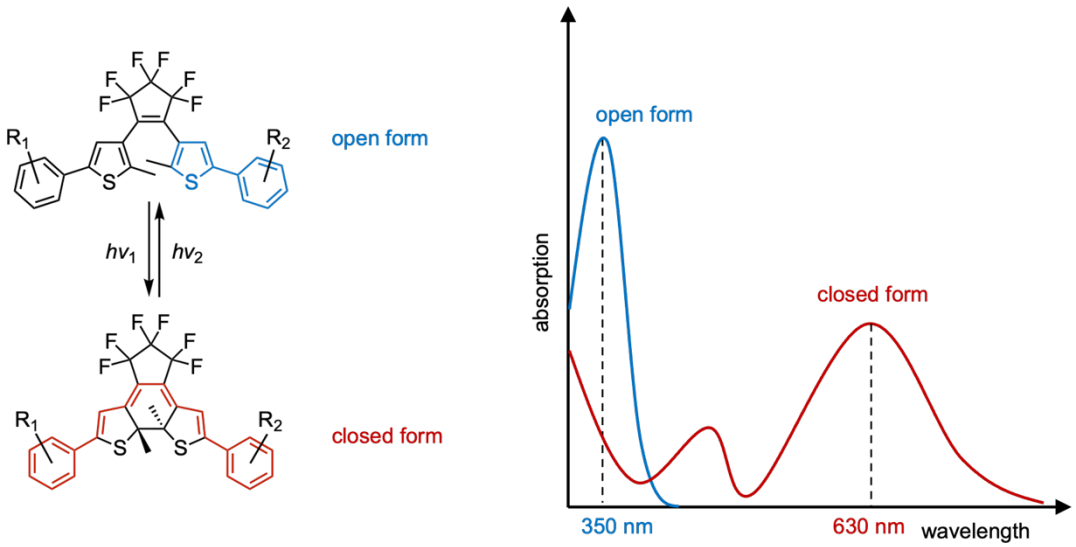
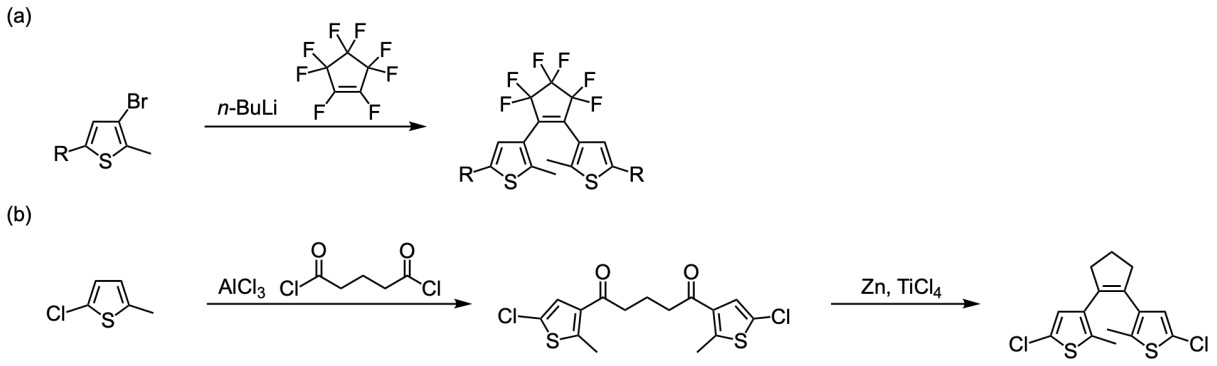


Figure 1.6 Photoswitching process of a DTE and typical UV-vis absorption of the open and the closed isomers. The color red and blue colors highlight the conjugation.

The photochemical and photophysical properties of DAEs, including the UV-vis absorption, PSDs, and photoswitching quantum yields, have been extensively researched but no systematic understanding has been established so far.[45, 46, 184-191] DTE, the most studied class of DAEs, typically exhibit excellent PSDs (70–100%) in the forward direction and quantitative PSD in the reverse direction.[192] The photocyclization quantum yield is dependent on the distribution of DAEs in different molecular conformations in a particular solvent. DAEs favoring an anti-parallel conformation, due to factors such as hydrogen bonding stabilization,[193] electronic repulsion,[45, 185, 194-196] polymer backbone restriction,[197] and electronic conjugation stabilization,[198] can have moderate to high photocyclization quantum yields ranging from 0.3 to 0.9. In the meanwhile, some DAE derivatives with stable parallel conformations can have extremely low photocyclization quantum yields of less than 0.01.[45] Photoreversion quantum yields of DTEs are significantly lower than photocyclization quantum yields, ranging from 0.001 to 0.5.[36, 45, 198] One key advantage of DTEs compared to other classes of photoswitches is fatigue resistance. The best-performing DTE can be switched for thousands of cycles.[199] Most DTEs are thermally bistable (P-type). However, the thermal reversion could be accelerated at elevated temperatures.[200]

The synthesis of DAEs can vary greatly depending on the desired structural features and targeted functionalization. Nevertheless, the central photoswitching core of DTEs is typically synthesized via two main routes (Scheme 1.23). For perfluorinated DTEs, the central core is constructed by condensing a lithiated thiophene with octafluorocyclopentene.[201] On the other

hand, the perhydro-cyclopentene analogue is generally synthesized through the McMurry reaction.[202]



Scheme 1.23 Synthesis of (a) perfluorinated DTEs and (b) DTEs with perhydro-cyclopentene bridge.

1.4.2.2 Dihydropyrene

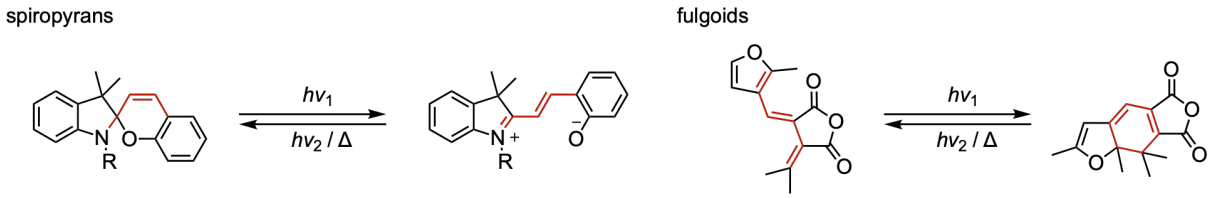
The dimethyldihydropyrene–cyclophanediene (DHP–CPD) photochromic couple is a unique derivative of DAE in a fused-ring system (Scheme 1.19). Unlike typical DAEs, the closed form of DHP–CPD is thermodynamically stable, while the open form is metastable. DHP–CPD couple can be structurally tuned by attaching substituents to various parts of the molecule, such as the ethene bridge[203, 204] and the aryl moieties.[204] The methyl groups can also be replaced with other functional groups.[205] Additionally, the conjugated π-system can be extended.[206]

The DHP form contains 14 delocalized π-electrons, resulting in an absorption profile that spans the visible to near-infrared range of the electromagnetic spectrum (500–700 nm). Similar to DAEs, the two central methyl groups in DHP–CPD prevent irreversible oxidation of the core. When exposed to visible light, the DHP undergoes a ring-opening reaction to form the metastable open isomer, CPD, which absorbs at 300–500 nm. [207] The PSD is not often reported for DHP–CPD due to the short thermal half-lives (milliseconds–seconds) of CPD. To the best of our knowledge, only one study has reported the quantitative switching of DHP–CPD in both directions, demonstrating good fatigue resistance over 20 cycles of photoswitching. The forward photoswitching quantum yield generally ranges between 0.05 and 0.2, while the reverse quantum yield is reported to be quantitative.[208]

1.4.3 Photoswitch Involving Mixed Switching Mechanisms

For photoswitches relying on mixed switching mechanisms (Scheme 1.24), pericyclic reactions are usually one key step in the photoswitching mechanism. The pericyclic reaction is accompanied with the light-induced formation or cleavage of a covalent bond, resulting in a change in the molecular structure and electronic properties. These photoswitches also undergo

additional isomerization processes, such as *trans–cis* isomerization or intramolecular proton transfer etc., which contribute to the overall photoswitching mechanism. In this section, spiropyrans and fulgoids will be explored.



Scheme 1.24 Spiropyrans and fulgoids with mixed photoswitching mechanisms. Spiropyrans undergo C–O bond cleavage followed by *cis–trans* isomerization. Fulgoids undergo a *trans–cis* isomerization first followed by electrocyclization. The red color highlights the photoactive unit.

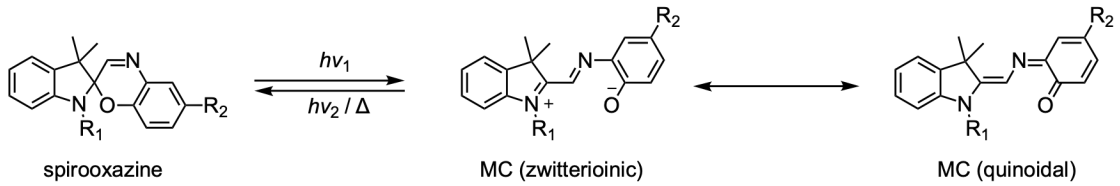
1.4.3.1 Spiropyrans

Spiropyrans have garnered significant attention due to their unique structural features and remarkable photoswitching properties.[209, 210] Spiropyrans consist of two rings, typically an indoline and a benzopyran moiety, connected through a shared sp^3-hybridized spiro carbon atom (Scheme 1.24). The benzopyran moiety can be replaced by other units, such as oxazines, giving rise to spirooxazines (Scheme 1.25).[211] To achieve specific functions and unique photoswitching behaviors, additional functionalization can be introduced to the benzopyran or oxazine moiety.[211]

The sp^3 spiro carbon acts as a junction point in the structure, forcing the two rings to be oriented perpendicular to each other. Such orthogonal arrangement perturbs the delocalization of π-electron across the molecule, resulting in an absorption peak in the UV or blue region (200–400 nm). The absorption spectrum of the closed-ring isomer shows two localized transitions. The blue band located below 300 nm is attributed to the π–π* transition in the indoline part of the molecule, and the red band around 350 nm band corresponds to the absorption of the chromene moiety.[212] Upon irradiation with UV light, the spiropyran (SP) isomer undergoes a rapid cleavage of the C–O bond in the benzopyran (or oxazine) moiety followed by a *cis–trans* isomerization (Scheme 1.24).[213, 214] This isomerization results in the formation of a ring-opened isomer known as merocyanine (MC). The merocyanine form is characterized by a zwitterionic structure, featuring a positively charged indolium and a negatively charged phenolate anion, connected through a conjugated benzopyran double bond. In the MC form, the two rings gain coplanarity, allowing for an extended π-conjugation throughout the molecule. This structural rearrangement leads to a large red shift in the UV-vis absorption spectrum, with the MC form exhibiting a strong absorption band in the visible region (500–600 nm).[215]

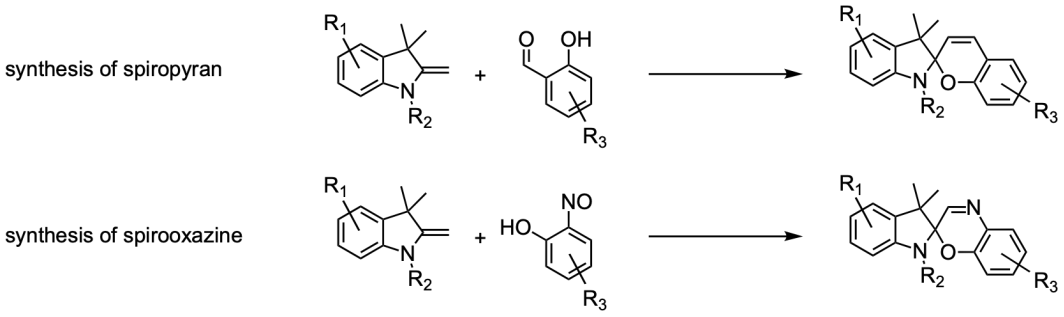
The PSD of spiropyran is not frequently reported due to the short thermal half-lives of these molecules (T-type) and the dependence of the PSD on the solvent.[209] As a result, the PSD of spiropyran photoswitches is typically estimated from UV-vis spectroscopy. According to a limited number of reports, the PSDs of spiropyrans range between 5% and 90%.[209, 216, 217] As for the photoswitching quantum yields, the ring-opening quantum yield usually falls between 1% and 10%,[209, 217, 218] while the ring-closure quantum yield ranges from 0.5% to 10%.[219, 220]

Spiropyran photoswitches exhibit an intriguing feature: the UV-vis absorption of the MC form displays strong solvatochromism. This phenomenon arises from the fact that the MC form can exist in two resonance forms: a zwitterionic form, characterized by a large charge separation, and a neutral quinoidal form (Scheme 1.25). In non-polar media, the quinoidal form is stabilized,[221, 222] which decreases the energy gap between the ground and excited states, leading to a bathochromic shift of the absorption band. Conversely, in polar media, the zwitterionic form is favored, resulting in a hypsochromic shift of the MC absorption band.[214]



Scheme 1.25 Photoswitching of spiropyrans, and the zwitterionic and quinoidal resonance forms of the MC isomer.

The synthesis of spiropyrans and spirooxazines has been well-established, following standard protocols reported in the literature.[223, 224] The formation of the spiro center typically involves a condensation reaction between a salicylaldehyde derivative and an indoline or naphthalene compound bearing an active methylene group (Scheme 1.26).



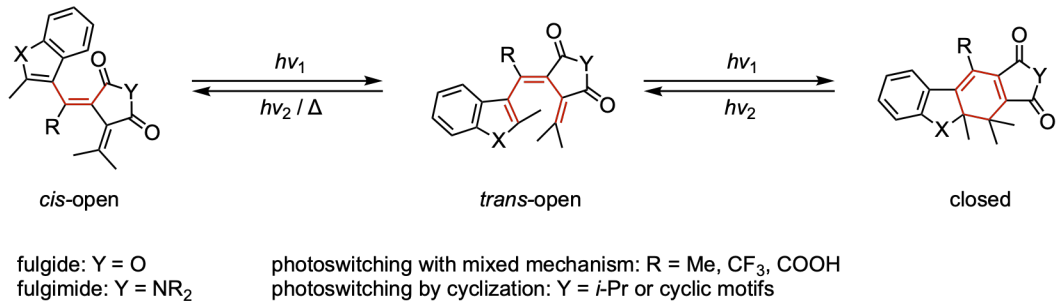
Scheme 1.26 Synthesis of spiropyran and spirooxazine.

1.4.3.2 Fulgoids

Fulgoid photoswitches encompass two major families: fulgides and fulgimides (Scheme 1.27). Fulgoids contain a (hetero)aromatic ring linked to either a succinic anhydride (fulgides) or a

succinimide (fulgimides) through an alkene bridge. Various aryl groups have been incorporated into fulgoid structures, including benzene,[225] (benzo)furan,[226, 227] thiophene,[226, 228, 229] thiazole,[226] oxazole,[228] pyrazole,[226] pyrrole,[228] and indole.[230-232] Early reports found that fulgides and fulgimides bearing thiazole group has significantly better fatigue resistance than other groups like thiophene, furan and pyrazole.[226] Modern fulgoids typically employ indole as the heteroaryl group, which results in red-shifted UV-vis absorption band, enabling the use of blue visible light to trigger the photoswitching.

In contrast to DTEs, fulgoids typically have an alkene that is not part of a cyclic ring. As a result, while DTEs exclusively undergo a photocyclization reaction, fulgoids often need to undergo a *cis–trans* isomerization followed by photocyclization (Scheme 1.27). The R group on plays a crucial role in influencing the photoswitching efficiency. When the R group is small (methyl or trifluoromethyl) the *cis* isomer fulgoid is thermodynamically stable.[230] However, when the R group is more sterically demanding (isopropyl), the *trans* fulgoid becomes thermodynamically stable and can directly photocyclize without the need for *cis–trans* isomerization.

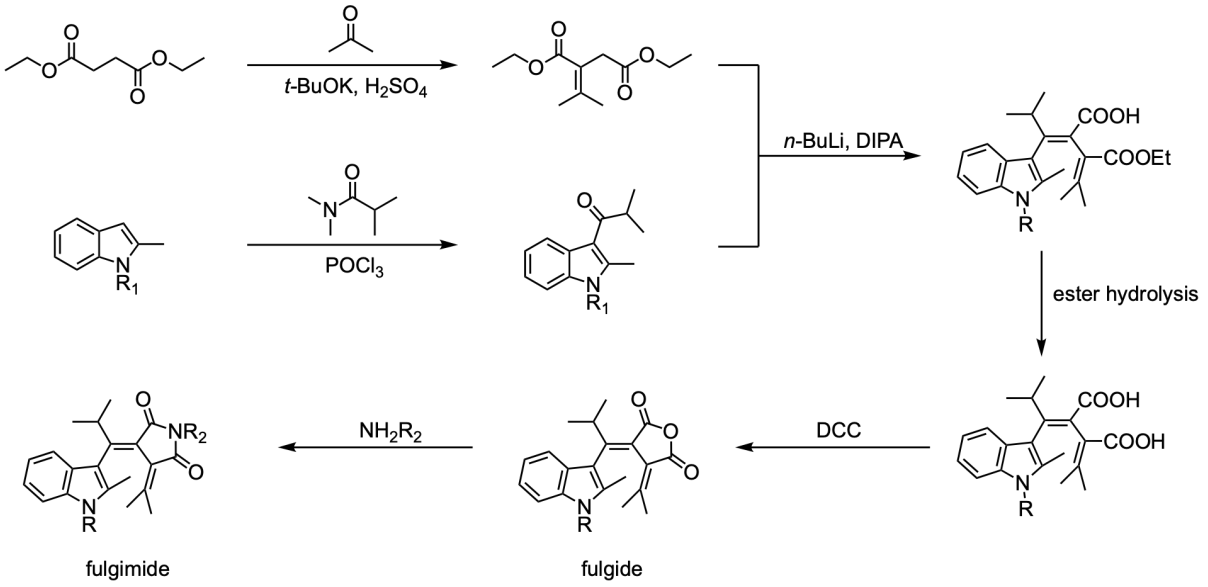


Scheme 1.27 The structural variation of fulgoid photoswitches and the general photoswitching mechanism. The red color highlights the photoactive unit.

The open fulgides (both *cis* and *trans*) typically absorb in the UV and blue visible region (200–400 nm). Fulgimides absorb at slightly longer wavelengths (250–420 nm). Photocyclization of fulgoids results in a new absorption band at 400–600 nm due to extended conjugation. Fulgoid derivatives can display exceptional photoswitching properties. Fulgimides bearing an isopropyl group at the R position (Scheme 1.27) can achieve PSDs of up to 93% under 365 nm irradiation.[227] With even small R groups like carboxylic acid PSD of 87% can be achieved.[232] Ring-closing quantum yield of fulgoids vary significantly, ranging from 0.04 to 0.54, depending on the substitution and solvent.[89, 233]

The synthesis of fulgides and fulgimides is more challenging compared to other photoswitches. The crucial step in the synthetic route involves a Stobbe condensation reaction

between an indole derivative and diethyl isopropylidenesuccinate (Scheme 1.28).[234] Despite the short synthetic pathway, several steps in the synthetic route suffer from low yields, making the overall process less efficient than the synthesis of many other photoswitches. This synthetic complexity can be a limiting factor in the widespread application of fulgides and fulgimides, as it may hinder their large-scale production and functionalization.



Scheme 1.28 Synthesis of fulgide and fulgimide through Stobbe condensation.

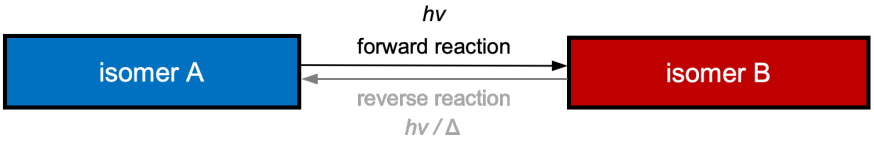
1.4.4 Summary of Photoswitching Parameters for Different Families of Photoswitches

The following Table 1 summarizes the findings of the literature survey conducted in Section 1.4, which reviews the photophysical and photochemical properties of various families of photoswitches. The table focuses on well-defined molecular photoswitches with clearly established photoswitching characteristics, while more exotic photochromic systems are not included. The table presents key photoswitching parameters, such as thermal stability, absorption, PSD, photoswitching quantum yield, and fatigue resistance, as well as the accessibility of these molecules in terms of the length of their synthetic routes. Table 1 does not aim to provide an exhaustive overview of all known photoswitches within each family. Instead, it summarizes the information from the parent molecule and a few closely related structures bearing the parent photoswitch.

In the context of this thesis, which aims to optimize the photoswitching parameters of the selected photoswitch and then utilize the optimized photoswitch as a key component in the development of organic switchable fluorophores and photopharmacological agents, several key parameters are highly valued. These include good absorption band separation, high PSD, good

fatigue resistance, and simple synthesis. The photoswitch families that meet these criteria primarily include diazocines, diarylethenes, spiropyrans (specifically, spirooxazines and spironaphthoxazines), fulgimides, hemiindigos, and hemithioindigos. Our group has focused mainly on the prior four classes of photoswitches and has published a number of papers on their syntheses, optimizations and applications in super-resolution microscopy.[209, 235-237] This thesis concentrates on optimizing diarylethene photoswitches and employing them in switchable fluorescence and photopharmacology, building upon the established expertise of our research group in this field.

Table 1 Summary of photoswitching parameters of different families of photoswitches.



Class	P or T Type	Absorption (nm) (A and B)	PSD (forward and reverse)	Switching Φ (forward and reverse)	Fatigue (cycles)	Synthetic Route (length)
stiff stilbene	T	320–340 340–360	~65% ~80%	~30% ~30%	10s	short
azobenzene	P or T	300–330 330–360	~75% ~100%	~20% ~40%	10–100s	medium
diazocine	P or T	300–420 480–600	~90% ~100%	~70% ~50%	100s	medium to long
indigoid	T	550–650 500–600	~70% ~80%	~20% ~60%	10–100s	medium
hemiindigo	P or T	450–550 550–650	~95% ~95%	~20% ~5%	100s	short to medium
hemithioindigo	P or T	400–450 400–500	~95% ~100%	~50% ~20%	100s	short to medium
aurone	T	350–450 380–490	<40% ~90%	~20% ~10%	10s	short to medium
iminoindigoid	T	400–500 500–600	~65% ~100%	~5% n.a.	10s	medium
hydrazone	P or T	350–450 320–420	>90% >80%	~15% ~10%	10s	medium
diarylethene	P	300–400 500–750	~70%–100% 100%	~1%–100% ~0.1%–50%	100–1000s	medium to long
dihydropyrene	T	500–700 300–500	>90% >90%	~5%–20% >80%	10–100s	medium to long
spiropyran	T	200–400 500–600	~10%–90% 100%	1%–10% 0.5%–10%	10–1000s	short to medium
fulgide	P	200–400 400–600	20%–90% 100%	~30% ~10%	10–1000s	medium to long
fulgimide	P	250–450 450–700	50%–95% 100%	~30% ~10%	10–1000s	medium to long

1.5 Project Aim

This introduction has provided an overview of modern molecular photoswitches. Despite the report on hundreds DAEs, there is still a lack of systematic studies on the structure-property relationships of these molecules, as many publications did not fully characterize all photochemical and photophysical parameters. This thesis aims to address this gap by first providing a systematic understanding of the structure-property relationships of DTE

photoswitches and then translating these findings to applications in switchable fluorescence and photopharmacology.

Chapter 2 will describe the synthesis of a family of eight DTEs bearing push-push, pull-pull, and push-pull substitution patterns. The chapter will explore different synthetic approaches to construct the photoactive hexatriene DTE core as well as the functionalization of the DAE arms. Following the synthesis, Chapter 2 also will also study the photophysical and photochemical behavior of the synthesized DTE photoswitches. The structure-property relationships, including UV-vis absorptions, PSDs, and photoswitching quantum yields, will be fully characterized. The observed trends will then be rationalized through computational studies. This chapter provides valuable insights into the factors that govern the performance of DTE photoswitches and guide the design of optimized molecules for specific applications.

In Chapter 3, the best-performing DTE photoswitch identified were covalently linked to fluorescent molecules. The DTE photoswitch serves as a control for modulating the fluorescence emission from the fluorophore. By exploiting the ability of DTEs to reversibly switch between two states, the fluorescence can be turned on and off, resulting in a bright and a dark state. This chapter will demonstrate the potential of DTE photoswitches as powerful tools for controlling photochemical and photophysical properties at the molecular level.

Chapter 4 involved the synthesis of four different DTEs and the analysis their binding affinities (in both the open and closed forms) towards DNA G-quadruplexes. G-quadruplexes are important secondary structures formed by guanine-rich DNA sequences and have been implicated in various biological processes, including gene regulation and telomere maintenance. By investigating the differential binding affinities of open and closed DTEs, this chapter will explore the potential of utilizing DTEs as photopharmacological agents.

References

1. H. Bouas-Laurent and H. Dürr, *Pure Appl. Chem.*, 2001, **73**, 639–665.
2. K. Nakatani, J. Piard, P. Yu and R. Métivier, *Photochromic Materials: Preparation, Properties and Applications*, Wiley-VCH Verlag GmbH & Co. KGaA., 2016.
3. D. Jago, E. E. Gaschk, G. A. Koutsantonis and C. Wentrup, *Aust. J. Chem.*, 2023, **76**, 635–654.
4. Z. L. Pianowski, *Molecular Photoswitches: Chemistry, Properties, and Applications*, Wiley-VCH GmbH, Weinheim, 2022.
5. M. Irie, *Chem. Rev.*, 2000, **100**, 1683–1684.
6. P. Bamfield and M. Hutchings, *Chromic Phenomena: Technological Applications of Colour Chemistry*, Royal Society of Chemistry, London, 2018.
7. S. Jordison, Making Alexander great: creating a hero from zero, https://www.theguardian.com/books/booksblog/2014/aug/12/mary-renault-alexander-trilogy-hero-from-zero, (accessed 1 June, 2024).
8. J. Fritzsche, *Comptes. Rendus. Acad. Sci.*, 1867, **69**, 1035.
9. I. Gillet and C. Dufraisse, *Compt. Rend. Acad. Sci. Paris*, 1949, **228**, 1812.
10. A. Maliakal, K. Raghavachari, H. Katz, E. Chandross and T. Siegrist, *Chem. Mater.*, 2004, **16**, 4980–4986.
11. J. M. Aubry, C. Pierlot, J. Rigaudy and R. Schmidt, *Acc. Chem. Res.*, 2003, **36**, 668–675.
12. D. Casanova, *Chem. Rev.*, 2018, **118**, 7164–7207.
13. K. Ono, H. Totani, T. Hiei, A. Yoshino, K. Saito, K. Eguchi, M. Tomura, J.-i. Nishida and Y. Yamashita, *Tetrahedron*, 2007, **63**, 9699–9704.
14. S. H. Chan, H. K. Lee, Y. M. Wang, N. Y. Fu, X. M. Chen, Z. W. Cai and H. N. Wong, *Chem. Commun.*, 2005, 66–68.
15. X. Zhou, M. Kitamura, B. Shen, K. Nakajima and T. Takahashi, *Chem. Lett.*, 2004, **33**, 410–411.
16. D. W. Bjarneson and N. O. Petersen, *J. Photochem. Photobiol., A*, 1992, **63**, 327–335.
17. K. S. Wei and R. Livingston, *Photochem. Photobiol.*, 2008, **6**, 229–232.
18. A. G. L. Olive, A. Del Guerzo, J. L. Pozzo, J. P. Desvergne, J. Reichwagen and H. Hopf, *J. Phys. Org. Chem.*, 2007, **20**, 838–844.
19. E. Ter Meer, *Annu. Chem.*, 1876, **181**, 1.
20. T. L. Phipson, *Chem. News*, 1881, **43**, 283.
21. J. B. Orr, *Chem. News*, 1881, **44**, 12.
22. W. Wislicenus, *Annu. Chem.*, 1893, **181**, 366.
23. W. Markwald, *Phys. Chem.*, 1899, **30**, 140.
24. H. Biltz, *Annu. Chem.*, 1899, **305**, 170.
25. H. Stobbe, *Ber. Dtsch. Chem. Ges.*, 1905, **38**, 3673–3682.
26. A. Santiago and R. S. Becker, *J. Am. Chem. Soc.*, 1968, **90**, 3654–3658.
27. M. Reinfelds, V. Hermanns, T. Halbritter, J. Wachtveitl, M. Braun, T. Slanina and A. Heckel, *ChemPhotoChem*, 2019, **3**, 441–449.
28. Y. Jiao, R. Yang, Y. Luo, L. Liu, B. Xu and W. Tian, *CCS Chem.*, 2022, **4**, 132–140.
29. E. Mitscherlich, *Ann. Pharm.*, 1834, **12**, 305–311.
30. G. S. Hartley, *Nature*, 1937, **140**, 281–281.
31. Y. Hirshberg and E. Fischer, *J. Chem. Soc.*, 1954, 297–303.
32. N. Y. C. Chu, *Can. J. Chem.*, 1983, **61**, 300–305.
33. N. Y. C. Chu, *Photochromism: Molecules and Systems*, Elsevier, Amsterdam, 1990.
34. S. Maeda, *Organic Photochromic and Thermochromic Compounds*, Kluwer Academic Publishers, New York, 2002.
35. S. Kawata and Y. Kawata, *Chem. Rev.*, 2000, **100**, 1777–1788.

36. M. Irie, T. Fukaminato, K. Matsuda and S. Kobatake, *Chem. Rev.*, 2014, **114**, 12174–12277.
37. K. Hull, J. Morstein and D. Trauner, *Chem. Rev.*, 2018, **118**, 10710–10747.
38. C. L. Sun, C. Wang and R. Boulatov, *ChemPhotoChem*, 2019, **3**, 268–283.
39. P. Hong, N.-H. Xie, K. Xiong, J. Liu, M.-Q. Zhu and C. Li, *J. Mater. Chem. A*, 2023, **11**, 5703–5713.
40. J. Kwon, J. Hwang, J. Park, G. R. Han, K. Y. Han and S. K. Kim, *Sci. Rep.*, 2015, **5**, 17804.
41. B. L. Feringa and W. R. Browne, *Molecular Switches*, Wiley-VCH Verlag GmbH & Co. KGaA, Weinheim, 2011.
42. J. Volaric, W. Szymanski, N. A. Simeth and B. L. Feringa, *Chem. Soc. Rev.*, 2021, **50**, 12377–12449.
43. K. Stranius and K. Borjesson, *Sci. Rep.*, 2017, **7**, 41145.
44. C. J. Otolski, A. M. Raj, V. Ramamurthy and C. G. Elles, *Chem. Sci.*, 2020, **11**, 9513–9523.
45. S. Qiu, A. T. Frawley, K. G. Leslie and H. L. Anderson, *Chem. Sci.*, 2023, **14**, 9123–9135.
46. P. Hong, J. Liu, K. X. Qin, R. Tian, L. Y. Peng, Y. S. Su, Z. Gan, X. X. Yu, L. Ye, M. Q. Zhu and C. Li, *Angew. Chem., Int. Ed.*, 2024, **63**, e202316706.
47. A. Boden, F. Pennacchietti, G. Coceano, M. Damenti, M. Ratz and I. Testa, *Nat. Biotechnol.*, 2021, **39**, 609–618.
48. J. Clayden, N. Greeves and S. Warren, *Organic Chemistry*, Oxford University Press, Oxford, 2012.
49. C. Dugave and L. Demange, *Chem. Rev.*, 2003, **103**, 2475–2532.
50. D. Villaron and S. J. Wezenberg, *Angew. Chem., Int. Ed.*, 2020, **59**, 13192–13202.
51. M. Oelgemöller, B. Brem, R. Frank, S. Schneider, D. Lenoir, N. Hertkorn, Y. Origane, P. Lemmen, J. Lex and Y. Inoue, *J. Chem. Soc., Perkin Trans. 2*, 2002, 1760–1771.
52. D. H. Waldeck, *Chem. Rev.*, 2002, **91**, 415–436.
53. M. Quick, F. Berndt, A. L. Dobryakov, I. N. Ioffe, A. A. Granovsky, C. Knie, R. Mahrwald, D. Lenoir, N. P. Ernsting and S. A. Kovalenko, *J. Phys. Chem. B*, 2014, **118**, 1389–1402.
54. W. Fuss, C. Kosmidis, W. E. Schmid and S. A. Trushin, *Angew. Chem., Int. Ed.*, 2004, **43**, 4178–4182.
55. N. Zhu, X. Li, Y. Wang and X. Ma, *Dyes Pigm.*, 2016, **125**, 259–265.
56. Y.-H. Wu, K. Huang, S.-F. Chen, Y.-Z. Chen, C.-H. Tung and L.-Z. Wu, *Sci. China: Chem.*, 2019, **62**, 1194–1197.
57. C. Cao, G. Chen and Y. Wu, *Sci. China: Chem.*, 2011, **54**, 1735–1744.
58. J. Saltiel and J. T. D'Agostino, *J. Am. Chem. Soc.*, 2002, **94**, 6445–6456.
59. T. van Leeuwen, A. S. Lubbe, P. Štacko, S. J. Wezenberg and B. L. Feringa, *Nat. Rev. Chem.*, 2017, **1**, 0096.
60. S. Kassem, T. van Leeuwen, A. S. Lubbe, M. R. Wilson, B. L. Feringa and D. A. Leigh, *Chem. Soc. Rev.*, 2017, **46**, 2592–2621.
61. H. M. Bandara and S. C. Burdette, *Chem. Soc. Rev.*, 2012, **41**, 1809–1825.
62. S. Crespi, N. A. Simeth and B. König, *Nat. Rev. Chem.*, 2019, **3**, 133–146.
63. N. A. Simeth and S. Crespi, *Photochemistry*, Royal Society of Chemistry, London, 2020.
64. E. Merino, *Chem. Soc. Rev.*, 2011, **40**, 3835–3853.
65. D. Larsen, P. M. Bjerre and S. R. Beeren, *Chem. Commun.*, 2019, **55**, 15037–15040.
66. S. Axelrod, E. Shakhnovich and R. Gomez-Bombarelli, *ACS Cent. Sci.*, 2023, **9**, 166–176.
67. J. Calbo, C. E. Weston, A. J. White, H. S. Rzepa, J. Contreras-Garcia and M. J. Fuchter, *J. Am. Chem. Soc.*, 2017, **139**, 1261–1274.
68. R. Siewertsen, H. Neumann, B. Buchheim-Stehn, R. Herges, C. Nather, F. Renth and F. Temps, *J. Am. Chem. Soc.*, 2009, **131**, 15594–15595.
69. S. Sun, S. Liang, W.-C. Xu, G. Xu and S. Wu, *Polym. Chem.*, 2019, **10**, 4389–4401.
70. F. A. Jerca, V. V. Jerca and R. Hoogenboom, *Nat. Rev. Chem.*, 2022, **6**, 51–69.
71. J. Garcia-Amoros, S. Nonell and D. Velasco, *Chem. Commun.*, 2011, **47**, 4022–4024.

72. J. Garcia-Amoros, S. Nonell and D. Velasco, *Chem. Commun.*, 2012, **48**, 3421–3423.
73. J. Otsuki, K. Harada and K. Araki, *Chem. Lett.*, 1999, **28**, 269–270.
74. J. Otsuki and K. Narutaki, *Bull. Chem. Soc. Jpn.*, 2004, **77**, 1537–1544.
75. S. Venkataramani, U. Jana, M. Dommaschk, F. D. Sonnichsen, F. Tuczek and R. Herges, *Science*, 2011, **331**, 445–448.
76. N. A. Simeth, S. Crespi, M. Fagnoni and B. Konig, *J. Am. Chem. Soc.*, 2018, **140**, 2940–2946.
77. S. Crespi, N. A. Simeth, A. Bellisario, M. Fagnoni and B. Konig, *J. Phys. Chem. A*, 2019, **123**, 1814–1823.
78. R. Travieso-Puente, S. Budzak, J. Chen, P. Stacko, J. T. Jastrzebski, D. Jacquemin and E. Otten, *J. Am. Chem. Soc.*, 2017, **139**, 3328–3331.
79. D. Kolarski, W. Szymanski and B. L. Feringa, *Org. Lett.*, 2017, **19**, 5090–5093.
80. D. Kolarski, A. Sugiyama, T. Rodat, A. Schulte, C. Peifer, K. Itami, T. Hirota, B. L. Feringa and W. Szymanski, *Org. Biomol. Chem.*, 2021, **19**, 2312–2321.
81. L. Cechova, J. Filo, M. Dracinsky, C. Slavov, D. Sun, Z. Janeba, T. Slanina, J. Wachtveitl, E. Prochazkova and M. Cigan, *Angew. Chem., Int. Ed.*, 2020, **59**, 15590–15594.
82. J. Garcia-Amoros, M. Diaz-Lobo, S. Nonell and D. Velasco, *Angew. Chem., Int. Ed.*, 2012, **51**, 12820–12823.
83. M. Schehr, C. Ianes, J. Weisner, L. Heintze, M. P. Muller, C. Pichlo, J. Charl, E. Brunstein, J. Ewert, M. Lehr, U. Baumann, D. Rauh, U. Knippschild, C. Peifer and R. Herges, *Photochem. Photobiol. Sci.*, 2019, **18**, 1398–1407.
84. T. Wendler, C. Schutt, C. Nather and R. Herges, *J. Org. Chem.*, 2012, **77**, 3284–3287.
85. J. Otsuki, K. Suwa, K. K. Sarker and C. Sinha, *J. Phys. Chem. A*, 2007, **111**, 1403–1409.
86. G. Davidson-Rozenfeld, L. Stricker, J. Simke, M. Fadeev, M. Vázquez-González, B. J. Ravoo and I. Willner, *Polym. Chem.*, 2019, **10**, 4106–4115.
87. K. Rustler, P. Nitschke, S. Zahnbrecher, J. Zach, S. Crespi and B. Konig, *J. Org. Chem.*, 2020, **85**, 4079–4088.
88. C. W. Chu, L. Stricker, T. M. Kirse, M. Hayduk and B. J. Ravoo, *Chem. - Eur. J.*, 2019, **25**, 6131–6140.
89. L. Stricker, M. Bockmann, T. M. Kirse, N. L. Doltsinis and B. J. Ravoo, *Chem. - Eur. J.*, 2018, **24**, 8639–8647.
90. L. Stricker, E. C. Fritz, M. Peterlechner, N. L. Doltsinis and B. J. Ravoo, *J. Am. Chem. Soc.*, 2016, **138**, 4547–4554.
91. C. E. Weston, R. D. Richardson, P. R. Haycock, A. J. P. White and M. J. Fuchter, *J. Am. Chem. Soc.*, 2014, **136**, 11878–11881.
92. S. Devi, M. Saraswat, S. Grewal and S. Venkataramani, *J. Org. Chem.*, 2018, **83**, 4307–4322.
93. P. Kumar, A. Srivastava, C. Sah, S. Devi and S. Venkataramani, *Chem. - Eur. J.*, 2019, **25**, 11924–11932.
94. P. R. Huddleston, V. V. Volkov and C. C. Perry, *Phys. Chem. Chem. Phys.*, 2019, **21**, 1344–1353.
95. C. Slavov, C. Yang, A. H. Heindl, H. A. Wegner, A. Dreuw and J. Wachtveitl, *Angew. Chem., Int. Ed.*, 2020, **59**, 380–387.
96. A. H. Heindl and H. A. Wegner, *Chem. - Eur. J.*, 2020, **26**, 13730–13737.
97. P. Lentes, E. Stadler, F. Rohricht, A. Brahms, J. Grobner, F. D. Sonnichsen, G. Gescheidt and R. Herges, *J. Am. Chem. Soc.*, 2019, **141**, 13592–13600.
98. R. Siewertsen, J. B. Schonborn, B. Hartke, F. Renth and F. Temps, *Phys. Chem. Chem. Phys.*, 2011, **13**, 1054–1063.
99. T. Tellkamp, J. Shen, Y. Okamoto and R. Herges, *Eur. J. Org. Chem.*, 2014, **2014**, 5456–5461.

100. L. Heintze, D. Schmidt, T. Rodat, L. Witt, J. Ewert, M. Kriegs, R. Herges and C. Peifer, *Int. J. Mol. Sci.*, 2020, **21**, 8961.
101. M. S. Maier, K. Hull, M. Reynders, B. S. Matsuura, P. Leippe, T. Ko, L. Schaffer and D. Trauner, *J. Am. Chem. Soc.*, 2019, **141**, 17295–s17304.
102. K. G. Leslie, DPhil, University of Oxford, 2023.
103. M. Schehr, D. Hugenbusch, T. Moje, C. Nather and R. Herges, *Beilstein J. Org. Chem.*, 2018, **14**, 2799–2804.
104. C. Petermayer and H. Dube, *Acc. Chem. Res.*, 2018, **51**, 1153–1163.
105. G. M. Wyman, *Chem. Rev.*, 2002, **55**, 625–657.
106. W. R. Brode and G. M. Wyman, *J. Res. Natl. Bur. Stand.*, 1951, **47**, 170–178.
107. C. Y. Huang, A. Bonasera, L. Hristov, Y. Garmshausen, B. M. Schmidt, D. Jacquemin and S. Hecht, *J. Am. Chem. Soc.*, 2017, **139**, 15205–15211.
108. K. Kuntze, J. Viljakka, M. Virkki, C. D. Huang, S. Hecht and A. Priimagi, *Chem. Sci.*, 2023, **14**, 2482–2488.
109. C. D. Huang and S. Hecht, *Chem. - Eur. J.*, 2023, **29**, e202300981.
110. C. Giuliano, L. Hess and J. Margerum, *J. Am. Chem. Soc.*, 2003, **90**, 587–594.
111. B. Koeppe, S. Rühl and F. Römpp, *ChemPhotoChem*, 2018, **3**, 71–74.
112. D. Farka, M. Scharber, E. D. Glowacki and N. S. Sariciftci, *J. Phys. Chem. A*, 2015, **119**, 3563–3568.
113. D. Pinheiro, A. M. Galvao, M. Pineiro and J. S. S. de Melo, *J. Phys. Chem. B*, 2021, **125**, 4108–4119.
114. L. A. Huber, P. Mayer and H. Dube, *ChemPhotoChem*, 2018, **2**, 458–464.
115. J. Z. Vlahakis, K. E. Maly and R. P. Lemieux, *J. Mater. Chem.*, 2001, **11**, 2459–2464.
116. G. Boice, B. O. Patrick, R. McDonald, C. Bohne and R. Hicks, *J. Org. Chem.*, 2014, **79**, 9196–9205.
117. D. Jacquemin, J. Preat, V. Wathelet, M. Fontaine and E. A. Perpete, *J. Am. Chem. Soc.*, 2006, **128**, 2072–2083.
118. D. L. Ross, *Appl. Opt.*, 1971, **10**, 571–576.
119. B. Koeppe and F. Rompp, *Chem. - Eur. J.*, 2018, **24**, 14382–14386.
120. S. Kitzig, M. Thilemann, T. Cordes and K. Ruck-Braun, *ChemPhysChem*, 2016, **17**, 1252–1263.
121. C. Petermayer, S. Thumser, F. Kink, P. Mayer and H. Dube, *J. Am. Chem. Soc.*, 2017, **139**, 15060–15067.
122. V. Smokal, O. Kharchenko, Y. Karabets, N. Iukhymenko, A. Kysil, O. Krupka and A. Kolendo, *Mol. Cryst. Liq. Cryst.*, 2019, **672**, 11–17.
123. M. W. H. Hoorens, M. Medved, A. D. Laurent, M. Di Donato, S. Fanetti, L. Slappendel, M. Hilbers, B. L. Feringa, W. Jan Buma and W. Szymanski, *Nat. Commun.*, 2019, **10**, 2390.
124. U. Burger and A. O. Bringhen, *Helv. Chim. Acta*, 1989, **72**, 93–100.
125. B. Maerz, S. Wiedbrauk, S. Oesterling, E. Samoylova, A. Nenov, P. Mayer, R. de Vivie-Riedle, W. Zinth and H. Dube, *Chem. - Eur. J.*, 2014, **20**, 13984–13992.
126. J. E. Zweig and T. R. Newhouse, *J. Am. Chem. Soc.*, 2017, **139**, 10956–10959.
127. V. Josef, F. Hampel and H. Dube, *Angew. Chem., Int. Ed.*, 2022, **61**, e202210855.
128. S. Wiedbrauk and H. Dube, *Tetrahedron Lett.*, 2015, **56**, 4266–4274.
129. D. V. Berdnikova, *Chem. - Eur. J.*, 2024, **30**, e202304237.
130. N. Shanker, O. Dilek, K. Mukherjee, D. W. McGee and S. L. Bane, *J. Fluoresc.*, 2011, **21**, 2173–2184.
131. M. Li, S. Yang, W. Liang, X. Zhang and D. Qu, *Dyes Pigm.*, 2019, **166**, 239–244.
132. X. Su and I. Aprahamian, *Chem. Soc. Rev.*, 2014, **43**, 1963–1981.
133. L. A. Tatum, X. Su and I. Aprahamian, *Acc. Chem. Res.*, 2014, **47**, 2141–2149.
134. I. Aprahamian, *Chem. Commun.*, 2017, **53**, 6674–6684.

135. S. M. Landge and I. Aprahamian, *J. Am. Chem. Soc.*, 2009, **131**, 18269–18271.
136. S. M. Landge, E. Tkatchouk, D. Benitez, D. A. Lanfranchi, M. Elhabiri, W. A. Goddard, 3rd and I. Aprahamian, *J. Am. Chem. Soc.*, 2011, **133**, 9812–9823.
137. X. Su and I. Aprahamian, *Org. Lett.*, 2011, **13**, 30–33.
138. X. Su, S. Voskian, R. P. Hughes and I. Aprahamian, *Angew. Chem., Int. Ed.*, 2013, **52**, 10734–10739.
139. M. J. Moran, M. Magrini, D. M. Walba and I. Aprahamian, *J. Am. Chem. Soc.*, 2018, **140**, 13623–13627.
140. M. L. Croteau, X. Su, D. E. Wilcox and I. Aprahamian, *ChemPlusChem*, 2014, **79**, 1214–1224.
141. X. Su and I. Aprahamian, *Org. Lett.*, 2013, **15**, 5952–5955.
142. J. T. Foy, D. Ray and I. Aprahamian, *Chem. Sci.*, 2015, **6**, 209–213.
143. J. D. Harris, M. J. Moran and I. Aprahamian, *Proc. Natl. Acad. Sci. U. S. A.*, 2018, **115**, 9414–9422.
144. B. Shao, H. Qian, Q. Li and I. Aprahamian, *J. Am. Chem. Soc.*, 2019, **141**, 8364–8371.
145. M. N. Chaur, D. Collado and J. M. Lehn, *Chem. - Eur. J.*, 2011, **17**, 248–258.
146. P. Courtot, R. Pichon and J. Le Saint, *Tetrahedron Lett.*, 1976, **17**, 1181–1184.
147. H. Qian, S. Pramanik and I. Aprahamian, *J. Am. Chem. Soc.*, 2017, **139**, 9140–9143.
148. R. B. Woodward and R. Hoffmann, *The Conservation of Orbital Symmetry*, Academic Press Inc., Weinheim, 1971.
149. K. Matsuda, H. Yamaguchi, T. Sakano, M. Ikeda, N. Tanifuji and M. Irie, *J. Phys. Chem. C*, 2008, **112**, 17005–17010.
150. M. Irie, *Chem. Rev.*, 2000, **100**, 1685–1716.
151. C. Zheng, C. Fan, S. Pu, B. Chen and B. Chen, *J. Mol. Struct.*, 2016, **1123**, 355–359.
152. X. Li, S. Pu, H. Li and G. Liu, *Dyes Pigm.*, 2014, **105**, 47–56.
153. M. Sacherer, S. Gracheva, H. Maid, C. Placht, F. Hampel and H. Dube, *J. Am. Chem. Soc.*, 2024, **146**, 9575–9582.
154. R. Wang, S. Pu, G. Liu and S. Cui, *Beilstein J. Org. Chem.*, 2012, **8**, 1018–1026.
155. C. Fleming, P. Remón, S. Li, N. A. Simeth, B. König, M. Grøtli and J. Andréasson, *Dyes Pigm.*, 2017, **137**, 410–420.
156. G. Liu, M. Liu, S. Pu, C. Fan and S. Cui, *Tetrahedron*, 2012, **68**, 2267–2275.
157. A. G. Lvov, M. Mortel, A. V. Yadykov, F. W. Heinemann, V. Z. Shirinian and M. M. Khusniyarov, *Beilstein J. Org. Chem.*, 2019, **15**, 2428–2437.
158. I. Colombier, S. Spagnoli, A. Corval, P. L. Baldeck, M. Giraud, A. Leaustic, P. Yu and M. Irie, *J. Chem. Phys.*, 2007, **126**, 011101.
159. L. Gundogdu, M. Kose, S. Takeuchi, Y. Yokoyama and E. Orhan, *J. Lumin.*, 2018, **203**, 568–575.
160. J. Zhang and H. Tian, *Adv. Opt. Mater.*, 2018, **6**, 1701278.
161. D. Wutz, C. Falenczyk, N. Kuzmanovic and B. König, *RSC Adv.*, 2015, **5**, 18075–18086.
162. C. Falenczyk, M. Schiedel, B. Karaman, T. Rumpf, N. Kuzmanovic, M. Grøtli, W. Sippl, M. Jung and B. König, *Chem. Sci.*, 2014, **5**, 4794–4799.
163. P. H. Lee, C. C. Ko, N. Zhu and V. W. Yam, *J. Am. Chem. Soc.*, 2007, **129**, 6058–6059.
164. T. Nakagawa, Y. Hasegawa and T. Kawai, *J. Phys. Chem. A*, 2008, **112**, 5096–5103.
165. V. W. Yam, C. C. Ko and N. Zhu, *J. Am. Chem. Soc.*, 2004, **126**, 12734–12735.
166. N. A. Simeth, A. C. Kneuttinger, R. Sterner and B. Konig, *Chem. Sci.*, 2017, **8**, 6474–6483.
167. E. Saito, T. Ako, Y. Kobori and A. Tsuda, *RSC Adv.*, 2017, **7**, 2403–2406.
168. D. Kolarski, P. Steinbach, C. Bannwarth, K. Klaue and S. Hecht, *Angew. Chem., Int. Ed.*, 2024, **63**, e202318015.
169. N. M.-W. Wu, T. H.-C. Fung, M. Ng and V. W.-W. Yam, *ACS Mater. Lett.*, 2023, **6**, 314–320.

170. R. Li, Q. Fang, M. Chen, M. Yamada, Y. Tsuji, Y. Kugai, W. Li and T. Kawai, *Chem. - Eur. J.*, 2023, **29**, e202302693.
171. E. C. Harvey, B. L. Feringa, J. G. Vos, W. R. Browne and M. T. Pryce, *Coord. Chem. Rev.*, 2015, **282**, 77–86.
172. N. M. Wu, M. Ng, W. H. Lam, H. L. Wong and V. W. Yam, *J. Am. Chem. Soc.*, 2017, **139**, 15142–15150.
173. Y. Yang, X. Bai and F. Hu, *Nat. Chem.*, 2024, **15**, 2578.
174. J. Bargstedt, M. Reinschmidt, L. Tydecks, T. Kolmar, C. M. Hendrich and A. Jaschke, *Angew. Chem., Int. Ed.*, 2024, **63**, e202310797.
175. Y.-P. Song, J.-N. Zhang, J.-R. Wang, K. Li, Y.-X. Yuan, B. Li and S.-Q. Zang, *Sci. China Mater.*, 2024, **67**, 698–704.
176. Y.-X. Wang, S.-R. Yang, G.-P. Li, L.-L. Ma and Y.-Y. Wang, *ACS Mater. Lett.*, 2023, **5**, 3074–3079.
177. A. Takeguchi, A. Kikuchi, K. Ueno, S. Ishihara, A. Nitta, T. Nakagawa, T. Ubukata and Y. Yokoyama, *Photochem. Photobiol. Sci.*, 2024, **23**, 133–151.
178. S. Takaku, R. Nishimura and M. Morimoto, *Dyes Pigm.*, 2023, **216**, 111354.
179. B. Tang, M. Pauls, C. Bannwarth and S. Hecht, *J. Am. Chem. Soc.*, 2024, **146**, 45–50.
180. S. He, S. Schog, Y. Chen, Y. Ji, S. Panitz, W. Richtering and R. Gostl, *Adv. Mater.*, 2023, **35**, e2305845.
181. X. Ma, S. Liuye, K. Ning, X. Wang, S. Cui and S. Pu, *Photochem. Photobiol. Sci.*, 2023, **22**, 2389–2399.
182. D. Y. Alene, V. Srinivasadesikan, M. C. Lin and W. S. Chung, *J. Org. Chem.*, 2023, **88**, 5530–5542.
183. M. P. O'Hagan, J. Ramos-Soriano, S. Haldar, S. Sheikh, J. C. Morales, A. J. Mulholland and M. C. Galan, *Chem. Commun.*, 2020, **56**, 5186–5189.
184. T. Fukaminato, T. Hirose, T. Doi, M. Hazama, K. Matsuda and M. Irie, *J. Am. Chem. Soc.*, 2014, **136**, 17145–17154.
185. K. Matsuda, Y. Shinkai, T. Yamaguchi, K. Nomiyama, M. Isayama and M. Irie, *Chem. Lett.*, 2003, **32**, 1178–1179.
186. R. Iwai, M. Morimoto and M. Irie, *Photochem. Photobiol. Sci.*, 2020, **19**, 783–789.
187. S. Fredrich, R. Gostl, M. Herder, L. Grubert and S. Hecht, *Angew. Chem., Int. Ed.*, 2016, **55**, 1208–1212.
188. H. Y. Jung, B. Kim, M. H. Jeon and Y. Kim, *Small*, 2022, **18**, e2103523.
189. K. Uno, M. L. Bossi, M. Irie, V. N. Belov and S. W. Hell, *J. Am. Chem. Soc.*, 2019, **141**, 16471–16478.
190. Z. Li, C. He, Z. Lu, P. Li and Y.-P. Zhu, *Dyes Pigm.*, 2020, **182**, 108623.
191. R. Murata, T. Yago and M. Wakasa, *Bull. Chem. Soc. Jpn.*, 2011, **84**, 1336–1338.
192. R. Gostl, B. Kobin, L. Grubert, M. Patzel and S. Hecht, *Chem. - Eur. J.*, 2012, **18**, 14282–14285.
193. R. Li, T. Nakashima, O. Galangau, S. Iijima, R. Kanazawa and T. Kawai, *Chem. - Asian J.*, 2015, **10**, 1725–1730.
194. S. H. Um, H. J. Kim, D. Kim, J. E. Kwon, J. W. Lee, D. Hwang, S. K. Kim and S. Y. Park, *Dyes Pigm.*, 2018, **158**, 36–41.
195. G. Naren, W. Larsson, C. Benitez-Martin, S. Li, E. Perez-Inestrosa, B. Albinsson and J. Andreasson, *Chem. Sci.*, 2021, **12**, 7073–7078.
196. D. Kim, A. Aktalay, N. Jensen, K. Uno, M. L. Bossi, V. N. Belov and S. W. Hell, *J. Am. Chem. Soc.*, 2022, **144**, 14235–14247.
197. F. Stellacci, C. Bertarelli, F. Toscano, M. C.Gallazzi, G. Zotti and G. Zerbi, *Adv. Mater.*, 1999, **11**, 292–295.

198. R. Kashihara, M. Morimoto, S. Ito, H. Miyasaka and M. Irie, *J. Am. Chem. Soc.*, 2017, **139**, 16498–16501.
199. M. Herder, B. M. Schmidt, L. Grubert, M. Patzel, J. Schwarz and S. Hecht, *J. Am. Chem. Soc.*, 2015, **137**, 2738–2747.
200. J. Ramos-Soriano and M. C. Galan, *JACS Au*, 2021, **1**, 1516–1526.
201. M. Irie, T. Lifka, S. Kobatake and N. Kato, *J. Am. Chem. Soc.*, 2000, **122**, 4871–4876.
202. T. Liu, X. Zhao, Q. Shen and L. Lu, *Tetrahedron*, 2012, **68**, 6535–6547.
203. E. Lognon, M. C. Heitz, A. Bakkar, S. Cobo, F. Loiseau, E. Saint-Aman, G. Royal and M. Boggio-Pasqua, *ChemPhysChem*, 2020, **21**, 1571–1577.
204. K. Klaue, W. Han, P. Liesfeld, F. Berger, Y. Garmshausen and S. Hecht, *J. Am. Chem. Soc.*, 2020, **142**, 11857–11864.
205. B. Saima, N. Khan, Y. S. S. Al-Faiyz, R. Ludwig, W. Rehman, M. Habib-Ur-Rehman, N. S. Sheikh and K. Ayub, *J. Mol. Graphics*, 2019, **88**, 261–272.
206. R. H. Mitchell, T. R. Ward, Y. Chen, Y. Wang, S. A. Weerawarna, P. W. Dibble, M. J. Marsella, A. Almutairi and Z. Q. Wang, *J. Am. Chem. Soc.*, 2003, **125**, 2974–2988.
207. K. Klaue, Y. Garmshausen and S. Hecht, *Angew. Chem., Int. Ed.*, 2018, **57**, 1414–1417.
208. Z. Ziani, S. Cobo, F. Loiseau, D. Jouvenot, E. Lognon, M. Boggio-Pasqua and G. Royal, *JACS Au*, 2023, **3**, 131–142.
209. Y. Xiong, A. Vargas Jentzsch, J. W. M. Osterrieth, E. Sezgin, I. V. Sazanovich, K. Reglinski, S. Galiani, A. W. Parker, C. Eggeling and H. L. Anderson, *Chem. Sci.*, 2018, **9**, 3029–3040.
210. S. Wang, M.-S. Choi and S.-H. Kim, *J. Photochem. Photobiol., A*, 2008, **198**, 150–155.
211. H. Xia, K. Xie and G. Zou, *Molecules*, 2017, **22**, 2236.
212. N. W. Tyer and R. S. Becker, *J. Am. Chem. Soc.*, 2002, **92**, 1289–1294.
213. Z. Tian, W. Wu, W. Wan and A. D. Li, *J. Am. Chem. Soc.*, 2011, **133**, 16092–16100.
214. J. T. C. Wojtyk, A. Wasey, P. M. Kazmaier, S. Hoz and E. Buncel, *J. Phys. Chem. A*, 2000, **104**, 9046–9055.
215. R. Klajn, *Chem. Soc. Rev.*, 2014, **43**, 148–184.
216. C. Kaiser, T. Halbritter, A. Heckel and J. Wachtveitl, *ChemistrySelect*, 2017, **2**, 4111–4123.
217. T. Stafforst and D. Hilvert, *Chem. Commun.*, 2009, 287–288.
218. H. Görner, *Phys. Chem. Chem. Phys.*, 2001, **3**, 416–423.
219. J. R. Nilsson, S. Li, B. Onfelt and J. Andreasson, *Chem. Commun.*, 2011, **47**, 11020–11022.
220. M. Hammarson, J. R. Nilsson, S. Li, P. Lincoln and J. Andreasson, *Chem. - Eur. J.*, 2014, **20**, 15855–15862.
221. X. Song, J. Zhou, Y. Li and Y. Tang, *J. Photochem. Photobiol., A*, 1995, **92**, 99–103.
222. S.-R. Keum, S.-J. Roh, S.-M. Ahn, S.-S. Lim, S.-H. Kim and K. Koh, *Dyes Pigm.*, 2007, **74**, 343–347.
223. C. Beyer and H. A. Wagenknecht, *J. Org. Chem.*, 2010, **75**, 2752–2755.
224. Q. Zou, X. Li, J. Zhou, K. Bai and H. Ågren, *Dyes Pigm.*, 2014, **107**, 174–181.
225. R. K. Weerasekara, H. Uekusa and C. V. Hettiarachchi, *Cryst. Growth Des.*, 2017, **17**, 3040–3047.
226. R. Matsushima and H. Sakaguchi, *J. Photochem. Photobiol., A*, 1997, **108**, 239–245.
227. K. Rustler, G. Maleeva, A. M. J. Gomila, P. Gorostiza, P. Bregestovski and B. Konig, *Chem. - Eur. J.*, 2020, **26**, 12722–12727.
228. Y. Kohno, Y. Tamura and R. Matsushima, *J. Photochem. Photobiol., A*, 2009, **201**, 98–101.
229. M. Seibold, M. Handschuh, H. Port and H. C. Wolf, *J. Lumin.*, 1997, **72-74**, 454–456.
230. N. A. Simeth, L. M. Altmann, N. Wossner, E. Bauer, M. Jung and B. Konig, *J. Org. Chem.*, 2018, **83**, 7919–7927.
231. J. Andreasson, S. D. Straight, T. A. Moore, A. L. Moore and D. Gust, *J. Am. Chem. Soc.*, 2008, **130**, 11122–11228.

232. C. Slavov, C. Boumrifak, C. A. Hammer, P. Trojanowski, X. Chen, W. J. Lees, J. Wachtveitl and M. Braun, *Phys. Chem. Chem. Phys.*, 2016, **18**, 10289–10296.
233. Y. Yokoyama, *Chem. Rev.*, 2000, **100**, 1717–1740.
234. Y. Liang, A. S. Dvornikov and P. M. Rentzepis, *J. Photochem. Photobiol., A*, 1999, **125**, 79–84.
235. A. T. Frawley, V. Wycisk, Y. Xiong, S. Galiani, E. Sezgin, I. Urbancic, A. Vargas Jentzsch, K. G. Leslie, C. Eggeling and H. L. Anderson, *Chem. Sci.*, 2020, **11**, 8955–8960.
236. A. T. Frawley, K. G. Leslie, V. Wycisk, S. Galiani, D. Shrestha, C. Eggeling and H. L. Anderson, *ChemPhysChem*, 2023, **24**, e202300125.
237. Y. Xiong, P. Rivera-Fuentes, E. Sezgin, A. Vargas Jentzsch, C. Eggeling and H. L. Anderson, *Org. Lett.*, 2016, **18**, 3666–3669.

2

Dithienylethenes – A Systematic Structure-Property Relationship

Contents

2.1 Introduction 53

2.1.1 Discovery of Bistable Dithienylethenes 53

2.1.2 DAEs Responsive to Visible-Light Photoswitching 54

2.1.2.1 Extending π Conjugation 55

2.1.2.2 Triplet Sensitization 59

2.1.3 DAEs with Aqueous Solubility 61

2.1.4 Project Aim 63

2.2 Results and Discussion 64

2.2.1 Design and Synthesis of DTE Photoswitches 64

2.2.2 Photochromism 71

2.2.3 Structural Impact on UV-vis Absorption Spectra 76

2.2.4 Photostationary State Distribution 79

2.2.5 Quantum Yield of Photoswitching 83

2.2.6 Calculation of PSD Based on Molar Absorption Coefficient and Quantum Yield 87

2.2.7 Fatigue Resistance 88

2.2.8 Decomposition of **Dy-yD** 91

2.2.9 Solvatochromism of **D-A** 95

2.2.10 Computational Benchmarking for DFT and TD-DFT Calculations 98

2.2.11 Conformational Analysis on Open DTEs 104

2.3 Conclusions 106

2.4 Experimental 107

2.4.1 General Synthetic and Characterization Methods 107
2.4.2 Acquisition of UV-vis Spectra 109
2.4.3 Determination of Molar Absorption Coefficient by NMR Reference Method..... 109
2.4.4 Ferric Oxalate Actinometry for Measuring the Power of LED Light Source 110
2.4.5 Determination of Photoswitching Quantum Yield 111
2.4.6 Determination of PSD by NMR Method..... 112
2.4.7 Determination of PSD by UV-Vis..... 117
2.4.8 Determination of Fatigue Resistance 117
2.4.9 Synthetic Procedures..... 118
2.5 Appendix 135

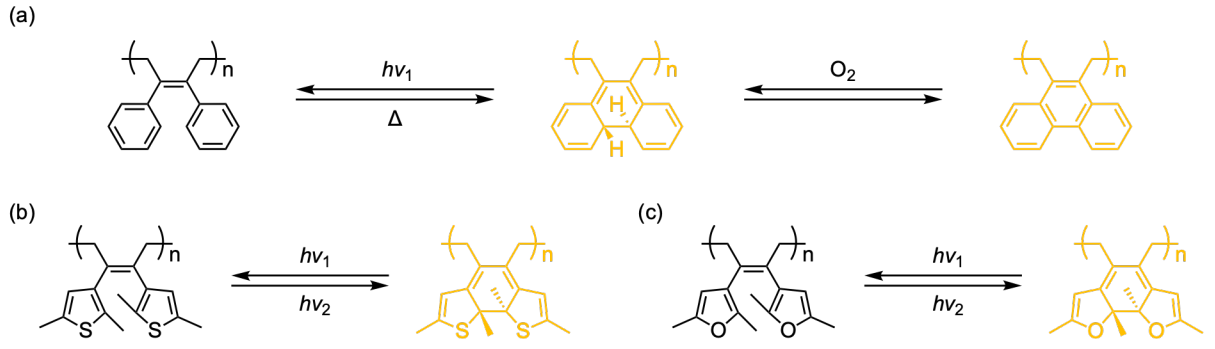
Chapter 2 - Dithienylethenes – A Systematic Structure-Property Relationship

2.1 Introduction

This section provides an overview of the property optimization efforts for DAE within the research community. The discussion begins with an examination of the selection of various aryl groups leading to bistable DTE. Subsequently, it progresses to the exploration of DTE photoswitching induced by visible light. Finally, the section concludes with an analysis of water-soluble DAE photoswitches.

2.1.1 Discovery of Bistable Dithienylethenes

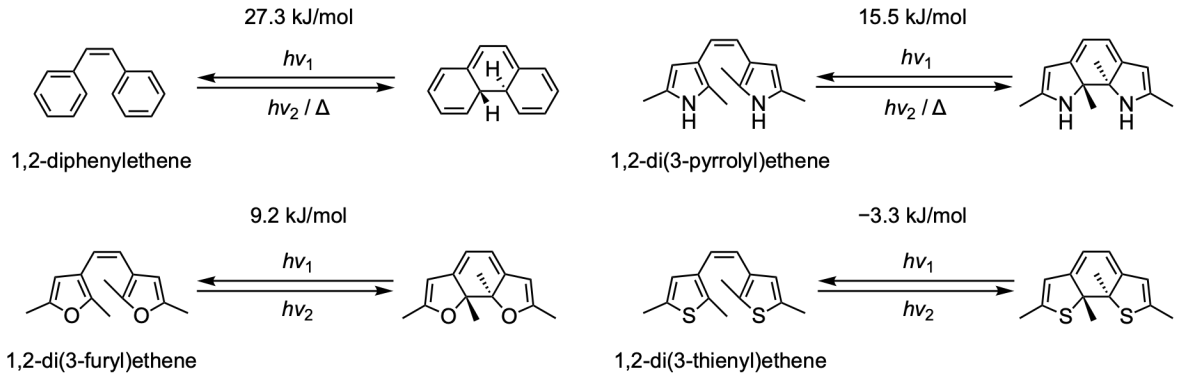
DAEs were discovered by Masahiro Irie while working with poly(2,3-diphenylbutadiene) (Scheme 2.1). Exposing this polymer to 313 nm light in oxygen-free condition led to the formation of yellow-colored dihydrophenanthrene units, which reverted to the original colorless 2,3-diphenylbutene units at room temperature. Like stilbenes, in presence of oxygen, the monomer can be oxidized to form phenanthrene. To avoid such oxidation, Irie prepared two more polymers containing thiophene and furan repeating units (Scheme 2.1).[1] The yellow polymer formed upon irradiation exhibited excellent stability, persisting overnight in the dark and even at 100 °C.



Scheme 2.1 Photoswitchable polymers leading to the discovery of bistable DTEs. (a) First polymer containing 2,3-dithienylbutene repeating unit. (b) and (c) polymers replacing the phenyl groups with thiophenes and furans.

Irie sought to explain the thermal irreversibility of thiophene analogues in several model systems (Scheme 2.2) by conducting semi-empirical MNDO ground-state energy calculations on both open and closed isomers.[2] The thermal stability of the closed isomers is determined by the activation energy barrier for the cycloreversion reaction, which is related to the energy difference between the ground-state energy of the two isomers (Figure 2.1). Calculations showed that the closed isomer of the thienyl model is more stable than the open isomer by 3.3 kJ/mol, contributing to a higher energy barrier for reverse reaction compared to the

pyrrolyl, furyl and phenyl models (Scheme 2.2, Figure 2.1). The closed isomers of pyrrolyl, furyl and phenyl models are less stable than the open form, resulting in lower photoreversion energy barrier.[2] Through more calculations, it was found that the energy difference between the open and the closed isomers mainly arises from the disruption of the aromatic stabilization during the photocyclization process.[2] The theoretical prediction was confirmed by the synthesis of DAEs with various types of aryl groups.[3-6] These studies led to the modern development of DTEs as P-type photoswitches.



Scheme 2.2 Model molecular systems for MNDO calculation. The numbers indicate the ground-state energy difference between the closed and the open isomer. Positive numbers indicate that the open form is more stable than the closed form.

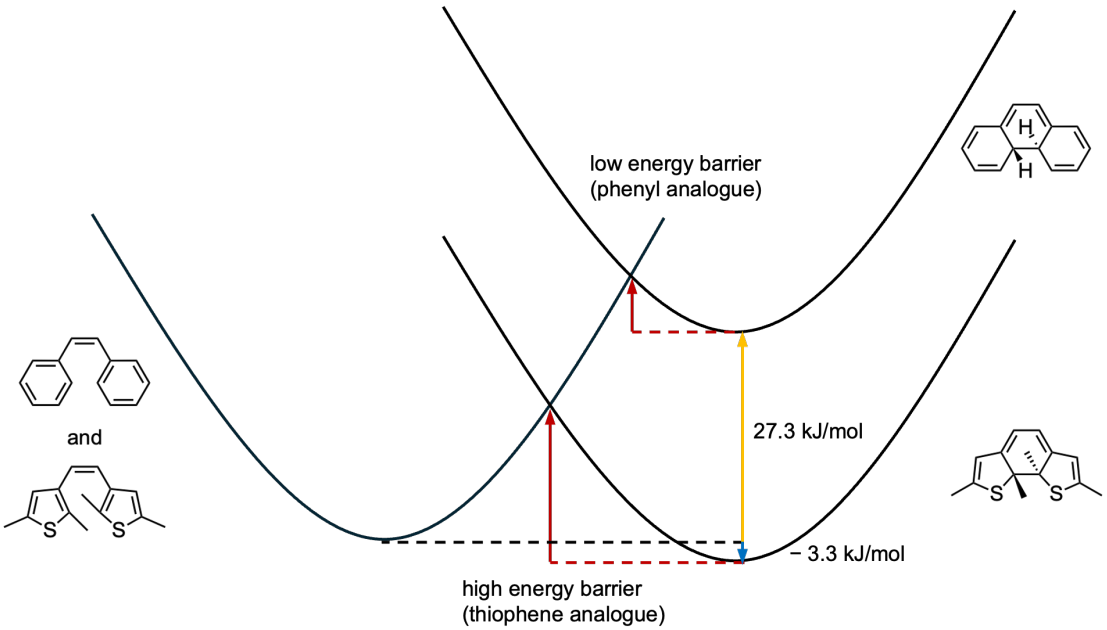


Figure 2.1 Graphic illustration of the energy barrier of the thermal reverse reaction. Small ground-state energy difference between the two isomers results in high thermal reversion energy barrier, and vice versa.

2.1.2 DAEs Responsive to Visible-Light Photoswitching

The use of visible or infrared light to trigger photoswitches in biological systems offers significant advantages over UV light, primarily due to reduced phototoxicity and deeper tissue penetration. UV light (Figure 2.2), particularly UVB (280–315 nm) and UVC (100–280 nm),

can cause direct DNA damage.[7] Even UVA (315–400 nm) can generate reactive oxygen species (ROS), which indirectly damage cellular components.[8] Furthermore, the wavelength of light directly influences its depth of penetration in biological tissues.[9, 10] Shorter wavelengths, such as UV light, are more readily absorbed and scattered by biological tissues, limiting their penetration depth. While UV light may only penetrate a few micrometers to a few hundred micrometers into tissue, visible light can penetrate several millimeters, and near-infrared light can penetrate even deeper, up to several centimeters.[11] Visible light is also essential for microscopy studies. Conventional microscopy and imaging techniques commonly employ visible or near-infrared light sources with wavelengths ranging from 400 to 650 nm. On the other hand, UV light is not frequently used in confocal microscopy due to several technical limitations, including the incompatibility of optical components.

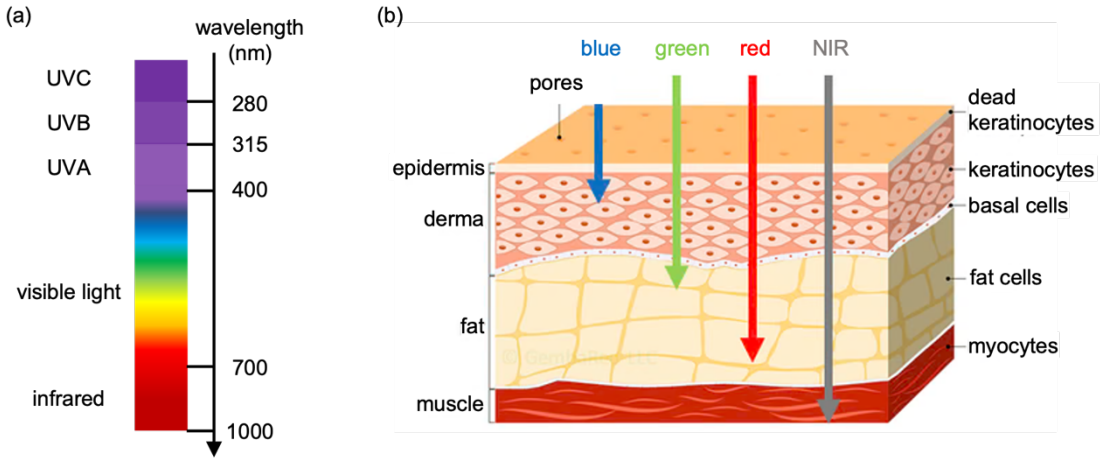


Figure 2.2 (a) Schematic representation of the electromagnetic spectrum ranges from UVC to infrared light, covering wavelengths from 100 nm to 1000 nm. (b) The penetration depth of light into biological tissues varies significantly depending on the wavelength. The figure is adopted from GembaRed. Reprint with permission.[12]

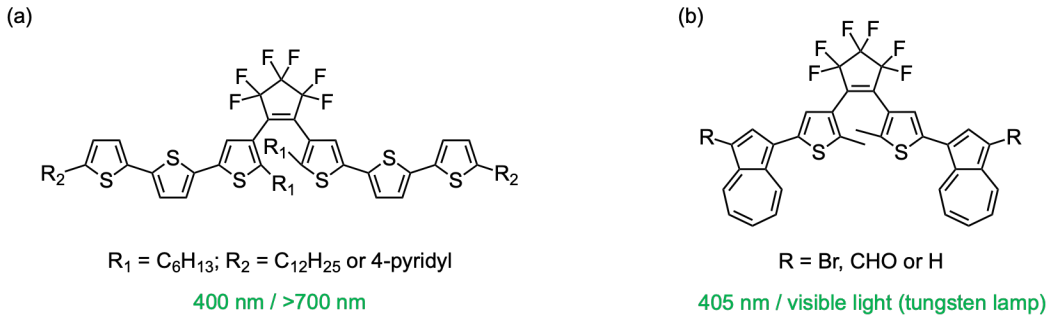
Researchers have invested significant efforts in fine-tuning the absorption properties of DAEs to enable their bidirectional switching using visible light.[13] Several strategies have been employed, including 1. extending π-conjugation,[14-20] 2. utilizing triplet sensitization,[21-30] 3. incorporating upconverting nanoparticles,[31] 4. multiphoton absorption,[32] 5. intermolecular electron transfer,[33] and 6. intramolecular proton transfer.[34] This section will evaluate the first two strategies.

2.1.2.1 Extending π Conjugation

To synthesize diarylethenes with extended π-conjugation, Lehn attached two additional thiophene units to the 5 and 5'-positions of the DTE (Scheme 2.3a). This structural modification caused substantial bathochromic shift of the absorption bands of both the open and closed forms, allowing the cyclization and cycloreversion reactions to be triggered by light at 400 nm

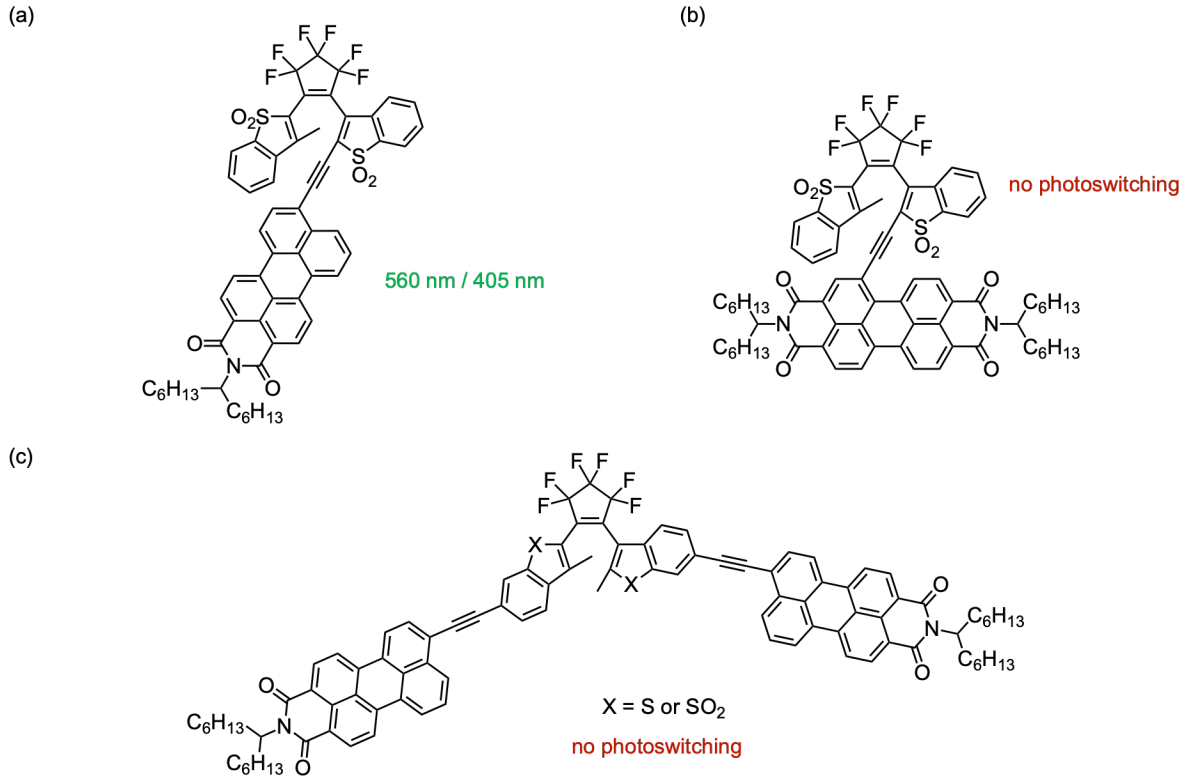
and 720 nm, respectively. The 4-pyridyl analogue is even more red-shifted due to additional π-conjugation.[14]

Drawing inspiration from the distinct electronic and optical attributes of azulene, Nica synthesized a collection of novel azulene-substituted DTEs (Scheme 2.3b).[15] These molecules photocyclize when exposed to visible light at 405 nm and demonstrated the ability to function as fluorescent switches (where the azulene fluorescence is turned off upon DAE photocyclization).



Scheme 2.3 DAEs with extended conjugation synthesized by (a) Lehn and (b) Nica.

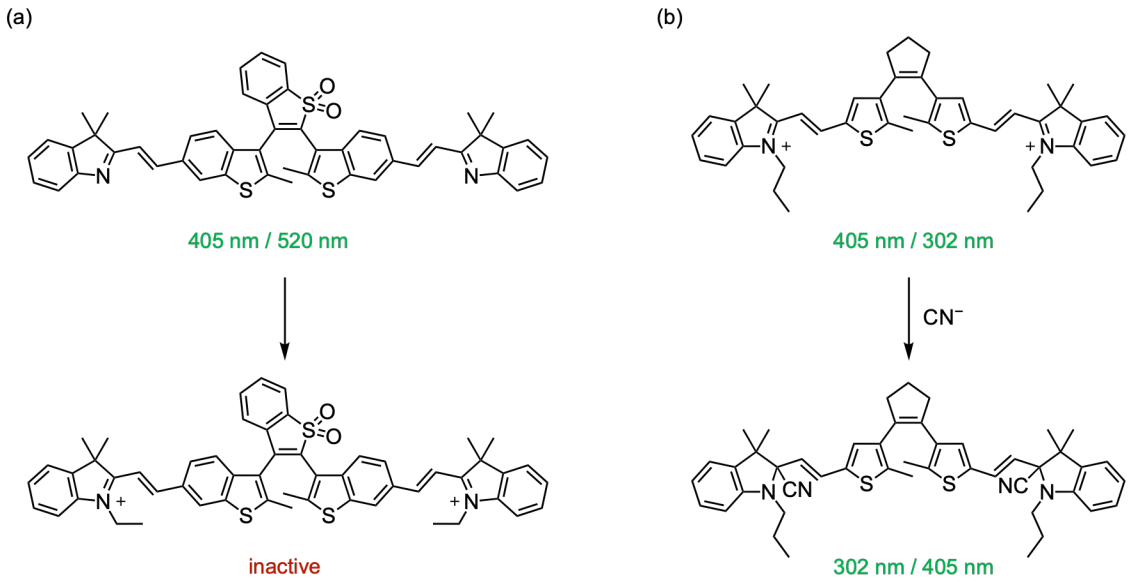
The 2,2'-positions of DTEs, which play crucial roles in bond formation during the ring closure process, provide an alternative route for extending π-conjugation. By introducing a conjugated antenna at the 2 or 2'-position, it is possible to create DTEs that exhibit a hypsochromic shift in the closed form compared to the open form. Fukaminato synthesized an all-visible-light-responsive DTE derivative by covalently linking a perylene monoimide (PMI) dye to the 2-position of the DTE (Scheme 2.4a).[16] The compound demonstrated the ability to undergo an isomerization reaction between the open and closed forms when exposed to visible light at 560 and 405 nm, achieving high PSDs of >90% for both cyclization and cycloreversion. However, the photocyclization quantum yield is less than 0.01. Modifying the position of attachment and changing PMI to perylenediimide (PDI) led to the loss of photoswitching ability (Scheme 2.4b and Scheme 2.4c). DFT calculations suggested that the localization of both HOMO and LUMO to the PMI or PDI moiety is responsible for the loss of photochromism.



Scheme 2.4 Structures of DAEs modified with PMI and PDI groups.

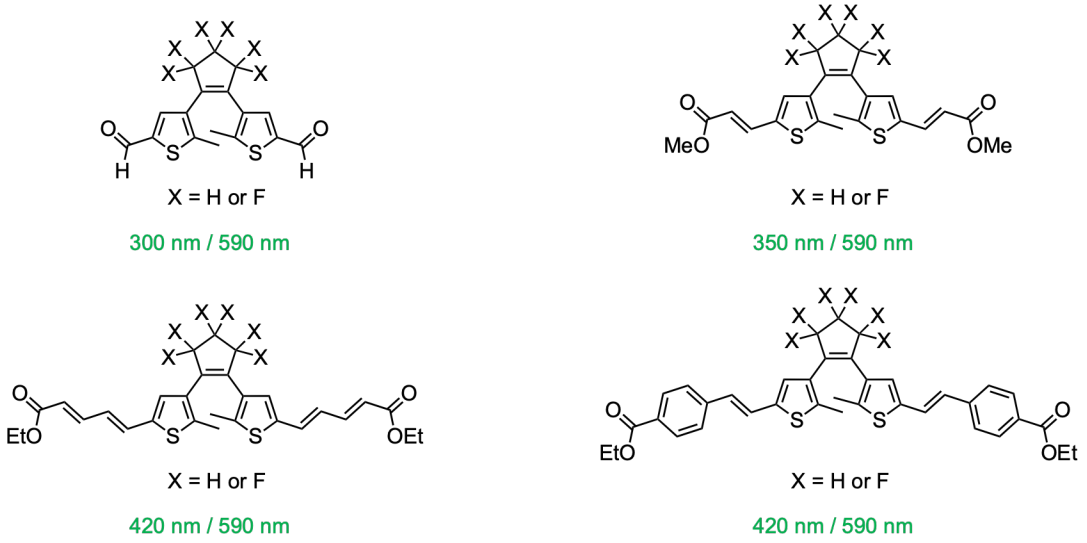
Tang synthesized a DAE derivative featuring extended π-conjugation with electron-donating groups (Scheme 2.5a, top).[17] The DAE can be controlled with 405 and 520 nm light in various solvents or living cells. However, when the electron-donating indolenine groups were replaced with electron-withdrawing indoleninium groups (Scheme 2.5a, bottom), the molecule failed to undergo photocyclization. Through DFT calculations, the authors found that, for the ethylated system, the LUMO and LUMO+1 molecular orbitals leading to photocyclization are not effectively distributed on the central hexatriene.

Hu developed a similar analogue by replacing the benzothiophene group with a traditional thiophene group (Scheme 2.5b).[18] They incorporated an electron-withdrawing indoleninium group to extend the π-conjugation on both sides of the DAE backbone. The cyanine-like structure results in a strong absorption band of the ring-open isomer near 470 nm. Upon irradiation with 405 nm light, a new absorption peak emerges at 840 nm. The authors triggered the photoreversion with 302 nm instead of NIR light. The high reactivity of the indoleninium group towards cyanide led to the development of a colorimetric and fluorescent probe for cyanide. The cyanide adducts did not display visible-light-triggered photochromic behavior due to the interruption of conjugation.



Scheme 2.5 DAEs bearing (a) indolenine and (b) indoleninium groups developed by Tang and Yin, respectively.

Tosic further synthesized a range of DTE derivatives featuring aldehyde or ester end groups (Scheme 2.6).[19] These DTEs involve extended π-conjugation, which was achieved through the incorporation of alkene or aryl functional groups. The authors reported red shifts in the absorption spectra for both the open and closed isomers of the DTEs with increased conjugation length. Each additional alkene or aryl group resulted in a red-shift of 10–20 nm in the open-form absorption spectra. Among all the DTEs investigated, only the analogues containing two alkenes, or one alkene and one aryl group could be switched using visible light at 420 nm. In the closed isomers, the UV-vis absorption band of the aryl analogue was found to be ~20 nm blue-shifted compared to the alkene analogue. This observation is likely due to the aryl group being slightly twisted out of plane, resulting in a reduction of the overall conjugation.



Scheme 2.6 DTEs developed by Tosic and co-workers, bearing alkene and/or aryl spacers for increasing π conjugation.

Investigations on DAEs with extended π-conjugation have revealed a complex relationship between molecular structure and photochemical behavior. While increasing π-conjugation can effectively reduce the HOMO-LUMO energy gap, it simultaneously impedes the photoswitching capabilities of DAEs. The mechanism of photochemical pericyclic reactions involves the excitation of a HOMO electron to the LUMO, with the subsequent chemical reaction occurring through LUMO orbital overlap (frontier molecular orbital theory and Woodward-Hoffmann rules). However, if the LUMO of a molecule becomes highly delocalized or localized on non-hexatriene regions of the molecule, the photoswitching process may be hindered or completely suppressed. This phenomenon elucidates the observed decrease in photocyclization quantum yields for many DAEs with increased π-conjugation.[35] Consequently, the strategy of employing extended π-conjugation to induce a bathochromic shift in the absorption spectrum of open-DAEs necessitates precise molecular engineering.

2.1.2.2 Triplet Sensitization

DTE photoswitches generally undergo photocyclization via the singlet excited state. However, in presence of suitable triplet sensitizer, the photocyclization may also proceed from the triplet excited state.

Triplet sensitization is a fundamental photophysical process, involving the transfer of energy from an excited triplet state of a sensitizer molecule to a ground state of a target molecule, leading to the formation of an excited triplet state in the target molecule. The sensitizer molecule, often referred to as a triplet sensitizer, is typically a compound with a high quantum yield of intersystem crossing (ISC) and a long-lived triplet excited state (Figure 2.3). Commonly used organic triplet sensitizers include iodinated or brominated organic chromophores, fullerenes, porphyrins, and biacetyl groups etc.[36]

The triplet sensitization process involves a series of steps (Figure 2.3). First, the sensitizer molecule (S) absorbs a photon, leading to the formation of an excited singlet state (S*, S_1 in Figure 2.3). Second, the excited singlet state of the sensitizer undergoes ISC, a non-radiative transition to an excited triplet state (T*, T_1 in Figure 2.3). The ISC process is facilitated by the presence of heavy atoms or certain molecular geometries that enhance spin-orbit coupling. Third, the excited triplet state of the sensitizer (T*) transfers its energy to a ground state of the target molecule (A), resulting in the formation of an excited triplet state in the target molecule (A*) and the return of the sensitizer to its ground state (S). Finally, the

excited triplet state of the target molecule (A*) can then undergo various photochemical reactions, depending on the specific molecular system.

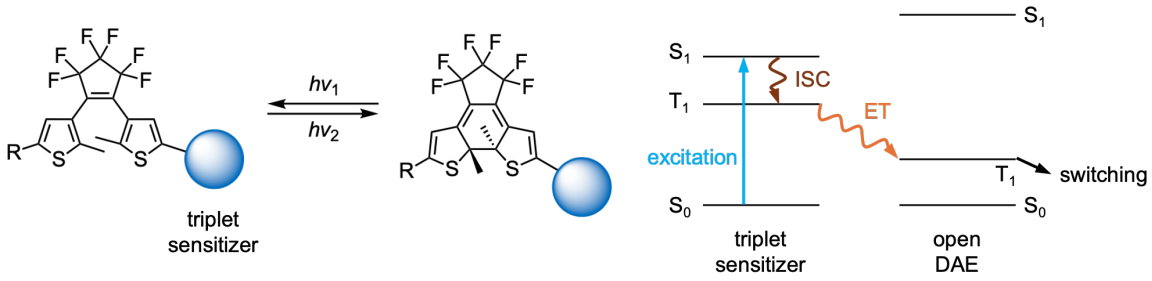
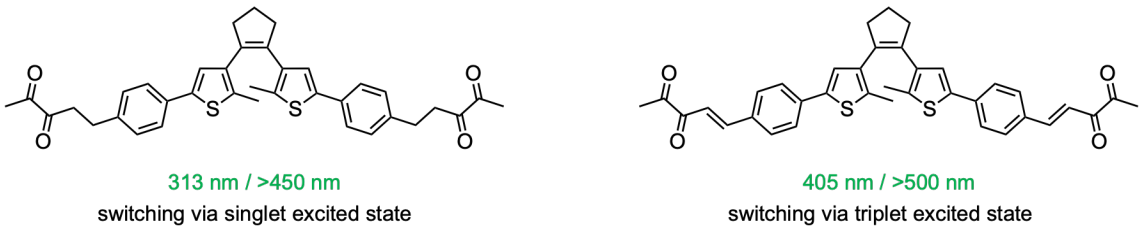


Figure 2.3 A DAE-sensitizer pair and the energy diagram for DAE photoswitching with triplet sensitization.

Transition metal complexes[26-29] and organic motifs[37-40] have been employed as triplet sensitizers to trigger the photocyclization reaction of DTEs. We highlight a study by Hecht, which synthesized two DTEs with covalently linked biacetyl triplet sensitizers,[41] one with an aliphatic linkage and the other with an unsaturated linkage (Scheme 2.7). The DTE-sensitizer pair with aliphatic linkage did not exhibit photocyclization through triplet sensitization. Similarly, no triplet sensitization was observed when 250 equivalents of biacetyl were added to the solution containing a DTE without covalently linked triplet sensitizer. In contrast, the DAE-biacetyl system with the conjugated linkage exhibits triplet-sensitized photocyclization, which can be suppressed in the presence of oxygen (O_2). Under 405 nm irradiation, the photocyclization quantum yield is 18% under inert atmosphere but decreases to 0.5% in the presence of oxygen. Other triplet quenchers also resulted in a reduced photocyclization quantum yield. This study highlights a significant limitation of employing triplet sensitizers in visible photoswitch design: the effectiveness of triplet sensitization is diminished by the presence of triplet quenchers, such as oxygen. This issue is particularly concerning for potential applications in biological contexts, as it is typically not feasible to remove oxygen in biological experiments.

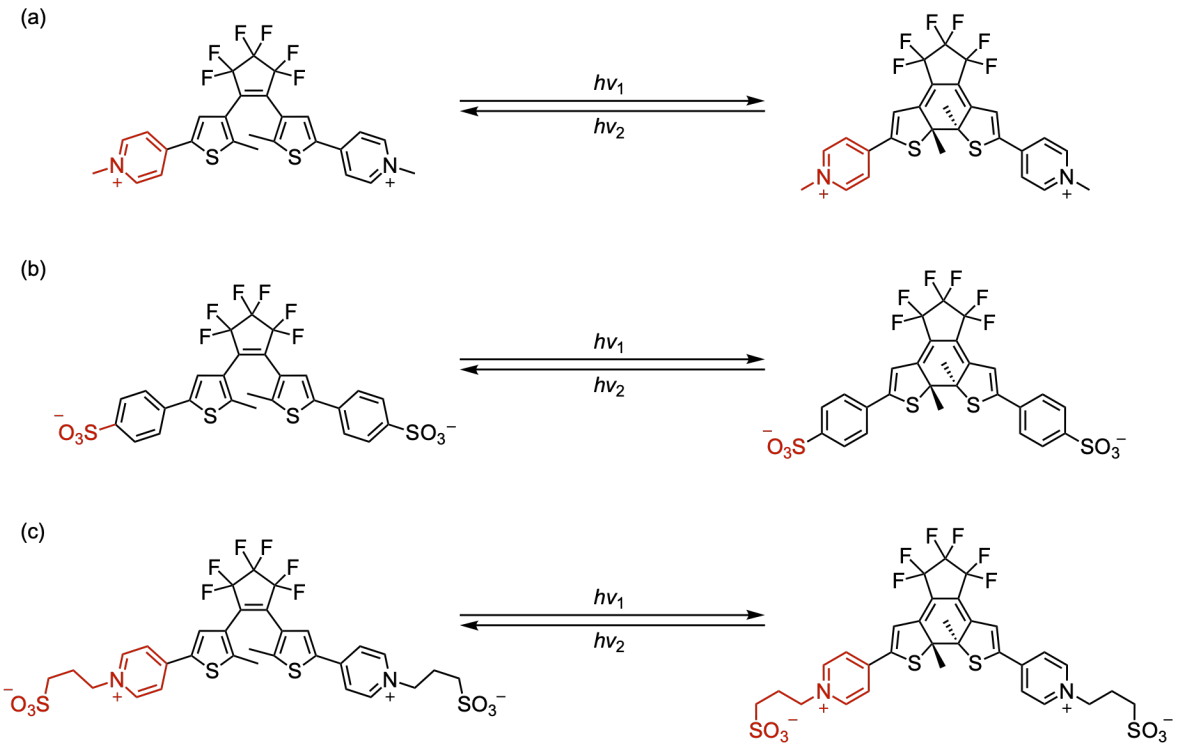


Scheme 2.7 Intramolecular triplet sensitization of DTE with diacetyl groups being linked through (a) aliphatic chains and (b) unsaturated linkage.

2.1.3 DAEs with Aqueous Solubility

Most DAEs reported in the literature are not water-soluble due to the hydrophobic hexatriene unit. However, numerous water-soluble DAEs have been developed using various strategies, such as introducing positive[35, 42-49] and negative[45, 50-56] charges, incorporating non-charged polar groups,[49, 56, 57] linking DAEs to water-soluble polymers,[58] enclosing DAEs into membranes or vesicles,[59] and utilizing host-guest chemistry.[43-45, 48, 51]

Matsuda and colleagues reported the first example of a doubly charged DTE in 2003.[42] They synthesized a DTE bearing two positively charged *N*-methylpyridinium groups (Scheme 2.8a). Interestingly, the primary goal of this study was not to introduce water solubility but rather to create a DTE that adopts an anti-parallel conformation through electrostatic repulsion, thereby achieving a high photocyclization quantum yield. The quantum yield of this DTE was measured to be 71% in methanol.



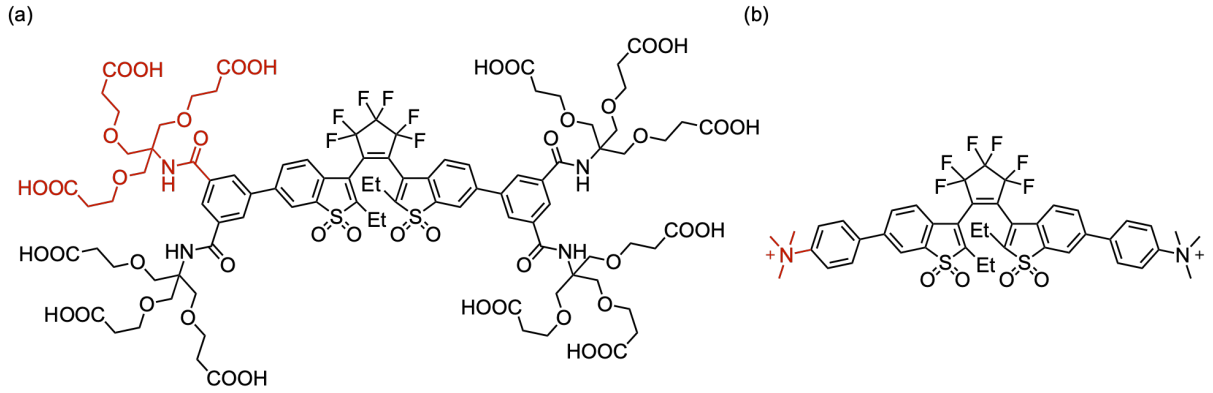
Scheme 2.8 DTE photoswitches bearing charged (a) *N*-methylpyridinium, (b) sulfonate groups, and (c) both. The red color highlights the solubilizing group.

Miyamoto synthesized a DTE bearing two sulfonate groups (Scheme 2.8b). Their aim was to investigate the host-guest chemistry between the DTE-sulfonate and cyclodextrins. The parent doubly charged DTE (as the sodium salt) exhibits excellent water solubility and undergoes photocyclization with a quantum yield of 73%, achieving a remarkable 96% PSD in

the forward direction. Upon addition of cyclodextrins, the DTE molecule forms inclusion complexes with β and γ cyclodextrins.

In a related study, Colaço and co-workers synthesized a zwitterionic DTE bearing both positively charged alkyl-pyridinium groups and negatively charged sulfonate groups to investigate the host-guest chemistry with cucurbit[8]uril (Scheme 2.8c).[45] The parent DTE is readily soluble in water and undergoes photocyclization with a quantum yield of 4%. After complexation, the photocyclization quantum yield increases to 25%.

The Irie and Hell groups have developed several water-soluble fluorescent DTEs for applications in super-resolution microscopy (Scheme 2.9). These DTEs, featuring oxidized benzothiophene heteroaryl rings, do not exhibit fluorescence in the open form but display strong fluorescence signals in the closed form, with fluorescence quantum yields reaching up to 60%.[52] The first fluorescent DTE (Scheme 2.9a) developed by these groups employed a branching approach to incorporate twelve carboxylic acids as solubilizing groups.[52] The resulting molecule is soluble in water and can achieve a PSD of 97% in the forward direction. The forward and reverse photocyclization quantum yields are 0.52 and 0.02, respectively.



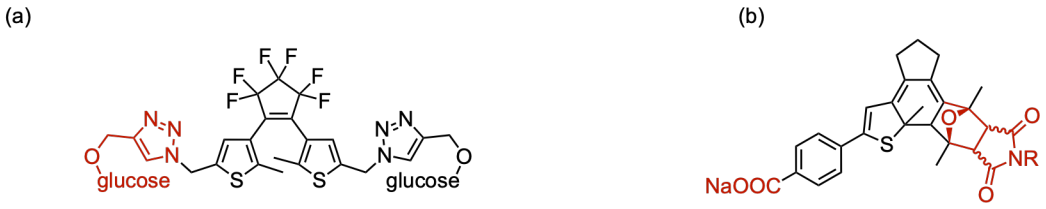
Scheme 2.9 Water-soluble fluorescent DTEs developed by the Irie group and the Hell group bearing (a) carboxylic acid solubilizing groups and (b) trimethylammonium solubilizing groups. The red color highlights the solubilizing group.

The second example also utilizes the fluorescent DTE motif but incorporates two trimethyl ammonium cations to achieve water solubility (Scheme 2.9b).[60] The parent DTE undergoes quantitative conversion when irradiated with 365 nm light in water. However, the fatigue resistance of this DTE is not optimal, with a photobleaching half-life of only 80 cycles. To address this issue, the parent DTE is complexed with a cucurbit[7]uril (CB7), extending the photobleaching half-life to an impressive 2560 cycles.

Tong and colleagues synthesized a glucose-DTE-glucose trimer using CuAAc chemistry (Scheme 2.10a).[57] The incorporation of triazole and glucose motifs significantly enhanced the

water solubility of the molecule. However, the molecule only has a PSD of 40% in the forward direction.

Göstl and co-workers developed an asymmetric DAE analogue for the photoswitchable release of maleimides.[56] The molecule features a conventional thiophene heterocycle on one end and a bicyclic ring system on the other (Scheme 2.10b). The water solubility of the molecule is enhanced by the charged carboxylate group and a maleimide moiety. The photoswitching of this DAE analogue involves the release of the maleimide functional group to restore a furan.



Scheme 2.10 (a) Water-soluble glucose-DTE-glycose trimer developed by Tong and co-workers. (b) Photochemical drug release system developed by Göstl and co-workers. The red color highlights the solubilizing group.

2.1.4 Project Aim

Although hundreds of DTEs have been synthesized,[4, 61, 62] there are few systematic structure-property studies of their photophysical and photochemical properties.[63, 64] Moreover, most reports focus on symmetrical DTEs. To the best of our knowledge, only a few push-pull DTEs bearing an electron donor on one arm and an electron acceptor on the other have been explored.[65-68] Moreover, there is little systematic information on the impact of electronic substitution patterns on the photophysical and photochemical properties of DTEs. This chapter aims to explore the synthesis of a family of symmetrical and asymmetrical DTEs using novel synthetic pathway and then evaluate the DTEs' photochemical and photophysical behaviors. Through systematic measurements of UV-vis absorption spectra, PSD, photoswitching quantum yields and further rationalization with DFT and TD-DFT calculations, this chapter will establish a structure-property relationship for push-push, pull-pull, and push-pull DTEs.

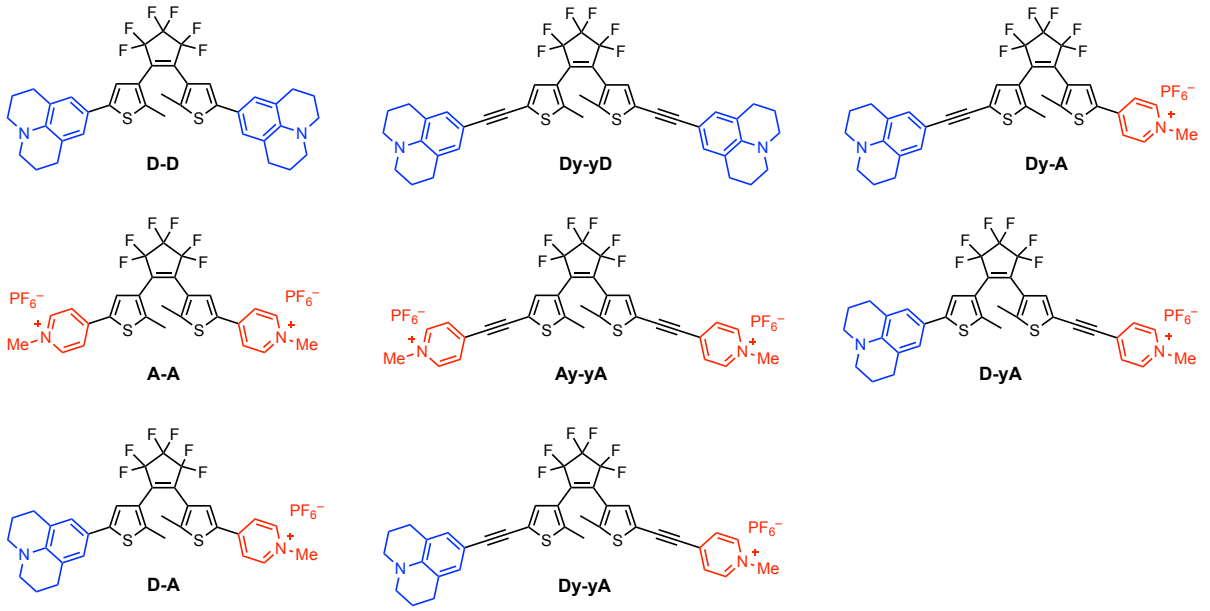
Organic π-systems end-capped with an electron donor (D) and an electron acceptor (A) are intriguing because the D-A interaction, or intramolecular charge transfer (ICT), reduces the HOMO-LUMO energy gap, leading to lower-energy π-π^* transitions.[69] Incorporating a photoswitchable π-system between the donor and acceptor would allow control of the ICT interaction. In push-pull DTEs, ICT can only occur in the closed form. The extent of ICT controls the wavelength of absorption, making it possible to shift the absorption band of the

closed form, while keeping the absorption of the open form unaffected, potentially leading to better control of the optimal wavelengths for switching in each direction.

2.2 Results and Discussion

2.2.1 Design and Synthesis of DTE Photoswitches

We prepared a collection of push-push, pull-pull, and push-pull DTEs with different lengths of conjugation (Scheme 2.11), intending to understand the impact of electron donor and acceptor, as well as the length of conjugation on the photophysical and photochemical properties of DTEs. We selected julolidine (blue, Scheme 2.11) to be a representative electron donor because the lone pair of electrons on the nitrogen is delocalized into the aromatic ring to a larger extent compared to other aniline derivatives. Charged *N*-methylpyridinium (red, Scheme 2.11) was selected as the electron acceptor. This ionic functional group has the added benefit of increasing the solubility of DTEs in polar solvents, facilitating biologically relevant applications. Compounds with short conjugation contain a functional end-group directly attached to the thiophene of the DTE core. The conjugation is extended by incorporating additional alkynes between the thiophene and the functional end-group. Extended conjugation with alkyne will result in red-shifted absorption spectra of open DTE and thus allow visible-light photoswitching at 405 nm. Previous work by Irie and co-workers[42] has shown that **A**-**A** is the DTE with the highest photocyclization quantum yield reported to date, due to the Coulombic repulsion between the two cationic moieties. The monocationic analogue with a *N*-methylpyridinium group on one arm and a phenyl group on the other arm has a moderate photochemical quantum yield, three times smaller than **A**-**A**.



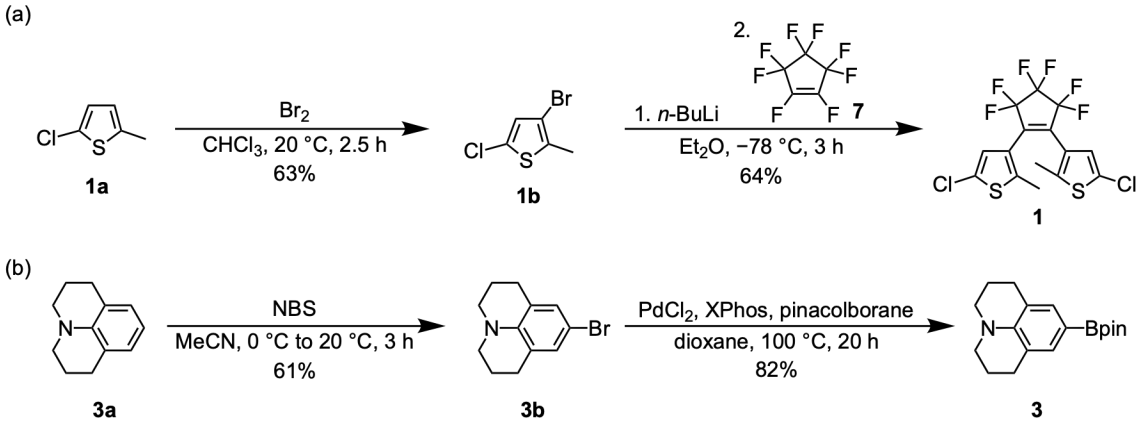
Scheme 2.11 Structures of the open-form DTEs synthesized, bearing donor-donor, acceptor-acceptor or donor-acceptor substitution patterns. Electron donor and acceptor are julolidine (blue) and *N*-methylpyridinium (red), respectively. D, A, y and - represent the donor, the acceptor, the alkyne, and the central DTE core respectively. Donor pushes electron density into π system while acceptor pulls electron density.

The synthesis of DTEs involves two key steps: formation of the photoresponsive DTE hexatriene core and attachment of the functionalized arms onto thiophene. The order of these two steps is not critical, provided that the functional groups on the thiophene arm are chemically compatible with the process of forming the DTE core (which typically requires *n*-BuLi). The synthetic approaches in which the DTE core is assembled prior to arm functionalization are referred to as core-to-arm methods, whereas the methodologies that introduce the DTE core at a later stage are known as arm-to-core methods. Both strategies enable the efficient synthesis of DTEs bearing functionalized arms.

Symmetrical push-push **D**-**D** and pull-pull **A**-**A**, and asymmetrical push-pull **D**-**A** with functional groups directly linked to the central thiophene were synthesized following the route shown in Scheme 2.12 and Scheme 2.13. The synthetic route started with the formation of a photoswitchable core DTE **1** dichloride following a procedure developed by Hermes with optimizations in the purification (Scheme 2.12a).[2] By optimizing the time required for lithium-halogen exchange with *n*-BuLi, we achieved a yield of 64%, which surpasses any previously reported yields in the literature. The aryl chloride site of DTE **1** can undergo Suzuki-Miyaura coupling reactions with chemical building blocks bearing boronic acid (or related) functional groups, allowing further functionalization of the DTE core.

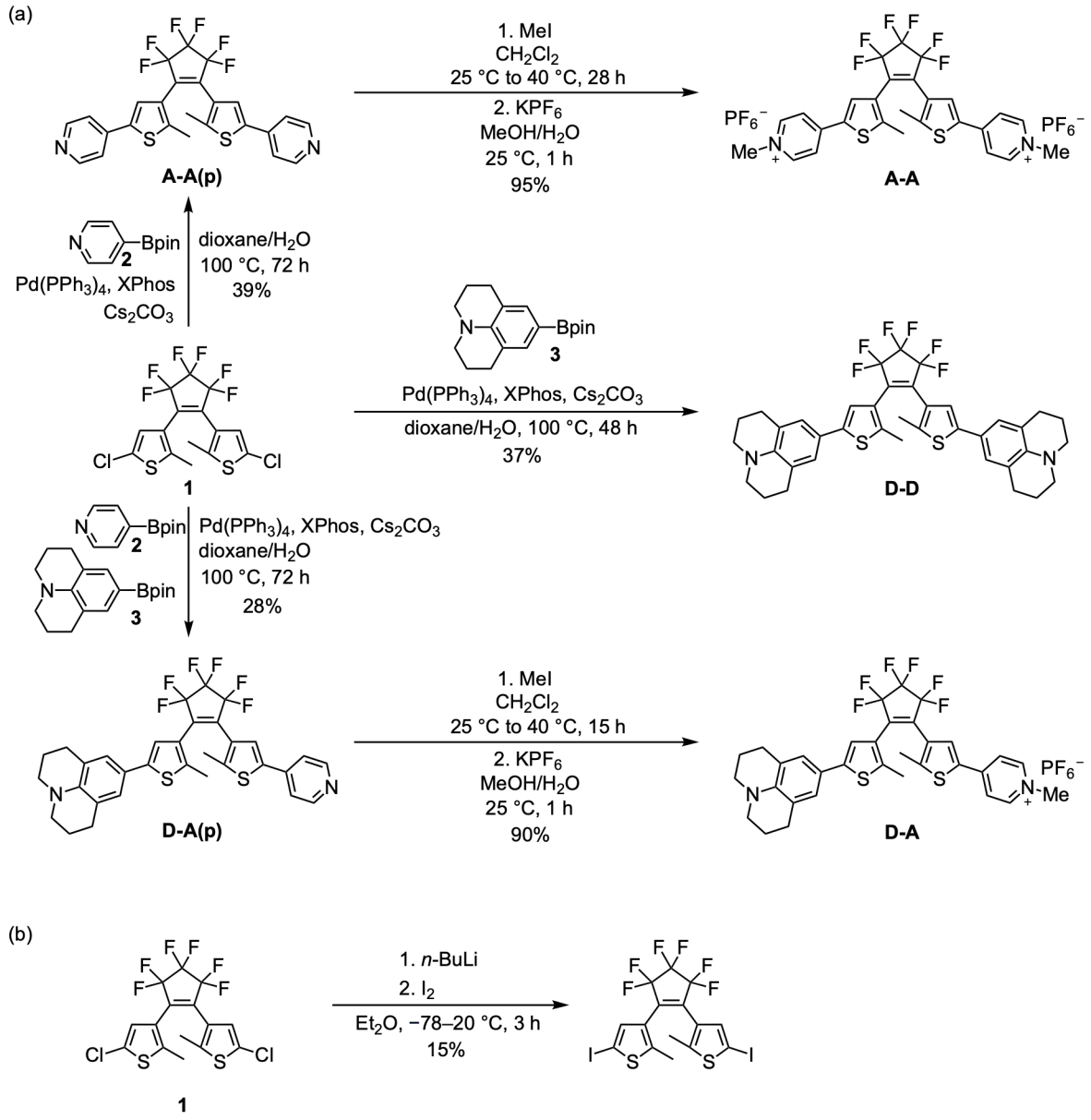
To incorporate julolidine groups, the boronate ester coupling partner **3** was synthesized by aromatic halogenation following a published procedure[70] with modification in the

purification method, followed by a Miyaura borylation with modified palladium catalyst ligand (Scheme 2.12b).[71]



Scheme 2.12 Synthesis of core DTE dichloride **1** and julolidine boronic acid pinacol ester **3**.

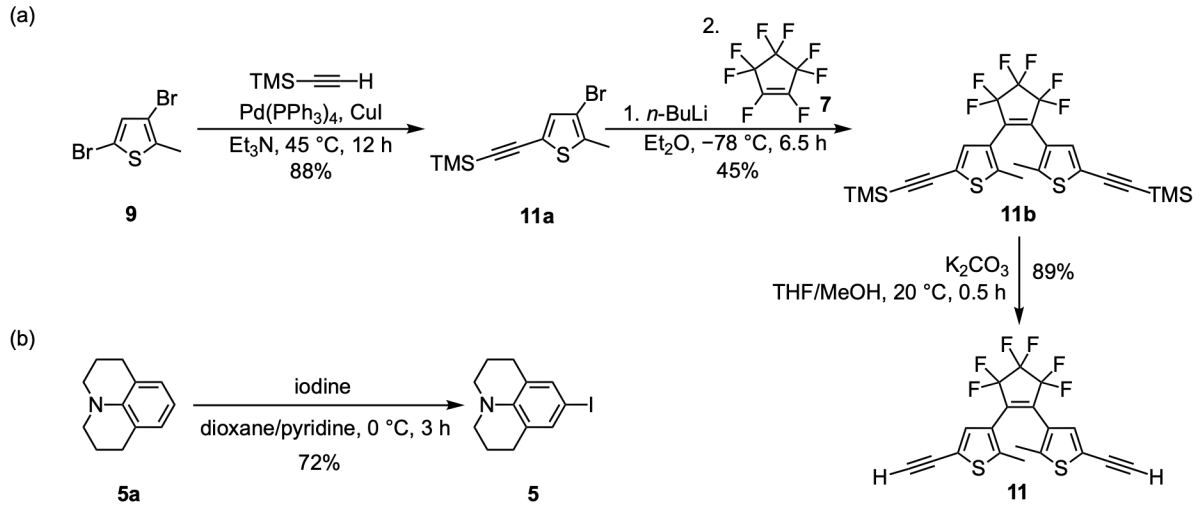
The structure of core DTE **1** was then extended by Suzuki-Miyaura coupling with julolidine-Bpin **3**, pyridine-Bpin **2**, or both in one pot to yield symmetrical **D-D** and **A-A(p)**, and asymmetrical **D-A(p)**, respectively (Scheme 2.13a). **D-D**, **A-A(p)** and **D-A(p)** could be separated easily by column chromatography on silica. One drawback of functionalization with Suzuki-Miyaura coupling at the aryl chloride site is that chloride is generally less reactive compared to aryl bromides or aryl iodides, as demonstrated by the 37% yield of **D-D** and 39% yield of **A-A(p)**. Although it is possible to replace the thienyl chloride with thienyl iodide using *n*-BuLi and iodine (Scheme 2.13b) for a more efficient Suzuki-Miyaura coupling, this method typically results in low yield of less than 20% and thus it was not employed.



Scheme 2.13 (a) Core-to-arm synthesis of **D-D**, **A-A** and **D-A** from DTE dichloride **1**. (b) Halogen exchange from aryl thienyl chloride to thienyl iodide.

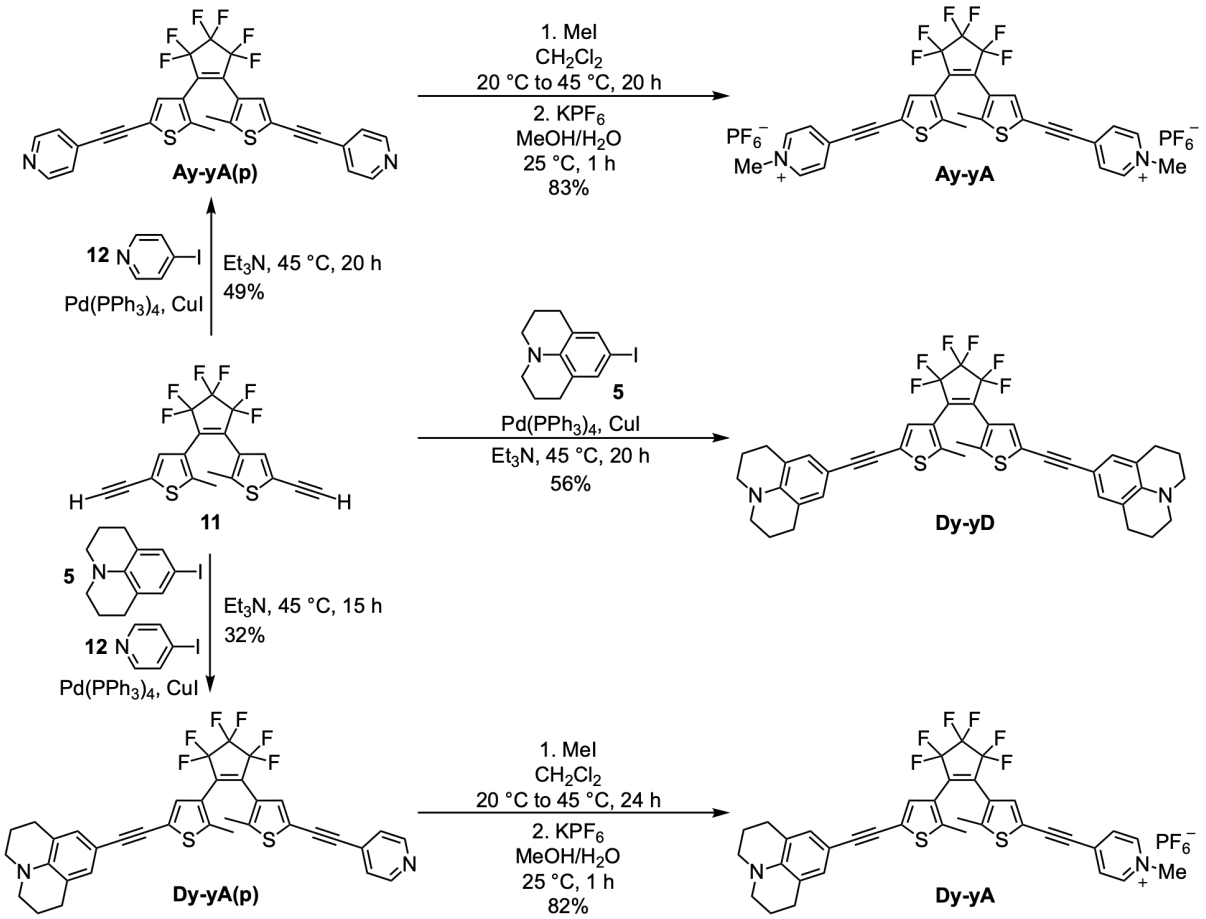
The final methylated **A-A** and **D-A** compounds were obtained by treating **A-A(p)** and **D-A(p)** with an excess of methyl iodide (Scheme 2.13a), generating an electron-withdrawing *N*-methylpyridinium group. To enhance the solubility in organic solvents for photophysical and photochemical studies, and to prevent the reverse reaction caused by iodide ion attacking the methyl group, the counterion was exchanged from iodide to hexafluorophosphate. This was achieved through a precipitation process using an aqueous solution of potassium hexafluorophosphate or ammonium hexafluorophosphate. The choice of counterion significantly influences the overall solubility of the molecule. For instance, the iodide and chloride salts of **A-A** exhibit high solubility in water, whereas the hexafluorophosphate salt of **A-A** is soluble in acetonitrile but not in water or methanol.

Push-push **Dy-yD**, pull-pull **Ay-yA**, and push-pull **Dy-yA** with additional alkynes were also synthesized following the core-to-arm approach (Scheme 2.14 and Scheme 2.15). The synthesis began with the preparation of a TMS-protected intermediate **11a** via a Sonogashira coupling. The TMS-protected DTE intermediate **11b** was then constructed using a strategy similar to the synthesis of DTE dichloride **1**, involving a lithium-halogen exchange between *n*-BuLi and the thienyl bromide, followed by addition-elimination on the sp^2 carbons of octafluorocyclopentene **7**. Photochromic behavior was observed on the TLC plate once the DTE core was formed. Subsequent deprotection of the TMS-protected compound **11b** with potassium carbonate yielded the key DTE intermediate **11**, bearing two free terminal alkynes (Scheme 2.14a).



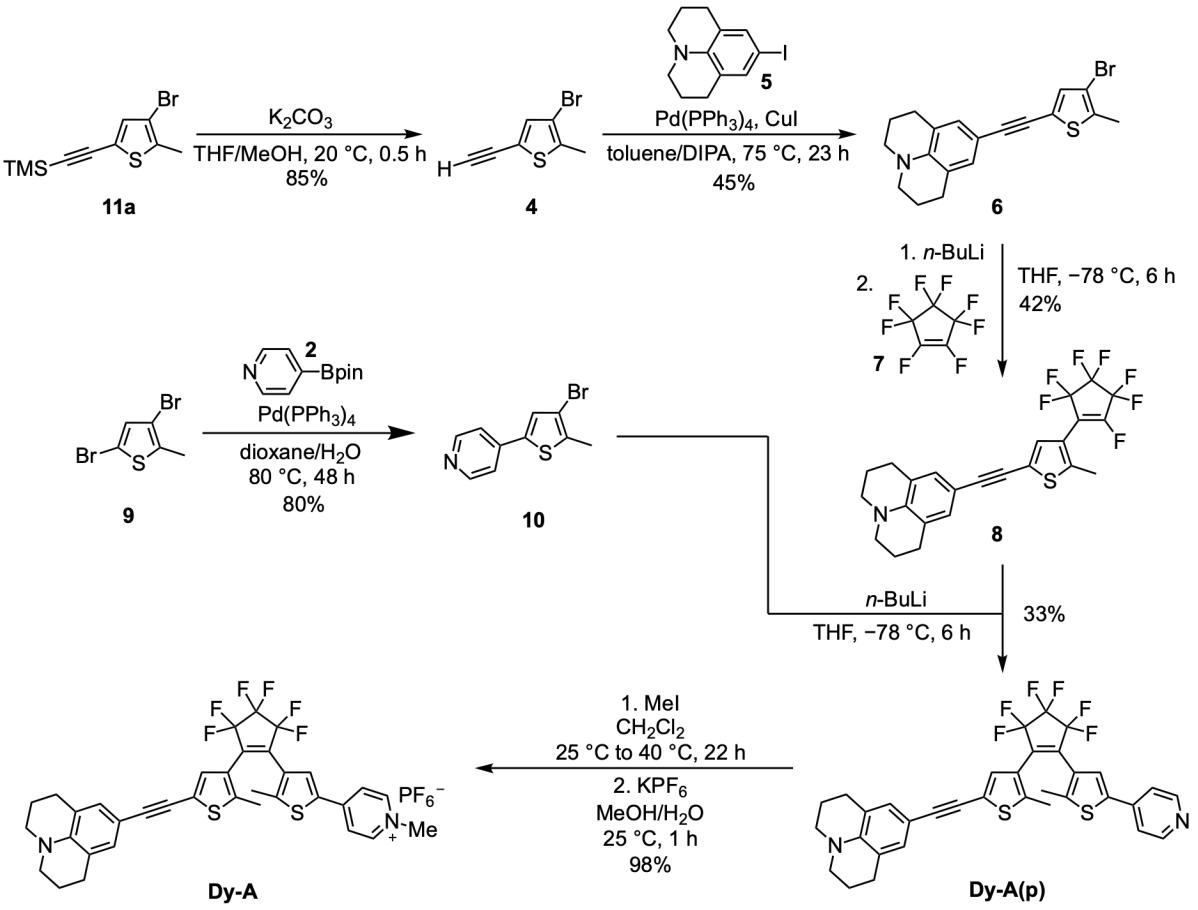
Scheme 2.14 (a) Synthesis of DTE core **11** bearing two free terminal alkynes and (b) iodination of julolidine.

The electron-rich Sonogashira coupling partner **5** was prepared by the iodination of julolidine with iodine in a 1:1 dioxane/pyridine solvent mixture (Scheme 2.14b). The structure of **11** was then extended through Sonogashira coupling reactions with 4-iodojulolidine **5**, 4-iodopyridine **12**, or both in a one-pot process, to afford **Dy-yD**, **Ay-yA(p)**, and **Dy-yA(p)**, respectively (Scheme 2.15). The Sonogashira coupling reactions result in higher yields than the Suzuki-Miyaura coupling reaction employed for preparing **D-D**, **A-A(p)** and **D-A(p)**. These three molecules also exhibit good separation on column, enabling efficient separation of **Dy-yA(p)** from the other two. To prepare **Ay-yA** and **Dy-yA**, the pyridine moiety was subjected to methylation to generate an electron-withdrawing *N*-methylpyridinium group. Finally, the counterion was exchanged from iodide to hexafluorophosphate.



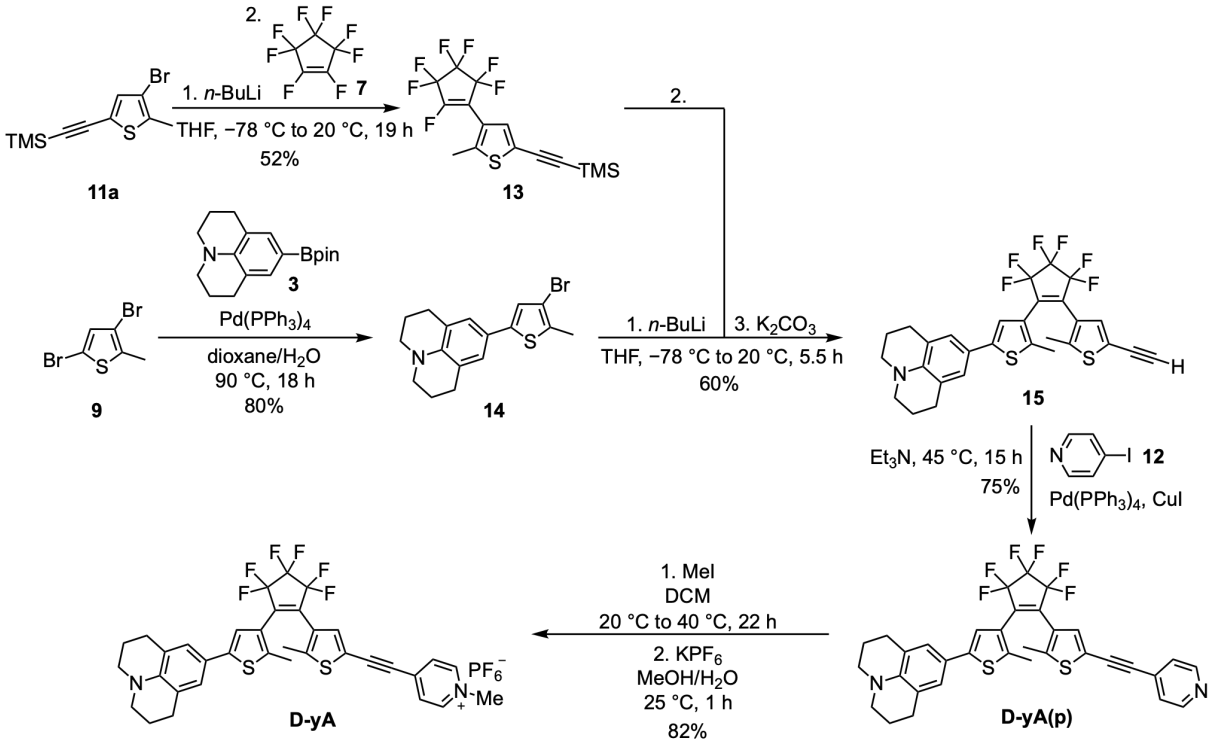
Scheme 2.15 Core-to-arm synthesis of **Dy-yD**, **Ay-yA** and **Dy-yA** from DTE **11**.

Due to the asymmetric conjugation pattern, **Dy-A** and **D-yA** cannot be prepared by from Suzuki or Sonogashira reactions alone. Instead, the DTE core must be assembled from two distinct thiophene fragments to break the symmetry. Thus, **Dy-A** (Scheme 2.16) and **D-yA** (Scheme 2.17) are prepared using arm-to-core strategies. These approaches involve the functionalization of the DTE arm prior to the reaction with octafluorocyclopentene **7**. In the case of **Dy-A** (Scheme 2.16), the electron-rich arm **6** and the electron-poor arm **10** were synthesized through Sonogashira and Suzuki coupling reactions, respectively. The two arms were then sequentially added to the perfluorinated bridge. The intermediate **8**, with one arm attached, can be isolated and purified before incorporating the second arm. Finally, the pyridine moiety was subjected to methylation.



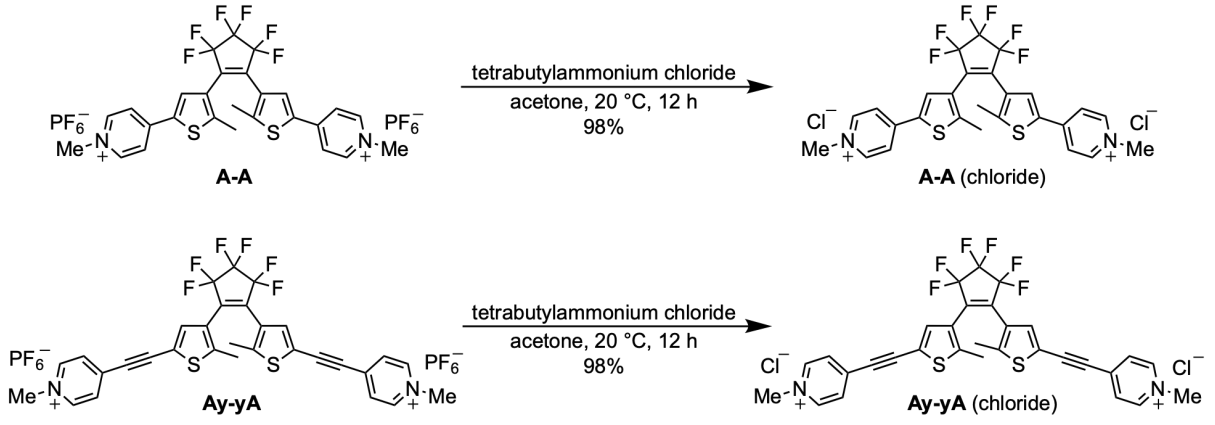
Scheme 2.16 Arm-to-core synthesis of **Dy-A**.

D-yA was prepared using a similar approach (Scheme 2.17). First, the TMS-protected thiophene was added to octafluorocyclopentene **7** to form the intermediate **13.** A fully functionalized electron-deficient arm bearing a pyridine group was not employed in this reaction, as it led to decomposition and failed to yield the desired product. Although the decomposition products were not characterized, it is probable that the electron-deficient arm with alkyne spacer is incompatible with *n*-BuLi. The electron-rich arm **14** was prepared via Suzuki-Miyaura coupling and subsequently added to the intermediate **13**, resulting in the DTE intermediate **15** after deprotection. The pyridine moiety was then incorporated through Sonogashira coupling. Finally, the pyridine group was subjected to methylation to afford **D-yA**. Ion exchange from iodide to hexafluorophosphate was performed for both **Dy-A** and **D-yA**.



Scheme 2.17 Arm-to-core synthesis of **D-yA**.

To enhance the water solubility of **A-A** and **Ay-yA** and facilitate the measurement of their photochemical and photophysical properties in aqueous media, the hexafluorophosphate counterion was replaced with chloride, yielding **A-A** (chloride) and **Ay-yA** (chloride). This ion exchange was performed following the procedure outlined by Pace et al. (Scheme 2.18), which involves the precipitation of the chloride salt from acetone.[72] By converting the compounds to their chloride salts, their solubility in water is significantly improved.



Scheme 2.18 Anion exchange to form **A-A** (chloride) and **Ay-yA** (chloride).

2.2.2 Photochromism

The photophysical and photochemical properties of each DTE were investigated in two solvents with varying polarity. The neutral push-push DTEs, **D-D** and **Dy-yD**, and the monocationic

push-pull DTEs, **D-A**, **Dy-yA**, **Dy-A**, and **D-yA**, were studied in THF and in MeCN. Due to their poor solubility in THF, **A-A** and **Ay-yA** were studied in MeCN but not THF. After changing the counterion of **A-A** and **Ay-yA** from hexafluorophosphate to chloride (Scheme 2.18), the resulting derivatives were studied in water.

Initial assessment of the photochromism of the DTEs was performed by UV-vis spectroscopy. UV-vis spectra of the compounds in their open forms were recorded in two solvents before irradiation with 365 nm light. All compounds exhibit strong absorption bands around 360 nm which gradually disappear upon UV irradiation (Figure 2.4). In all cases, irradiation at 365 nm leads to the emergence of broad absorption bands in the visible to NIR regions. The switching causes a color change of the sample from colorless to green/blue, except for **D-A**, which changes to pale yellow. Switching most of these DTEs in the two solvents usually results in similar colors, indistinguishable by eye. However, for **Dy-yA** and **D-yA**, only very faint colors achieved in MeCN while much more intense colors are achieved in THF, indicative of a large difference in the PSD with lower conversion in MeCN. Irradiation at 630 nm was used to drive the photoreversion. UV-vis spectra showed that the closed-form absorption band of all DTEs at >600 nm completely disappeared after irradiation at 630 nm, indicating 100% conversion back to the open form.

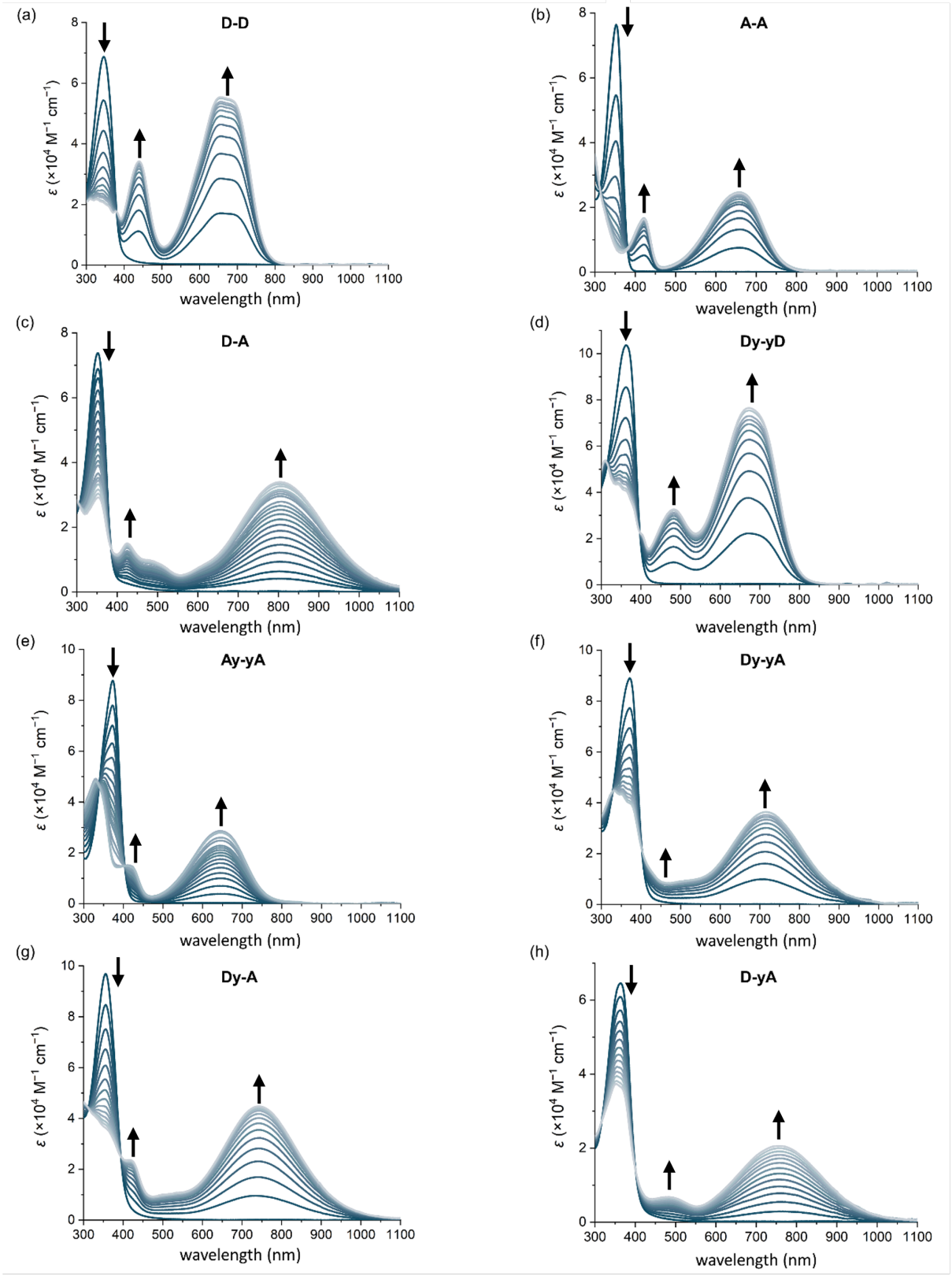


Figure 2.4 UV-vis-NIR spectra of DTEs showing the photocyclization from open form to PSS upon 365 nm light irradiation at 25 °C. **D-D**, **D-A**, **Dy-yD**, **Dy-yA**, **Dy-A** and **D-yA** were measured in THF. **A-A** and **Ay-yA** were measured in MeCN. Each DTE was switched with a different power setting and irradiation time due to different rate of switching. The power and irradiation time between two consecutive spectra are summarized in Table 2.1.

Table 2.1 Irradiation power (365 nm) and irradiation time between two consecutive spectra for acquiring the spectra shown in Figure 2.4.

Compound	Solvent	Power (mW)	Irradiation Time (s)
D-D	THF	18.9	1
A-A	MeCN	12.3	1
D-A	THF	159	60
Dy-yD	THF	18.9	1
Ay-yA	MeCN	12.3	1
Dy-yA	THF	159	20
Dy-A	THF	159	20
D-yA	THF	159	30

Kinetic traces of the photoswitching for all compounds were shown in Figure 2.5 by plotting the absorbance of the closed-form absorption band in the red-NIR region against time. The data were fitted using a first-order kinetic model. Although the *k* values provided in the Figure 2.5 allow for a comparison of the rates of photocyclization, it is important to note that different light intensities (Table 2.1) were used to trigger the processes. Therefore, the *k* values alone do not provide a direct measure of the intrinsic switching rates. However, based on the available data, it can be concluded that **A-A** exhibits the most efficient photocyclization among the compounds studied, as it has the highest *k* value despite being switched with the lowest light intensity. In contrast, **D-A** exhibits the least efficient photocyclization. In the concentration range of 2.5–5 μM (Figure 2.4 and Figure 2.5), under irradiation at 365 nm, **A-A** reaches the PSS in 15 s in MeCN with 12.33 mW irradiation (0.56 mol of photons), whereas **D-A** takes 800 s in THF with 159 mW irradiation (388 mol of photons).

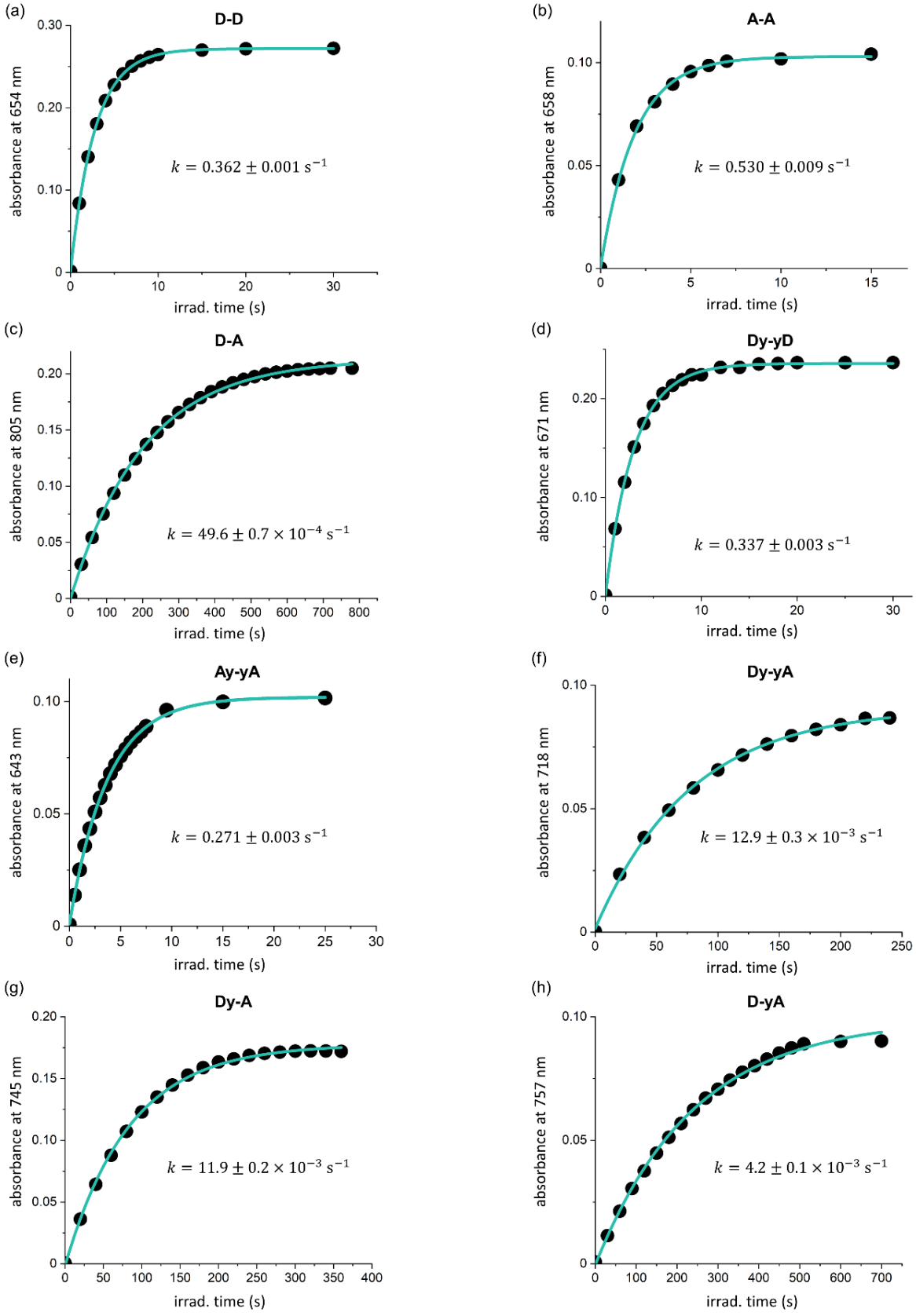


Figure 2.5 The kinetic trace of photocyclization upon 365 nm light irradiation (monitored at the absorption maxima of the closed-form) extracted from the UV-vis-NIR spectra shown in Figure 2.4 and the fitted first-order curve with respect to time of irradiation.

2.2.3 Structural Impact on UV-vis Absorption Spectra

The absorption spectra of all the compounds were recorded in two different solvents, as summarized in Table 2.2 and Figure 2.6 to deduce structure-property relationships between the absorption wavelengths and the substitution pattern. The molar absorption coefficients were measured by an NMR reference method (Section 2.4.3). The closed-form UV-vis absorption spectra were calculated from the PSD (Section 2.2.4) obtained by NMR.

The open isomers of all the DTEs have λ_{max} between 350 nm and 400 nm. The substitution pattern does not significantly affect the absorption spectra of the open DTEs, as **D-D**, **A-A**, and **D-A** absorb at 346 nm, 357 nm, and 350 nm, respectively, in MeCN (Table 2.2 and Figure 2.7a). The additional alkyne units in **Dy-yD**, **Ay-yA** and **Dy-yA** lead to a 15–20 nm bathochromic shift of the absorption spectra compared to **D-D**, **A-A** and **D-A** (Table 2.2). These red-shifts caused by alkyne spacer on both arms significantly increase the molar absorption coefficient at 405 nm (from 271 M^{-1} cm^{-1} for **A-A** to 11700 M^{-1} cm^{-1} for **Ay-yA**), allowing the compounds to be switched at this wavelength. The closed DTEs have two main absorption bands in the visible region, one in the 400–500 nm range (minor, closed-DTE absorption band 1) and another in the red-NIR range (major, closed-DTE absorption band 2, Table 2.2 and Figure 2.6).

Table 2.2 Absorption maxima and molar absorption coefficients of open and closed DTEs in different solvents.

DTE	Solvent	λ_{max}^{o} (nm)	ε (10^3 M^{-1} cm^{-1})	$\lambda_{max}^{c\text{-}1}$ (nm)	ε (10^3 M^{-1} cm^{-1})	$\lambda_{max}^{c\text{-}2}$ (nm)	ε (10^3 M^{-1} cm^{-1})
D-D	THF	346	52.4	439	24.8	654	42.7
	MeCN	346	53.0	439	25.1	667	43.1
A-A[a]	MeCN	353	61.2	421	12.8	658	19.1
	water	357	61.5	424	12.7	659	19.0
D-A	THF	352	57.4	425	17.4	805	38.2
	MeCN	350	57.2	423	17.8	792	38.1
Dy-yD	THF	362	85.1	483	26.7	671	47.3
	MeCN	363	84.8	479	27.4	673	41.9
Ay-yA[a]	MeCN	371	67.1	411	11.8	643	22.3
	water	377	69.5	415	11.6	650	23.1
Dy-yA	THF	371	71.0	/	/	718	37.8
	MeCN	369	72.4	/	/	693	37.6
Dy-A	THF	356	76.1	418	20.2	745	29.4
	MeCN	354	74.2	417	16.6	724	26.5
D-yA	THF	364	58.6	484	10.8	757	32.3
	MeCN	364	55.7	484	10.4	753	35.1

[a] Measured in MeCN as the hexafluorophosphate salt and in water as the chloride salt.

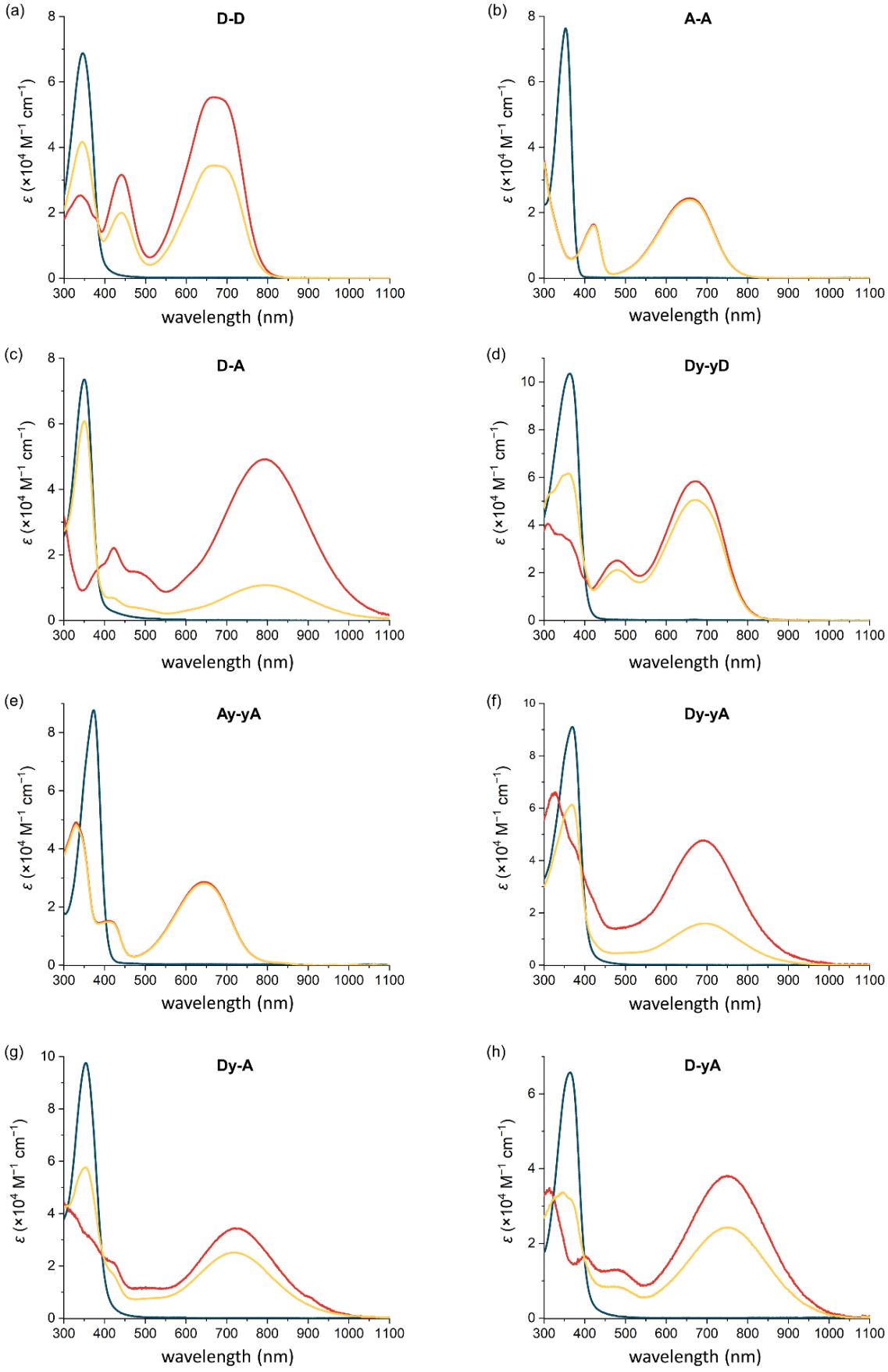


Figure 2.6 UV-vis-NIR absorption spectra of DTEs in acetonitrile. The blue line represents the open-DTE absorption; the yellow line represents the absorption at PSS (365 nm); the red line represents calculated spectra of the closed DTE.

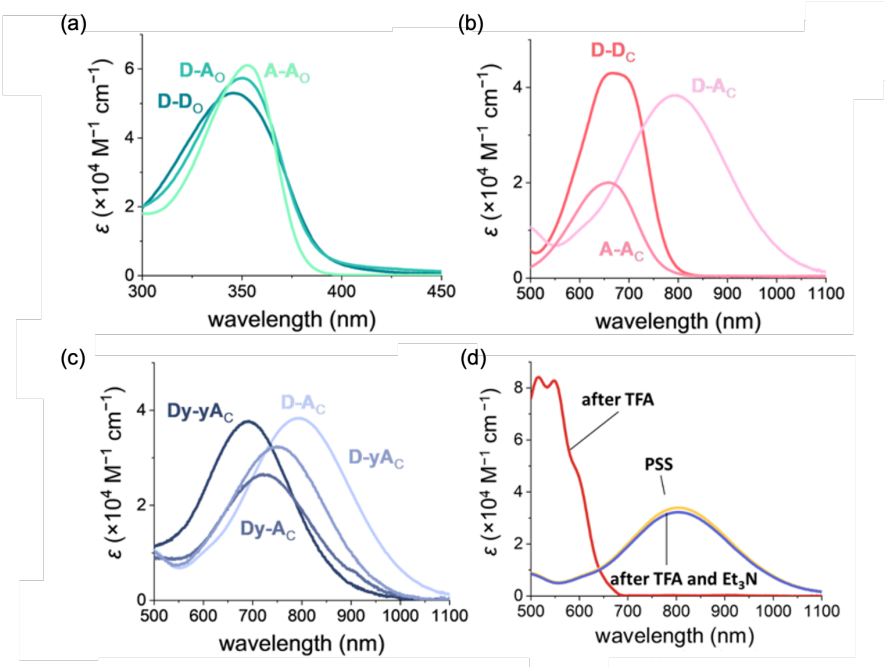


Figure 2.7 Absorption spectra of (a) open and (b) closed **D-D**, **A-A** and **D-A** in MeCN. (c) Absorption spectra of closed **D-A**, **Dy-A**, **D-yA** and **Dy-yA** in MeCN. (d) Absorption spectra of **D-A** at PSD in MeCN (yellow), MeCN + 0.5% TFA (red), and MeCN + 0.5% TFA + excess Et_3N (blue).

The impact of additional alkynes on the closed push-push and pull-pull DTEs is subtle, with a 6 nm red shift of the lowest-energy absorption of **Dy-yD** compared to **D-D** and 15 nm blue-shift of the lowest-energy absorption of **Ay-yA** compared to **A-A** (Table 2.2). The red-shift of **Dy-yD** compared to **D-D** can be attributed to the extended length of π-conjugation. In contrast, for **A-A** and **Ay-yA**, ICT can readily take place between the electron-rich central thiophene groups and the electron-deficient *N*-methylpyridinium groups. The charge transfer is strongest when the electron acceptor is directly connected to the electron donor, and becomes weaker with additional alkynes.[73] Therefore, the excited state of **Ay-yA** is less stabilized by the polar MeCN compared to **A-A**, resulting in the hypsochromic shift of the absorption band.

Despite having no clear impact on the absorption maximum of the open DTEs, the push-pull substitution patterns significantly red-shift the absorption maximum of the closed DTEs, as illustrated by the closed **D-A** absorbing at 792 nm while **D-D** and **A-A** absorbing at 667 nm and 658 nm, respectively (Figure 2.7b). The >100 nm bathochromic shift of the absorption band is attributed to the ICT between the electron-donating julolidine group and the electron-accepting *N*-methylpyridinium group. Similar red shifts of the closed DTE absorption due to donor-acceptor interaction is observed in other push-pull DTEs (Figure 2.7c). However, the red-shift of **Dy-yA** (50 nm red-shift compared to **Ay-yA**) is less profound than that of **D-A**. The closed-form absorption maxima of **Dy-A** and **D-yA** with one alkyne in the backbone lie in between the absorption of **D-A** and **Dy-yA**, at 724 nm and 753 nm,

respectively, indicative of the insulating effect of triple bonds in the donor-π-acceptor conjugated system. In a protonation experiment, the absorption band of closed **D-A** is blue-shifted by >100 nm upon TFA protonation but recovered with excess triethylamine (Figure 2.7d).

2.2.4 Photostationary State Distribution

After an initial assessment of photochromism and UV-vis absorption, we measured the PSD upon 365 nm irradiation for each compound in two different solvents, i.e., THF and MeCN for neutral and monocationic species; MeCN (as hexafluorophosphate salts) and water (as chloride salts) for **A-A** and **Ay-yA**. In the less polar solvent, the PSD was determined using an NMR integration method (Section 2.4.6). The ratios of the open and closed isomers were determined by comparing the ^{1}H NMR integrations of the thiophene protons before and after irradiation at 365 nm (Figure 2.8 and Section 2.4.6).

Figure 2.8 shows the ^{1}H NMR signal of the thiophene proton and aromatic protons of **D-D** in its open and closed forms. In the open form, the thiophene proton of **D-D** has a shift of 7.08 ppm while the julolidine aromatic proton has a shift of 6.94 ppm. Upon exposure to 365 nm light, which converts the open DTE to the closed form, the thiophene proton shifted upfield to 6.50 ppm while the julolidine aromatic proton shifted downfield to 7.03 ppm. The NMR spectra show quantitative photoswitching of **D-D** in THF, achieving >99% PSD. Other NMR spectra for PSD determination are given in experimental Section 2.4.6.

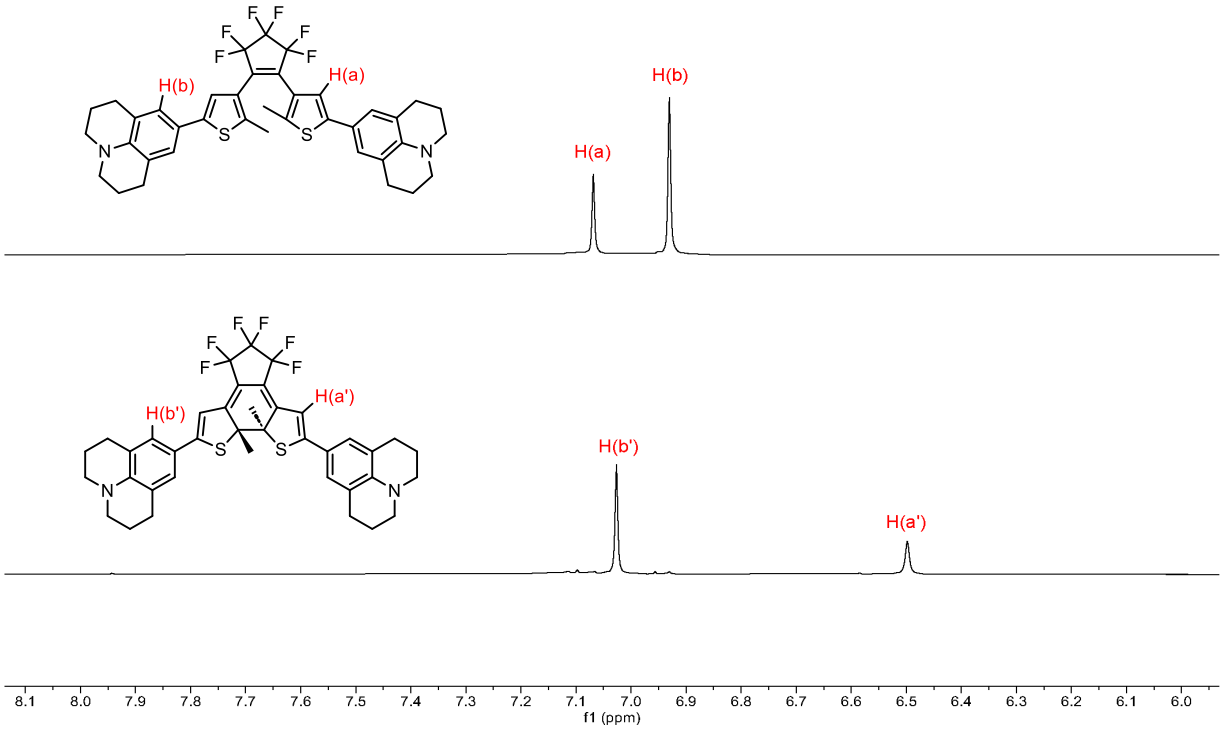


Figure 2.8 ^{1}H NMR spectra (500 MHz) of open **D-D** (top) and at PSS after 365 nm irradiation (bottom) in THF-d_8.

Due to slow switching, the PSD of **D-D**, **D-A**, **Dy-yD**, **Dy-yA**, **Dy-A**, and **D-yA** in MeCN could not be characterized by NMR. Even after several hours of irradiation at NMR concentrations, it was not possible to reach the PSS. As an alternative, UV-vis spectroscopy was employed to determine the PSD for these compounds. The UV-vis spectroscopy method involves measuring the absorption spectra of both the open DTEs and a DTE sample containing a known amount of the closed form in MeCN. The photoswitching process was then initiated in MeCN to reach the PSS. The PSD in MeCN was subsequently deconvoluted based on the principle that the absorption spectrum at the PSS is a linear combination of the absorption spectra of the open and closed forms of the DTE (Section 2.4.7).

Figure 2.9 shows the absorption spectra of open **Dy-yA** (blue), a **Dy-yA** sample containing 80% closed form (the PSS reached in THF, red) and at the PSS of **Dy-yA** achieved in MeCN (yellow). A quantitative model was established to calculate the UV-vis absorption spectra of **Dy-yA** and 33% PSD of **Dy-yA** in MeCN results in excellent match between the calculated spectra (green) and the experimental spectra (yellow).

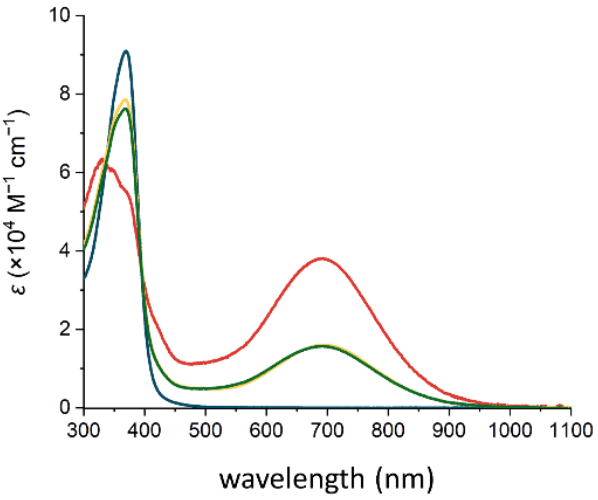


Figure 2.9 Determining the PSD of **Dy-yA** by a UV-vis method. The blue line represents the absorption of open-form **Dy-yA** in MeCN. The red line represents the absorption of a **Dy-yA** sample containing 80% closed isomer (the PSD in THF) in MeCN. The yellow line represents the experimental PSS achieved after 365 nm light irradiation in MeCN. The green line represents the calculated PSD containing 33% closed form in MeCN.

The PSDs of all the DTEs are summarized in Table 2.3. For the forward photocyclization reaction (365 nm), exceedingly high PSDs (>99%) are achieved by push-push **D-D** and **Dy-yD** in THF, and by pull-pull **A-A** and **Ay-yA** in MeCN and water. Changing from THF to more polar MeCN has a significant impact on the PSDs of push-push DTEs, illustrated by reductions of over 10% in the PSDs of both compounds. Solvent polarity has negligible impact on the PSDs of **A-A** and **Ay-yA**. These two molecules can be quantitatively switched in both MeCN and water. Push-pull DTEs have lower PSDs compared to push-push or pull-pull DTEs. The highest PSD of 85% is achieved by **Dy-A** in THF and the lowest PSD of 21% is achieved by **D-A** in MeCN. The PSDs of push-pull compounds are strongly affected by the solvent polarity, manifested by a reduction from 71% to 21% (**D-A**) when changing from THF to MeCN. While the photocyclization PSDs vary for different DTEs and in different solvents, the PSDs of the photoreversion upon 630 nm irradiation are quantitative for all compounds in all solvents, due to lack of absorption by the open DTEs at 630 nm.

Table 2.3 Summary of PSDs measured by NMR and UV-vis spectroscopy. Open-to-closed PSSs were achieved by irradiation with 365 nm or 405 nm light. Closed-to-open PSSs were achieved by irradiation with 630 nm light.

Compound	Solvent	PSD_{O-C} (365 nm) (%)	PSD_{O-C} (405 nm) (%)	PSD_{C-O} (630 nm) (%)
D-D	THF	>99	/	100
	MeCN	69	/	100
A-A[a]	MeCN	>99	/	100
	water	>99	71	100
D-A	THF	71	/	100
	MeCN	21	/	100
Dy-yD	THF	>99	/	100
	MeCN	86	/	100
Ay-yA[a]	MeCN	>99	/	100
	Water	>99	96	100
Dy-yA	THF	80	/	100
	MeCN	33	/	100
Dy-A	THF	85	/	100
	MeCN	64	/	100
D-yA	THF	66	/	100
	MeCN	26	/	100

[a] Measured in MeCN as the hexafluorophosphate salt and water as the chloride salt.

To investigate whether the additional alkyne, and the resulting redshift of the open absorption band, could permit DTEs to be switched with visible light, we measured the PSD of the chloride salts of **A-A** and **Ay-yA** in water upon 405 nm irradiation. The results in Table 2.3 demonstrate that **A-A** can achieve 71% PSD while **Ay-yA** can achieve 96% PSD, i.e. the additional alkyne on each arm leads to a 25% boost in PSD under 405 nm irradiation. To the best of our knowledge, the chloride salt of **Ay-yA** is the first example of water-soluble non-fluorescent DTE that can be switched to over 95% PSD in the forward direction and quantitatively in the reverse reaction with visible light.

The extent of spectral separation (or difference in molar absorption coefficient at a given wavelength) between the open and closed DTEs is a key contributing factor that affects the PSDs. For push-push and push-pull DTEs, the band separation is not optimal at 365 nm, the wavelength of irradiation. Generally, the molar absorption coefficient of the open form is two to five times greater than the closed form. In this poor band separation scenario, the predominant factor leading to the 99% PSD of **D-D** and **Dy-yD** in THF is the much greater quantum yield of photocyclization compared to the quantum yield of photoreversion (Section 2.2.5). The sensitivity of the PSD to the polarity of solvent environment can be mainly attributed to the different ratio of photocyclization quantum yield to photoreversion quantum yield in different solvents. For **A-A** at 365 nm, the molar absorption coefficient of the open form (42300 M^{-1} cm^{-1}) is approximately nine times greater than that of the closed form (4800 M^{-1} cm^{-1}). Thus, the band separation plays a more important role leading to >99% PSD

upon 365 nm irradiation. Photocyclization of **Ay-yA** triggered by 405 nm light is an intriguing example of a photoswitch in the poor band separation scenario, where the closed form (11800 M^{-1} cm^{-1}) absorbs more strongly than the open form (9800 M^{-1} cm^{-1}). Nevertheless, a high PSD of 96% is achieved due to the exceedingly high photocyclization quantum yield and low photoreversion quantum yield (Section 2.2.5). This example breaks the traditional rule for photoswitch design, which states that large band separation is crucial for a photoswitch to achieve high PSD.

2.2.5 Quantum Yield of Photoswitching

Quantum yields of photocyclization and photoreversion reactions were measured using the "initial slope" method in the low-concentration regime[74] with the experimental setup reported by Stadler and co-workers.[75] The photochemical quantum yield was calculated using Equation 2.1 as reported by Heckel and co-workers,[76] which is a general method for measuring the photochemical quantum yields of P-type (thermally irreversible) photoswitches, where Φ is the photochemical quantum yield of the reaction, m is the slope of the linear fit for the time-dependent absorbance change during irradiation (either appearance or disappearance of closed DTE monitored at the absorption maxima in the visible region, e.g. monitored at 654 nm for **D-D**), V is the volume of solution under irradiation, N_A is the Avogadro constant, h is the Planck constant, c is the speed of light, P is the irradiation power (in W), λ is the excitation wavelength, A is the absorbance at excitation wavelength, ε_{prod} is the molar absorption coefficient of the formed product at the monitoring wavelength (e.g. at 42700 M^{-1} cm^{-1} for **D-D** at 654 nm), l is the pathlength (1 cm).

$$\Phi = \frac{m \cdot V \cdot N_A \cdot h \cdot c}{P \cdot \lambda \cdot (1 - 10^{-A}) \cdot \varepsilon_{prod} \cdot l} \tag{2.1}$$

The power, P, of the light sources mic-LED-365, mic-LED-405 and mic-LED-630 were first measured with a Coherent® PowerMaxTM-USB/RS Sensor System power meter at various points of indicated power percentage (Table 2.4). These measurements were carried out at the end of the liquid light guide, immediately before the cuvette, so they give a measure of the light being delivered to the sample.

Table 2.4 Power of LED light sources measured from a Coherent® PowerMaxTM-USB/RS Sensor System.

Indicated Power Percentage (%)	Power of mic-LED-365 (mW)	Power of mic-LED-405 (mW)	Power of mic-LED-630 (mW)
2	10.4	12.1	7.17
5	16.8	18.6	10.9
10	27.6	29.7	17.3
20	47.2	50.5	28.8
30	68.3	71.1	39.8
40	88.5	90.3	51.7
50	107	109	63.4
60	127	127	75.3
70	147	144	86.5
80	/*	160	97.8
90	/	176	108
100	/	190	118

*The mic-LED-365 light source can be operated at a maximum percentage of 70%.

The power of the mic-LED-365 and mic-LED-405 light sources was also confirmed by a chemical actinometry method described in the experimental Section 2.4.4.[77, 78] A linear correlation between the power (mW) and the indicated output percentage was derived (Figure 2.10). The power obtained from the power meter matches well with that from the chemical actinometry measurement.

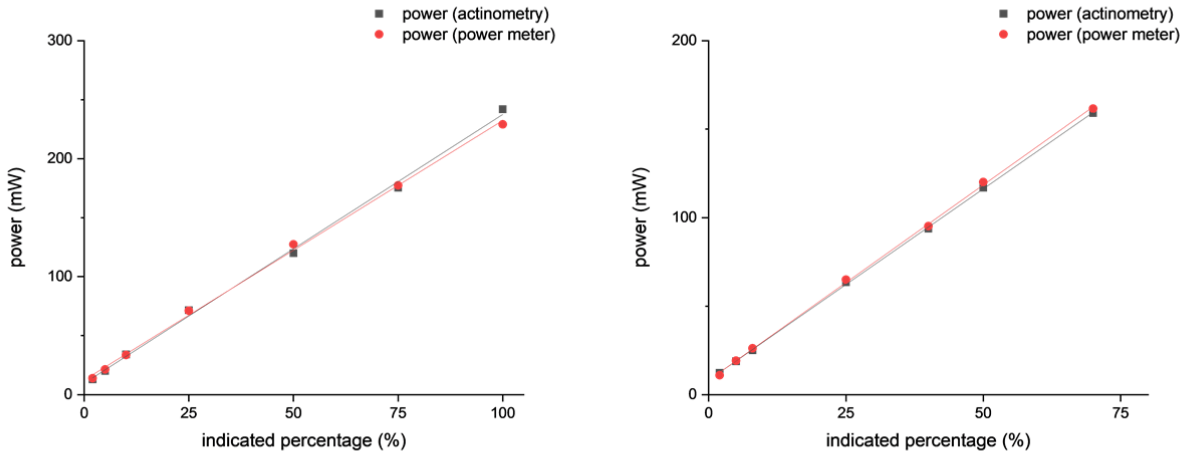


Figure 2.10 Linear correlation between the output percentage and power from actinometry or the power meter for mic-LED-365 (left) and mic-LED-405 light sources (right). For mic-LED-365 light source, the measurement points from actinometry are shown as black squares (linear fit: black line, $y = 2.16x + 8.19$, $R^2 = 0.998$). Measurement points from the power meter are shown as red circles (linear fit: red line, $y = 2.21x + 8.10$, $R^2 = 0.998$). For mic-LED-405 light source, the measurement points from actinometry are shown as black squares (linear fit: black line, $y = 2.29x + 9.64$, $R^2 = 0.997$). Measurement points from the power meter are shown as red circles (linear fit: red line, $y = 2.20x + 12.4$, $R^2 = 0.998$).

In the measurement of the photoswitching quantum yields, to accurately determine the initial slope (m) of the photochemical process, the power of the LED light source was turned down sufficiently that the formation of the product is linear (only 5%–10% of the product is formed during the process of measurement). Typical results are shown in Figure 2.11, demonstrating the linear fit of the initial slope of photocyclization and photoreversion of **D-D**

in THF and MeCN monitored at the closed-form λ_{max} in the visible region. The experimentally determined initial slope *m* was inserted into Equation 2.1 to determine the photoswitching quantum yields.

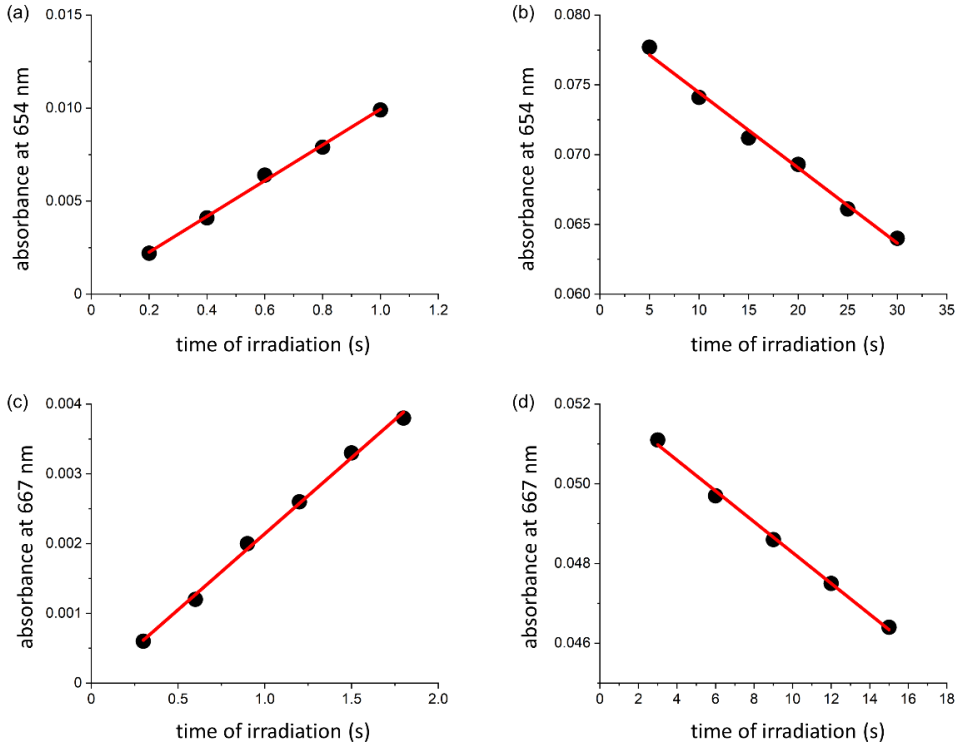


Figure 2.11 The initial region of the kinetic trace of (a) photocyclization and (b) photoreversion in THF, and (c) photocyclization and (d) photoreversion in MeCN of **D-D** and their linear fits. The gradient *m* of (a) 0.0100 ± 0.0004 s^{-1}, (b) 0.00057 ± 0.00002 s^{-1}, (c) 0.00222 ± 0.00005 s^{-1} and (d) 0.00036 ± 0.00002 s^{-1} were used in the calculation of photochemical quantum yields.

The gradients of linear fits and the photochemical quantum yields of all the DTEs are listed in Table 2.5. The quantum yields of UV-induced photocyclization are generally medium to high ($\Phi_{O\text{-}C}$ = 5–38%) for push-push DTEs (in non-polar solvents like THF) and pull-pull DTEs, but over two orders of magnitude lower for push-pull DTEs (in THF). **A-A** exhibits the highest photocyclization quantum yield (38% in water), which is over five times higher than **D-D** in THF (7.7%). Similarly, the photocyclization quantum yield of dicationic **Ay-yA** in water (17%) is approximately three-times higher than **Dy-yD** (5.5%) in THF. We observe a reduction in photocyclization quantum yield with insertion of alkynes into both push-push and pull-pull compounds This can be attributed to the smaller orbital contribution of the singlet excited state to the photoactive central hexatriene moiety.[13] However the cyclization quantum yields of push-pull DTEs increase from 0.020% (**D-A**) to 0.077% (**Dy-yA**).

Table 2.5 Summary of quantum yields of photocyclization and photoreversion measured by the initial slope method.

Compound	Solvent	$m_{o\text{-}c}$	$\varphi_{o\text{-}c}$ (%)	$m_{c\text{-}o}$	$\varphi_{c\text{-}o}$ (%)
D-D	THF	$100 \pm 4 \times 10^{-4}$ s^{-1}	7.7 ± 0.4	$5.7 \pm 0.2 \times 10^{-4}$ s^{-1}	0.043 ± 0.002
	MeCN	$22.2 \pm 4 \times 10^{-4}$ s^{-1}	0.18 ± 0.01	$3.6 \pm 0.2 \times 10^{-4}$ s^{-1}	0.039 ± 0.001
A-A[a]	MeCN	$183 \pm 4 \times 10^{-4}$ s^{-1}	31 ± 2	$5.0 \pm 0.2 \times 10^{-4}$ s^{-1}	0.16 ± 0.01
	water	$300 \pm 20 \times 10^{-4}$ s^{-1}	38 ± 3	$4.3 \pm 0.1 \times 10^{-4}$ s^{-1}	0.16 ± 0.01
D-A	THF	$2.1 \pm 0.1 \times 10^{-4}$ s^{-1}	0.020 ± 0.001	$2.6 \pm 0.4 \times 10^{-5}$ s^{-1}	0.015 ± 0.002
	MeCN	$1.5 \pm 0.1 \times 10^{-5}$ s^{-1}	$1.2 \pm 0.2 \times 10^{-3}$	$2.3 \pm 0.1 \times 10^{-5}$ s^{-1}	0.014 ± 0.001
Dy-yD	THF	$90 \pm 2 \times 10^{-4}$ s^{-1}	5.5 ± 0.2	$4.7 \pm 0.2 \times 10^{-4}$ s^{-1}	0.026 ± 0.002
	MeCN	$14.2 \pm 0.3 \times 10^{-4}$ s^{-1}	0.11 ± 0.01	$1.9 \pm 0.1 \times 10^{-4}$ s^{-1}	0.026 ± 0.001
Ay-yA[a]	MeCN	$95 \pm 2 \times 10^{-4}$ s^{-1}	9.2 ± 0.5	$4.0 \pm 0.1 \times 10^{-4}$ s^{-1}	0.13 ± 0.01
	water	$172 \pm 7 \times 10^{-4}$ s^{-1}	17 ± 1	$4.5 \pm 0.1 \times 10^{-4}$ s^{-1}	0.12 ± 0.01
Dy-yA	THF	$10 \pm 1 \times 10^{-4}$ s^{-1}	0.077 ± 0.004	$1.7 \pm 0.1 \times 10^{-4}$ s^{-1}	0.039 ± 0.003
	MeCN	$1.8 \pm 0.2 \times 10^{-4}$ s^{-1}	0.012 ± 0.001	$1.3 \pm 0.1 \times 10^{-4}$ s^{-1}	0.039 ± 0.004
Dy-A	THF	$7.7 \pm 0.7 \times 10^{-4}$ s^{-1}	0.059 ± 0.004	$9.4 \pm 0.5 \times 10^{-5}$ s^{-1}	0.041 ± 0.002
	MeCN	$8.6 \pm 0.7 \times 10^{-5}$ s^{-1}	0.015 ± 0.001	$5.9 \pm 0.3 \times 10^{-5}$ s^{-1}	0.043 ± 0.003
D-yA	THF	$2.5 \pm 0.2 \times 10^{-4}$ s^{-1}	0.028 ± 0.002	$1.7 \pm 0.1 \times 10^{-4}$ s^{-1}	0.047 ± 0.003
	MeCN	$3.6 \pm 0.2 \times 10^{-5}$ s^{-1}	$5.0 \pm 0.3 \times 10^{-3}$	$1.3 \pm 0.1 \times 10^{-4}$ s^{-1}	0.040 ± 0.003

[a] Measured in MeCN as the hexafluorophosphate salt and in water as the chloride salt.

We observe a reduction of more than an order of magnitude in the photocyclization quantum yield for push-push compounds when changing from THF to MeCN. A smaller two-fold reduction is observed for push-pull DTEs. In contrast, pull-pull DTEs demonstrate a slight increase in quantum yield when changing from MeCN to water (accompanied by counterion exchange from hexafluorophosphate to chloride). The reduced cyclization quantum yields of DTEs in polar solvents have been reported previously and attributed to the formation of twisted intramolecular charge transfer (TICT) states.[79, 80] The most thorough investigation comes from a study of fluorescent DTEs with a maleic anhydride central bridge.[79] The fluorescence signal of the compounds demonstrated a two-component decay and the contribution of the slower decaying component increased with the increasing solvent polarity. Together with a bathochromic shift of fluorescence spectra and a reduction in fluorescence intensity in more polar solvents, the authors postulated a TICT state in the excited state that does not lead to cyclization. A related study found that a TICT state can be formed in DTEs when one or both thiophene arms are substituted with electron-rich *N*,*N*-dimethylaniline.[80] As julolidine is an extremely good electron donor and all our DTEs have perfluorinated central bridges, the formation of a TICT state could explain the lower cyclization quantum yield of both push-push and push-pull DTEs in MeCN. Other possible explanations for the low quantum yields of the julolidine-functionalized DTEs in polar solvents include the formation of other types of intramolecular or intermolecular charge-separated states.

2.2.6 Calculation of PSD Based on Molar Absorption Coefficient and Quantum Yield

Given the large discrepancies in photoswitching quantum yields reported in the literature, we further analyzed the reliability of our result by calculating the forward PSDs based on the experimental molar absorption coefficients and photoswitching quantum yields and comparing the calculated PSDs with the experimental PSDs. All the experimental and calculated PSD values are listed in Table 2.6. The PSD of the forward reaction (PSD_λ) is expressed as the fraction of closed DTE and is calculated using Equation 2.2:

$$PSD_\lambda = \frac{\varepsilon_{\text{open},\lambda} \cdot \Phi_{\text{o-c}}}{\varepsilon_{\text{closed},\lambda} \cdot \Phi_{\text{c-o}} + \varepsilon_{\text{open},\lambda} \cdot \Phi_{\text{o-c}}} \quad (2.2)$$

where $\varepsilon_{\text{open},\lambda}$ and $\varepsilon_{\text{closed},\lambda}$ are the molar absorption coefficients of the open and closed isomers, respectively, at the excitation wavelength; $\Phi_{\text{o-c}}$ and $\Phi_{\text{c-o}}$ are the quantum yields for isomerization in each direction.

Table 2.6 Experimental and calculated PSD in different solvents

Compound	Solvent	Exp. PSD_{o-c} (365 nm) (%)	Exp. PSD_{o-c} (405 nm) (%)	Calc. PSD_{o-c} (365 nm) (%)	Calc. PSD_{o-c} (405 nm) (%)
D-D	THF	>99	/	100	/
	MeCN	69	/	79	/
A-A[a]	MeCN	>99	71	100	79
	water	>99	/	100	/
D-A	THF	71	/	82	/
	MeCN	21	/	29	/
Dy-yD	THF	>99	/	100	/
	MeCN	86	/	93	/
Ay-yA[a]	MeCN	>99	/	100	/
	water	>99	96	100	99
Dy-yA	THF	80	/	79	/
	MeCN	33	/	37	/
Dy-A	THF	85	/	81	/
	MeCN	64	/	55	/
D-yA	THF	66	/	72	/
	MeCN	26	/	36	/

[a] Measured in MeCN for the hexafluorophosphate salt and water for the chloride salt.

As shown in Table 2.6, the theoretical PSDs calculated from the molar absorption coefficients and photoswitching quantum yields generally agree with experimental PSDs

determined either by NMR or UV-vis methods with error of less than 10%, indicating the experimentally measured photoswitching quantum yields are reliable.

2.2.7 Fatigue Resistance

The fatigue resistance of DTEs is characterized by repeatedly switching the DTE between the open form and the closed form and monitoring the change of the closed-DTE λ_{max} in the visible region, as shown in Figure 2.12. The change in absorbance after a certain number of cycles of switching gives an indication of whether decomposition occurs.

Given that each DTE has different photocyclization and photoreversion quantum yields, we did not use a uniform sample concentration in the cuvette. Irradiation time and irradiation power also vary for each DTE to reach the PSS. The optimal combination of parameters was measured so that the PSS of photocyclization and photoreversion are just reached on each cycle. The optimized conditions were used to trigger the forward and reverse photoswitching to avoid decomposition resulting from over-irradiation.

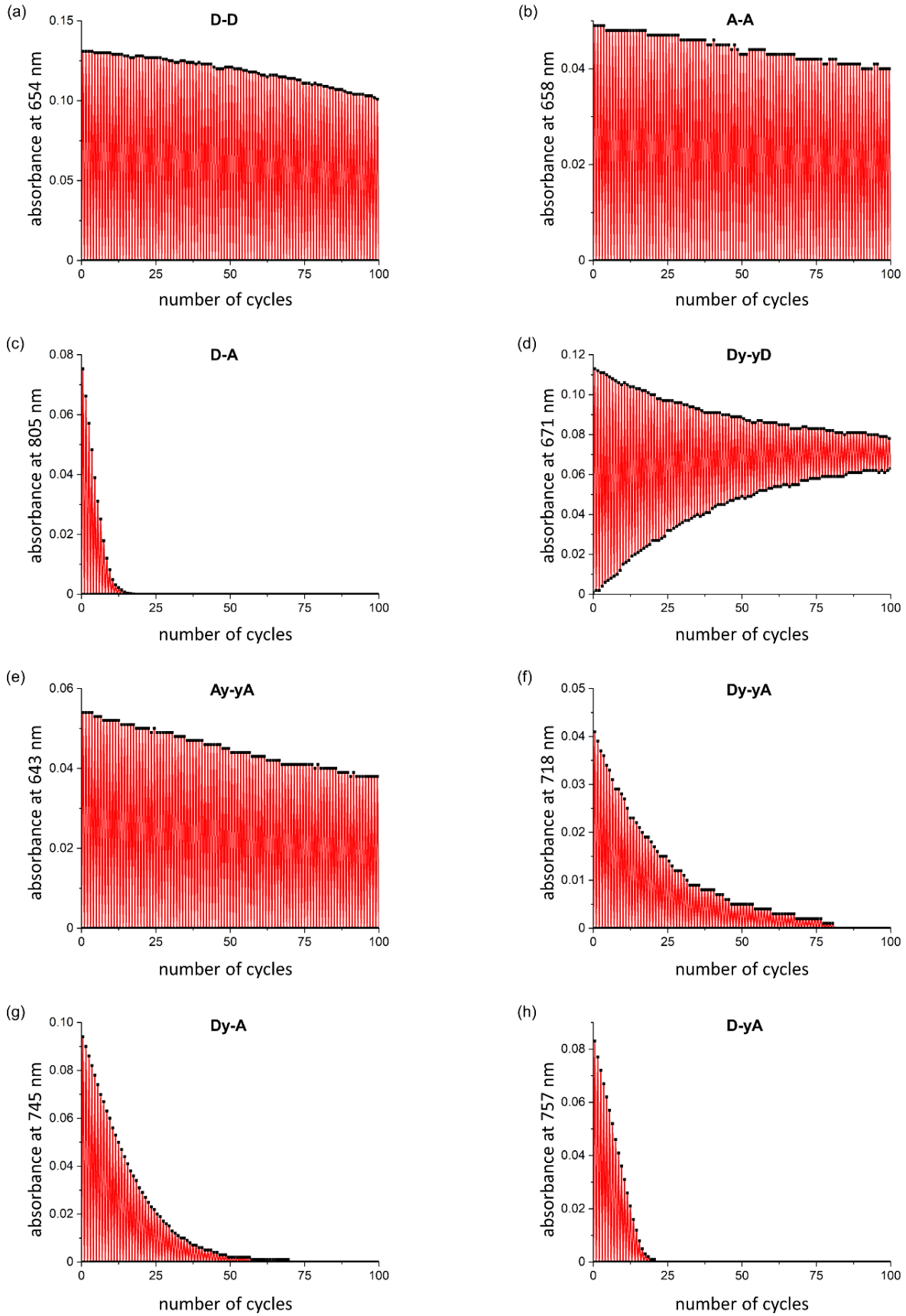


Figure 2.12 Fatigue resistance of **D-D** (THF), **A-A** (MeCN), **D-A** (THF), **Dy-yD** (THF), **Ay-yA** (MeCN), **Dy-yA** (THF), **Dy-A** (THF) and **D-yA** (THF).

Among the eight DTEs, **D-D**, **A-A** and **Ay-yA** exhibit good fatigue resistance as they remain switchable after a hundred cycles of photoswitching. Comparing the final closed-form absorbance after photoswitching with the initial absorbance, we found that 33% of **D-D**, 21% of **A-A** and 24% of **Ay-yA** decomposed after a hundred switching cycles.

Push-pull DTEs generally have worse fatigue resistance. The most fatigue resistant push-pull DTE, **Dy-yA**, has a photoswitching half-life of 18 cycles while **D-A** has a photoswitching half-life of only 5 cycles, at the same irradiation power. Instead of indicating fast decomposition per photon (high decomposition quantum yield), the poor fatigue resistance of push-pull DTEs mainly originates from the low photocyclization quantum yield, as the fatigue resistance curve is a measure of how many cycles a photoswitch can be switched. While the PSS of pull-pull DTEs can be achieved in ten seconds, it takes over ten minutes to reach the PSS of **D-A**. Thus, the push-pull samples are exposed to more photons during the process of measuring fatigue resistance. Even if the decomposition quantum yields of the pull-pull and push-pull DTEs were the same, we would expect much worse fatigue in the push-pull DTEs due to slow cyclization.

Most DTEs decompose into by-products that do not absorb in the visible region as the absorbance decays. However, **Dy-yD** shows a distinctive decomposition pathway as the absorbance after 630 nm light irradiation gradually increases, indicating the formation of a by-product that resembles the closed DTE. This by-product cannot be switched back by visible light. The decomposition pathway is further explored in Section 2.2.8.

Although almost all previous work on photoswitches report the fatigue resistance in the number of switching cycles, such method has an intrinsic drawback. It is not possible to determine the exact time required to reach the PSS, and therefore, the sample is usually over-irradiated in each cycle. The over-irradiation could have a significant impact on the number of cycles that the photoswitch can be switched. To better understand the kinetics of decomposition, herein we assume that **A-A** (chloride) and **Ay-yA** (chloride) decompose from their closed forms. We monitored their decomposition under extended time of 365 nm irradiation through UV-vis spectroscopy (Figure 2.13). The decomposition data were fitted as first-order decays. The initial gradient of the two curves were obtained by taking the first derivative of the fitting function and setting the time to zero. The initial gradients were used to calculate the photochemical quantum yield of decomposition of **A-A** (chloride) and **Ay-yA** (chloride), yielding results of 0.0020% ± 0.0003% and 0.0026% ± 0.0003%, respectively. For **A-A**

and **Ay-yA**, these decomposition quantum yields are 13,000- and 5,700-times smaller than the photocyclization quantum yields, respectively.

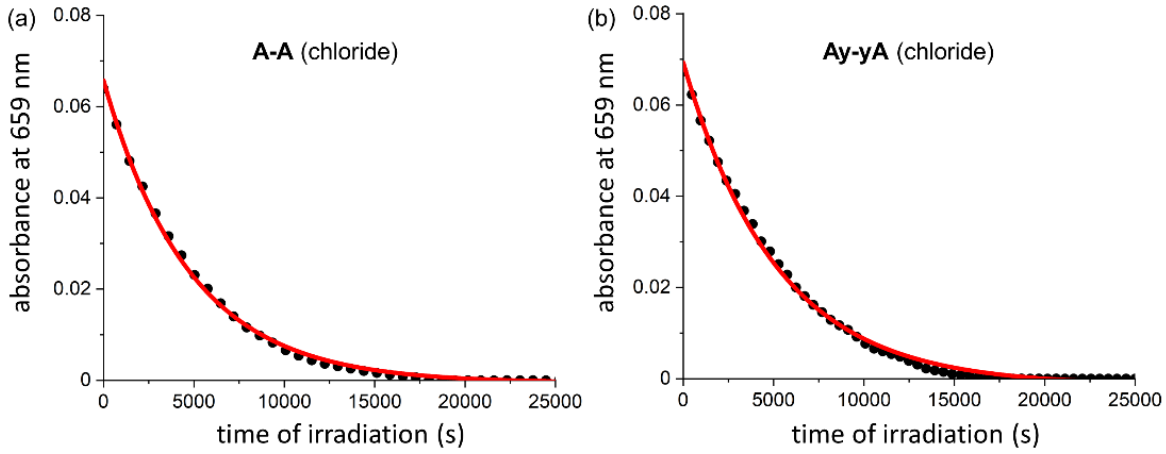


Figure 2.13 Photo-induced decomposition of the closed forms of (a) **A-A** (chloride) and (b) **Ay-yA** (chloride). The fitted equations are (a) $y = 0.0713 \cdot e^{\left(-\frac{x}{7323}\right)} - 0.0022$ and (b) $y = 0.0566 \cdot e^{\left(-\frac{x}{5141}\right)} - 0.0003$. The initial gradients of (a) and (b) were used to calculate the quantum yield of photochemical decomposition, yielding results of 0.0020% ± 0.0003% and 0.0026% ± 0.0006%, respectively.

2.2.8 Decomposition of Dy-yD

In order to characterize the distinctive decomposition pathway, a sample of **Dy-yD** at the PSD (i.e. >99% closed, as determined by NMR after irradiation at 365 nm), was further irradiated with 365 nm light for 3 hours in THF. **Dy-yD** converted into a single clean product, according to NMR (Figure 2.14c) and TLC, with an absorption band resembling the closed form **Dy-yD** but hypsochromically shifted by approximately 20 nm (Figure 2.14b), indicating that the length of π-conjugation resembles that of closed **Dy-yD**. ^{1}H NMR spectra (Figure 2.15 and Figure 2.16) show that the two methyl groups on the thiophene moieties are chemically equivalent for **Dy-yD** (open) and **Dy-yD** (closed) but become inequivalent after decomposition. Moreover, the two quaternary thiophene carbon centers and the two methyl carbons of closed **Dy-yD** are equivalent according to ^{13}C NMR (Figure 2.17) but become inequivalent after decomposition (Figure 2.18). The inequivalent carbon signal is also demonstrated with HSQC (Figure 2.19 and Figure 2.20). Therefore, we conclude that **Dy-yD** decomposes in a pathway shown in Figure 2.14a, similar to the previous report by Irie and co-workers,[81] which was further investigated by the Hecht group.[40] This decomposition pathway was rationalized by Jacquemin's computational study, which used all molecular mechanics-valence bond (MMVB), complete active space self-consistent field (CASSCF) and complete active-space second order perturbation theory (CASPT2) methods to predict a canonical insertion that leads to the formation of the annulated by-product.[82]

As only **Dy-yD** (but not **D-D**) among the eight DTEs cleanly decomposes into the annulated product, we conclude that the electron-donating ability of the aryl substituent is not the only factor contributing to the by-product formation, although Hecht and co-workers reported that the yield of annulated by product formation is generally higher for DTEs with electron donating substituents.[40]

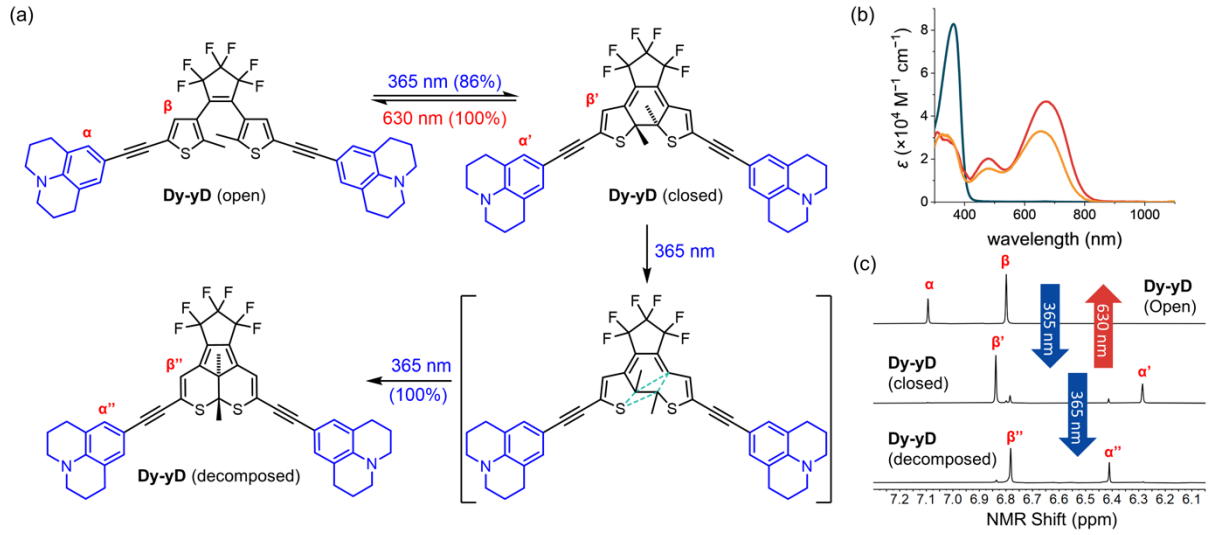


Figure 2.14 (a) Proposed decomposition pathway of **Dy-yD**. (b) Absorption spectra of open form (blue), closed form (red), and decomposed product (orange) of **Dy-yD** recorded in THF (c) Partial ^{1}H NMR spectra of open form, closed form, and decomposed product of **Dy-yD** (500 MHz, THF-d_8).

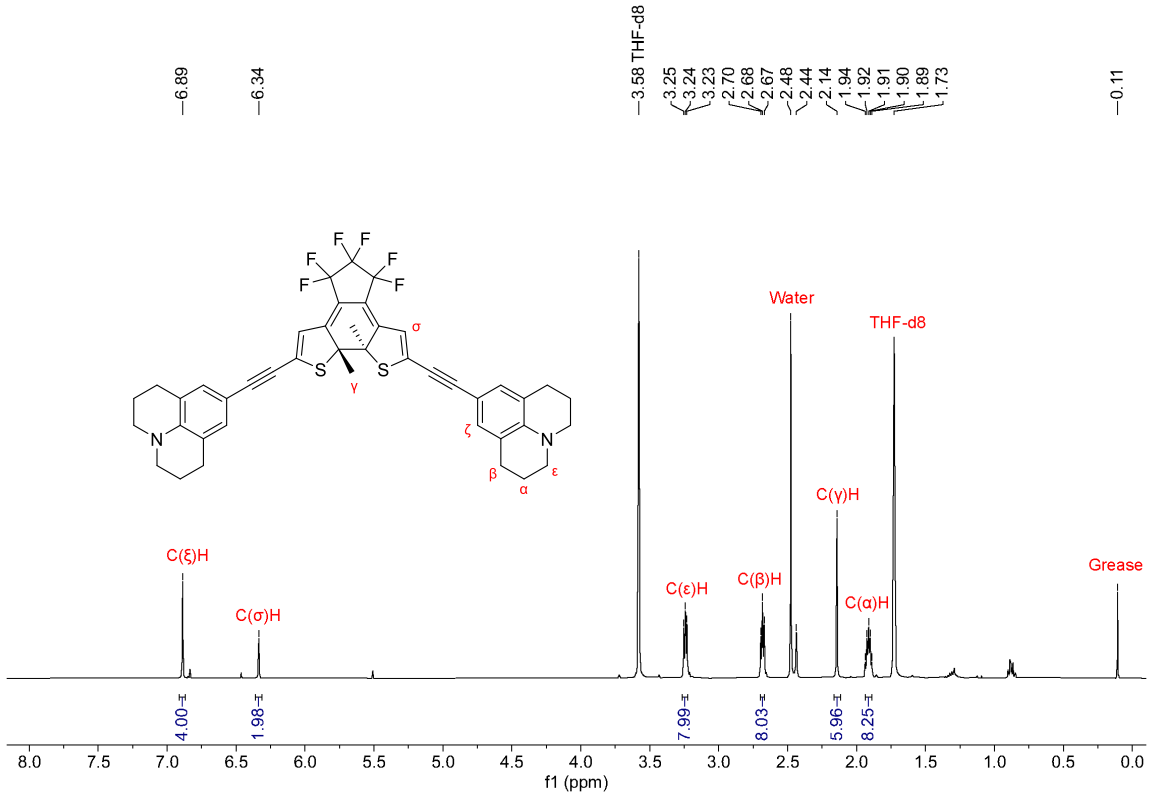


Figure 2.15 ^{1}H NMR spectrum (500 MHz, THF-d_8) of closed **Dy-yD**.

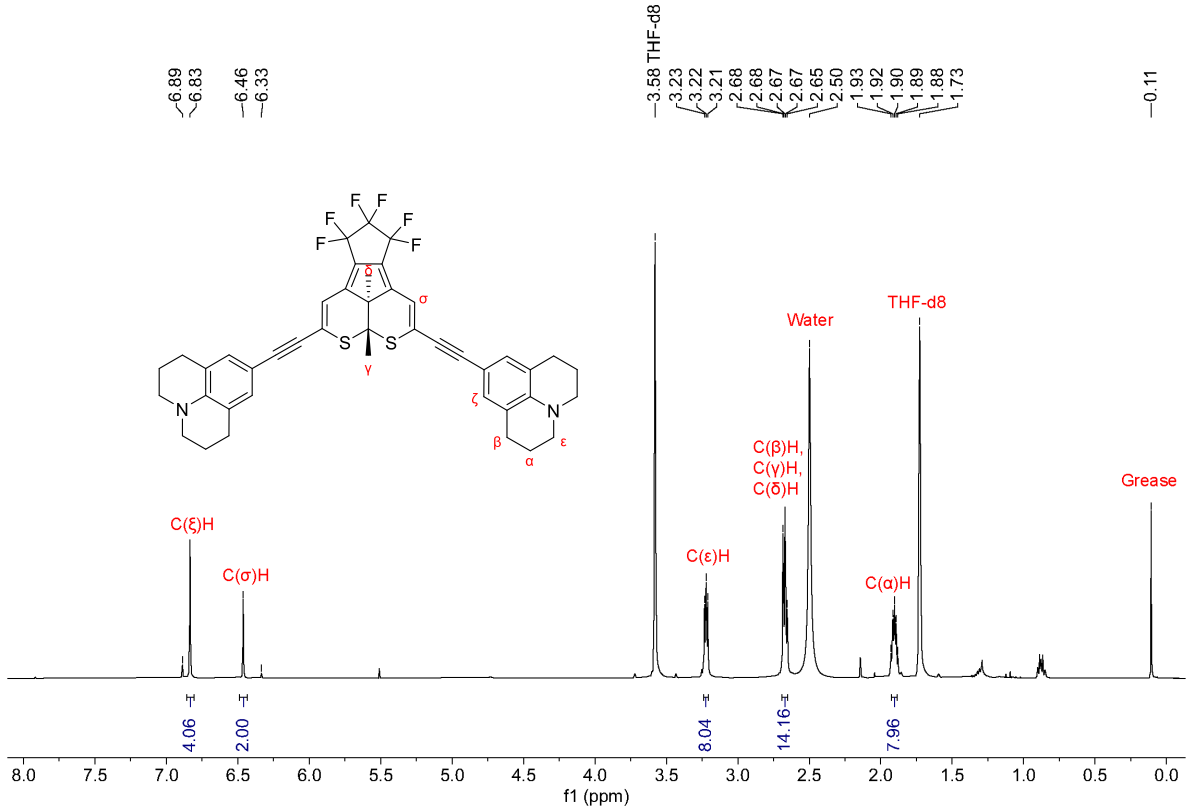


Figure 2.16 ^{1}H NMR spectrum (500 MHz, THF-d_8) of decomposed **Dy-yD** containing 6% closed-form **Dy-yD**.

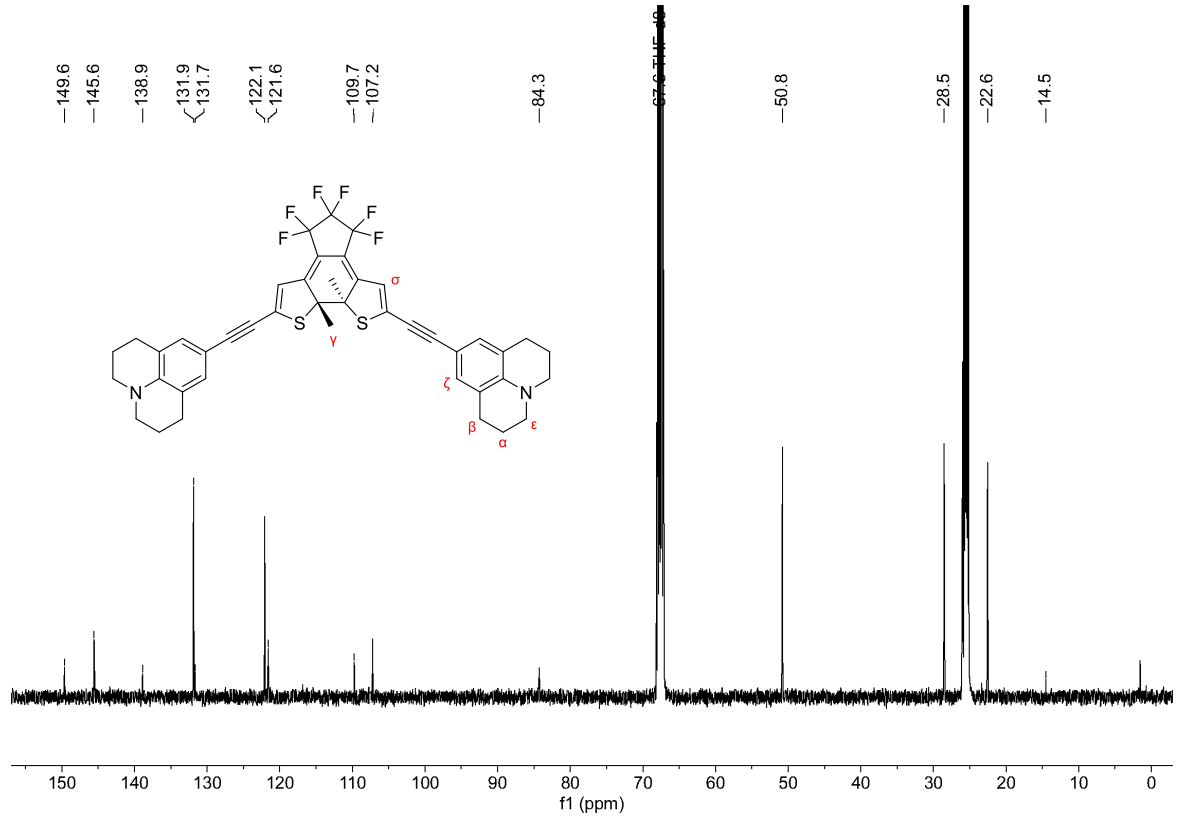


Figure 2.17 ^{13}C NMR spectrum (101 MHz, THF-d_8) of closed **Dy-yD.**

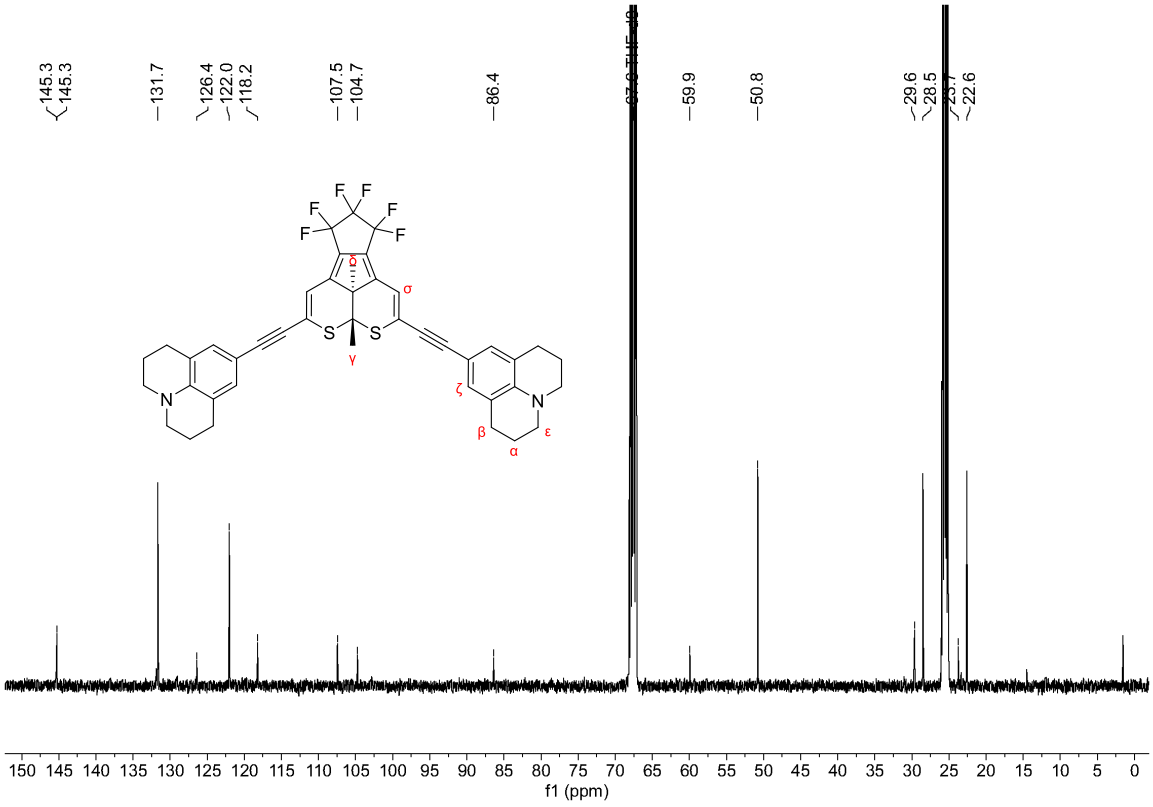


Figure 2.18 ^{13}C NMR spectrum (101 MHz, THF-d$_8$) of decomposed **Dy-yD**.

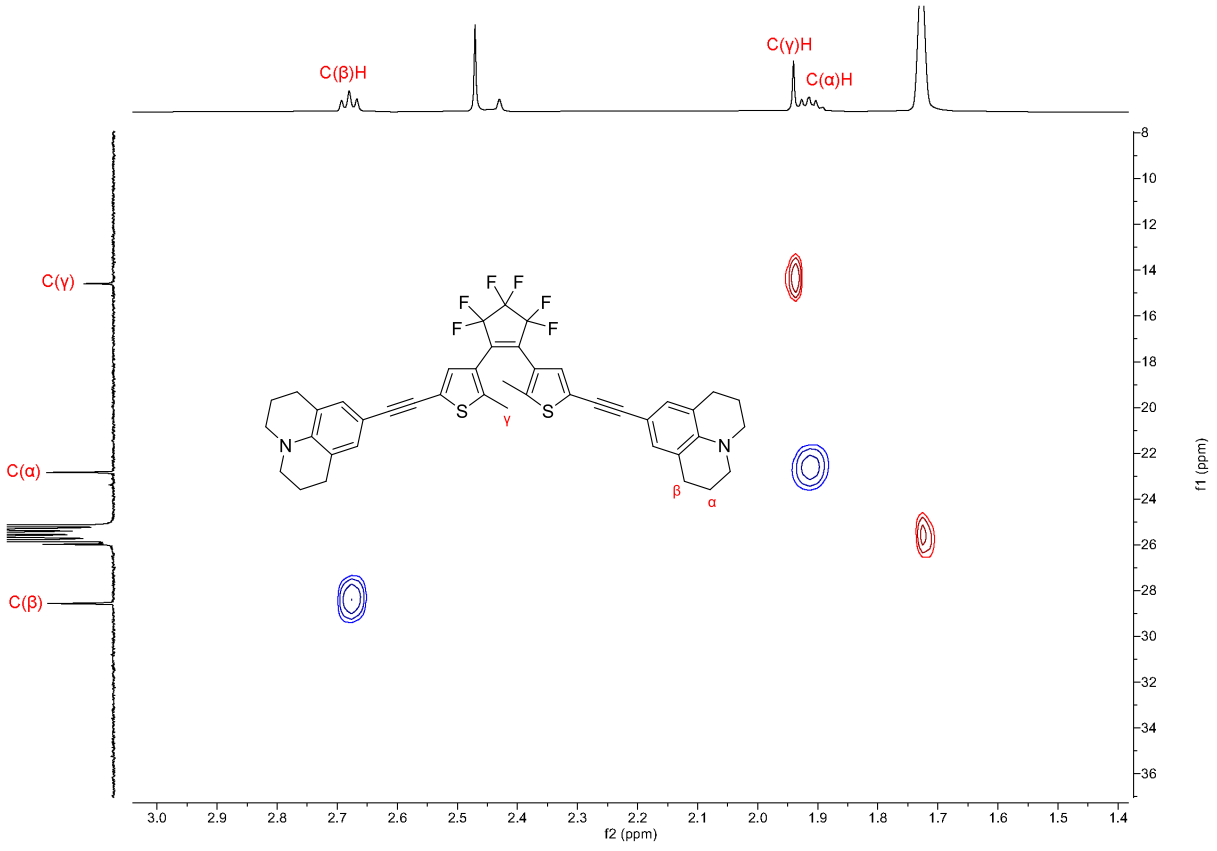


Figure 2.19 HSQC assignment of open **Dy-yD**.

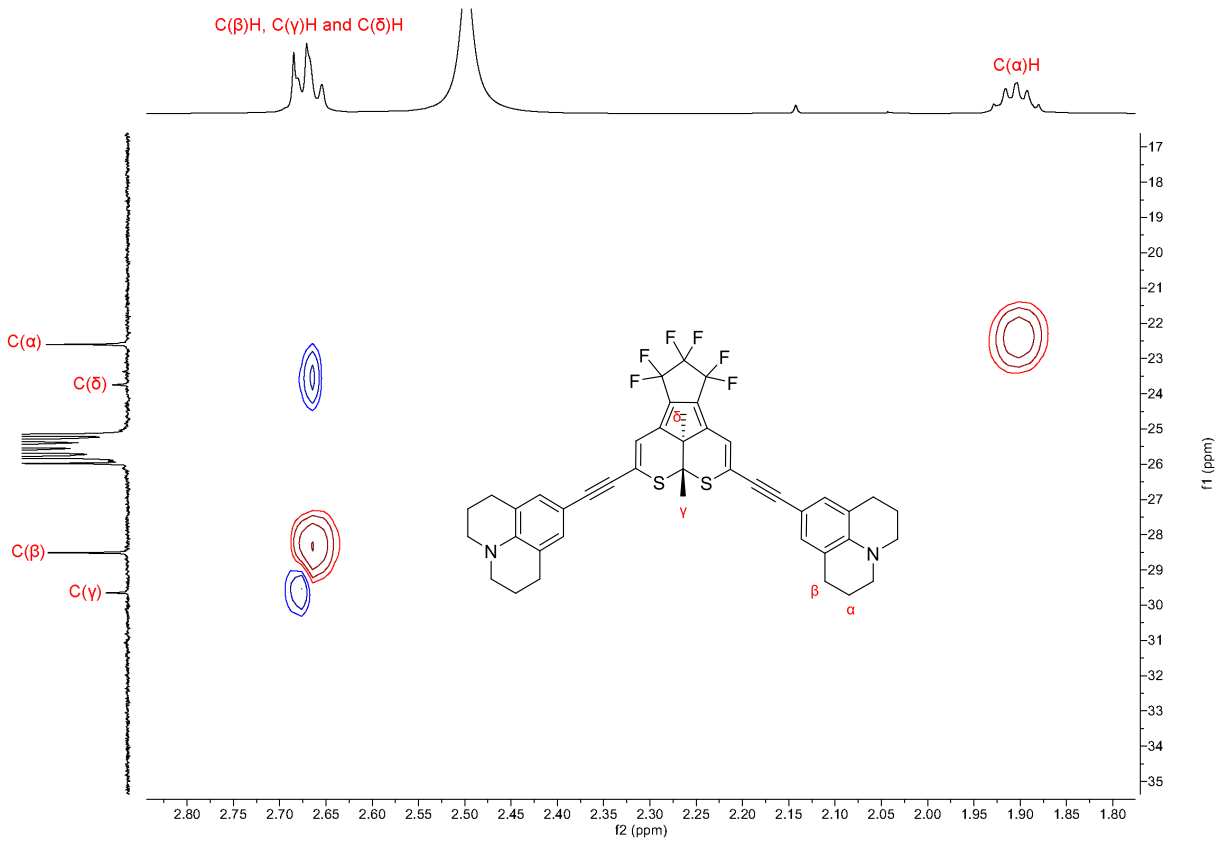


Figure 2.20 HSQC assignment of decomposed **Dy-yD** showing that C(γ) and C(δ) are no longer equivalent.

2.2.9 Solvatochromism of D-A

The solvatochromic behavior of compounds **D-D**, **A-A**, **D-A**, and **Dy-yA** was investigated by recording their UV-vis absorption spectra in various solvents (Figure 2.21). Open DTEs exhibited minimal or no solvatochromism. For closed DTEs, **D-D** (Figure 2.21a) and **A-A** (Figure 2.21b) displayed no discernible solvatochromic effects in THF and MeCN. The push-pull system **D-A** demonstrated a slight hypsochromic shift in polar solvents, with approximately 8 nm difference between THF and MeCN. **Dy-yA** exhibited more pronounced hypsochromic shifts, showing a 25 nm difference between THF and MeCN. The observed negative solvatochromism in **D-A** and **Dy-yA** is consistent with expectations, as the formation of the ICT state displaces positive charge from the pyridinium acceptor. This charge displacement becomes energetically less favorable when the acceptor is well-solvated in polar media.[83-85]

A more complex solvatochromic behavior was observed in halogenated solvents. Compounds **A-A**, **D-A**, and **Dy-yA** exhibited bathochromic shifts in their absorption spectra when dissolved in halogenated media (Figure 2.21b, Figure 2.21d, and Figure 2.21e). This effect was most pronounced for **D-A** in dichloromethane, where the absorption maxima experienced

a substantial red-shift exceeding 150 nm compared to non-halogenated solvents. Similar bathochromic shifts were noted in other halogenated solvents, including chloroform, dibromomethane, iodomethane, and chlorobenzene. Interestingly, carbon tetrachloride did not induce this effect. A plot correlating the energy of absorption with the dielectric constant of the solvents (Figure 2.21f) revealed a linear relationship between the absorption maxima of **D-A** and solvent polarity. However, the gradients of the linear fits differed significantly between non-halogenated and halogenated solvents, indicating distinct solvent-solute interactions in these two classes of solvents.

To further characterize the abnormal solvatochromic behavior, we fitted the energies of the maxima of the closed-form absorption in different solvents to a simplified version of the Kamlet-Abboud-Taft (KAT) solvatochromic model, a linear solvation energy relationship (LSER).[86-88] The KAT model is a multi-regression analytic model with the general Equation 2.3, where ν is the observed energy of the absorption maximum in different solvents, $\nu_{max,0}$ is the energy of the absorption maximum in vacuum obtained from linear regression in different solvents, α is a measure of hydrogen bond donor acidity and describes the ability of the solvent to donate a proton in a solvent-to-solute hydrogen bond. The β value is a measure of hydrogen bond acceptor basicity and describes a solvent's ability to accept a proton in a solute-to-solvent hydrogen bond. The π^* value is an index of dipolarity and polarizability of the solvent and measures the ability of the solvent to stabilize a charge or a dipole. The δ term is the discontinuous polarizability correction term. The correction term is incorporated because the polarizability of different classes of solvents varies significantly. The discontinuous polarizability correction term is 1 for aromatic solvents, 0.5 for chlorinated aliphatic solvents and 0 for other solvents. Despite assigning δ values to different classes of solvents for correction, there is currently no clear physical interpretation why aromatic and halogenated solvents deviate from others. The δ_H (Hildebrand solubility) and ξ (coordinate valency) terms in the original KAT model are neglected because the δ_H term is a measure of the solvent/solvent interactions that are interrupted in creating a cavity for the solute and is most relevant for the solvation of polymers while the ξ term provide a measure of basicity in presence of C=O, S=O, P=O, pyridine, or amine groups.[86] The α, β, $\pi^\star$ and δ parameters are published for THF, MeOH, MeCN, EtOH, acetone, CH_2Cl_2 and chloroform (Table 2.7).[86]

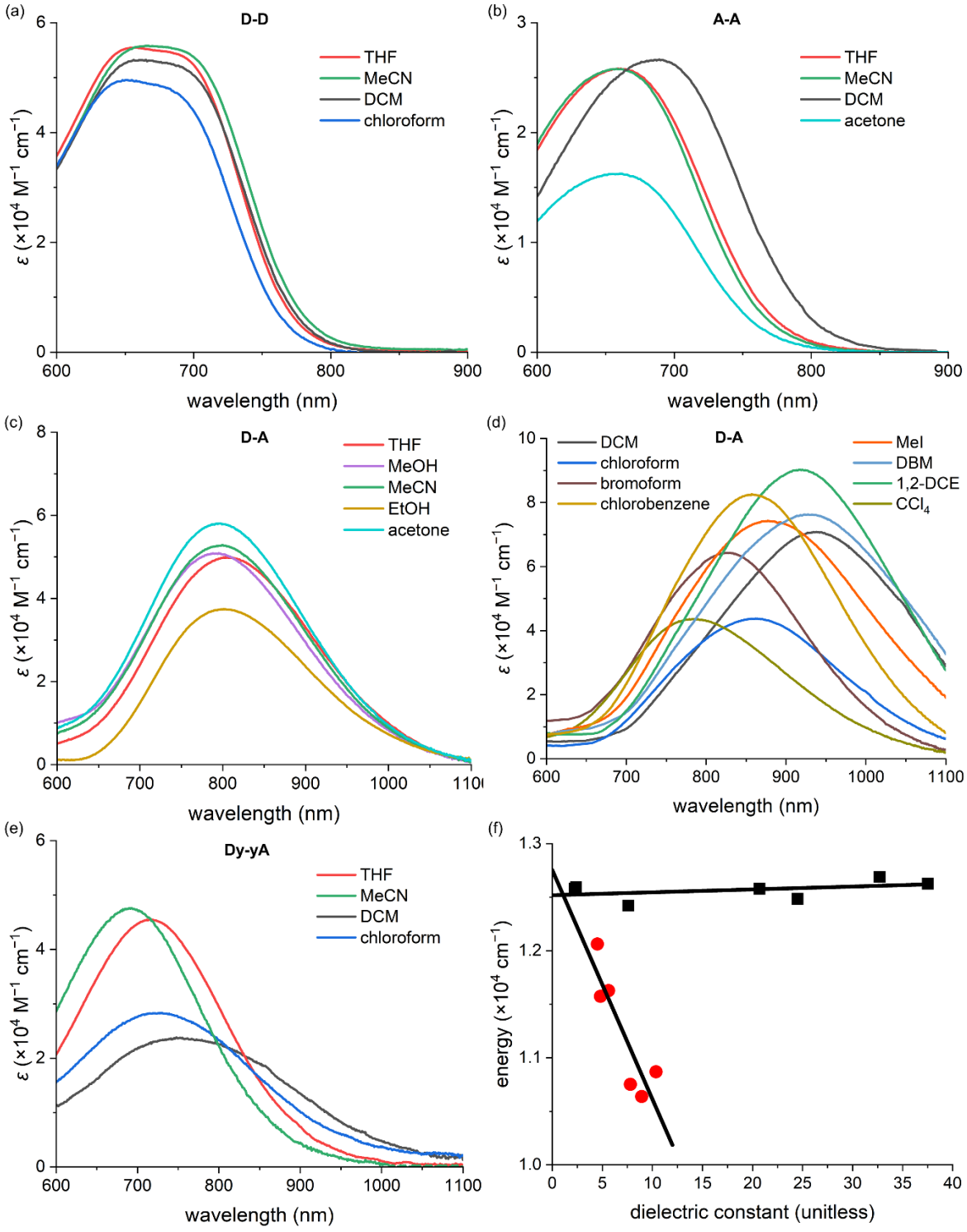


Figure 2.21 UV-vis absorption solvatochromism of (a) D-D, (b) A-A, (c) D-A in non-halogenated solvents, (d) D-A in halogenated solvents and (e) linear fits of solvatochromic behavior of D-A in non-halogenated solvents (black squares) and halogenated solvents (red dots). The intercept dielectric constant of the two linear fit is 1.08.

$$\nu_{max} = \nu_{max,0} + a\alpha + b\beta + s(\pi^* + d\delta) \tag{2.3}$$

Table 2.7 The values of α, β, π* and δ parameters of selected solvents for the KAT model analysis.[86]

Solvent	α	β	π^*	δ
THF	0.00	0.55	0.58	0
MeOH	0.93	0.62	0.60	0
MeCN	0.19	0.31	0.75	0
EtOH	0.83	0.77	0.54	0
acetone	0.08	0.48	0.71	0
CH_2Cl_2	0.30	0.00	0.82	0.5
chloroform	0.44	0.00	0.58	0.5

Table 2.8 Multi-regression results of the KAT model.

Term	$\nu_{max,0}$ (cm^{-1})	a (cm^{-1})	b (cm^{-1})	s (cm^{-1})	d
Value	12600±300	14±500	−300±800	−300±1400	13±4

The multi-regression analysis yields the results as shown in Table 2.8. Small *a*, *b* and *s* values close to zero with significantly greater error ranges indicate that the abnormal solvatochromism is not related to hydrogen-bond donation, hydrogen-bond acceptance, dipolarity or polarizability of the solvent. The value of *d* is expected to be zero when only one class of solvents is considered and small ($|d| < 0.5$) and negative when different classes of solvents are considered together. The significantly greater value of *d* than what has commonly been reported in the literature suggests that it is not the polarizability leading to the abnormal solvatochromism. After fitting the measured absorption maxima with the KAT model, a multi-regression solvent model that takes solvent polarity, hydrogen-bond donating ability, and hydrogen-bond accepting ability into consideration, we ruled out all three factors being responsible for the abnormal red-shift of the absorption of pull-pull and push-pull DTEs.

Comparing the extent of absorption peak shift in dichloromethane, dibromomethane and diiodomethane, we found that the spectral shift is most prominent in chlorinated solvents and least prominent in iodinated solvents. This observation is not consistent with the rationalization provided by Ponnusamy and co-workers,[87] who concluded that halogen bonding between the counterion and the halogenated solvents leads to the abnormal shift of absorption. It appears that halogenated solvents have special impact on the ion pairing between the ionic DTE and the counterion, but the exact nature of this interaction remains unclear.

2.2.10 Computational Benchmarking for DFT and TD-DFT Calculations

To rationalize the observed trend in the the measured UV-vis absorption spectra of the DTEs, we performed density functional theory (DFT) geometry optimizations and time-dependent

density functional theory (TD-DFT) calculations for calculating the vertical transition energies of all compounds. Note that these vertical transition energies do not account for vibronic coupling, which may not be insignificant.

Ground-state geometry benchmarking was carried out with **D-D**, **A-A**, and **D-A** (both open and closed forms) as the prototype DTEs. Calculations were performed in the gas phase, and numerical frequency calculations were used to confirm stationary points as minima. Benchmarked geometries were calculated at B3LYP/Def2SVP, PBE0/Def2SVP, ωB97X-D/Def2SVP, and tuned CAM-B3LYP/Def2SVP levels of theory. B3LYP and PBE0 are two hybrid functionals without long-range correction. Tuned CAM-B3LYP (μ = 0.150, α = 0.0799 and β = 0.9201) with long-range correction was adopted from a report published by Okuno and co-workers,[89] which demonstrated that CAM-B3LYP with the tuned parameters could semi-quantitatively reproduce several excitation energies obtained from the experimental UV-vis spectra of 15 closed-form DTE derivatives. The ωB97X-D functional includes both long-range correction and empirical dispersion. The GD3BJ empirical dispersion was applied to the functionals without empirical dispersion, i.e. B3LYP, PBE0 and tuned CAM-B3LYP, during both DFT and TD-DFT calculations.

The output geometries were aligned and RMSD values between each pair of optimized geometries of **D-D**, **A-A**, and **D-A** were calculated and are summarized in Table 2.9, Table 2.10, and Table 2.11. An example of aligned structures is shown in Figure 2.22.

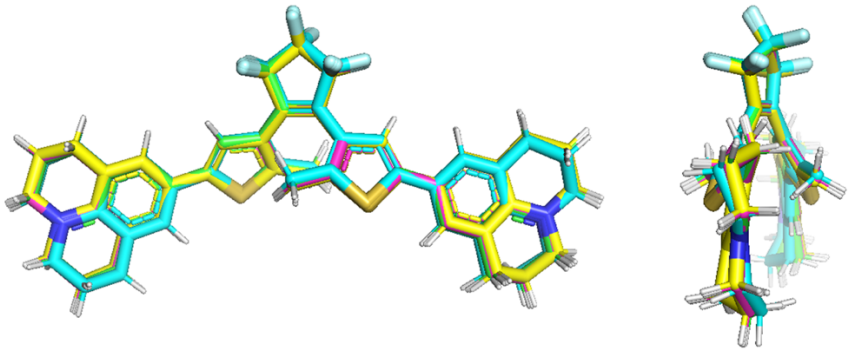


Figure 2.22 Front (left) and side view (right) of superposed geometries of open-form D-D optimized at B3LYP/Def2SVP (pink), PBE0/Def2SVP (green), tuned CAM-B3LYP/Def2SVP (yellow), and ωB97X-D/Def2SVP (blue) levels of theory. Hydrogen, fluorine, sulfur, and nitrogen atoms are shown in white, light blue, dark yellow and dark blue, respectively.

Table 2.9 Summary of RMSD values between each pair of optimized geometries of **D-D** (open) and **D-D** (closed).

D-D (open)					**D-D** (closed)				
	B3LYP	PBE0	CAM	ωB97X-D		B3LYP	PBE0	CAM	ωB97X-D
B3LYP	/	/	/	/	B3LYP	/	/	/	/
PBE0	0.059	/	/	/	PBE0	0.080	/	/	/
CAM	0.079	0.131	/	/	CAM	0.078	0.053	/	/
ωB97X-D	0.280	0.235	0.340	/	ωB97X-D	0.452	0.397	0.420	/

Table 2.10 Summary of RMSD values between each pair of optimized geometries of **A-A** (open) and **A-A** (closed).

A-A (open)					**A-A (closed)**				
	B3LYP	PBE0	CAM	ωB97X-D		B3LYP	PBE0	CAM	ωB97X-D
B3LYP	/	/	/	/	B3LYP	/	/	/	/
PBE0	0.046	/	/	/	PBE0	0.057	/	/	/
CAM	0.104	0.140	/	/	CAM	0.045	0.050	/	/
ωB97X-D	0.091	0.063	0.191	/	ωB97X-D	0.196	0.177	0.197	/

Table 2.11 Summary of RMSD values between each pair of optimized geometries of **D-A** (open) and **D-A** (closed).

D-A (open)					**D-A (closed)**				
	B3LYP	PBE0	CAM	ωB97X-D		B3LYP	PBE0	CAM	ωB97X-D
B3LYP	/	/	/	/	B3LYP	/	/	/	/
PBE0	0.091	/	/	/	PBE0	0.057	/	/	/
CAM	0.214	0.251	/	/	CAM	0.036	0.045	/	/
ωB97X-D	0.305	0.230	0.346	/	ωB97X-D	0.040	0.054	0.061	/

The RMSD values demonstrate that the geometries are fairly similar between different functionals, except for those calculated with ωB97X-D, which tend to have larger deviations. Analysis of the structures showed the dihedral angle between the central perfluorinated five-membered ring and the thiophene ring (C-T dihedral), as well as the dihedral angle between the thiophene ring and the aromatic ring attached to thiophene (T-A dihedral) as the main sources of the geometry deviation (Figure 2.23). The average C-T and T-A dihedral angles of each optimized geometry was measured and summarized in Table 2.12, Table 2.13, and Table 2.14. Geometries optimized with ωB97X-D functional have larger T-A dihedral angles than the geometries optimized with other functionals, which better resemble the angles in X-ray crystallographic data of several reported DTEs.[42, 90, 91]

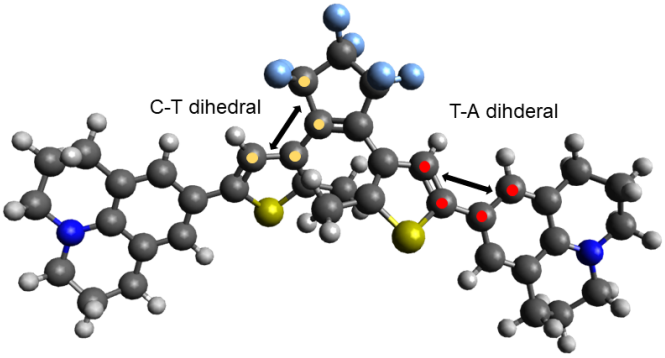


Figure 2.23 Optimized geometry of **D-D** at B3LYP/Def2SVP level of theory for measuring the dihedral angles.

Table 2.12 Summary of average C-T and T-A dihedral angles of optimized **D-D** geometry with different functionals.

D-D (open)					**D-D (closed)**				
	B3LYP	PBE0	CAM	ωB97X-D		B3LYP	PBE0	CAM	ωB97X-D
Avg. C-T (°)	44.0	44.3	41.8	47.5	Avg. C-T (°)	7.6	7.0	7.2	6.3
Avg. T-A (°)	18.8	16.1	20.2	27.6	Avg. T-A (°)	1.2	1.8	2.8	15.9

Table 2.13 Summary of average C-T and T-A dihedral angles of optimized **A-A** geometry with different functionals.

A-A (open)					**A-A (closed)**				
	B3LYP	PBE0	CAM	ωB97X-D		B3LYP	PBE0	CAM	ωB97X-D
Avg. C-T (°)	40.5	41.0	37.6	43.3	Avg. C-T (°)	8.4	7.8	7.8	7.0
Avg. T-A (°)	1.2	1.2	0.5	2.1	Avg. T-A (°)	4.9	6.4	5.7	17.1

Table 2.14 Summary of average C-T and T-A dihedral angles of optimized **D-A** geometry with different functionals.

D-A (open)					**D-A (closed)**				
	B3LYP	PBE0	CAM	ωB97X-D		B3LYP	PBE0	CAM	ωB97X-D
Avg. C-T (°)	45.0	45.2	40.9	46.9	Avg. C-T (°)	11.1	10.7	11.0	10.8
Avg. T-A (°)	6.1	8.4	5.4	13.8	Avg. T-A (°)	1.0	0.8	1.0	1.4

We further analyzed the impact of different optimized ground-state geometries on the predicted transitions with TD-DFT calculations. For all optimized ground-state geometries, TD-DFT was performed at tuned CAM-B3LYP/Def2SVP level of theory with solvation model based on density (SMD, acetonitrile), using GD3BJ empirical dispersion. The resulting transition data were analyzed with Gaussian broadening (35 nm, Chemcraft software) to simulate the full width at half maximum (FWHM) of experimental absorption spectra, and the peak maximum was compared between the different geometries. The experimental and calculated absorption maxima are summarized in Table 2.15, Table 2.16, and Table 2.17. We

found that the different ground-state geometries of open DTEs have little impact on the TD-DFT calculations while significant impact is observed in the closed DTEs. Different ground-state geometries led to > 60 nm difference for closed **D-D** and >100 nm difference for closed-form **A-A,** moreover, TD-DFT at tuned CAM-B3LYP/Def2SVP level of theory yields very poor prediction of absorption spectra for closed **A-A** and **D-A**. As ωB97X-D-optimized ground-state geometry most closely resemble literature crystal data,[19-21] and gave TD-DFT results closer to literature values, we chose the ωB97X-D functional for the geometry optimization of all other DTEs.

Table 2.15 Calculated absorption maxima (tuned CAM-B3LYP/Def2SVP) of ground-state geometries obtained from geometry optimization with different functionals, and the experimental absorption maxima of **D-D**.

D-D (open)					**D-D (closed)**				
	B3LYP	PBE0	CAM	ωB97X-D		B3LYP	PBE0	CAM	ωB97X-D
Calc. (nm)	358.1	354.6	359.6	342.9	Calc. (nm)	720.2	712.9	696.3	653.6
Exp. (nm)	346				Exp. (nm)	667			

Table 2.16 Calculated absorption maxima (tuned CAM-B3LYP/Def2SVP) of ground-state geometries obtained from geometry optimization with different functionals, and the experimental absorption maxima of **A-A**.

A-A (open)					**A-A (closed)**				
	B3LYP	PBE0	CAM	ωB97X-D		B3LYP	PBE0	CAM	ωB97X-D
Calc. (nm)	366.6	364.1	365.8	350.0	Calc. (nm)	847.7	837.4	797.0	723.6
Exp. (nm)	353				Exp. (nm)	658			

Table 2.17 Calculated absorption maxima (tuned CAM-B3LYP/Def2SVP) of ground-state geometries obtained from geometry optimization with different functionals, and the experimental absorption maxima of **D-A**.

D-A (open)					**D-A (closed)**				
	B3LYP	PBE0	CAM	ωB97X-D		B3LYP	PBE0	CAM	ωB97X-D
Calc. (nm)	369.2	364.5	369.9	353.2	Calc. (nm)	1077	1071	1063	1045
Exp. (nm)	350				Exp. (nm)	792			

After benchmarking the ground-state geometry, we decided to employ the tuned CAM-B3LYP and ωB97X-D functionals to calculate the spectroscopic features of all eight compounds in both isomeric forms (open and closed forms) because the long-range correction of these two functionals are important for properties influenced by charge transfer. The Def2SVP basis set was used throughout the calculation. The transitions were calculated at three combinations of functionals, including ωB97X-D/ωB97X-D (where both geometry optimization and TD-DFT calculation were performed with ωB97X-D), ωB97X-D/CAM-B3LYP (where geometry optimization was performed with ωB97X-D and TD-DFT was performed with tuned CAM-B3LYP), and CAM-B3LYP/CAM-B3LYP (where both geometry optimization and TD-DFT calculation were performed with tuned

CAM-B3LYP). The calculated vertical transition energies are summarized in Table 2.18, where CAM represents the tuned CAM-B3LYP functional. It is important to notice that the calculated vertical transition energies do not take into account vibronic effects, and therefore are strictly equivalent to the (0,0) transition, rather than λ_{max}. Figure 2.24 shows the comparison between calculated vertical transition energies and experimental excitation wavelengths of all DTEs in both isomers.

Table 2.18 Calculated wavelengths (nm) of absorption maxima of DTEs at three different combinations of functionals.

DTE	isomer	CAM/CAM	ωB97X-D/ωB97X-D	ωB97X-D/CAM
D-D	open	360	312	343
	closed	696	580	654
A-A	open	369	332	359
	closed	797	616	724
D-A	open	370	328	353
	closed	1063	975	1045
Dy-yD	open	389	347	379
	closed	745	613	697
Ay-yA	open	406	360	395
	closed	825	640	751
Dy-yA	open	406	360	393
	closed	1125	827	957
Dy-A	open	390	348	379
	closed	1109	926	1035
D-yA	open	410	368	402
	closed	1111	911	1023

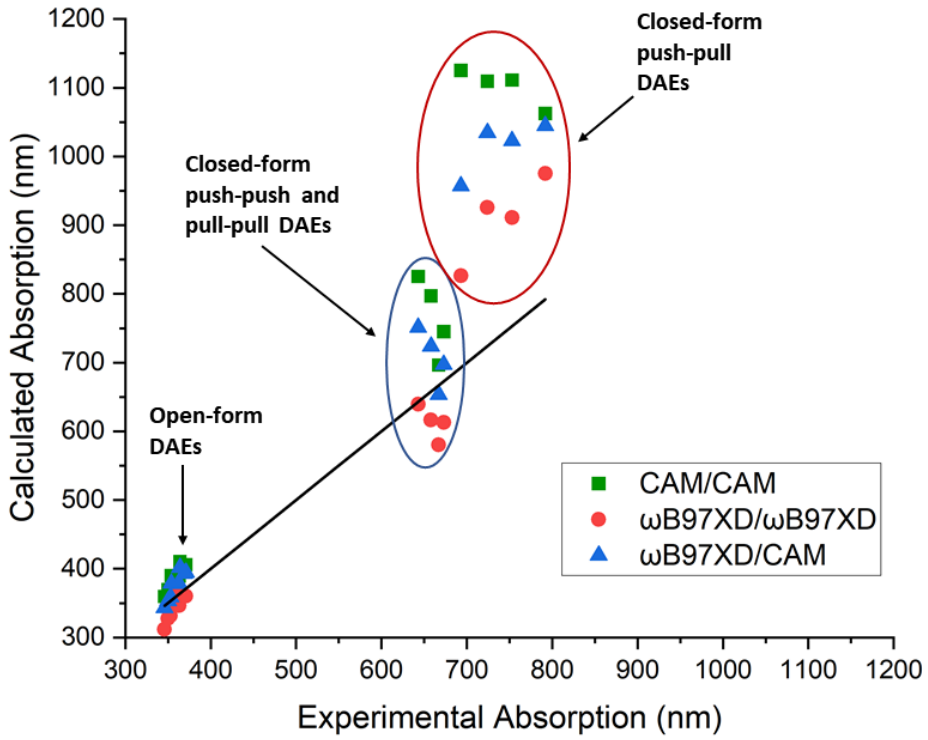


Figure 2.24 Comparison between the experimental and theoretical absorption maxima of the DTEs in their open and closed forms calculated by tuned CAM-B3LYP/tuned CAM-B3LYP, ωB97X-D/ωB97X-D, and ωB97X-D/tuned CAM-B3LYP functionals with Def2SVP basis set.

Overall, analysis of the data presented in Figure 2.24 demonstrates that all functional combinations employed for geometry optimization and TD-DFT calculations provide accurate estimations of the absorption maxima for open DTEs. For closed DTEs, theoretical predictions for push-push and pull-pull systems show moderate agreement with experimental data. However, there is a significant overestimation of the stabilization of intramolecular charge transfer states. Upon comparison of the three functional combinations, we determined that geometry optimization at the ωB97X-D/Def2SVP level of theory, followed by TD-DFT calculations at the same level, yields theoretical absorption maxima wavelengths that most closely align with experimental data. This combination appears to offer the best balance between computational efficiency and accuracy for predicting the spectroscopic properties of these DTE systems.

2.2.11 Conformational Analysis on Open DTEs

Conformational analysis of the open DTEs is utilized to better understand the trend observed in photocyclization quantum yields (Section 2.2.5, Table 2.5). Conformational searches of molecules **A-A**, **D-A**, **D-D**, and **Dy-yA** were performed using CREST, starting from a parallel-1 geometry input (Figure 2.25).[92] Six different conformers were generated for **A-A** and they were manually grouped into the three main types (anti-parallel, parallel 1 and parallel 2).

Significantly more conformers were generated with the incorporation of julolidine (e.g. 40 for **D-A** and 74 for **D-D**) due to the flexible julolidine aliphatic side chain. Since fluctuations in julolidine have small energy barriers (3 kJ/mol for an inversion of the CH_2 in julolidine) and are equally common across all three categories of conformation, we neglected the impact of such displacements in julolidine groups. Among the three main conformation groups (Figure 2.25), anti-parallel conformers and parallel 2 conformers exist as mirror-imaged pairs. Parallel 1 conformer consists of two mirror-imaged pairs if the two arms are different. Geometry optimizations were performed on the representative structures (anti-parallel, parallel 1 and parallel 2) at the ωB97X-D/def2-SVP level of theory with SMD solvent model (acetonitrile). The Boltzmann distributions of each molecule at different conformations (Table 2.19) were calculated with the sum of electronic and zero-point energies as well as the sum of electronic and thermal free energies (accounting for entropic contributions, Table 2.20) by the Equation 2.4, where p_i is the probability of state i, g_i is the number of degenerate states (mirror-image), ε_i is the energy of state i, k is the Boltzmann constant, T is the absolute temperature, M is the number of all states accessible to the system of interest, and Q is the normalization denominator.

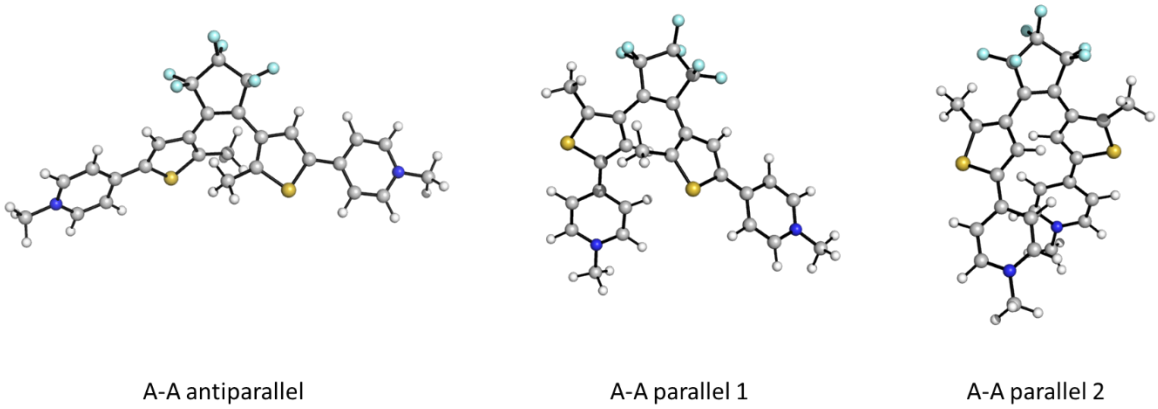


Figure 2.25 Representative **A-A** structures for the three main conformers of the studied DTEs.

$$p_i = \frac{1}{Q} \cdot e^{-\frac{\varepsilon_i}{kT}} = \frac{g_i e^{-\frac{\varepsilon_i}{kT}}}{\sum_{j=1}^{M} g_j e^{-\frac{\varepsilon_j}{kT}}} \tag{2.4}$$

Table 2.19 Relative energy (calculated from the sum of electronic and zero-point energies) and Boltzmann distribution (%) of different conformers of **D-D**, **A-A**, **D-A** and **Dy-yA**. The values in the bracket denote the number of degenerate structures, *M*, used in Boltzmann distribution calculation.

	D-D		**A-A**		**D-A**		**Dy-yA**	
	energy (kJ/mol) (M)	distribution (%)	energy (kJ/mol) (M)	distribution (%)	energy (kJ/mol) (M)	distribution (%)	energy (kJ/mol) (M)	distribution (%)
anti	5.3 (2)	10.3%	0 (2)	>99.9%	12.4 (2)	0.5%	8.2 (2)	3.4%
para-1	16.8 (2)	0.2%	25.4 (2)	<0.1%	16.0 (4)	0.4%	16.2 (4)	0.2%
para-2	0 (2)	89.5%	/[a]	0%	0 (2)	99.1%	0 (2)	96.4%

[a] local energy minimum was not found for A-A in parallel 2 conformation.

Table 2.20 Relative energy (calculated from the sum of electronic and thermal free energies) and Boltzmann distribution (%) of different conformers of **D-D**, **A-A**, **D-A** and **Dy-yA**. The values in the bracket denote the number of degenerate structures being accounted for Boltzmann distribution calculation.

	D-D		**A-A**		**D-A**		**Dy-yA**	
	energy (kJ/mol) (M)	distribution (%)	energy (kJ/mol) (M)	distribution (%)	energy (kJ/mol) (M)	distribution (%)	energy (kJ/mol) (M)	distribution (%)
anti	4.9 (2)	12.1%	0 (2)	>99.9%	11.2 (2)	0.8%	7.1 (2)	3.9%
para-1	14.2 (2)	0.6%	20.8 (2)	<0.1%	12.2 (4)	1.4%	9.9 (4)	3.1%
para-2	0 (2)	87.3%	/[a]	0%	0 (2)	97.8%	0 (2)	93.0%

[a] local energy minimum was not found for A-A in parallel 2 conformation.

For neutral **D-D** and mono-cationic **D-A** and **Dy-yA**, the parallel-2 conformation with the two DTE arms stacking with each other has the lowest energy. This conformation accounts for 99.1% of the population for **D-A**, 96.4% for **Dy-yA** and 89.5% for **D-D** at room temperature, negatively correlating with the photocyclization quantum yield. This result demonstrates that in molecules where the most stable parallel-2 conformer is heavily populated, photocyclization is disfavored. For dicationic **A-A**, the anti-parallel conformation is most the stable. A Boltzmann distribution of >99% in the anti-parallel conformation indicates that **A-A** exists in a conformation predisposed for photocyclization.

2.3 Conclusions

In this chapter, we have described the synthesis, photochemistry, photophysics, and DFT and TD-DFT calculations of eight DTEs bearing push-push, pull-pull and push-pull substitution patterns with different conjugation lengths in the backbone. The DTEs with symmetrical conjugated patterns (with or without alkynes) on both arms can be synthesized starting with the formation of the DTE core, and then functionalizing with the arms using Suzuki or Sonogashira coupling, while DTEs with an alkyne on one arm can be prepared with DTE core

formation at a late stage. Both routes permit straightforward synthesis of DTEs bearing versatile substituents.

The photocyclization and photoreversion abilities of DTEs critically depend on the substitution pattern. The cationic pull-pull DTEs generally demonstrate higher photocyclization quantum yields than push-push or push-pull DTEs due to Coulomb repulsion between the two positive charges, forcing the DTE to adopt an anti-parallel conformation in the ground state that can photocyclize in a conrotatory fashion, leading to extremely high PSDs. In contrast, the parallel conformations of push-pull DTEs are stabilized by interactions between the two arms, inhibiting photocyclization. Solvent polarity also affects the quantum yield of photoswitching. The impact of solvent polarity is most pronounced on push-push DTEs where TICT states may be accessed by rotation around the thiophene-phenyl bond.

Fatigue resistance measurements show that the fatigue does not simply relate to the substitution pattern. **D-D**, **A-A** and **Ay-yA** are highly fatigue resistant. However, **Dy-yD** decomposes in a distinct mechanism leading to the formation of an annulated ring. Push-pull DTEs generally show poor fatigue resistance due to slow photocyclization, i.e. the compounds need to be irradiated longer in each cycle of switching, resulting in decomposition.

Overall, we have completed a systematic study on the structure-property relationship of DTEs bearing push-push, pull-pull and push-pull substitution patterns, offering guidance for future DTE design for different applications. **Ay-yA** is the first reported DTE that is water-soluble, can be switched in both directions with visible light, reaching over 95% PSD in the forward reaction and 100% PSD in the reverse reaction. These properties make **Ay-yA** a promising candidate for potential application in biological contexts such as switchable fluorescence and photopharmacology.

2.4 Experimental

2.4.1 General Synthetic and Characterization Methods

All reactions were performed using oven-dried reaction vessels under an argon atmosphere unless stated otherwise. Anhydrous acetonitrile (MeCN), 1,4-dioxane, chloroform ($CHCl_3$), dichloromethane (CH_2Cl_2), diethyl ether (Et_2O), dimethylformamide (DMF), tetrahydrofuran (THF), toluene, triethylamine (Et_3N) and pyridine were obtained from an MBraun MBSPS-5-BenchTop solvent purification system, having been passed through an activated alumina column under nitrogen. Methanol was dried over 4 Å molecular sieves under argon.

DIPEA was distilled before each reaction using a Hickman distillation head. All other chemical reagents used were commercially available from Alfa Aesar, Fluorochem, Merck, and TCI Chemicals and were used as supplied.

Thin layer chromatography (TLC) and reverse-phase TLC analyses were carried out using Merck aluminum-backed TLC silica gel 60 F_{254} plates and Merck aluminum-backed TLC silica gel 60 RP-18 F_{254} plates, respectively. Plates were visualized directly under ambient light (for colored fluorescent dyes), by the quenching of fluorescence under ultraviolet light (λ = 254 nm), by the turn-on of fluorescence under ultraviolet light (λ = 365 nm) or by color changes of photoswitches after ultraviolet light (λ = 365 nm) irradiation. Flash column chromatography and reverse-phase flash-column chromatography was performed using Merck Geduran® 60 silica gel (particle size 63–200 μm) and C18-reversed phase silica gel, respectively, with the solvent system given. All solvents used for chromatography purification were HPLC grade or equivalent and were supplied by Merck, Fisher Scientific, VWR, or Honeywell.

Proton (^{1}H) and carbon (^{13}C) NMR spectra were recorded on either a Bruker AVIII HD 400, a Bruker AVIII HD 500, a Bruker AVII 500 with a ^{13}C(^{1}H) dual cryo-probe, or a Bruker AVIII 600 instrument with a broadband cryo-probe in deuterated solvents. Fluorine (^{19}F) NMR spectra were recorded on either a Bruker AVIII HD 400 or a Bruker AVIII HD 500 instrument in deuterated solvents. Boron (^{11}B) NMR spectra were recorded on a Bruker AVIII HD 400 instrument in deuterated solvents. Experiments on the Bruker AVIII 600 instrument were performed by the staff from the Chemistry Department NMR Research Facility, University of Oxford. All NMR experiments were performed at 298 K. ^{1}H NMR chemical shifts are reported in ppm to the nearest 0.01 ppm relative to $SiMe_4$ (δ = 0) and were referenced internally with respect to residual protons in the deuterated solvent (1.94 for acetonitrile-d_3, 7.26 for chloroform-d, 2.50 for DMSO-d_6, 4.79 for D_2O, and 3.31 for methanol-d_4). ^{13}C NMR spectra were recorded with broadband decoupling. ^{13}C chemical shifts were reported in ppm to the nearest 0.1 ppm relative to $SiMe_4$ (δ = 0) and were referenced internally with respect to carbons in the solvent (δ = 118.6 for acetonitrile-d_6, 77.2 for chloroform-d, 39.5 for DMSO-d_6, and 49.0 for methanol-d_4). ^{19}F NMR chemical shifts were reported to the nearest 0.1 ppm relative to $CFCl_3$ (δ = 0). ^{11}B chemical shifts were reported in ppm to the nearest 0.1 ppm relative to $BF3{\cdot}OEt_2$ (δ = 0). Peak assignments were made based on chemical shifts, integrations, coupling constants, comparison to known compounds, and using COSY, HSQC, and HMBC experiments where appropriate. Multiplets are described as singlet (s), doublet (d), triplet (t),

quartet (q), pentet (p) multiplet (m), broad (br), or combinations thereof. Coupling constants (*J*) are reported to the nearest 0.1 Hz.

High resolution mass spectra (HRMS) were recorded by the staff from the Chemistry Research Laboratory Mass Spectrometry Facility, University of Oxford, using a Bruker MicroTOF spectrometer or a Thermo Orbitrap Exactive mass spectrometer. The mass reported was that containing the isotopes with the lowest mass, with each value to 7 significant figures and within 5 ppm of the calculated mass. Mass to charge ratios (*m*/*z*) are reported in Daltons.

2.4.2 Acquisition of UV-vis Spectra

A typical experiment is as follows: a stock solution of **D-D** in THF-d_8 of known concentration from NMR integration relative to a dioxane standard was diluted with THF in a cuvette (3.0 mL, 4.2 μM) and then irradiated with 630 nm light (0.11 W, 1 min) to convert all residual closed **D-D** into open-form **D-D**. The open-form UV-vis spectrum was recorded between 280 nm and 1100 nm. The solution of **D-D** was then irradiated with cycles of 365 nm LED (18.9 mW, 1 s irradiation, 3 min interval) and the UV-vis spectrum was recorded during the intervals until no further changes in the UV-vis spectrum were observed. The final UV-vis spectrum with no further change after irradiation is the absorption spectrum of the PSS. The UV-vis spectrum of the closed-form **D-D** was then calculated based on the fact that the absorption spectrum of the PSS at a certain wavelength is a linear combination of open-form absorption and the closed-form absorption. The composition of **D-D** solution at PSS under 365 nm light irradiation was measured by ^{1}H NMR.

2.4.3 Determination of Molar Absorption Coefficient by NMR Reference Method

The concentration of the stock solution was determined by ^{1}H NMR spectroscopy by using a known concentration of dioxane as a reference. An NMR relaxation delay of 30 s was used to measure accurate integrals. A typical experiment for determining the molar absorption coefficient at the band maximum is as follows: a stock solution of **D-D** in THF-d_8 containing 2.24 mM dioxane was prepared and the exact concentration of **D-D** was determined by NMR to be 1.93 mM. The stock solution of **D-D** was diluted into THF and the absorption spectra of various concentrations were recorded following irradiation with 630 nm light at 112.0 mW for 5 minutes. The absorbance at 346 nm was plotted against concentration to give a graph of the form $y = mx$ where m gives the molar absorption coefficient according to the Beer-Lambert Law.

2.4.4 Ferric Oxalate Actinometry for Measuring the Power of LED Light Source

A solution of ferric oxalate (0.0060 M) was prepared by dissolving $K_3[Fe(C_2O_4)_3]\cdot 3H_2O$ (300 mg, 0.60 mmol) in aqueous sulfuric acid (100 mL, 0.050 M). From this stock solution, 2.00 mL of it was transferred to a quartz cuvette, and while stirring, irradiated with mic-LED-365 at the power of the indicated output percentage for 10 s, while an identical control sample was kept in the dark. A sample of the irradiated ferric oxalate sodium (0.20 mL) and a control sample (0.20 mL) were transferred to vials containing a mixture of 0.1% phenanthroline solution (0.90 mL, prepared by dissolving 13.56 g CH_3CO_2Na and 0.100 g of phenanthroline in 100 mL of 0.50 M H_2SO_4) and H_2O (0.90 mL). Samples were kept in the dark for 1 h to allow the complexation to occur and the absorption spectra were acquired in the 250–850 nm range. The LED power intensities and irradiation lengths were chosen to ensure that the photoconversion of ferric oxalate does not exceed 5% and that the absorbance of $Fe(phen)_3^{2+}$ complex is within the range 0.5–1.0.

Upon exposure to light, $K_3[Fe(C_2O_4)_3]$ is converted to Fe^{2+}, and the quantum yield of the formation of Fe^{2+} (Φ_R) is well-known for a range of wavelengths (220–500 nm, Φ_R = 1.16 at 365 nm, Φ_R = 1.14 at 405 nm). The photon flux f was calculated using the Equation 2.5, where Φ_R is the quantum yield of the ferric oxalate conversion at the irradiation wavelength, t is the irradiation time in seconds, $(1-10^{-A})$ is the fraction of light absorbed by the ferric oxalate solution while A is the absorbance of 0.006 M solution at the irradiation wavelength. Formation of the coloured $Fe(phen)_3^{2+}$complex (ε_{510} = 11,100 M^{-1} cm^{-1}) allows quantification of Fe^{2+} generated during the irradiation by measuring the absorbance of the irradiated and non-irradiated samples (Equation 2.6), where V_1 (mL) is the irradiated volume, V_2 (mL) is the aliquot of the irradiated solution being transferred to the solution of buffered phenanthroline, V_3 (mL) is the final volume of the complexation solution , l (cm) is the optical path length of the quartz cuvette used for irradiation, ΔA is the difference in the absorbance between the irradiated solution and the control stored in dark, and ε (510 nm) is the molar absorption coefficient of $Fe(phen)_3^{2+}$ complex at 510 nm.

$$f = \frac{\text{no. of moles of } Fe^{2+}}{\Phi_R \cdot t \cdot (1 - 10^{-A})} \tag{2.5}$$

$$\text{no. of moles of } Fe^{2+} = \frac{V_1 \cdot V_3 \cdot \Delta A\ (510\ \text{nm})}{10^3 \cdot V_2 \cdot l \cdot \varepsilon} \tag{2.6}$$

The calculated value of the photon flux was expressed in $E \cdot s^{-1}$ and was converted to mW using Equation 2.7.

$$P(\mathrm{mW}) = 1000 \cdot f\ (\mathrm{E} \cdot \mathrm{s}^{-1}) \cdot N_{\mathrm{A}} \cdot h \cdot \frac{c}{\lambda} \tag{2.7}$$

2.4.5 Determination of Photoswitching Quantum Yield

A typical photocyclization experiment is as follows: a THF solution of **D-D** (1.6 μM) was placed in a cuvette in the sample holder of the UV-vis spectrometer and stirred at 25 °C. After irradiating the sample with 365 nm light (18.9 mW, 200 ms irradiation), the absorption intensity at 654 nm corresponding to peak maximum of the formed product was recorded. The irradiation-recording process was repeated for five cycles to acquire a kinetic trace of the photochemical conversion (8% of the open-form **D-D** was converted to the closed-form). The determination of the initial slope was carried out twice for each compound in each solvent and showed good reproducibility. The parameters being used to calculate the photoswitching quantum yields are summarized in Table 2.21.

Table 2.21 Absorbance at excitation wavelength (365 nm and 630 nm), power of LED, wavelength of irradiation (365 nm and 630 nm), and molar absorption coefficient at monitoring wavelength used for calculating the photochemical quantum yield of each compound in different solvents.

DTE	Solvent	Process	*A*	*P* (W)	exci. λ (nm)	moni. λ (nm)	ε_{prod} (M^{-1} cm^{-1})
D-D	THF	O-C	0.0749	0.0189	365	654	42700
		C-O	0.0754	0.1120	630		
	MeCN	O-C	0.0134	0.1591	365	667	43100
		C-O	0.0504	0.1120	630		
A-A	MeCN	O-C	0.0743	0.0189	365	658	19100
		C-O	0.0374	0.1120	630		
	water	O-C	0.1068	0.0189	365	659	19000
		C-O	0.0319	0.1120	630		
D-A	THF	O-C	0.0803	0.1591	365	805	38200
		C-O	0.0098	0.1120	630		
	MeCN	O-C	0.1004	0.1591	365	792	38100
		C-O	0.0102	0.1120	630		
Dy-yD	THF	O-C	0.0887	0.0189	365	671	47300
		C-O	0.0930	0.1120	630		
	MeCN	O-C	0.0878	0.1591	365	673	41900
		C-O	0.0401	0.1120	630		
Ay-yA	MeCN	O-C	0.0978	0.0189	365	643	22300
		C-O	0.0323	0.1120	630		
	water	O-C	0.1089	0.0189	365	650	23100
		C-O	0.0372	0.1120	630		
Dy-yA	THF	O-C	0.1024	0.1591	365	718	37800
		C-O	0.0259	0.1120	630		
	MeCN	O-C	0.1209	0.1591	365	693	37600
		C-O	0.0199	0.1120	630		
Dy-A	THF	O-C	0.1393	0.1591	365	745	29400
		C-O	0.0176	0.1120	630		
	MeCN	O-C	0.0632	0.1591	365	724	26500
		C-O	0.0115	0.1120	630		
D-yA	THF	O-C	0.8092	0.1591	365	757	32300
		C-O	0.0254	0.1120	630		
	MeCN	O-C	0.05836	0.1591	365	753	35100
		C-O	0.02147	0.1120	630		

2.4.6 Determination of PSD by NMR Method

A typical procedure for determining the percentage conversion at PSS is as follows: a sample of **D-D** in THF-d_8 was irradiated with 630 nm light at 112.0 mW for 3 minutes and then the NMR spectrum of the open-form was recorded. The sample was then irradiated with 365 nm light at 159 mW for 5 minutes and then the NMR spectrum was recorded. Irradiation with 365 nm light for 5 minutes followed by taking NMR spectrum was repeated for 7 times until no further change in the NMR spectrum was observed. The integration ratios of the peaks H(a):H(a') and H(b):H(b') at the PSD were measured to give a PSD of >99% conversion to the closed form, i.e. no detectable trace of the open isomer. The uncertainty associated with NMR integration is evaluated by setting the integration of H(a) peak to 2.00 and randomly integrate on the baseline

where no peak occurs (with the width of 0.05 ppm) for ten times, giving average uncertainty of ± 0.02, which corresponds to 1% error in the integration value.

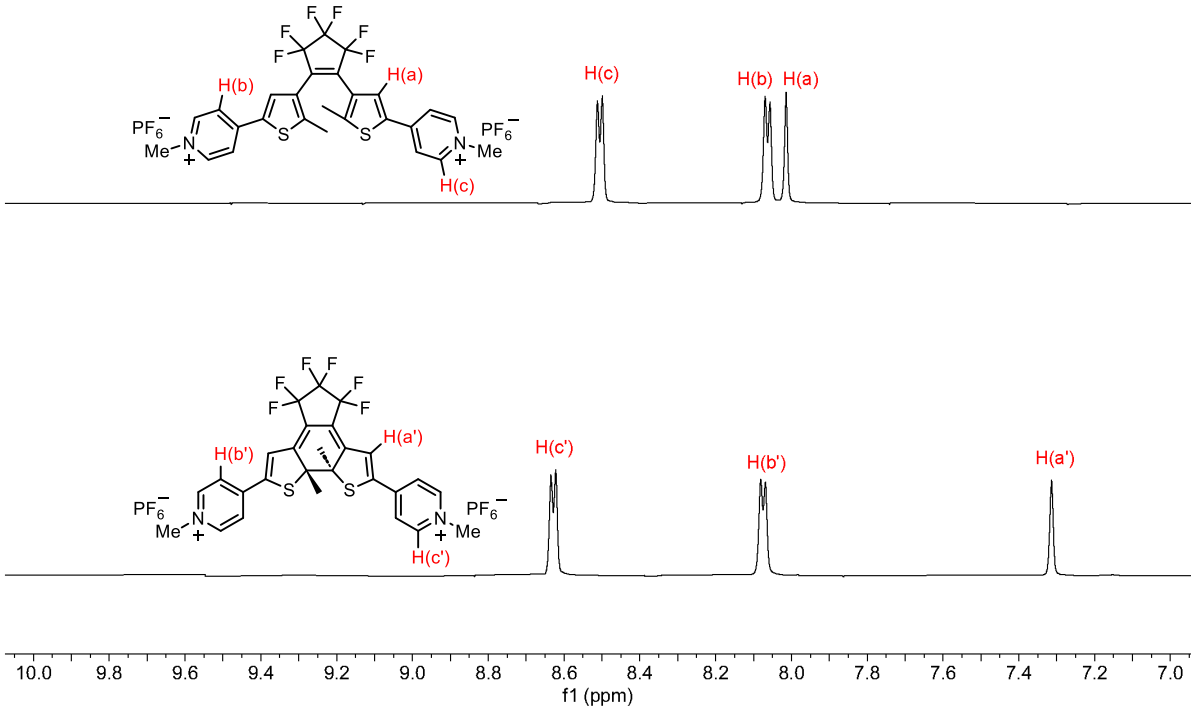


Figure 2.26 ^{1}H NMR spectra (500 MHz) of open-form **A**-**A** (top) and >99% conversion reached at PSS by 365 nm irradiation (bottom) in MeCN-d_3.

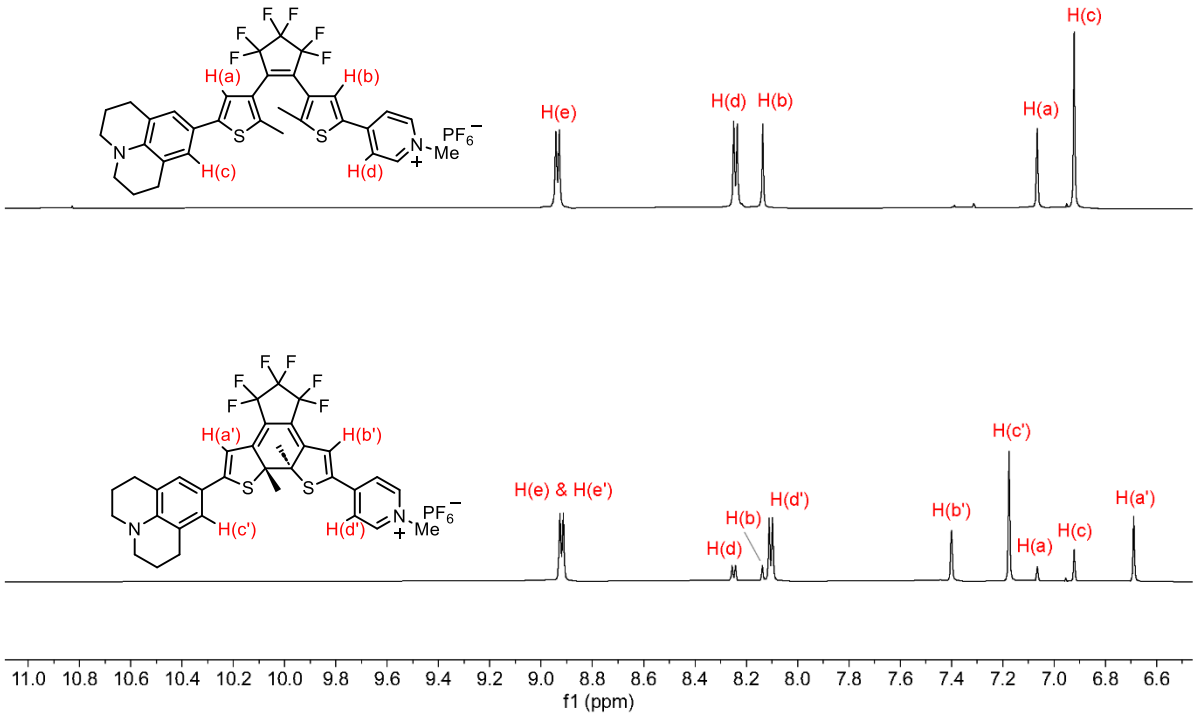


Figure 2.27 ^{1}H NMR spectra (500 MHz) of open-form **D**-**A** (top) and 71% ± 1% conversion reached at PSS by 365 nm irradiation (bottom) in THF-d_8.

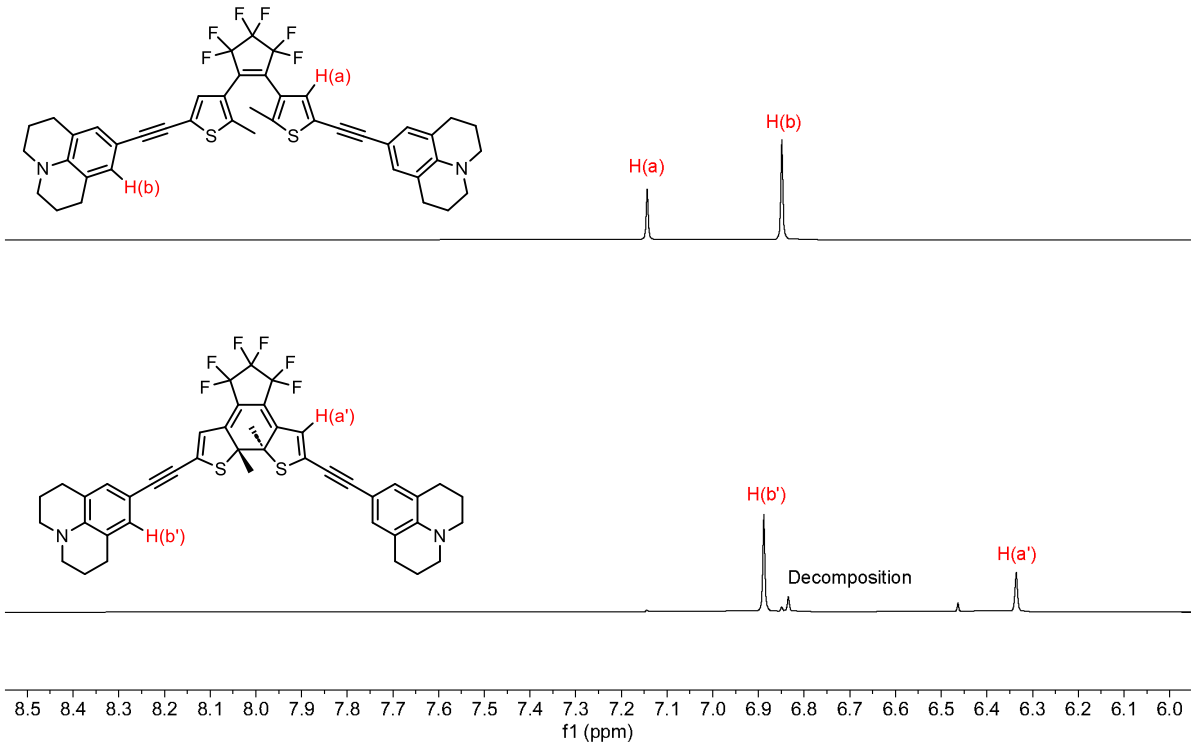


Figure 2.28 ^{1}H NMR spectra (500 MHz) of open-form **Dy-yD** (top) and >99% conversion reached at PSS by 365 nm irradiation (bottom) in THF-d_8.

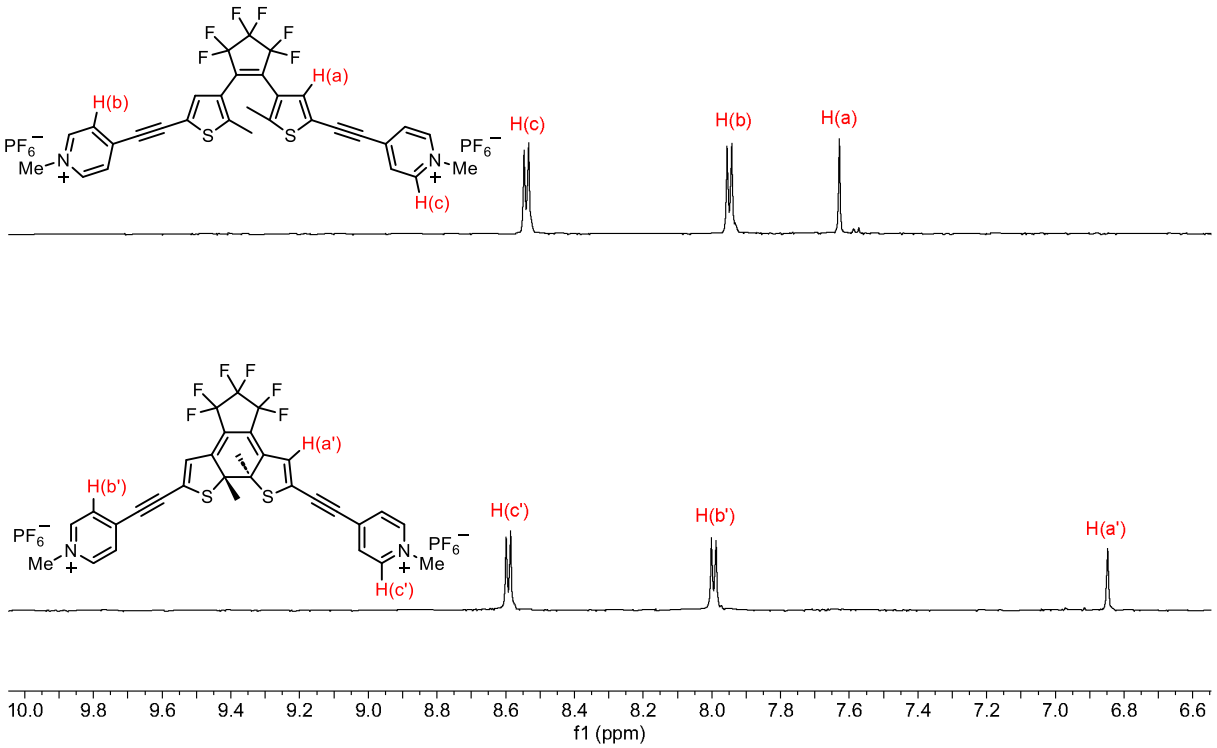


Figure 2.29 ^{1}H NMR spectra (500 MHz) of open-form **Ay-yA** (top) and >99% conversion reached at PSS by 365 nm irradiation (bottom) in MeCN-d_3.

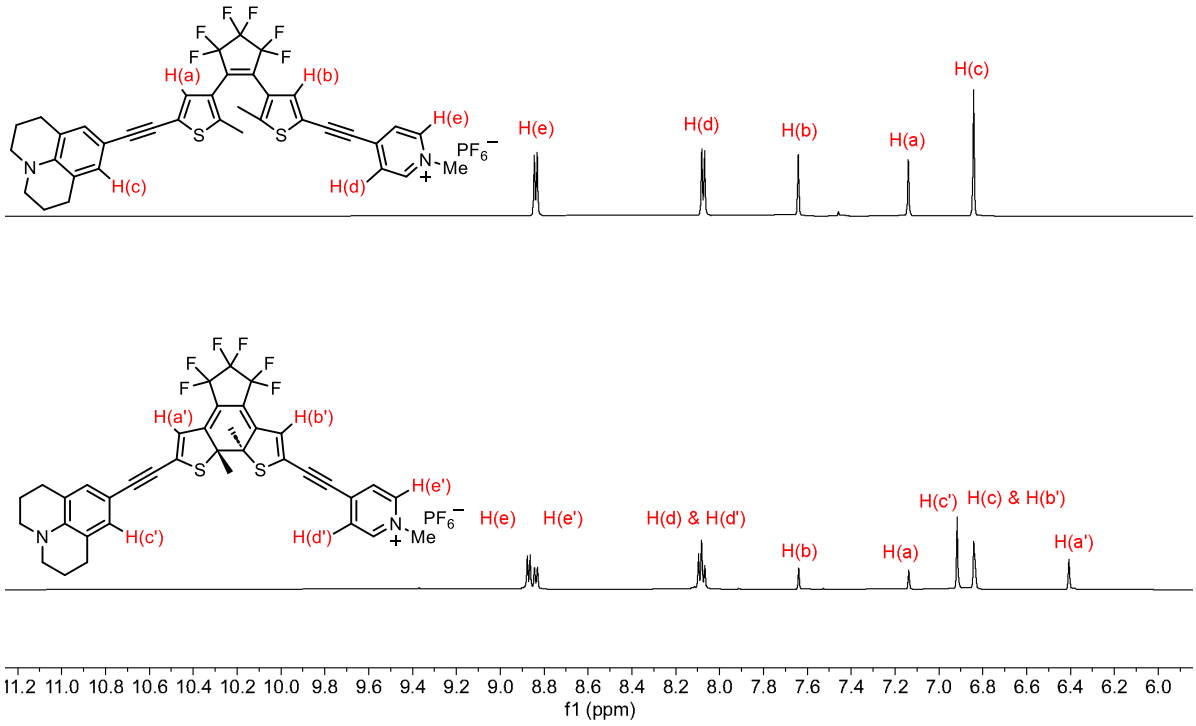


Figure 2.30 ^{1}H NMR spectra (500 MHz) of open-form **Dy-yA** (top) and 80% ± 1% conversion reached at PSS by 365 nm irradiation (bottom) in THF-d_8.

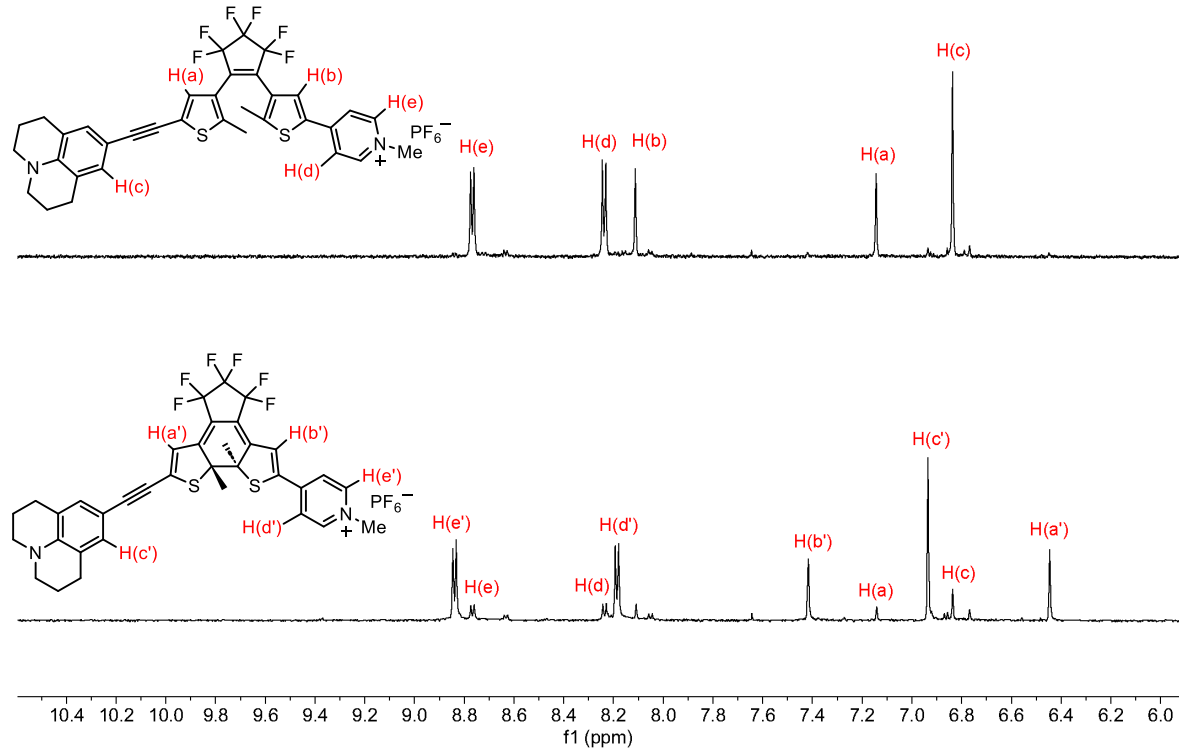


Figure 2.31 ^{1}H NMR spectra (500 MHz) of open-form **Dy-A** (top) and 85% ± 1% conversion reached at PSS by 365 nm irradiation (bottom) in THF-d_8.

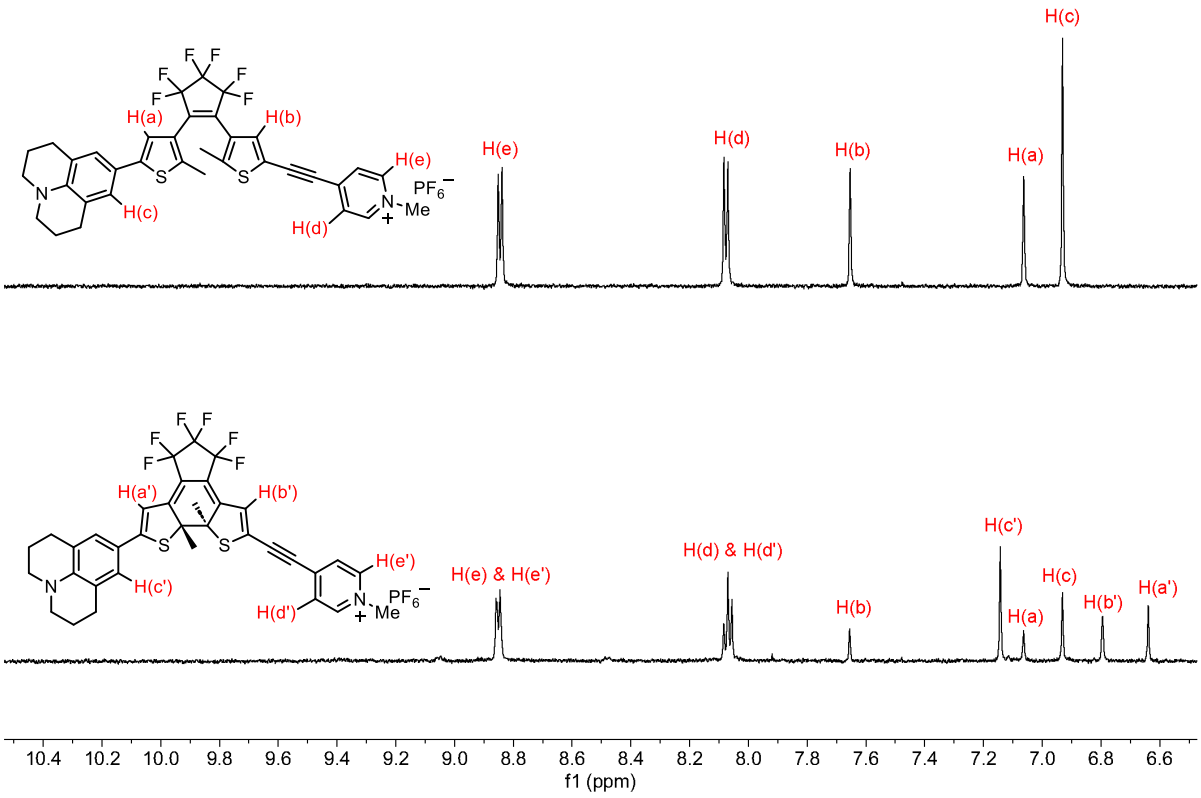


Figure 2.32 ^{1}H NMR spectra (500 MHz) of open-form **D-yA** (top) and 66% ± 1% conversion reached at PSS by 365 nm irradiation (bottom) in THF-d_8.

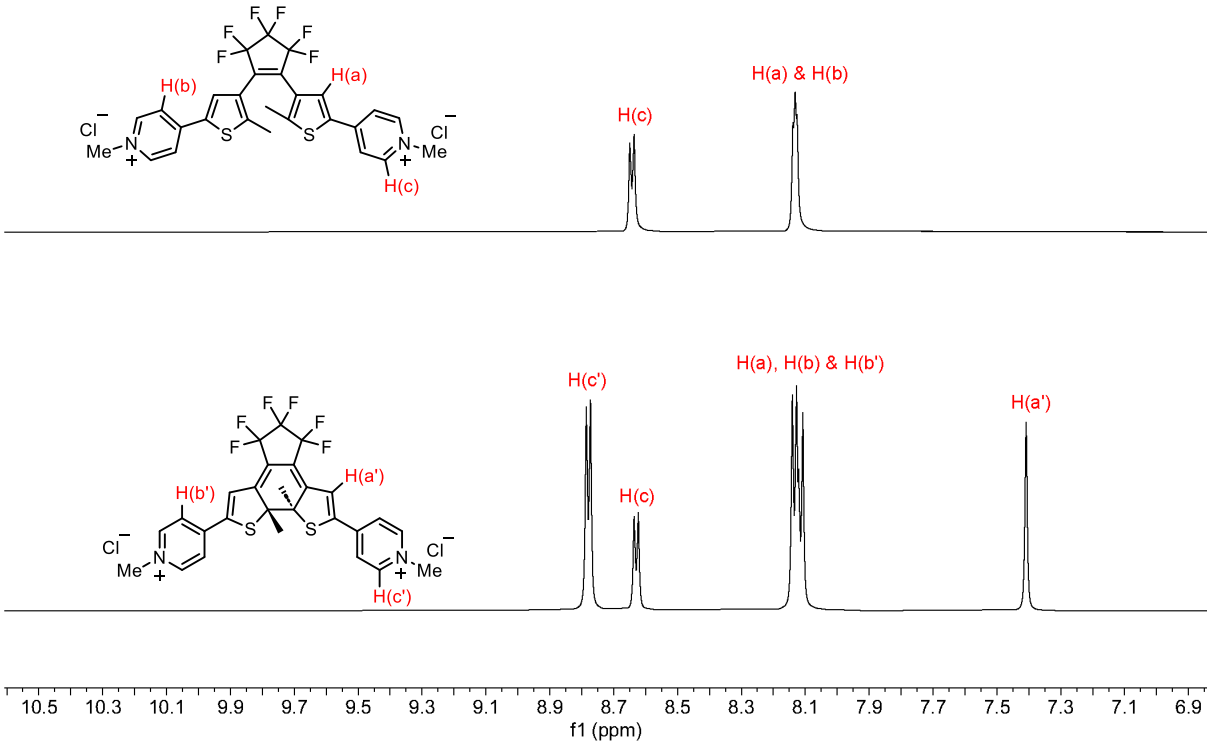


Figure 2.33 ^{1}H NMR spectra (500 MHz) of open-form **A-A** (chloride) (top) and 71% ± 1% conversion reached at PSS by 405 nm light irradiation (bottom) in D_2O.

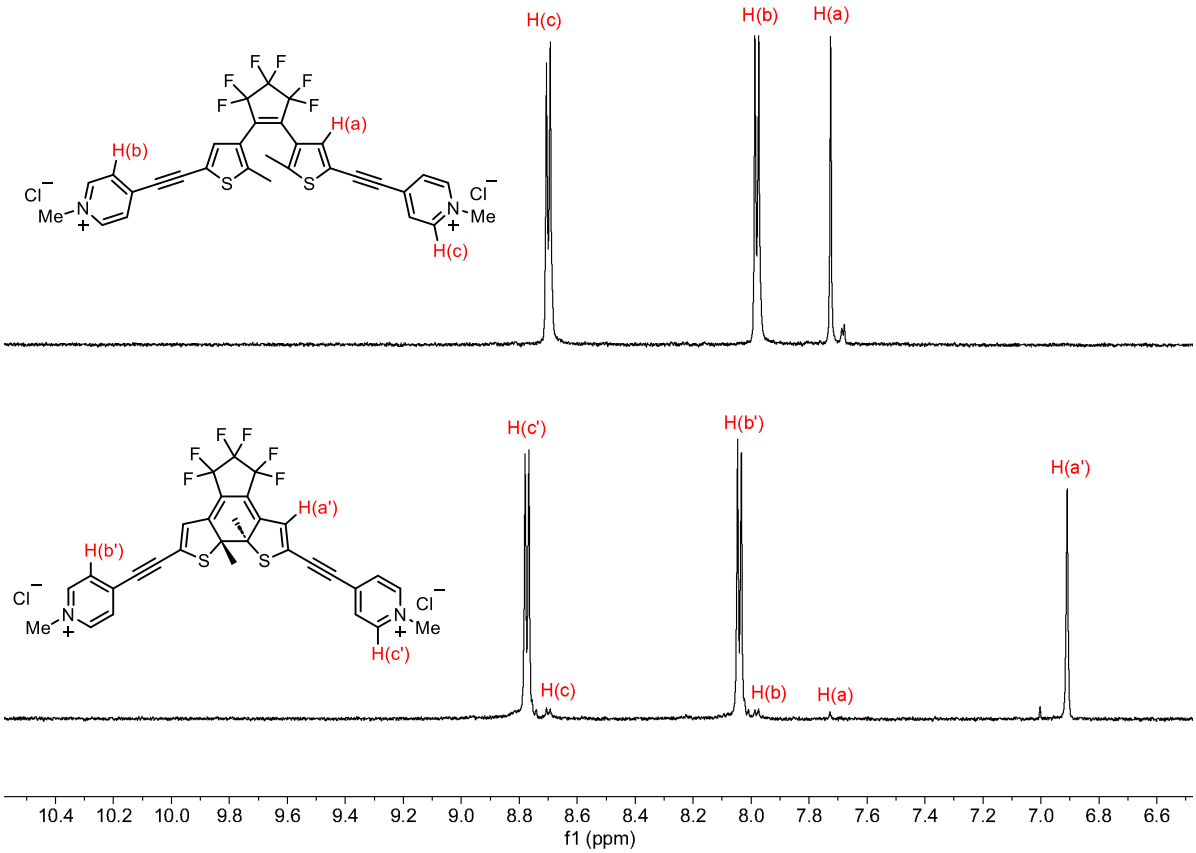


Figure 2.34 ^{1}H NMR spectra (500 MHz) of open-form **Ay-yA** (chloride) (top) and 96% ± 1% conversion reached at PSS by 405 nm irradiation (bottom) in D_2O.

2.4.7 Determination of PSD by UV-Vis

A typical procedure for obtaining the percentage conversion at PSD in acetonitrile is as follows: the UV-vis spectra of the open-form and the PSD reached in THF of **Dy-yA** were measured in acetonitrile. An open-form **Dy-yA** sample in acetonitrile was then repeatedly irradiated with 365 nm light and the UV-vis absorption was monitored after each cycle of irradiation until no further change in the UV-vis spectrum was observed, representing the UV-vis absorption of the PSS reached in acetonitrile. The percentage conversion at PSS in acetonitrile was then calculated taking the closed-form absorption maximum (693 nm) as the reference point based on the fact that the PSS absorption spectrum is a linear combination of open-form absorption and closed-form absorption, yielding the result of 33% conversion at PSS in acetonitrile with 365 nm light irradiation.

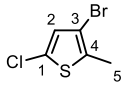
2.4.8 Determination of Fatigue Resistance

A typical procedure for measuring the fatigue resistance is as follows: a THF solution of **D-D** (2.8 μM, 3.0 mL) was placed in a cuvette in the sample holder of the UV-vis spectrometer and stirred at 25 °C. The absorbance of the sample at 654 nm was recorded. The solution was then

irradiated with a pulse of 365 nm light (18.9 mW, 10 s) and the absorption at 654 nm was recorded. Afterwards, the sample was irradiated with a pulse of 630 nm (112 mW, 3 min) and the absorbance at 653 nm was recorded. This procedure of irradiation with alternative light sources was repeated for 100 cycles and the absorption at 654 nm was recorded after each pulse of irradiation. The UV-vis absorption at 654 nm was plotted against the number of switching cycles.

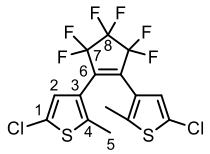
2.4.9 Synthetic Procedures

3-Bromo-5-chloro-2-methylthiophene 1b



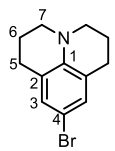
This compound was prepared from **1a** using a procedure published by Lucas and co-workers,[93] yielding a pale-yellow oil (10.1 g, 63%). δ_H (400 MHz, $CDCl_3$): 6.73 (1H, s, C(2)H), 2.32 (3H, s, C(5)H); δ_C (101 MHz, $CDCl_3$): 133.3, 128.6, 127.0, 107.7, 14.9.

3,3'-(Perfluorocyclopent-1-ene-1,2-diyl)bis(5-chloro-2-methylthiophene) 1



This compound was prepared using a procedure published by Hermes and co-workers,[94] yielding a brown solid (5.97 g, 64%). δ_H (400 MHz, $CDCl_3$): 6.88 (2H, s, C(2)H), 1.89 (6H, s, C(5)H); δ_C (101 MHz, $CDCl_3$): 140.7, 128.2, 125.7, 124.2, 14.5, C(6), C(7) and C(8) are too weak to be observed due to C-F coupling; δ_F (376 MHz, $CDCl_3$): −110.3 (4F, t, $^3J_{FF}$ 5.4, C(7)F), −131.9 (2F, p, $^3J_{FF}$ 5.4, C(8)F).

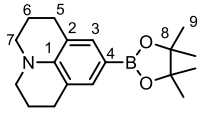
4-Bromojulolidine 3b



The compound **3b** was prepared following a published procedure[70] with modifications in the purification method. To a solution of julolidine (2.24 g, 12.9 mmol) in MeCN (40 mL) under inert atmosphere at 0 °C was slowly added a solution of NBS (2.53 g, 14.2 mmol, 1.1 equiv.) in MeCN (15 mL). The reaction mixture was warmed to room temperature and stirred for 3 h. After confirming the total consumption of julolidine by TLC (CH_2Cl_2), the mixture was poured into water, basified with a saturated solution of sodium bicarbonate, and extracted with CH_2Cl_2. The organic extracts were combined, washed with brine, dried with $MgSO_4$, and concentrated in vacuo to give the crude product as a red-wine-colored oil. The crude compound was purified by flash column chromatography (CH_2Cl_2) to yield the product as a red-wine-colored oil (1.99 g, 61%). δ_H (400 MHz, $CDCl_3$): 6.88 (2H, s,

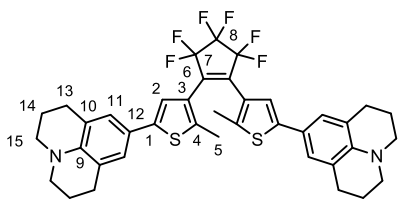
C(3)H), 3.11 (4H, t, $^3J_{HH}$ 5.8, C(7)H), 2.71 (4H, t, $^3J_{HH}$ 6.6, C(5)H), 1.94 (4H, tt, $^3J_{HH}$ 5.8, $^3J_{HH}$ 6.6, C(6)H); δ_C (101 MHz, $CDCl_3$): 142.0, 129.3, 123.7, 107.3, 49.9, 27.6, 21.9.

9-(4,4,5,5-Tetramethyl-1,3,2-dioxaborolan-2-yl)-2,3,6,7-tetrahydro-1*H*,5*H*-pyrido[3,2,1-*ij*]quinolone 3



Compound **3** was prepared following a published procedure with modification in the catalytic system.[71] Dry dioxane and triethylamine were degassed by three cycles of freeze-pump-thaw. A solution of **3b** (6.00 g, 23.8 mmol), $Pd(OAc)_2$ (267 mg, 1.19 mmol, 5 mol%), XPhos (1.13 mg, 2.38 mmol, 10 mol%) in dioxane (200 mL) and triethylamine 40 mL) was stirred at 80 °C for 10 min before adding pinacolborane (13.8 mL, 95.2 mmol, 4 equiv.). The reaction mixture was further stirred at 80 °C for 20 h. After confirming the full consumption of **5** by TLC (CH_2Cl_2), the reaction mixture was cooled to room temperature, concentrated in vacuo, dispersed in water (20 mL) and extracted with hexane/EtOAc (1:1). The crude product was purified by flash column chromatography (EtOAc/hexane 1:20) to yield the product as a white solid (5.81 g, 82%). δ_H (400 MHz, $CDCl_3$): 7.25 (2H, s, C(3)H), 3.17 (4H, t, $^3J_{HH}$ 5.4, C(7)H), 2.74 (4H, t, $^3J_{HH}$ 6.3, C(5)H), 1.94 (4H, tt, $^3J_{HH}$ 5.4, $^3J_{HH}$ 6.3, C(6)H), 1.31 (12H, s, C(9)H); δ_C (101 MHz, $CDCl_3$): 145.5, 133.8, 120.4, 83.1, 50.1, 27.7, 24.9, 22.0, C(4) was not observed due to coupling with ^{10}B and ^{11}B; δ_B (128 MHz, $CDCl_3$): 31.3 (C(4)B).

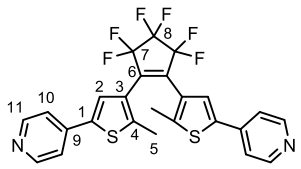
9,9'-((Perfluorocyclopent-1-ene-1,2-diyl)bis(5-methylthiophene-4,2-diyl))bis(2,3,6,7-tetrahydro-1*H*,5*H*-pyrido[3,2,1-*ij*]quinoline) D-D



1 (200 mg, 0.457 mmol), **3** (300 mg, 1.00 mmol), $Pd(PPh_3)_4$ (53.0 mg, 0.0458 mmol, 10 mol%), XPhos (50.0 mg, 0.105 mmol), and Cs_2CO_3 (1.0 g, 3.1 mmol) were added to the reaction vessel. Dioxane and water were degassed by three cycles of freeze-pump-thaw. To the mixture of solids under an argon atmosphere was added dioxane (10 mL) and water (2.5 mL). The reaction mixture was heated at reflux for 48 h before being allowed to cool to room temperature. The reaction mixture was poured into water (50 mL) and extracted with Et_2O. The organic extracts were combined, washed with brine, dried ($MgSO_4$), and concentrated in vacuo to yield the crude product as a brown oil. The crude

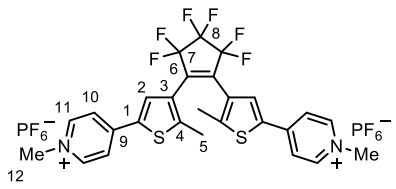
product was purified by flash column chromatography (PE/EtOAc 19:1) and precipitated in a mixture of CH_2Cl_2 and PE to yield the final product as a dark green solid (97 mg, 37%). δ_H (400 MHz, $CDCl_3$): 7.05 (2H, s, C(2)H), 6.98 (4H, s, C(11)H), 3.17 (8H, t, $^3J_{HH}$ 5.8, C(15)H), 2.78 (8H, t, $^3J_{HH}$ 6.5, C(13)H), 1.99 (8H, tt, $^3J_{HH}$ 5.8, $^3J_{HH}$ 6.5, C(14)H), 1.88 (6H, s, C(5)H); δ_C (101 MHz, $CDCl_3$): 143.4, 142.9, 138.9, 125.8, 124.5, 121.8, 121.0, 119.7, 50.1, 27.8, 22.1, 14.5, C(6), C(7) and C(8) are too weak to be observed due to C-F coupling; δ_F (376 MHz, $CDCl_3$): −110.0 (4F, t, $^3J_{FF}$ 5.7, C(7)F), −131.9 (2F, p, $^3J_{FF}$ 5.7, C(8)F); HRMS (ESI^+) *m/z*: $[M+H]^+$ calcd. for $C_{39}H_{37}N_2F_6S_2^+$ 711.2273; found 711.2272. UV-vis (MeCN): λ_{max} 346 nm (ε = 53000 M^{-1} cm^{-1}).

4,4'-((Perfluorocyclopent-1-ene-1,2-diyl)bis(5-methylthiophene-4,2-diyl))dipyridine. A-A(p)



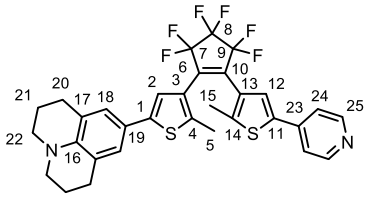
The compound **A-A(p)** was prepared following published procedure with slight modifications in the catalytic system.[72] **1** (300 mg, 0.686 mmol), 4-(4,4,5,5-tetramethyl-1,3,2-dioxaborolan-2-yl)pyridine (563 mg, 2.74 mmol), $Pd(PPh_3)_4$ (79.3 mg, 0.0686 mmol, 10 mol%), XPhos (56.3 mg, 0.137 mmol, 20 mol%), and Cs_2CO_3 (1.12 g, 3.43 mmol) were added to the reaction vessel. Dioxane and water were degassed by three cycles of freeze-pump-thaw. To the dried mixture of solids under an argon atmosphere was added dioxane (20 mL) and water (5 mL). The reaction mixture was heated at reflux for 72 h before being allowed to cool to room temperature. The reaction mixture was poured into water (70 mL) and then extracted with CH_2Cl_2. The organic extracts were combined, washed with brine, dried ($MgSO_4$), and concentrated in vacuo to yield the crude product as a brown oil. The crude product was purified by flash column chromatography (PE/EtOAc 1:5, 1% Et_3N) to yield the product as a white solid (141 mg, 39%). With contamination of triphenylphosphine oxide (18% by ^1H NMR), the crude product was not further purified. δ_H (400 MHz, $CDCl_3$): 8.61 (4H, d, $^3J_{HH}$ 4.3, C(11)H), 7.47 (2H, s, C(2)H), 7.40 (4H, d, $^3J_{HH}$ 4.3, C(10)H), 1.99 (6H, s, C(5)H); δ_C (101 MHz, $CDCl_3$): 150.7, 143.8, 140.2, 139.5, 126.3, 124.8, 119.7, 14.9, C(6), C(7) and C(8) are too weak to be observed due to C-F coupling; δ_F (376 MHz, $CDCl_3$): −110.1 (4F, t, $^3J_{FF}$ 5.3, C(7)F), −131.8 (2F, p, $^3J_{FF}$ 5.3, C(8)F).

4,4'-((Perfluorocyclopent-1-ene-1,2-diyl)bis(5-methylthiophene-4,2-diyl))bis(1-methylpyridin-1-ium) bishexafluorophosphate A-A



The compound **A-A(p)** was prepared following published procedure with modifications in the purification method.[72] To a solution of **A-A(p)** (260 mg, 0.498 mmol) in CH_2Cl_2 (15 mL) was added iodomethane (1.50 mL, 24.1 mmol). The reaction mixture was stirred at room temperature for 28 h and the precipitate in the reaction mixture was filtered off. The precipitate was dissolved in methanol (100 mg, 0.129 mmol) and then added to a solution of potassium hexafluorophosphate (8.0 g, 43.46 mmol) in water (100 mL). The solution was stirred at room temperature for 1 h for ion exchange and the precipitate was filtered off to yield the final product as a pale green solid (110 mg, 95%). δ_H (400 MHz, CD_3CN): 8.52 (4H, d, $^3J_{HH}$ 7.1, C(11)H), 8.06 (4H, d, $^3J_{HH}$ 7.1, C(10)H), 8.01 (2H, s, C(2)H), 4.22 (6H, s, C(12)H), 2.11 (6H, s, C(5)H); δ_C (101 MHz, $CDCl_3$): 151.3, 148.6, 146.2, 136.4, 132.0, 127.6, 123.5, 48.4, 15.4, C(6), C(7) and C(8) are too weak to be observed due to C-F coupling; δ_F (376 MHz, CD_3CN): −72.9 (6F, d, $^1J_{FP}$ 705.7, hexafluorophosphate), −110.9 (4F, t, $^3J_{FF}$ 4.9, C(7)F), −132.4 (2F, p, $^3J_{FF}$ 4.9, C(8)F). HRMS (ESI$^+$) *m/z*: $[M]^{2+}$ calcd. for $C_{27}H_{22}F_6N_2S_2^{2+}$ 276.0559; found 276.0558. UV-vis (MeCN): λ_{max} = 353 nm (ε = 661200 $M^{-1}\,cm^{-1}$).

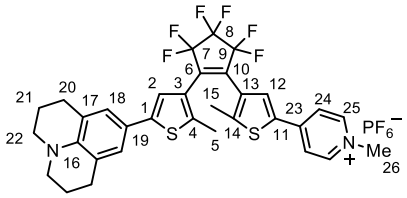
9-(4-(3,3,4,4,5,5-Hexafluoro-2-(2-methyl-5-(pyridin-4-yl)thiophen-3-yl)cyclopent-1-en-1-yl)-5-methylthiophen-2-yl)-2,3,6,7-tetrahydro-1*H*,5*H*-pyrido[3,2,1-*ij*]quinoline D-A(p)



1 (1.53 g, 3.50 mmol), **3** (1.10 g, 3.67 mmol, 1.05 equiv.), 4-(4,4,5,5-tetramethyl-1,3,2-dioxaborolan-2-yl)pyridine (753 mg, 3.67 mmol, 1.05 equiv.), $Pd(PPh_3)_4$ (202 mg, 175 μmol, 5 mol%), XPhos (167 mg, 350 μmol, 10 mol%), and Cs_2CO_3 (4.40 g, 13.5 mmol) were dried under high vacuum for 2 h. Dioxane and water were degassed by three cycles of freeze-pump-thaw. To the dried mixture of solids under an argon atmosphere was added dioxane (100 mL) and water (20 mL). The reaction mixture was heated at reflux for 72 h before being allowed to cool to room temperature. The reaction mixture was concentrated in vacuo to remove dioxane and then poured into water and extracted with CH_2Cl_2. The organic extracts were combined, washed with brine, dried ($MgSO_4$), and concentrated in vacuo to yield the crude product as a brown oil. The crude product was purified by flash column chromatography (PE/EtOAc 4:1, 1% Et_3N) to yield the product as a green solid (210 mg, 28%). δ_H (400 MHz,

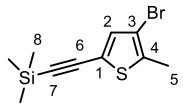
$CDCl_3$): 8.60 (2H, d, $^3J_{HH}$ 4.4, C(25)H), 7.47 (1H, s, C(12)H), 7.40 (2H, d, $^3J_{HH}$ 4.4, C(24)H), 7.02 (1H, s, C(2)H), 6.96 (2H, s, C(18)H), 3.17 (4H, t, $^3J_{HH}$ 5.8, C(22)H), 2.76 (4H, t, $^3J_{HH}$ 6.4, C(20)H), 2.00–1.94 (overlapping s and tt, 7H, $^3J_{HH}$ 5.8, $^3J_{HH}$ 6.4, C(15)H and C(21)H), 1.90 (s, 3H, C(5)H); δ_C (101 MHz, $CDCl_3$): 150.7, 144.0, 143.9, 143.0, 140.5, 138.9, 138.8, 126.7, 125.4, 125.1, 124.5, 121.8, 120.6, 119.7, 119.4, 50.1, 27.8, 22.0, 14.9, 14.6, C(6), C(7) and C(8) are too weak to be observed due to C-F coupling; δ_F (376 MHz, $CDCl_3$): −109.8 (2F, t, $^3J_{FF}$ 8.1, C(7)F), −110.2 (2F, t, $^3J_{FF}$ 8.6, C(9)F), −131.9 (4F, tt, $^3J_{FF}$ 8.1, $^3J_{FF}$ 8.6, C(8)F). HRMS (ESI$^+$) *m/z*: $[M+H]^+$ calcd. for $C_{32}H_{27}F_6N_2S_2^+$ 617.1514; found 617.1513.

4-(4-(3,3,4,4,5,5-Hexafluoro-2-(2-methyl-5-(2,3,6,7-tetrahydro-1*H*,5*H*-pyrido[3,2,1-*ij*]quinolin-9-yl)thiophen-3-yl)cyclopent-1-en-1-yl)-5-methylthiophen-2-yl)-1-methylpyridin-1-ium hexafluorophsphate D-A



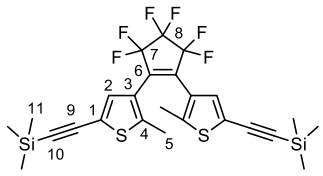
To a solution of **D-A(p)** (100 mg, 162 μmol) in CH_2Cl_2 (10 mL) was added iodomethane (1.00 mL, 16.2 mmol, 100 equiv.). The reaction mixture was stirred at 40 °C for 15 h until the starting material was fully consumed (monitored by MS). The reaction mixture was then cooled to room temperature and concentrated in vacuo to yield a green oil. The green oil was dissolved in methanol (2 mL) and then added to a solution of potassium hexafluorophosphate (1.5 g, 8.1 mmol) in water (20 mL). The reaction mixture for ion exchange was stirred at room temperature for 1 h and the precipitation was filtered off to yield the crude product as a yellow solid. The crude product was further purified by flash column chromatography (CH_2Cl_2/MeOH 95:5) to yield the product as a pale green solid (113 mg, 90%). δ_H (400 MHz, DMSO): 8.89 (2H, d, $^3J_{HH}$ 7.5, C(25)H), 8.36 (2H, d, $^3J_{HH}$ 7.5, C(24)H), 8.30 (1H, s, C(12)H), 7.14 (1H, s, C(2)H), 6.95 (2H, s, C(18)H), 4.26 (3H, s, C(26)H), 3.14 (4H, t, $^3J_{HH}$ 5.7, C(22)H), 2.68 (4H, t, $^3J_{HH}$ 6.4, C(20)H), 2.08 (3H, s, C(15)H), 1.91 (3H, s, C(5)H), 1.86 (4H, tt, $^3J_{HH}$ 5.7, $^3J_{HH}$ 6.4, C(21)H); δ_C (101 MHz, DMSO): 149.0, 146.4, 145.7, 143.7, 142.7, 138.3, 135.2, 131.1, 126.7, 124.2, 123.8, 122.1, 121.1, 119.2, 118.5, 49.2, 47.0, 27.0, 21.3, 14.5, 14.0, C(6), C(7), C(8), C(9) and C(10) are not observed because the carbon signals are very weak resulting from the C-F coupling; δ_F (376 MHz, DMSO): −70.2 (6F, d, $^1J_{FP}$ 710.1, hexafluorophosphate), −109.2 (2F, t, $^3J_{FF}$ 8.9, C(7)F), −109.6 (2F, t, $^3J_{FF}$ 8.1, C(9)F), −131.1 (2F, tt, $^3J_{FF}$ 8.9, $^3J_{FF}$ 8.1, C(8)F). HRMS (ESI$^+$) *m/z*: $[M]^+$ calcd. for $C_{33}H_{29}F_6N_2S_2^+$ 631.1671; found 631.1660. UV-vis (MeCN): λ_{max} = 350 nm (ε = 57200 M^{-1} cm^{-1}).

((4-Bromo-5-methylthiophen-2-yl)ethynyl)trimethylsilane 11a



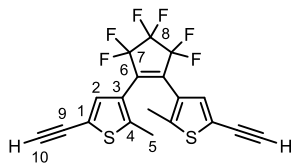
Compound **11a** was synthesized following a published procedure,[95] yielding the product as a white solid (4.69 g, 88%, including by-product) with around 12% (estimated by ^{1}H NMR) contamination by the by-product 1,4-bis(trimethylsilyl)butadiyne from trimethylsilylacetylene homocoupling. The product was not further purified as the by-product does not react in the next step. δ_H (400 MHz, $CDCl_3$): 7.02 (1H, s, C(2)H), 2.36 (3H, s, C(5)H), 0.23 (9H, s, C(8)H); δ_C (101 MHz, $CDCl_3$): 136.5, 135.0, 120.8, 108.9, 99.7, 96.6, 15.0, −0.1.

(((Perfluorocyclopent-1-ene-1,2-diyl)bis(5-methylthiophene-4,2-diyl))bis(ethyne-2,1-diyl))bis(trimethylsilane) 11b



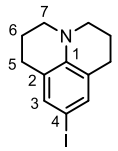
The compound **11** was prepared from a published procedure,[95] yielding a white solid (2.40 g, 45%). δ_H (400 MHz, $CDCl_3$): 7.19 (2H, s, C(2)H), 1.88 (6H, s, C(5)H), 0.25 (18H, s, C(11)H); δ_C (101 MHz, $CDCl_3$): 143.5, 132.2, 124.7, 121.9, 100.2, 96.3, 14.6, −0.1, C(6), C(7) and C(8) are too weak to be observed due to C-F coupling; δ_F (376 MHz, ($CDCl_3$): −110.4 (4F, t, $^{3}J_{FF}$ 5.3, C(7)F), −131.9 (2F, p, $^{3}J_{FF}$ 5.3, C(8)F).

3,3'-(Perfluorocyclopent-1-ene-1,2-diyl)bis(5-ethynyl-2-methylthiophene) 11



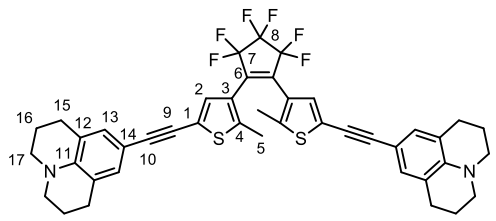
The TMS-deprotection was carried out following a published procedure, yielding a white solid (747 mg, 89%).[95] δ_H (400 MHz, $CDCl_3$): 7.23 (2H, s, C(2)H), 3.35 (2H, s, C(10)H), 1.91 (6H, s, C(5)H); δ_C (101 MHz, $CDCl_3$): 143.8, 132.7, 124.7, 120.8, 82.4, 75.9, 14.5 C(6), C(7) and C(8) are too weak to be observed due to C-F coupling; δ_F (376 MHz, ($CDCl_3$): −110.4 (4F, t, $^{3}J_{FF}$ 5.4, C(7)F), −131.9 (2F, p, $^{3}J_{FF}$ 5.4, C(8)F).

4-Iodojulolidine 5



To a solution of julolidine **5a** (2.00 g, 11.5 mmol) in a mixture of 1,4-dioxane (25 mL) and pyridine (25 mL) under an argon atmosphere at 0 °C was slowly added a solution of iodine (5.30 g, 21.0 mmol, 1.8 equiv.) in 1,4-dioxane (10 mL). The reaction mixture was stirred at 0 °C for 2 h before being allowed to warm to room temperature. Iodine (2.93 g, 11.5 mmol, 1 equiv.) was further added and the reaction was stirred at room temperature for 1 h. The reaction mixture was then poured into a saturated aqueous solution of sodium thiosulfate and extracted with CH_2Cl_2. The organic extracts were combined, dried with $MgSO_4$, and concentrated in vacuo to give the crude product as a brown oil. The crude compound was purified by flash column chromatography (CH_2Cl_2) to yield the product as a brown oil (2.50 g, 72%). δ_H (400 MHz, $CDCl_3$): 7.06 (2H, s, C(3)H), 3.13 (4H, t, $^3J_{HH}$ 6.1, C(7)H), 2.70 (4H, t, $^3J_{HH}$ 6.8, C(5)H), 1.94 (4H, tt, $^3J_{HH}$ 6.1, $^3J_{HH}$ 6.8, C(6)H); δ_C (101 MHz, $CDCl_3$): 142.5, 135.1, 124.1, 76.2, 49.8, 27.4, 21.8. HRMS (ESI^+) *m/z*: $[M+H]^+$ calcd. for $C_{12}H_{15}IN$ 300.0559; found 300.0559.

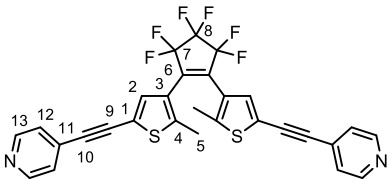
3,3'-(Perfluorocyclopent-1-ene-1,2-diyl)bis(5-((2,3,7,8,9,9a-hexahydro-1*H*-phenalen-5-yl)ethynyl)-2-methylthiophene) Dy-yD



11 (150 mg, 360 µmol), **5** (269 mg, 900 µmol, 2.5 equiv.), $Pd(PPh_3)_4$ (41.6 mg, 36.0 µmol, 10 mol%), and CuI (13.6 mg, 71.3 µmol, 20 mol%) were dried under high vacuum for 30 min. Dry triethylamine was degassed by three cycles of freeze-pump-thaw. To the dried mixture of solids under an argon atmosphere was added triethylamine. The reaction mixture was stirred at 45 °C for 20 h before being allowed to cool to room temperature. Upon completion of the reaction verified by TLC (PE/EtOAc 9:1 with 1% triethylamine), the reaction mixture was concentration in vacuo to yield the crude product as a green oil. The crude product was then purified by flash column chromatography (PE/EtOAc 9:1 with 1% triethylamine) to yield the product as a green solid (244 mg, 56%). δ_H (400 MHz, $CDCl_3$): 7.13 (2H, s, C(2)H), 6.94 (4H, s, C(13)H), 3.19 (8H, t, $^3J_{HH}$ 6.0, C(17)H), 2.71 (8H, t, $^3J_{HH}$ 6.2, C(15)H), 1.95 (8H, tt, $^3J_{HH}$ 6.2, $^3J_{HH}$ 6.0, C(16)H), 1.89 (6H, s, C(5)H); δ_C (101 MHz, $CDCl_3$): 143.4, 142.2, 130.3, 130.0, 124.8, 123.2, 121.1, 107.8, 96.0, 79.1, 50.0, 27.7, 21.8, 14.6, C(6), C(7) and C(8) are too weak to be observed due to C-F coupling; δ_F (376 MHz, ($CDCl_3$): −110.2 (4F, t, $^3J_{FF}$ 5.2, C(7)F), −131.9

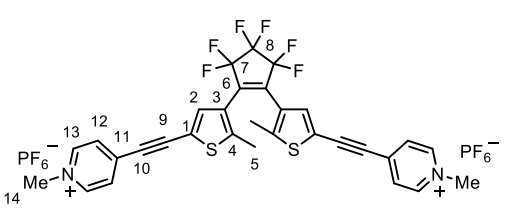
(2F, p, $^3J_{FF}$ 5.2, C(8)F). HRMS (ESI$^+$) *m/z*: [M+H]$^+$ calcd. for $C_{43}H_{36}F_6N_2S_2^+$ 758.2219; found 758.2212. UV-vis (MeCN): λ_{max} = 363 nm (ε = 84800 M^{-1} cm^{-1}).

4,4'-(((Perfluorocyclopent-1-ene-1,2-diyl)bis(5-methylthiophene-4,2-diyl))bis(ethyne-2,1-diyl))dipyridine Ay-yA(p)



11 (223 mg, 535 µmol), 4-iodopyridine (329 mg, 1.60 mmol, 3 equiv.), $Pd(PPh_3)_4$ (30.9 mg, 26.7 µmol, 5 mol%), and copper(I) iodide (10.2 mg, 53.5 µmol, 10 mol%) were dried under high vacuum for 30 min. Anhydrous triethylamine was degassed by three cycles of freeze-pump-thaw. To the dried mixture of solids under an argon atmosphere was added degassed triethylamine (20 mL). The reaction mixture was stirred at 45 °C for 20 h before being allowed to cool to room temperature. Upon completion of the reaction verified by TLC (PE/EtOAc 4:1 with 1% triethylamine), the reaction mixture was concentration in vacuo. The crude product was then purified by flash column chromatography (PE/EtOAc 4:1 with 1% triethylamine) to yield the product as an off-white solid (150 mg, 49%). δ_H (400 MHz, $CDCl_3$): 8.61 (4H, d, $^3J_{HH}$ 4.5, C(13)H), 7.35 (4H, d, $^3J_{HH}$ 4.5, C(12)H), 7.33 (2H, s, C(2)H), 1.97 (6H, s, C(5)H); δ_C (101 MHz, $CDCl_3$): 150.0, 144.9, 132.8, 130.7, 125.2(4), 125.1(5), 120.8, 91.5, 86.0, 14.7, C(6), C(7) and C(8) are too weak to be observed due to C-F coupling; δ_F (376 MHz, ($CDCl_3$): −110.3 (4F, t, $^3J_{FF}$ 5.0, C(7)F), −131.8 (2F, p, $^3J_{FF}$ 5.0, C(8)F); HRMS (ESI$^+$) *m/z*: [M+H]$^+$ calcd. for $C_{29}H_{17}F_6N_2S_2^+$ 571.0732; found 571.0721.

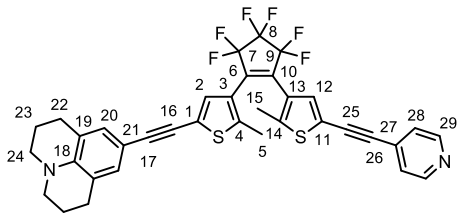
4,4'-(((Perfluorocyclopent-1-ene-1,2-diyl)bis(5-methylthiophene-4,2-diyl))bis(ethyne-2,1-diyl))bis(1-methylpyridin-1-ium) bishexafluorophosphate Ay-yA



To a solution of **Ay-yA(p)** (55.0 mg, 96.4 µmol) in CH_2Cl_2 (5 mL) was added iodomethane (2.0 mL, 34 mmol). The reaction mixture was stirred at room temperature for 24 h and the precipitation was filtered off. The precipitate was dissolved in methanol (2 mL) and added to a solution of potassium hexafluorophosphate (4.00 g, 21.7 mmol) in water (50 mL). The solution was stirred at room temperature for 1 h for ion exchange and the precipitate was filtered off to yield the product as a dark green solid (95 mg, 83%). δ_H (400 MHz, CD_3CN): 8.56 (4H, d, $^3J_{HH}$ 6.7,

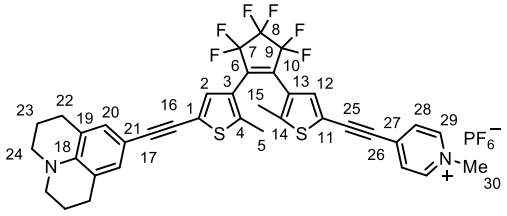
C(13)H), 7.95 (4H, d, $^3J_{HH}$ 6.7, C(12)H), 7.61 (2H, s, C(2)H), 4.26 (6H, s, C(14)H), 2.19 (6H, s, C(5)H); δ_C (101 MHz, CD_3CN): 150.0, 146.2, 140.3, 136.8, 129.7, 126.1, 119.8, 96.3, 90.7, 49.1, 15.1, C(6), C(7) and C(8) are too weak to be observed due to C-F coupling; δ_F (376 MHz, (CD_3CN): −72.8 (12F, d, $^1J_{FP}$ 707.6, hexafluorophosphate), −110.8 (4F, t, J_{FF} 5.0, C(7)F), −132.3 (2F, p, $^3J_{FF}$ 5.0, C(8)F). HRMS (ESI$^+$) *m/z*: [M^{2+}] calcd. for $C_{31}H_{22}F_6N_2S_2^{2+}$ 300.0559; found 300.0559. UV-vis (MeCN): λ_{max} = 371 nm (ε = 67100 M^{-1} cm^{-1}).

9-((4-(3,3,4,4,5,5-Hexafluoro-2-(2-methyl-5-(pyridin-4-ylethynyl)thiophen-3-yl)cyclopent-1-en-1-yl)-5-methylthiophen-2-yl)ethynyl)-2,3,6,7-tetrahydro-1*H*,5*H*-pyrido[3,2,1-*ij*]quinoline Dy-yA(p)



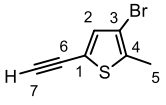
11 (0.395 g, 0.704 mmol, 1 equiv.), 4-iodopyridine (0.159 g, 0.775 mmol, 1.1 equiv.), **5** (0.232 g, 0.775 mmol, 1.1 equiv.), $Pd(PPh_3)_4$ (81.4 mg, 70.4 μmol, 10 mol%), and CuI (26.8 mg, 141 μmol, 20 mol%) were dried under high vacuum for 30 min. Dry triethylamine was degassed by three cycles of freeze-pump-thaw. To the dried mixture of solids under an argon atmosphere was added degassed triethylamine (20 mL). The reaction mixture was stirred at 45 °C for 20 h before being allowed to cool to room temperature. Upon completion of the reaction verified by TLC (PE/EtOAc 4:1 with 1% triethylamine), the reaction mixture was concentrated in vacuo. The crude product was then purified by flash column chromatography (PE/EtOAc 4:1 with 1% triethylamine) to yield the product as a dark green solid (150 mg, 32%). δ_H (400 MHz, $CDCl_3$): 8.61 (2H, d, $^3J_{HH.}$ 4.7, C(29)H), 7.35 (2H, d, $^3J_{HH.}$ 4.7, C(28)H), 7.33 (1H, s, C(12)H), 7.12 (1H, s, C(2)H), 6.94 (2H, s, C(20)H), 3.19 (4H, t, $^3J_{HH}$ 5.6, C(24)H), 2.71 (4H, t, $^3J_{HH}$ 6.3, C(22)H), 1.98-1.91 (7H, overlapping s and tt, $^3J_{HH}$ 5.6, $^3J_{HH}$ 6.3, C(15)H and C(23)H), 1.91 (3H, s, C(5)H); δ_C (101 MHz, $CDCl_3$): 150.0, 145.0, 143.5, 142.0, 133.0, 130.8, 130.3, 129.8, 125.4, 125.3, 124.6, 123.6, 121.1, 120.5, 107.6, 96.3, 91.3, 86.2, 78.9, 50.0, 27.7, 21.8, 14.8, 14.6, C(6), C(7), C(8), C(9) and C(10) are too weak to be observed due to C-F coupling; δ_F (376 MHz, ($CDCl_3$): −110.1 (2F, t, $^3J_{FF}$ 9.8, C(9)F), −110.3 (2F, t, $^3J_{FF}$ 10.3, C(7)F), −131.8 (2F, tt, $^3J_{FF}$ 9.8, $^3J_{FF}$ 10.3, C(8)F). HRMS (ESI$^+$) *m/z*: $[M+H]^+$ calcd. for $C_{36}H_{27}F_6N_2S_2^+$ 665.1514; found 665.1506.

4-((4-(3,3,4,4,5,5-Hexafluoro-2-(2-methyl-5-((2,3,6,7-tetrahydro-1*H*,5*H*-pyrido[3,2,1-*ij*]quinolin-9-yl)ethynyl)thiophen-3-yl)cyclopent-1-en-1-yl)-5-methylthiophen-2-yl)ethynyl)-1-methylpyridin-1-ium hexafluorophosphate Dy-yA



To a solution of **Dy-yA(p)** (200 mg, 312 μmol) in CH_2Cl_2 (20 mL) was added iodomethane (2.0 mL, 32 mmol). The reaction mixture was stirred at room temperature for 20 h and at 45 °C for 4 h before being concentrated in vacuo. The crude product was dissolved in methanol and added to a solution of potassium hexafluorophosphate (4.00 g, 21.7 mmol) in water (50 mL). The solution was stirred at room temperature for 1 h for ion exchange and the precipitate was filtered off to yield the crude product as a brown solid. The crude product was further purified by flash column chromatography (CH_2Cl_2/MeOH 95:5) to yield the product as a pale green solid (206 mg, 82%). δ_H (400 MHz, CD_3CN): 8.53 (2H, d, $^3J_{HH}$ 6.8, C(29)H), 7.95 (2H, d, $^3J_{HH}$ 6.8, C(28)H), 7.60 (1H, s, C(12)H), 7.13 (1H, s, C(2)H), 6.86 (2H, s, C(20)H), 4.24 (3H, s, C(30)H), 3.20 (4H, t, $^3J_{HH}$ 5.7, C(24)H), 2.68 (4H, t, $^3J_{HH}$ 6.3, C(22)H), 2.05 (3H, s, C(15)H), 1.96 (3H, s, C(5)H), 1.89 (4H, tt, $^3J_{HH}$ 5.7, $^3J_{HH}$ 6.3, C(23)H); δ_C (101 MHz, CD_3CN): 149.9, 146.0, 144.5, 143.9, 140.3, 136.9, 130.8, 130.6, 129.6, 126.4, 125.1, 124.2, 122.1, 119.4, 107.5, 97.2, 96.2, 90.5, 79.1, 50.4, 49.0, 28.1, 22.2, 15.0, 14.6, C(6), C(7), C(8), C(9) and C(10) are too weak to be observed due to C-F coupling; δ_F (376 MHz, (CD_3CN): −73.0 (6F, d, $^1J_{FP}$ 708.2, hexafluorophosphate), −110.7 (2F, t, $^3J_{FF}$ 5.1, C(9)F), −110.9 (2F, t, $^3J_{FF}$ 6.3, C(7)F), −132.4 (2F, tt, $^3J_{FF}$ 5.1, $^3J_{FF}$ 6.3, C(8)F). HRMS (ESI$^+$) *m/z*: [M$^+$] calcd. for $C_{37}H_{29}F_6N_2S_2^+$ 679.1642; found 679.1661. UV-vis (MeCN): λ_{max} = 369 nm (ε = 72400 M^{-1} cm^{-1}).

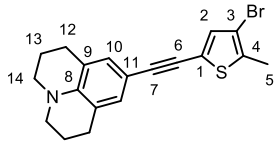
3-Bromo-5-ethynyl-2-methylthiophene 4



To a solution of **11a** (170 mg, 622 μmol) in a mixture of THF (5 mL) and methanol (5 mL) was added solid potassium carbonate (1.00 g, 7.20 mmol) and the reaction mixture was stirred at room temperature for 30 min. Upon the completion of the reaction verified by TLC (PE), the reaction mixture was poured into water (30 mL) and extracted with CH_2Cl_2. The organic extracts were combined, washed with water, dried ($MgSO_4$), and concentrated in vacuo. The crude product was purified by flash column chromatography (PE) to yield the final product as a colorless oil (106 mg, 85%). δ_H (400 MHz,

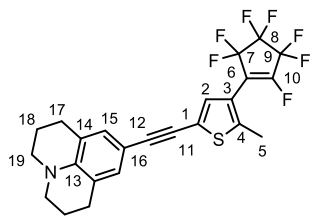
$CDCl_3$): 7.07 (1H, s, C(2)H), 3.33 (1H, s, C(7)H), 2.38 (3H, s, C(5)H); δ_C (101 MHz, $CDCl_3$): 136.9, 135.5, 119.6, 108.9, 82.0, 76.2, 15.0.

9-((4-Bromo-5-methylthiophen-2-yl)ethynyl)-2,3,6,7-tetrahydro-1*H*,5*H*-pyrido[3,2,1-*ij*]quinoline 6



5 (1.00 g, 4.97 mmol), **4** (1.49 g, 4.97 mmol), $Pd(PPh_3)_4$ (575 mg, 497 μmol, 10 mol%), and CuI (189 mg, 995 μmol, 20 mol%) were dried under high vacuum for 30 min. Dry toluene and DIPA were degassed by three cycles of freeze-pump-thaw. To the dried mixture of solids under an argon atmosphere was added degassed toluene (50 mL) and DIPA (50 mL). The reaction mixture was stirred at 75 °C for 23 h before being allowed to cool to room temperature. Upon completion of the reaction verified by TLC (PE/EtOAc 20:1), the reaction mixture was concentration in vacuo. The crude product was then purified by flash column chromatography (PE/EtOAc 20:1) to yield the product as an off-white solid (831 mg, 45%). δ_H (400 MHz, $CDCl_3$): 6.94 (1H, s, C(2)H), 6.92 (2H, s, C(10)H), 3.19 (4H, t, $^3J_{HH}$ 5.8, C(14)H), 2.71 (4H, t, $^3J_{HH}$ 6.4, C(12)H), 2.37 (3H, s, C(5)H), 1.94 (4H, tt, $^3J_{HH}$ 5.8, $^3J_{HH}$ 6.4, C(13)H); δ_C (101 MHz, $CDCl_3$): 143.4, 134.9, 132.7, 130.3, 122.4, 121.1, 108.8, 108.0, 95.8, 79.2, 50.0, 27.7, 21.8, 15.0. HRMS (ESI^+) *m/z*: $[M+H]^+$ calcd. for $C_{19}H_{13}N_1Br_1S_1$ 372.0416; found 372.0417.

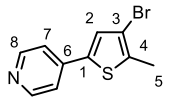
9-((5-Methyl-4-(perfluorocyclopent-1-en-1-yl)thiophen-2-yl)ethynyl)-2,3,6,7-tetrahydro-1*H*,5*H*-pyrido[3,2,1-*ij*]quinoline 8



To a solution of **6** (830 mg, 2.23 mmol) in anhydrous THF (70 mL) was added *n*-BuLi (1.6 M in hexane, 1.53 mL, 2.45 mmol, 1.1 equiv.) dropwise at −78 °C. The mixture was stirred for 2 h before adding octafluorocyclopentene (1.00 mL, 7.45 mmol, 3.3 equiv.). The reaction mixture was stirred at −78 °C for 2 h and then at room temperature for 2 h followed by quenching with water and extracting with CH_2Cl_2. The organic extracts were combined and washed with saturated aqueous solution of sodium bicarbonate and water, dried ($MgSO_4$), and concentrated in vacuo. The crude product was purified by flash column chromatography (PE/EtOAc 20:1) followed by precipitation in methanol to yield the product as an off-white solid (450 mg, 42%). δ_H (400 MHz, $CDCl_3$): 7.12 (1H, s, C(2)H), 6.94

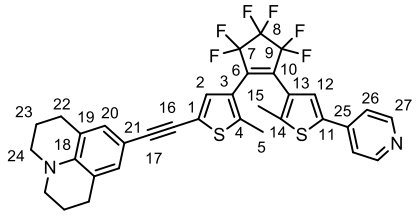
(2H, s, C(15)H), 3.19 (4H, t, $^3J_{HH}$ 5.9, C(19)H), 2.71 (4H, t, $^3J_{HH}$ 6.9, C(17)H), 2.43 (3H, d, $^6J_{HF}$ 3.3, C(5)H, 1.95 (4H, tt, $^3J_{HH}$ 5.9, $^3J_{HH}$ 6.9, C(18)H); δ_C (101 MHz, $CDCl_3$): 143.8, 143.5, 130.3, 129.8, 123.6, 121.1, 107.7, 96.3, 78.7, 51.0, 50.0, 27.7, 21.8, 14.8; C(6), C(7), C(8), C(9), and C(10) are too weak to be observed due to C-F coupling; δ_F (376 MHz, $CDCl_3$): −108.5 (2F, m, C(8)F), −118.0 (2F, m, C(9)F), −127.2 (1F, m, C(10)F), −130.0 (2F, m, C(7)F).

4-(4-Bromo-5-methylthiophen-2-yl)pyridine 9



9 (3.00 g, 11.7 mmol, 1 equiv.), 4-(4,4,5,5-tetramethyl-1,3,2-dioxaborolan-2-yl)pyridine (2.52 g, 12.3 mmol, 1.05 equiv.), $Pd(PPh_3)_4$ (135 mg, 117 μmol, 10 mol%), and Cs_2CO_3 (2.00 g, 6.14 mmol) were dried under high vacuum for 2 h. Anhydrous 1,4-dioxane and water were degassed by three cycles of freeze-pump-thaw. To the dried mixture of solids under an argon atmosphere was added 1,4-dioxane (40 mL) and water (5 mL). The reaction mixture was stirred at 80 °C for 48 h before being allowed to cool to room temperature. The reaction was concentrated in vacuo, dispersed in water, and then extracted with CH_2Cl_2. The organic extracts were combined, dried ($MgSO_4$), and concentrated in vacuo. The crude product was purified by flash column chromatography (EtOAc) followed by precipitation with pentane at −78 °C to yield the product as an off-white solid (2.38 g, 80%). δ_H (400 MHz, $CDCl_3$): 8.58 (2H, d, $^3J_{HH}$ 5.9, C(8)H), 7.38 (2H, d, $^3J_{HH}$ 5.9, C(7)H), 7.31 (1H, s, C(2)H), 2.44 (3H, s, C(5)H); δ_C (101 MHz, $CDCl_3$): 150.6, 140.5, 138.0, 136.6, 128.1, 119.3, 110.8, 15.2. HRMS (ESI^+) *m/z*: $[M+H]^+$ calcd. for $C_{10}H_9NBrS$ 253.9634; found 253.9635.

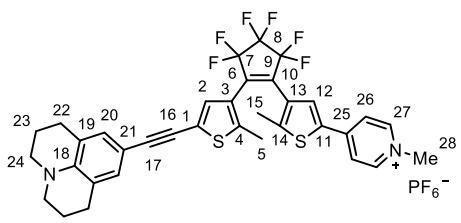
9-((4-(3,3,4,4,5,5-Hexafluoro-2-(2-methyl-5-(pyridin-4-yl)thiophen-3-yl)cyclopent-1-en-1-yl)-5-methylthiophen-2-yl)ethynyl)-2,3,6,7-tetrahydro-1*H*,5*H*-pyrido[3,2,1-*ij*]quinoline Dy-A(p)



To a solution of **10** (240 mg, 944 μmol, 1 equiv.) in anhydrous THF (50 mL) was added *n*-BuLi (1.6 M in hexane, 0.70 mL, 1.1 mmol, 1.2 equiv.) dropwise at −78 °C. The mixture was stirred for 1.5 h before adding a solution of **8** (413 mg, 850 μmol, 0.9 equiv.) in anhydrous THF (5 mL). The reaction mixture was stirred for 2.5 h at −78 °C and then 2 h at room temperature followed by quenching with water (100 mL) and extraction with CH_2Cl_2. The organic extracts were

combined and washed with saturated aqueous sodium bicarbonate solution and water, dried ($MgSO_4$), and concentrated in vacuo. The crude product was purified by flash column chromatography (PE/EtOAc 5:1) followed by size exclusion chromatography (with $CHCl_3$ eluent) to yield the product as a brown solid (201 mg, 33%). δ_H (400 MHz, $CDCl_3$): 8.60 (2H, d, $^3J_{HH}$ 4.7, C(27)H), 7.45 (1H, s, C(12)H), 7.41 (2H, d, $^3J_{HH}$ 4.7, C(26)H), 7.13 (1H, s, C(2)H), 6.93 (2H, s, C(20)H), 3.19 (4H, t, $^3J_{HH}$ 5.9, C(24)H), 2.71 (4H, t, $^3J_{HH}$ 6.5, C(22)H), 2.00 (3H, s, C(15)H), 1.95 (4H, tt, $^3J_{HH}$ 5.9, $^3J_{HH}$ 6.5, C(23)H), 1.91 (3H, s, C(5)H); δ_C (101 MHz, $CDCl_3$): 150.7, 143.9, 143.5, 142.0, 140.4, 139.2, 130.3, 129.9, 126.4, 124.9, 124.7, 123.5, 121.1, 119.7, 107.6, 96.3, 78.9, 50.0, 27.7, 21.8, 14.9, 14.6, C(6), C(7), C(8), C(9) and C(10) are too weak to be observed due to C-F coupling; δ_F (376 MHz, $CDCl_3$): −110.0 (2F, t, $^3J_{FF}$ 6.1, C(9)F), −110.3 (2F, t, $^3J_{FF}$ 5.8, C(7)F), −131.8 (2F, tt, $^3J_{FF}$ 5.8, $^3J_{FF}$ 6.1, C(8)F). HRMS (ESI$^+$) *m/z*: $[M+H]^+$ calcd. for $C_{34}H_{27}F_6N_2S_2^+$ 641.1514; found 641.1508.

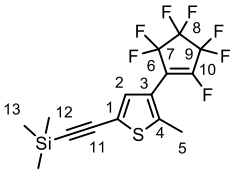
4-(4-(3,3,4,4,5,5-Hexafluoro-2-(2-methyl-5-((2,3,6,7-tetrahydro-1*H*,5*H*-pyrido[3,2,1-*ij*]quinolin-9-yl)ethynyl)thiophen-3-yl)cyclopent-1-en-1-yl)-5-methylthiophen-2-yl)-1-methylpyridin-1-ium hexafluorophosphate Dy-A



To a solution of **Dy-A(p)** (40.0 mg, 62.4 μmol) in CH_2Cl_2 (20 mL) was added iodomethane (0.50 mL, 8.0 mmol). The reaction mixture was stirred at room temperature for 20 h and then at 45 °C for 2 h before being concentrated in vacuo. The dried crude product was dissolved in methanol and then added to a solution of potassium hexafluorophosphate (4.0 g, 22 mmol) in water (50 mL). The solution was stirred at room temperature for 1 h for ion exchange and the precipitate was collected by centrifugation to yield the crude product as a brown solid. The crude product was purified by recrystallisation from CH_2Cl_2/cyclohexane to yield a brown solid. The brown solid was further purified by flash column chromatography (CH_2Cl_2/MeOH 95:5) to yield the product as a pale green solid (40 mg, 98%). δ_H (400 MHz, CD_3CN): 8.55 (2H, d, $^3J_{HH}$ 6.8, C(27)H), 8.05 (2H, d, $^3J_{HH}$ 6.8, C(26)H), 7.98 (1H, s, C(12)H), 7.15 (1H, s, C(2)H), 6.85 (2H, s, C(20)H), 4.22 (3H, s, C(28)H), 3.20 (4H, t, $^3J_{HH}$ 5.8, C(24)H), 2.67 (4H, t, $^3J_{HH}$ 6.5, C(22)H), 2.10 (3H, s, C(15)H), 1.97 (3H, s, C(5)H), 1.89 (4H, tt, $^3J_{HH}$ 6.8, $^3J_{HH}$ 6.5, C(23)H); δ_C (101 MHz, CD_3CN): 151.2, 148.7, 146.2, 144.5, 144.0, 136.1, 132.1, 130.8, 130.5, 128.1, 125.0, 124.2, 123.3, 122.2, 107.5, 97.2, 79.1, 50.3, 48.3, 28.1, 22.2, 15.3, 14.7; C(6), C(7), C(8), C(9) and C(10) are too

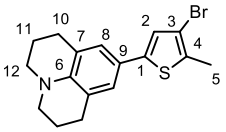
weak to be observed due to C-F coupling; δ_F (376 MHz, CD_3CN): −72.9 (6F, d, $^1J_{FP}$ 706.8, hexafluorophosphate), −107.3 (2F, t, $^3J_{FF}$ 5.5, C(7)F), −107.6 (2F, t, $^3J_{FF}$ 6.4, C(9)F), −129.1 (2F, tt, , $^3J_{FF}$ 5.5, $^3J_{FF}$ 6.4, C(8)F). HRMS (ESI$^+$) *m/z*: [M$^+$] calcd. for $C_{35}H_{29}F_6N_2S_2^+$ 655.1671; found 655.1669. UV-vis (MeCN): λ_{max} = 354 nm (ε = 74200 M^{-1} cm^{-1}).

Trimethyl((5-methyl-4-(perfluorocyclopent-1-en-1-yl)thiophen-2-yl)ethynyl)silane 13



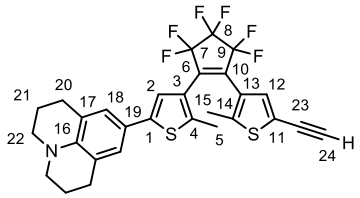
The compound **13** was synthesized following a published procedure,[27] yielding a yellow oil (657 mg, 52%). δ_H (400 MHz, $CDCl_3$): 7.20 (1H, s, C(2)H), 2.43 (3H, d, $^6J_{HF}$ 2.9, C(5)H), 0.25 (9H, s, C(13)H); δ_C (101 MHz, $CDCl_3$): 145.1, 132.1, 122.2, 119.6, 100.4, 96.1, 14.7, −0.2, C(6), C(7), C(8), and C(9) are too weak to be observed due to C-F coupling; δ_F (376 MHz, $CDCl_3$): −108.7 (2F, m, C(7)F), −118.3 (2F, m, C(9)F), −126.9 (1F, m, C(10)F), −130.1 (2F, m, C(8)F).

9-(4-Bromo-5-methylthiophen-2-yl)-2,3,6,7-tetrahydro-1*H*,5*H*-pyrido[3,2,1-*ij*]quinoline 14



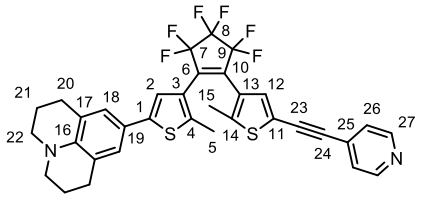
9 (3.00 g, 11.7 mmol), **3** (3.51 g, 11.7 mmol), $Pd(PPh_3)_4$ (667 mg, 586 µmol, 5 mol%), and Cs_2CO_3 (3.00 g, 9.21 mmol) were dried under high vacuum for 2 h. 1,4-Dioxane and water were degassed by three cycles of freeze-pump-thaw. To the dried mixture of solids under an argon atmosphere was added 1,4-dioxane (40 mL) and water (5 mL). The reaction mixture was stirred at 90 °C for 18 h before being allowed to cool to room temperature. The reaction mixture was concentrated in vacuo, dissolved in CH_2Cl_2, and washed with water and brine. The organic layer was dried ($MgSO_4$), and concentrated in vacuo. The crude product was purified by flash column chromatography (PE/EtOAc 20:1) to yield the product as a yellow solid (3.25 g, 80%). δ_H (400 MHz, $CDCl_3$): 6.95 (2H, s, C(8)H), 6.88 (1H, s, C(2)H), 3.17 (4H, t, $^3J_{HH}$ 5.7, C(12)H), 2.76 (4H, t, $^3J_{HH}$ 6.8, C(10)H), 1.98 (4H, tt, $^3J_{HH}$ 5.7, $^3J_{HH}$ 6.8, C(11)H); δ_C (101 MHz, $CDCl_3$): 142.9, 142.6, 130.9, 124.3, 122.8, 121.7, 121.1, 109.4, 50.1, 27.8, 22.1, 14.9. HRMS (ESI$^+$) *m/z*: [M+H]$^+$ calcd. for $C_{17}H_{19}BrNS$ 348.0416; found 348.0416.

9-(4-(2-(5-Ethynyl-2-methylthiophen-3-yl)-3,3,4,4,5,5-hexafluorocyclopent-1-en-1-yl)-5-methylthiophen-2-yl)-2,3,6,7-tetrahydro-1*H*,5*H*-pyrido[3,2,1-*ij*]quinoline 15



To a solution of **14** (650 mg, 1.87 mmol) in anhydrous THF (15 mL) at −78 °C was added *n*-BuLi (1.6 M in hexane, 1.28 mL, 2.05 mmol, 1.1 equiv.) dropwise. The mixture was stirred for 1 h before being transferred to a separate flask containing a solution of **13** (721 mg, 1.87 mmol) in anhydrous THF (40 mL) at −78 °C through a cannula. The reaction mixture was stirred at −78 °C for 2 h and then at room temperature for 2 h followed by quenching with water (10 mL). To the quenched mixture was added potassium carbonate (3.00 g, 21.7 mmol) and the reaction mixture was stirred for 30 min. The reaction mixture was then poured into water (100 mL) and extracted with CH_2Cl_2. The organic extracts were combined, washed with water, dried ($MgSO_4$), and concentrated in vacuo. The crude product was purified by flash column chromatography (PE/EtOAc 20:1) to yield the product as a pale green solid (630 mg, 60%). δ_H (400 MHz, $CDCl_3$): 7.27 (1H, s, C(12)H), 6.99 (1H, s, C(2)H), 6.95 (2H, s, C(18)H), 3.34 (1H, s, C(24)H), 3.17 (4H, t, $^3J_{HH}$ 5.8, C(22)H), 2.77 (4H, t, $^3J_{HH}$ 6.5, C(20)H), 1.98 (4H, tt, $^3J_{HH}$ 5.8, $^3J_{HH}$ 6.5, C(21)H), 1.89 (3H, s, C(15)H), 1.87 (3H, s, C(5)H); δ_C (101 MHz, $CDCl_3$): 143.9, 143.8, 143.0, 138.8, 133.0, 125.3, 125.2, 124.5, 121.8, 120.7, 120.3, 119.3, 82.1, 76.1, 50.1, 27.8, 22.1, 14.5(5), 14.5(2), C(6), C(7), C(8), C(9) and C(10) are too weak to be observed due to C-F coupling; δ_F (376 MHz, $CDCl_3$): −101.1 (2F, t, $^3J_{FF}$ 6.7, C(7)F), −110.2 (2F, t, $^3J_{FF}$ 7.9, C(9)F), −131.9 (2F, tt, $^3J_{FF}$ 6.7, $^3J_{FF}$ 7.9 C(8)F). HRMS (ESI$^+$) *m/z*: $[M+H]^+$ calcd. for $C_{29}H_{24}F_6NS_2^+$ 564.1249; found 564.1247.

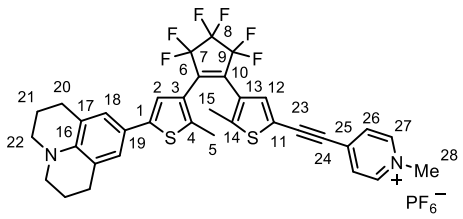
9-(4-(3,3,4,4,5,5-Hexafluoro-2-(2-methyl-5-(pyridin-4-ylethynyl)thiophen-3-yl)cyclopent-1-en-1-yl)-5-methylthiophen-2-yl)-2,3,6,7-tetrahydro-1*H*,5*H*-pyrido[3,2,1-*ij*]quinoline D-yA(p)



15 (550 mg, 976 µmol), 4-iodopyridine (300 mg, 1.45 mmol, 1.5 equiv.), $Pd(PPh_3)_4$ (113 mg, 97.6 µmol, 10 mol%), and CuI (31.2 mg, 195 µmol, 20 mol%) were dried under high vacuum for 30 min. Anhydrous triethylamine was degassed by three cycles of freeze-pump-thaw. To the dried mixture of solids under an argon atmosphere was added degassed triethylamine (60 mL). The reaction mixture was stirred at 45 °C for 15 h before being allowed to cool to room temperature. Upon completion of the reaction verified by

TLC (PE/EtOAc 4:1 with 1% triethylamine), the reaction mixture was concentration in vacuo. The crude product was then purified by flash column chromatography (PE/EtOAc 4:1 with 1% triethylamine) to yield the product as a green solid (472 mg, 75%). δ_H (400 MHz, $CDCl_3$): 8.61 (2H, d, $^3J_{HH}$ 5.9, C(27)H), 7.33-7.37 (3H, overlapping s and d, $^3J_{HH}$ 5.9, C(12)H and C(26)H), 7.01 (1H, s, C(2)H), 6.96 (2H, s, C(18)H), 3.17 (4H, t, $^3J_{HH}$ 5.8, C(22)H), 2.77 (4H, t, $^3J_{HH}$ 6.4, C(20)H), 1.98 (4H, tt, $^3J_{HH}$ 5.8, $^3J_{HH}$ 6.4, C(21)H), 1.94 (3H, s, C(15)H), 1.90 (3H, s, C(5)H); δ_C (101 MHz, $CDCl_3$): 150.0, 145.0, 144.0, 143.0, 138.8, 133.2, 130.9, 125.7, 125.3, 125.3, 124.5, 121.8, 120.6, 120.2, 119.3, 91.3, 86.4, 50.0, 27.8, 22.0, 14.6(4), 14.5(7), C(6), C(7), C(8), C(9) and C(10) are too weak to be observed due to C-F coupling; δ_F (376 MHz, ($CDCl_3$): −110.0 (2F, t, $^3J_{FF}$ 6.7, C(7)F), −110.3 (2F, t, $^3J_{FF}$ 8.1, C(9)F), −131.9 (2F, tt, $^3J_{FF}$ 6.7, $^3J_{FF}$ 8.1, C(8)F). HRMS (ESI^+) *m/z*: $[M+H]^+$ calcd. for $C_{29}H_{24}NF_6S_2$ 564.1249; found 564.1247.

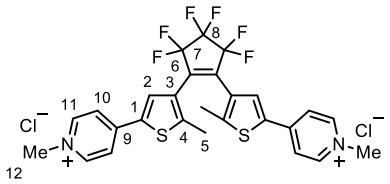
4-((4-(3,3,4,4,5,5-Hexafluoro-2-(2-methyl-5-(2,3,6,7-tetrahydro-1*H*,5*H*-pyrido[3,2,1-*ij*]quinolin-9-yl)thiophen-3-yl)cyclopent-1-en-1-yl)-5-methylthiophen-2-yl)ethynyl)-1-methylpyridin-1-ium hexafluorophosphate D-yA



To a solution of **D-yA(p)** (200 mg, 312 μmol) in CH_2Cl_2 (20 mL) was added iodomethane (2.0 mL, 22 mmol). The reaction mixture was stirred at room temperature for 20 h and then at 45 °C for 2 h before being concentrated in vacuo. The dried crude product was dissolved in methanol and then added to a solution of potassium hexafluorophosphate (4.0 g, 21.73 mmol) in water (50 mL). The solution was stirred at room temperature for 1 h for ion exchange and the precipitate was collected by centrifugation to yield the crude product as a brown solid. The crude product was purified by recrystallisation from CH_2Cl_2/cyclohexane to yield the product as a brown solid. The brown solid was further purified by flash column chromatography (CH_2Cl_2/MeOH 95:5) to yield the product as a pale brown solid (205 mg, 82%). δ_H (400 MHz, CD_3CN): 8.98 (2H, d, $^3J_{HH}$ 6.5, C(27)H), 8.23 (2H, d, $^3J_{HH}$ 6.5, C(26)H), 7.75 (1H, s, C(12)H), 7.13 (1H, s, C(2)H), 6.95 (2H, s, C(18)H), 4.30 (3H, s, C(28)H), 3.14 (4H, t, $^3J_{HH}$ 5.8, C(24)H), 2.69 (4H, t, $^3J_{HH}$ 6.5, C(22)H), 2.02 (3H, s, C(15)H), 1.90 (3H, s, C(5)H), 1.86 (4H, tt, $^3J_{HH}$ 5.8, $^3J_{HH}$ 6.5, C(23)H); δ_C (101 MHz, CD_3CN): 148.1, 145.5, 143.7, 142.7, 138.4, 137.6, 135.7, 128.5, 125.2, 124.3, 123.8, 121.1, 119.2, 118.5, 118.0, 94.1, 90.1, 49.2, 47.8, 27.1, 21.3, 14.3, 14.0, C(6), C(7), C(8), C(9) and C(10) are too weak to be observed due to C-F coupling; δ_F (376 MHz,

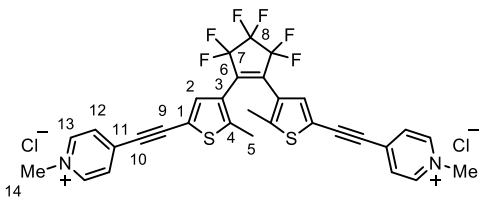
(CD_3CN): −67.9 (6F, d, $^1J_{FP}$ 707.0, hexafluorophosphate), −109.1 (2F, m, C(7)F), −109.4 (2F, m, C(9)F), −130.9 (2F, m, C(8)F). HRMS (ESI$^+$) *m/z*: [M$^+$] calcd. for $C_{35}H_{29}F_6N_2S_2^+$ 655.1671; found 655.1651. UV-vis (MeCN): λ_{max} = 364 nm (ε = 55700 M^{-1} cm^{-1}).

4,4'-((Perfluorocyclopent-1-ene-1,2-diyl)bis(5-methylthiophene-4,2-diyl))bis(1-methylpyridin-1-ium) dichloride A-A (chloride)



To a solution of tetrabutylammonium chloride (500 mg, 1.80 mmol) in acetone (30 mL) was added a solution of **A-A** (30 mg, 0.035 mmol) in THF (1 mL). The reaction mixture was stirred at room temperature for 1 h for ion exchange and the precipitate was filtered off to yield the crude product as an off-white solid. The crude product was purified by dissolving in MeOH and recrystallizing with a 1:1 mixture of THF and PE (22 mg, 98%). δ_H (400 MHz, CD_3OD): 8.79 (4H, d, $^3J_{HH}$ 7.1, C(11)H), 8.26 (4H, d, $^3J_{HH}$ 7.1 C(10)H), 8.18 (2H, s, C(2)H), 4.34 (6H, s, C(12)H), 2.17 (6H, s, C(5)H); δ_C (101 MHz, CD_3OD): 151.3, 149.2, 146.8, 137.1, 132.3, 128.3, 123.6, 48.0, 15.2, C(6), C(7) and C(8) are too weak to be observed due to C-F coupling; δ_F (376 MHz, CD_3OD): −118.8 (4F, t, $^3J_{FF}$ 5.3, C(7)F), −133.3 (2F, p, $^3J_{FF}$ 5.3, C(8)F). UV-vis (water): λ_{max} = 357 nm (ε = 61500 M^{-1} cm^{-1}).

4,4'-(((Perfluorocyclopent-1-ene-1,2-diyl)bis(5-methylthiophene-4,2-diyl))bis(ethyne-2,1-diyl))bis(1-methylpyridin-1-ium) dichloride Ay-yA (chloride)



To a solution of tetrabutylammonium chloride (500 mg, 1.80 mmol) in acetone (20 mL) was added a solution of **Ay-yA** (50 mg, 0.056 mmol) in acetone (10 mL). The reaction mixture was stirred at room temperature for 1 h for ion exchange and the precipitate was filtered off to yield the product as an off-white solid (37 mg, 98%). δ_H (400 MHz, CD_3OD): 8.87 (4H, d, $^3J_{HH}$ 6.7, C(13)H), 8.11 (4H, d, $^3J_{HH}$ 6.7, C(12)H), 7.68 (2H, s, C(2)H), 4.38 (6H, s, C(14)H), 2.07 (6H, s, C(5)H); δ_C (101 MHz, CD_3OD): 149.6, 146.6, 147.0, 130.7, 129.9, 126.7, 120.4, 96.1, 90.9, 14.8, C(14) was not resolved due to overlapping with solvent peak, C(6), C(7) and C(8) are too weak to be observed due to C-F coupling. δ_F (376 MHz, (CD_3OD): −119.9 (4F, t, J_{FF} 5.0, C(7)F), −133.4 (2F, p, $^3J_{FF}$ 5.0, C(8)F). UV-vis (water): λ_{max} = 377 nm (ε = 69500 M^{-1} cm^{-1}).

2.5 Appendix

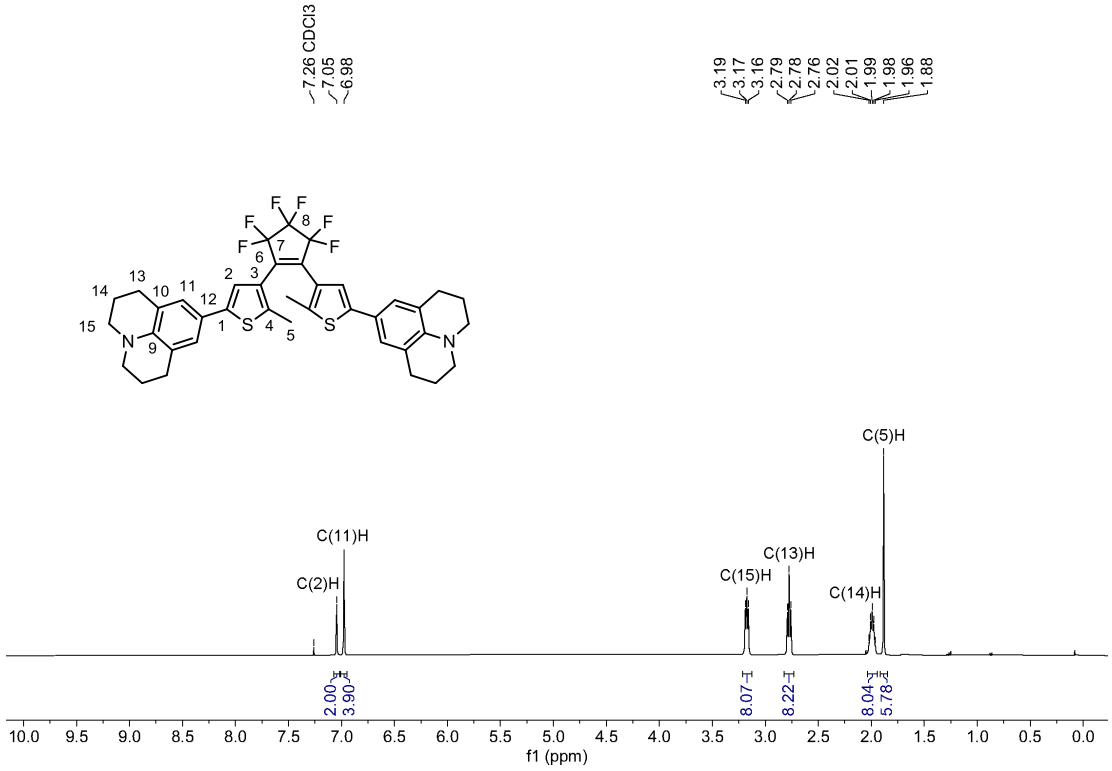


Figure 2.35 ^{1}H NMR spectrum (400 MHz, $CDCl_3$) of **D**-**D**.

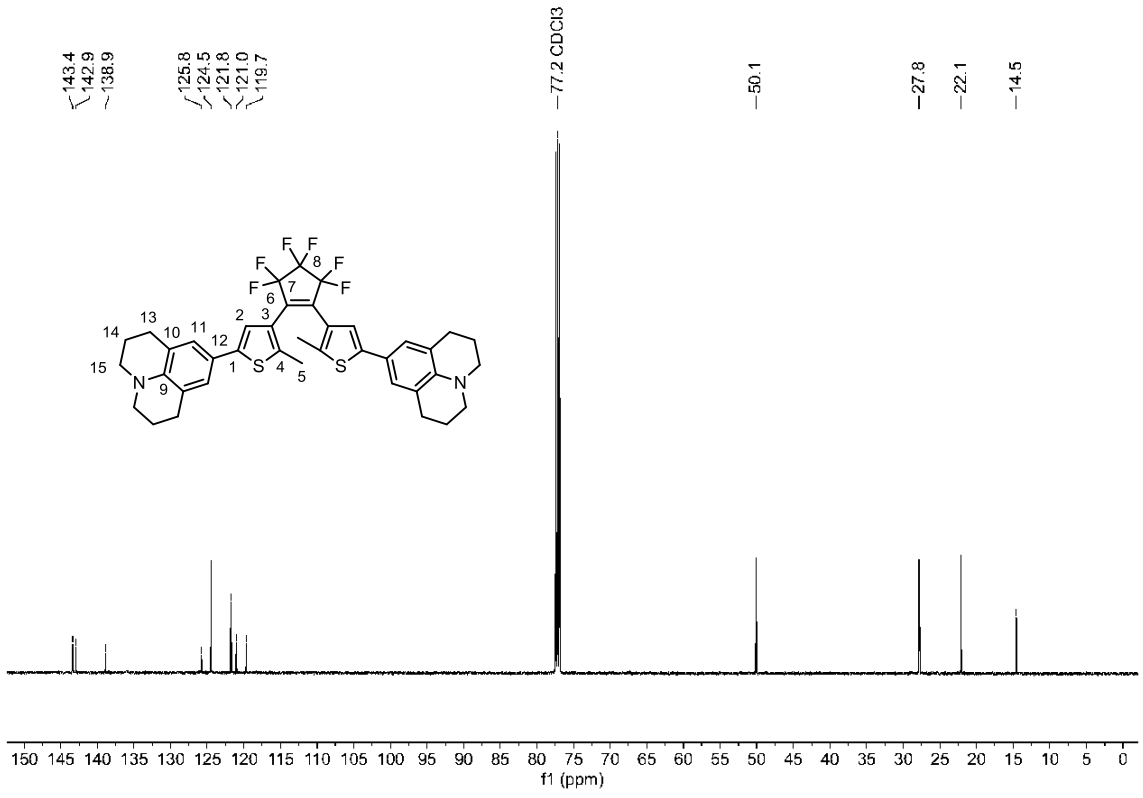


Figure 2.36 ^{13}C NMR spectrum (101 MHz, $CDCl_3$) of **D**-**D**.

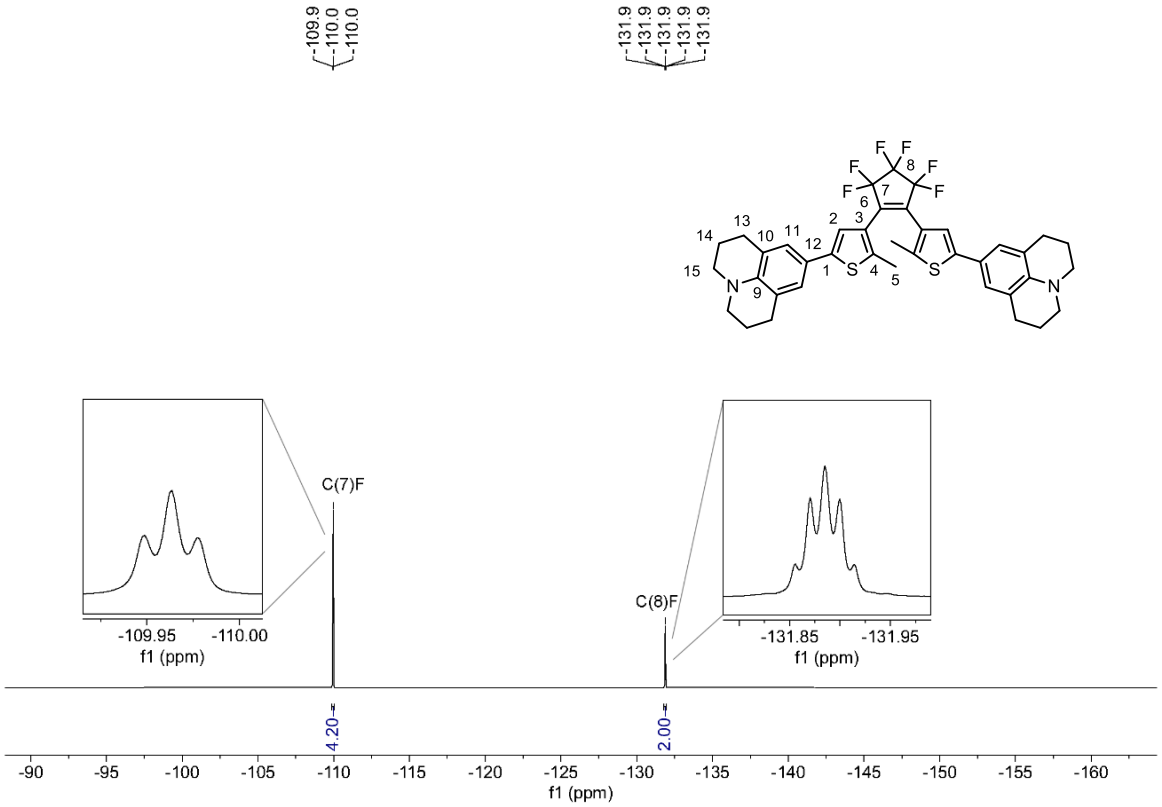


Figure 2.37 ^{19}F NMR spectrum (376 MHz, $CDCl_3$) of **D-D**.

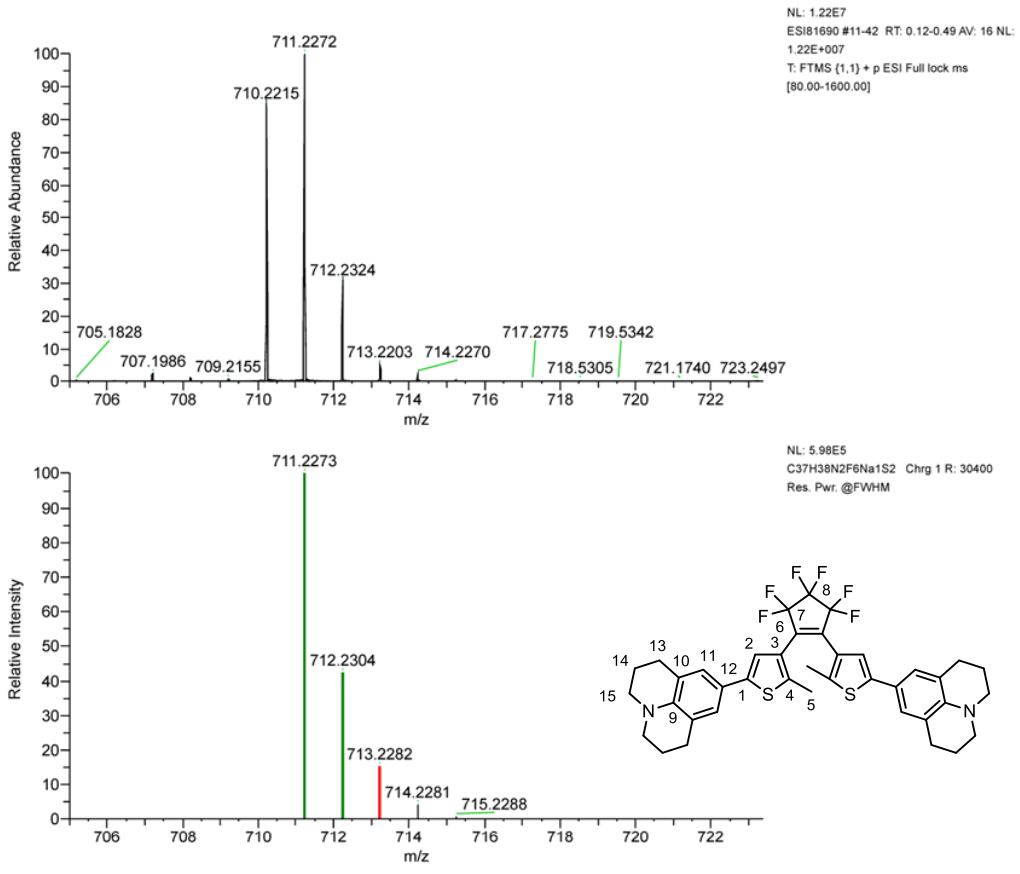


Figure 2.38 HRMS (ESI$^+$) of **D-D**, *m/z*: $[M+H]^+$ calcd. for $C_{39}H_{37}N_2F_6S_2^+$ 711.2273; found 711.2272.

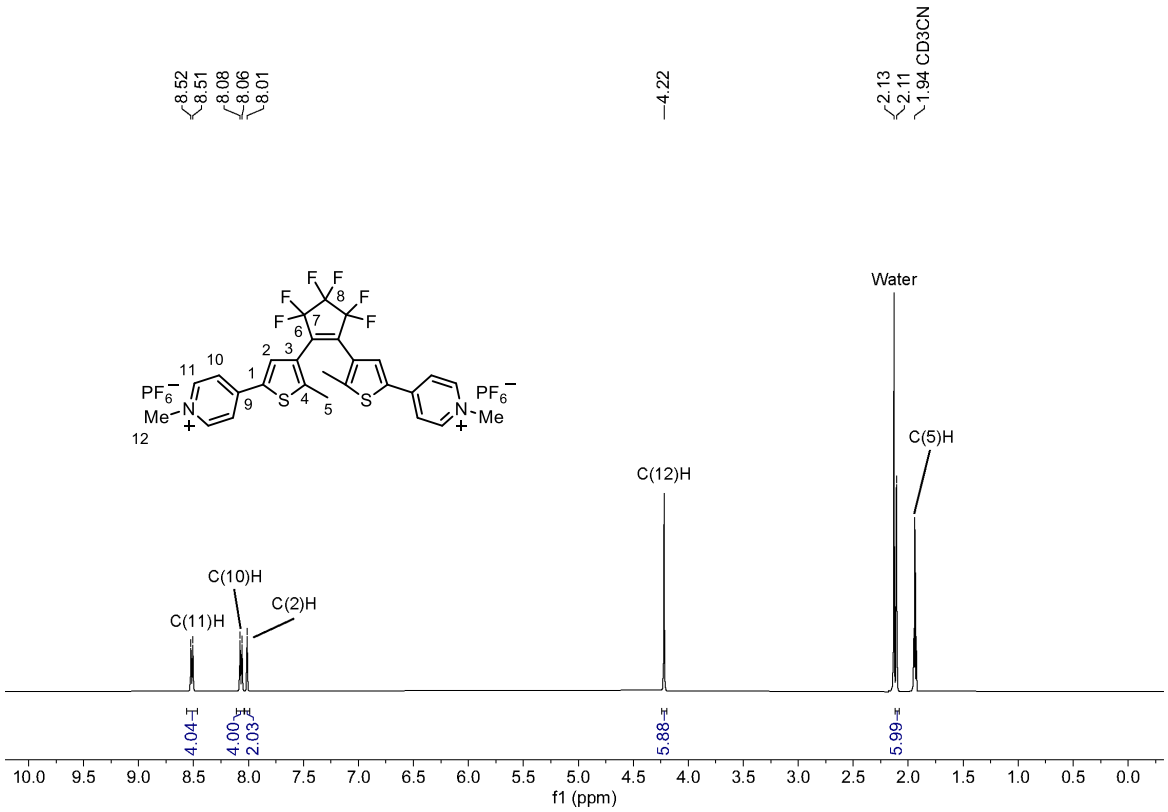


Figure 2.39 ^{1}H NMR spectrum (400 MHz, CD_3CN) of **A**-**A**.

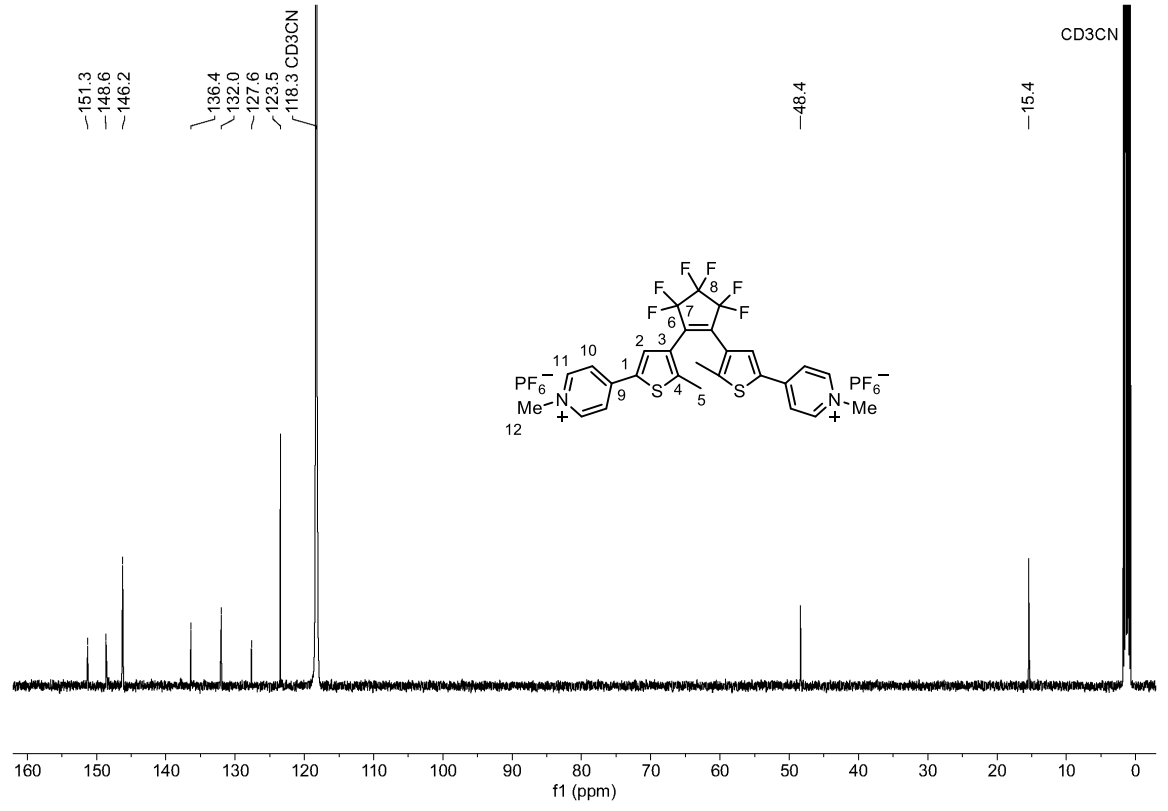


Figure 2.40 ^{13}C NMR spectrum (101 MHz, CD_3CN) of **A**-**A**.

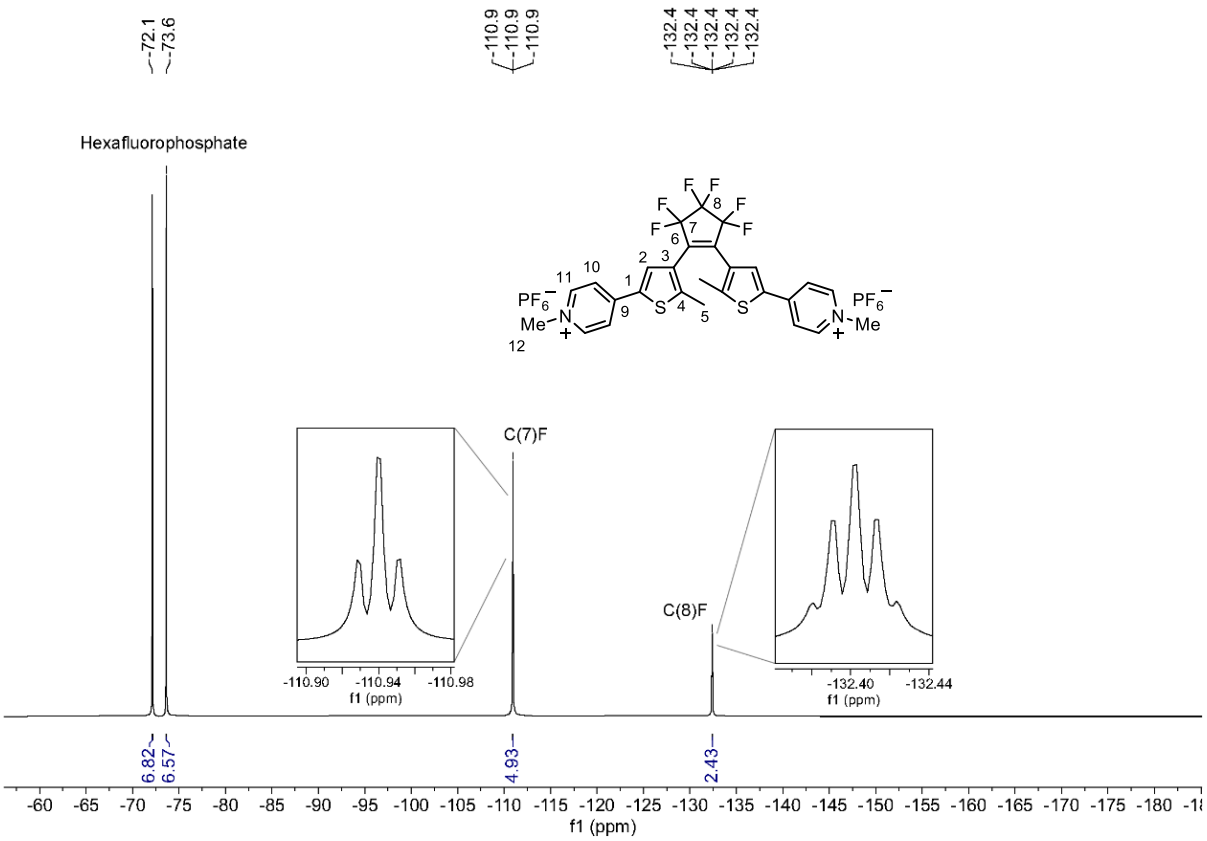


Figure 2.41 ^{19}F NMR spectrum (376 MHz, CD_3CN) of **A**-**A**.

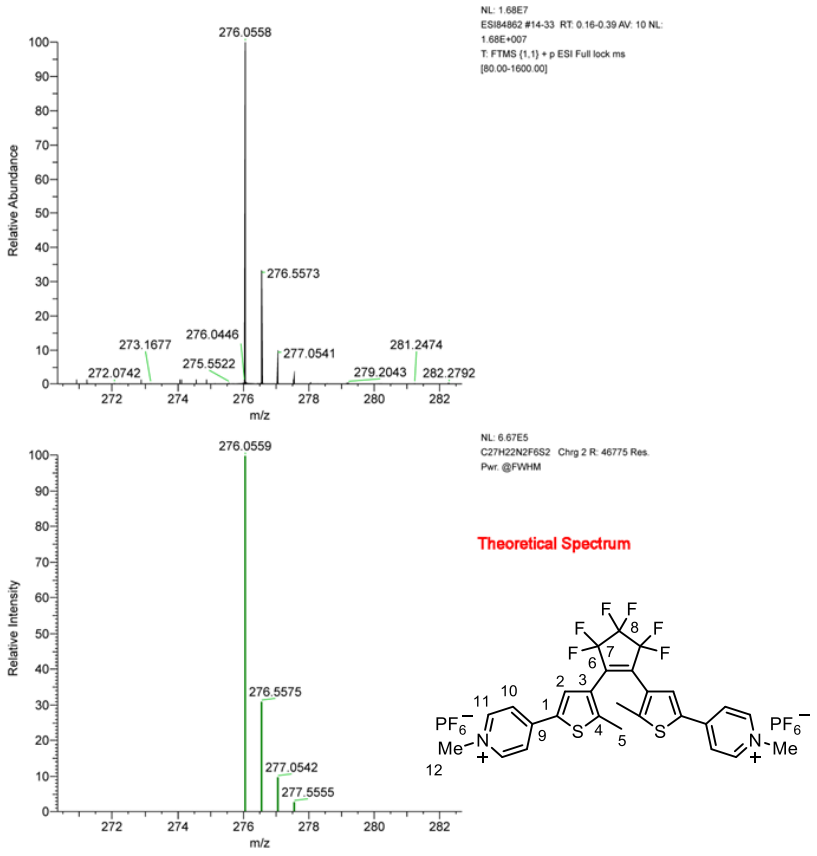


Figure 2.42 HRMS (ESI$^+$) of **A**-**A**, *m/z*: $[M]^{2+}$ calcd. for $C_{27}H_{22}F_6N_2S_2^{2+}$ 276.0559; found 276.0558.

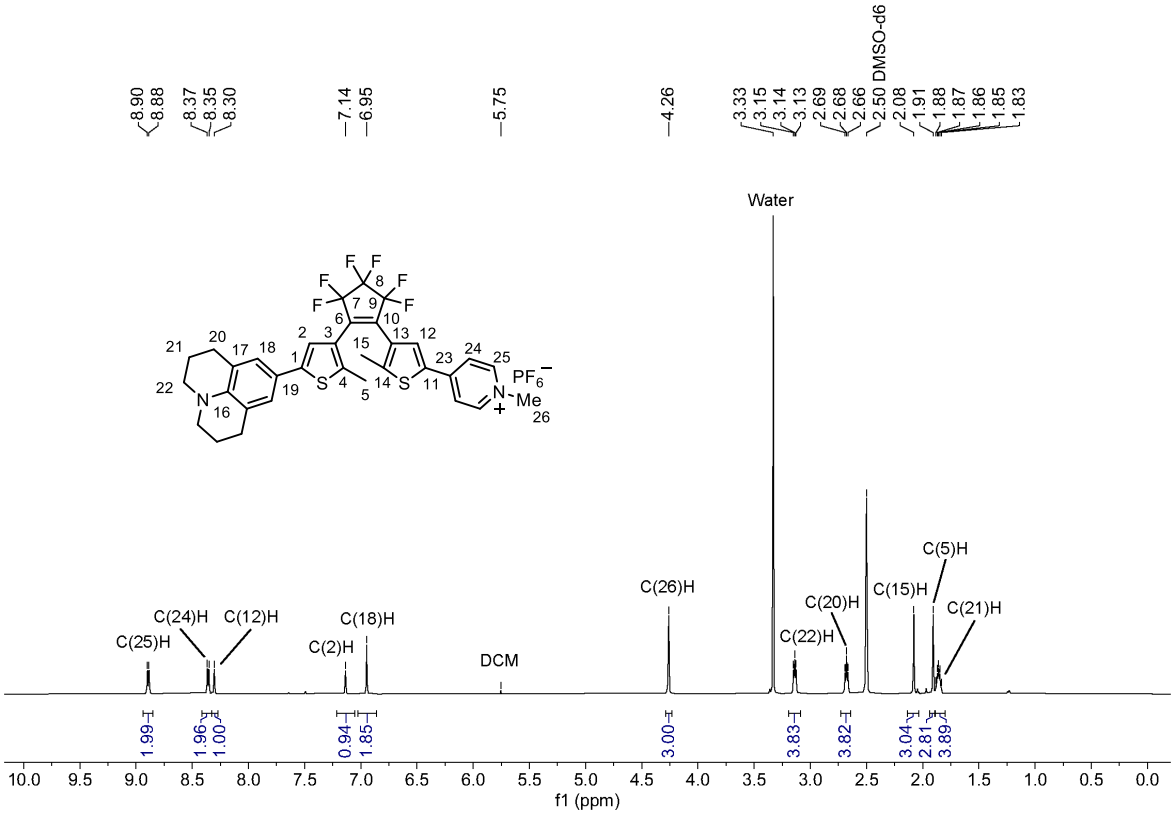


Figure 2.43 ^{1}H NMR spectrum (400 MHz, DMSO-d_6) of **D-A**.

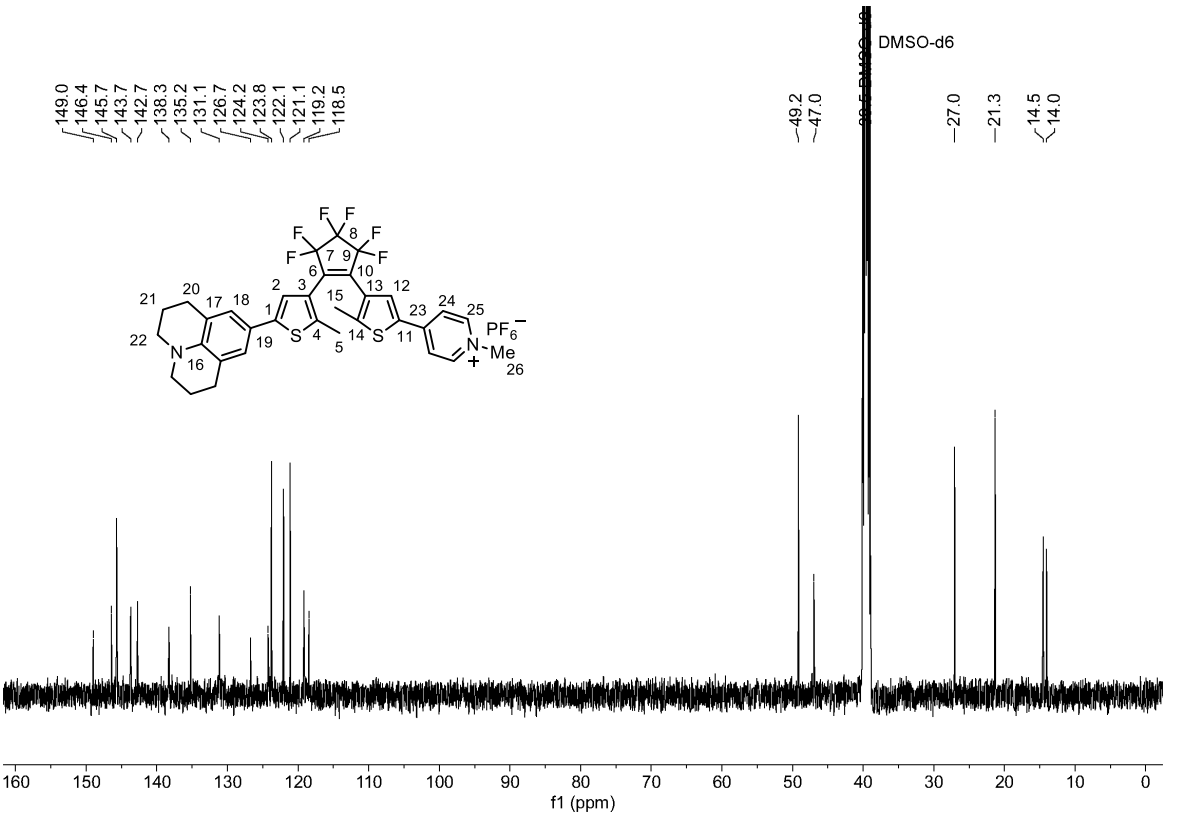


Figure 2.44 ^{13}C NMR spectrum (101 MHz, DMSO-d_6) of **D-A**.

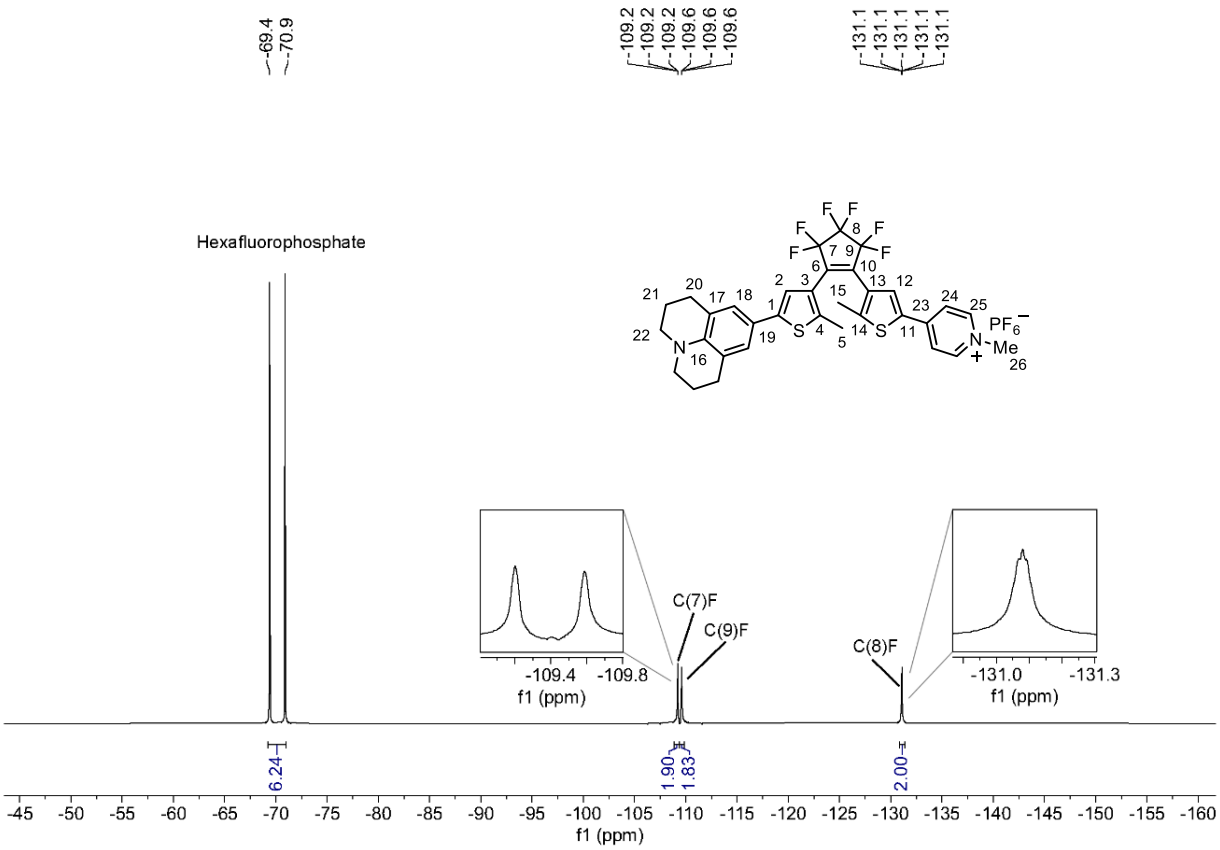


Figure 2.45 ^{19}F NMR spectrum (376 MHz, DMSO-d_6) of **D-A**.

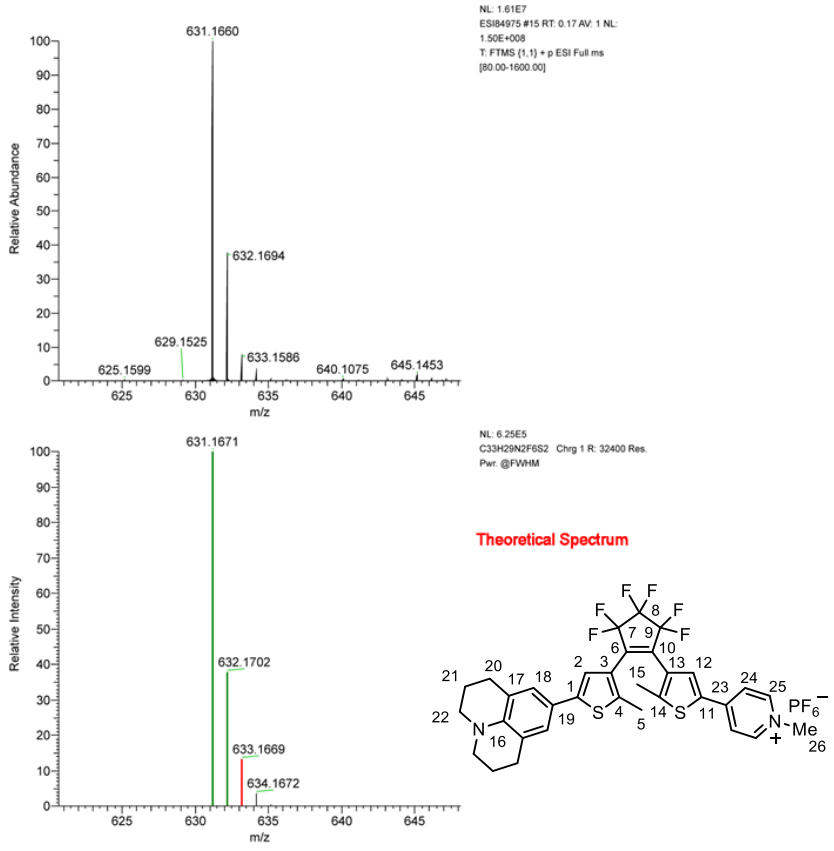


Figure 2.46 HRMS (ESI$^+$) of **D-A**, *m/z*: $[M]^+$ calcd. for $C_{33}H_{29}F_6N_2S_2^+$ 631.1671; found 631.1660.

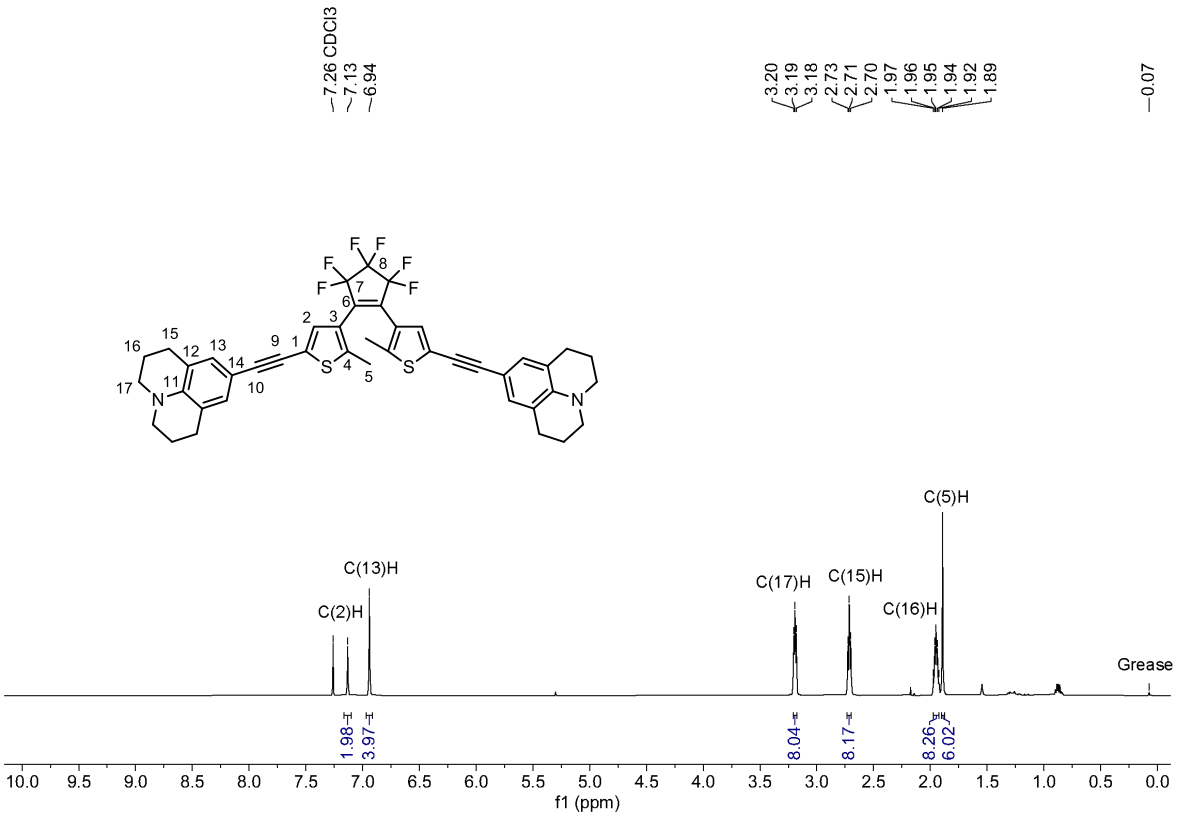


Figure 2.47 ^{1}H NMR spectrum (400 MHz, $CDCl_3$) of **Dy-yD**.

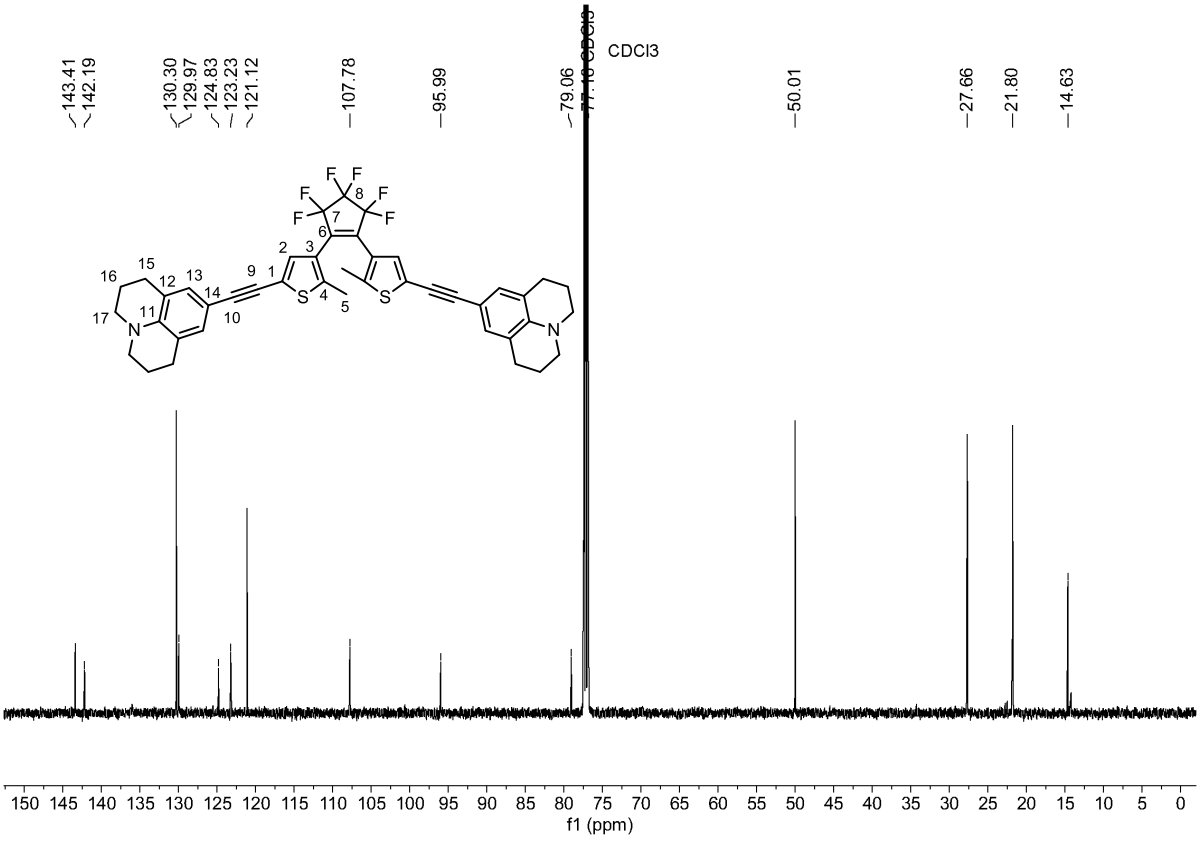


Figure 2.48 ^{13}C NMR spectrum (101 MHz, $CDCl_3$) of **Dy-yD**.

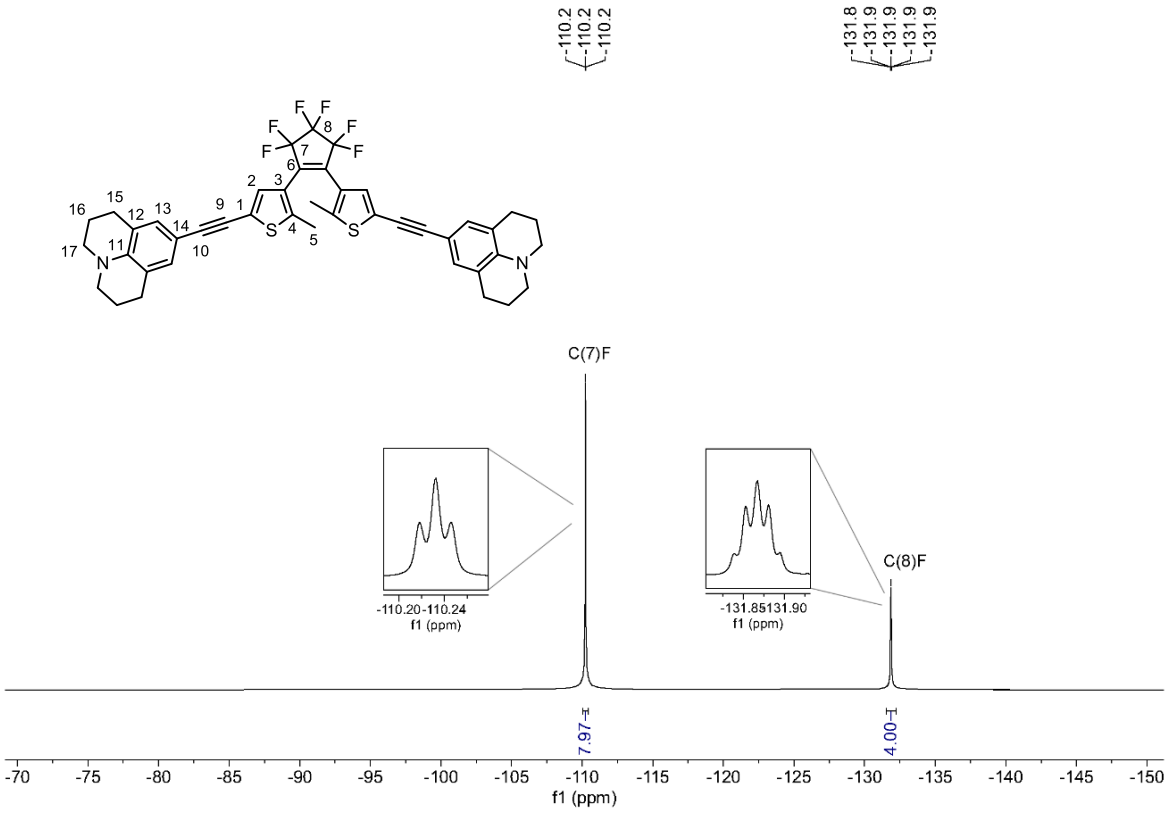


Figure 2.49 ^{19}F NMR spectrum (376 MHz, $CDCl_3$) of **Dy-yD**.

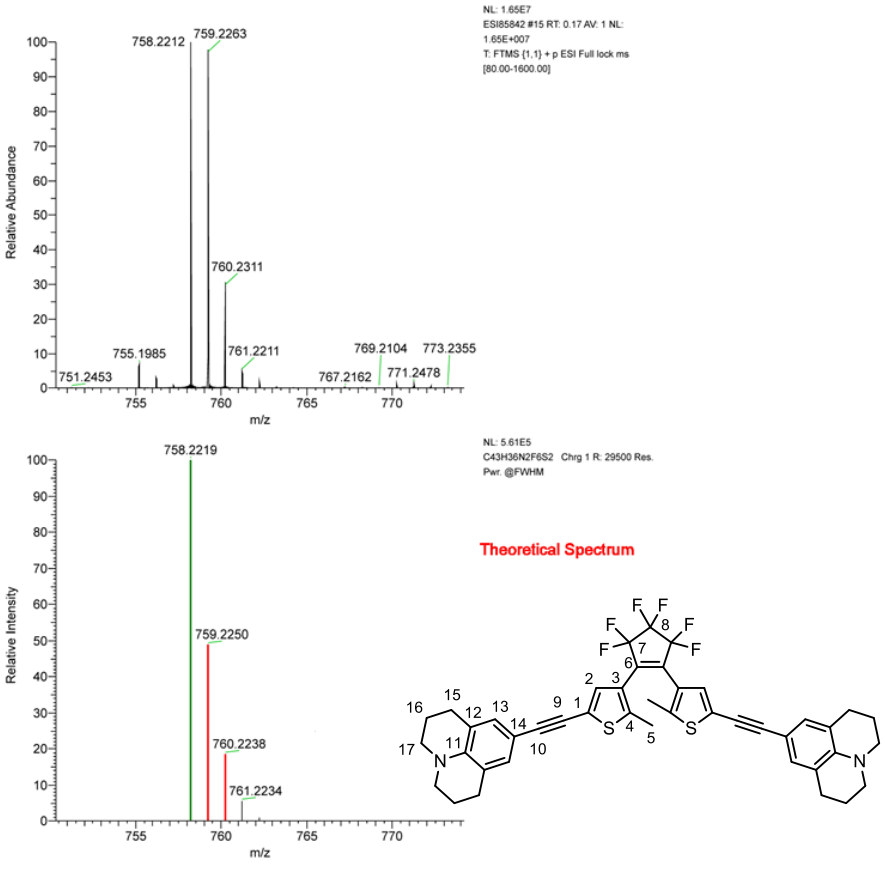


Figure 2.50 HRMS (ESI$^+$) of **Dy-yD**, *m/z*: $[M+H]^+$ calcd. for $C_{43}H_{36}F_6N_2S_2^+$ 758.2219; found 758.2212.

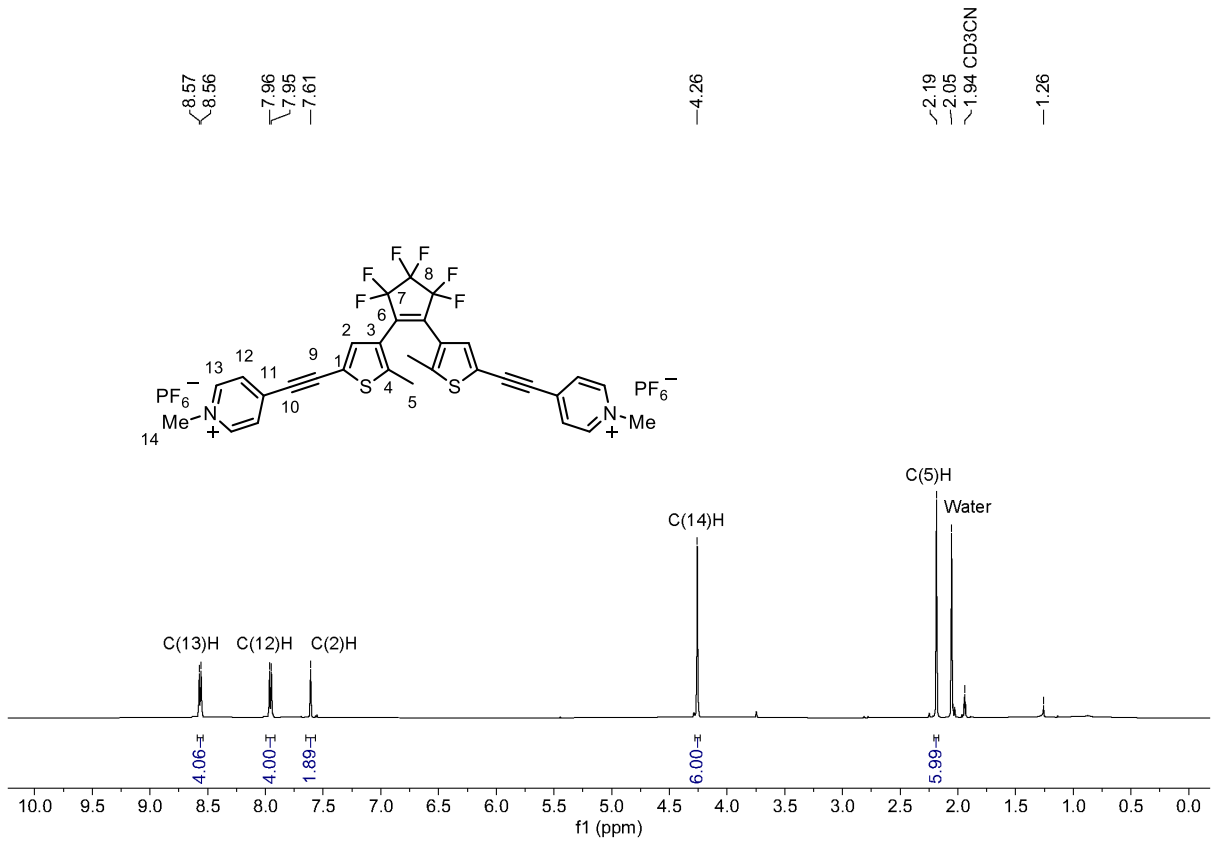


Figure 2.51 ^{1}H NMR spectrum (400 MHz, CD_3CN) of **Ay-yA**.

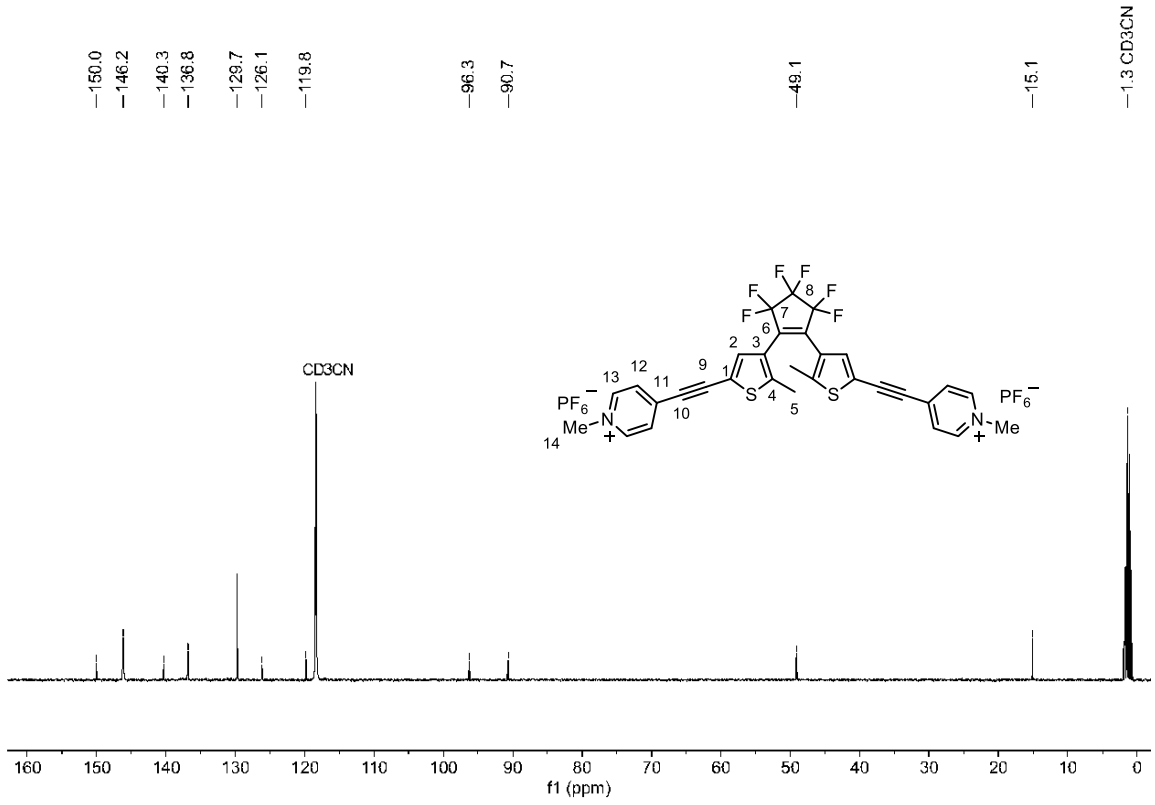


Figure 2.52 ^{13}C NMR spectrum (101 MHz, CD_3CN) of **Ay-yA**.

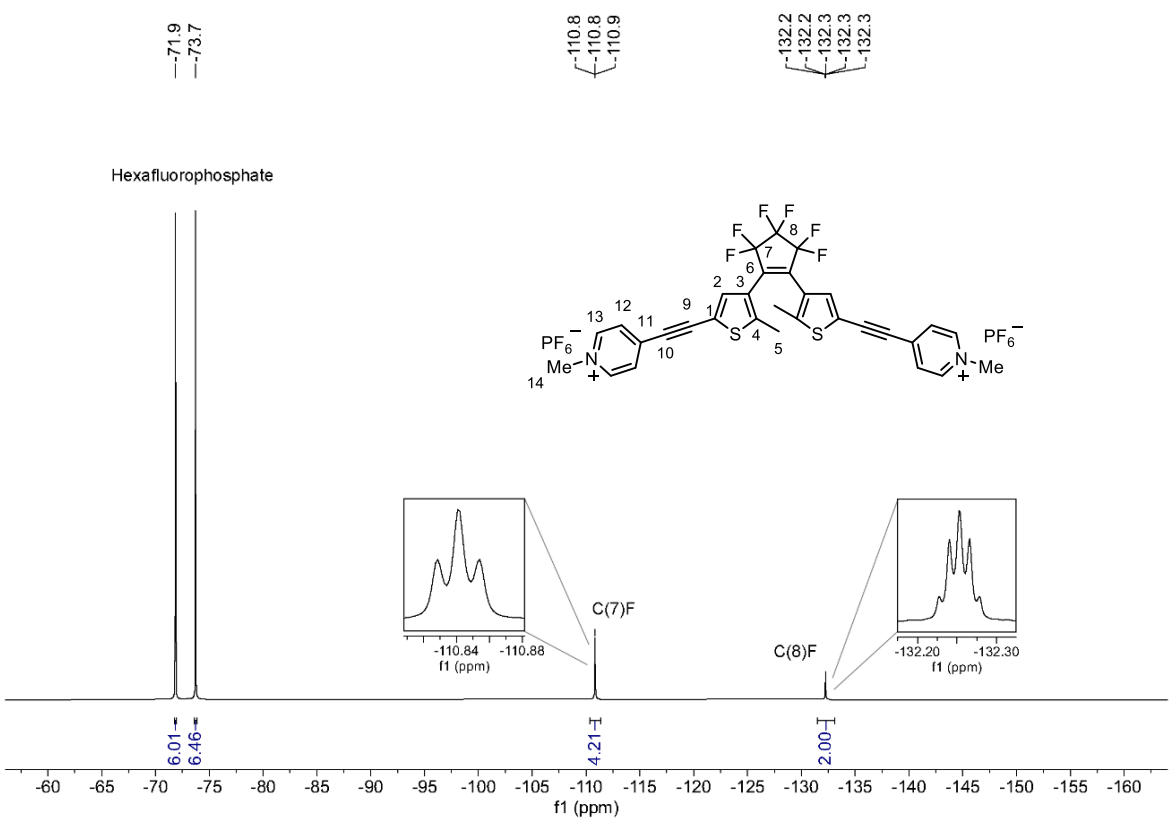


Figure 2.53 ^{19}F NMR spectrum (376 MHz, CD_3CN) of **Ay-yA**.

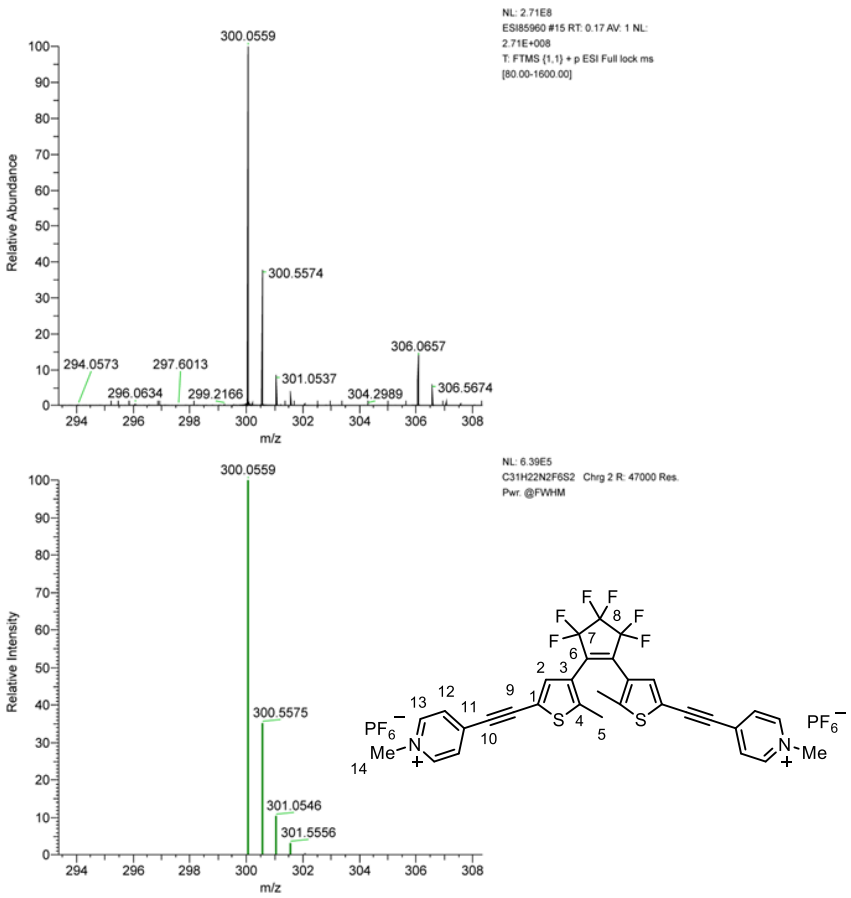


Figure 2.54 HRMS (ESI$^+$) of **Ay-yA**, *m/z*: $[M]^{2+}$ calcd. for $C_{31}H_{22}F_6N_2S_2^{2+}$ 300.0559; found 300.0559.

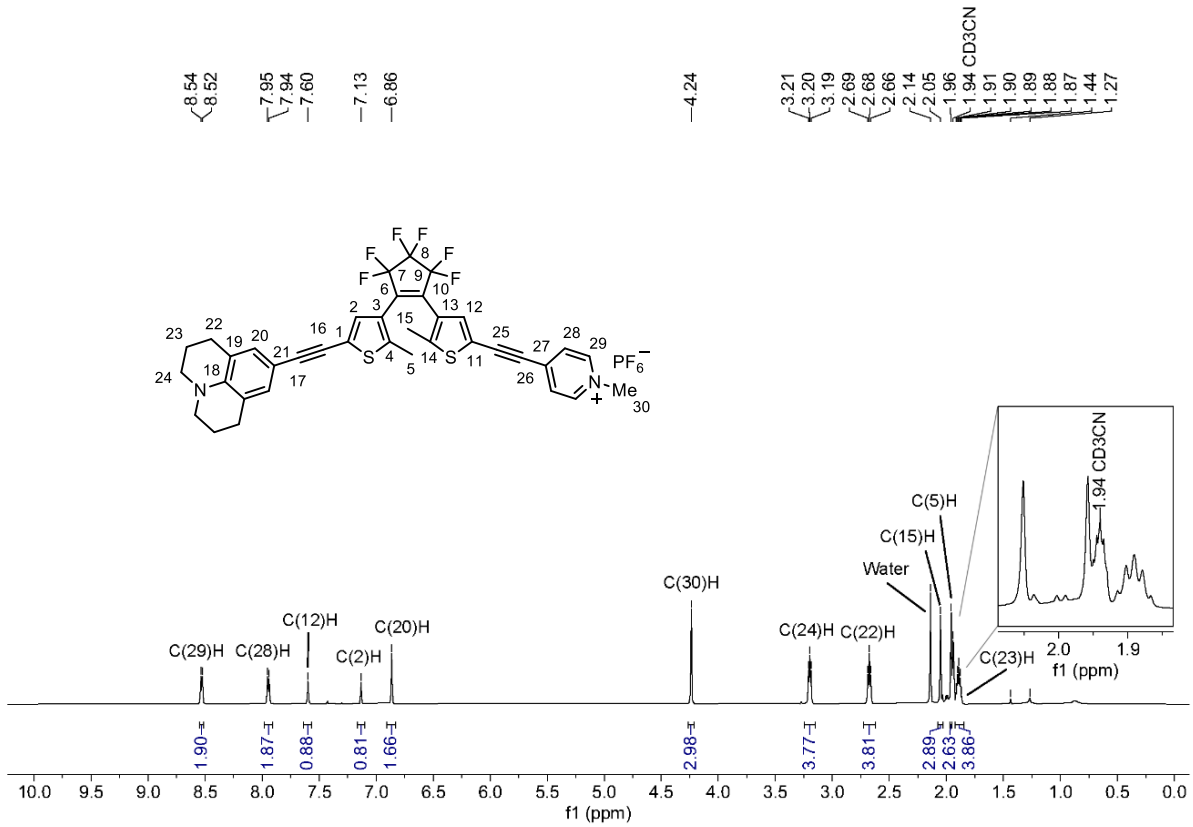


Figure 2.55 ^{1}H NMR spectrum (400 MHz, CD_3CN) of **Dy-yA**.

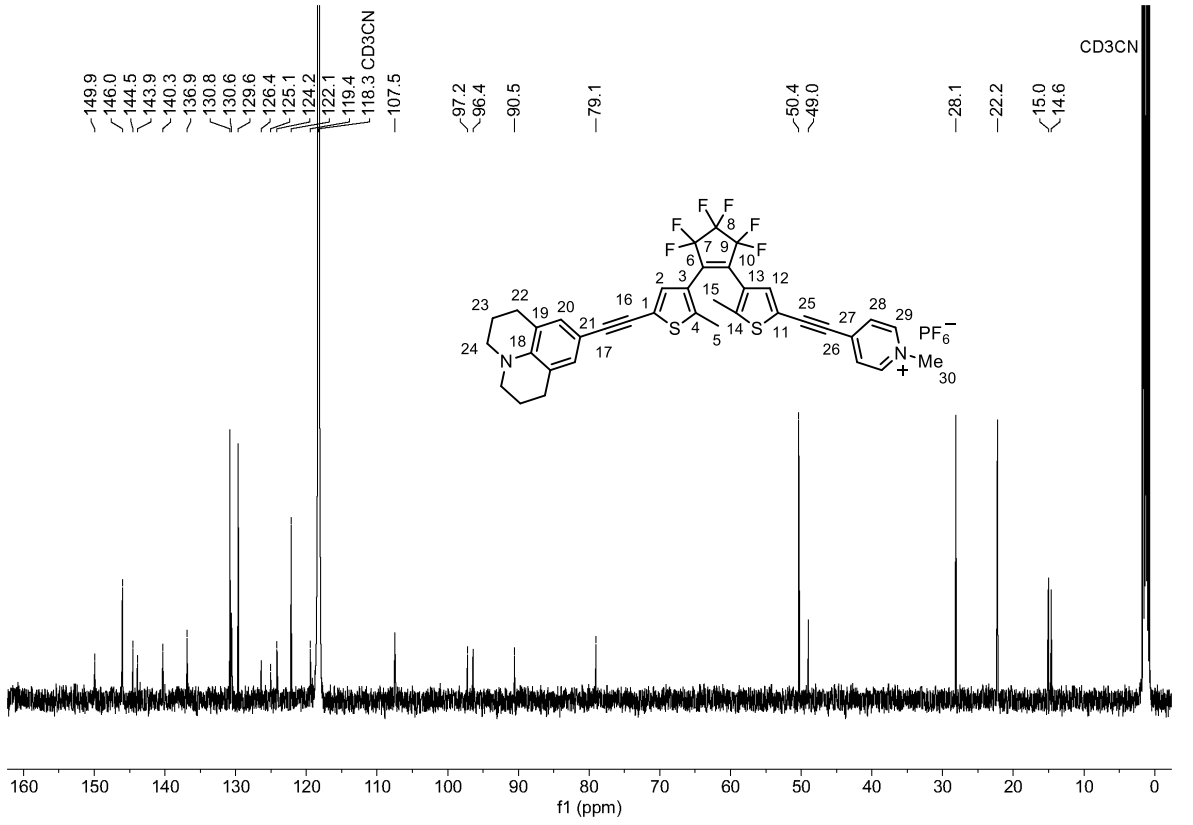


Figure 2.56 ^{13}C NMR spectrum (101 MHz, CD_3CN) of **Dy-yA**.

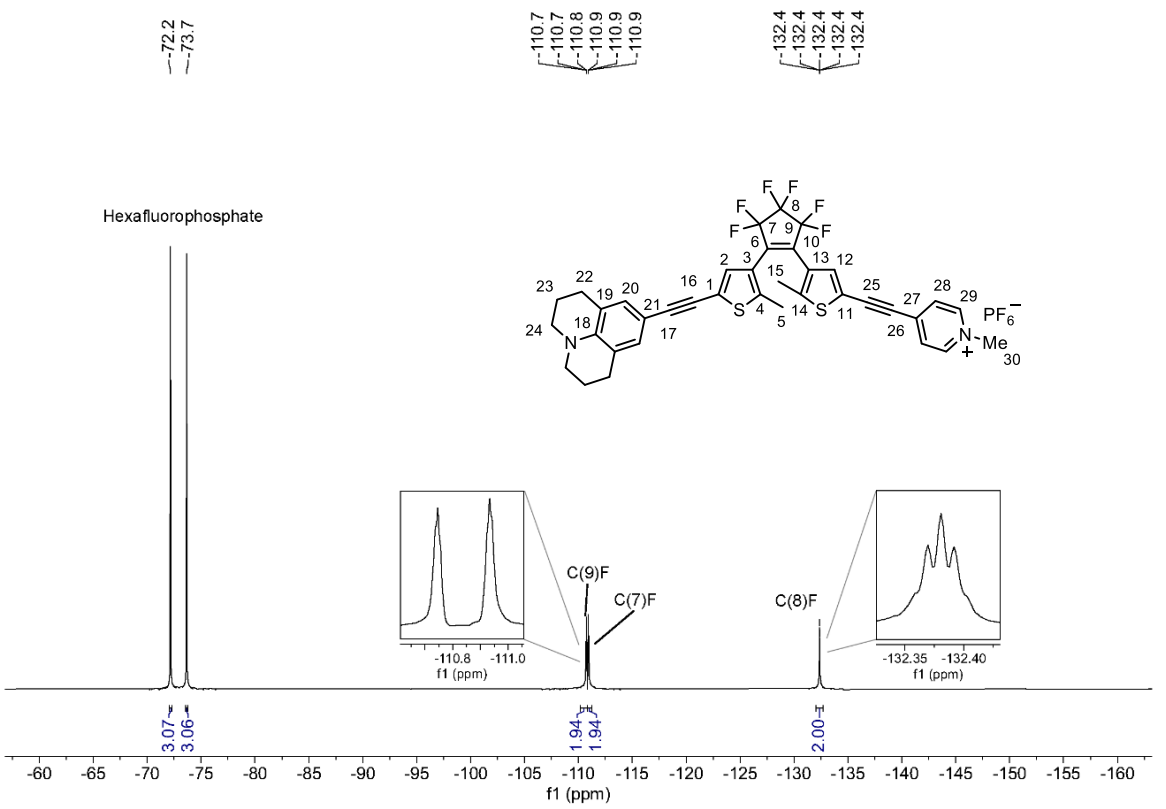


Figure 2.57 ^{19}F NMR spectrum (376 MHz, CD_3CN) of **Dy-yA**.

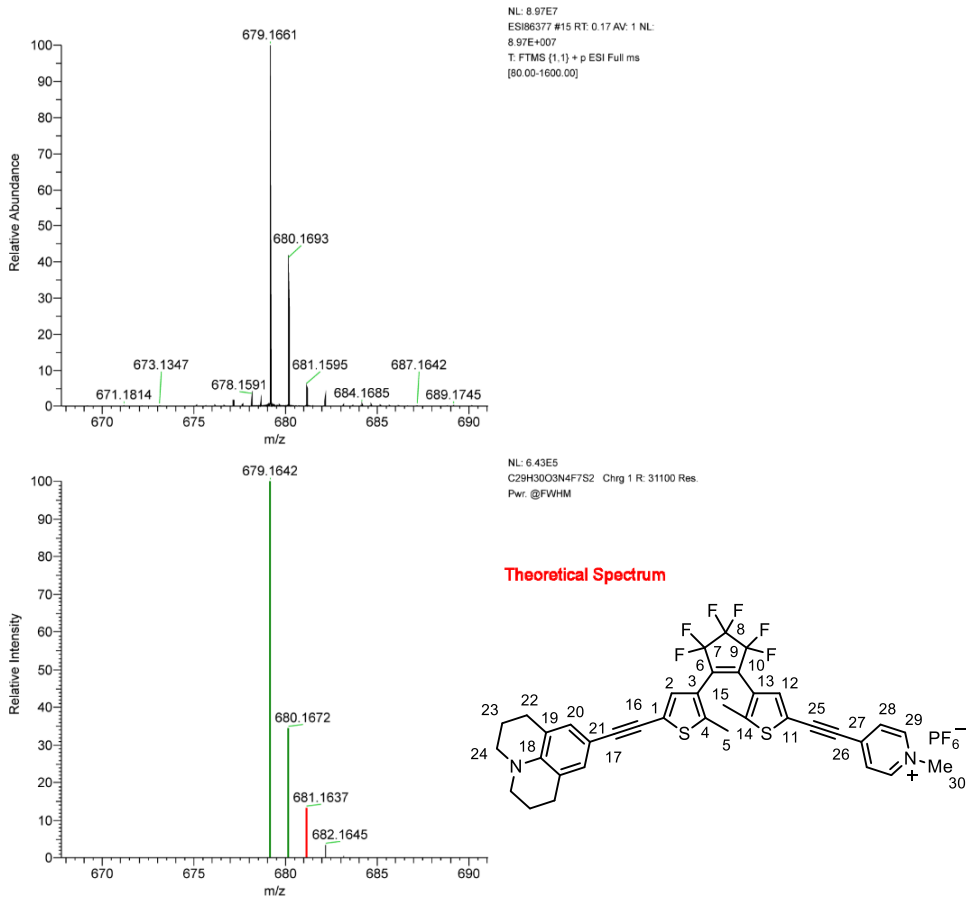


Figure 2.58 HRMS (ESI$^+$) of **Dy-yA**, *m/z*: [M$^+$] calcd. for $C_{37}H_{29}F_6N_2S_2^+$ 679.1642; found 679.1661.

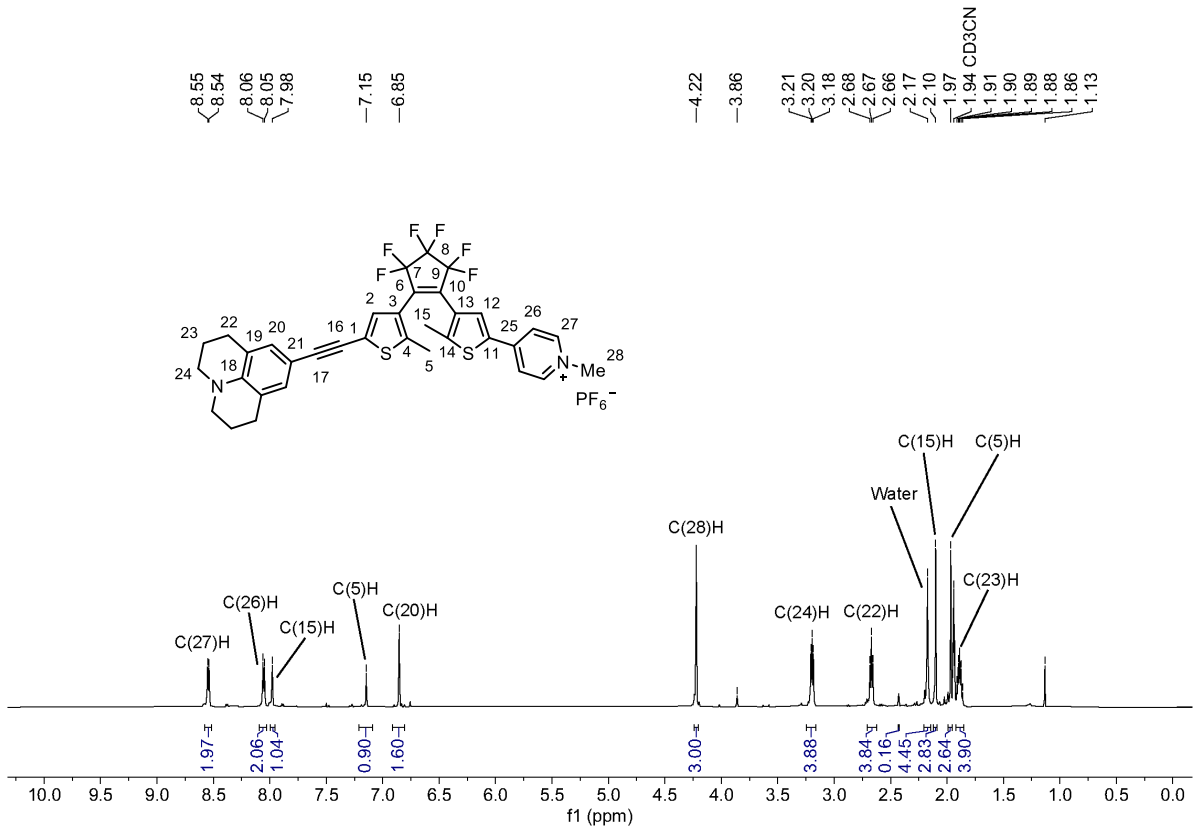


Figure 2.59 ^{1}H NMR spectrum (400 MHz, CD_3CN) of **Dy-A**.

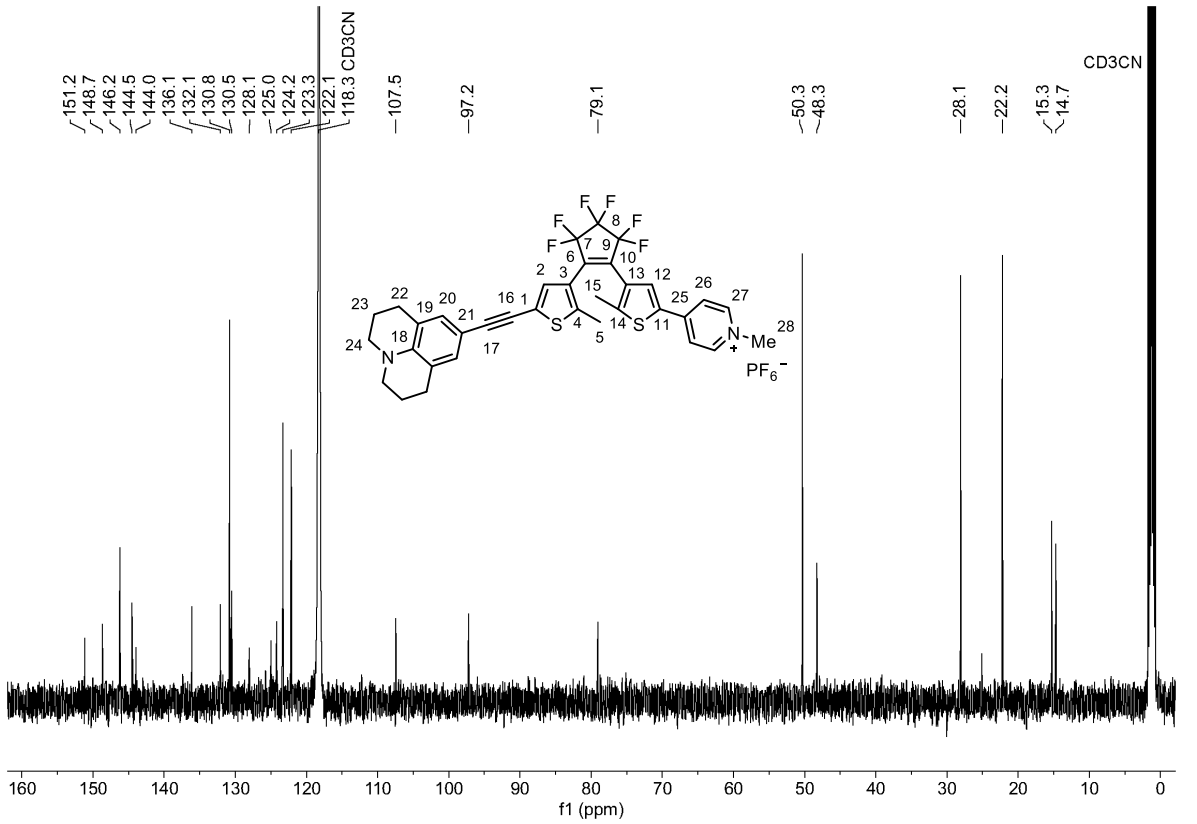


Figure 2.60 ^{13}C NMR spectrum (101 MHz, CD_3CN) of **Dy-A**.

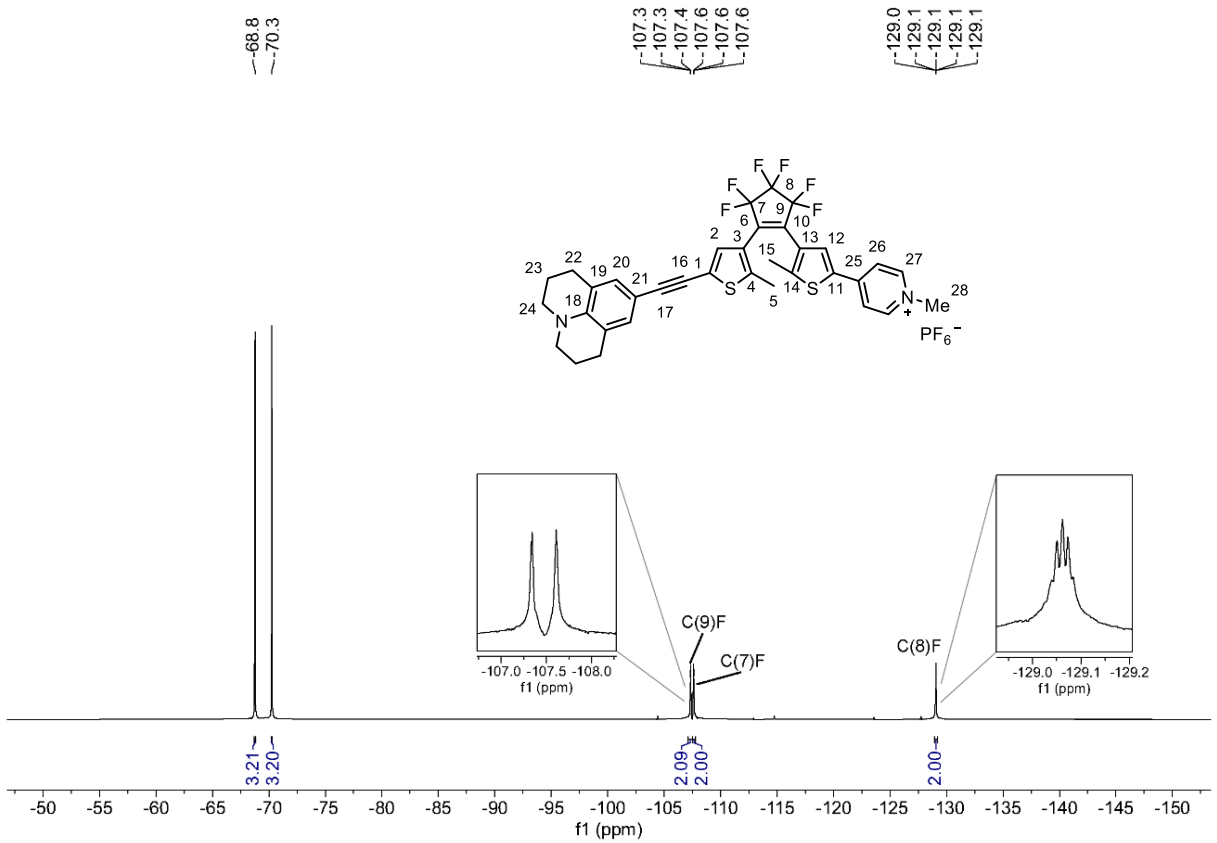


Figure 2.61 ^{19}F NMR spectrum (376 MHz, $CDCl_3$) of **Dy-A**.

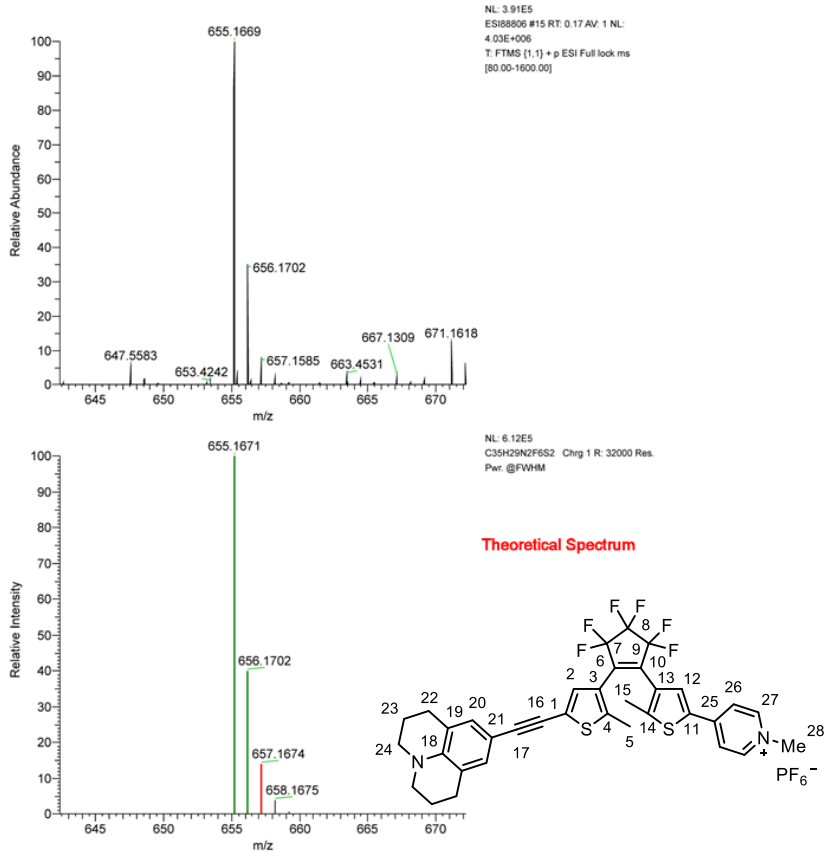


Figure 2.62 HRMS (ESI$^+$) of **Dy-A**, *m/z*: $[M]^+$ calcd. for $C_{35}H_{29}F_6N_2S_2^+$ 655.1671; found 655.1669.

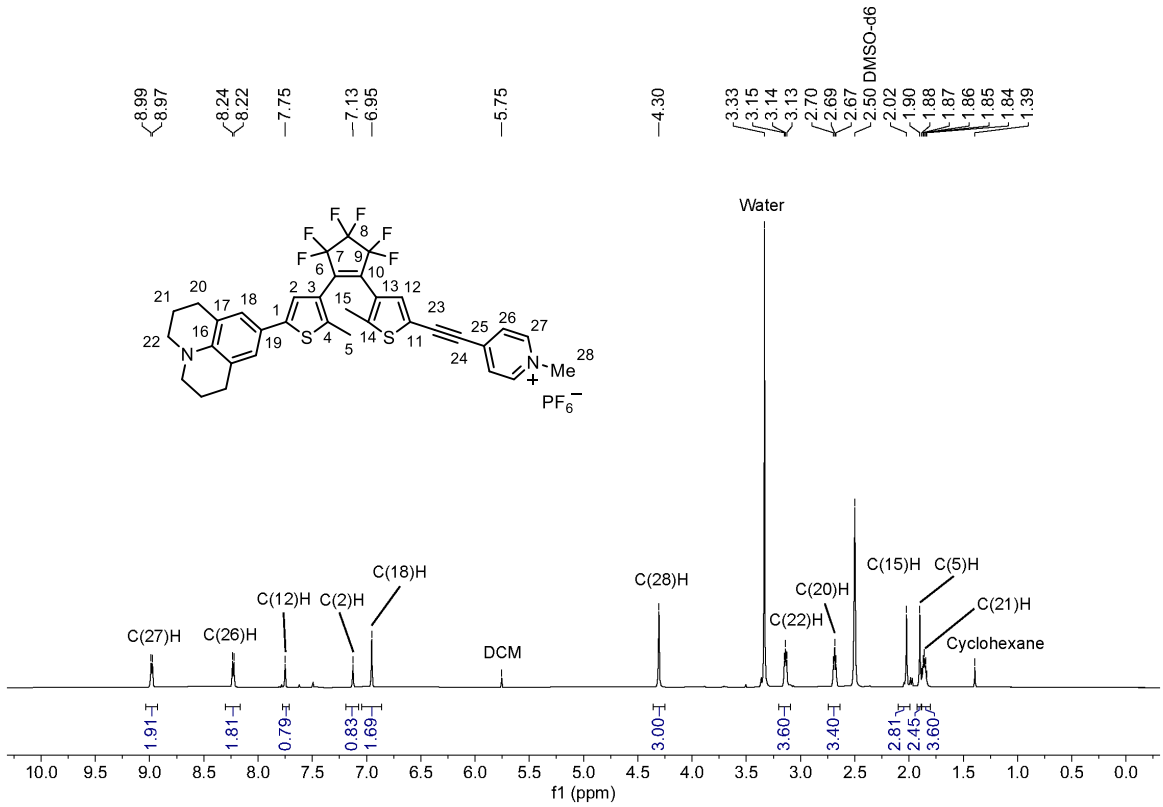


Figure 2.63 ^{1}H NMR spectrum (400 MHz, DMSO-d_6) of **D-yA**.

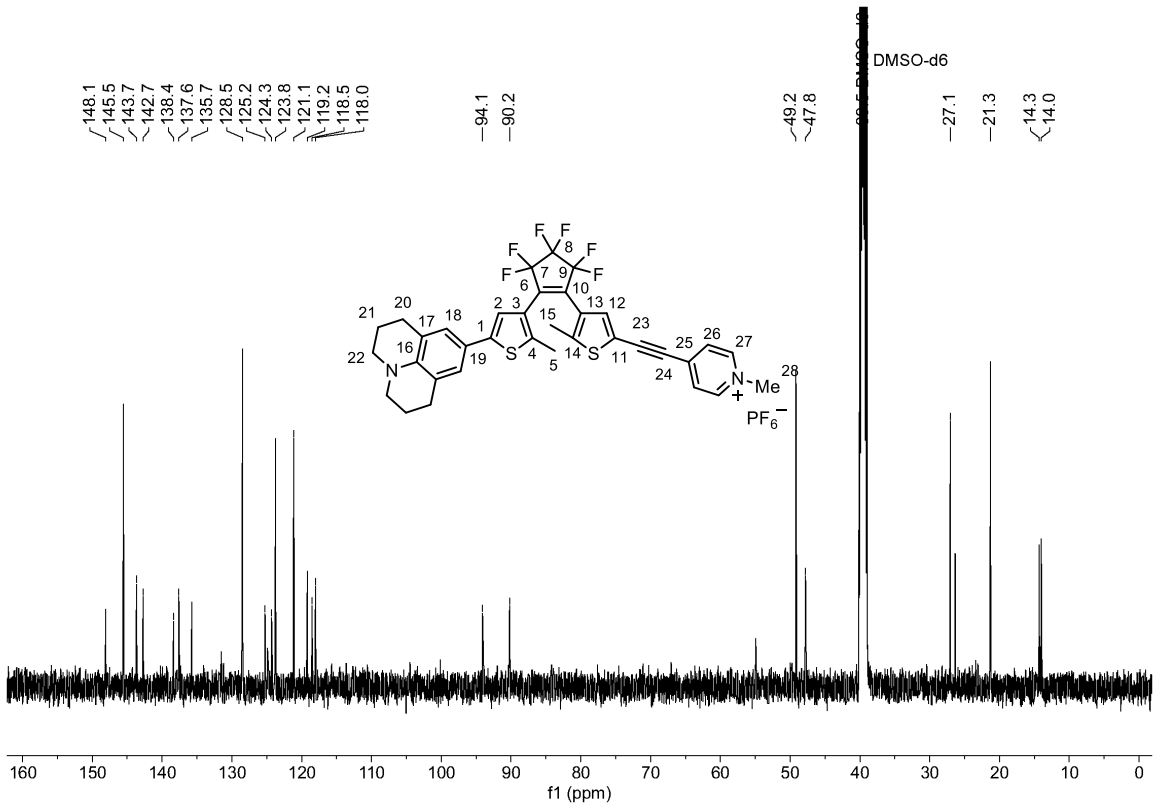


Figure 2.64 ^{13}C NMR spectrum (101 MHz, DMSO-d_6) of **D-yA**.

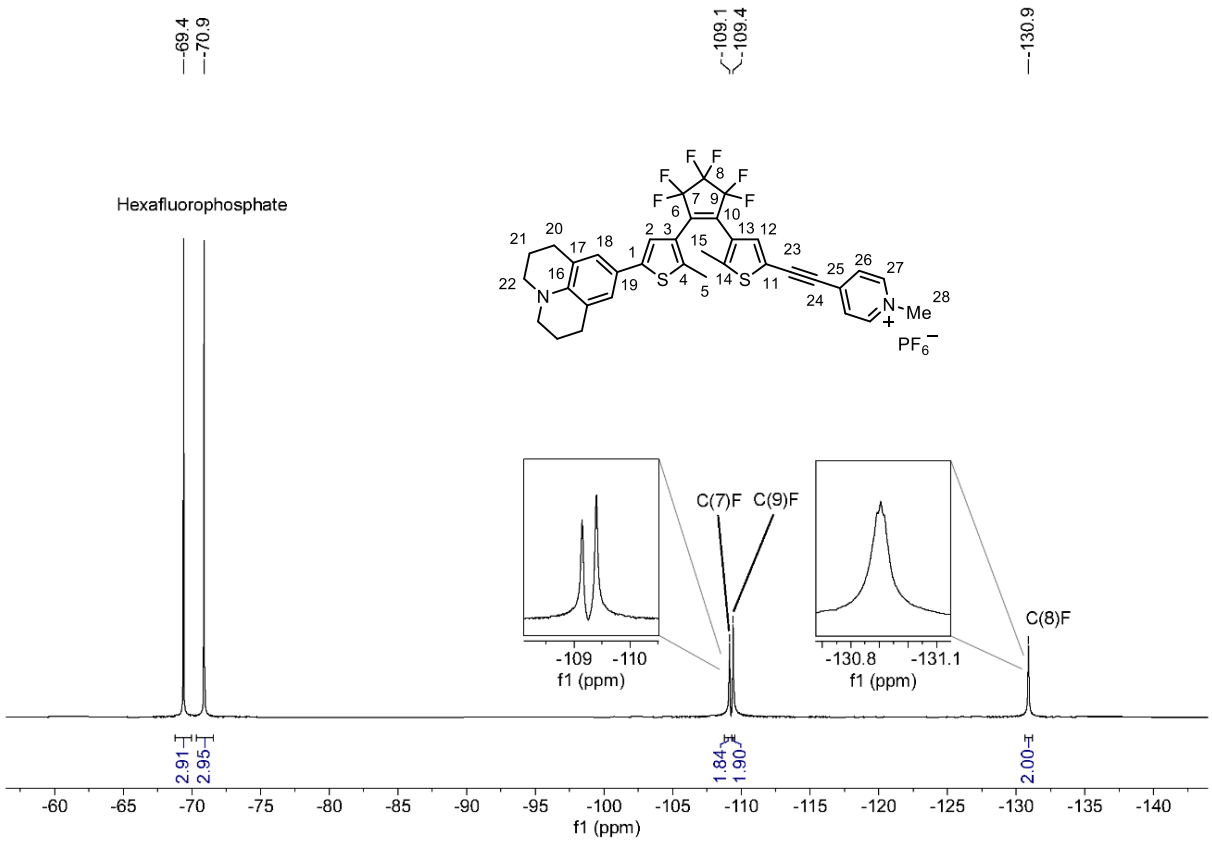


Figure 2.65 ^{19}F NMR spectrum (376 MHz, DMSO-d_6) of **D-yA**.

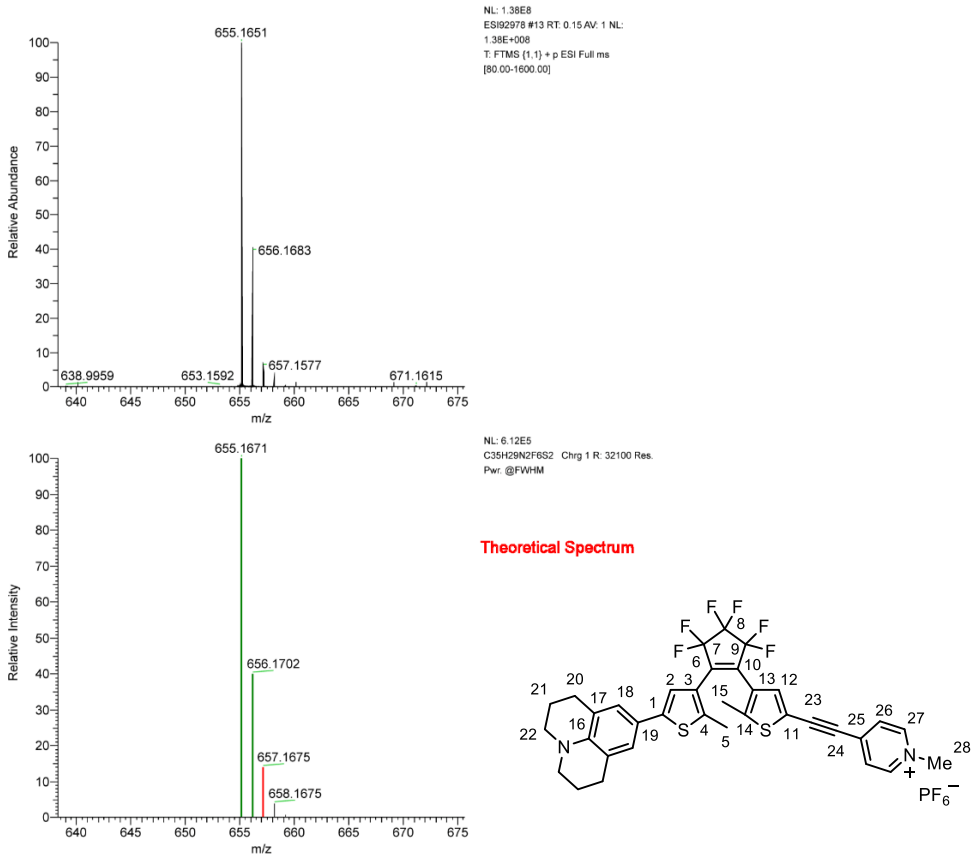


Figure 2.66 HRMS (ESI$^+$) of D-yA, *m/z*: $[M]^+$ calcd. for $C_{35}H_{29}F_6N_2S_2^+$ 655.1671; found 655.1651.

References

1. M. Irie and W. Schnabel, *Eur. Polym. J.*, 1982, **18**, 15–18.
2. M. Irie, *Pure Appl. Chem.*, 2015, **87**, 617–626.
3. M. Irie, *Chem. Rev.*, 2000, **100**, 1685–1716.
4. M. Irie, T. Fukaminato, K. Matsuda and S. Kobatake, *Chem. Rev.*, 2014, **114**, 12174–12277.
5. K. Uchida, T. Matsuoka, K. Sayo, M. Iwamoto, S. Hayashi and M. Irie, *Chem. Lett.*, 1999, **28**, 835–836.
6. S. Takami, S. Kobatake, T. Kawai and M. Irie, *Chem. Lett.*, 2003, **32**, 892–893.
7. M. Zhivagui, A. Hoda, N. Valenzuela, Y. Y. Yeh, J. Dai, Y. He, S. P. Nandi, B. Otlu, B. Van Houten and L. B. Alexandrov, *Nat. Commun.*, 2023, **14**, 276.
8. M. Wei, X. He, N. Liu and H. Deng, *Cell Div.*, 2024, **19**, 1.
9. J. L. Sandell and T. C. Zhu, *J. Biophotonics*, 2011, **4**, 773–787.
10. S. L. Jacques, *Phys. Med. Biol.*, 2013, **58**, R37.
11. M. V. Padalkar and N. Pleshko, *Analyst*, 2015, **140**, 2093–2100.
12. GembaRed, How Deep Does Red and Near-Infrared Light Penetrate into the Body? Marketing vs. Science, https://gembared.com/blogs/musings/how-deep-does-red-and-near-infrared-wavelengths-penetrate-into-the-body-marketing-vs-science, (accessed April 2024).
13. Z. Li, C. He, Z. Lu, P. Li and Y.-P. Zhu, *Dyes Pigm.*, 2020, **182**, 108623.
14. G. M. Tsivgoulis and J. M. Lehn, *Adv. Mater.*, 2004, **9**, 627–630.
15. E. A. Dragu, A. E. Ion, S. Shova, D. Bala, C. Mihailciuc, M. Voicescu, S. Ionescu and S. Nica, *RSC Adv.*, 2015, **5**, 63282–63286.
16. T. Fukaminato, T. Hirose, T. Doi, M. Hazama, K. Matsuda and M. Irie, *J. Am. Chem. Soc.*, 2014, **136**, 17145–17154.
17. S. Tang, F. Song, M. Lu, K. Han and X. Peng, *Sci. China: Chem.*, 2019, **62**, 451–459.
18. F. Hu, M. Cao, X. Ma, S. H. Liu and J. Yin, *J. Org. Chem.*, 2015, **80**, 7830–7835.
19. O. Tosic, K. Altenhoner and J. Mattay, *Photochem. Photobiol. Sci.*, 2010, **9**, 128–130.
20. N. M. Wu, M. Ng, W. H. Lam, H. L. Wong and V. W. Yam, *J. Am. Chem. Soc.*, 2017, **139**, 15142–15150.
21. C. C. Ko and V. W. Yam, *Acc. Chem. Res.*, 2018, **51**, 149–159.
22. Y. Hasegawa, T. Nakagawa and T. Kawai, *Coord. Chem. Rev.*, 2010, **254**, 2643–2651.
23. C.-C. Ko and V. Wing-Wah Yam, *J. Mater. Chem.*, 2010, **20**, 2063–2070.
24. M. Akita, *Organometallics*, 2011, **30**, 43–51.
25. S. Kume and H. Nishihara, *Dalton Trans.*, 2008, 3260–3271.
26. R. T. Jukes, V. Adamo, F. Hartl, P. Belser and L. De Cola, *Inorg. Chem.*, 2004, **43**, 2779–2792.
27. V. W. Yam, C. C. Ko and N. Zhu, *J. Am. Chem. Soc.*, 2004, **126**, 12734–12735.
28. C. C. Ko, W. M. Kwok, V. W. Yam and D. L. Phillips, *Chem. - Eur. J.*, 2006, **12**, 5840–5848.
29. J. K.-W. Lee, C.-C. Ko, K. M.-C. Wong, N. Zhu and V. W.-W. Yam, *Organometallics*, 2006, **26**, 12–15.
30. S. K. Brayshaw, S. Schiffers, A. J. Stevenson, S. J. Teat, M. R. Warren, R. D. Bennett, I. V. Sazanovich, A. R. Buckley, J. A. Weinstein and P. R. Raithby, *Chem. - Eur. J.*, 2011, **17**, 4385–4395.
31. J. C. Boyer, C. J. Carling, B. D. Gates and N. R. Branda, *J. Am. Chem. Soc.*, 2010, **132**, 15766–15772.
32. K. Mori, Y. Ishibashi, H. Matsuda, S. Ito, Y. Nagasawa, H. Nakagawa, K. Uchida, S. Yokojima, S. Nakamura, M. Irie and H. Miyasaka, *J. Am. Chem. Soc.*, 2011, **133**, 2621–2625.
33. G. Liu, Y. M. Zhang, C. Wang and Y. Liu, *Chem. - Eur. J.*, 2017, **23**, 14425–14429.

34. H. Xi, Z. Zhang, W. Zhang, M. Li, C. Lian, Q. Luo, H. Tian and W. H. Zhu, *J. Am. Chem. Soc.*, 2019, **141**, 18467–18474.
35. S. Qiu, A. T. Frawley, K. G. Leslie and H. L. Anderson, *Chem. Sci.*, 2023, **14**, 9123–9135.
36. J. Zhao, W. Wu, J. Sun and S. Guo, *Chem. Soc. Rev.*, 2013, **42**, 5323–5351.
37. R. Murata, T. Yago and M. Wakasa, *J. Phys. Chem. A*, 2015, **119**, 11138–11145.
38. R. Murata, T. Yago and M. Wakasa, *Bull. Chem. Soc. Jpn.*, 2011, **84**, 1336–1338.
39. T. Fukaminato, T. Doi, M. Tanaka and M. Irie, *J. Phys. Chem. C*, 2009, **113**, 11623–11627.
40. M. Herder, B. M. Schmidt, L. Grubert, M. Patzel, J. Schwarz and S. Hecht, *J. Am. Chem. Soc.*, 2015, **137**, 2738–2747.
41. S. Fredrich, R. Gostl, M. Herder, L. Grubert and S. Hecht, *Angew. Chem., Int. Ed.*, 2016, **55**, 1208–1212.
42. K. Matsuda, Y. Shinkai, T. Yamaguchi, K. Nomiyama, M. Isayama and M. Irie, *Chem. Lett.*, 2003, **32**, 1178–1179.
43. C. Wang, Y. H. Liu and Y. Liu, *Small*, 2022, **18**, e2201821.
44. D. Sun, Y. Wu, X. Han and S. Liu, *Mater. Chem. Front.*, 2022, **6**, 2929–2934.
45. M. Colaco, P. Maximo, A. Jorge Parola and N. Basilio, *Chem. - Eur. J.*, 2021, **27**, 9550–9555.
46. G. Naren, W. Larsson, C. Benitez-Martin, S. Li, E. Perez-Inestrosa, B. Albinsson and J. Andreasson, *Chem. Sci.*, 2021, **12**, 7073–7078.
47. D. Sun, Y. Wu, X. Han and S. Liu, *Chem. - Eur. J.*, 2021, **27**, 16153–16160.
48. P. Ferreira, B. Ventura, A. Barbieri, J. P. Da Silva, C. A. T. Laia, A. J. Parola and N. Basilio, *Chem. - Eur. J.*, 2019, **25**, 3477–3482.
49. Y. Zou, T. Yi, S. Xiao, F. Li, C. Li, X. Gao, J. Wu, M. Yu and C. Huang, *J. Am. Chem. Soc.*, 2008, **130**, 15750–15751.
50. Q.-F. Li, A. Liu, L. Fu, E. Li, D. Yue, J.-T. Wang and Z. Wang, *Dyes Pigm.*, 2024, **223**, 111934.
51. R. Miyamoto, D. Kitagawa and S. Kobatake, *Bull. Chem. Soc. Jpn.*, 2022, **95**, 639–645.
52. K. Uno, M. L. Bossi, M. Irie, V. N. Belov and S. W. Hell, *J. Am. Chem. Soc.*, 2019, **141**, 16471–16478.
53. S. H. Um, H. J. Kim, D. Kim, J. E. Kwon, J. W. Lee, D. Hwang, S. K. Kim and S. Y. Park, *Dyes Pigm.*, 2018, **158**, 36–41.
54. B. Roubinet, M. Weber, H. Shojaei, M. Bates, M. L. Bossi, V. N. Belov, M. Irie and S. W. Hell, *J. Am. Chem. Soc.*, 2017, **139**, 6611–6620.
55. Y. Takagi, M. Morimoto, R. Kashihara, S. Fujinami, S. Ito, H. Miyasaka and M. Irie, *Tetrahedron*, 2017, **73**, 4918–4924.
56. R. Gostl and S. Hecht, *Chem. - Eur. J.*, 2015, **21**, 4422–4427.
57. Z. Tong, S. Pu, Q. Xiao, G. Liu and S. Cui, *Tetrahedron Lett.*, 2013, **54**, 474–477.
58. H. Y. Jung, B. Kim, M. H. Jeon and Y. Kim, *Small*, 2022, **18**, e2103523.
59. H. Cheng, P. Ma, Y. Wang, G. Hu, S. Fang, Y. Fang and Y. Lin, *Chem. - Asian J.*, 2017, **12**, 248–253.
60. D. Kim, A. Aktalay, N. Jensen, K. Uno, M. L. Bossi, V. N. Belov and S. W. Hell, *J. Am. Chem. Soc.*, 2022, **144**, 14235–14247.
61. H. Tian and S. Yang, *Chem. Soc. Rev.*, 2004, **33**, 85–97.
62. H. B. Cheng, S. Zhang, E. Bai, X. Cao, J. Wang, J. Qi, J. Liu, J. Zhao, L. Zhang and J. Yoon, *Adv. Mater.*, 2022, **34**, 2108289.
63. M. Irie, K. Sakemura, M. Okinaka and K. Uchida, *J. Org. Chem.*, 2002, **60**, 8305–8309.
64. Y. Nakagawa, T. Hishida, E. Hatano, K. Sumaru, K. Morishita, M. Morimoto, S. Yokojima, S. Nakamura and K. Uchida, *Org. Biomol. Chem.*, 2022, **20**, 3211–3217.
65. S. L. Gilat, S. H. Kawai and J.-M. Lehn, *J. Chem. Soc., Chem. Commun.*, 1993, 1439–1442.
66. S. L. Gilat, S. H. Kawai and J. M. Lehn, *Chem. - Eur. J.*, 1995, **1**, 275–284.
67. E. Kim, M. Kim and K. Kim, *Tetrahedron*, 2006, **62**, 6814–6821.
68. K. J. Chen, A. D. Laurent and D. Jacquemin, *J. Phys. Chem. C*, 2014, **118**, 4334–4345.

69. F. Bureš, *RSC Adv.*, 2014, **4**, 58826-58851.
70. E. Zysman-Colman, K. Arias and J. S. Siegel, *Can. J. Chem.*, 2009, **87**, 440–447.
71. R. Saito, *Heterocycles*, 2010, **81**, 2831–2840.
72. T. C. S. Pace, V. Müller, S. Li, P. Lincoln and J. Andréasson, *Angew. Chem., Int. Ed.*, 2013, **52**, 4393–4396.
73. A. Slama-Schwok, M. Blanchard-Desce and J. M. Lehn, *J. Phys. Chem.*, 1990, **94**, 3894–3902.
74. K. Stranius and K. Borjesson, *Sci. Rep.*, 2017, **7**, 41145.
75. E. Stadler, A. Eibel, D. Fast, H. Freißmuth, C. Holly, M. Wiech, N. Moszner and G. Gescheidt, *Photochem. Photobiol. Sci.*, 2020, **17**, 660–669.
76. C. Özçoban, T. Halbritter, S. Steinwand, L.-M. Herzig, J. Kohl-Landgraf, N. Askari, F. Groher, B. Fürtig, C. Richter, H. Schwalbe, B. Suess, J. Wachtveitl and A. Heckel, *Org. Lett.*, 2015, **17**, 1517–1520.
77. M. Montalti, A. Credi, L. Prodi and M. T. Gandolfi, *Handbook of Photochemistry*, CRC Press, 2006.
78. Y. Xiong, DPhil, University of Oxford, 2018.
79. M. Irie and K. Sayo, *J. Phys. Chem.*, 2002, **96**, 7671–7674.
80. S. Kobatake, Y. Terakawa and H. Imagawa, *Tetrahedron*, 2009, **65**, 6104–6108.
81. M. Irie, T. Lifka, K. Uchida, S. Kobatake and Y. Shindo, *Chem. Commun.*, 1999, 747–750.
82. D. Mendive-Tapia, A. Perrier, M. J. Bearpark, M. A. Robb, B. Lasorne and D. Jacquemin, *Phys. Chem. Chem. Phys.*, 2014, **16**, 18463–18471.
83. P. Plaza, D. Laage, M. M. Martin, V. Alain, M. Blanchard-Desce, W. H. Thompson and J. T. Hynes, *J. Phys. Chem. A*, 1999, **104**, 2396–2401.
84. E. Fluhler, V. G. Burnham and L. M. Loew, *Biochemistry*, 2002, **24**, 5749–5755.
85. M. Barzoukas, C. Runser, A. Fort and M. Blanchard-Desce, *CHem. Phys. Lett.*, 1996, **257**, 531–537.
86. M. J. Kamlet, J. L. M. Abboud, M. H. Abraham and R. W. Taft, *J. Org. Chem.*, 1983, **48**, 2877–2887.
87. K. Ponnusamy, S. Chellappan, C. M. Singaravelu and J. Kandasamy, *J. Lumin.*, 2018, **202**, 253–262.
88. L. G. Nandi, F. Facin, V. G. Marini, L. M. Zimmermann, L. A. Giusti, R. d. Silva, G. F. Caramori and V. G. Machado, *J. Org. Chem.*, 2012, **77**, 10668–10679.
89. K. Okuno, Y. Shigeta, R. Kishi, H. Miyasaka and M. Nakano, *J. Photochem. Photobiol. A: Chem.*, 2012, **235**, 29–34.
90. R. Castagna, V. Nardone, G. Pariani, E. Parisini and A. Bianco, *J. Photochem. Photobiol. A: Chem.*, 2016, **325**, 45–54.
91. M. Morimoto, S. Kobatake and M. Irie, *Chem. Eur. J.*, 2003, **9**, 621–627.
92. P. Pracht, F. Bohle and S. Grimme, *Phys. Chem. Chem. Phys.*, 2020, **22**, 7169–7192.
93. L. N. Lucas, J. van Esch, R. M. Kellogg and B. L. Feringa, *Tetrahedron Lett.*, 1999, **40**, 1775–1778.
94. S. Hermes, G. Dassa, G. Toso, A. Bianco, C. Bertarelli and G. Zerbi, *Tetrahedron Lett.*, 2009, **50**, 1614–1617.
95. A. Osuka, D. Fujikane, H. Shinmori, S. Kobatake and M. Irie, *J. Org. Chem.*, 2001, **66**, 3913–3923.

3

DTE-Cyanine Dyads with Photoswitchable Fluorescence

Contents

3.1 Introduction 157

3.1.1 Fluorescence 157

3.1.2 Activatable, Convertible and Switchable Fluorescence 158

3.1.3 Switchable Fluorescent Probes for Super-Resolution Microscopy 161

3.1.4 Switchable Fluorescent Probes for Studying Cellular Dynamics 169

3.1.5 Project Aim 169

3.2 Results and Discussion 170

3.2.1 Molecular Design of Photoswitchable Dyads 170

3.2.2 Selection of the Fluorescent Dye 171

3.2.3 Modelling of FRET Quenching 175

3.2.4 Synthesis of Cy3 and Cy3B Dyes 179

3.2.5 Characterization of Cy3 and Cy3B Photophysics 181

3.2.6 Synthesis of Photoswitchable Fluorophores 184

3.2.7 Photoswitching of **DTE-Cy3** and **DTE-Cy3B** 187

3.2.8 Regulation of Cyanine Fluorescence by DTE 190

3.2.9 Fatigue Resistance of **DTE-Cy3** and **DTE-Cy3B** 193

3.2.10 Conclusion 194

3.3 Experimental 195

3.3.1 General Synthetic and Characterization Methods 195

3.3.2 HPLC Analysis and Purification 196

3.3.3 Optical Analysis 197

3.3.4 Measurement of Fatigue Resistance 198
3.3.5 Synthetic Procedures 198
3.4 Appendix 211

Chapter 3 - DTE-Cyanine Dyads with Photoswitchable Fluorescence

3.1 Introduction

3.1.1 Fluorescence

Fluorescence is a fundamental phenomenon in chemistry and biology that has become an essential tool for studying various processes at the molecular level, primarily through fluorescence assays and fluorescence microscopy. Fluorescence assays provide quantitative information on the intensity, lifetime, polarization, and other characteristics of fluorescence, while fluorescence microscopy adds locational information, enabling the formation of images.

Fluorescence is a form of luminescence, where a molecule absorbs light and subsequently emits light.[1] The fluorescence emission spectrum is characterized by several key features. First, due to the rapid vibrational relaxation and internal conversion processes, the emission spectrum is typically shifted to longer wavelengths compared to the absorption spectrum. This shift is known as the Stokes shift. The magnitude of the Stokes shift can vary depending on the molecular structure and the environment of the fluorophore. Another important characteristic of fluorescence is the fluorescence quantum yield (Φ) (Equation 3.1, where k_r is the emission rate constant and k_{nr} is the collective non-radiative rate constant), which is defined as the ratio of the number of photons emitted to the number of photons absorbed. A high quantum yield indicates that most of the absorbed energy is released as fluorescence, while a low quantum yield suggests that non-radiative relaxing processes are more dominant. The fluorescence lifetime (τ) is another key parameter (Equation 3.2), which represents the average time a molecule spends in the excited state before returning to the ground state. Fluorescence lifetimes typically range from picoseconds to nanoseconds, depending on the molecular structure and the environment.[2]

$$\Phi_f = \frac{\text{photons emitted}}{\text{photons absorbed}} = \frac{k_r}{k_r + k_{nr}} \tag{3.1}$$

$$\tau = \frac{1}{k_r + k_{nr}} \tag{3.2}$$

3.1.2 Activatable, Convertible and Switchable Fluorescence

Conventional fluorescence techniques rely on standard fluorophores, which emit light upon illumination at a specific excitation wavelength.[3] However, activatable, convertible and switchable fluorophores offer an additional level of control over the fluorescence signal by requiring an external stimulation that can turn the fluorescence on and off. This advanced molecular design allows for greater manipulation of the fluorescence emission, enabling more sophisticated applications in imaging and sensing.

Activatable fluorescence refers to probes that can be irreversibly converted from a dark state to a bright state through stimulation, while convertible fluorescence refers to probes that can be irreversibly switched from a bright state to a dark state. Switchable fluorescence involves probes that can be reversibly converted between the two states (Figure 3.1).[4]

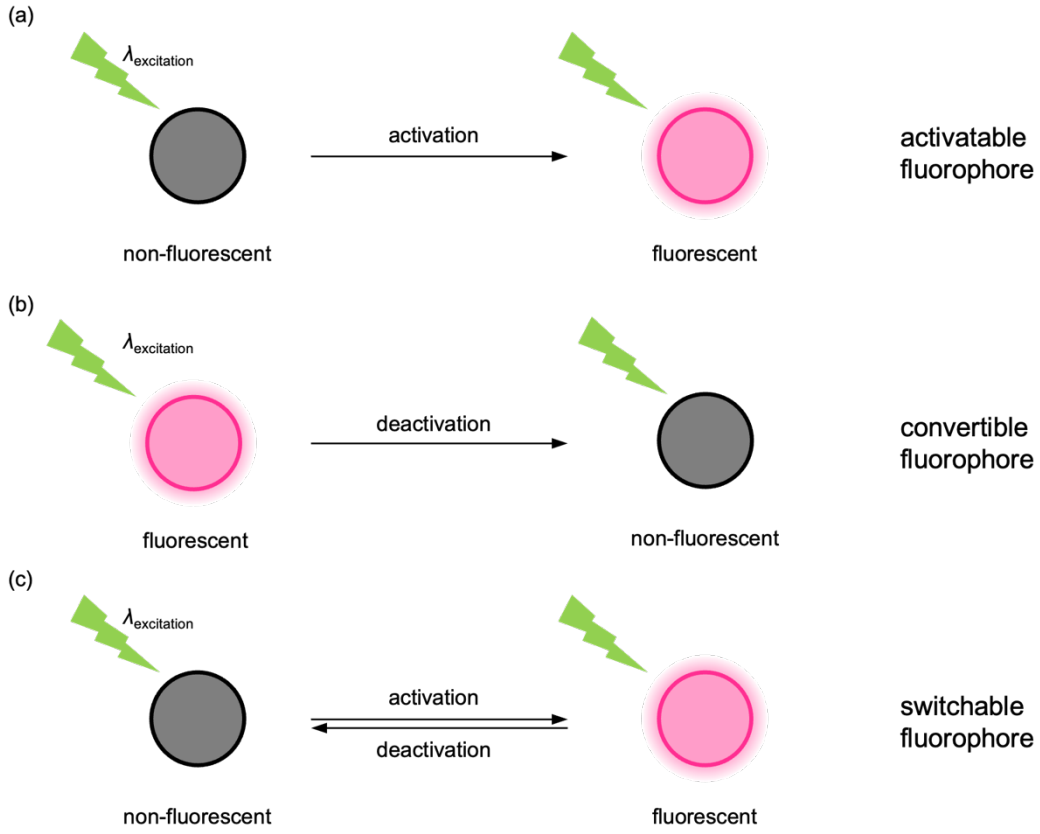
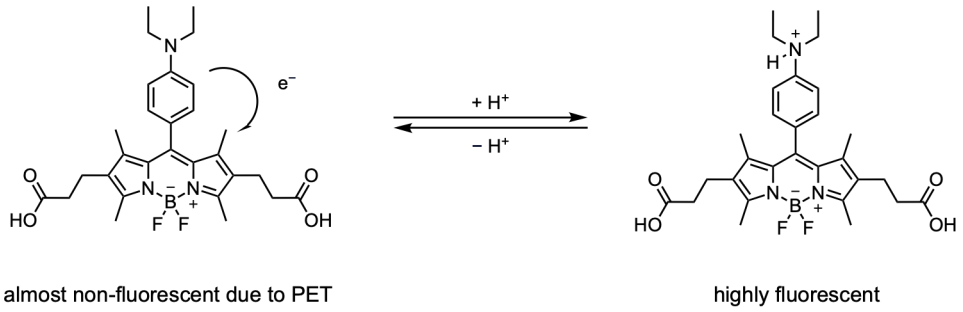


Figure 3.1 Schematic demonstration of (a) activable, (b) convertible and (c) switchable fluorophores.

The interplay between the external stimulation (for activation, deactivation or switching) and excitation enables precise control over fluorescence emission in both space and time. The controllable fluorescence is particularly advantageous for advanced microscopy studies, as it allows for the selective activation of fluorescence in specific regions of interest at desired time. By applying the stimulation to a targeted area at a specific time, fluorescence can

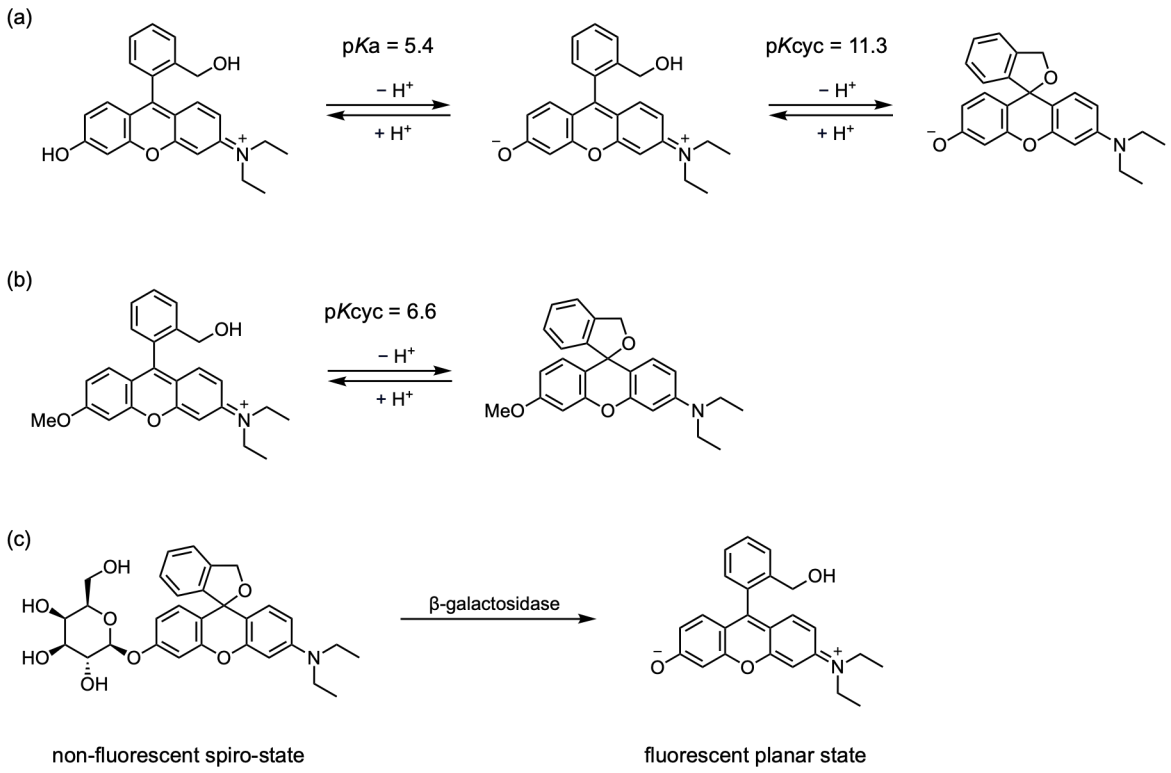
be switched on with high spatial and temporal resolution. This level of control opens up new possibilities for imaging schemes that would be unattainable with conventional fluorophores, which emit light continuously upon excitation.

De Silva developed the first pH-switchable fluorophore based on photoinduced electron transfer (PET) by attaching various nitrogen-bearing functional groups, including NEt_2, to anthracene.[5] The fluorescence is quenched when the nitrogen center is not protonated and restored upon protonation. Building on this concept, Urano and colleagues applied it to BODIPY dyes, developing an activatable fluorescence system using pH as a stimulus (Scheme 3.1).[6] They synthesized a series of BODIPY dyes with anilines serving as proton-reactive moieties. In the unprotonated state, fluorescence is quenched via PET from the *N*,*N*-dialkylated anilines to the BODIPY fluorophore. Protonation suppresses the PET pathway, resulting in a 300-fold increase in fluorescence quantum yield. The researchers coupled this pH-sensitive fluorophore to trastuzumab, an antibody that recognizes overexpressed HER2 receptors in cancer cells. When applied to cancer cells, the activatable probes exhibited intense fluorescent spots that co-localized with LysoTracker dyes, indicating fluorophore activation in the acidic lysosomal environment.



Scheme 3.1 Acid-induced fluorescence activation of the BODIPY probe bearing an aniline group.

Doura and co-workers developed a class of functionalized fluorogenic substrates for selective imaging of *lac*Z(+) cells.[7] The activatable fluorophore is based on rhodol, a hybrid structure derived from fluorescein and rhodamine (Scheme 3.2a). In its native form, the rhodol fluorophore is highly fluorescent at neutral pH. However, the researchers discovered that alkylation of the terminal oxygen causes the rhodol to isomerize into a weakly fluorescent spiro isomer at neutral pH (Scheme 3.2b). To create a probe that can be activated with the enzyme β-galactosidase, the researchers attached a β-galactopyranoside moiety to the rhodol fluorophore, rendering it non-fluorescent in cells. When β-galactosidase enzyme cleaves off the β-galactopyranoside, the molecule undergoes a structural change from the spiro form to a planar fluorescent rhodol, resulting in 75-fold increase in fluorescence intensity (Scheme 3.2c).[8]

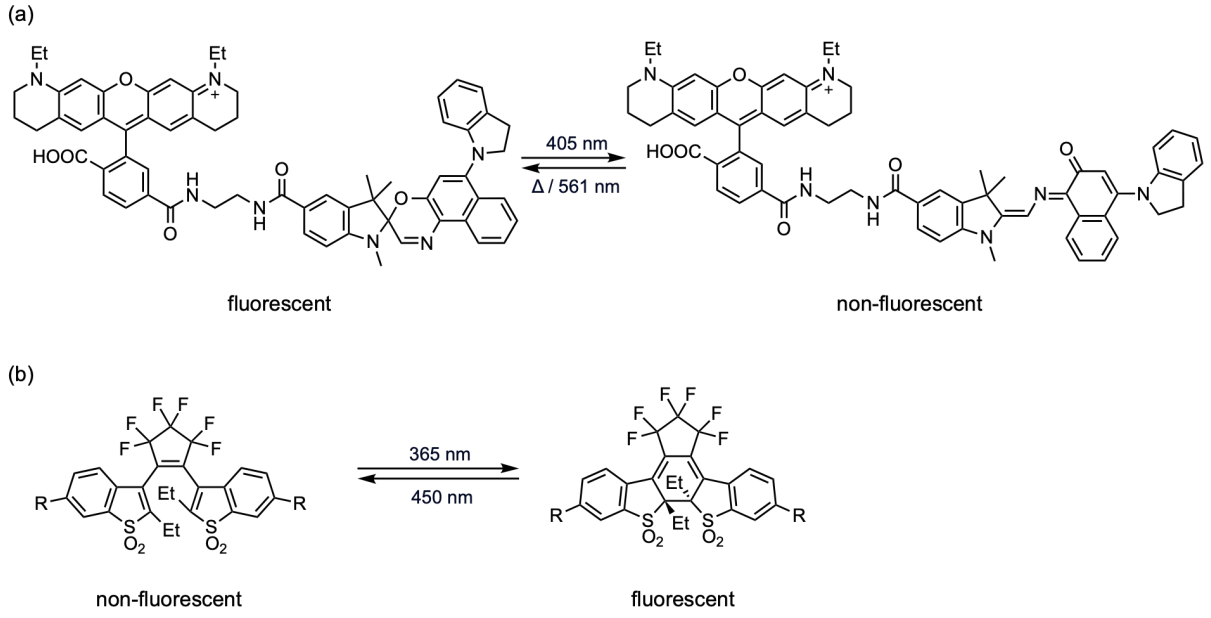


Scheme 3.2 The structures present at different pH conditions of (a) parent rhodol and (b) methylated rhodol and (c) Rhodol bearing β-galactopyranoside that can be cleaved in presence of the β-galactosidase enzyme.

Another commonly used external stimulus for controlling fluorescence is light. Two common systems are photoactivatable fluorescence (irreversible activation) and photoswitchable fluorescence (reversible switching). Photoswitchable fluorophore usually involves the incorporation of molecular photoswitches that can be toggled between two states. Two main strategies exist for constructing a photoswitchable fluorophore. The first approach entails linking a molecular photoswitch to an established fluorophore. In this case, the photoswitch can quench the fluorescence in one state through mechanisms such as PET or FRET, while leaving the fluorophore unaffected in the other state. This approach benefits from a wide range of available photoswitches and fluorophores that can be combined. However, it necessitates the separate synthesis of the fluorophore and the photoswitch, which must subsequently be linked together. The second approach involves the development of intrinsically fluorescent molecular photoswitches, which exhibit fluorescence in one state but not in the other, eliminating the need for a separate fluorophore. Although this approach may entail more complex molecular design and synthesis, it can result in more compact and integrated photoswitchable fluorophores. However, when a photoswitch itself fluoresces, the radiative process can compete with the photoswitching process, potentially leading to diminished switching performance.

Our group followed the first strategy for developing a photoswitchable fluorophore by linking a spironaphthoxazine photoswitch to an Atto565 fluorescent dye through an ethylenediamine linker (Scheme 3.3a).[9] When the photoswitch is in its spiro form, the fluorophore can be excited at 561 nm and emits light at 590 nm. However, when the photoswitch is converted into its merocyanine form, the fluorescence from Atto565 is quenched by FRET, achieving a quenching efficiency of around 85%, which is consistent with the PSD of the photoswitch under 405 nm irradiation.

In contrast, Irie and co-workers developed a turn-on-type fluorescent photoswitch following the second strategy (Scheme 3.3b).[10] The DAE molecule is not fluorescent in its open form. Upon photoswitching to its closed form under 365 nm irradiation, the molecule becomes fluorescent when excited at 450 nm. However, the 450 nm irradiation triggers both the radiative pathway and reverse photoswitching, resulting in a lower reverse photoswitching quantum yield compared to non-fluorescent DAEs.



Scheme 3.3 Photoswitchable fluorophores following (a) a photoswitch-fluorophore dyad design strategy and (b) an intrinsic fluorescent photoswitch strategy.

3.1.3 Switchable Fluorescent Probes for Super-Resolution Microscopy

In far-field optical microscopy, the spatial resolution is limited due to the diffraction of light that occurs when it passes through a lens system. This phenomenon results in the formation of an Airy disk, a diffraction pattern consisting of a bright central region surrounded by a series of concentric rings of decreasing intensity (Figure 3.2a). The diameter of the Airy disk is related

to the wavelength (λ) of the illuminating light and the size of the circular aperture, and it represents the smallest point to which a beam of light can be focused.[11]

As the focused Airy patterns from different object details approach one another, they begin to overlap. When the overlapping patterns create enough constructive interference to reduce contrast, they eventually become indistinguishable from each other (Figure 3.2b). This limitation is known as Abbe's diffraction limit[12] and arises from a fundamental barrier: as light propagates away from a point source in both excitation and fluorescence detection pathways, diffraction is inevitable, resulting in an ellipsoid pattern, or a point spread function (PSF) of a finite size, rather than an infinitely small spot. Consequently, even on a perfect far-field fluorescence microscope, when two objects simultaneously emit within the volume of the PSF, they cannot be discerned, and instead, a blurred image is formed.[11]

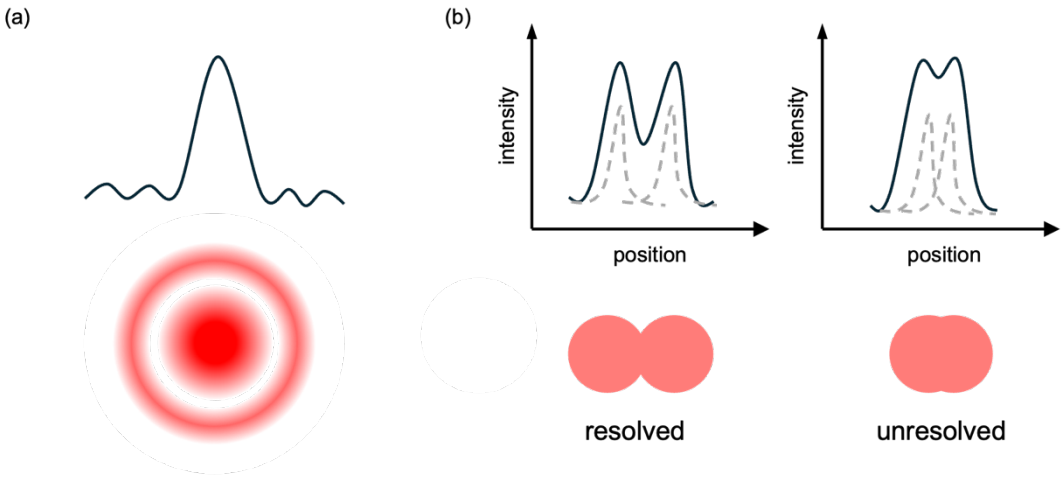


Figure 3.2 (a) Schematic representation of the Airy pattern of a focused optical imaging system and the corresponding Airy disk. (b) The ellipsoid point spread functions of two emitters, far enough apart to be resolved (left) and too close to be resolved (right).

For a long time, the diffraction barrier was considered an insurmountable limit in microscopy. However, in the late 1990s, researchers proposed innovative super-resolution microscopy techniques that aimed to overcome this barrier by exploiting the properties of fluorescent molecules themselves. These techniques relied on photoswitching to turn molecules on and off, either with specific irradiation patterns or stochastically. By controlling the fluorescence emission of individual molecules, it became possible to localize fluorophores with a precision far below the diffraction limit. The groundbreaking work of Stefan Hell, Eric Betzig, and William Moerner in developing these technologies was recognized with the Nobel Prize in Chemistry in 2014, highlighting the significance of their contributions to the field of microscopy and the potential impact of super-resolution microscopy (SRM) on various areas of scientific research.[13-15]

SRM methods differ fundamentally in their approach to exciting fluorescently labeled samples and detecting the emitted photons. Schermelleh and co-workers have reviewed the various types of SRM techniques and their relationships.[16] These techniques can be broadly classified into three main families: super-resolved structured illumination microscopy (SR-SIM), deterministic super-resolution techniques, and stochastic super-resolution techniques. Each family employs distinct strategies to overcome the diffraction limit and achieve high-resolution imaging of biological structures and processes.

SR-SIM techniques, which have been reviewed elsewhere,[17, 18] include traditional interference-based linear 2D and 3D SIM[19-21] and more recently introduced point scanning SIM approaches.[22, 23] These methods exploit the large-scale interference (moiré) patterns that emerge when two patterned objects are overlaid. By using patterned excitation irradiation generated by a grating, sub-diffraction features in samples form moiré patterns in the recorded emission.[24]

Diffraction-unlimited SRM techniques, including stochastic and deterministic methods, can theoretically push resolution levels down to infinitesimally small scales. However, in practice, experimental constraints such as high irradiation intensities, labeling density, and prolonged imaging times limit the achievable resolution, particularly in live-cell experiments. The unifying basic principle of these techniques is the modulation or switching of fluorescence emission.

Stochastic methods, collectively known as single-molecule localization microscopy (SMLM), rely on the fact that the spatial coordinates of single fluorescent molecules can be determined with high precision if their PSFs do not overlap (Figure 3.3). SMLM methods appear under various acronyms, primarily STORM (stochastic optical reconstruction microscopy)[25] and (f)PALM ((fluorescence) photoactivated localization microscopy),[26, 27] depending on the types of fluorophores and imaging conditions used. To avoid overlaps between the PSFs of individual molecules, fluorescent emissions of distinct molecules are separated in time. The most common approach to achieve this temporal separation exploits the phenomenon of switching, where fluorescent molecules can switch between an active 'on' or 'bright' state, in which they emit fluorescent light when excited, and one or more inactive 'off' or 'dark' states, in which they do not fluoresce. This allows the acquisition of the individual 2D PSF for each molecule, which is then used in data processing to decipher its position. The precision of determining the centroid position of a fluorescent signal mainly depends on the

photon count (roughly the square root of the number of photons detected). At the end of an acquisition, the individual molecule positions are then used to reconstruct a final super-resolution image. SMLM approaches are popular because they can be implemented at low cost on conventional, camera-based, wide-field setups, shifting the complexity to biological sample preparation and downstream reconstruction and data analysis. Most SMLM implementations can separate individual dyes with distances reduced to 20 nm lateral and 50 nm axial resolution. However, structural resolution, such as the ability to distinguish biological features like filaments, depends on the sample's labeling density and switching properties.[28, 29] As a general rule, achieving a specific structural resolution requires that the distance between neighboring localizations to be at least 2-fold smaller to meet the Nyquist sampling criterion.[30-32]

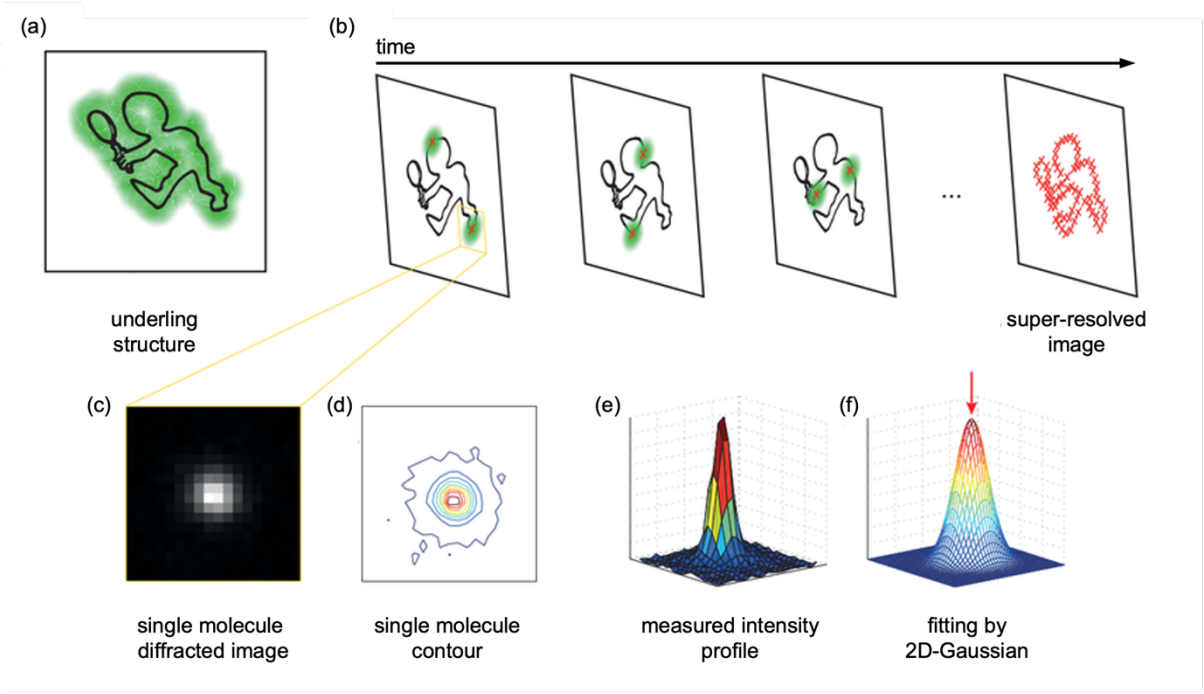
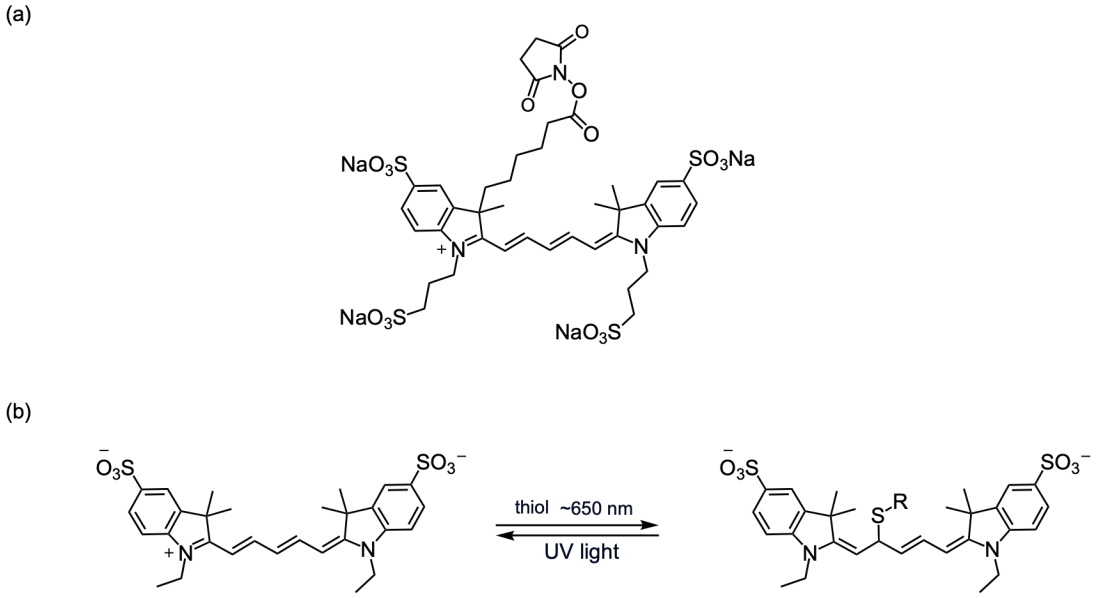


Figure 3.3 The principle behind SMLM. (a) The underlying object as well as the image resulting from conventional widefield microscopy in green. (b) Stochastic blinking allows localization of the individual fluorophores with nanoscopic precision. The process is repeated for many frames to yield a pointillistic reconstruction of the object, bypassing the diffraction limit. (c) The image of a single fluorescent molecule in widefield microscopy. (d) Contour plot of the intensity profile. (e) 3D plot of measured intensity profile. (f) The 2D Gaussian that is fitted to the measured intensity profile. Reprint with permission.[33]

Alexa Fluor 647 (Scheme 3.4a), a functionalized Cy5 dye, has been regarded as the gold standard fluorophore for SMLM since its inception, consistently delivering the best imaging results. Despite ongoing efforts to develop new fluorophores, no dye has outperformed Alexa Fluor 647 to date.[34] SMLM relies on a fluorophore's ability to switch, which can occur through various mechanisms. One commonly studied mechanism is Cy5 switching in the presence of a thiol (Scheme 3.4b).[35] Cy5 starts in the on-state and can be reversibly switched on and off or

enter a permanent dark state due to photobleaching. The reversible dark state is caused by the thiol bonding to the bridge structure, disrupting the molecule's conjugation and making it nonfluorescent. The thiol spontaneously detaches from the bridge, restoring the fluorescent state, a process that can be assisted by low-dosage ultraviolet light irradiation. Other switchable fluorophores specifically designed for SMLM have been reviewed elsewhere.[36, 37]



Scheme 3.4 (a) Chemical structure of Alexa Fluor 647. (b) Mechanism of switchable fluorescence Cy5 fluorophores. Upon illumination with ~650 nm light in the presence of thiol, Cy5 transitions to a non-fluorescent state consisting of the phosphine or thiol bound to the polymethine bridge of molecule. This process is reversible, and the reverse reaction can be driven by irradiation with UV light.

Stimulated emission depletion (STED) microscopy is the most common deterministic approach for super-resolution imaging.[38] STED microscopy achieves sub-diffraction resolution by selectively deactivating fluorophores in the sample, effectively reducing the size of the fluorescent spot. A typical STED microscope setup utilizes two laser beams: an excitation laser, with a wavelength matched to the fluorophore's absorption spectrum, and a donut-shaped depletion laser, with a wavelength that falls within the fluorophore's emission spectrum (Figure 3.4a). The excitation laser excites the fluorescent molecules, while the depletion laser selectively suppresses fluorescence in the outer regions of the excitation spot. The depletion is achieved through stimulated emission. In the presence of an external electromagnetic field with a frequency that matches the energy difference between the excited state and the ground state, the excited atom or molecule can be stimulated to emit a photon. The emitted photon has the same frequency, phase, polarization, and direction as the incident photon from the external field. The resolution of STED microscopy is positively correlated with the depletion laser power, as a more intense depletion donut results in a smaller effective central zero point.[39]

The donut-shaped depletion beam is created by passing the depletion laser through a vortex phase plate, which shifts the phase of the laser beam in a spiral around the center, resulting in a hollow central cylinder in the intensity distribution. As STED is a scanning technique, out-of-focus emission can be filtered out using a pinhole, enabling optical sectioning of tissues into different focal planes. The emission is collected as an intensity in each pixel using photodetectors and can be filtered by wavelength for multi-color imaging.[40]

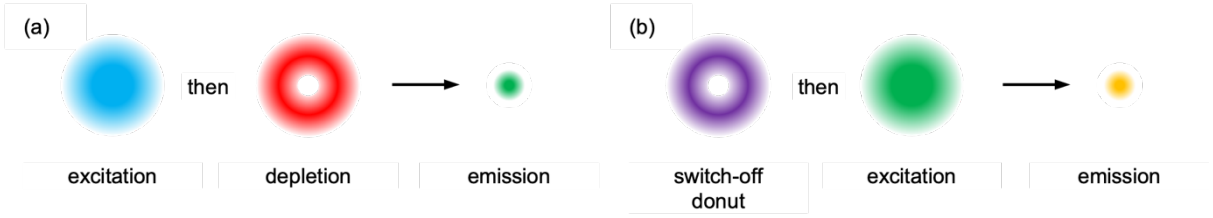


Figure 3.4 Deterministic SRM techniques. (a) The laser sequence for STED microscopy: excitation is followed by depletion with a donut-shaped laser, resulting in diffraction unlimited emission at the central node of zero intensity. (b) RESOLFT laser illumination pattern: the switch-off donut triggers photochemical switching to an off state, so that when the excitation laser is applied, only emission from the central node is observed.

The main limitation of STED microscopy is the high intensity laser irradiation required to deplete the excited state before spontaneous emission occurs, which can lead to photobleaching and phototoxicity. However, STED microscopy routinely achieves lateral resolutions of 30–80 nm and axial resolutions of 100 nm. In cells, current commercial STED systems typically achieve down to 50–60 nm lateral resolution.[41] More recent 3D STED setups also operate along the *z*-direction, allowing for tunable lateral and axial resolution.[38]

Reversible saturable optical fluorescence transitions (RESOLFT) microscopy is an SRM technique that shares similarities with STED. Both techniques employ an overlaid donut-shaped laser beam to selectively allow only a small population of fluorophores to emit, thereby achieving sub-diffraction resolution. However, RESOLFT utilizes photochemical switching rather than stimulated emission from the excited state to turn molecules off (Figure 3.4b), as reported in the first RESOLFT microscopy study published 10 years after the introduction of STED.[42] In RESOLFT microscopy, reversibly photoswitchable fluorophores are used, which can be switched between a fluorescent "on" state and a non-fluorescent "off" state using light of different wavelengths.[43] The imaging process involves three laser beams: an activation laser to switch the fluorophores from the "off" state to the "on" state, an excitation laser to excite the fluorophores in the "on" state and induce fluorescence emission, and a deactivation laser shaped into a donut-like pattern to selectively switch the fluorophores in the outer regions of the excitation spot back to the "off" state. The main advantage of RESOLFT microscopy over STED is that the light intensity required for photoswitching is similar to that used for excitation in

confocal fluorescence microscopy and up to six orders of magnitude lower than the intensities needed for STED.[44] This significant reduction in light intensity makes RESOLFT microscopy a more suitable choice for live-cell imaging experiments conducted over long timeframes, as it minimizes the phototoxicity and photobleaching associated with the high-intensity depletion lasers used in STED.[45]

The first application of the RESOLFT microscopy utilized photoswitchable proteins, demonstrating the advantage of using photochemical switching over stimulated emission. The laser intensities required for photochemical switching were eight orders of magnitude lower than the comparable STED intensities at the time.[42] Photoswitchable proteins contain a chromophore that can adopt either a fluorescent "on" state or a dark "off" state through a photochemical *trans–cis* isomerization .[46] These proteins are derivatives of the green fluorescent protein (GFP) family, consisting of a central chromophore on an alpha helix, surrounded by a barrel of beta sheets (Figure 3.5).[44] The emission properties of the chromophores depend on their protonation state, isomeric form, and interactions with the surrounding amino acid residues. The ability to tune the chromophore environment has led to the development of many mutants with varying spectral properties, often through the rational design of structural changes.[47] As with any super-resolution dye, the important properties of photoswitchable fluorescent proteins for their application include brightness, switching speed, background (off-state fluorescence), and fatigue. These parameters are often the target of optimization mutation studies,[44] with around 30 reported photoswitchable proteins and variants produced to have improved photostability,[48] switching kinetics (and therefore imaging speed),[49, 50] switching direction (and therefore laser sequence),[51] red-shifted emission,[52] and lifetime.[53]

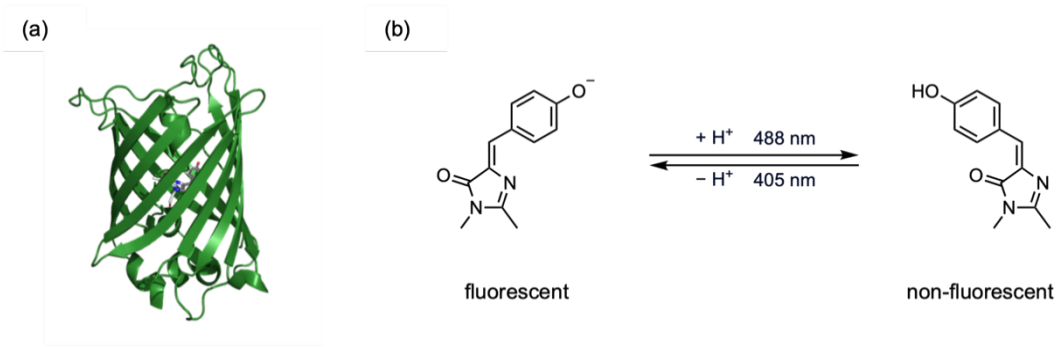
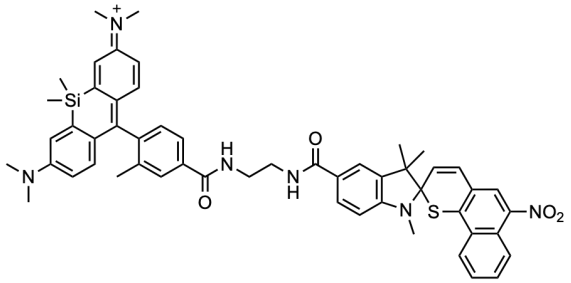


Figure 3.5 Schematic of the overall structure and photoswitching mechanisms of reversibly switchable fluorescent proteins. (a) Crystal structure of the wild-type green fluorescent protein. (b) The photoinduced structural and protonation state changes of the chromophore during reversible switching. Reprint with permission.[54]

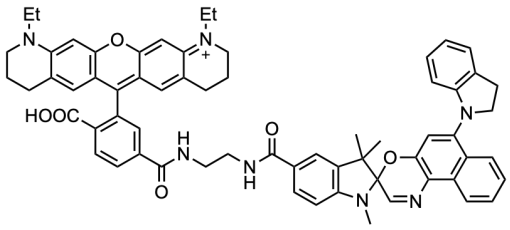
However, there are some drawbacks associated with fluorescent proteins. These include their relatively large size, sensitivity to local pH, and oxygen dependence. They also require

genetic mutation to introduce them into cells and often have slow switching kinetics and poor photostability. Importantly, there is a limit to how much these parameters can be improved by protein modification, as the core scaffold and chromophore cannot be easily altered. The use of synthetic dyes in RESOLFT microscopy opens up a much wider range of photoswitching mechanisms and chromophores that can be explored. However, to date, only a few organic dyes have been reported for use in RESOLFT.[55] The development of organic dyes specifically designed for RESOLFT would not only expand the available options for imaging but also provide the opportunity to incorporate organelle targeting and chemical sensing moieties.

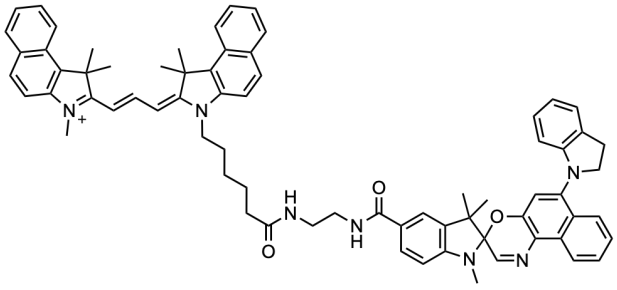
Our group has developed several photoswitchable dyads that utilize FRET quenching with molecular photoswitches (Scheme 3.5). In these dyads, the photoswitch quenches the fluorescence from the fluorophore in one state ("off" state) but not in the other ("on" state). Initially, we created a FRET dyad composed of a silicon rhodamine dye and a spiropyran photoswitch, which demonstrated good switching properties and high brightness in confocal experiments. However, the fatigue resistance of this dyad was insufficient for RESOLFT microscopy.[56] To address this issue, we developed a better-optimized visible light spironaphthoxazine photoswitch. This improved photoswitch enabled the successful creation of RESOLFT FRET dyads with Atto565,[9] Atto590 and cyanine dyes.[57] These dyads were imaged in giant unilamellar vesicle (GUV) membranes. The best resolutions are around 80 nm, with 2.7-fold resolution enhancements under RESOLFT compared to confocal.



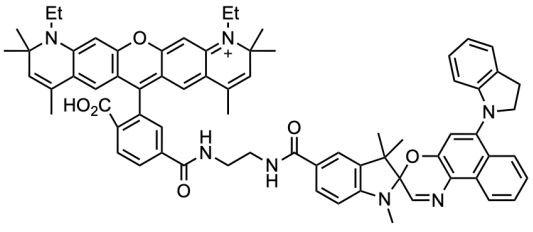
spiropyran-SiRhodamine



spironaphthoxazine-Atto565



spironaphthoxazine-Cy3.5



spironaphthoxazine-Atto590

Scheme 3.5 Photoswitchable fluorophores developed in our group.

3.1.4 Switchable Fluorescent Probes for Studying Cellular Dynamics

Photoswitchable fluorophores have not only improved the resolution in SRM but have also revolutionized the study of cellular dynamics using advanced fluorescence microscopy techniques. Traditionally, the dynamics of cellular processes, such as protein mobility, diffusion, and interactions, have been studied using various techniques, including fluorescence recovery after photobleaching (FRAP), inverse FRAP (iFRAP), fluorescence loss in photobleaching (FLIP), fluorescence lifetime imaging (FLIM), fluorescence correlation spectroscopy (FCS), and single-particle tracking.[58, 59]

In FRAP, a small region of interest (ROI) containing fluorescently labeled molecules is selectively photobleached, and the recovery of fluorescence intensity over time is monitored as unbleached molecules from the surrounding area diffuse into the bleached ROI.[60] Conventionally, FRAP experiments have relied on fluorescent proteins that undergo irreversible photobleaching, which requires high-power lasers to fully photobleach the fluorophores within the ROI, potentially causing phototoxicity in living cells. The emergence of photoswitchable fluorophores has introduced switchable fluorescence, which can be switched off with much lower laser power compared to photobleaching, thus minimizing phototoxicity. They can also be reversibly switched for multiple measurements within a single sample.

Patterson and co-workers reported an early example of using switchable fluorophores to study cell dynamics.[61] They developed new variants of GFP through site-directed mutagenesis, with the T203H GFP variant exhibiting outstanding photochemical and photophysical behavior. The weakly fluorescent native form of T203H GFP can be activated under 413 nm irradiation, resulting in a 100-fold increase in fluorescence. The activated GFP can be excited at 488 nm, leading to emission with a maximum at 520 nm. The authors demonstrated the utility of GFP photoactivation for measuring protein dynamics within living cells by selectively photoactivating a subpopulation of GFP molecules in expressing cells and observing their behavior over time. Rapid movement of the photoactivated molecules across the nuclear envelope and into the cytoplasm was observed, resulting in their equilibration throughout the cell within minutes.

3.1.5 Project Aim

Fluorescence has proven to be a powerful tool for investigating cellular processes, enabling researchers to visualize and track various biological events with high spatial and temporal

resolution. The development of advanced photoswitchable fluorophores has further expanded the capabilities of fluorescence-based techniques, allowing for more in-depth investigations of cellular processes using advanced imaging methods.

However, majority of these studies have been based on photoswitchable fluorescent proteins, which have inherent limitations. While fluorescent proteins offer genetic encodability and can be expressed in living cells, their photoswitching and fluorescent properties are determined by their amino acid sequence and are difficult to fine-tune. This lack of flexibility in optimizing the properties of photoswitchable fluorescent proteins has hindered their broader application in studying complex biological systems.

To overcome these limitations, this project aims to harness the power of small molecule photoswitches, specifically the best performing DTE photoswitch identified in the Chapter 2, to develop a novel photoswitchable fluorophore. The bistable nature of the DTE photoswitch will enable the fluorophore to be switched between two stable states, giving high contrast between the bright and the dark states.

3.2 Results and Discussion

3.2.1 Molecular Design of Photoswitchable Dyads

In Chapter 2, the DTE candidate with the most promising photoswitching parameters (**Ay-yA**) has been identified. Building on this foundation, this chapter describes the development of a fluorophore that exhibits photoswitchable fluorescence incorporated with this photoswitch. The proposed switchable dyad (Figure 3.6) comprises a fluorophore and a DTE photoswitch that can regulate the fluorescence emitted by the fluorophore. When the DTE is in its open form, the fluorophore emits light upon excitation, resulting in a fluorescent "on" state. However, when the DTE is switched to its closed form, the fluorescence is quenched through FRET, resulting in a non-fluorescent "off" state. The photoswitchable nature of the DTE allows for the reversible toggling of the fluorescence. By exposing the dyad to specific wavelengths (405 nm and 630 nm) the DTE can be switched between its open and closed forms. The excitation of the fluorophore is achieved using light of a different wavelength. This spectral separation allows for the independent control of the photoswitching and fluorescence excitation processes, ensuring minimal interference.

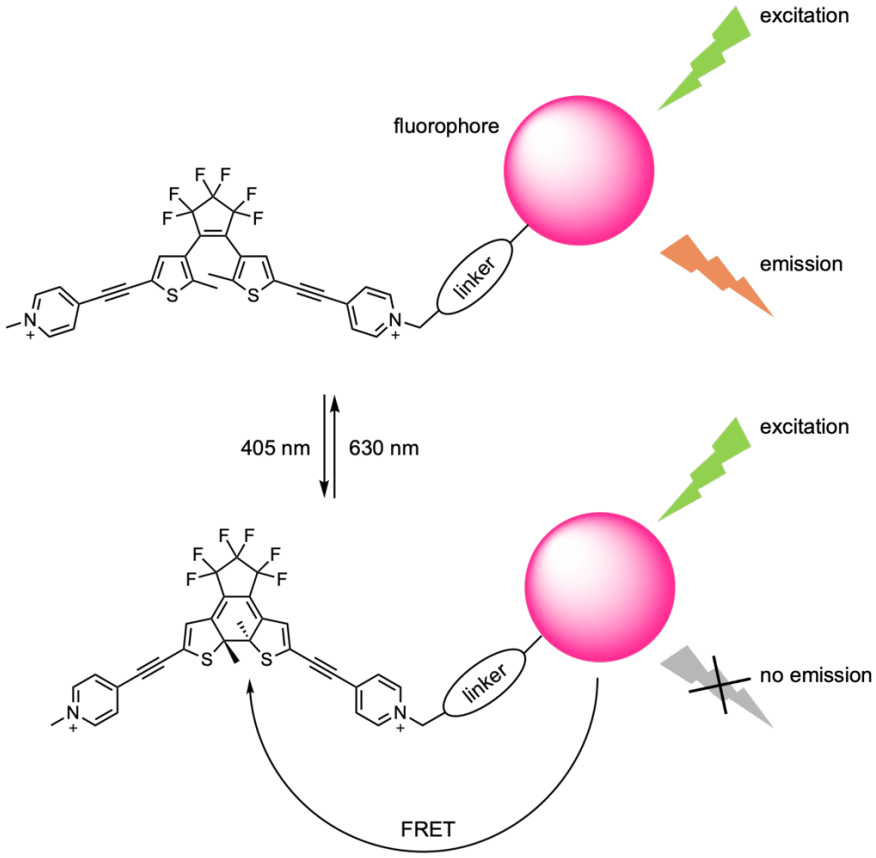


Figure 3.6 Molecular design of the photoswitchable dyad. The fluorophore emits light upon excitation when the DTE is in the open form while the fluorescence is quenched by FRET when the DTE is in the closed form.

3.2.2 Selection of the Fluorescent Dye

For efficient modulation of fluorescence in a photoswitchable dyad, the chosen fluorophore should meet three key spectroscopic requirements to ensure efficient FRET quenching of the fluorophore while minimizing the compromise on the DTE's performance.

1. Spectral overlap between the donor and acceptor: The fluorescence spectrum of the fluorophore should significantly overlap with the absorption spectrum of the closed DTE. This overlap is necessary for efficient FRET to occur, allowing the closed the DTE to effectively quench the fluorescence of the fluorophore, resulting in a substantial difference in fluorescence intensity between the "on" and "off" states of the photoswitchable fluorophore.
2. Wavelength of fluorophore excitation: The fluorophore should be excited at a wavelength where the closed DTE has a low molar absorption coefficient. This requirement is crucial to avoid the simultaneous photoreversion of the DTE during the excitation of the fluorophore. However, this criterion may be relaxed if the

photoreversion quantum yield of the photoswitch is low and the fluorophore can be excited using a low-power light source.

3. Wavelengths for DTE control: The fluorophore should have minimal absorption at the wavelength used for triggering the photocyclization of the DTE (405 nm). If the fluorophore absorbs significantly at this wavelength, FRET from the fluorophore to the DTE will trigger the photoreversion of DTE, potentially resulting in a pseudo-PSS with lower PSD due to this additional pathway.

While the first two criteria are essential for a good switchable dyad, the third criterion might be easily overlooked. However, previous research from our group has highlighted the importance of this criterion.[62] We prepared a diazocine-rhodamine dyad (Figure 3.7) that exhibited only 10% fluorescence quenching upon diazocine photoswitching, even though the diazocine moiety on its own could achieve a 72% PSD under 405 nm irradiation. Further investigation revealed that the photoswitch quickly returned to its stable *cis* form due to energy transfer from the fluorophore. The issue arises because the rhodamine dye also absorbs light at 405 nm. Irradiation at 405 nm excites both the photoswitch and the dye, leading to energy transfer from the excited dye to the photoswitch. This energy transfer results in diazocine's isomerization back to the *cis* isomer. Consequently, the PSD of the dyad under constant irradiation differs from that observed for the isolated photoswitch.

Several experimental observations support this conclusion. When the dyad emission was remeasured immediately after recording it in the quenched form, it returned to the original experimental maximum, indicating that the process of measuring the emission spectrum was altering the sample and that exciting the dye caused the sample composition to change. A control experiment was also conducted where a diazocine sample at its 405 nm PSD was subjected to the fluorometer conditions used to acquire the dyad's emission spectra. In the absence of the dye, the photoswitch did not relax back to the *cis* form under these conditions, implying that the dye absorption was responsible for the reversion of the photoswitch.

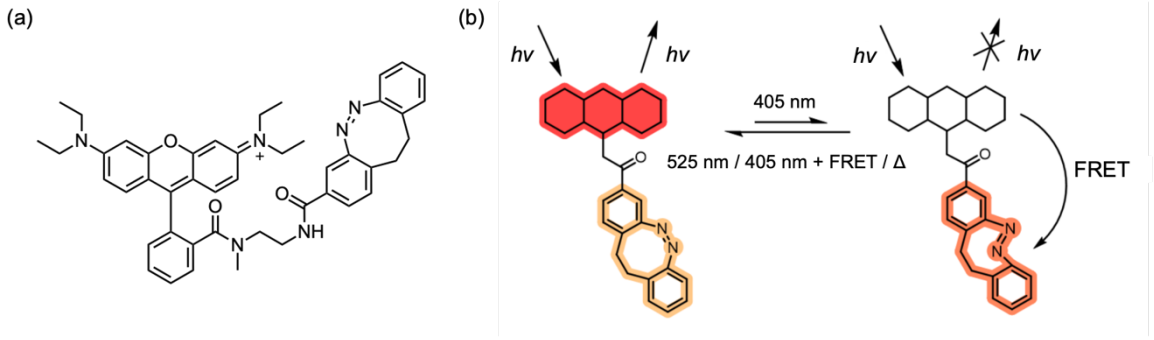


Figure 3.7 (a) The diazocine-rhodamine dyad. (b) Proposed underlying mechanism resulting in poor fluorescence quenching.

The three criteria discussed above are summarized in Figure 3.8, which highlights the optimal excitation and fluorescence spectral ranges for the fluorophore. To achieve the best performance in a DTE-fluorophore dyad system, the ideal fluorophore should have the ability to be excited between 450 and 530 nm and have an emission maximum between 560 and 720 nm. Meeting these spectral requirements is essential for efficient FRET quenching and minimizing any interference with the DTE's photoswitching process.

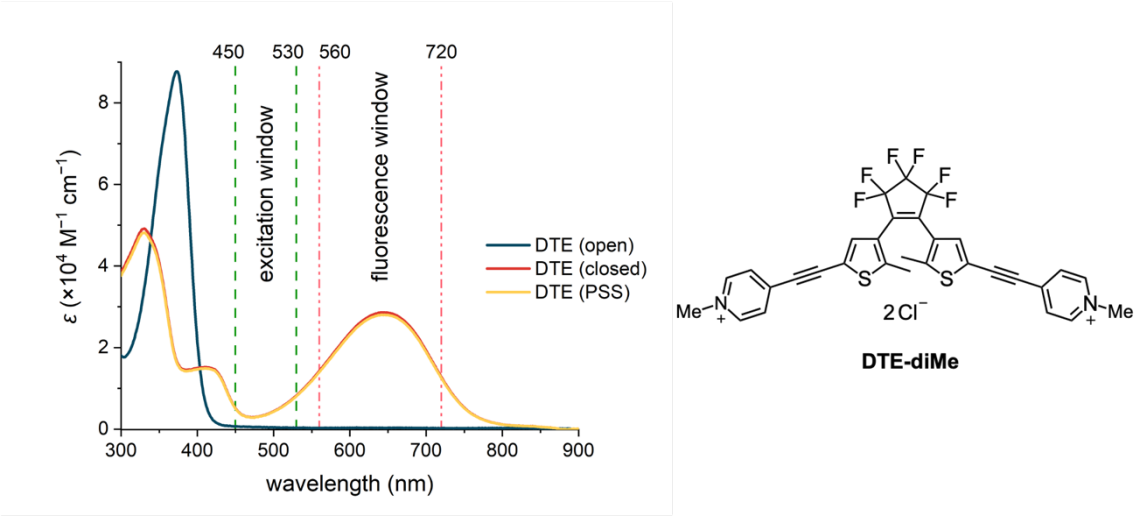


Figure 3.8 Schematic fluorophore selection criteria for the DTE-fluorophore system, plotted with the UV-vis absorption of **DTE-diMe**, which is equivalent to **Ay-yA** in Chapter 2.

In order to identify fluorophores that fulfill these criteria, an extensive survey was performed, covering both published literature and products from leading chemical suppliers (including AAT Bioquest, ATTO-TEC, Lumiprobe, Merck, Thermo Fisher Scientific, and Vector Laboratories). The photophysical parameters (including absorption maxima, emission maxima, and fluorescence quantum yields) of the main fluorophore families were collated and are presented in the Table 3.1.

Table 3.1 Notable fluorescent dyes and their photophysical parameters.

Dye	Excitation Maximum (nm)	Emission Maximum (nm)	Fluorescent Quantum Yield (%)	Solvent
Atto-532[a,*]	532	552	90	water
Atto-550[a,*]	554	576	80	water
BODIPY-FL[b]	502	511	90	methanol
Cy2[b]	492	508	12	PBS
Cy3[b]	555	569	15	PBS
Cy3B[b]	560	571	58	PBS
Cy3.5[c]	580	610	35	ethanol
Cy5[c]	646	662	20	ethanol
Cy5.5[c]	684	710	20	ethanol
Cy7[c]	750	773	30	ethanol
Rhodamine 110[d,e]	498	520	92	ethanol
Rhodamine 6G[b]	525	548	95	water
Rhodamine B[d,e]	553	627	65	ethanol
Rhodamine-X[b]	578	604	94	buffer (pH 7.2)
Rhodamine-Si[f]	648	663	34	PBS
Fluorescein	498	517	79	ethanol

[*] Structurally related to rhodamine 6G. [a] Data from ATTO-TEC. [b] Data from AAT Bioquest. [c] Data from Lumiprobe. [d] Data from Merck. [e] Reported by Kubin and co-workers.[63] [f] Reported by Rao and co-workers.[64]

Based on the survey, fluorophores derived from cyanine 3 (Cy3 and Cy3B) were selected (Figure 3.9) for further modeling validation. Cy3B is a rigidified version of Cy3 with highly similar absorption and fluorescence properties but significantly higher fluorescence quantum yield. Cy3 dyes typically exhibit an emission maximum around 570 nm, which overlaps well with the absorption spectrum of the closed form of the DTE, ensuring efficient FRET quenching (Figure 3.9). Although Cy3s typically have an absorption maximum around 560 nm, they can be effectively excited using light ranging from 450 nm to 600 nm. Importantly, in the field of microscopy, Cy3 dyes are commonly excited with 488 nm laser line to produce images of live biological samples while DTE has minimal absorption at this wavelength. Another key advantage of cyanine dyes, compared to other major classes of dyes such as rhodamines and BODIPYs, is their very weak absorption at 405 nm, the wavelength used for DTE photoswitching. In contrast, rhodamines and BODIPYs can absorb reasonably strongly at 405 nm, potentially having a negative impact on the PSD of the photoswitch due to fluorophore excitation followed by FRET to the photoswitch.

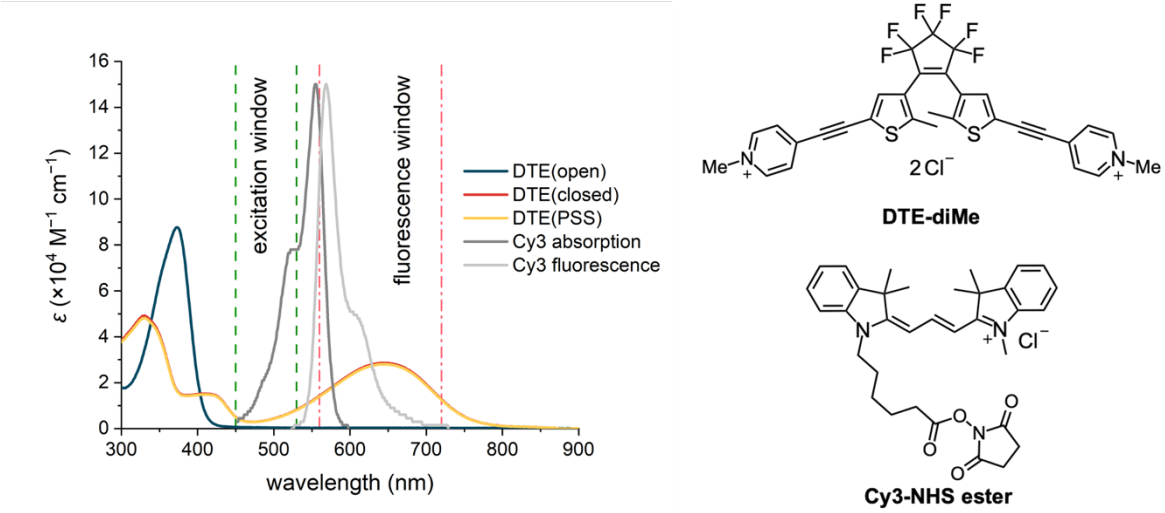


Figure 3.9 The UV-vis absorption of open and closed **DTE-diMe** and the absorption and fluorescence of an example Cy3 dye.

3.2.3 Modelling of FRET Quenching

Before synthesizing and testing the dyad system, the FRET-based fluorescent quenching was modelled. FRET is the process by which the energy of an excited state donor fluorophore is non-radiatively transferred to an acceptor molecule. The requirements for FRET quenching to occur include physical proximity, the alignment of the donor and acceptor transition dipole moments, and spectral overlap between the FRET donor emission and the FRET acceptor absorption. The FRET efficiency (E) is defined as the quantum yield of the FRET process and can be calculated for a given donor and acceptor pair using Equation 3.3.

$$E = \frac{k_{\mathrm{ET}}}{k_{\mathrm{FL}} + k_{\mathrm{ET}} + \sum k_{\mathrm{i}}} \tag{3.3}$$

where k_{ET} is the rate of energy transfer from the donor to the acceptor, k_{FL} is the radiative decay rate of the donor, and k_{i} is the rate of any other non-radiative relaxation pathways excluding the energy transfer. FRET efficiency depends on the donor-to-acceptor separation distance (r) with an inverse 6$^{\mathrm{th}}$-power relationship shown in Equation 3.4.

$$E = \frac{1}{1 + \left(\frac{r}{R_0}\right)^6} \tag{3.4}$$

The Förster radius R_0 term is the distance at which FRET is 50% efficient and can be approximated with Equation 3.5:

$$R_0 = 0.2108 \left[\frac{\kappa^2 \cdot \Phi_D \cdot J(\lambda)}{n^4} \right]^{\frac{1}{6}} \quad (3.5)$$

where Φ_D is the fluorescence quantum yield of the donor, and n is the refractive index of the solvent. The term κ^2 is the dipole orientation factor, which describes the relative orientation of the transition dipoles of the donor and acceptor. The value can range from 0 to 4, (0 for perpendicular, 1 for parallel, 4 for antiparallel) but is assumed to be an average of 0.667 given free rotation between the donor and acceptor. The term $J(\lambda)$ is the spectral overlap integral, which is given by Equation 3.6:

$$J(\lambda) = \int f_D(\lambda) \cdot \varepsilon_A(\lambda) \cdot \lambda^4 \cdot d\lambda \quad (3.6)$$

where f_D is the normalised donor emission spectrum, ε_A is the acceptor molar absorption coefficient at wavelength λ.

Table 3.2 summarizes the parameters used to calculate the Förster radius and the corresponding results, assuming a dipole orientation factor of 0.667. The spectral overlap integral is calculated using the absorption spectrum of closed **DTE-diMe** (**Ay-yA** from Chapter 2) and the emission spectra of Cy3 and Cy3B provided by AAT Bioquest. The DTE-Cy3B system exhibits a larger Förster radius compared to the DTE-Cy3 system. This difference can be attributed to two factors: first (major), Cy3B has a significantly higher fluorescent quantum yield than Cy3, and second (minor), the fluorescence of Cy3B is red shifted by approximately 2 nm relative to Cy3 (according to the supplier's data), resulting in slightly better spectral overlap with the DTE acceptor. When compared to previous studies conducted in our group, the calculated Förster radii for DTE-Cy3 and DTE-Cy3B dyads are higher than those reported for diazocine-rhodamine dyads.[62] However, they are slightly lower than the Förster radius of 66.4 Å reported for spironaphthoxazine-Atto565 dyads.[65]

Table 3.2 FRET quenching model parameters for DTE-Cy3 and DTE-Cy3B systems.

System	$J(\lambda)$ (mol^{-1} dm^3 cm^{-1} nm^4)	Φ_D (%)	n	R_0 (Å)
DTE-Cy3	1.81×10^{15}*	15	1.33	41.4
DTE-Cy3B	1.85×10^{15}*	58		53.1

* The spectral overlap integral is calculated using the closed **DTE-diMe** absorption spectrum measured in the previous chapter, and Cy3 and Cy3B emission spectra supplied by AAT Bioquest.

To estimate the distance between the DTE and the fluorophore molecular models **M1** and **M2** (corresponding to DTE-Cy3 and DTE-Cy3B dyads, respectively) were constructed using a twelve-carbon linker (Figure 3.10). Although the exact nature of the linker chemistry is not considered at this modeling stage, a twelve-carbon linker is likely to be longer than the linker used in the actual synthesis. The molecular models were optimized using the MM2 force field to achieve a fully extended conformation. The distance between the center of the DTE hexatriene and the middle of the cyanine was measured as an estimate of the donor-acceptor distance.

The **M1** and **M2** dyads have estimated donor-acceptor distances of 25.2 Å and 27.3 Å, respectively. This difference in distance mainly arises from the different connection sites on the cyanine dyes. Cy3 dyes are typically connected to other motifs through the indolenine nitrogen atom, whereas Cy3B dyes are connected through a linker on the aromatic ring of the indolenine. These structural differences lead to the slight variation in the donor-acceptor distance between the two dyads.

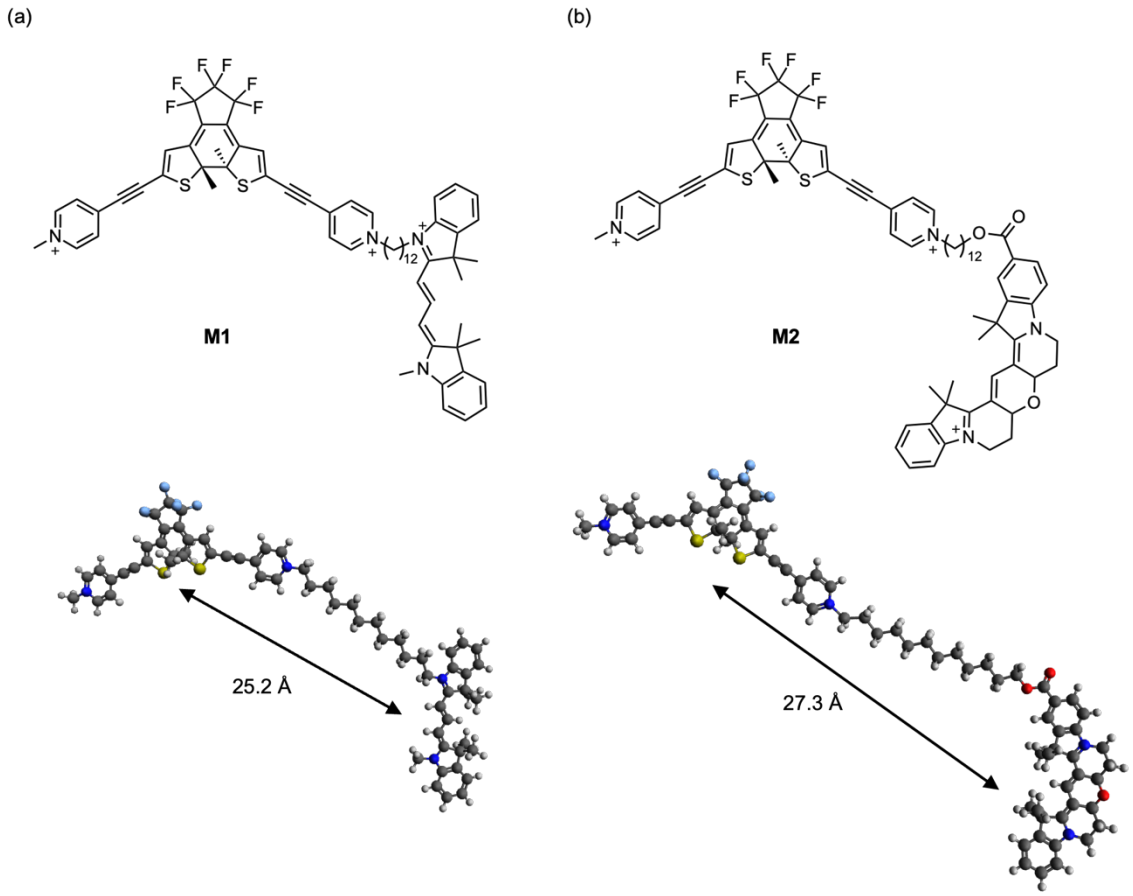


Figure 3.10 Model compounds **M1** and **M2** for estimating the FRET donor-acceptor distance.

The FRET efficiencies for the models **M1** and **M2** were calculated using the donor-acceptor distances estimated from the molecular models **M1** and **M2**, respectively. The results, presented in Table 3.3, show that model **M1** has a FRET efficiency of 95.2%, while model **M2** has a FRET efficiency of 98.1%. It is important to note that these molecular models were constructed assuming that the molecules adopt fully extended conformations. In reality, the synthesized molecules are expected to have higher FRET efficiencies when the linkers randomly fold up in solution due to their flexibility, bringing the donor and acceptor closer together.

Table 3.3 Calculated FRET efficiency of models **M1** and **M2**.

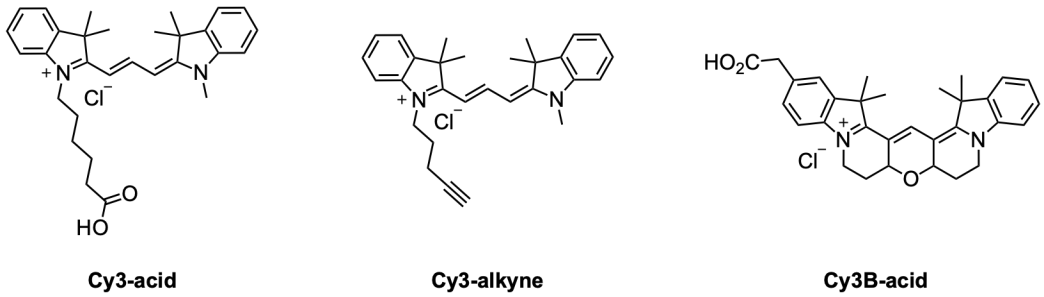
Model	R_0 (Å)	Maximum D-A Distance (Å)	FRET Efficiency (lower limit)
M1	41.4	25.2	95.2%
M2	53.1	27.3	98.1%

The FRET quenching model demonstrates that the closed DTE photoswitch will effectively quench the cyanine fluorescence in the dyad. In contrast, when the DTE is in the

open form, it will not quench the fluorescence, as there is no spectral overlap between the open DTE and the cyanine dyes.

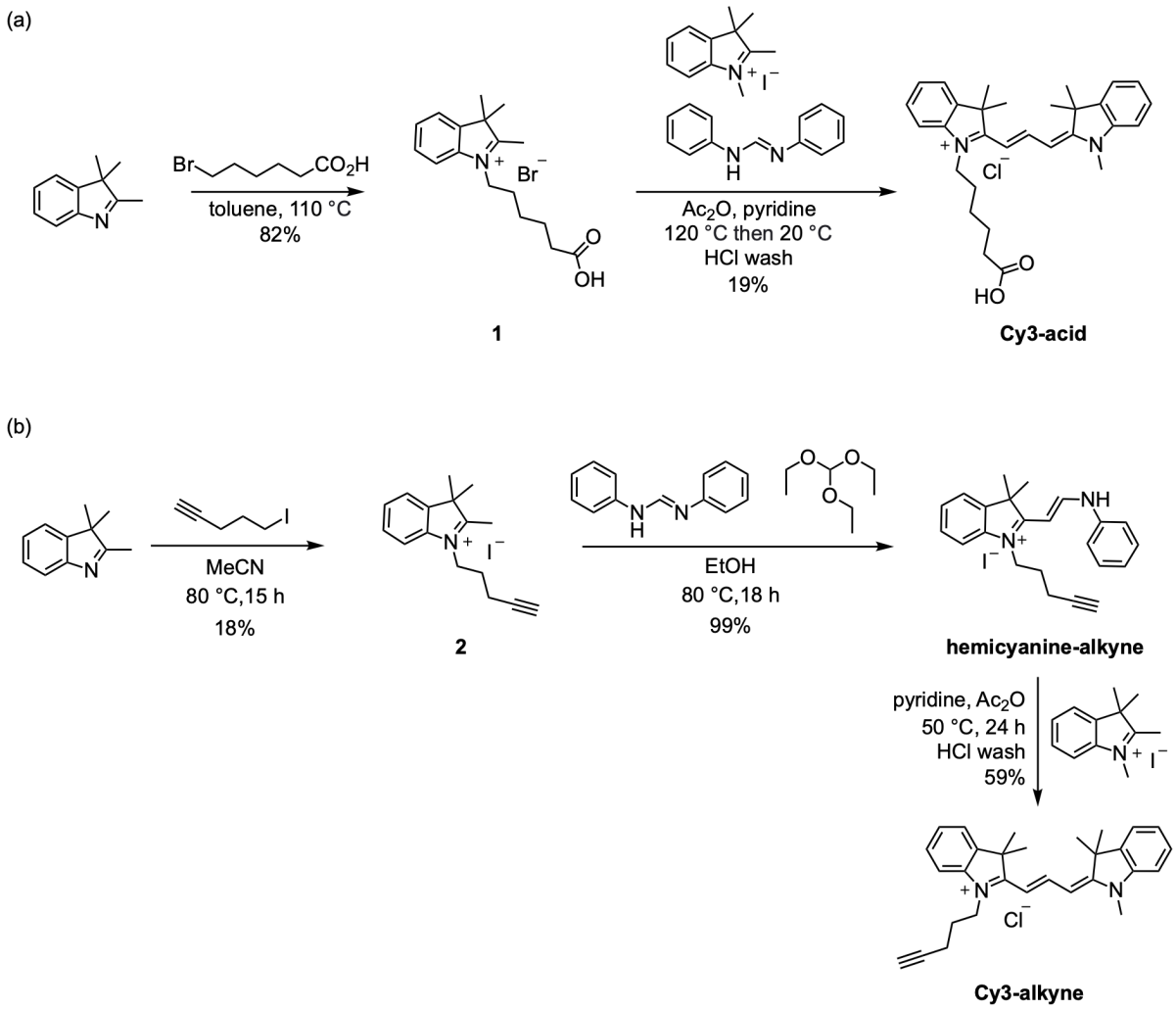
3.2.4 Synthesis of Cy3 and Cy3B Dyes

Cyanine dyes with specific functional groups required for constructing the desired dyads are often not commercially available or are prohibitively expensive. To overcome this challenge, I synthesized two analogues of Cy3 (**Cy3-acid** and **Cy3-alkyne**) and one analogue of Cy3B (**Cy3B-acid**) (Scheme 3.6). **Cy3-acid** and **Cy3B-acid** possess a carboxylic acid functional group, which can facilitate dyad formation through various coupling strategies, such as amide coupling. On the other hand, the **Cy3-alkyne** features an alkyne functional group, which can potentially enable the formation of dyads through a click reaction.



Scheme 3.6 Derivatives of Cy3 dyes (as chloride salts) being prepared in our laboratory.

The synthesis of **Cy3-acid** was carried out following the route developed by Miao and co-workers, with a modification in the reaction condition of the second step of the reaction as well as the purification method (Scheme 3.7a).[66] In this approach, the hemicyanine intermediate is generated in-situ, followed by the formation of the cyanine dye. On the other hand, **Cy3-alkyne** was synthesized using the route developed by Gerowska and coworkers (Scheme 3.7b).[67] However, instead of forming the cyanine in a one-pot reaction, a stepwise approach was employed. In this modified route, the hemicyanine intermediate **hemicyanine-alkyne** is first formed and isolated, followed by the subsequent formation of the cyanine dye. This stepwise cyanine synthesis has been found to provide better overall yields compared to the one-pot approach, as it reduces the formation of the undesired homocoupled product.



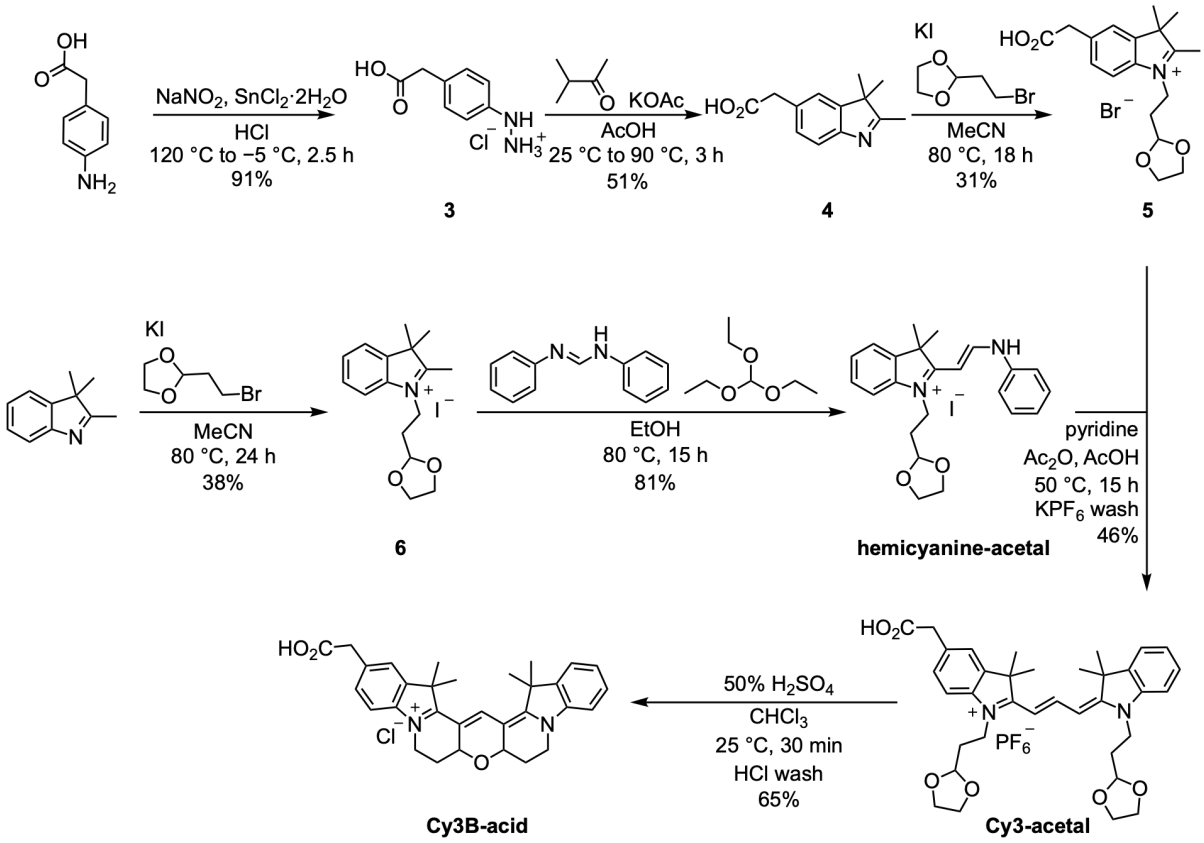
Scheme 3.7 Synthesis of (a) **Cy3-acid** and (b) **Cy3-alkyne**.

The synthesis of **Cy3B-acid** was carried out following the general Cy3B synthetic route developed by Hall and co-workers (Scheme 3.8),[68] with a modification to incorporate a carboxylic acid functionality on the indolenine aromatic ring. The synthesis of **Cy3B-acid** is more complex compared to the Cy3 derivatives, primarily because the required starting indolenines are not commercially available and need to be prepared beforehand.

The synthesis begins with the preparation of indolenines **5** and **6**. Indolenine **5**, functionalized with a carboxylic acid group, was prepared starting from 2-(4-aminophenyl) acetic acid. This starting material was converted into hydrazine **3** using sodium nitrite and tin(II) chloride dihydrate.[69] Subsequently, indole **4**, bearing a carboxylic acid group, was synthesized through a Fischer indole synthesis.[70] Indolenines **5** and **6** were then obtained by alkylating the indole nitrogen with 2-(2-bromoethyl)-1,3-dioxolane.

Since the stepwise cyanine synthesis provided higher overall yields compared to the one-pot approach in the previous Cy3 synthesis, a similar stepwise strategy was adopted for the

synthesis of **Cy3B-acid**. First, the hemicyanine intermediate **hemicyanine-acetal** was prepared and isolated. Then, **hemicyanine-acetal** was condensed with the other indolenine to form **Cy3-acetal**, which further underwent cyclization under acidic conditions to yield the desired **Cy3B-acid**. This synthetic route allowed us to easily prepare **Cy3B-acid** on a half gram to gram scale.



Scheme 3.8 Synthesis of **Cy3B-acid**.

3.2.5 Characterization of Cy3 and Cy3B Photophysics

The absorption and fluorescence spectra were of **Cy3-acid**, **Cy3-alkyne**, and **Cy3B-acid** were acquired in deionized water (Figure 3.11), and the results are summarized in Table 3.4. **Cy3-acid** and **Cy3-alkyne** exhibit identical absorption and fluorescence maxima, and their spectra are highly alike, since they share the same photoactive cyanine structure. The only difference between these two molecules lies in their linker functional groups, which do not significantly influence their photophysical properties. In contrast, the absorption and emission spectra of **Cy3B-acid** are red-shifted by 12 nm compared to the Cy3 derivatives. This bathochromic shift can be attributed to the more rigid structure of Cy3B. Furthermore, **Cy3B-acid** exhibits a smaller Stokes shift of 12 nm compared to the 15 nm Stokes shift observed

for the Cy3 analogues. The molar absorption coefficients of the cyanine dyes were measured using the same NMR reference method as described in Chapter 2 (Section 2.4.3).

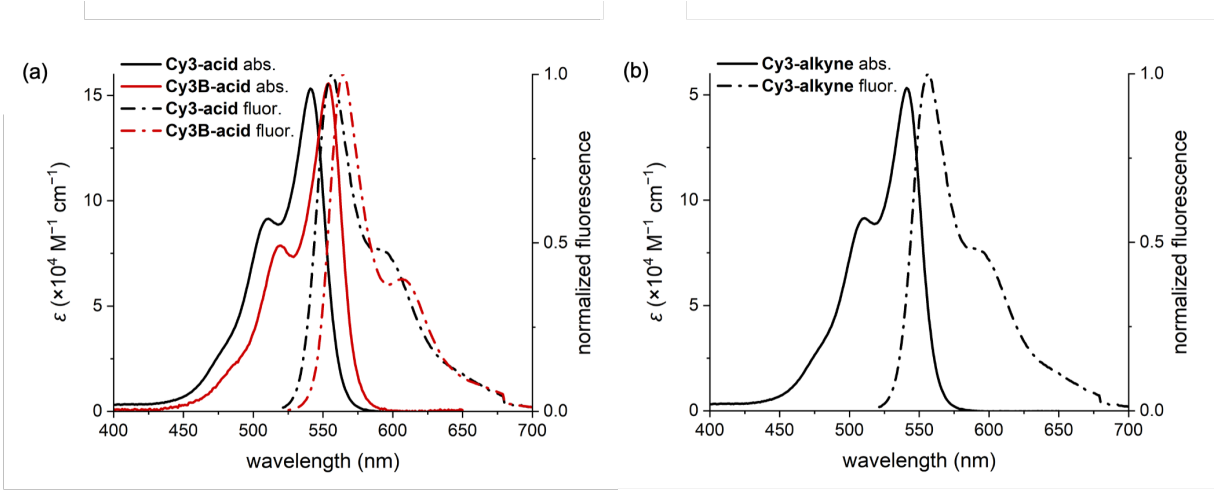


Figure 3.11 Absorption and fluorescence spectra of (a) **Cy3-acid** and **Cy3B-acid**, and (b) **Cy3-alkyne** measured in water.

Table 3.4 The absorption and fluorescence parameters of the synthesized Cy3 dyes.

	absorption				fluorescence	
Molecule	λ_{max}^{m} (nm)	ε (M^{-1} cm^{-1})	λ_{max}^{s} (nm)	ε (M^{-1} cm^{-1})	λ_{max}^{m} (nm)	λ_{max}^{s} (nm)
Cy3-acid	541	153000	510	91400	556	595
Cy3-alkyne	541	154000	510	91200	556	595
Cy3B-acid	553	156000	520	78600	564	607

The letter m and s in the λ_{max} section indicates the main band and the shoulder band, respectively.

The fluorescence quantum yields of the synthesized Cy3 dyes were measured using a combination of absolute and relative methods. First, the fluorescence quantum yield of **Cy3B-acid** was determined in water using an absolute method with an integrating sphere, resulting in a value of 63%. This value served as a reference for the subsequent determination of the fluorescence quantum yields of **Cy3-acid**, **Cy3-alkyne**, and **Cy3B-acid** in three different solvents: water, methanol, and glycerol.

The relative method was employed for measuring the fluorescence quantum yields of **Cy3-acid** and **Cy3-alkyne** because their values in water and methanol were too low (less than 5%) to be accurately determined using the absolute method. By referencing all other fluorescence quantum yields of these dyes to that of **Cy3B-acid** in water, reliable results could be obtained because all three Cy3 dyes have similar fluorescence spectra in the same wavelength range, ensuring the validity of the relative measurements. The fluorescence quantum yields of the three dyes in different solvents are presented in Table 3.5.

Table 3.5 Fluorescence quantum yields of the synthesized Cy3s measured in water, methanol and glycerol.

Solvent	**Cy3-acid**	**Cy3-alkyne**	**Cy3B-acid**
water	2.8%	2.9%	63%*
methanol	3.7%	3.9%	68%
glycerol	29%	27%	57%

* Value measured by absolute fluorescence method with an integrating sphere and all other fluorescence quantum yields are referenced to this value.

The measured data reveal a striking difference in the fluorescence quantum yields of **Cy3-acid**, **Cy3-alkyne**, and **Cy3B-acid** in various solvents. In pure water, **Cy3-acid** and **Cy3-alkyne** exhibit very low fluorescence quantum yields of 2.8% and 2.9%, respectively. In contrast, **Cy3B-acid** displays a significantly higher fluorescence quantum yield of 63%. A similar trend is observed in methanol.

A significant discrepancy was found between the fluorescence quantum yields measured by us and the values reported by various chemical suppliers, including Lumiprobe, AAT Bioquest, and Merck. While most chemical suppliers reported the fluorescence quantum yield of **Cy3-acid** to be in the range of 15%–30% in water and PBS solutions, our results indicate that the fluorescence of this molecule is considerably lower. Our results align more closely with a previous study by Sanborn,[71] which reported a fluorescent quantum yield of 7% for a sulfonated Cy3 derivative.

One possible explanation for the low fluorescence quantum yields of **Cy3-acid** and **Cy3-alkyne** is that these conventional Cy3 dyes can undergo *trans–cis* isomerization along their polymethine backbone, providing a relaxation pathway that competes with fluorescence.[72, 73] However, this photoisomerization pathway is not accessible for **Cy3B-acid** due to its rigidized structure, which prohibits *trans–cis* isomerization. This hypothesis is supported by the quantum yields measurements in glycerol, a highly viscous solvent known to reduce the rate of photoinduced molecular motion.[74] The fluorescence quantum yields of **Cy3-acid** and **Cy3-alkyne** were found to be almost ten times higher in glycerol compared to water and methanol, supporting the hypothesis that the restriction of molecular motion can enhance the fluorescence quantum yields of these dyes.

The fluorescence lifetimes of **Cy3-acid** and **Cy3B-acid** were also measured in water and glycerol using time-correlated single photon counting (TCSPC) technique and the results are summarized in Table 3.6.

Table 3.6 Fluorescence lifetime of **Cy3-acid** and **Cy3B-acid** in water and glycerol.

	Fluorescent Lifetime (ns)	
Solvent	**Cy3-acid**	**Cy3B-acid**
water	<0.2*	2.75
glycerol	1.91	2.47

* The lifetime was very short, and the data could not be fitted with an exponential tail fit.

The data reveal that **Cy3B-acid** exhibits longer fluorescence lifetimes compared to **Cy3-acid** in both water and glycerol. Notably, the fluorescence lifetime of **Cy3-acid** in water was too short to be reliably fitted, indicating a rapid decay of the excited state. However, in glycerol, the fluorescence lifetime of **Cy3-acid** was significantly prolonged. These findings provide additional support for the hypothesis that viscous solvents, such as glycerol, can slow down photoinduced molecular motion, thereby increasing the fluorescence lifetime and fluorescence quantum yield of **Cy3-acid**. The longer fluorescence lifetime observed in glycerol suggests that the excited state of **Cy3-acid** is stabilized, allowing for more efficient radiative decay and a higher fluorescence quantum yield.

The characterization of the fluorescence properties of the synthesized cyanine dyes (**Cy3-acid**, **Cy3-alkyne**, and **Cy3B-acid**) confirms that all three molecules are suitable for use as fluorophores in conjunction with the DTE photoswitch to create photoswitchable dyads. However, among the three candidates, **Cy3B-acid** stands out as the most promising option due to its high fluorescence quantum yield. This suggests that a dyad incorporating **Cy3B-acid** would exhibit a significantly brighter "on" state compared to the Cy3 analogue.

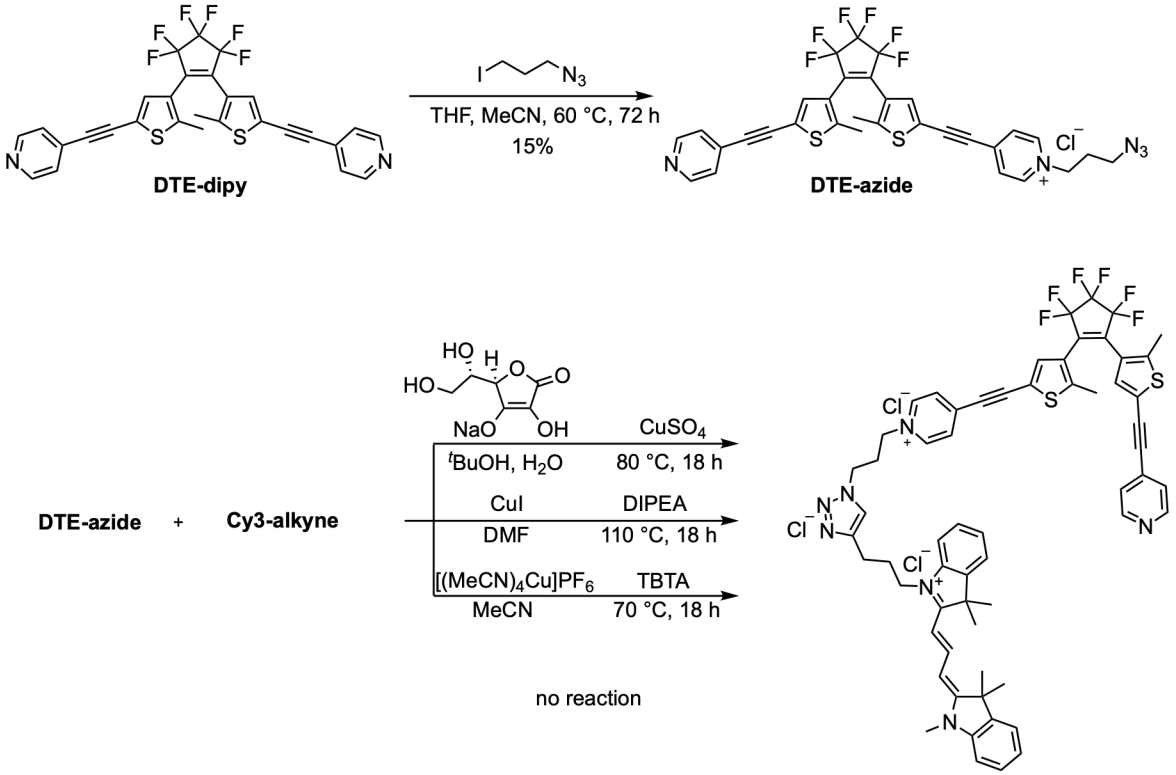
Despite the advantageous photophysical properties of **Cy3B-acid**, it is important to consider the synthetic complexity of the cyanine dyes when selecting a fluorophore for the photoswitchable dyad. The synthesis of Cy3 derivatives (**Cy3-acid** and **Cy3-alkyne**) is generally simpler compared to the more elaborate synthetic route required for **Cy3B-acid**. Therefore, Cy3 dyes may serve as a more accessible model system for initial studies and proof-of-concept experiments.

3.2.6 Synthesis of Photoswitchable Fluorophores

Two distinct photoswitchable dyads, **DTE-Cy3** and **DTE-Cy3B**, were synthesized by linking a DTE photoswitch with either a Cy3 dye or a Cy3B dye, respectively, using different linker chemistries.

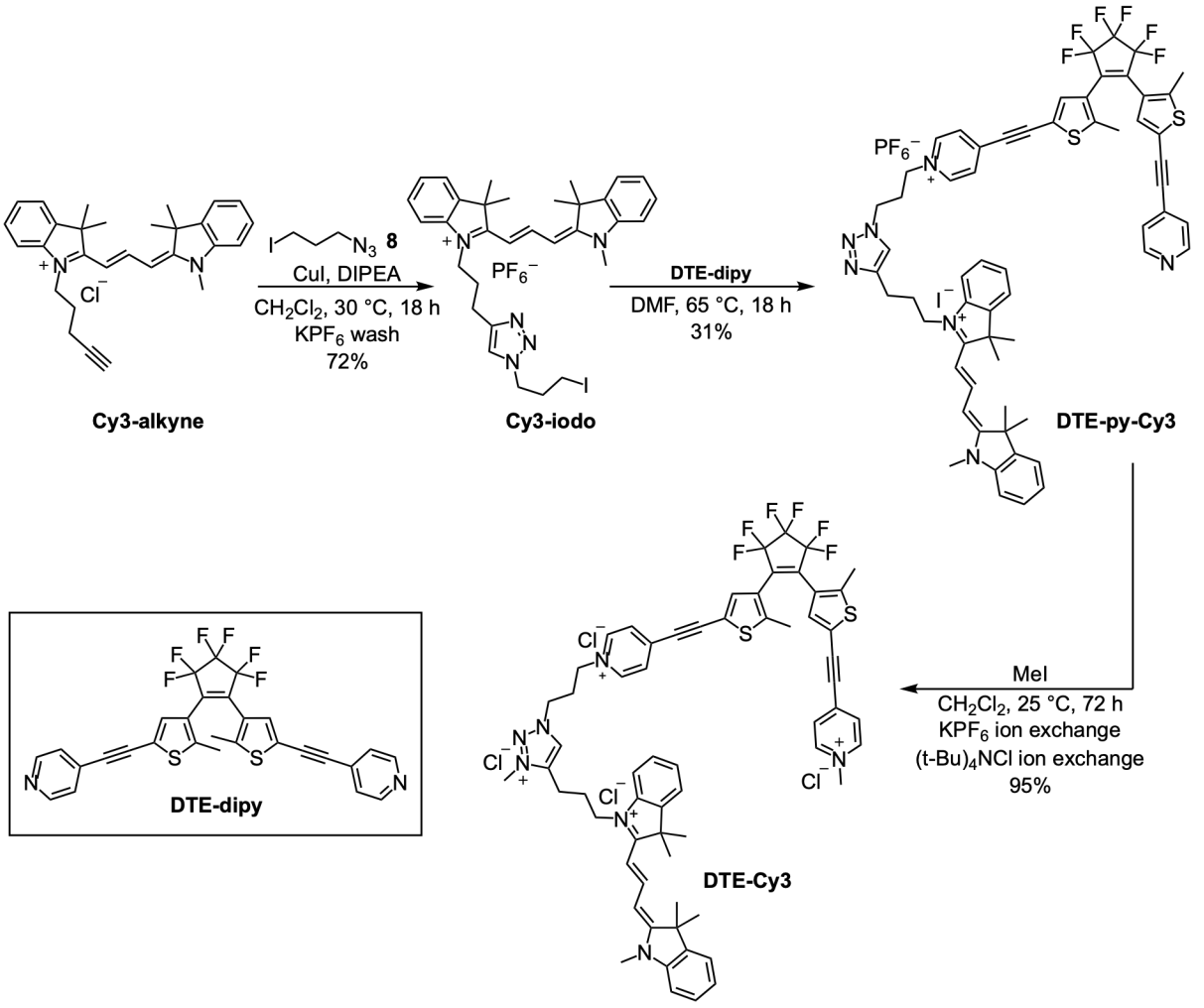
I initially designed a route to prepare **DTE-Cy3** dyad utilizing CuAAc (click) chemistry but later proved to be unsuccessful (Scheme 3.9). The failed route involved synthesizing **DTE-azide** by substituting one pyridine group of the **DTE-dipy** through S_N2 chemistry. Subsequently, the click reaction between **DTE-azide** and **Cy3-alkyne** was attempted using a variety of copper catalysts, including the most active copper catalyst with TBTA ligand, but the reaction did not proceed. Even under microwave conditions, the click reaction was unsuccessful.

Although the exact reason for the lack of reactivity is unknown, electrostatic repulsion between the two charged species may disfavor the coordinated state, as the two charged moieties would be forced to stay in close proximity to each other.



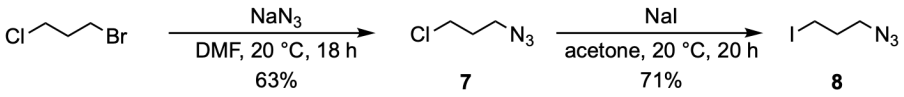
Scheme 3.9 Unsuccessful attempts to prepare the dyad through CuAAc reaction.

To surpass the lack of reactivity in the click coupling between the **DTE-azide** and **Cy3-alkyne**, **Cy3-alkyne** was first converted into **Cy3-iodo**, which bears a terminal iodide, through a CuAAc reaction (Scheme 3.10). Subsequently, the DTE and Cy3 components were linked together via an S_N2 reaction, where the terminal pyridine of the **DTE-dipy** attacks the alkyl iodide of **Cy3-iodo**. Finally, the remaining free pyridine of the DTE was methylated using iodomethane. During this process, the triazole nitrogen also undergoes methylation, resulting in a tetracationic dyad. In this approach, the alkyne group functional group on the **Cy3-alkyne** serves as a masked iodide, enabling the efficient S_N2 coupling of the DTE and Cy3 moieties.



Scheme 3.10 Synthesis of **DTE-Cy3**.

The linker **8** is prepared following the route reported by Yao and co-workers (Scheme 4.11),[75] starting with the selective azidation of 1-bromo-3-chloropropane using sodium azide. The chloride is further replaced with iodide to form the linker **8**.

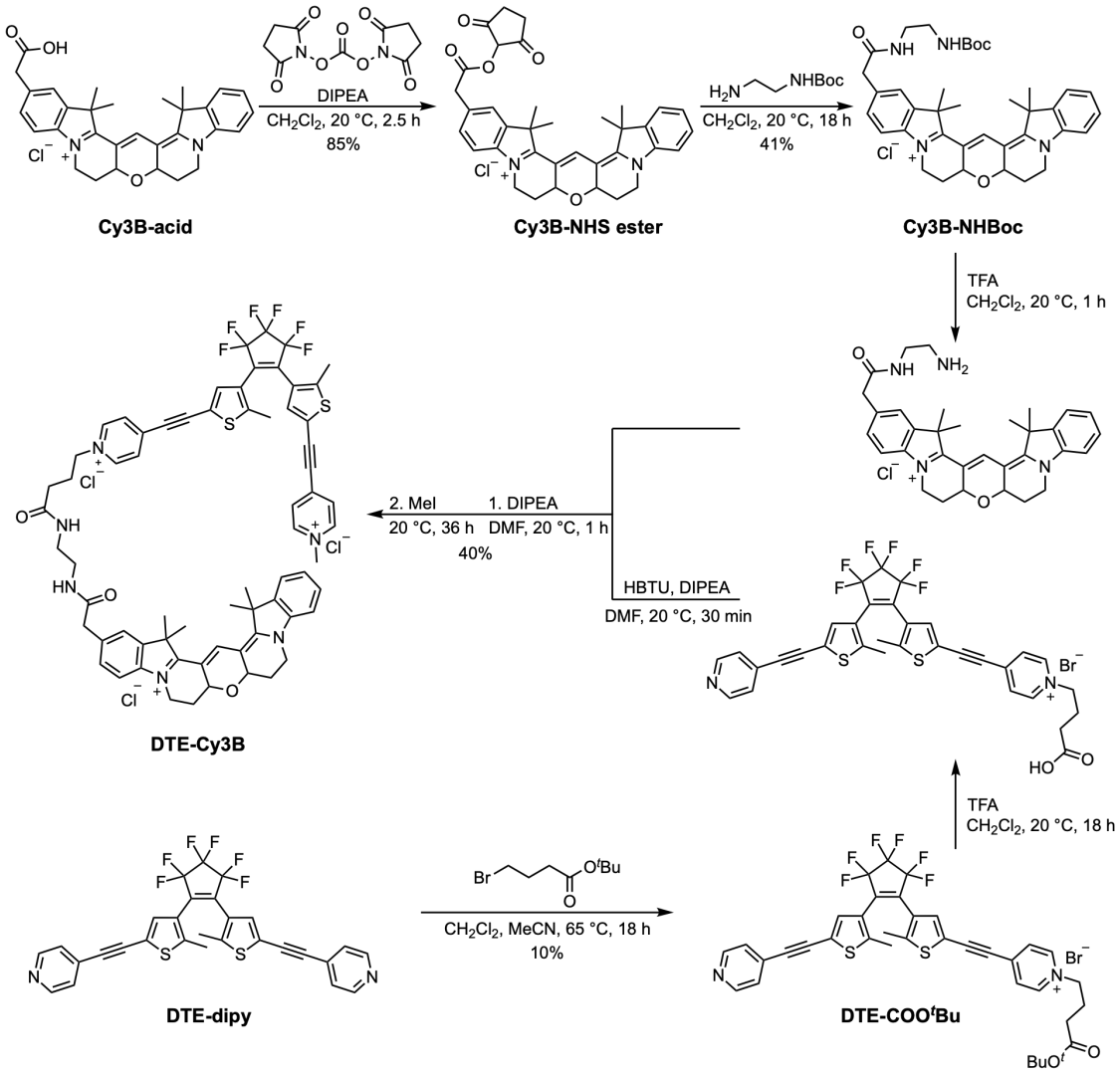


Scheme 4.11 Preparation of linker **8**.

DTE-Cy3B was synthesized using amide coupling reactions with an ethylenediamine linker in contrast to the CuAAc route (Scheme 3.12). The synthesis began by converting **Cy3B-acid** to **Cy3B-NHS ester**, which can easily react with nucleophiles. The ethylenediamine linker, with one end protected by a Boc group, was reacted with the NHS ester to form **Cy3B-NHBoc**. In parallel, the **DTE-dipy** was modified with an alkyl linker bearing a protected carboxylic acid, yielding **DTE-COO^{t}Bu**. Both the *t*-butyl ester protecting group on the DTE and the Boc protecting group on the cyanine were removed using trifluoroacetic acid separately. The deprotected DTE was then activated with HBTU and coupled to the deprotected cyanine,

which featured a free amine group. Without any purification, the coupled product was finally methylated with iodomethane to form **DTE-Cy3B**.

The main challenge encountered in the amide coupling route is the instability of the positively charged DTE moiety after alkylation in the presence of base or nucleophile. In a control experiment, it was discovered that **DTE-COO^{t}Bu** and the deprotected analogue decompose overnight in the amide coupling condition containing 5 equivalents of DIPEA. Therefore, the amide coupling step needs to be closely monitored with HPLC and DIPEA needs to be quenched with excess iodomethane (which also methylates the pyridine of the DTE) once the amide coupling is complete.



Scheme 3.12 Synthesis of **DTE-Cy3B** trough amide coupling with an ethylenediamine linker.

3.2.7 Photoswitching of DTE-Cy3 and DTE-Cy3B

The photoswitching behavior of these dyads was investigated using NMR and UV-vis spectroscopy. The results were compared to those of **DTE-dime** (**Ay-yA** in Chapter 2) on its

own to assess the impact of the fluorophore attachment on the photoswitching properties. Figure 3.12 and Figure 3.13 present an overview of the photoswitching process, changes in UV-vis absorption spectra during photoswitching, and NMR spectra used for quantifying the PSD for **DTE-Cy3** and **DTE-Cy3B**, respectively. The UV-vis absorption parameters are summarized in Table 3.7.

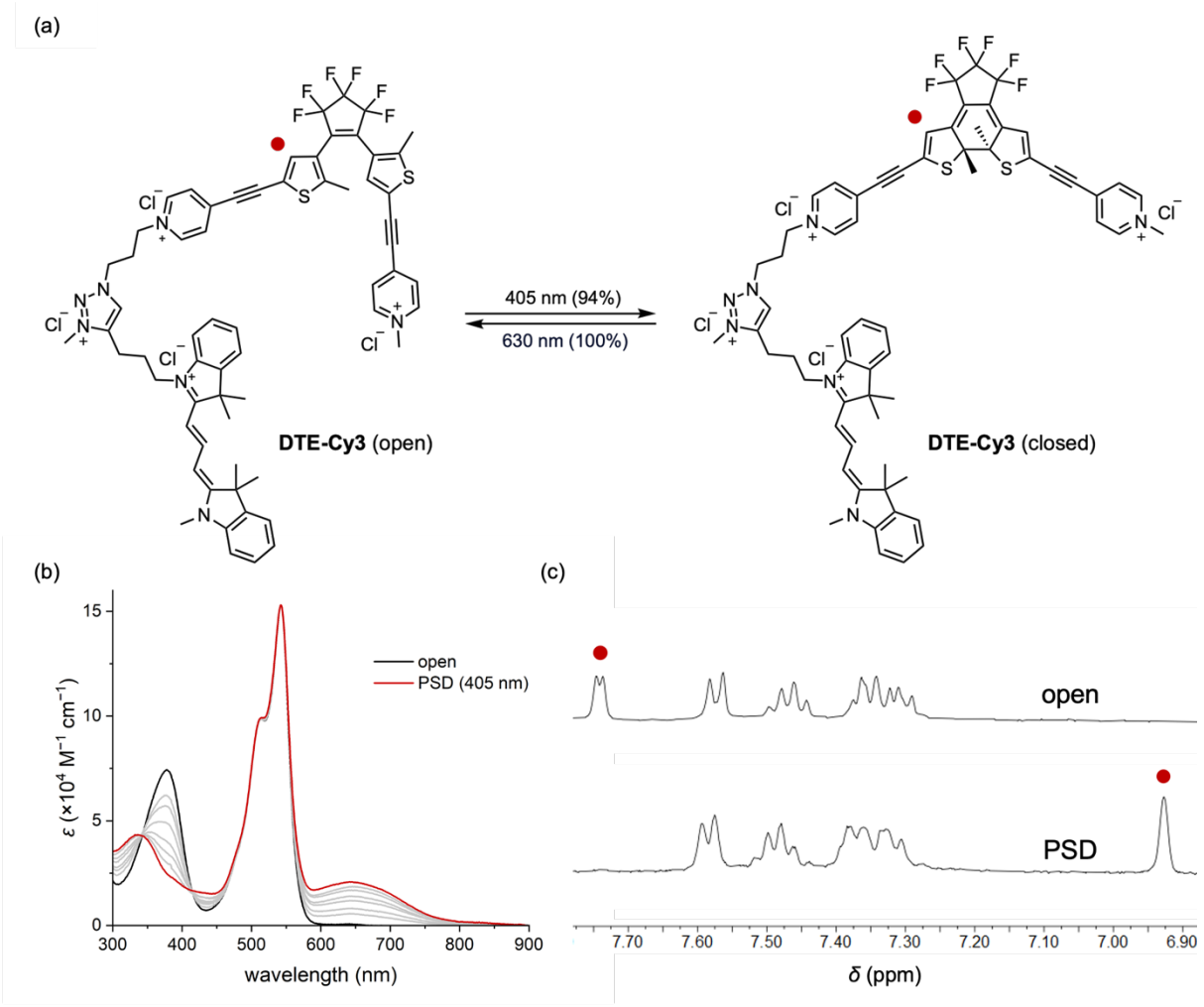


Figure 3.12 (a) Photoswitching of dyad **DTE-Cy3** in water under 405 nm and 630 nm irradiation and the corresponding change in (b) UV-vis absorption spectrum (25 °C) and (c) NMR spectra (D_2O, 500 MHz).

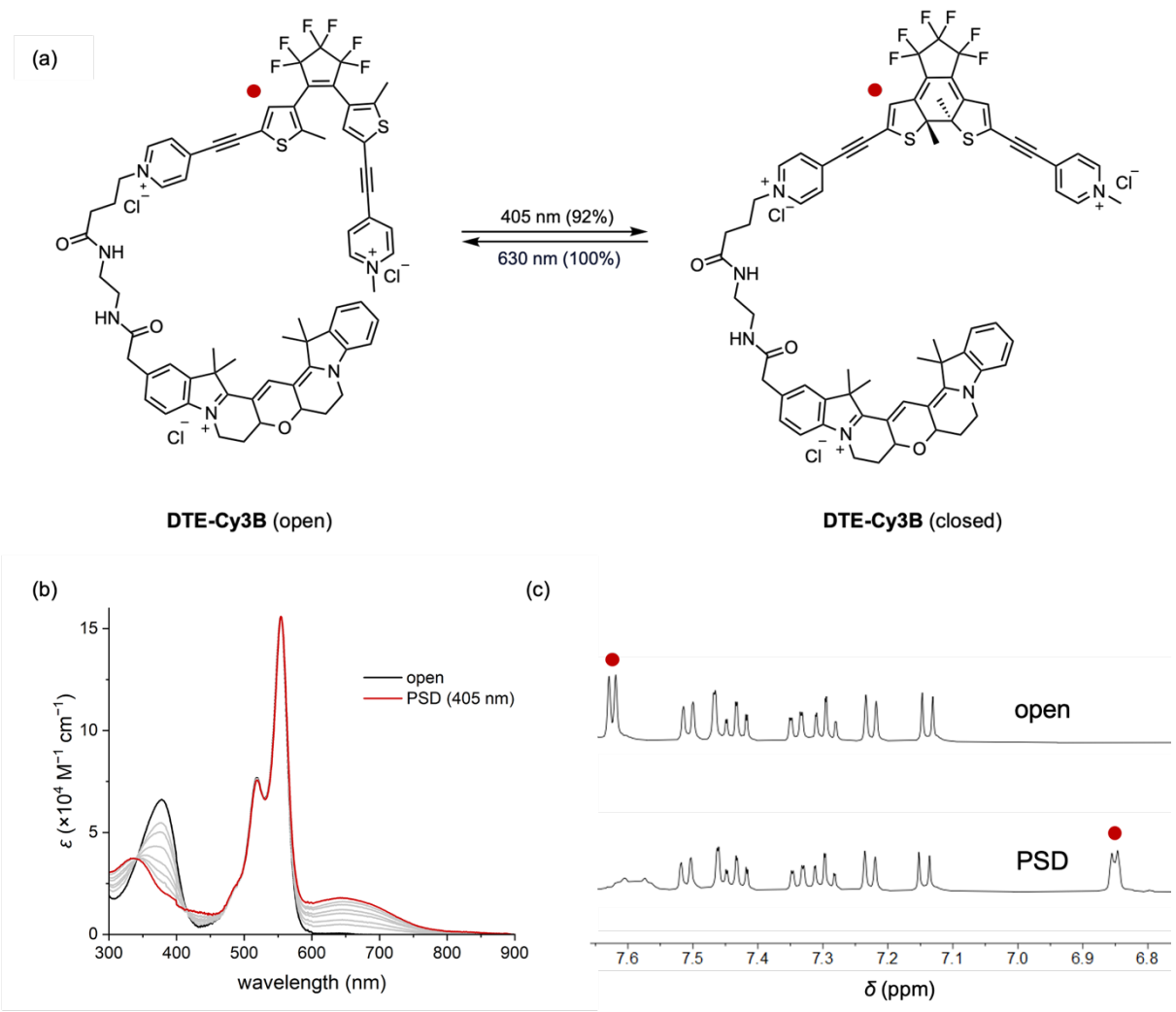


Figure 3.13 (a) Photoswitching of dyad **DTE-Cy3B** in water under 405 nm and 630 nm irradiation and the corresponding change in (b) UV-vis absorption spectrum (25 °C) and (c) NMR spectra (D_2O, 500 MHz).

Table 3.7 Summary of UV-vis absorption parameters of **DTE-Cy3** and **DTE-Cy3B** in open and closed form in water.

	$\lambda_{DTE\text{-}o}$ (nm)	ε (M^{-1} cm^{-1})	$\lambda_{cyanine}$ (nm)	ε (M^{-1} cm^{-1})	$\lambda_{DTE\text{-}c}$ (nm)	ε (M^{-1} cm^{-1})
DTE-Cy3	377	71200	542	151000	647	22100
DTE-Cy3B	377	69500	555	158000	648	21500

The values are summarized from the UV-vis absorption spectra from Figure 14 and Figure 15.

The UV-vis absorption spectra and NMR spectra confirm that both **DTE-Cy3** and **DTE-Cy3B** demonstrate promising photoswitching behavior. The UV-vis spectra of these dyads reveal distinct absorption bands: a DTE absorption band at 377 nm and cyanine absorption bands at 543 nm for **DTE-Cy3** and 555 nm for **DTE-Cy3B**. Upon irradiation with 405 nm light for 1–30 seconds in water, the DTE absorption band gradually decreases, while a new band emerges at approximately 650 nm, corresponding to the closed form of the DTE moiety. The cyanine absorption remains unaffected during this process. The molar absorption coefficients of these bands correlate well with individual cyanine dyes (**Cy3-alkyne** and **Cy3B-acid**) as well as individual **DTE-dime** before dyad formation with difference of less than

5%. Such result indicates the DTE and the Cy3 have been linked at a 1:1 ratio and excess cyanine impurities have been successfully removed.

In the case of **DTE-Cy3**, the DTE photoswitch undergoes photocyclization under 405 nm irradiation to achieve a PSD of 94% in the forward direction. This PSD value is similar to that observed for **DTE-dime** alone (96%), subjecting to ±1% error associated with NMR integration of a flat region, indicating that the attachment of the Cy3 fluorophore does not significantly impact the photoswitching efficiency of the DTE moiety. Similarly, the **DTE-Cy3B** dyad exhibits a forward PSD of 92%, as determined by ^{1}H NMR spectroscopy. However, it is important to note that the amide proton signal at the PSS partially overlaps with the thiophene proton signal of the open form in the NMR spectrum. This overlap can introduce a larger error when using the NMR integration method to quantify the PSD, potentially resulting in a lower observed value. In the reverse direction, both **DTE-Cy3** and **DTE-Cy3B** achieve complete conversion under 630 nm irradiation, indicating that the photoreversion process is highly efficient in both dyads.

3.2.8 Regulation of Cyanine Fluorescence by DTE

To assess the change in fluorescence emission associated with the photoswitching of the DTE moiety, fluorescence spectra were acquired in water for both **DTE-Cy3** and **DTE-Cy3B** in their open form and at PSSs after irradiation with 405 nm and 365 nm light. For **DTE-Cy3**, the measurements of the "on" and the "off" states were performed under identical instrument parameters. Figure 3.14 depicts the change in fluorescence intensity, measured in counts per second, for both the **DTE-Cy3** and **DTE-Cy3B** dyads. When the DTE moiety is switched from the open form to the closed form using either 405 nm or 365 nm light, a significant reduction in fluorescence intensity is observed for both dyads. This substantial fluorescence quenching demonstrates that the closed form of the DTE effectively suppresses the emission of the attached cyanine fluorophores, indicating efficient energy transfer from the fluorophore to the DTE. To quantitatively evaluate the fluorescence quenching, the absolute area under the curves was calculated for all the fluorescence spectra presented in Figure 3.14, and the results are summarized in Table 3.8. The percentage of fluorescence quenching at the PSS was determined by dividing the change in fluorescence by the initial fluorescence intensity when the DTE is in the open form. The calculations reveal that **DTE-Cy3** and **DTE-Cy3B** exhibit fluorescence quenching of 94% and 93%, respectively, after irradiation with 405 nm light. These fluorescence quenching values closely resemble the PSD of 94% for **DTE-Cy3** and 92% for **DTE-Cy3B**.

Photoswitching with 365 nm light results in even more pronounced fluorescence quenching of 97% and 95% for **DTE-Cy3** and **DTE-Cy3B**, respectively. This enhanced quenching can be attributed to the slightly higher PSD achieved when irradiating the dyads with 365 nm light. According to NMR integration, **DTE-dime**, which serves as a reference, can achieve 96% PSD in the forward direction under 405 nm irradiation, while irradiation with 365 nm light can lead to a PSD exceeding 99%.[76]

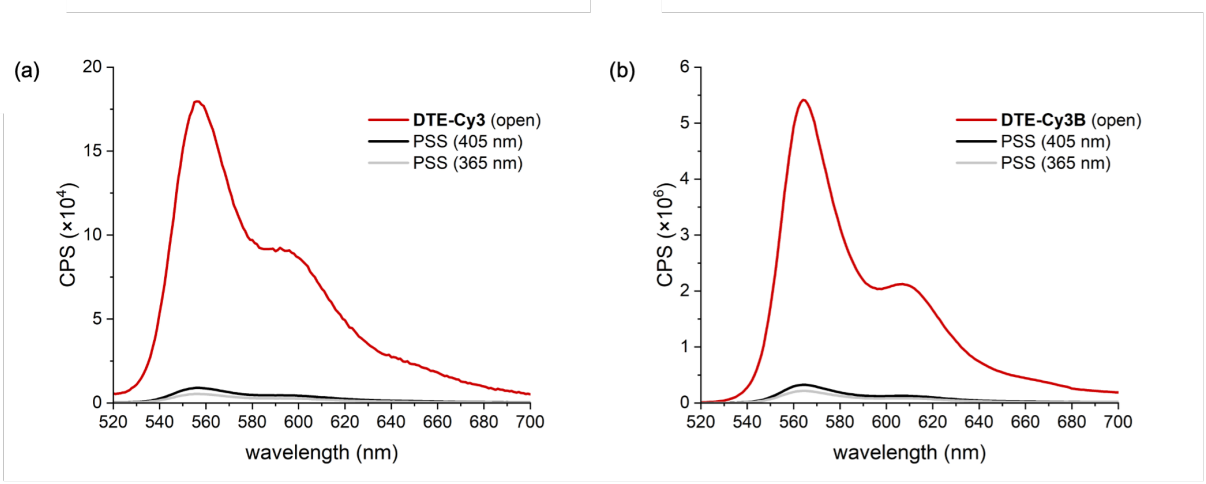


Figure 3.14 Fluorescence quenching of **DTE-Cy3** and **DTE-Cy3B** under identical measurement conditions.

Table 3.8 Mathematical areas under the fluorescence spectra and the percent quenching at PSS compared to the open form.

	DTE-Cy3		**DTE-Cy3B**	
	absolute area	% quenching	absolute area	% quenching
open	1.05×10^{7}	/	2.51×10^{8}	/
PSS (405 nm)	5.83×10^{6}	94%	1.71×10^{7}	93%
PSS (365 nm)	3.34×10^{6}	97%	1.23×10^{7}	95%

Percentage quenching is calculated by dividing the change in fluorescence by the initial fluorescence intensity when the DTE is in the open form.

The fluorescence quenching of **DTE-Cy3** and **DTE-Cy3B** was further quantified by measuring their fluorescence quantum yields in both the open forms and at the PSS (405 nm) in water. The fluorescence quantum yields were determined using a relative method, with **Cy3B-acid** in water (63%) as the reference. The results are presented in Table 3.9. It is important to note that the fluorescence quantum yield measured at the PSS ($\Phi_{F,obs.}$) represents the overall quantum yield of a sample containing both open and closed forms of the DTE. As a result, the fluorescence quantum yield at the PSS does not represent an intrinsic fluorescence property of **DTE-Cy3** and **DTE-Cy3B** with the DTE exclusively in either the open or closed form. Instead, it reflects the average behavior of the population.

Table 3.9 Fluorescence quantum yield of **DTE-Cy3** and **DTE-Cy3B** when the DTE is in the open form and at PSS (405 nm) in water.

	DTE-Cy3		**DTE-Cy3B**	
	$\Phi_{F,obs.}$ (%)	% quenching	Φ_F (%)	% quenching
open	2.5	/	61	/
PSS (405 nm)	0.15	94%	3.5	93%

The fluorescence quantum yields of **DTE-Cy3** (2.5%) and **DTE-Cy3B** (61%) in water are similar to those of **Cy3-alkyne** (2.9%) and **Cy3B-acid** (63%), respectively. This similarity indicates that the attachment of the DTE moiety does not significantly interfere with the fluorescence of the cyanine fluorophores when the DTE is in its open form. Upon reaching the PSS at 405 nm, the fluorescence quantum yields decrease to 0.15% for **DTE-Cy3** and 3.5% for **DTE-Cy3B**, corresponding to fluorescence quenching of 94% and 93%, respectively. The observed residual fluorescence is likely attributed to the remaining dyads with DTEs in their open form, rather than inefficient FRET quenching.

To verify the efficiency of FRET quenching, the fluorescence lifetimes of **DTE-Cy3** and **DTE-Cy3B** were measured when the DTE moiety was in the open form and at the PSS (405 nm). The results are presented in Table 3.10.

Table 3.10 Fluorescence lifetime (ns) of **DTE-Cy3** and **DTE-Cy3B** when the DTE is in the open form and at PSS (405 nm).

	DTE-Cy3		**DTE-Cy3B**	
Solvent	water	glycerol	water	glycerol
open	<0.2*	1.84	2.70	2.51
PSS (405 nm)	<0.2*	1.85	2.68	2.53

* The lifetime was very short, and the data could not be fitted with an exponential tail fit.

For both **DTE-Cy3** and **DTE-Cy3B**, the results show that the fluorescence lifetime of the dyad with the DTE in the open form is similar to that of the molecule at the PSS. This observation indicates that the FRET quenching in these dyads are efficient and the fluorescence signal measured at the PSS mainly originates from the remaining **DTE-Cy3** and **DTE-Cy3B** with the DTE in the open form. If the FRET quenching is not efficient, the FRET process competes with the radiative decay and would result in shorter fluorescence lifetimes. Overall, the darkness of the off state of these dyad systems is governed by the PSD of the DTE photoswitch.

3.2.9 Fatigue Resistance of DTE-Cy3 and DTE-Cy3B

The use of switchable fluorophores **DTE-Cy3** and **DTE-Cy3B** in biological applications, such as super-resolution microscopy and FRAP, requires multiple cycles of photoswitching. Fatigue of switchable dyads can originate from both the fluorophore and the DTE. The stability of the DTE determines the darkness of the dark state, as DTE decomposition would result in deteriorated FRET quenching in the sample. If the decomposition products of the DTE do not quench fluorescence, the fluorescence of the dark state is expected to increase, while the fluorescence signal of the bright state would not be affected. On the other hand, decomposition (photobleaching) of the cyanine dye would cause both the bright state and the dark state to become less bright, as the decomposed molecules become non-fluorescent.

To characterize the fatigue resistance of both the DTE photoswitch and the cyanine dye in the dyad, the absorption signals of DTE (in both open and closed states), the absorption signal of the cyanine, and the fluorescence signal of cyanine were tracked over 20 cycles in water (Figure 3.15). Photocyclization of DTE is triggered by 405 nm LED light (27.6 mW, 5 s) and the photoreversion of DTE is triggered by 630 nm LED light (118 mW, 30 s). Overall, both **DTE-Cy3** and **DTE-Cy3B** demonstrate outstanding photostability during the photoswitching cycles. The high fatigue resistance of the DTE molecule in both dyads resembles that of the **DTE-dime** on its own. For both **DTE-Cy3** and **DTE-Cy3B**, approximately 4% signal reduction is observed in the closed-DTE absorption channel, which is comparable to the decomposition of the parent **DTE-dime**.[76] Regarding the cyanine stability, both dyads show a gradual loss of cyanine absorption signal over the 20 photoswitching cycles. However, the cyanine in **DTE-Cy3** is considerably less stable (8% absorption signal decrease) than that in **DTE-Cy3B** (3% absorption decrease), as illustrated by the faster decomposition in Figure 3.15c. In terms of the fluorescence signal, the fluorescence and quenching are well-maintained over 20 cycles. **DTE-Cy3** shows 7% fluorescence decrease in the bright state and 2% fluorescence decrease in the dark state over 20 cycles. Interestingly, for **DTE-Cy3B**, 3% fluorescence reduction and 3% fluorescence increase are observed for the bright state and the dark state, respectively. These results show that the dark state of **DTE-Cy3** gradually gets darker while the dark state of **DTE-Cy3B** gradually gets brighter. This observation can be attributed to the fact that DTE decomposition in **DTE-Cy3B** is faster than cyanine photobleaching.

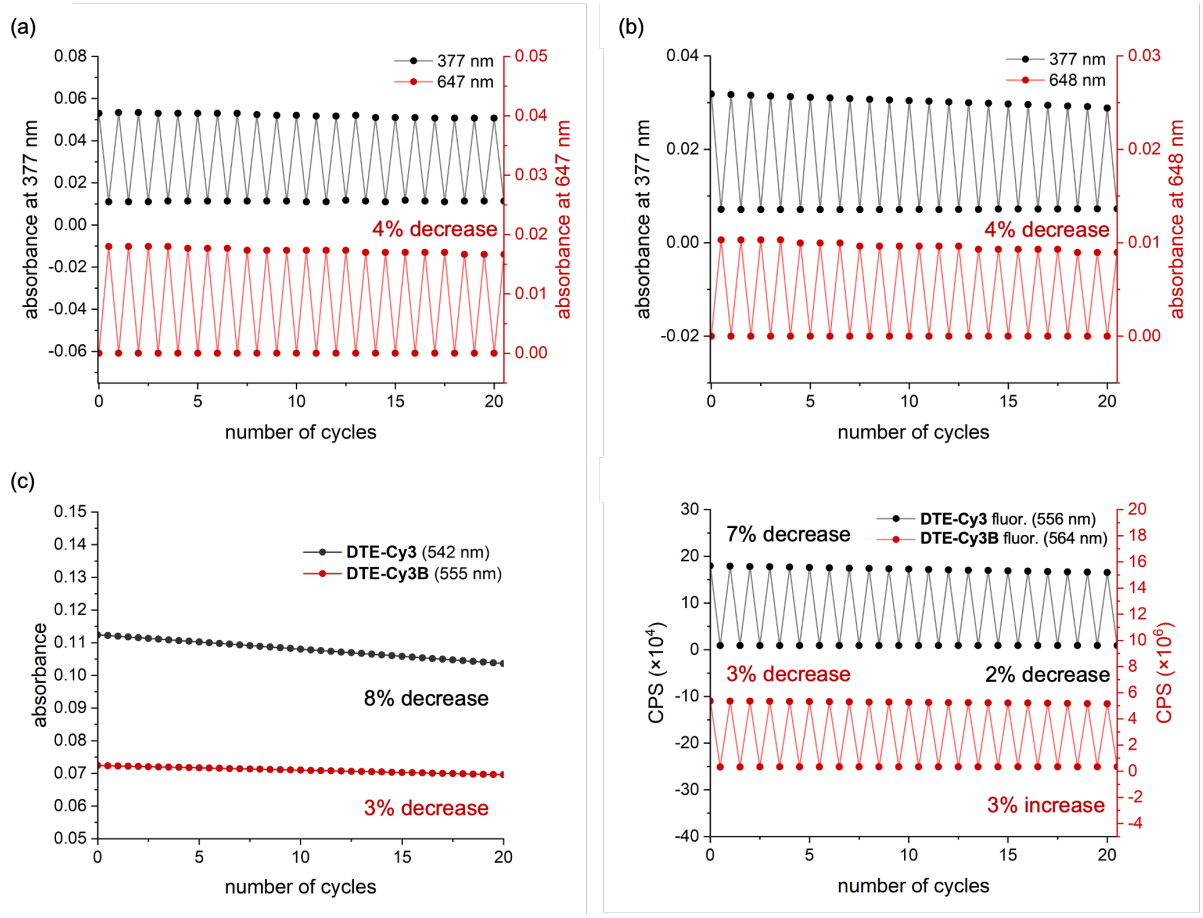


Figure 3.15 Fatigue resistance of DTE photoswitch monitored at the open-state absorption maximum (black) and closed-form absorption maximum (red) during the dyad photoswitching of (a) **DTE-Cy3** and (b) **DTE-Cy3B**. (c) Fatigue resistance of the cyanine dye monitored at the absorption maximum. (d) Overall fatigue resistance of DTE-Cy3 and DTE-Cy3B monitored by fluorescence emission maxima. All experiments were performed in water.

3.2.10 Conclusion

In this work, I have designed, prepared, and characterized two novel water-soluble switchable fluorophores, **DTE-Cy3** and **DTE-Cy3B**. These switchable fluorophores are based on a dyad design, where a well-established organic fluorophore (Cy3 or Cy3B) is linked to an optimized DTE (**DTE-diMe**) molecular photoswitch. The fluorescence emitted by the fluorophore is not affected when the photoswitch is in the open form, but it is quenched through the FRET when the photoswitch is in the closed form. Both **DTE-Cy3** and **DTE-Cy3B** exhibit excellent fluorescence quenching of 94% and 93%, respectively, upon DTE photocyclization triggered by 405 nm irradiation in water. The quenching can be further enhanced to 97% for **DTE-Cy3** and 95% for **DTE-Cy3B** by using 365 nm irradiation, as the DTE moiety achieves a higher PSD at this wavelength. In addition to their impressive fluorescence quenching, both switchable fluorophores demonstrate exceptional fatigue resistance, with less than 5% change in the fluorescence signal after 20 cycles of photoswitching. This stability is crucial for their potential application in biological systems, where multiple rounds of photoswitching are required. When

considering potential biological applications, **DTE-Cy3B** would be a better candidate compared to **DTE-Cy3**, as the Cy3B dye is significantly brighter than the Cy3 dye. This higher brightness allows for easier detection of the fluorescence signal.

3.3 Experimental

3.3.1 General Synthetic and Characterization Methods

All reactions were performed using oven-dried reaction vessels under an argon atmosphere unless stated otherwise. Anhydrous acetonitrile (MeCN), chloroform ($CHCl_3$), dichloromethane (CH_2Cl_2), diethyl ether (Et_2O), dimethylformamide (DMF), tetrahydrofuran (THF), toluene, and pyridine were obtained from an MBraun MBSPS-5-BenchTop solvent purification system, having been passed through an activated alumina column under nitrogen. Methanol was dried over 4 Å molecular sieves under argon. All other chemical reagents used were commercially available from Alfa Aesar, Fluorochem, Merck, and TCI Chemicals and were used as supplied.

Thin layer chromatography (TLC) and reverse-phase TLC analyses were carried out using Merck aluminum-backed TLC silica gel 60 F_{254} plates and Merck aluminum-backed TLC silica gel 60 RP-18 F_{254} plates, respectively. Plates were visualized directly under ambient light (for colored fluorescent dyes), by the quenching of fluorescence under ultraviolet light (λ = 254 nm), or by the turn-on of fluorescence under ultraviolet light (λ = 365 nm). Flash column chromatography and reverse-phase flash-column chromatography was performed using Merck Geduran® 60 silica gel (particle size 63–200 μm) and C18-reversed phase silica gel, respectively, with the solvent system given. All solvents used for chromatography purification were HPLC grade or equivalent and were supplied by Merck, Fisher Scientific, VWR, or Honeywell.

Proton (^{1}H) and carbon (^{13}C) NMR spectra were recorded on either a Bruker AVIII HD 400, a Bruker AVIII HD 500, a Bruker AVII 500 with a ^{13}C(^{1}H) dual cryo-probe, or a Bruker AVIII 600 instrument with a broadband cryo-probe in deuterated solvents. Experiments on the Bruker AVIII 600 instrument were performed by the staff from the Chemistry Department NMR Research Facility, University of Oxford. All NMR experiments were conducted at 298 K. ^{1}H NMR chemical shifts are reported in ppm to the nearest 0.01 ppm relative to $SiMe_4$ (δ = 0) and were referenced internally with respect to residual protons in the deuterated solvent (1.94 for acetonitrile-d_3, 7.26 for chloroform-d, 2.50 for DMSO-d_6, 4.79 for D_2O, and 3.31 for methanol-d_4). ^{13}C NMR spectra were recorded with broadband decoupling. ^{13}C chemical shifts

were reported in ppm to the nearest 0.1 ppm relative to $SiMe_4$ (δ = 0) and were referenced internally with respect to carbons in the solvent (δ = 118.6 for acetonitrile-d_6, 77.2 for chloroform-d, 39.5 for DMSO-d_6, and 49.0 for methanol-d_4). Peak assignments were made based on chemical shifts, integrations, coupling constants, comparison to known compounds, and using COSY, HSQC, and HMBC experiments where appropriate. Multiplets are described as singlet (s), doublet (d), triplet (t), quartet (q), pentet (p) multiplet (m), broad (br), or combinations thereof. Coupling constants (*J*) are reported to the nearest 0.1 Hz.

High resolution mass spectra (HRMS) were recorded by the staff from the Chemistry Research Laboratory Mass Spectrometry Facility, University of Oxford, using a Bruker MicroTOF spectrometer or a Thermo Orbitrap Exactive mass spectrometer. The mass reported was that containing the isotopes with the lowest mass, with each value to 7 significant figures and within 5 ppm of the calculated mass. Mass to charge ratios (*m*/*z*) are reported in Daltons.

3.3.2 HPLC Analysis and Purification

Analytical reverse phase HPLC was performed at 298 K using an Agilent 1100 Series system comprising an autosampler (G1313A), a vacuum degassing unit (G1379A), a quaternary pump (G1311A), a column oven (G1316A), a diode array detector (G1315B), and a fraction collector (G1364C). Preparative reverse phase HPLC was performed at 298 K using an Agilent 1260 Infinity II system comprising a binary pump. Both analytical and preparative instruments were operated using ChemStation software. For analytical HPLC an Agilent Eclipse XDB-C18 column (4.6 × 150 mm, 5 μm particle size) was used with a flow rate of 1.0 mL/min. For preparative HPLC, an Agilent InfinityLab ZORBAX Eclipse Plus C18 column (21.2 × 150 mm, 5 μm particle size) was used with a flow rate of 21.0 mL/min.

Method A (analytical): monitoring at 250 nm, 360 nm, 560 nm and 650 nm. Using MeCN and H_2O (with 0.1% TFA additive) as eluents. Starting with 5% MeCN, 5–100% MeCN over 20 min, then 100% MeCN for 10 min, eventually 100–5% MeCN over 5 min to restore the starting setting.

Method B (preparative): monitoring at 400 nm and 500 nm. Using MeCN and H_2O (with 0.1% TFA additive) as eluents. Starting with 5% MeCN, 5–100% MeCN over 20 min, then 100% MeCN for 15 min, eventually 100–5% MeCN over 5 min to restore the starting setting.

3.3.3 Optical Analysis

All spectroscopic measurements were conducted in HPLC grade solvents or deionized water (purified with ELGA LabWater PURELAB® Chorus 1 Complete water purification system) using fused silica cuvettes (10 mm path length, Starna Scientific Ltd, UK). UV-vis absorption spectra were acquired on a Perkin Elmer Lambda 20 spectrometer. Unless otherwise stated, all absorption spectra were recorded at 298 K, with temperature control by a PTP-1 Peltier unit from Perkin Elmer. Fluorescence spectra were acquired at 298K using an Edinburgh Instruments FS5 spectrofluorometer operating with Fluoracle® software and equipped with a xenon arc lamp (providing 230–1000 nm excitation range), a thermostatic sample holder (SC-20) and both an R13456 PMT detector (200–950 nm spectral coverage, Hamamatsu) and an InGaAs analogue NIR detector (850–1650 nm spectral coverage).

Fluorescence quantum yields were measured by an absolute method using an integrating sphere (SC-30) or by a relative method referencing to the quantum yield of **Cy3B-acid** (63%, synthesized in-house) fluorescent dye in water, using the Equation 4.7:

$$\Phi_S = \Phi_R \cdot \frac{I_S}{I_R} \cdot \frac{1 - 10^{-A_R}}{1 - 10^{-A_S}} \cdot \left(\frac{n_S}{n_R}\right)^2 \tag{4.7}$$

where the subscripts S and R denote the sample and reference respectively. Φ_R is the known quantum yield of the reference standard, I is the integrated fluorescence spectrum intensity, A is the absorbance of the solution at the excitation wavelength (λ_{ex}), and n is the refractive index of the solvent.

Fluorescence lifetimes were measured in time-correlated single photon counting (TCSPC) mode using a picosecond pulsed diode laser (EPL-475; 473.4 nm, pulse width 100 ps) as the excitation source. Once a time-resolved fluorescence decay and the instrument response function were measured, a reconvolution fit analysis was carried out using Fluoracle® (Edinburgh Instruments) by fitting in a mono-exponential function (Equation 4.8):

$$A + B \cdot e^{-\frac{t}{\tau}} \tag{4.8}$$

where A is the calculated background, B is the calculated pre-exponential factor, and the goodness of fit is given as χ^2.

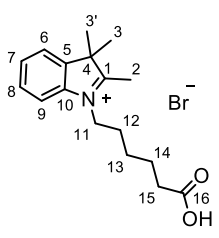
3.3.4 Measurement of Fatigue Resistance

The fatigue resistance is measured by tracking the absorption signals of DTE (in both open and closed states), the absorption signal of the cyanine, and the fluorescence signal of cyanine were tracked over 20 cycles in water. Tracking fatigue resistance in four different channels ensures the characterization of both DTE and cyanine decomposition.

A typical procedure for measuring the fatigue resistance is as follows: an aqueous solution of **DTE-Cy3** (0.74 μM) was prepared from a stock solution of **DTE-Cy3** (0.1 mM) and placed in a cuvette (1 cm pathlength) in the UV-vis spectrometer and stirred at 25 °C. The absorbance of the sample at 377 nm, 542 nm, and 647 nm was recorded. The cuvette containing the sample was transferred to the spectrofluorometer and the fluorescence was measured. The solution was then irradiated with a pulse of 365 nm light (18.9 mW, 10 s) and the absorption and fluorescence were recorded with the same instrument setting. Afterwards, the solution was irradiated with a pulse of 630 nm light (118 mW, 60 s) and the absorption and fluorescence were recorded. This procedure of irradiation with alternative light sources was repeated for 20 cycles and the absorption and fluorescence were recorded after each pulse of irradiation. The UV-vis absorption at 377 nm, 542 nm and 647 nm, and the fluorescence at 556 nm were plotted against the number of switching cycles.

3.3.5 Synthetic Procedures

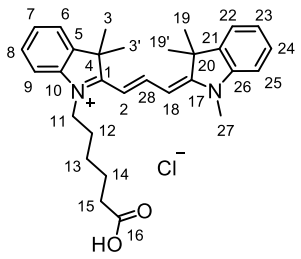
1-(5-Carboxypentyl)-2,3,3-trimethyl-3*H*-indol-1-ium bromide 1



The compound was prepared following a procedure developed by Kvach and co-workers with modification in the purification method.[77] 2,3,3-Trimethylindolenine (3.20 mL, 20.0 mmol) and 6-bromohexanoic acid (3.90 g, 20.0 mmol) were dissolved in toluene (5 mL). The reaction mixture was heated at reflux for 19 h before being allowed to cool to room temperature. The precipitate was collected by filtration then washed with Et_2O. The crude product was dissolved in nitromethane and precipitated with EtOAc twice to yield the product as a pale pink solid (5.80 g, 82%). δ_H (400 MHz, DMSO-d_6): 7.98 (1H, m, H^9), 7.84 (1H, m, H^6), 7.62 (2H, m, H^7 and H^8), 4.46 (2H, t, J_{HH} 7.5, H^{11}), 2.84 (3H, s, H^2), 2.23 (2H, t, J_{HH} 7.2, H^{15}), 1.84 (2H, m, H^{12}), 1.61–1.49 (8H, m, H^{14}, H^3 and $H^{3'}$), 1.43 (2H, m, H^{13}); δ_C (101 MHz, DMSO): 196.5,

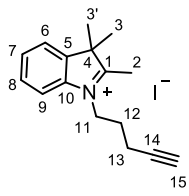
174.3, 141.9, 141.1, 129.4, 128.9, 123.5, 115.5, 54.2, 47.4, 33.4, 26.9, 25.4, 24.0, 22.0, 14.0. HRMS (ESI+) m/z: $[M]^+$ calcd. for $C_{17}H_{24}NO_2$ 274.1802, found 274.1791.

Cy3-acid



The compound was synthesized following a procedure developed by Miao and co-workers with modification in the purification method.[66] **1** (550 mg, 1.55 mmol) and *N*,*N*'-diphenylformamidine (305 mg, 1.55 mmol, 1 equiv.) were dissolved in acetic anhydride (7.5 mL) and the reaction mixture was heated at 120 °C for 30 min. The reaction mixture was then cooled to room temperature followed by the addition of 1,2,3,3-tetramethyl-3*H*-indolium iodide (468 mg, 1.55 mmol, 1 equiv.) and pyridine (7.5 mL). The reaction mixture was stirred at room temperature for 18 h and then precipitated with Et_2O (200 mL). The precipitate was collected by filtration, dried with a nitrogen stream, and purified by flash column chromatography (0–15% MeOH in CH_2Cl_2). The resulting compound was dissolved in CH_2Cl_2. The solution was washed with 0.5 M aqueous HCl solution followed by brine, dried ($MgSO_4$) and concentrated in vacuo to yield the product as a shiny green solid (145 mg, 19%). δ_H (500 MHz, CD_3OD): 8.55 (1H, m, H^{28}), 7.59–7.26 (8H, m, H^{6-9} & H^{22-25}), 6.51 (2H, m, H^2 & H^{18}), 4.17 (2H, t, J_{HH} 7.3, H^{11}), 3.70 (3H, s, H^{27}), 2.32 (2H, t, J_{HH} 7.1, H^{15}), 1.91–1.65 (16H, m, includes H^3, $H^{3'}$, H^{19} & $H^{19'}$, H^{12} & H^{14}), 1.54 (2H, m, H^{13}); δ_C (126 MHz, CD_3OD): 178.0, 176.6, 175.9, 152.1, 144.1, 143.4, 142.2, 142.1, 130.0, 129.9, 126.7, 126.6, 123.5, 123.4, 112.4, 112.3, 103.9, 103.8, 50.6, 50.5, 45.1, 35.0, 32.0, 28.3, 28.2, 27.4, 25.9, 25.1. UV-Vis (water): λ_{max} (ε) = 541 nm (153,000 mol^{-1} dm^3 cm^{-1}); fluorescence (water): λ_{em} = 556 nm; $\Phi_{fl.}$ = 2.8%. HRMS (ESI+) m/z: $[M]^+$ calcd. for $C_{30}H_{37}N_2O_2$ 457.2850, found 457.2840.

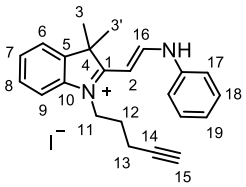
2,3,3-Trimethyl-1-(pent-4-yn-1-yl)-3*H*-indol-1-ium iodide 2



The compound was synthesized following a procedure developed by Gerowska and co-workers with modification in the purification method.[78] 2,3,3-Trimethylindolenine (7.8 mL, 49 mmol) and 5-chloro-1-pentyne (8.0 mL, 76 mmol, 1.6 equiv.) were dissolved in acetonitrile (50 mL). The reaction mixture was heated at reflux for 18 h before being allowed to cool to room temperature. The precipitate was collected by filtration and then washed with Et_2O. The crude product was dissolved in

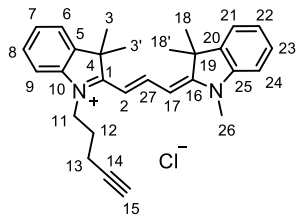
nitromethane and precipitated with EtOAc twice to yield the product as a pale pink solid (3.0 g, 18%). δ_H (400 MHz, DMSO): 7.98 (1H, m, H^9), 7.84 (1H, m, H^6), 7.62 (2H, m, H^7 and H^8), 4.46 (2H, t, J_{HH} 7.5, H^{11}), 2.84 (3H, s, H^2), 2.23 (2H, t, J_{HH} 7.2, H^{15}), 1.84 (2H, m, H^{12}), 1.61–1.49 (8H, m, H^{14}, H^3 and $H^{3'}$), 1.43 (2H, m, H^{13}); δ_C (101 MHz, DMSO): 196.5, 174.3, 141.9, 141.1, 129.4, 128.9, 123.5, 115.5, 54.2, 47.4, 33.4, 26.9, 25.4, 24.0, 22.0. HRMS (ESI+) m/z: $[M]^+$ calcd. for $C_{17}H_{24}NO_2$ 274.1802, found 274.1791.

Hemicyanine-alkyne



2 (2.50 g, 7.08 mmol) and *N*,*N*'-diphenylformamidine (1.53 g, 7.78 mmol, 1.1 equiv.) were suspended in ethanol (40 mL). Triethylorthoformate (1.15 g, 7.78 mmol, 1.1 equiv.) was then added and the suspension was heated at reflux for 15 h. The reaction mixture was cooled to room temperature. The remaining oil was dissolved in EtOH and precipitated with Et_2O to yield the product as a dark red solid (3.2 g, 99%). δ_H (500 MHz, CD_3CN): 11.26 (1H, s, NH), 8.61 (1H, d, J_{HH} 12.5, H^2), 7.56–7.25 (9H, m, ArH), 6.97 (1H, d, J_{HH} 12.5, H^{16}), 4.16 (2H, t, J_{HH} 7.7, H^{11}), 2.46 (2H, td, J_{HH} 7.7, J_{HH} 2.7, H^{13}), 2.33 (1H, t, J_{HH} 2.7, H^{15}), 2.04 (2H, appr. p., H^{12}), 1.70 (6H, s, H^3 & $H^{3'}$); δ_C (126 MHz, CD_3CN): 179.6, 152.7, 142.8, 142.3, 139.3, 130.8, 129.7, 127.5, 127.0, 123.5, 119.0, 112.5, 92.0, 83.8, 71.2, 57.9, 50.8, 44.8, 28.6, 26.7, 18.7, 16.7. HRMS (ESI^+) *m/z*: $[M^+]$ calcd. for $C_{23}H_{25}N_2^+$ 363.2012; found 329.2000.

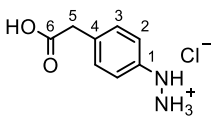
Cy3-alkyne



Hemicyanine-alkyne (3.20 g, 7.01 mmol), 1,2,3,3-tetramethyl-3*H*-indolium iodide (3.17 g, 10.5 mmol, 1.5 equiv.) and acetic anhydride (6.6 mL, 70.1 mmol, 10 equiv.) were dissolved in pyridine (40 mL). The reaction mixture was stirred at 50 °C for 18 h before being cooled to room temperature and precipitated with diethyl ether (500 mL, 4 °C) overnight. The supernatant liquid layer was decanted, and the remaining thick dark-brown oil was redissolved in chloroform. The chloroform solution was subsequently washed with HCl (aq. 0.5 M) and brine, dried ($MgSO_4$) and concentrated in vacuo. The crude product was purified by flash column chromatography (CH_2Cl_2, CH_2Cl_2 1:1 EtOAc, CH_2Cl_2 1:2 EtOAc and 1–5% MeOH in CH_2Cl_2 to yield the product as a shiny green solid (2.20 g, 59%). δ_H (500 MHz, CD_3OD): 8.56 (1H, appr. t, H^{27}), 7.58–7.26 (8H, m, H^{6-9} & H^{21-24}), 6.56–6.43 (2H, m, H^2 & H^{17}),

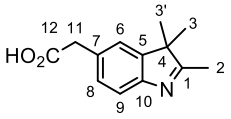
4.27 (2H, t, J_{HH} 7.6, H^{11}), 3.70 (3H, s, H^{26}), 2.51 (1H, t, J_{HH} 2.6, H^{15}), 2.43–2.38 (2H, td, J_{HH} 6.8, J_{HH} 2.6, H^{13}), 2.04 (2H, appr. p, H^{12}), 1.79–1.75 (12H, two singlets overlapping, H^{3}, $H^{3'}$, H^{18} & $H^{18'}$); δ_C (126 MHz, CD_3OD): 176.9, 176.0, 152.2, 144.1, 143.4, 142.2, 142.1, 130.0, 129.8, 126.9, 126.7, 123.6, 123.41, 112.4, 112.2, 104.0, 103.6, 83.7, 71.4, 50.7, 50.6, 44.1, 31.9, 28.4, 28.1, 27.3, 23.8. UV-Vis (water): λ_{max} (ε) = 541 nm (154,000 mol^{-1} dm^3 cm^{-1}); fluorescence (water): λ_{em} = 556 nm; $\Phi_{fl.}$ = 2.9%. HRMS (ESI$^+$) *m/z*: [M^+] calcd. for $C_{29}H_{33}N_2^+$ 409.2638; found 409.2626.

2-(4-(Carboxymethyl)phenyl)hydrazin-1-ium chloride 3



The compound was synthesized following the procedure developed by Ahlström and co-workers.[2] 2-(4-Aminophenyl)acetic acid (10.0 g, 66.2 mmol) was dissolved in aqueous hydrochloric acid (37%, 100 mL). The slurry was heated to 120 °C until a clear solution was formed. The solution was rapidly cooled down to −5 °C. A solution of $NaNO_2$ (5.48 g, 79.4 mmol, 1.2 equiv.) in water (5 mL) was then added dropwise and the mixture was stirred at −5 °C for 15 min. A solution of $SnCl_2{\cdot}2H_2O$ (29.9 g, 132 mmol, 2 equiv.) in HCl (37%, aq., 10 mL) was further added to the reaction mixture at −20 °C. After stirring at −20°C for 25 min and at −5°C for another 25 min, the precipitate was collected by filtration and successively washed with ethanol to yield the product as an off-white solid (12.1 g, 91%). δ_H (500 MHz, DMSO-d_6): 10.07 (s, br, COOH and NH_3^+), 8.15 (1H, s, NH), 7.17 (2H, d, J_{HH} 8.7, H^3), 6.90 (2H, d, J_{HH} 8.7, H^2), 3.48 (2H, s, H^5); HRMS (ESI$^+$) *m/z*: [$M]^+$ calcd. for $C_8H_{11}N_2O_2^+$ 167.0815; found 167.0813.

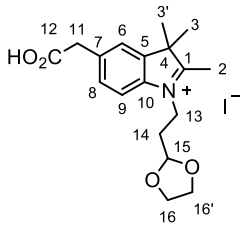
2-(2,3,3-Trimethyl-3*H*-indol-5-yl)acetic acid 4



3 (12.0 g, 59.2 mmol), 3-methylbutan-2-one (12.8 g, 148 mmol, 2.5 equiv.) and potassium acetate (11.6 g, 118 mmol, 2 equiv.) were dissolved acetic acid (200 mL). The reaction mixture was heated at 90 °C for 3 h before being allowed to cool to room temperature. The reaction mixture was concentrated in vacuo, dissolved in CH_2Cl_2 and washed with water and brine. The organic layer was dried ($MgSO_4$), filtered and concentrated in vacuo to yield the product as a pale red solid (6.50 g, 51%). No purification was required. δ_H (500 MHz, DMSO-d_6): 12.28 (1H, s, br, COOH), 7.34 (1H, d, J_{HH} 7.8, H^8), 7.29 (1H, s, H^6), 7.15 (1H, d, J_{HH} 7.8, H^9), 3.57 (2H, s, H^{11}), 2.19 (3H, s, H^2), 1.23 (6H, s,

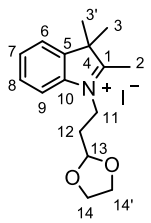
H^3 & $H^{3'}$); δ_C (126 MHz, DMSO-d_6): 187.4, 172.9, 152.4, 146.0, 131.6, 128.5, 122.7, 118.9, 53.1, 40.7, 22.6, 15.0. HRMS (ESI^+) *m/z*: $[M+H]^+$ calcd. for $C_{13}H_{16}NO_2^+$ 218.1176; found 218.1170.

1-(2-(1,3-Dioxolan-2-yl)ethyl)-5-(carboxymethyl)-2,3,3-trimethyl-3*H*-indol-1-ium iodide 5



4 (2.80 g, 12.9 mmol), 2-(2-bromoethyl)-1,3-dioxolane (11.7 g, 64.4 mmol, 5 equiv.) and potassium iodide (6.42 g, 38.7 mmol, 3 equiv.) were dissolved in acetonitrile (50 mL). The reaction mixture was heated at 80 °C for 18 h before being allowed to cool to room temperature. The reaction mixture was concentrated in vacuo. The resulting slurry was dissolved in CH_2Cl_2 and then filtered to remove inorganic salts. After concentrating the solution in vacuo, the remaining oil was dissolved in MeCN and precipitated with EtOAc to yield the product as a dark red solid (1.8 g, 31%). δ_H (500 MHz, DMSO-d_6): 7.85 (1H, d, J_{HH} 8.2, H^9), 7.72 (1H, s, H^6), 7.51 (1H, d, J_{HH} 8.2, H^8), 4.99 (1H, t, J_{HH} 4.3, H^{15}), 4.56 (2H, t, J_{HH} 6.6, H^{13}), 3.84–3.70 (8H, m, incl. a singlet at 3.74, H^{16}, $H^{16'}$ & H^2), 2.79 (2H, s, H^{11}), 2.24 (2H, m, H^{14}), 1.51 (6H, s, H^3 & $H^{3'}$); δ_C (126 MHz, DMSO-d_6): 172.2, 141.7, 139.7, 136.8, 130.2, 124.5, 115.1, 101.4, 64.2, 59.7, 54.1, 43.3, 30.5, 21.8, 20.8, 14.1. HRMS (ESI^+) *m/z*: $[M^+]$ calcd. for $C_{18}H_{24}NO_4^+$ 318.1700; found 318.1696.

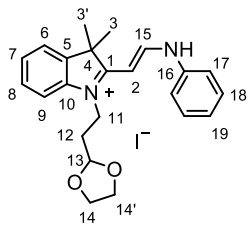
1-(2-(1,3-Dioxolan-2-yl)ethyl)-2,3,3-trimethyl-3*H*-indol-1-ium iodide 6



The compound was synthesized following a patent assigned to SFC Co., Ltd. with longer reaction time and modification in the purification method.[79] 2-(2-Bromoethyl)-1,3-dioxolane (4.43 g, 24.5 mmol, 1.3 equiv.) and potassium iodide (9.38 g, 3 equiv.) were stirred in acetonitrile (100 mL) at 50 °C for 1 hour. To the reaction mixture was added 2,3,3-trimethylindolenine (3.00 g, 18.8 mmol, 1 equiv.). The resulting reaction mixture was stirred at 85 °C for 36 h before being cooled to room temperature. The insoluble inorganic salt was filtered off and the filtrate was concentrated in vacuo. The crude product was redissolved in acetonitrile (15 mL) and precipitated with CH_2Cl_2 (7.5 mL) to remove the last trace of inorganic salt. The filtrate was concentrated in vacuo, further redissolved in acetonitrile (10 mL) and precipitated with EtOAc (50 mL) overnight at 4 °C. The supernatant was decanted and the remaining solid was dried to yield the final product

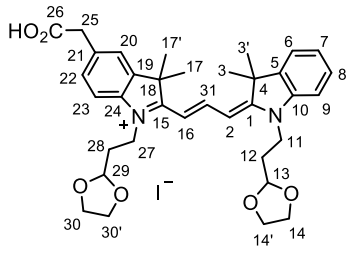
as a pale brown solid (2.73 g, 38%). δ_H (500 MHz, CD_3CN): 7.80–7.75 (1H, m, H^9), 7.74–7.70 (1H, m, H^6), 7.66–7.58 (2H, m, H^7 & H^8), 4.99 (1H, t, J_{HH} 4.1, H^{13}), 4.54 (2H, t, J_{HH} 6.6, H^{11}), 3.84–3.74 (4H, m, H^{14} & $H^{14'}$), 2.76 (3H, s, H^2), 2.35–2.30 (2H, td, J_{HH} 4.1, J_{HH} 6.6, H^{12}), 1.54 (6H, s, H^3 & $H^{3'}$); δ_C (126 MHz, CD_3CN): 197.9, 142.9, 142.1, 130.8, 130.2, 124.41, 116.4, 102.4, 65.6, 55.6, 44.6, 31.3, 22.5, 15.3. HRMS (ESI^+) *m/z*: $[M]^+$ calcd. for $C_{16}H_{22}NO_2^+$ 260.1645; found 260.1639.

Hemicyanine-acetal



6 (2.35 g, 6.07 mmol) and *N*,*N*'-diphenylformamidine (1.31 g, 6.67 mmol, 1.1 equiv.) were suspended in ethanol (40 mL). Triethylorthoformate (989 mg, 6.67 mmol, 1.1 equiv.) was then added and the suspension was heated at reflux for 15 h. The reaction mixture was cooled to room temperature and concentrated in vacuo. The remaining oil was dissolved in EtOH and precipitated with Et_2O to yield the product as a dark red solid (2.40 g, 81%). δ_H (500 MHz, CD_3CN): 8.59 (1H, d, J_{HH} 12.5, H^{15}), 7.56–7.27 (9H, m, ArH), 6.82 (1H, d, J_{HH} 12.5, H^2), 5.05 (1H, t, J_{HH} 4.0, H^{13}), 4.21 (2H, t, J_{HH} 7.3, H^{11}), 3.93–3.75 (4H, m, H^{14} & $H^{14'}$), 2.22 (2H, m, H^{12}), 1.69 (6H, s, H^3 & $H^{3'}$). δ_C (126 MHz, CD_3CN): 179.5, 152.5, 142.7, 142.1, 139.4, 130.8, 129.6, 127.3, 126.91, 123.3, 118.9, 112.8, 102.5, 92.0, 65.7, 50.9, 40.9, 31.2, 22.4. HRMS (ESI^+) *m/z*: $[M^+]$ calcd. for $C_{23}H_{27}N_2O_2^+$ 363.2057; found 363.2067.

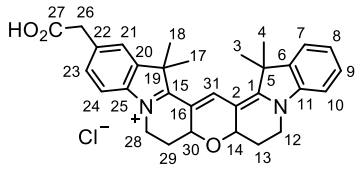
Cy3-acetal



Hemicyanine-acetal (2.50 g, 5.10 mmol) and **5** (2.72 g, 6.12 mmol, 1.2 equiv.) were dissolved in a mixture of pyridine (30 mL), acetic acid (30 mL) and acetic anhydride (6.67 mL) (pyridine : acetic acid : acetic anhydride = 4.5 : 4.5 : 1). The reaction mixture was heated at 50 °C for 18 h before being allowed to cool to room temperature. The reaction mixture was precipitated with cold ether. The precipitate was purified by flash column chromatography (DCM, DCM/EtOAc 1:1, DCM/EtOAc 1:2, 1%–5% MeOH in DCM) to yield the product as a shiny green solid (1.7 g, 46%). δ_H (500 MHz, CD_3CN): 8.45 (1H, dd, appr. t, J_{HH} 13.6, H^{31}), 7.54–7.21 (7H, m, H^6, H^7, H^8, H^9, H^{20}, H^{22} & H^{23}), 6.35–6.28 (2H, d × 2, J_{HH} 13.6, H^2 & H^{16}), 4.98 (2H, t, J_{HH} 4.0, H^{13} & H^{29}), 4.17 (4H, t × 2, appr. q, H^{11} &

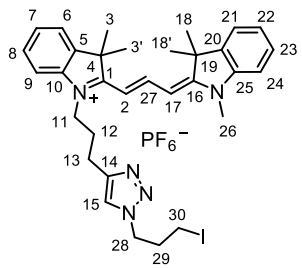
H^{27}), 3.95–3.79 (8H, m, H^{14}, $H^{14'}$, H^{30} & $H^{30'}$), 3.68 (2H, s, H^{25}), 2.22–2.11 (H^{12} & H^{28} under water peak), 1.72–1.69 (12H, s × 2, H^{3}, $H^{3'}$, H^{17} & $H^{17'}$). δ_C (126 MHz, CD_3CN): 175.6, 173.0, 151.3, 143.1, 142.1, 142.1, 141.9, 133.2, 130.8, 129.6, 126.4, 124.6, 123.3, 112.3, 112.2, 103.5, 103.5, 102.6, 79.1, 65.7, 50.3, 40.6, 40.4, 40.3, 31.4, 31.4, 28.0. HRMS (ESI$^+$) *m/z*: [M$^+$] calcd. for $C_{35}H_{43}N_2O_6^+$ 587.3104; found 587.3116.

Cy3B-acid (chloride)



To a solution of **Cy3-acetal** (1.20 g, 1.68 mmol) in chloroform (100 mL) was added aqueous sulfuric acid (50%, 20 mL). The reaction mixture was stirred at 25 °C for 30 min. The reaction mixture was then diluted with chloroform (100 mL), washed with water, and then washed with 0.5 M aqueous HCl to exchange the counterion to chloride. The organic layer was collected, dried ($MgSO_4$) and concentrated in vacuo. The crude product was purified by flash column chromatography (CH_2Cl_2 to 5% MeOH in CH_2Cl_2) to yield the product as a shiny green solid (600 mg, 57%). δ_H (500 MHz, CD_3CN): 8.10 (1H, s, H^{31}), 7.51 (1H, d, J_{HH} 7.4, H^{10}), 7.45–7.40 (2H, m, H^{8} & H^{21}), 7.34–7.27 (2H, m, H^{9} & H^{24}), 7.23 (1H, d, J_{HH} 7.7, H^{7}), 7.18 (1H, d, J_{HH} 7.9, H^{23}), 4.60 (2H, m, H^{14} & H^{30}), 4.22 (2H, m, equatorial H^{12} & H^{28}), 3.86 (2H, m, axial H^{12} & H^{28}), 3.68 (2H, s, H^{26}), 2.52 (2H, m, equatorial H^{13} & H^{29}), 1.98 (2H, m, axial H^{13} & H^{29}), 1.72 (12H, m, H^{3}, H^{4}, H^{17} & H^{18}). δ_C (126 MHz, CD_3CN): 173.2, 169.4, 169.3, 143.0, 142.1, 142.2, 141.9, 138.9, 133.5, 131.0, 129.7, 126.5, 124.6, 123.3, 111.7, 111.5, 110.7, 110.6, 70.7, 70.6, 49.7, 42.3, 42.2, 40.8, 28.3, 28.2, 27.7, 27.3, 27.2. UV-Vis (water): λ_{max} (ε) = 553 nm (156,000 mol^{-1} dm^3 cm^{-1}); fluorescence (water): λ_{em} = 564 nm; $\Phi_{fl.}$ = 63%. HRMS (ESI$^+$) *m/z*: [M$^+$] calcd. for $C_{31}H_{33}N_2O_3^+$ 481.2486; found 481.2474.

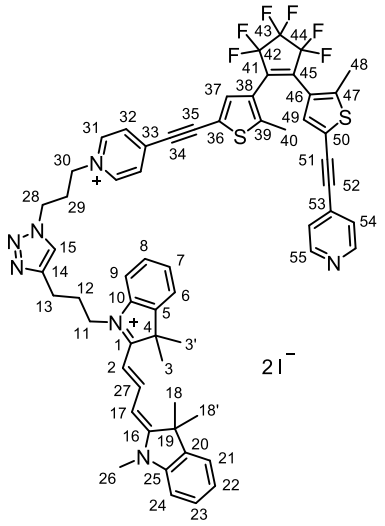
Cy3-iodo



Cy3-alkyne (500 mg, 1.12 mmol), 1-azido-3-iodopropane (**13**, 2.37 g, 11.2 mmol, 10 equiv.), copper(I) iodide (107 mg, 562 mmol, 0.5 equiv.) and DIPEA (200 μL, 1.15 mmol, 1 equiv.) were dissolved in CH_2Cl_2 (100 mL). The reaction mixture was heated at 30 °C for 40 h and concentrated in vacuo. The crude product was purified by flash column chromatography (CH_2Cl_2 1:1 EtOAc, then 1–5% MeOH in CH_2Cl_2). The purified

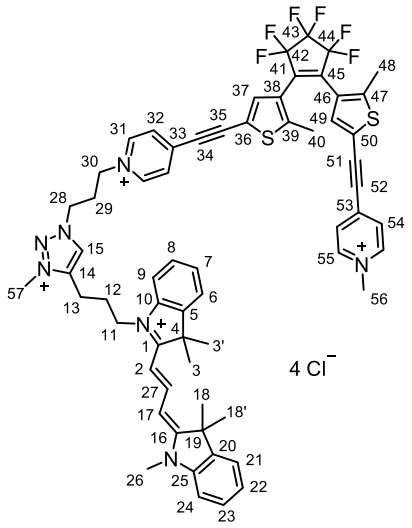
compound was dissolved in CH_2Cl_2 and washed with an aqueous solution of potassium hexafluorophosphate (5% w/v) to exchange the counterion to hexafluorophosphate. The solution was concentrated in vacuo to yield the final compound as a shiny green solid (250 mg, 30%). δ_H (500 MHz, CD_3OD): 8.54 (1H, appr. t, J_{HH} 13.5, H^{27}), 7.86 (1H, s, H^{15}), 7.58–7.28 (8H, m, H^{6-9} & H^{21-24}), 6.50–6.43 (2H, 2×d, J_{HH} 13.5, H^2 & H^{17}), 4.49 (2H, t, J_{HH} 6.7, H^{30}), 4.23 (2H, t, J_{HH} 7.6, H^{11}), 3.73 (3H, s, H^{26}), 3.18 (2H, t, J_{HH} 6.7, H^{28}), 2.92 (2H, t, J_{HH} 7.6, H^{13}), 2.38 (2H, appr. p., J_{HH} 6.7, H^{29}), 2.25 (2H, appr. p, J_{HH} 7.6, H^{12}), 1.78–1.75 (12H, 2×s, H^3, $H^{3'}$, H^{18} & $H^{18'}$); δ_C (126 MHz, CD_3OD): 176.8, 175.9, 152.1, 147.7, 144.1, 143.3, 142.1, 130.0, 129.9, 126.8, 126.7, 124.1, 123.6, 123.4, 112.4, 112.3, 104.1, 103.8, 54.8, 51.5, 50.7, 50.6, 44.6, 34.9, 32.0, 30.7, 28.3, 28.2, 27.7, 23.4. HRMS (ESI^+) *m/z*: [M^+] calcd. for $C_{32}H_{39}IN_5^+$ 620.2245; found 620.2237.

DTE-py-Cy3 (iodide)



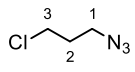
Cy3-iodo (100 mg, 134 μmol, 1 equiv.) and **DTE-dipy** (763 mg, 10 equiv.) were dissolved in DMF (20 mL). The reaction mixture was stirred at 45 °C for 45 h. Upon confirmation of full consumption of **Cy3-iodo** and the formation of the dyad by analytical HPLC (monitored at 360 nm corresponding to DTE absorption and 550 nm corresponding to cyanine absorption), the reaction mixture was concentrated in vacuo and purified by flash column chromatography (CH_2Cl_2 1:1 EtOAc, then 1–10% MeOH in CH_2Cl_2) to remove excess **DTE-dipy** used in the reaction. The purified product was dissolved in CH_2Cl_2 and the solution was washed with an aqueous solution of sodium iodide (10% w/v). The washed organic layer was concentrated in vacuo to yield the product as a black solid (55 mg, 31%). The compound was analyzed by analytical HPLC to confirm full removal of **DTE-dipy** and directly used in the next step. Analytical HPLC (Method A): t_R = 14.4 min (in both 360 nm and 550 nm channels).

DTE-Cy3



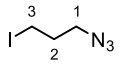
DTE-py-Cy3 iodide (30 mg, 14.8 μmol) was dissolved in a mixture of iodomethane (5 mL) and CH_2Cl_2 (5 mL). The reaction mixture was stirred at 20 °C for 3 days. Upon full consumption of the starting material **DTE-py-Cy3** and conversion into a new dyad species verified by analytical HPLC, the reaction mixture was concentrated in vacuo. The crude product was purified by reverse phase flash column chromatography (10–80% MeOH in water). The purified product was dissolved in MeCN (1 mL) and added to an aqueous solution of potassium hexafluorophosphate (5% w/v, 50 mL). The precipitate (**DTE-Cy3** as an hexafluorophosphate salt) was collected and washed with water. The resulting solid was dissolved in MeCN (1 mL) and added to a solution of tetrabutylammonium chloride in acetone (10% w/v, 20 mL). The mixture was stirred at room temperature for 18 h to exchange the counterion to chloride. The precipitate was collected to yield the product as a black solid (15 mg, 82%). δ_H (600 MHz, CD_3OD): 9.05 (2H, d, J_{HH} 7.0, H^{31}), 8.86 (2H, d, J_{HH} 6.8, H^{55}), 8.80 (1H, s, H^{15}), 8.58 (1H, appr. t, J_{HH} 13.5, H^{27}), 8.15 (2H, d, J_{HH} 7.0, H^{32}), 8.11 (2H, d, J_{HH} 6.8, H^{54}), 7.69–7.66 (2H, 2×s, H^{37} & H^{49}), 7.57–7.29 (8H, m, H^{6-9} & H^{21-24}), 6.69–6.61 (2H, 2×d, J_{HH} 13.5, H^2 & H^{17}), 4.79 (m, overlapping with water peak, confirmed with COSY, H^{30}), 4.41–4.29 (10H, m incl. 2×s, H^{11}, H^{28}, H^{56} & H^{57}), 3.73 (3H, s, H^{26}), 3.19 (2H, t, J_{HH} 8.3, H^{13}), 2.77 (2H, appr. p, J_{HH} 7.7, H^{29}), 2.34 (2H, appr. p, J_{HH} 8.3, H^{12}), 2.07–2.05 (6H, 2×s, H^{40} & H^{48}), 1.82–1.75 (12H, 2×s, H^3, $H^{3'}$, H^{18} & $H^{18'}$); δ_C (151 MHz, CD_3OD): 177.2, 175.7, 152.4, 150.1, 149.9, 146.6, 146.0, 145.5, 144.0, 143.3, 142.2, 142.1, 141.5, 140.7, 137.2, 137.0, 130.4, 130.2, 130.1, 130.0, 129.9, 127.1, 126.8, 126.7, 123.6, 123.4, 120.4, 120.3, 112.5, 112.2, 104.7, 103.7, 96.9, 96.2, 91.1, 90.9, 59.0, 51.4, 50.8, 50.5, 44.2, 38.4, 32.1, 31.4, 28.5, 28.1, 25.8, 24.8, 24.2, 21.9, 20.7, 14.8, 14.8, 13.9. UV-Vis (water): $\lambda_{max,\ DTE}$ (ε) = 377 nm (71200 mol^{-1} dm^3 cm^{-1}); $\lambda_{max,\ cyanine}$ (ε) = 541 nm (154,000 mol^{-1} dm^3 cm^{-1}); fluorescence (water): λ_{em} = 556 nm; $\Phi_{fl.}$ = 2.5%. HRMS (ESI^+) *m/z*: [M^{4+}] calcd. for $C_{63}H_{61}F_6N_7S_2^{4+}$ 273.3584; found 273.3580. Analytical HPLC (Method A): t_R = 12.6 min (in both 360 nm and 560 nm channels).

1-Azido-3-chloropropane 7



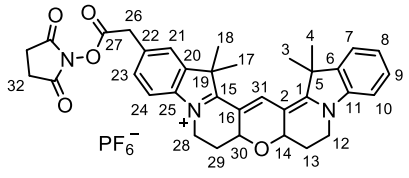
The compound was synthesized following the procedure developed by Yao and co-workers.[75] To a solution of 1-bromo-3-chloropropane (3.3 mL, 33 mmol) in DMF was added sodium azide (2.15 g, 33 mmol, 1 equiv.). The reaction mixture was stirred at 20 °C for 18 h and concentrated in vacuo. The resulting oil was dissolved in Et_2O (50 mL) and the organic solution was washed with water (3 × 50 mL). The Et_2O solution was concentrated in vacuo to yield the product as a brown oil (2.5 g, 63%). δ_H (400 MHz, $CDCl_3$): 3.63 (2H, t, J_{HH} 6.2, H^3), 3.50 (2H, t, J_{HH} 6.4, H^1), 2.02 (2H, appr. p, J_{HH} 6.3, H^2); δ_C (101 MHz, $CDCl_3$): 48.4, 41.7, 31.8.

1-Azido-3-iodopropane 8



The compound was synthesized following the procedure developed by Yao and co-workers.[75] To a solution of **7** (10.5 g, 87.8 mmol) in acetone was added sodium iodide (26.3 g, 176 mmol, 2 equiv.). The reaction mixture was stirred at reflux for 18 h and concentrated in vacuo. The resulting oil was dissolved in EtOAc and the organic solution was washed with water. The organic layer was dried ($MgSO_4$) and concentrated in vacuo. The crude product was purified by flash column chromatography (PE : EtOAc = 9 : 1) to yield the product as a pale yellow oil (13.1 g, 71%). δ_H (400 MHz, $CDCl_3$): 3.46 (2H, t, J_{HH} 6.2, H^1), 3.27 (2H, t, J_{HH} 6.4, H^3), 2.09 (2H, m, appr. p, J_{HH} 6.3, H^2); δ_C (101 MHz, $CDCl_3$): 52.0, 32.7, 2.8.

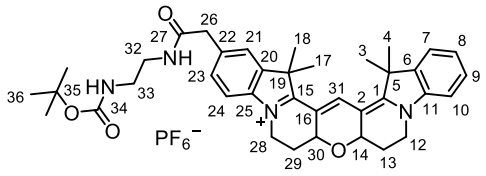
Cy3B-NHS ester (hexafluorophosphate)



Cy3B-acid (chloride, 275 mg, 534 μmol) was dissolved in MeCN and added to an aqueous solution of potassium hexafluorophosphate (5%) to exchange the counter ion to hexafluorophosphate. The precipitate (320 mg, 96%) was filtered and used in further reactions. To a solution of **Cy3B-acid** (hexafluorophosphate, 200 mg, 319 μmol) in CH_2Cl_2 (5 mL) was added DIPEA (110 μL, 638 μmol, 2 equiv.) and *N*,*N*'-disuccinimidyl carbonate (98 mg, 383 μmol, 1.2 equiv.). The reaction mixture was stirred at 25 °C for 2 h. Upon the completion verified by analytical HPLC (method A), the reaction mixture was diluted (with 50 mL CH_2Cl_2), washed with water, and then washed with an aqueous solution of KPF_6 (5% w/v). The organic layer was separated and concentrated in vacuo. The crude

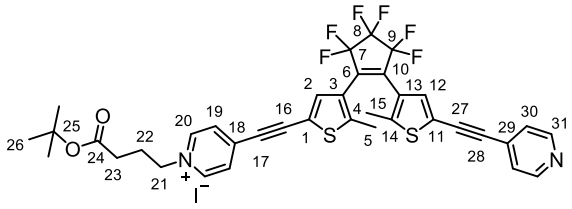
product was purified by flash column chromatography (gradient from CH_2Cl_2 to 5% MeOH in CH_2Cl_2) to yield the product as a dark brown solid (180 mg, 78%). δ_H (400 MHz, CD_3CN): 8.11 (1H, s, H^{31}), 7.54–7.19 (7H, m, H^{7-10}, H^{21}, H^{23} & H^{24}), 4.69 (2H, m, H^{14} & H^{30}), 4.23 (2H, m, equatorial H^{12} & H^{28}), 4.04 (2H, s, H^{26}), 3.87 (2H, m, axial H^{12} & H^{28}), 2.77 (4H, s, H^{32}), 2.52 (2H, m, equatorial H^{13} & H^{29}), 2.04–1.96 (2H, m, axial H^{13} & H^{29}), 1.76–1.69 (12H, m, H^3, H^4, H^{17} & H^{18}). δ_C (126 MHz, CD_3CN): 171.0, 169.7, 169.1, 168.4, 143.0, 142.6, 142.3, 141.9, 139.1, 130.9, 130.6, 129.8, 126.6, 124.5, 123.3, 111.8, 111.7, 111.0, 110.6, 70.7, 70.7, 49.8, 49.6, 42.3, 42.3, 37.9, 28.3, 28.3, 27.7, 27.6, 27.3, 27.2, 26.4. HRMS (ESI^+) *m/z*: [M^+] calcd. for $C_{35}H_{36}N_3O_5^+$ 578.2650; found 578.2631. Analytical HPLC (Method A): t_R = 12.3 min (in 560 nm channel).

Cy3B-NHBoc (hexafluorophosphate)



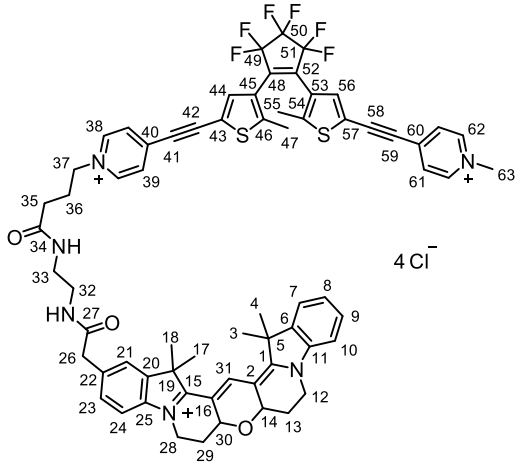
To a solution of **Cy3B-NHS ester** (270 mg, 373 μmol) in CH_2Cl_2 was added a solution of *N*-Boc-ethylenediamine (63.0 mg, 392 μmol, 1.05 equiv.). The reaction mixture was stirred at 20° C for 18 h and concentrated in vacuo. The reaction mixture was diluted with CH_2Cl_2 (50 mL) and the solution was washed with water (150 mL) and an aqueous solution of KPF_6 (4% w/v, 100 mL). The organic layer was dried ($MgSO_4$) and concentrated in vacuo. The crude product was purified by flash column chromatography (0–7% MeOH in CH_2Cl_2) to yield the product as a black solid (200 mg, 70%). δ_H (400 MHz, CD_3CN): 8.10 (1H, s, H^{31}), 7.54–7.15 (7H, m, H^{7-10}, H^{21}, H^{23} & H^{24}), 6.66 (1H, s, br, carbamate NH), 5.42 (1H, s, br, amide NH), 4.60 (2H, m, H^{14} & H^{30}), 4.22 (2H, m, equatorial H^{12} & H^{28}), 3.85 (2H, m, axial H^{12} & H^{28}), 3.51 (2H, s, H^{26}), 3.24–3.06 (4H, m, H^{32} & H^{33}), 2.53 (2H, m, equatorial H^{13} & H^{29}), 2.04–1.96 (2H, m, axial H^{13} & H^{29}), 1.74–1.70 (12H, m, H^3, H^4, H^{17} & H^{18}), 1.40 (9H, s, H^{36}); δ_C (101 MHz, CD_3CN): 171.4, 168.9, 168.8, 142.6, 141.6, 141.4, 138.4, 134.5, 130.2, 129.3, 126.0, 124.0, 122.9, 111.2, 111.1, 110.3, 110.1, 79.0, 70.3, 70.2, 54.9, 49.3, 49.2, 43.0, 41.9, 41.8, 40.7, 40.1, 28.2, 27.9, 27.9, 27.3, 27.3, 26.9. HRMS (ESI^+) *m/z*: [M^+] calcd. for $C_{35}H_{36}N_3O_5^+$ 578.2655; found 578.2648. Analytical HPLC (Method A): t_R = 12.5 min (in 560 nm channel).

DTE-COO^{t}Bu



To a solution of *t*-butyl-4-bromobutanoate (450 mg, 2.02 mmol, 1 equiv.) and potassium iodide (502 mg, 1.5 equiv.) in MeCN (50 mL) was added a solution of **DTE-dipy** (1.73 g, 3.03 mmol, 1.5 equiv.) in CH_2Cl_2 (10 mL). The reaction mixture was stirred at 65 °C for 60 h before being cooled to room temperature and concentrated in vacuo. The resulting solid was dissolved in MeCN and precipitated with CH_2Cl_2 twice to remove inorganic salts. The crude product was purified by flash column chromatography (CH_2Cl_2 1:1 EtOAc, then 1–10% MeOH in CH_2Cl_2) to yield the product as an off-white solid (310 mg, 18%). δ_H (400 MHz, CD_3CN): 8.64 (2H, d, J_{HH} 6.3, H^{20}), 8.60 (2H, d, J_{HH} 4.7, H^{31}), 7.98 (2H, d, J_{HH} 6.3, H^{19}), 7.61 (1H, s, H^2), 7.42–7.38 (3H, m, H^{12} & H^{30}), 4.52 (2H, t, J_{HH} 7.5, H^{21}), 2.34 (2H, t, J_{HH} 7.2, H^{23}), 2.19 (2H, appr. p, H^{22}), 2.06 (3H, s, H^5), 2.02 (3H, s, H^{14}), 1.42 (9H, s, H^{26}). HRMS (ESI$^+$) *m/z*: [M^+] calcd. for $C_{37}H_{31}F_6N_2O_2S_2^+$ 713.1731; found 713.1738. Analytical HPLC (Method A): t_R = 13.5 min (in 360 nm channel).

DTE-Cy3B



Deprotection of **DTE-COO^{t}Bu**: **DTE-COO^{t}Bu** (iodide, 20 mg, 24 μmol) was dissolved in a 9:1 mixture CH_2Cl_2/TFA (1 mL) and the resulting solution was stirred at 20 °C for 18 h. The solvent was evaporated under reduced pressure and the residue was co-distilled with dichloromethane (5 × 5 mL). The pale green solid and was used immediately without further purification. Analytical HPLC (Method A): t_R = 11.8 min (in 360 nm channel).

Deprotection of **Cy3B-NHBoc**: **Cy3B-NHBoc** (hexafluorophosphate, 19 mg, 24 μmol, 1 equiv.) was dissolved in a 9:1 mixture CH_2Cl_2/TFA (1 mL) and the resulting solution was stirred at 20 °C for 1.5 h. The solvent was evaporated under reduced pressure and the residue was co-distilled with dichloromethane (5 × 5 mL). Analytical HPLC (Method A): t_R = 9.5 min (in 560 nm channel).

The deprotected **DTE-COO^{t}Bu**, HBTU (10 mg, 26 μmol, 1.1 equiv.) and DIPEA (33 μL, 190 μmol, 8 equiv.) were mixed in DMF (0.5 mL). The reaction mixture for activating the carboxylic acid group was stirred at 20° C for 30 min and then transferred to the solution of deprotected **Cy3B-NHBoc** in DMF. The amide coupling reaction mixture was stirred at 20 °C for 1.5 h. Upon completion of the amide coupling reaction verified by analytical HPLC, excess iodomethane (10 mL) was added to the reaction mixture to methylate the DTE pyridine and quench the remaining DIPEA. The methylation reaction mixture was stirred at 20 °C for 40 h and then concentrated in vacuo. The resulting compound was purified by preparative HPLC (method B). The purified compound was dissolved in MeCN (1 mL) and added to an aqueous solution of KPF_6 (4% w/v, 30 mL) and stirred for 30 min. The precipitate was collected, dissolved in MeCN (1 mL) and then added to a solution of tetrabutylammonium chloride in acetone (10% w/v, 20 mL). The ion exchange reaction was stirred at 20 °C for 18 h. The precipitate was collected to yield the final product as a black solid (16 mg, 51%). δ_H (600 MHz, CD_3CN): 8.74 (2H, d, J_{HH} 6.9, H^{38}), 8.58 (2H, d, J_{HH} 6.9, H^{62}), 8.09 (1H, s, H^{31}), 7.99–7.90 (4H, m, H^{39} & H^{61}), 7.81–7.71 (2H, m, NH), 7.64–7.58 (2H, 2 × s, H^{44} & H^{56}), 7.54–7.10 (7H, m, $H^{7–10}$, H^{21}, H^{23}, H^{24} & H^{25}), 4.59 (2H, m, H^{14} & H^{30}), 4.53 (2H, t, J_{HH} 7.1, H^{37}), 7.27–7.16 (5H, m incl. s, H^{63} & equatorial H^{12} & H^{28}), 3.85 (2H, m, axial H^{12} & H^{28}), 3.54 (2H, s, H^{26}), 3.21 (4H, m, H^{32} & H^{33}), 2.52 (2H, m, equatorial H^{13} & H^{29}), 2.27 (2H, t, J_{HH} 7.1, H^{35}), 2.22 (2H, appr. p, J_{HH} 7.1, H^{36}), 2.05–2.03 (6H, 2 × s, H^{47} & H^{55}), 2.00–1.96 (2H, m, axial H^{13} & H^{29}), 1.73–1.68 (12H, 4 × s, H^3, H^4, H^{17} & H^{18}); δ_C NMR (151 MHz, CD^3CN) 172.3, 171.9, 169.4, 169.2, 160.7, 160.4, 150.1, 146.2, 145.7, 143.1, 142.0, 141.8, 141.7, 140.5, 140.3, 138.8, 136.8, 136.7, 135.4, 130.6, 129.9, 129.7, 126.4, 126.1, 124.4, 123.3, 119.8, 118.7, 116.8, 111.6, 111.4, 110.7, 110.5, 96.4, 96.3, 90.8, 90.7, 70.7, 70.7, 61.9, 49.7, 49.6, 49.1, 43.4, 42.3, 42.2, 40.0, 39.9, 34.5, 32.5, 28.4, 27.7, 27.3, 26.5, 25.8, 15.1. UV-Vis (water): $\lambda_{max,\ DTE}$ (ε) = 377 nm (69500 mol^{-1} dm^3 cm^{-1}); $\lambda_{max,\ cyanine}$ (ε) = 555 nm (158,000 mol^{-1} dm^3 cm^{-1}); fluorescence (water): λ_{em} = 564 nm; $\Phi_{fl.}$ = 61%. HRMS (ESI^+) *m/z*: [M^{3+}] calcd. for $C_{67}H_{63}F_6N_6O_3S_2^{3+}$ 392.4764, found 392.4757. Analytical HPLC (Method A): t_R = 12.8 min (in both 360 nm and 560 nm channels).

3.4 Appendix

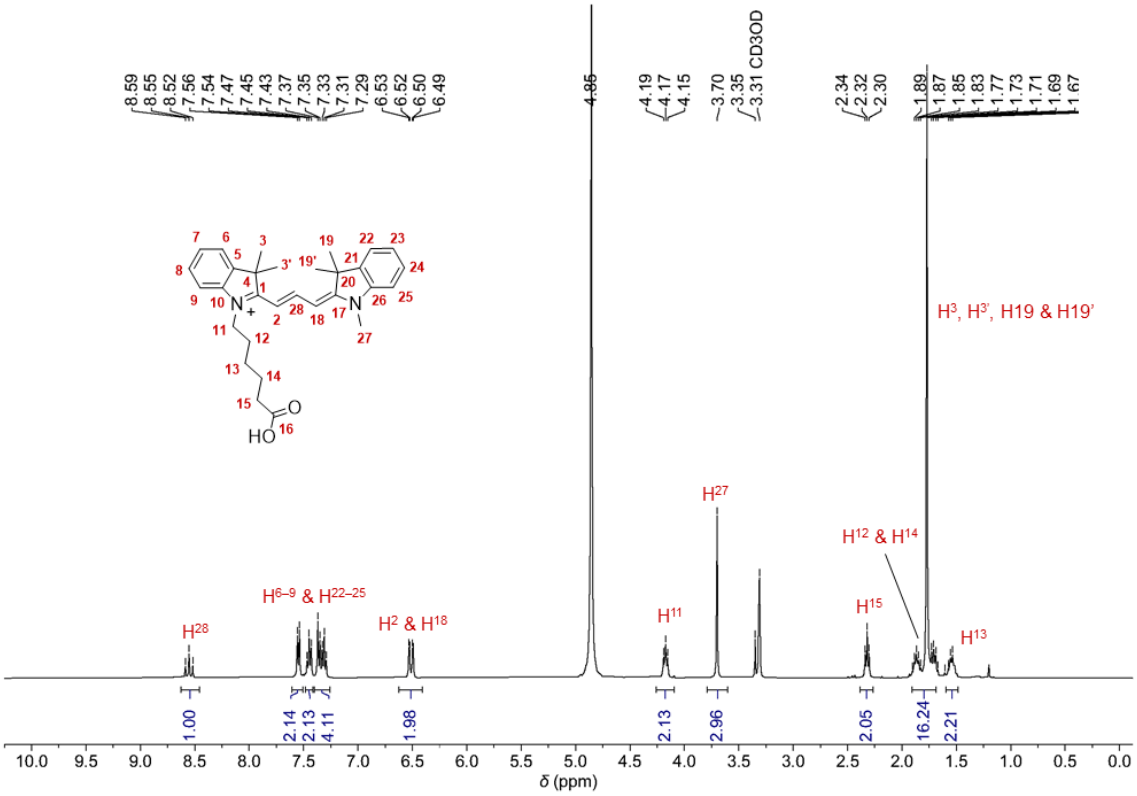


Figure 3.16 ^{1}H NMR spectrum (500 MHz, CD_3OD) of **Cy3-acid**.

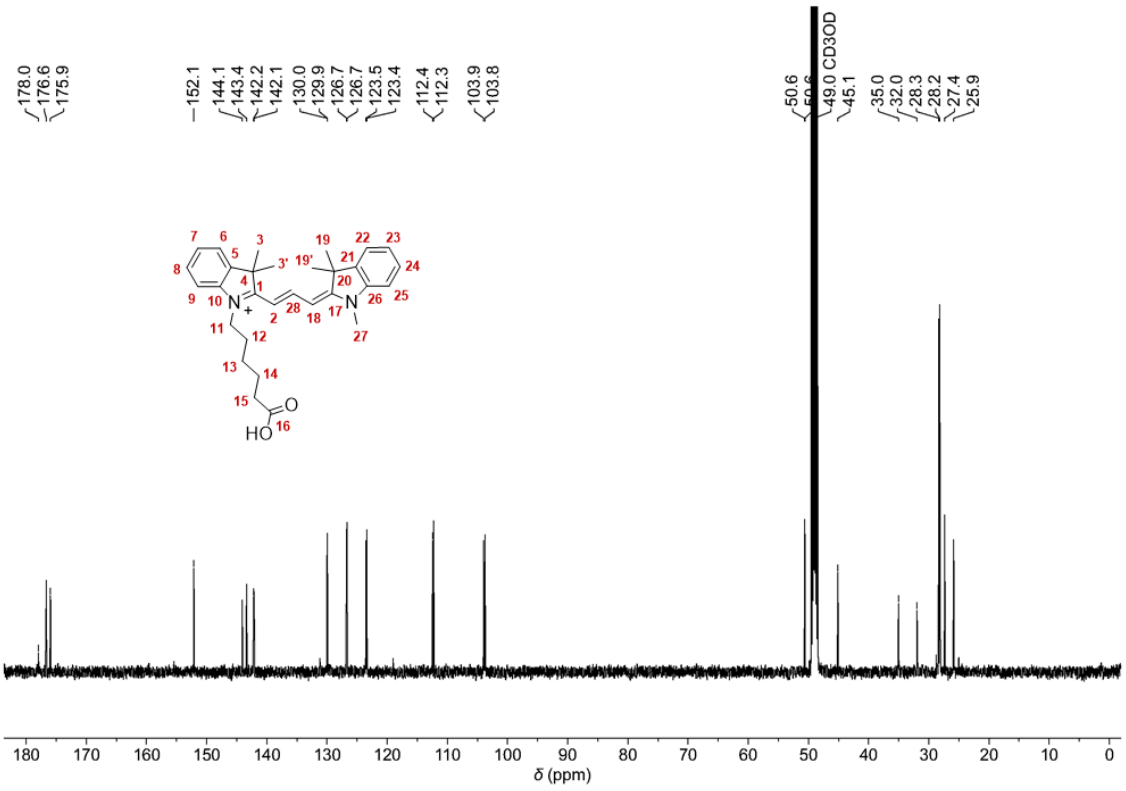


Figure 3.17 ^{13}C NMR spectrum (126 MHz, CD_3OD) of **Cy3-acid**.

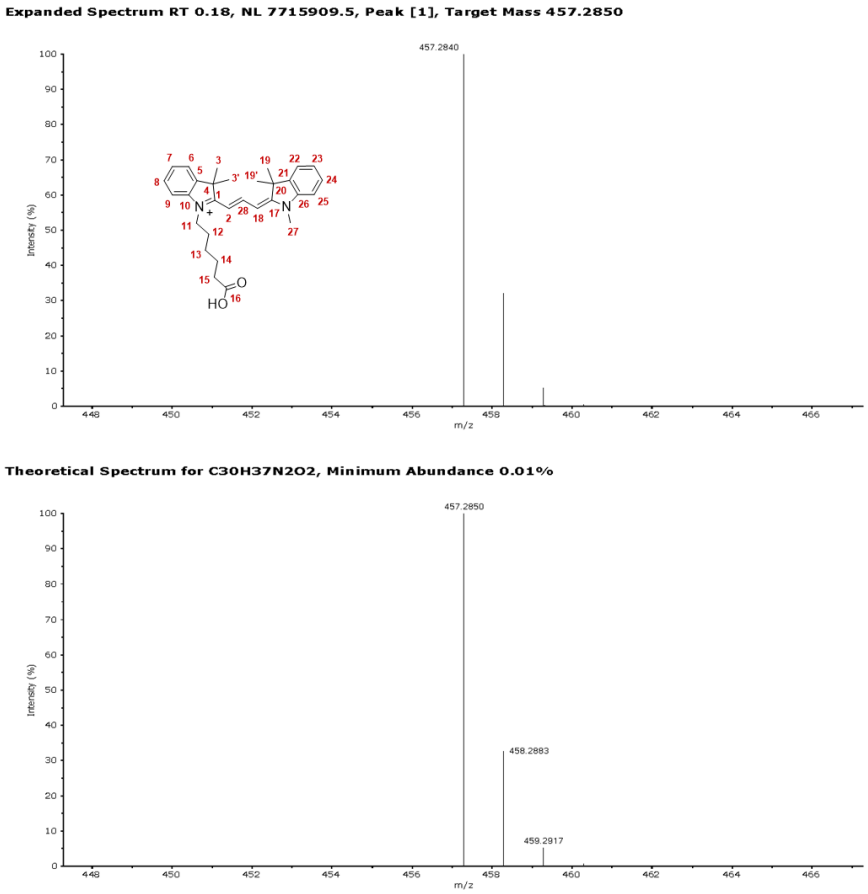


Figure 3.18 Experimental HRMS (ESI⁺) pattern of **Cy3-acid** and the theoretical pattern.

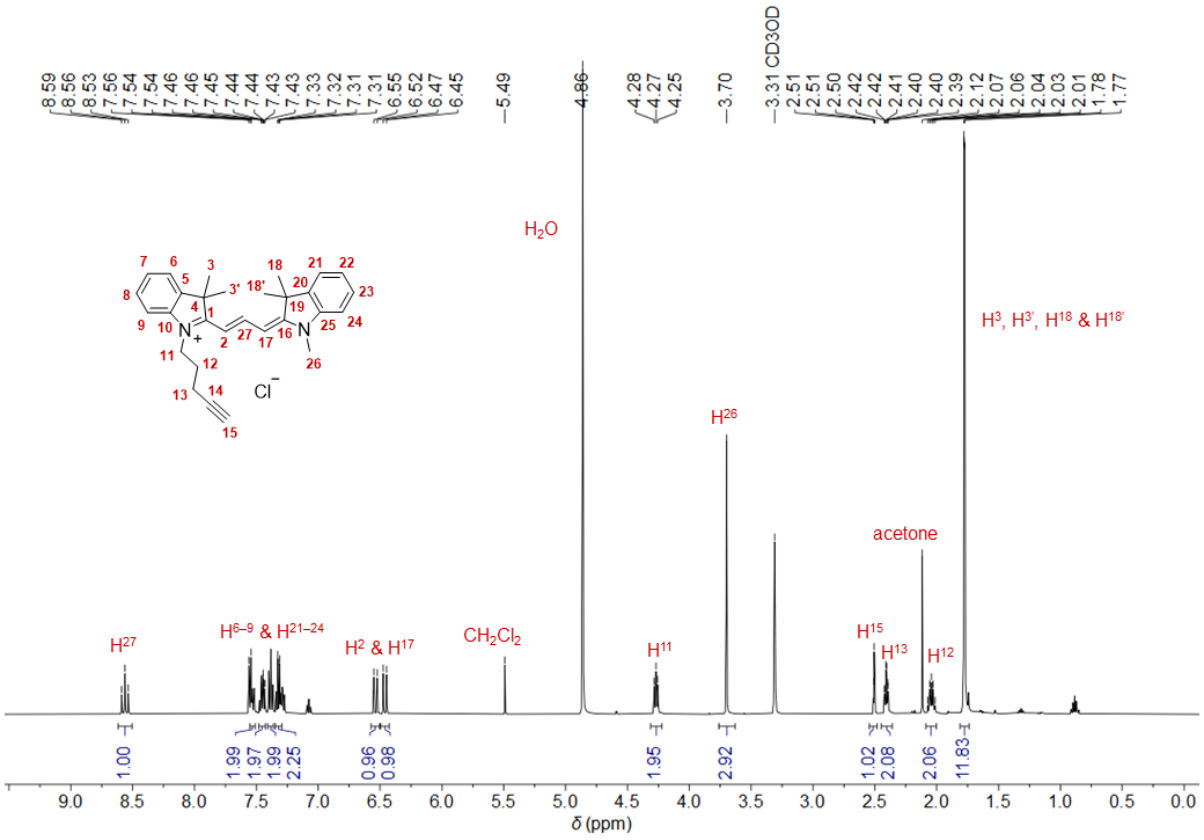


Figure 3.19 ^{1}H NMR spectrum (500 MHz, CD_3OD) of **Cy3-alkyne**.

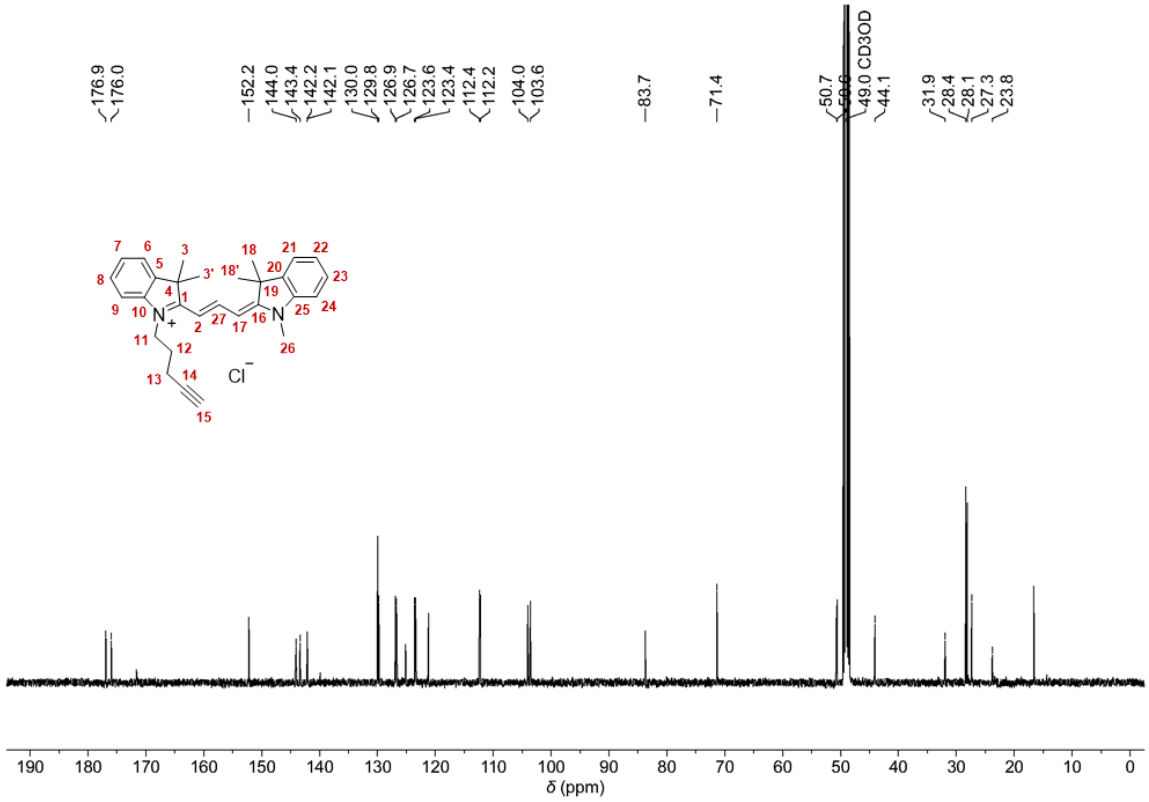


Figure 3.20 ^{13}C NMR spectrum (126 MHz, CD_3OD) of **Cy3-alkyne**.

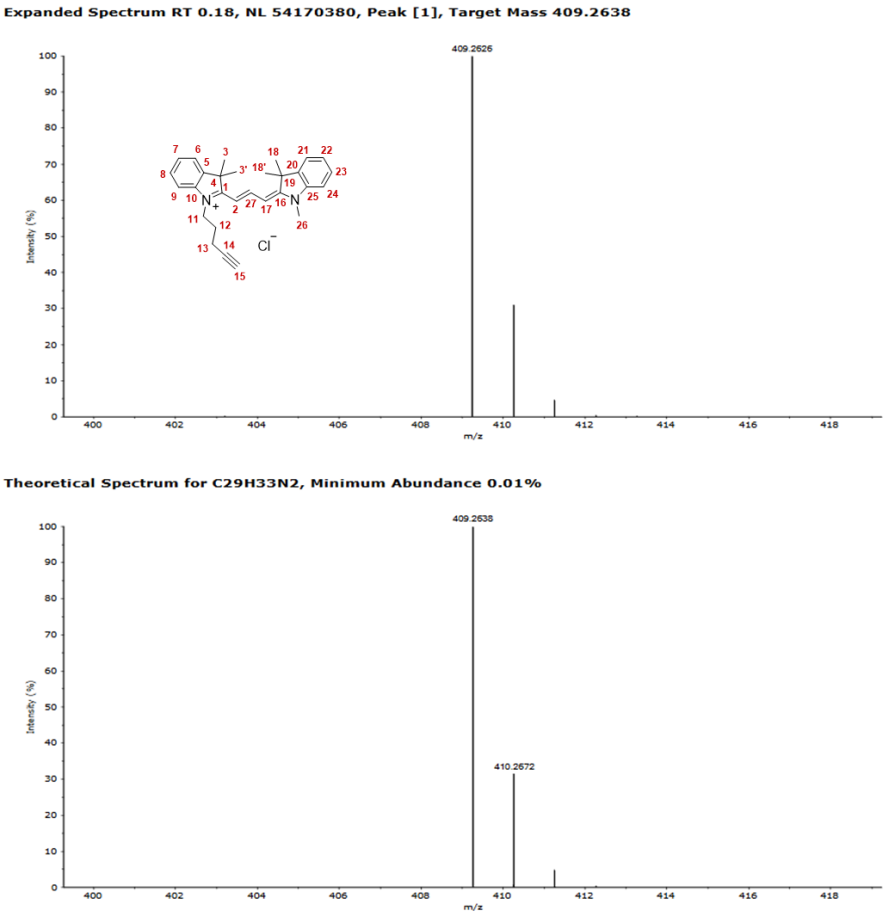


Figure 3.21 Experimental HRMS (ESI^+) pattern of **Cy3-alkyne** and the theoretical pattern.

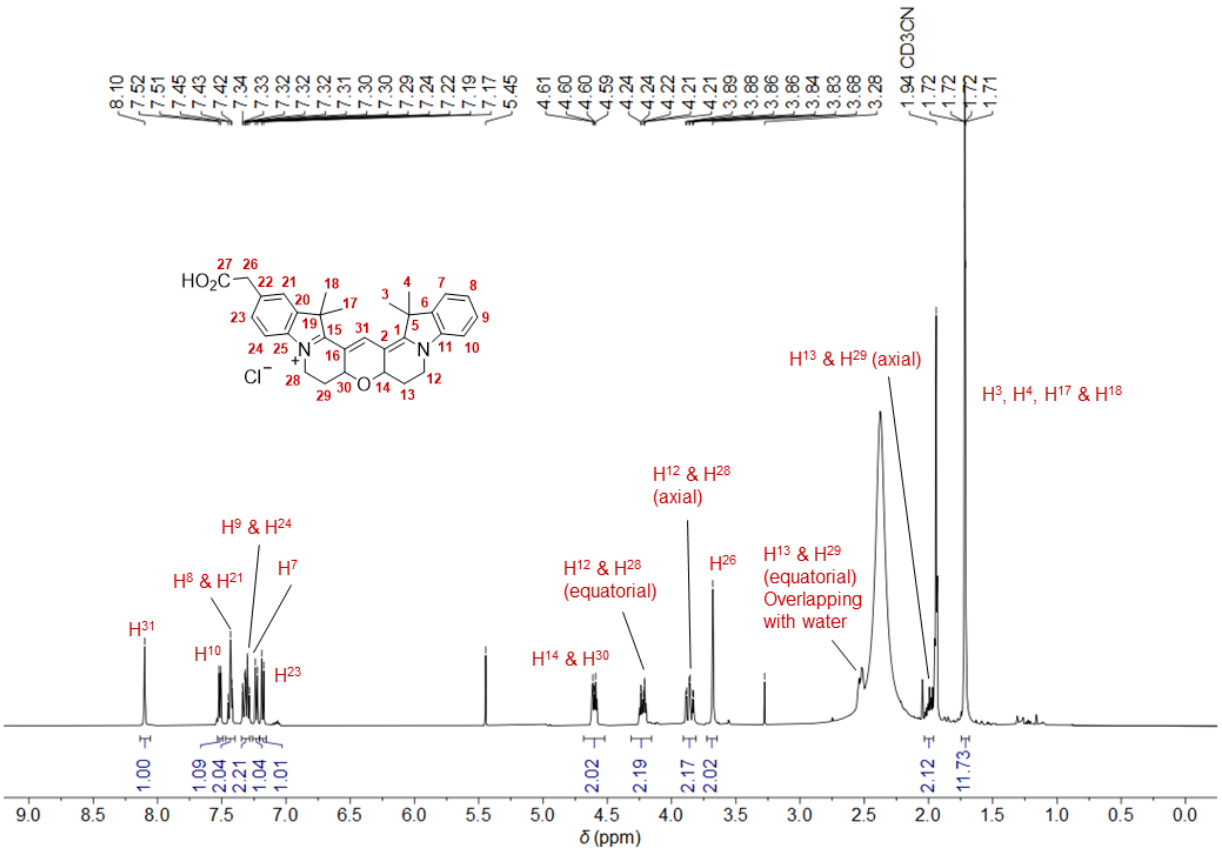


Figure 3.22 ^{1}H NMR spectrum (500 MHz, CD_3CN) of **Cy3-acid**.

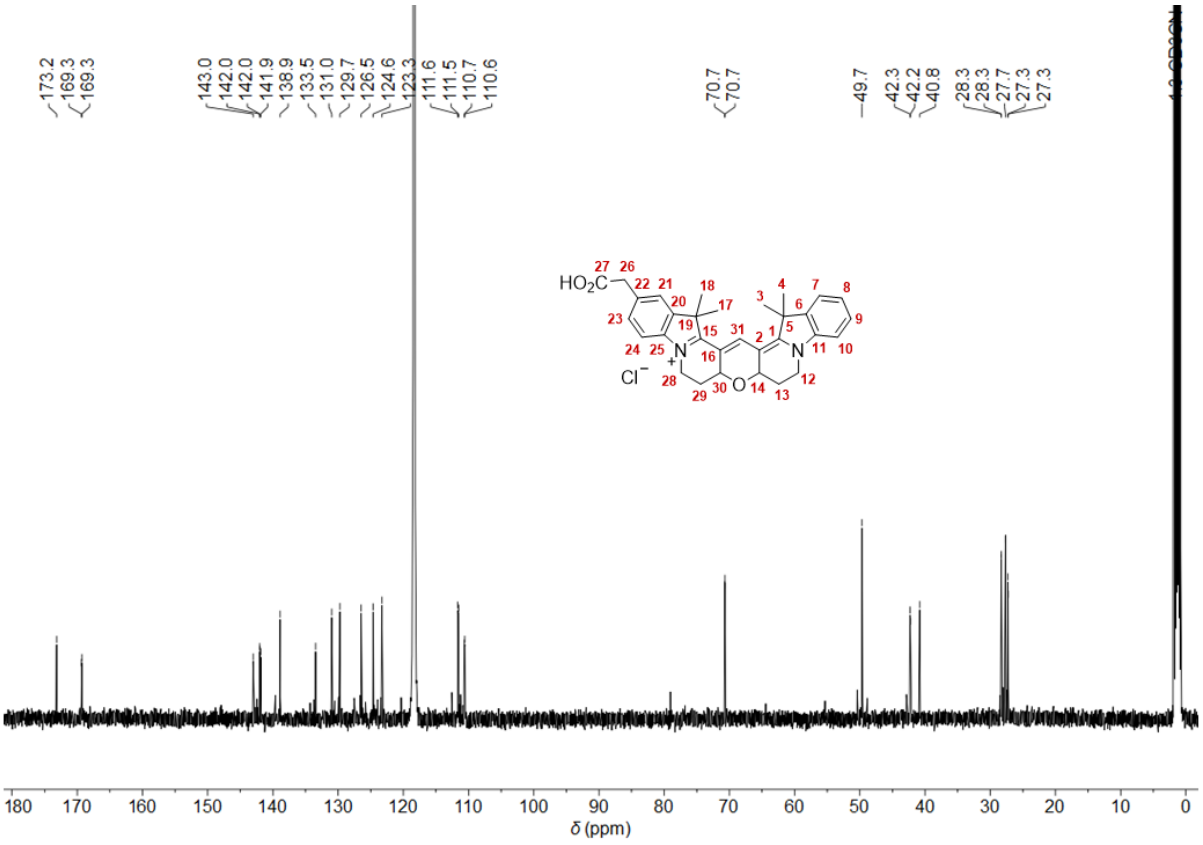


Figure 3.23 ^{13}C NMR spectrum (126 MHz, CD_3CN) of **Cy3B-acid**.

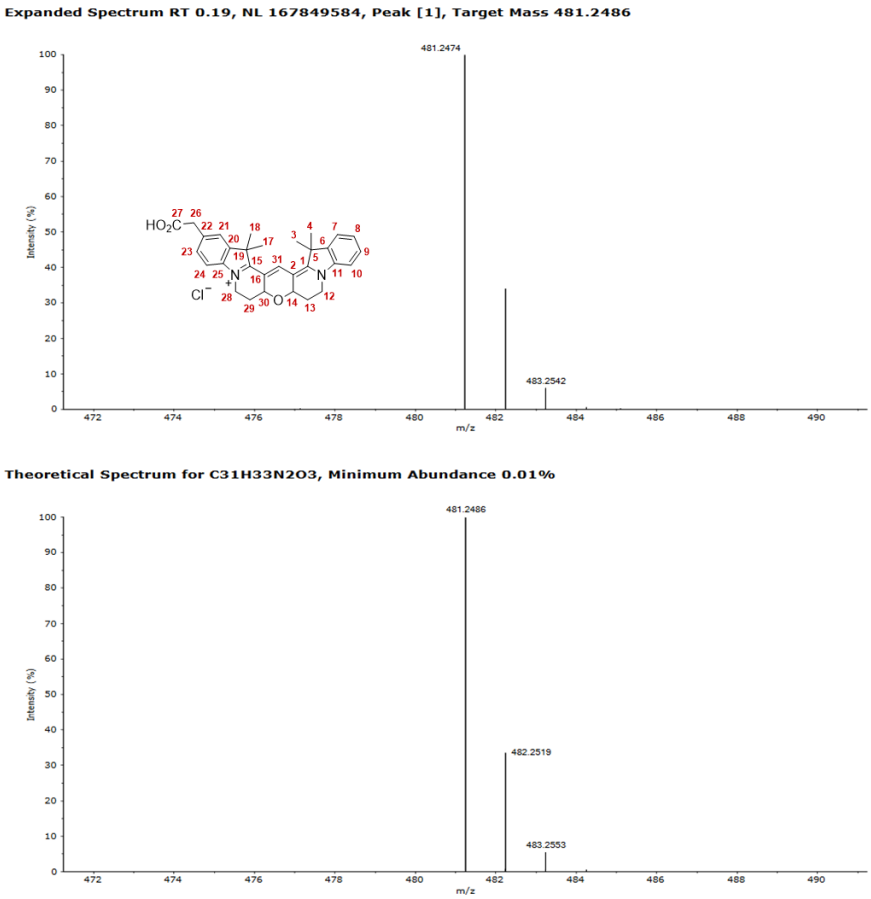


Figure 3.24 Experimental HRMS (ESI$^+$) pattern of **Cy3B-acid** and the theoretical pattern.

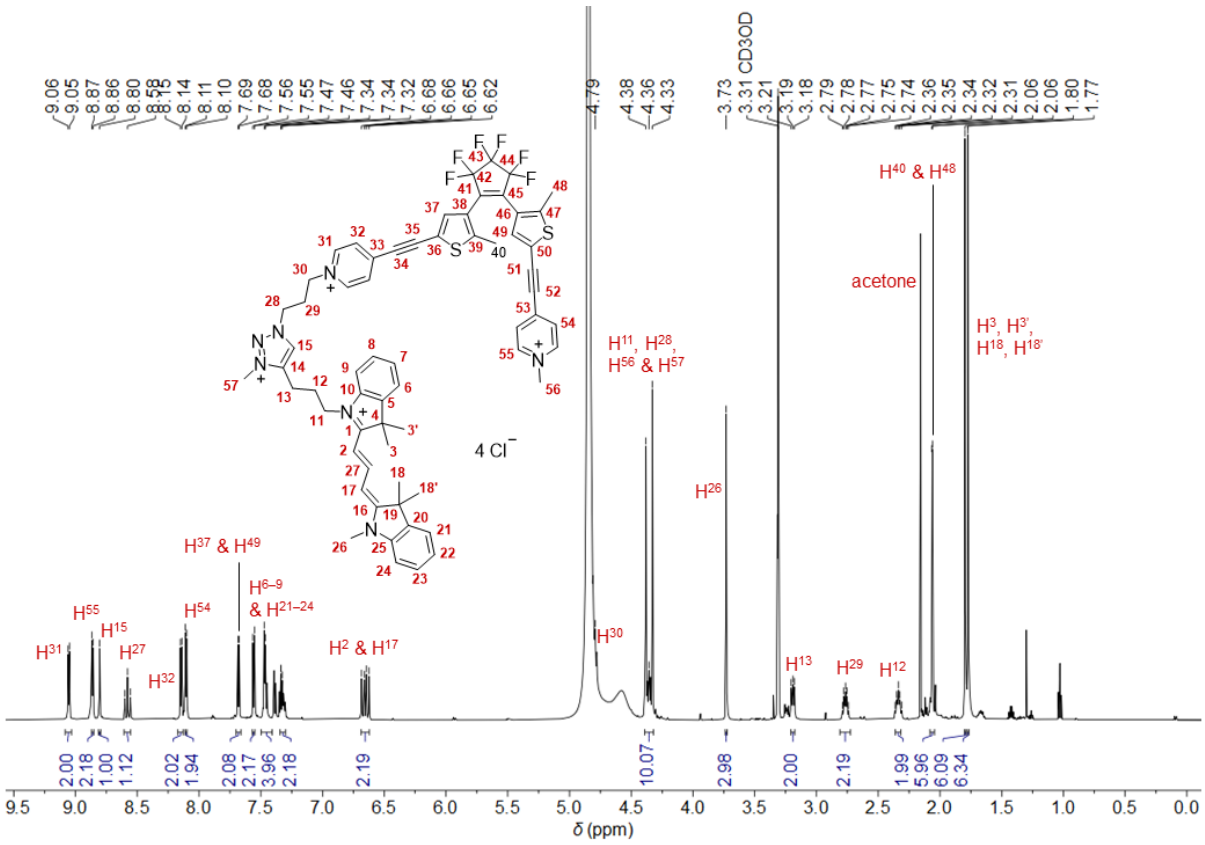


Figure 3.25 ^{1}H NMR spectrum (600 MHz, CD_3OD) of **DTE-Cy3**.

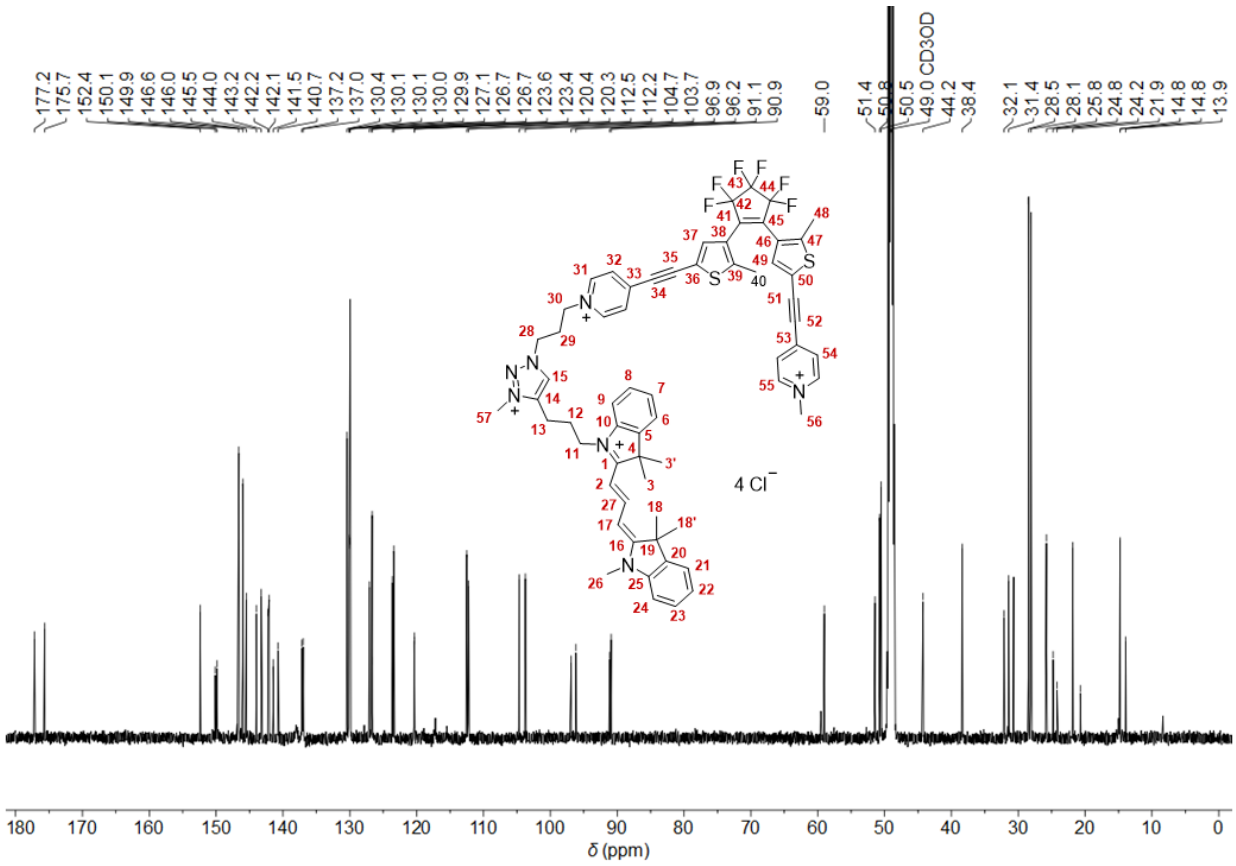


Figure 3.26 ^{13}C NMR spectrum (151 MHz, CD_3OD) of **DTE-Cy3**.

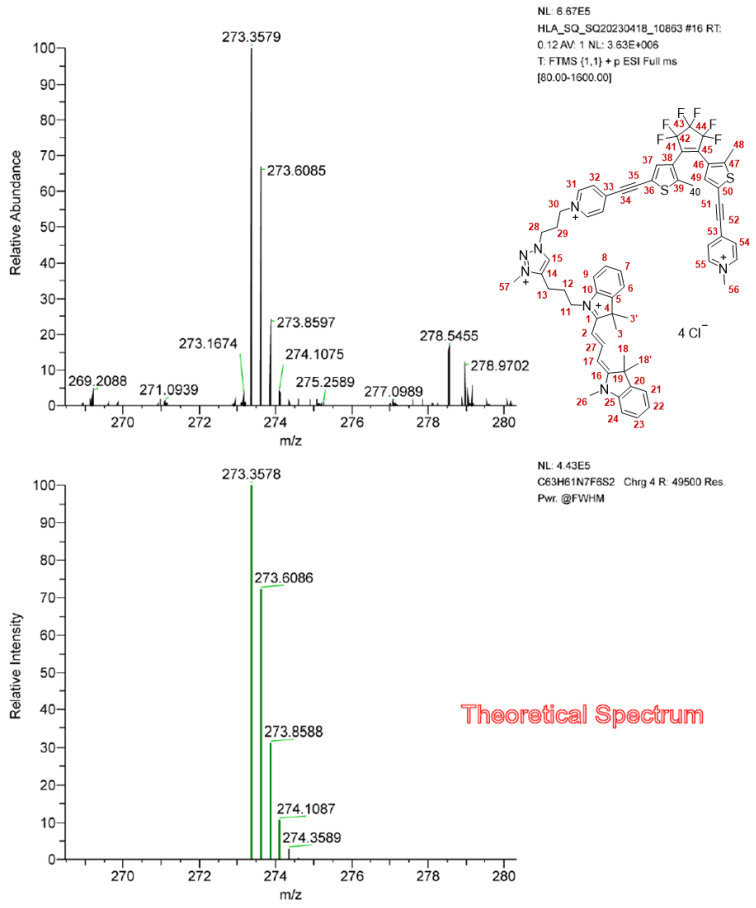


Figure 3.27 Experimental HRMS (ESI$^+$) pattern of **Cy3-acid** and the theoretical pattern.

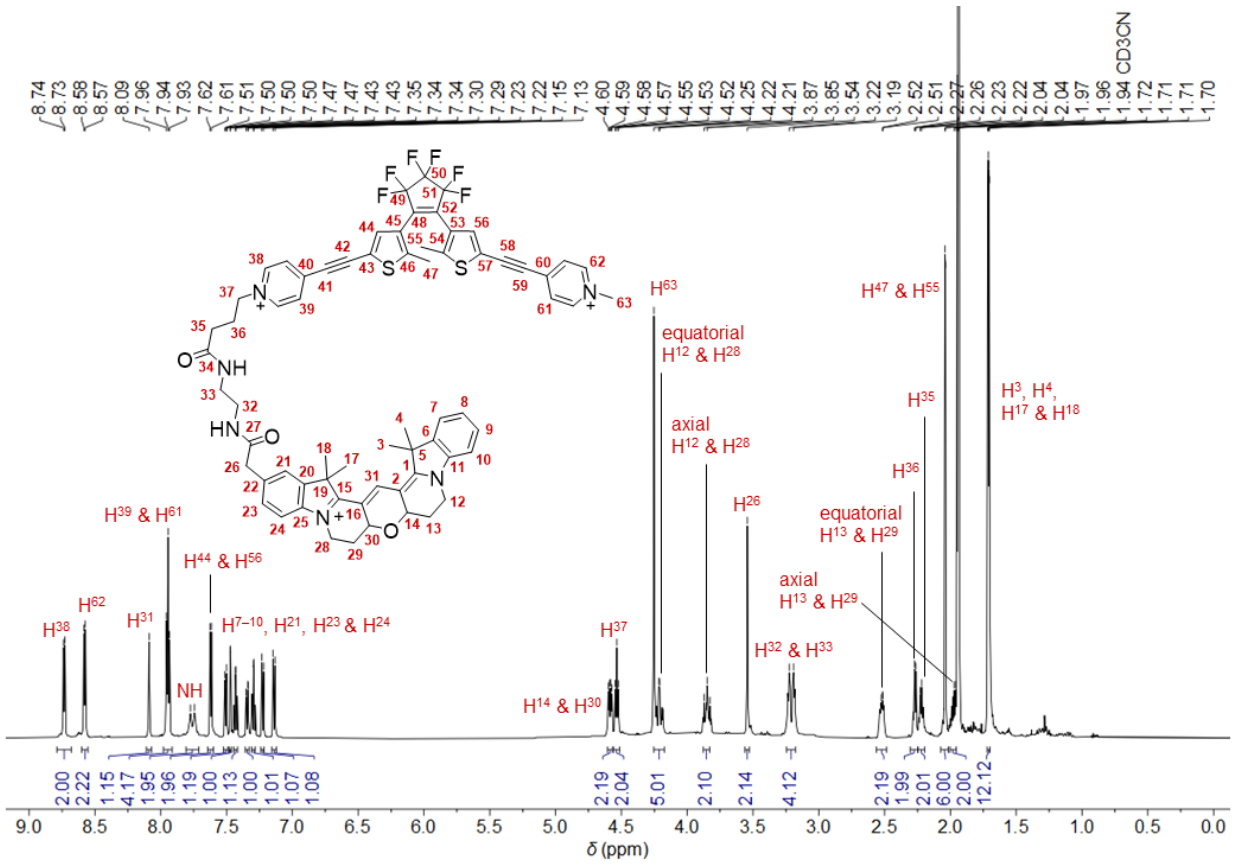


Figure 3.28 ^{1}H NMR spectrum (600 MHz, CD_3CN) of **DTE-Cy3B**.

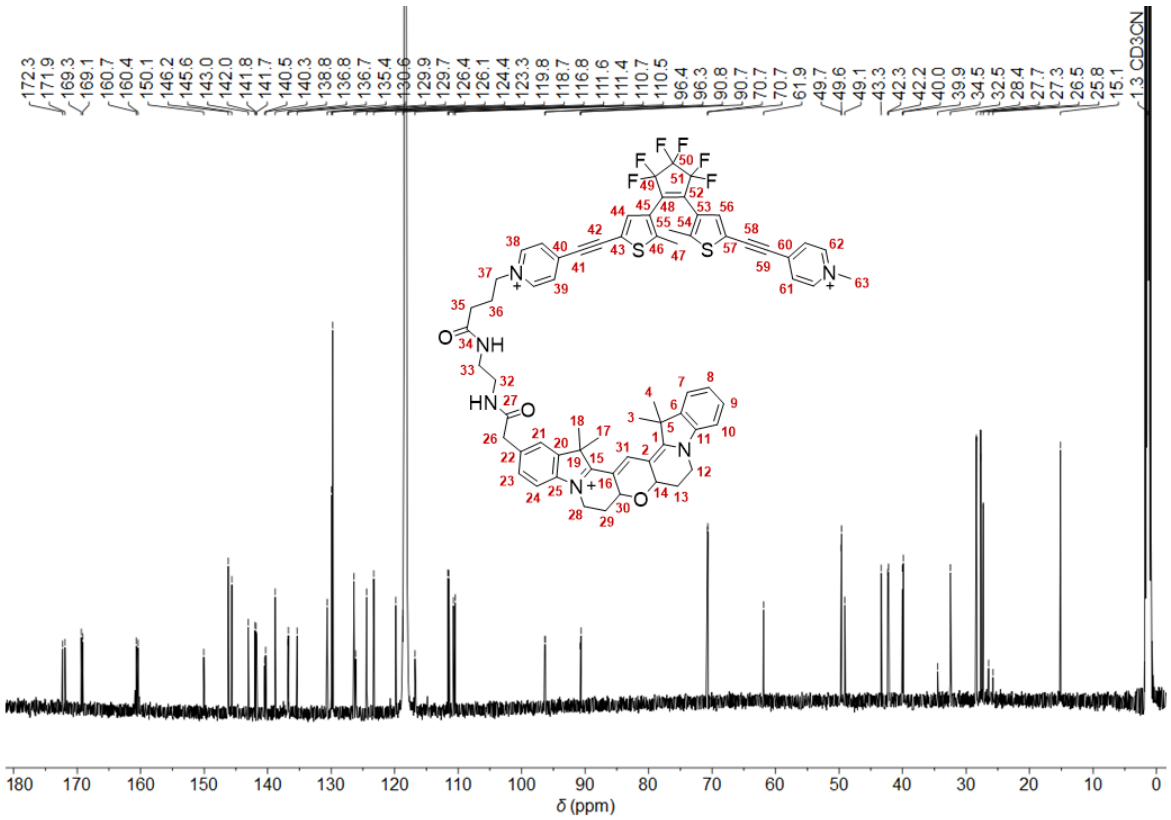


Figure 3.29 ^{13}C NMR spectrum (151 MHz, CD_3CN) of **DTE-Cy3B**.

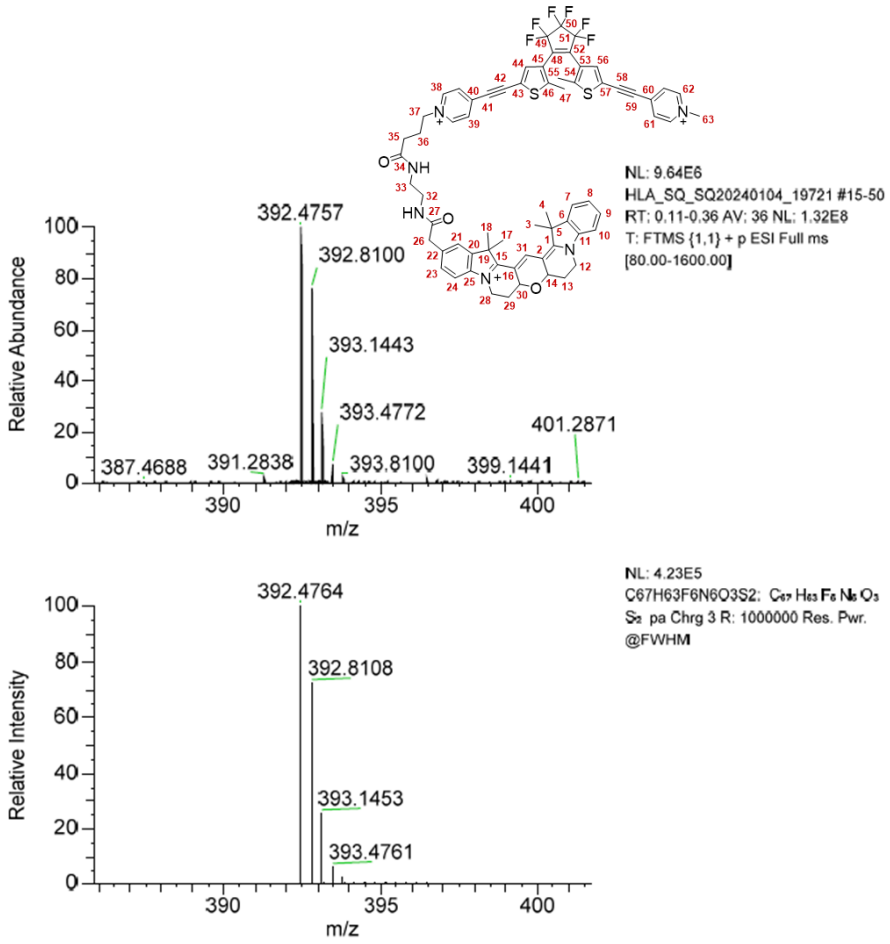


Figure 3.30 Experimental HRMS (ESI$^+$) pattern of **Cy3B-acid** and the theoretical pattern.

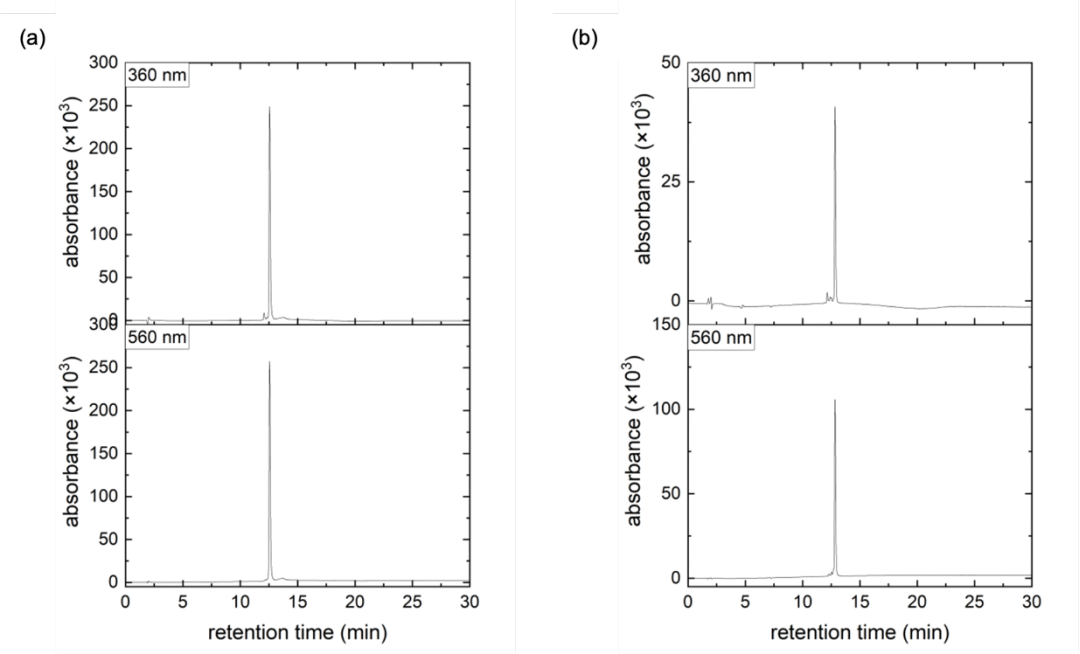


Figure 3.31 Analytical HPLC trace (method A) of (a) **DTE-Cy3** and (b) **DTE-Cy3B** monitored at 360 nm (DTE absorption range) and 560 nm (Cy3 absorption range).

References

1. M. Kasha, *Discussions of the Faraday Society*, 1950, **9**.
2. P. Atkins and J. de Paula, *Atkins' Physical Chemistry*, Oxford University Press, Oxford, 2014.
3. J. R. Lakowicz, *Principles of Fluorescence Spectroscopy*, Springer, 2006.
4. G. Christoph, Photoactivatable, Photoconvertible, and Photoswitchable Fluorescent Proteins, https://www.leica-microsystems.com/science-lab/life-science/photoactivatable-photoconvertible-and-photoswitchable-fluorescent-proteins/, (accessed 2 July, 2024).
5. A. P. de Silva and R. A. D. D. Rupasinghe, *J. Chem. Soc., Chem. Commun.*, 1985.
6. Y. Urano, D. Asanuma, Y. Hama, Y. Koyama, T. Barrett, M. Kamiya, T. Nagano, T. Watanabe, A. Hasegawa, P. L. Choyke and H. Kobayashi, *Nat. Med.*, 2009, **15**, 104–109.
7. T. Doura, M. Kamiya, F. Obata, Y. Yamaguchi, T. Y. Hiyama, T. Matsuda, A. Fukamizu, M. Noda, M. Miura and Y. Urano, *Angew. Chem., Int. Ed.*, 2016, **55**, 9620–9624.
8. M. Kamiya, D. Asanuma, E. Kuranaga, A. Takeishi, M. Sakabe, M. Miura, T. Nagano and Y. Urano, *J. Am. Chem. Soc.*, 2011, **133**, 12960–12963.
9. Y. Xiong, A. Vargas Jentzsch, J. W. M. Osterrieth, E. Sezgin, I. V. Sazanovich, K. Reglinski, S. Galiani, A. W. Parker, C. Eggeling and H. L. Anderson, *Chem. Sci.*, 2018, **9**, 3029–3040.
10. R. Kashihara, M. Morimoto, S. Ito, H. Miyasaka and M. Irie, *J. Am. Chem. Soc.*, 2017, **139**, 16498–16501.
11. M. Born and E. Wolf, *Principles of Optics*, Cambridge University Press, Cambridge, 1999.
12. E. Abbe, *Archiv für Mikroskopische Anatomie*, 1873, **9**, 413-468.
13. S. W. Hell, *Angew. Chem., Int. Ed.*, 2015, **54**, 8054–8066.
14. E. Betzig, *Angew. Chem., Int. Ed.*, 2015, **54**, 8034–8053.
15. W. E. Moerner, *Angew. Chem., Int. Ed.*, 2015, **54**, 8067–8093.
16. L. Schermelleh, A. Ferrand, T. Huser, C. Eggeling, M. Sauer, O. Biehlmaier and G. P. C. Drummen, *Nat. Cell. Biol.*, 2019, **21**, 72–84.
17. R. Heintzmann and T. Huser, *Chem. Rev.*, 2017, **117**, 13890–13908.
18. X. Chen, S. Zhong, Y. Hou, R. Cao, W. Wang, D. Li, Q. Dai, D. Kim and P. Xi, *Light: Sci. Appl.*, 2023, **12**, 172.
19. M. G. L. Gustafsson, L. Shao, P. M. Carlton, C. J. R. Wang, I. N. Golubovskaya, W. Z. Cande, D. A. Agard and J. W. Sedat, *Biophys. J.*, 2008, **94**, 4957–4970.
20. P. Kner, B. B. Chhun, E. R. Griffis, L. Winoto and M. G. L. Gustafsson, *Nat. Methods*, 2009, **6**, 339–342.
21. L. Schermelleh, P. M. Carlton, S. Haase, L. Shao, L. Winoto, P. Kner, B. Burke, M. C. Cardoso, D. A. Agard, M. G. L. Gustafsson, H. Leonhardt and J. W. Sedat, *Science*, 2008, **320**, 1332–1336.
22. A. G. York, S. H. Parekh, D. D. Nogare, R. S. Fischer, K. Temprine, M. Mione, A. B. Chitnis, C. A. Combs and H. Shroff, *Nat. Methods*, 2012, **9**, 749–754.
23. A. G. York, P. Chandris, D. D. Nogare, J. Head, P. Wawrzusin, R. S. Fischer, A. Chitnis and H. Shroff, *Nat. Methods*, 2013, **10**, 1122–1126.
24. Y. Ma, K. Wen, M. Liu, J. Zheng, K. Chu, Z. J. Smith, L. Liu and P. Gao, *JPhys Photonics*, 2021, **3**, 024009.
25. M. J. Rust, M. Bates and X. Zhuang, *Nat. Methods*, 2006, **3**, 793–796.
26. E. Betzig, G. H. Patterson, R. Sougrat, O. W. Lindwasser, S. Olenych, J. S. Bonifacino, M. W. Davidson, J. Lippincott-Schwartz and H. F. Hess, *Science*, 2006, **313**, 1642–1645.
27. S. T. Hess, T. P. K. Girirajan and M. D. Mason, *Biophys. J.*, 2006, **91**, 4258–4272.

28. S. van de Linde, M. Heilemann and M. Sauer, *Annu. Rev. Phys. Chem.*, 2012, **63**, 519–540.
29. S. van de Linde, A. Löschberger, T. Klein, M. Heidbreder, S. Wolter, M. Heilemann and M. Sauer, *Nat. Protoc.*, 2011, **6**, 991–1009.
30. J. Demmerle, E. Wegel, L. Schermelleh and I. M. Dobbie, *Methods*, 2015, **88**, 3–10.
31. H. Deschout, F. C. Zanacchi, M. Mlodzianoski, A. Diaspro, J. Bewersdorf, S. T. Hess and K. Braeckmans, *Nat. Methods*, 2014, **11**, 253–266.
32. D. Baddeley and J. Bewersdorf, *Annu. Rev. Biochem.*, 2018, **87**, 965–989.
33. D. L. H. v. d. Haven, Master, Eindhoven University of Technology, 2020.
34. L. Gagnon, *Microsc. Today*, 2023, **31**, 14–23.
35. G. T. Dempsey, M. Bates, W. E. Kowtoniuk, D. R. Liu, R. Y. Tsien and X. Zhuang, *J. Am. Chem. Soc.*, 2009, **131**, 18192–18193.
36. H. Li and J. C. Vaughan, *Chem. Rev.*, 2018, **118**, 9412–9454.
37. M. Lelek, M. T. Gyparaki, G. Beliu, F. Schueder, J. Griffié, S. Manley, R. Jungmann, M. Sauer, M. Lakadamyali and C. Zimmer, *Nat. Rev. Methods Primers*, 2021, **1**, 39.
38. C. Eggeling, K. I. Willig, S. J. Sahl and S. W. Hell, *Q. Rev. Biophys.*, 2015, **48**, 178–243.
39. H. Blom and J. Widengren, *Chem. Rev.*, 2017, **117**, 7377–7427.
40. H. Blom and J. Widengren, *Curr. Opin. Chem. Biol.*, 2014, **20**, 127–133.
41. E. Wegel, A. Göhler, B. C. Lagerholm, A. Wainman, S. Uphoff, R. Kaufmann and I. M. Dobbie, *Sci. Rep.*, 2016, **6**, 27290.
42. M. Hofmann, C. Eggeling, S. Jakobs and S. W. Hell, *Proc. Natl. Acad. Sci. U. S. A.*, 2005, **102**, 17565–17569.
43. J. Kwon, J. Hwang, J. Park, G. R. Han, K. Y. Han and S. K. Kim, *Sci. Rep.*, 2015, **5**, 17804.
44. T. Salditt, A. Egner and D. R. Luke, *Nanoscale Photonic Imaging*, Springer, New York, 2020.
45. S. Wäldchen, J. Lehmann, T. Klein, S. van de Linde and M. Sauer, *Sci. Rep.*, 2015, **5**, 15348.
46. J. Woodhouse, G. Nass Kovacs, N. Coquelle, L. M. Uriarte, V. Adam, T. R. M. Barends, M. Byrdin, E. de la Mora, R. Bruce Doak, M. Feliks, M. Field, F. Fieschi, V. Guillon, S. Jakobs, Y. Joti, P. Macheboeuf, K. Motomura, K. Nass, S. Owada, C. M. Roome, C. Ruckebusch, G. Schirò, R. L. Shoeman, M. Thepaut, T. Togashi, K. Tono, M. Yabashi, M. Cammarata, L. Foucar, D. Bourgeois, M. Sliwa, J.-P. Colletier, I. Schlichting and M. Weik, *Nat. Commun.*, 2020, **11**.
47. V. Adam, K. Hadjidemetriou, N. Jensen, R. L. Shoeman, J. Woodhouse, A. Aquila, A. S. Banneville, T. R. M. Barends, V. Bezchastnov, S. Boutet, M. Byrdin, M. Cammarata, S. Carbajo, N. Eleni Christou, N. Coquelle, E. De la Mora, M. El Khatib, T. Moreno Chicano, R. Bruce Doak, F. Fieschi, L. Foucar, O. Glushonkov, A. Gorel, M. L. Grünbein, M. Hilpert, M. Hunter, M. Kloos, J. E. Koglin, T. J. Lane, M. Liang, A. Mantovanelli, K. Nass, G. Nass Kovacs, S. Owada, C. M. Roome, G. Schirò, M. Seaberg, M. Stricker, M. Thépaut, K. Tono, K. Ueda, L. M. Uriarte, D. You, N. Zala, T. Domratcheva, S. Jakobs, M. Sliwa, I. Schlichting, J. P. Colletier, D. Bourgeois and M. Weik, *ChemPhysChem*, 2022, **23**, e202200192.
48. T. Grotjohann, I. Testa, M. Leutenegger, H. Bock, N. T. Urban, F. Lavoie-Cardinal, K. I. Willig, C. Eggeling, S. Jakobs and S. W. Hell, *Nature*, 2011, **478**, 204–208.
49. T. Grotjohann, I. Testa, M. Reuss, T. Brakemann, C. Eggeling, S. W. Hell and S. Jakobs, *eLife*, 2012, **1**, e00248.
50. C. Gregor, S. C. Sidenstein, M. Andresen, S. J. Sahl, J. G. Danzl and S. W. Hell, *Sci. Rep.*, 2018, **8**, 2724.
51. F. Lavoie-Cardinal, N. A. Jensen, V. Westphal, A. C. Stiel, A. Chmyrov, J. Bierwagen, I. Testa, S. Jakobs and S. W. Hell, *ChemPhysChem*, 2014, **15**, 655–663.

52. F. Pennacchietti, E. O. Serebrovskaya, A. R. Faro, I. I. Shemyakina, N. G. Bozhanova, A. A. Kotlobay, N. G. Gurskaya, A. Bodén, J. Dreier, D. M. Chudakov, K. A. Lukyanov, V. V. Verkhusha, A. S. Mishin and I. Testa, *Nat. Methods*, 2018, **15**, 601–604.
53. M. Barbry, P. Koval, F. Marchesin, R. Esteban, A. G. Borisov, J. Aizpurua and D. Sánchez-Portal, *Nano. Lett.*, 2015, **15**, 3410–3419.
54. L. Tang and C. Fang, *Int. J. Mol. Sci.*, 2022, **23**, 6459.
55. T. J. Chozinski, L. A. Gagnon and J. C. Vaughan, *FEBS Lett.*, 2014, **588**, 3603–3612.
56. Y. Xiong, P. Rivera-Fuentes, E. Sezgin, A. Vargas Jentzsch, C. Eggeling and H. L. Anderson, *Org. Lett.*, 2016, **18**, 3666–3669.
57. A. T. Frawley, V. Wycisk, Y. Xiong, S. Galiani, E. Sezgin, I. Urbancic, A. Vargas Jentzsch, K. G. Leslie, C. Eggeling and H. L. Anderson, *Chem. Sci.*, 2020, **11**, 8955–8960.
58. H. C. Ishikawa-Ankerhold, R. Ankerhold and G. P. C. Drummen, *Molecules*, 2012, **17**, 4047–4132.
59. N. Cai, A. C.-K. Lai, K. Liao, P. R. Corridon, D. J. Graves and V. Chan, *Polymers*, 2022, **14**, 1913.
60. D. Axelrod, D. E. Koppel, J. Schlessinger, E. Elson and W. W. Webb, *Biophys. J.*, 1976, **16**, 1055–1069.
61. G. H. Patterson and J. Lippincott-Schwartz, *Science*, 2002, **297**, 1873–1877.
62. K. G. Leslie, DPhil, University of Oxford, 2023.
63. R. F. Kubin and A. N. Fletcher, *J. Lumin.*, 1982, **27**, 455–462.
64. D. N. Rao, X. Ji and S. C. Miller, *Chem. Sci.*, 2022, **13**, 6081–6088.
65. Y. Xiong, DPhil, University of Oxford, 2018.
66. S. Miao, Y. Liang, I. Marathe, J. Mao, C. DeSantis and D. Bong, *J. Am. Chem. Soc.*, 2019, **141**, 9365–9372.
67. M. Gerowska, L. Hall, J. Richardson, M. Shelbourne and T. Brown, *Tetrahedron*, 2012, **68**, 857–864.
68. L. M. Hall, M. Gerowska and T. Brown, *Nucleic Acids Res.*, 2012, **40**, e108.
69. M. M. Ahlström, M. Ridderström, I. Zamora and K. Luthman, *J. Med. Chem.*, 2007, **50**, 4444–4452.
70. *United States Pat.,* 2003, US20030224391A1.
71. M. E. Sanborn, B. K. Connolly, K. Gurunathan and M. Levitus, *J. Phys. Chem. B*, 2007, **111**, 11064–11074.
72. E. Sandberg, J. Piguet, U. Kostiv, G. Baryshnikov, H. Liu and J. Widengren, *J. Phys. Chem. B*, 2023, **127**, 3208–3222.
73. F. Momicchioli, I. Baraldi and G. Berthier, *Chem. Phys.*, 1988, **123**, 103–112.
74. T. R. Evans, *J. Photochem.*, 1982, **19**, 55–58.
75. L. Yao, B. T. Smith and J. Aubé, *J. Org. Chem.*, 2004, **69**, 1720–1722.
76. S. Qiu, A. T. Frawley, K. G. Leslie and H. L. Anderson, *Chem. Sci.*, 2023, **14**, 9123–9135.
77. M. V. Kvach, A. V. Ustinov, I. A. Stepanova, A. D. Malakhov, M. V. Skorobogatyi, V. V. Shmanai and V. A. Korshun, *Eur. J. Org. Chem.*, 2008, **2008**, 2107–2117.
78. Z. Ziani, S. Cobo, F. Loiseau, D. Jouvenot, E. Lognon, M. Boggio-Pasqua and G. Royal, *JACS Au*, 2023, **3**, 131–142.
79. *United States Pat.,* 2019, US10473666B2.

4

Photoswitchable DNA G-Quadruplex Ligands

Contents

4.1 Introduction 225

4.1.1 Photopharmacology 225

4.1.2 Azobenzene-Based Agents 229

4.1.3 Agents Bearing Diarylethenes 230

4.1.4 Diarylethenes Targeting DNA G-Quadruplex 233

4.1.5 Project Aim 234

4.2 Results and Discussion 235

4.2.1 Synthesis of DTEs 235

4.2.2 UV-vis Absorption 237

4.2.3 Photostationary State Distribution 238

4.2.4 Photoswitching Quantum Yields 240

4.2.5 Fluorescence Quenching Assay 241

4.2.6 Circular Dichroism Titration 243

4.2.7 FRET Melting Assay 245

4.2.8 Cell Viability Assay 247

4.2.9 Conclusion 249

4.3 Experimental 250

4.3.1 Fluorescence Quenching Assay 250

4.3.2 Circular Dichroism Titration 250

4.3.3 FRET Melting 250

4.3.4 Cell Viability Assay 251

4.3.5 Synthetic Procedures 251
4.4 Appendix 254

Chapter 4 - Photoswitchable DNA G Quadruplex Ligands

4.1 Introduction

4.1.1 Photopharmacology

Pharmaceuticals (pharmacotherapy) have revolutionized medicine, significantly improving quality of life and treating a wide array of diseases.[1] However, they face substantial challenges, primarily due to poor drug selectivity and the emergence of drug resistance. These issues stem from uncontrolled drug activity in time and space, leading to side effects, toxicity, and reduced efficacy.[2]

Poor drug selectivity occurs when pharmaceuticals interact with unintended targets, causing adverse effects. This problem is particularly evident in cancer treatment. Cytotoxic anti-neoplastic agents, such as vinca alkaloids and taxanes, while effective against cancer cells, also affect healthy, fast-dividing cells.[3] This lack of selectivity results in severe side effects including hair loss, mucositis, and anemia. Despite efforts to develop targeted therapies, selectivity remains a major hurdle in oncology and other fields of medicine.[4] The issue of selectivity extends beyond side effects. It narrows the therapeutic window of drugs, often necessitating suboptimal dosing to avoid toxicity. This limitation is a significant factor in drug development, with over 85% of small-molecule drugs in clinical research being discarded, partly due to insufficient selectivity.[5] Consequently, many promising drug candidates that could potentially improve current treatments or address unmet medical needs are abandoned. Recent advances in drug discovery have revealed that many effective pharmaceuticals act by modulating multiple targets simultaneously, a concept known as network pharmacology.[6] Network pharmacology further complicates the selectivity problem, as drugs need to interact with multiple sites to achieve maximum activity while avoiding interactions that lead to side effects.

Beyond inducing side effects, drug resistance, particularly in antibacterial therapy, poses another significant challenge. The accumulation of antibiotics in both community and hospital environments promotes the survival and growth of resistant bacterial strains.[7] This phenomenon can also be viewed as a selectivity issue, where the drug affects not only the targeted pathogenic bacteria but also other bacteria in the environment, leading to widespread resistance.

The challenges associated with inadequate drug selectivity stem from the inability to precisely control drug activity in both temporal and spatial dimensions (Figure 4.1). This lack of control results in drug action at inappropriate times and locations, both within and outside the target organism, where such activity is not only unnecessary but potentially detrimental.[8] This significant limitation serves as a driving force for the development of innovative molecular strategies aimed at dynamically modulating drug activity. These novel approaches seek to circumvent the complications arising from poor drug selectivity, potentially revolutionizing therapeutic interventions and improving patient outcomes.

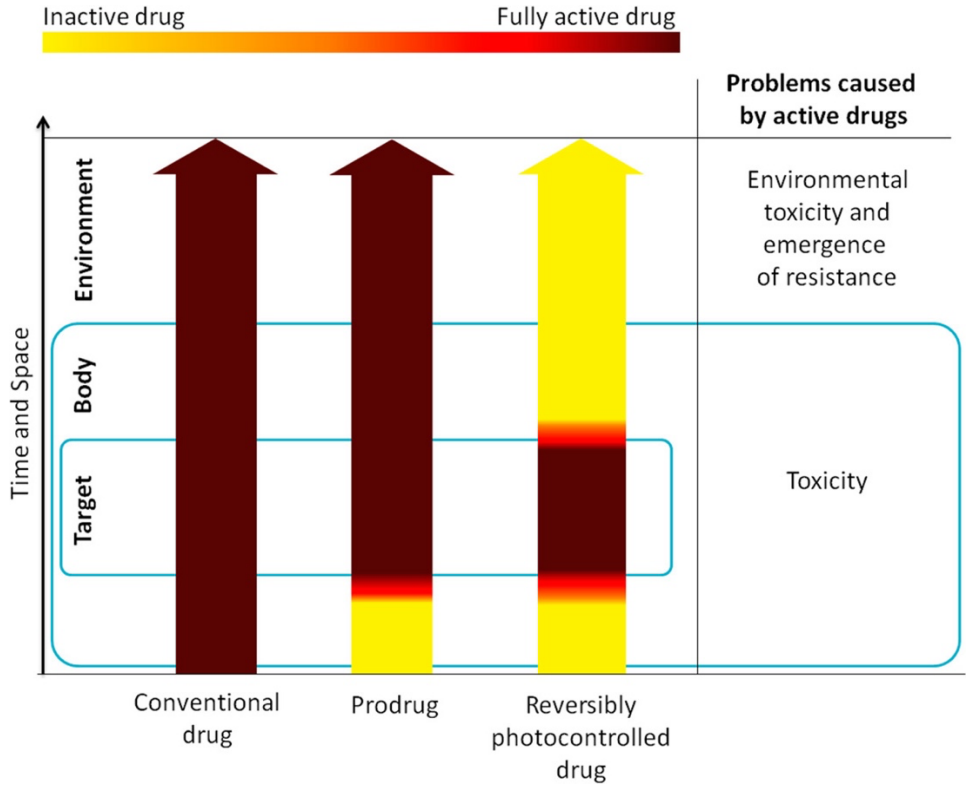


Figure 4.1 Drug activity over time and space for a conventional drug, a prodrug, and a reversibly photocontrolled drug. For conventional drugs, activity is present throughout the body of a patient during the time the drug is present, which may cause adverse effects; after excretion, the buildup of active drug can have a negative impact on the environment and/or lead to the emergence of drug-resistant pathogens. Some of the adverse effects can be avoided by using prodrugs, which liberate the active substance at a later stage. Adverse effects and environmental buildup of drugs might be completely avoided by using drugs whose activity can be controlled reversibly in space and time. Reprint with permission.[8]

The challenge associated with drug selectivity calls for novel approaches to increase drug selectivity and control drug activity dynamically. Photopharmacology emerges as a promising solution, leveraging light's unique properties to regulate biological processes with unprecedented precision.[9,10] Light offers several advantages as a regulatory element in biological applications:

1. Orthogonality: Unlike chemical regulators, light does not contaminate or interfere with most elements of chemical and biochemical systems. It has low or negligible toxicity, making it ideal for biological applications.[11]
2. Precision: Light can be delivered with high spatial and temporal accuracy, allowing for precise control of drug activity, if the drug can be activated or deactivated by light.
3. Tunability: The wavelength and intensity of light can be adjusted, providing qualitative and quantitative control over drug action. This allows for fine-tuning of drug activity based on specific needs.[12]

Photopharmacology seeks to overcome the challenges of traditional pharmacotherapy by coupling the action of light to the therapeutic efficacy of drugs.[13] The advantages of light-responsive therapeutic agents over conventional drugs are multifaceted and depend on the specific approach or agent in question. However, one fundamental principle stands out, stemming from the spatial selectivity that light offers. Consider a scenario where a photoactive drug with minimal inherent toxicity in its inactive (dark) state is administered systemically to a patient. Subsequently, precise light irradiation is applied to a specific area, converting the drug to its biologically active state only in that defined region. This approach has the potential to significantly enhance the drug's therapeutic index. The key benefit is that only the illuminated areas will experience the drug's effects, even if the inactive form of the photoactive drug is not exclusively localized to the target region. This method allows for targeted drug activation, potentially reducing systemic side effects and improving overall treatment efficacy. It provides a level of spatial control over drug activity that is challenging to achieve with conventional pharmaceutical approaches.

However, photopharmacology also faces inherent limitations. The primary challenge is the limited tissue penetration of light, which is heavily dependent on the wavelength of irradiation. For in vivo applications, red and NIR light are preferred due to their deeper penetration. Additionally, the absorption, distribution, metabolism, and excretion (ADME) processes of photoactive drugs, along with interindividual variability, constrain the window of opportunity for effective light-triggered drug activation. This temporal aspect is crucial, as the drug needs to be in the right location and not yet metabolized at the moment of light activation.

Photodynamic therapy (PDT) represents the most well-established application of light-activated therapeutic interventions (Figure 4.2a). The PDT protocol involves initial administration of a photosensitizing agent to the patient, followed by targeted light exposure.

Upon light absorption, the photosensitizer transitions to an excited state, catalyzing the production of reactive oxygen species (ROS).[14] A key advantage of PDT is its catalytic nature, where each photosensitizer molecule can generate multiple singlet oxygen ($^1O_2$) molecules. PDT has achieved regulatory approval for the treatment of various conditions, including malignancies, dermatological disorders, and ophthalmic diseases.[15] Furthermore, analogous techniques show promise in addressing infectious diseases, a field known as photodynamic inactivation.[16] Consequently, PDT has played a pivotal role in establishing the foundation for the development and clinical acceptance of light-based therapeutic modalities.

Forming an active drug by photouncaging from a prodrug is another prominent strategy relying on the irreversible photochemistry (Figure 4.2b).[17] In photouncaging, a photoactive protecting group, or "cage", is attached to a biological ligand. This cage masks crucial pharmacophoric features of the ligand, effectively deactivating its ability to interact with its target. Upon light irradiation, the protecting group undergoes photochemical cleavage, releasing the active biological agent.

Incorporating photoswitchable moieties into biologically active molecules is another important photopharmacological approach (Figure 4.2c). These photoswitches can undergo reversible structural changes upon exposure to specific wavelengths of light, altering the molecule's shape, polarity, or electronic properties. This, in turn, affects the molecule's ability to interact with its biological target, effectively switching its activity on or off.[18] Common photoswitches used in photopharmacology include azobenzenes, spiropyrans, and diarylethenes. Each of these molecular switches has unique properties suitable for different applications.

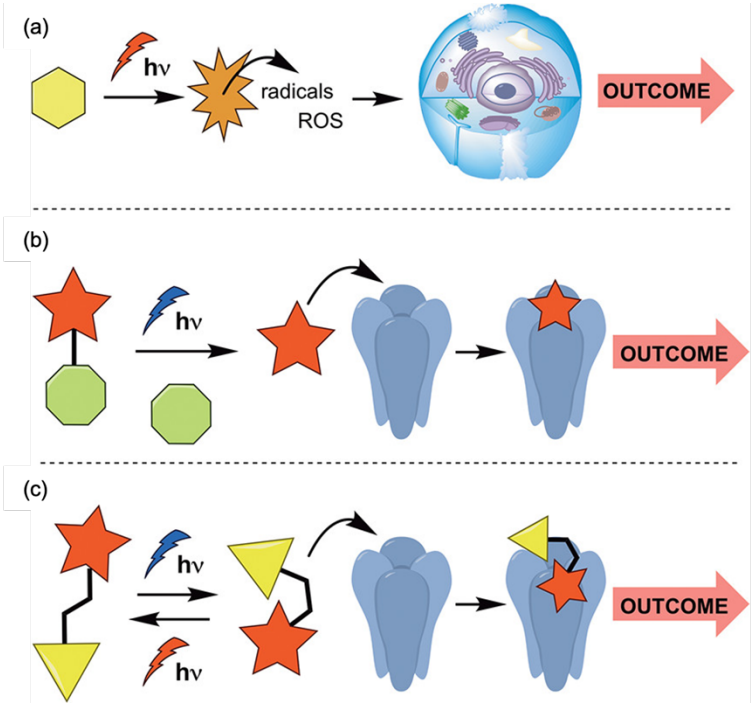


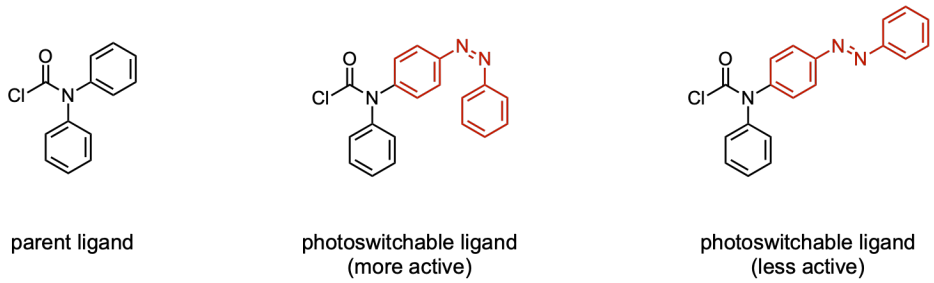
Figure 4.2 Light-dependent pharmacological approaches: (a) photodynamic therapy (ROS = reactive oxygen species); (b) irreversible photopharmacology (photouncaging); (c) reversible photopharmacology with a ligand that is active only in one structural state. Reprint with permission.[13]

4.1.2 Azobenzene-Based Agents

Among these three strategies, incorporating photoswitchable moieties offers the best control over drug activity and selectivity (Figure 4.1). Azobenzene is the most used photoswitchable unit. The practice of converting stilbene-based systems into their azobenzene counterparts is known as azologization and involves replacing the central ethylene bridge of stilbenes with an azo (N=N) group, thereby creating photoswitchable azobenzene derivatives. Azobenzene can also be introduced as an external motif using a different chemical strategies summarized by Kobauri and co-workers.[19]

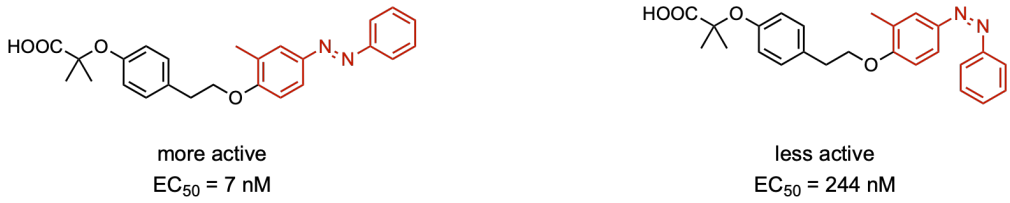
An early demonstration of a photoswitchable liagnd was presented in Kauffman's research.[20] Their study involved the creation of a light-responsive variant of diphenylcarbamic chloride by integrating an azobenzene photoswitch into its structure (Scheme 4.1). Both the parent ligand and the photoswitchable version react with a serine residue in at the active site of chymotrypsin, causing its inhibition. Although the researchers did not fully characterize the photochemical properties, such as the PSD or photoswitching quantum yields, they successfully isolated the metastable *cis* isomer. This was achieved through chromatographic separation after exposing the sample to 320 nm light. Notably, the study revealed that the *cis* isomer of the modified molecule exhibited significantly higher potency against chymotrypsin, a digestive

enzyme, compared to its *trans* counterpart. Specifically, the *cis* form was found to be five times more effective in inhibiting the enzyme's activity.



Scheme 4.1 Parent diphenylcarbamic chloride and the photoswitchable variant that inhibit chymotrypsin.

In a more recent study, Willems and co-workers developed a few photoswitching ligands targeting peroxisome proliferator-activated receptors (PPAR) PPARα and PPARδ (Scheme 4.2). A priori molecular docking indicated that the alkoxy spacer of the compound had the optimal length for *trans*-on agonism with significant light-induced differences. With a structure-based design approach, different substituents (i.e., methyl, chlorine, or trifluoromethyl) were evaluated in silico in the *ortho*- and *para*-position of the inner or outer ring of azobenzene, respectively. The docking process suggested that a methyl group in the *ortho*-position of the inner ring could occupy a lipophilic subpocket. As a result, the rationally designed *trans*-on agonist is extremely potent (EC_{50} = 7 nM) with a high contrast compared to the *cis* isomer (EC_{50} = 244 nM).



Scheme 4.2 PPAR ligands developed by Willems and co-workers.

4.1.3 Agents Bearing Diarylethenes

While azobenzenes have been extensively studied in photopharmacology,[19] other photoswitches remain relatively underexplored. Azobenzenes offer inherent advantages, including a compact photoswitching unit and a significant geometric change from *trans* to *cis* during photoswitching. Their small size allows them to fit into conventional protein binding pockets, while the substantial geometric shift typically results in markedly different interaction profiles within these pockets for each isomer. Photoswitches based on *trans–cis* isomerization, such as hemithioindigos, share the benefit of large geometric changes but require more spacious

binding pockets. Recent studies have investigated hemithioindigos for their isomer-dependent antimitotic bioactivity.[21] In contrast, photoswitches relying on pericyclic reactions and mixed mechanisms are seldom used in photopharmacology. Diarylethenes, for instance, are traditionally considered less suitable in this field because the transition from open to closed form does not produce a significant geometric change, thus minimally affecting binding strength. Furthermore, larger photoswitches necessitate biological targets with binding pockets capable of accommodating such sizeable molecules.

Nevertheless, diarylethenes find special applications in regulating peptide secondary structures.[22-25] Instead of using the DAEs directly as ligands to biological targets, Fujimoto designed and prepared the first peptide bearing a photoswitchable DAE crosslink.[22] In α-helices, hydrogen bonds between amide groups are formed along the axis of the helices and contribute to stabilize the helical structures. When even part of the hydrogen bonding is broken, the whole helicity will largely be influenced (Figure 4.3). A diarylethene cross-linker can vary its molecular diameter in a range of about 0.3 nm during photoisomerization. The authors envisaged that the structural change of the cross-linker is enough to disturb the hydrogen bonds in α-helices. Indeed, in the peptides **qk^DAE** and **hnf^DAE** bearing DAE photoswitch, photocyclization of DAE results in change in the CD spectra corresponding to the loss of α-helical character. Moreover, the K_d values of the two photoisomers of **qk^DAE** for its target DNA were estimated to be 1 μM and 4 μM for the open and closed isomers, respectively.

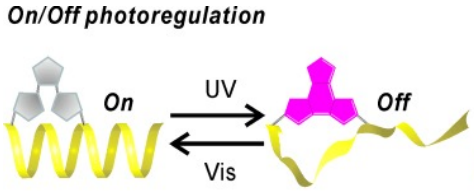


Figure 4.3 Schematic representation showing crosslinked DAE regulating the secondary structure of peptides. Reprint with permission.[22]

Babii expanded on the concept of using DAEs to modulate peptide secondary structure, applying it to PDT.[24] This approach differs from traditional PDT, which typically relies on photochrome-generated ROS. In their study, Babii synthesized two cyclic peptidomimetics by integrating a photoswitchable DAE unit into the backbone of the antibiotic gramicidin S (GS, Figure 4.4). This modification allowed the GS to switch between two distinct forms. The open configuration demonstrated significant cytotoxicity across all healthy and cancer cell lines tested. Notably, its half maximal inhibitory concentration (IC_{50}) values were comparable to those of unmodified GS. In contrast, the closed isomer exhibited markedly reduced cytotoxicity,

with a 5.5- to 8.0-fold decrease compared to the open form. The closed isomer shows minimal toxicity in the healthy mouse aortic endothelial cell line. In an in vivo study, the closed GS was injected into the mouse model and the cancerous tissue was irradiated with 664 nm light to generate the active open GS. The results showed that animal survival in the groups that received the PDT was improved by 60 % compared to the control.

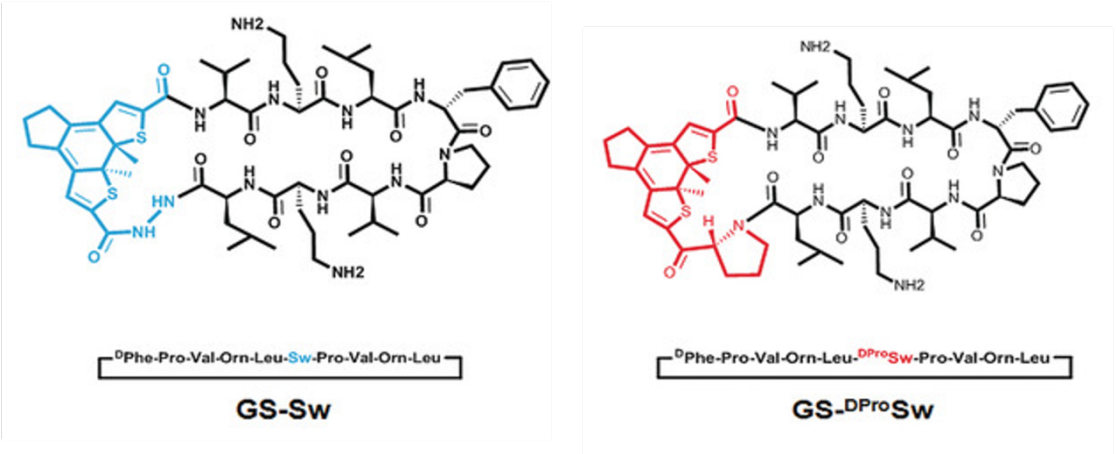


Figure 4.4 Structures of two GS bearing a photoswitchable DAE in their backbone. Reprint with permission.[24]

Al-Atar's research demonstrated that DTE itself can function as a photopharmaceutical, specifically in regulating paralysis in living organisms (Figure 4.5).[26] Their study revealed that both the open and closed forms of DTE exhibit toxicity towards the worms used in the experiment. However, the degree of toxicity differed significantly between the two forms. The closed form of DTE showed a more pronounced effect, causing paralysis in 40% of the treated worm population. In contrast, the open form of DTE resulted in paralysis for only about 20% of the treated worms. Interestingly, the researchers also explored an in vivo photoswitching approach. They first fed the worms with the open form of DTE and then used light to convert it to the closed form within the living organisms. This *in situ* transformation led to an increase in toxicity.

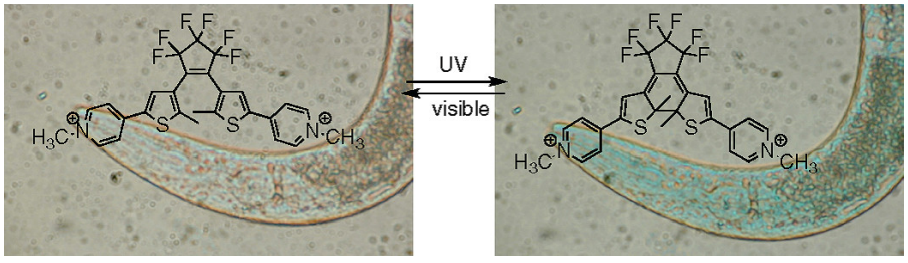


Figure 4.5 A DTE that can be reversibly triggered in a living organism and induces paralysis in *Caenorhabditis elegans* only when specific wavelengths of light convert it to one of its structural forms. Reprint with permission.[26]

4.1.4 Diarylethenes Targeting DNA G-Quadruplex

DNA G-quadruplexes (G4s) are non-canonical secondary structures formed in guanine-rich nucleic acid sequences. These structures consist of stacked planar arrangements of four guanine bases, known as G-quartets, which are stabilized by Hoogsteen hydrogen bonding and monovalent cations, particularly potassium.[27] G-quadruplexes can form within a single strand of DNA (intramolecular) or between multiple strands (intermolecular), and they can adopt various topologies depending on factors such as sequence composition, loop length, and environmental conditions.

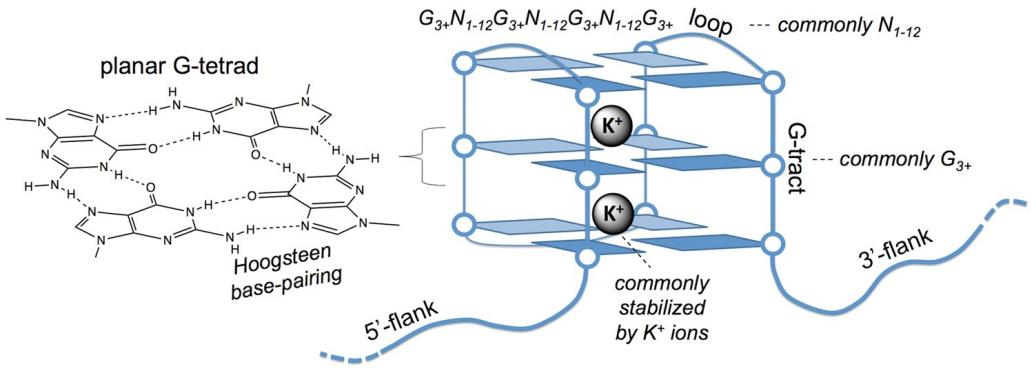


Figure 4.6 Schematic representation of canonical G-quadruplex (G4) structures in DNA, along with a common sequence motif used to identify such structures. Reprint with permission.[28]

First discovered in 1910 by Bang, who observed the gel-like behavior of guanylic acid at high concentrations,[29] G-quadruplexes have since become a subject of intense research due to their potential biological significance. These structures have been found to be prevalent in important genomic regions, including telomeres, gene promoters, and 5' untranslated regions (UTRs) of mRNAs.[30] The human genome contains an estimated 376,000 sequences with G4-forming potential, highlighting their widespread occurrence.[31] G-quadruplexes have been implicated in various cellular processes, including DNA replication, transcription, and telomere maintenance.[32] In telomeres, G4 structures are thought to play a role in protecting chromosome ends and regulating telomerase activity.[33] In gene promoters, G-quadruplexes can act as regulatory elements, influencing gene expression. For instance, the formation of G4 structures in the c-MYC promoter has been shown to suppress transcription of this important oncogene.[34]

The potential biological roles of G-quadruplexes have made them attractive targets for therapeutic interventions. Small molecules that can selectively bind to and stabilize G4 structures have been developed as potential anticancer agents.[35] These G4 ligands can interfere with telomere maintenance and oncogene expression, offering new avenues for cancer treatment.[36]

Galan's research group reported the first DAE-based photoswitchable ligand designed to bind to G4s.[37] They synthesized a conventional DTE molecule and evaluated its binding affinity to G4s (Figure 4.7). Both the open and closed forms of the DTE exhibited selective binding to G4s over duplex DNA. However, NMR studies revealed distinct binding modes for the two isomeric forms with different G4 topologies. The closed DTE demonstrated a 2:1 binding ratio with G4s, providing greater stabilization to the G4 structures. This isomer stacked onto both G-tetrad surfaces without disrupting the G4 fold. In contrast, the open form showed a 1:1 binding ratio, associating externally with terminal capping residues and causing partial disruption of the G4 structure. Importantly, the ligand showed cytotoxicity against HeLa cancer cells, with the closed form exhibiting approximately twice the potency of the open form.

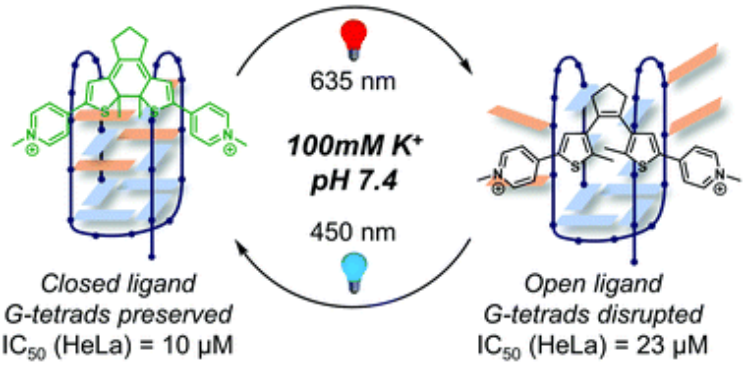


Figure 4.7 Differential binding of DTE to G4. Reprint with permission.[37]

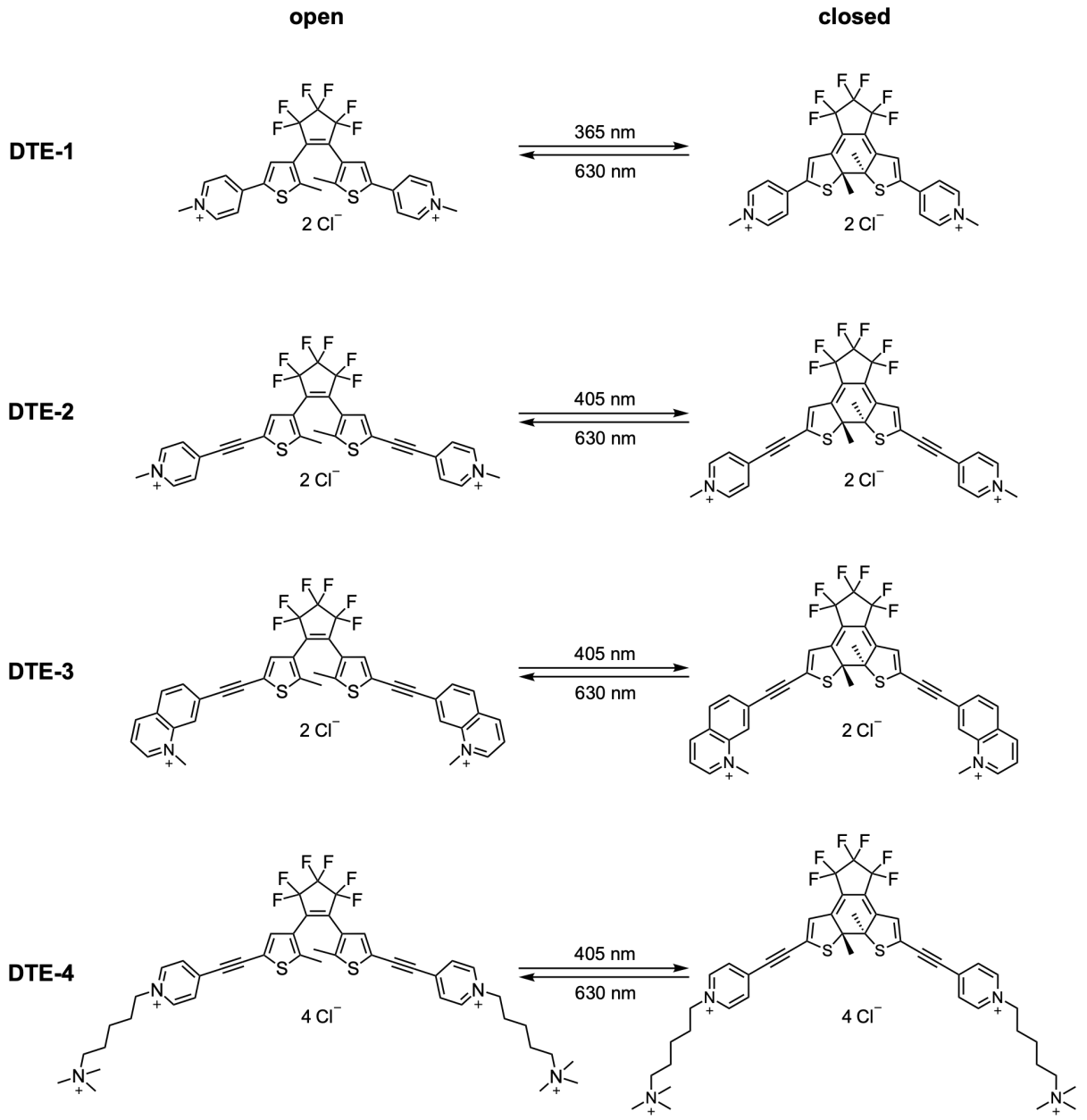
4.1.5 Project Aim

Our research aims to advance the field of photoswitchable G4 ligands by synthesizing and evaluating a series of novel DTE derivatives. We planned to design and create a diverse array of DTE variants with enhanced properties tailored for G4 binding. These modifications will include systems with extended conjugation and larger aromatic surfaces to promote stronger π-stacking interactions with G-tetrads, and the incorporation of additional positive charges to increase electrostatic interactions with the negatively charged DNA backbone. Our study will assess the binding affinity and selectivity of these newly synthesized DTE variants against various G4 topologies, including parallel, antiparallel, and hybrid structures, as well as double-stranded DNA for comparison. Furthermore, we will investigate the photoswitching properties of these compounds and evaluate how structural changes in the DTE core influence their ability to modulate G4 binding upon photoisomerization. We will also explore the biological activity of these novel DTE derivatives.

4.2 Results and Discussion

4.2.1 Synthesis of DTEs

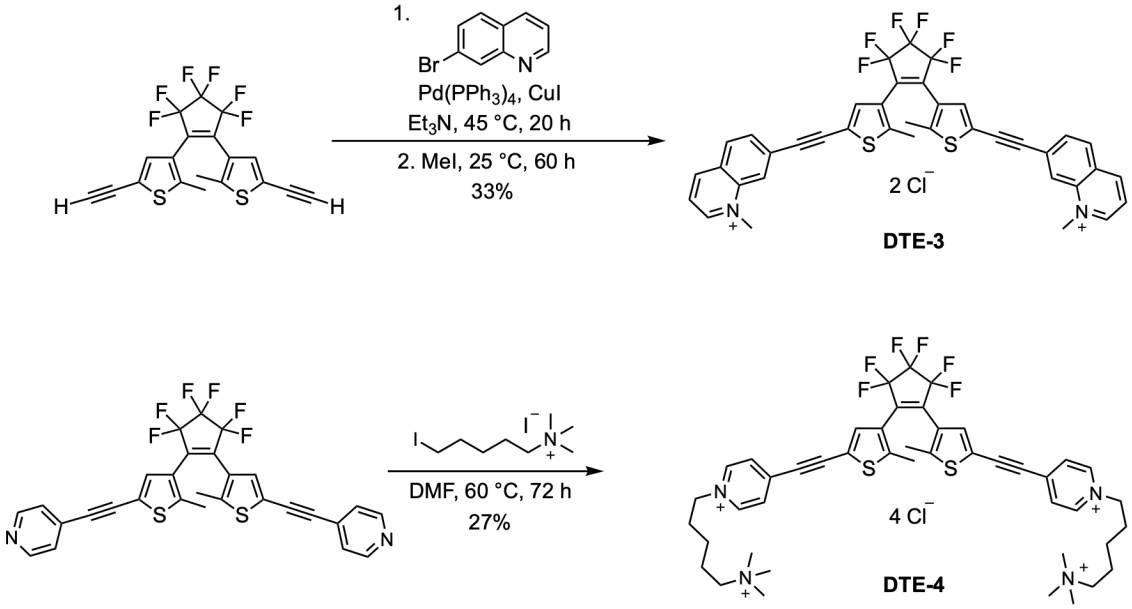
We have synthesized four derivatives of DTE (Scheme 4.3). The first two ligands, **DTE-1** and **DTE-2** were synthesized in Chapter 2 and were given the compound code **A-A** and **Ay-yA**, respectively. **DTE-1** is structurally analogous to the ligand previously reported by O'Hagan,[37] but incorporates a perfluorinated pentacyclic central bridge instead of a perhydrogenated one. The choice of fluorinated DTEs is motivated by their simpler synthesis, easier functionalization, and enhanced fatigue resistance compared to their perhydrogenated counterparts.[38] **DTE-2** features additional alkynes in the backbone, which result in red-shifted absorption spectra, enabling visible-light photoswitching. Furthermore, the alkyne introduces a larger hydrophobic surface that may promote stacking interactions with the G-tetrad surface. In **DTE-3**, we have replaced the *N*-methyl pyridinium group with an *N*-methyl quinolinium group, providing a larger aromatic surface for enhanced stacking interactions. **DTE-4** incorporates additional positively charged groups connected to the pyridinium moiety through a spacer. We hypothesize that these additional charged groups could interact with the negatively charged DNA backbone, potentially resulting in stronger binding. This design is based on the observation that positive charges play a critical role in G4 binding, as evidenced by many reported G4 ligands bearing positive charges.[39, 40]



Scheme 4.3 Prepared DTE derivatives and their photoswitching process.

The synthesis of **DTE-1** and **DTE-2** followed the core-to-arm approach described in Chapter 2. **DTE-3** and **DTE-4** were synthesized following the route shown in Scheme 4.4. **DTE-3** was prepared starting from a DTE intermediate bearing two free alkynes. A Sonogashira reaction was employed to incorporate the quinoline functionality. Notably, the product of this coupling reaction had the same R_f value as 7-bromoquinoline, making it impossible to remove excess starting material by column chromatography. Consequently, the crude mixture was carried forward to the methylation step without further purification. The final methylated **DTE-3** was then purified using flash column chromatography. For the synthesis of **DTE-4**, we started with an intermediate DTE bearing two free pyridine groups. The additional two positive

charges were introduced via an S_N2 reaction with 5-iodo-*N*,*N*,*N*-trimethylpentan-1-aminium iodide, which was prepared following a procedure developed by Reeve.[41]



Scheme 4.4 Synthesis of **DTE-3** and **DTE-4**.

4.2.2 UV-vis Absorption

The UV-vis absorption spectra of the synthesized DTEs were analyzed in water for their open isomers, at the PSS (365 nm for **DTE-1**, 405 nm for **DTE-2**, **DTE-3**, and **DTE-4**), and in their closed forms (Figure 4.8). Table 4.1 summarizes the key parameters of the UV-vis absorption spectra.

The incorporation of an additional alkyne in the molecular structure resulted in a 20 nm bathochromic shift of the open-form absorption spectra. Notably, further extension of conjugation on the arms by replacing the *N*-methyl pyridinium group with *N*-methyl quinolinium moiety led to an additional red-shift of 21 nm, bringing the λ_{max} to 398 nm. This shift into the visible region enables visible-light-triggered photocyclization for **DTE-3**. The addition of positive charges did not significantly alter the UV-vis absorption features, as evidenced by the similar spectra of **DTE-2** and **DTE-4**, which share the same photochromic core. However, slight shifts in λ_{max} were observed for both open and closed forms of **DTE-4**, likely due to differences in solvation stabilization caused by the additional charged groups.

Table 4.1 Absorption maxima and molar absorption coefficients of open and closed DTEs in water.

DTE	λ_{max}^{o} (nm)	ε (10^3 M^{-1} cm^{-1})	λ_{max}^{c1} (nm)	ε (10^3 M^{-1} cm^{-1})	λ_{max}^{c2} (nm)	ε (10^3 M^{-1} cm^{-1})
DTE-1	357	61.2	424	12.7	659	19.0
DTE-2	377	63.0	415	11.4	650	22.1
DTE-3	398	52.3	/	/	634	18.5
DTE-4	382	62.7	413	11.8	648	21.0

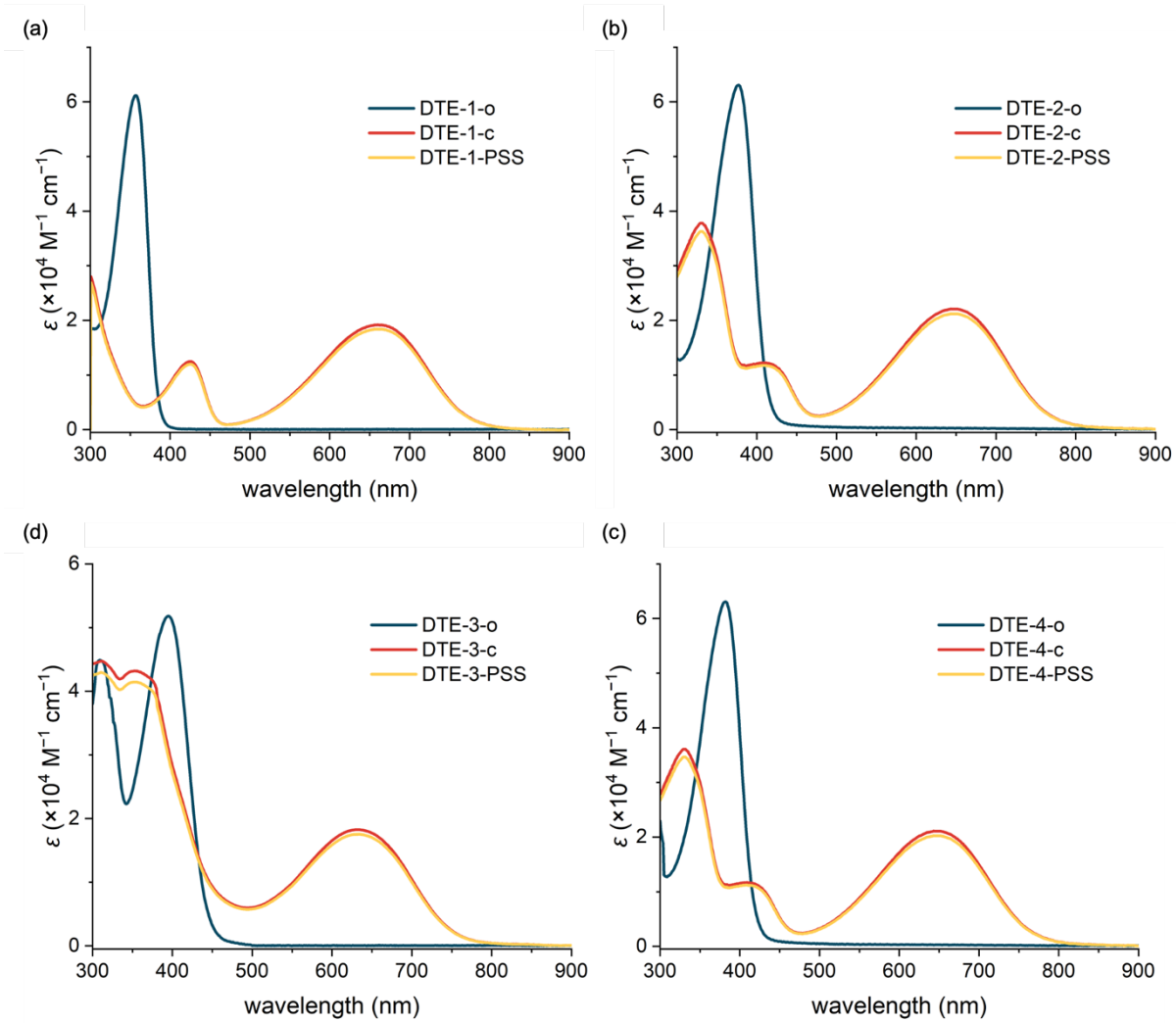


Figure 4.8 UV-vis absorption spectra of the DTEs measured in water. The PSS of **DTE-1** was achieved under 365 nm irradiation while the PSSs of **DTE-2**, **DTE-3** and **DTE-4** were achieved under 405 nm irradiation.

4.2.3 Photostationary State Distribution

The PSDs of all DTEs were characterized using the NMR integration method described in Chapter 2 (Section 2.2.4 and Section 2.4.6), following the change in the thiophene proton signal (Figure 4.9 and Figure 4.10). The PSDs of all DTEs under 365 nm and 405 nm irradiations are summarized in Table 4.2.

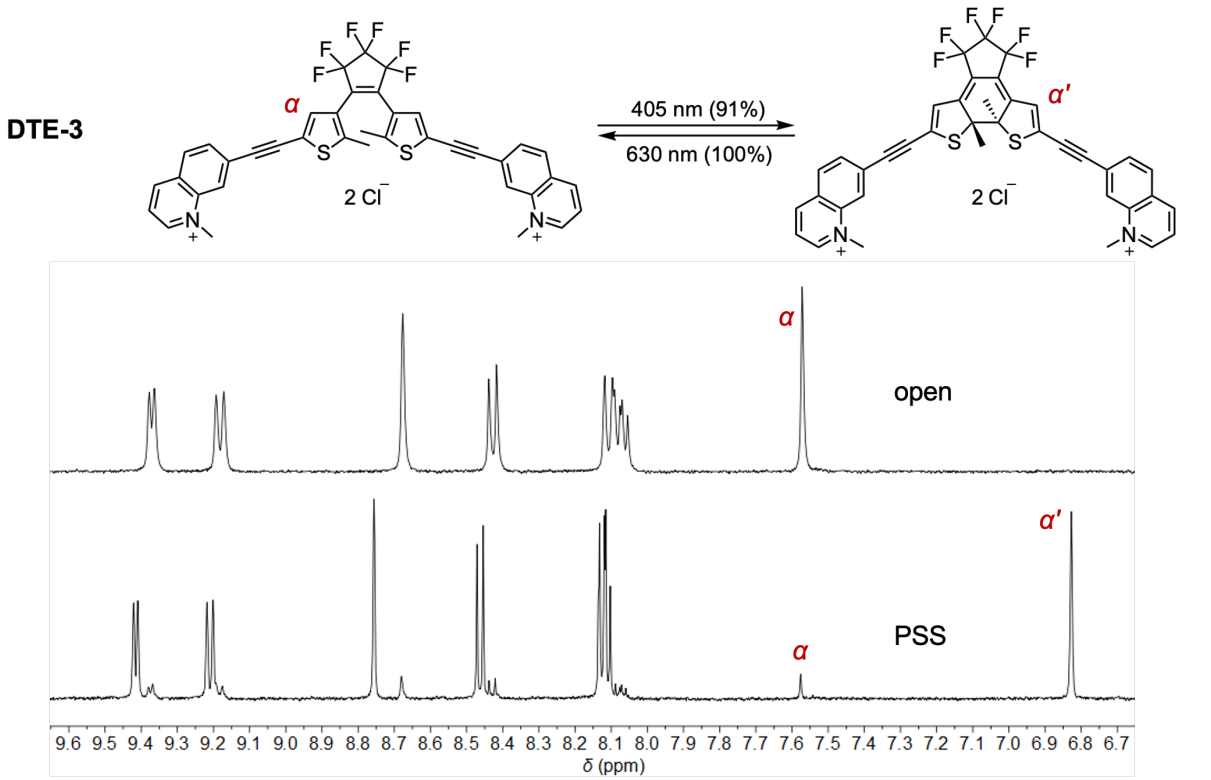


Figure 4.9 Photoswitching of **DTE-3** (405 nm) monitored by ^{1}H NMR (500 MHz, water).

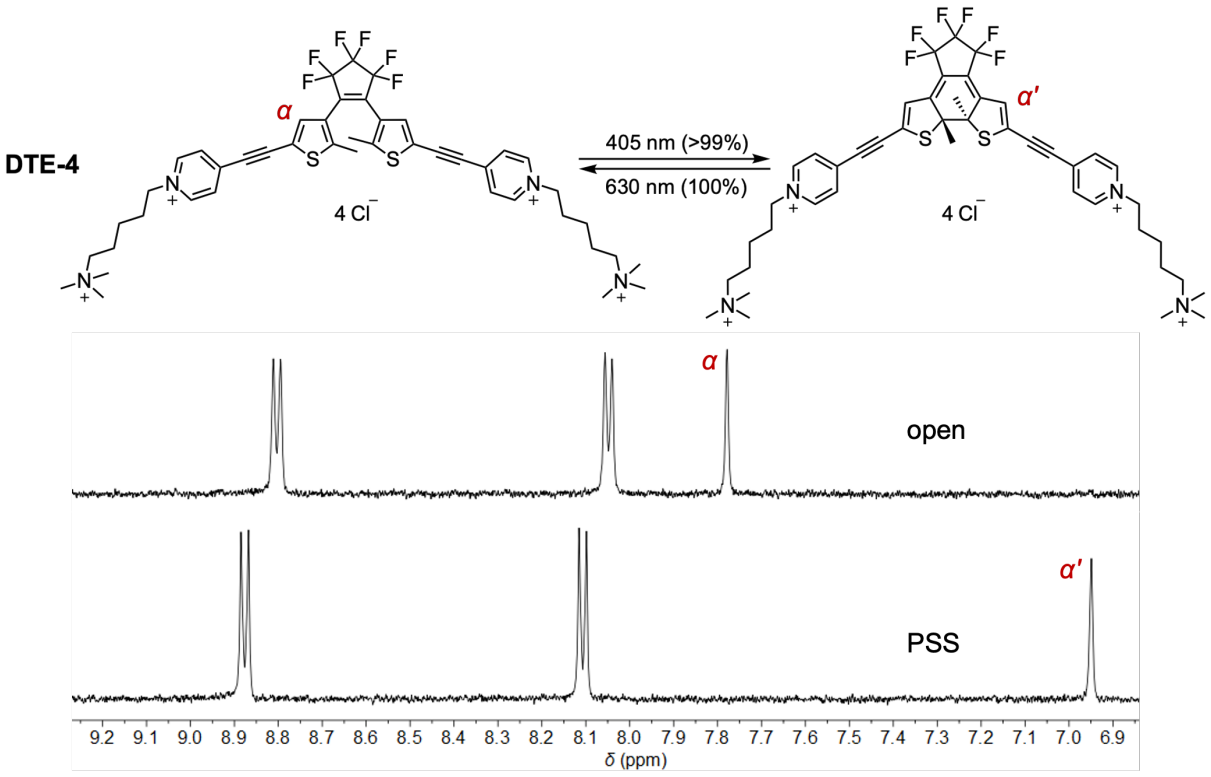


Figure 4.10 Photoswitching of **DTE-4** (405 nm) monitored by ^{1}H NMR (500 MHz, water).

Table 4.2 Summary of PSDs measured by NMR in water.

DTE	PSD_{O-C} (365 nm) (%)	PSD_{O-C} (405 nm) (%)	PSD_{C-O} (630 nm) (%)
DTE-1	>99	71	100
DTE-2	>99	96	100
DTE-3	75	91	100
DTE-4	>99	>99	100

All the synthesized DTEs exhibit excellent photoswitching behavior. **DTE-1** achieves a 71% PSD under 405 nm irradiation, limited by insufficient red-shift of its open-form absorption spectra. However, irradiation at 365 nm results in >99% conversion for this compound. **DTE-2**, previously identified as the best photoswitch in Chapter 2 (as **Ay-yA**), maintains its superior performance. Interestingly, the attachment of additional charged groups in **DTE-4** enhances the PSD (405 nm) from 96% for **DTE-2** to >99%, despite sharing the same photochromic core. This improvement may be attributed to a slight redshift in the open-form absorption spectra (by 5 nm) and increased electrostatic repulsion forcing the DTE to maintain an anti-parallel conformation, both contributing to higher photocyclization PSD. **DTE-3** demonstrates a unique behavior, achieving 75% PSD under 365 nm irradiation and 91% conversion under 405 nm irradiation. The strong absorption of closed **DTE-3** at 365 nm probably promotes photoreversion at this wavelength, explaining the lower PSD compared to other derivatives.

4.2.4 Photoswitching Quantum Yields

The photoswitching quantum yields were evaluated using the initial slope method described in Chapter 2 (Section 2.2.5 and Section 2.4.5), with results summarized in Table 4.3. All DTE derivatives exhibited markedly higher photocyclization quantum yields compared to their photoreversion quantum yields. **DTE-1** showed the highest photocyclization quantum yield, which can be attributed to the localization of its LUMO on the photoactive hexatriene unit. In comparison, **DTE-2** and **DTE-3**, featuring extended conjugation, displayed lower photocyclization quantum yields. This reduction is probably a consequence of their more delocalized LUMO, leading to less efficient photocyclization. An intriguing observation was made for **DTE-4**, which, despite sharing the same photochromic core as **DTE-2**, demonstrated a higher photocyclization quantum yield. This enhancement may be attributed to the additional positive charges, which potentially constrain the DTE molecule in an anti-parallel conformation more favorable for photocyclization. This increased photocyclization quantum yield also explains the observed higher PSD for **DTE-4** (>99%) compared to **DTE-2** (96%) under 405 nm irradiation.

Table 4.3 Photocyclization and photoreversion quantum yields of DTEs in water under 405 nm and 630 nm irradiation.

DTE	$\varphi_{o\text{-}c}$ / %	$\varphi_{c\text{-}o}$ / %
DTE-1[*]	38 ± 3	0.16 ± 0.01
DTE-2	17 ± 1	0.12 ± 0.01
DTE-3	8.2 ± 0.4	0.072± 0.004
DTE-4	22 ± 1	0.13 ± 0.01

[*]Photocyclization of **DTE-1** was triggered by 365 nm light source.

4.2.5 Fluorescence Quenching Assay

Following the characterization of the photochemical and photophysical parameters of all the DTEs, we proceeded to evaluate their interactions with G4s using a fluorescence quenching assay (Figure 4.11).[42] This assay utilizes oligonucleotides labeled with a cyanine-5 (Cy5) fluorescent dye at the 5' end. The strong fluorescence signal of Cy5 is quenched upon ligand complexation. This assay has been cross-validated and widely used as a quick screening method for discovering G4 ligands, but the exact fluorescence quenching mechanism was not fully elucidated.[42] We determined the apparent dissociation constant (K_D^{app}) of the DTEs in both their open and closed forms against five different oligonucleotides using this fluorescence quenching method. These included three G4-forming oligonucleotides: cKIT, cMYC, and hTELO. Additionally, we used a control double-stranded oligonucleotide (dsDNA) and a control single-stranded oligonucleotide (hTELO-mut) to assess the selectivity of our compounds. The sequences of all these oligonucleotides are presented in Table 4.4. The experimentally measured fluorescence quenching curves are shown in Figure 4.12 and the K_D^{app} values are shown in Table 4.5.

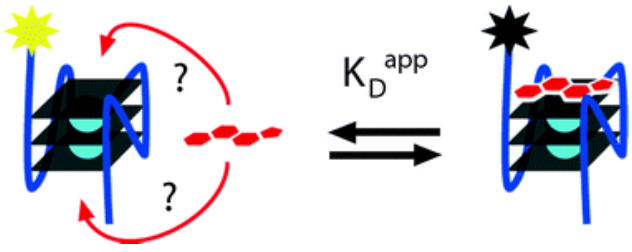


Figure 4.11 Schematic representation of the fluorescence quenching assay. Reprint with permission.[42]

Table 4.4 Sequence of the oligonucleotides tested for DTE binding.

Name	Sequence (5'→3')	Notes
cKIT	AGGGTTAGGGTTAGGGTTAGGGT	G4 DNA sequence (hybrid)
cMYC	AGGGAGGGCGCTGGGAGGAGGG	G4 DNA sequence (parallel)
hTELO	TGGGGAGGGTGGGGAGGGTGGGGAAGG	G4 DNA sequence (parallel)
dsDNA	CAATCGGATCGAATTCGATCCGATTG	dsDNA control
hTELO-mut	AAAATTAAAATTAAAATTAAAAT	ss DNA control (mutated G4)

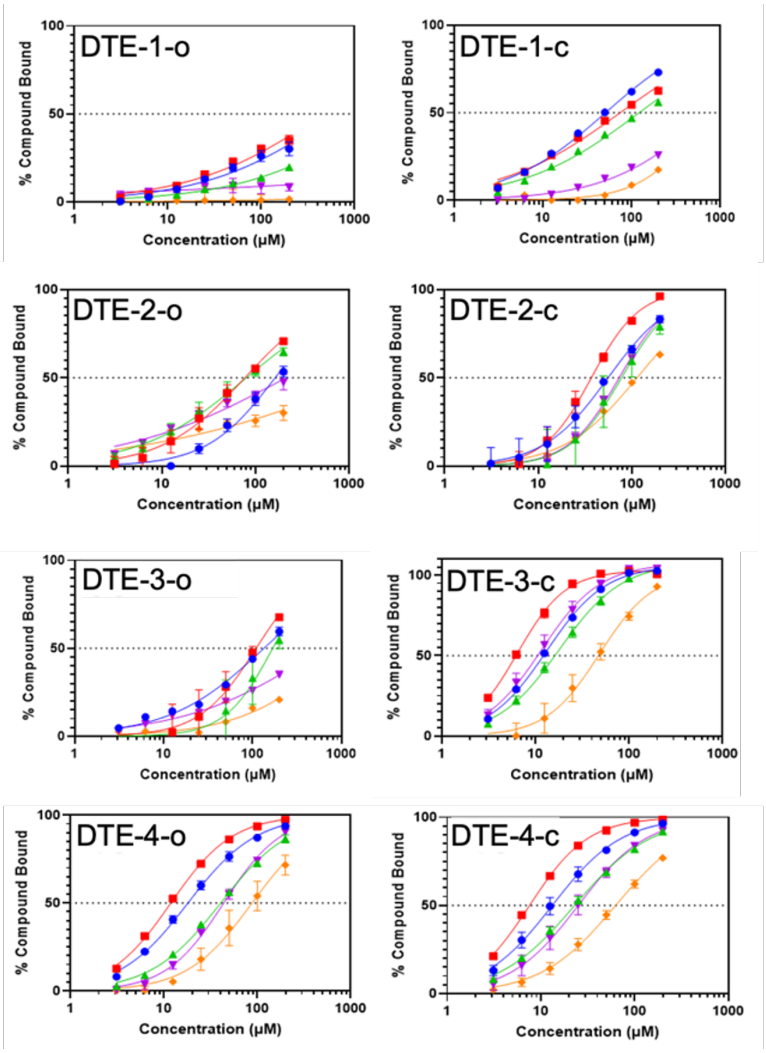


Figure 4.12 Fluorescence quenching assay curves of each ligand, with cKIT (blue curve, G4 DNA), cMYC (red curve, G4 DNA), hTELO (green curve, G4 DNA), hTELO-mut (purple curve, single-stranded DNA) and dsDNA (orange curve, double-stranded DNA). The experiment was performed in in 50 mM TrisHCl, pH 7.2 (50 mM KCl, 0.5 w/v % CHAPS, 0.05 v/v % Triton X-100, assay buffer), at a final concentration of 10 nM DNA.

Table 4.5 K_d^{app} values (in μM) obtained from the fluorescence quenching curves shown in Figure 4.11.

	DTE-1-o	**DTE-1-c**	**DTE-2-o**	**DTE-2-c**	**DTE-3-o**	**DTE-3-c**	**DTE-4-o**	**DTE-4-c**
cKIT	>200	50.8	162	55.8	125	13.2	18.1	13.6
cMYC	>200	70.3	77.1	37.0	111	6.42	11.9	7.5
hTELO	>200	121.1	80.1	77.7	168	18.1	40.6	22.9
hTELO-mut	>200	>200	>200	73.3	>200	11.6	43.7	25.0
dsDNA	>200	>200	>200	114	>200	48.4	88.0	62.9

The fluorescence quenching assay revealed varying binding affinities among the DTE derivatives. While **DTE-1-o** exhibited minimal fluorescence quenching, the other DTEs showed more substantial interactions. All DTEs, in both open and closed states, demonstrated a preference for G4 structures over double-stranded DNA, aligning with O'Hagan's findings.[37] **DTE-2**, **DTE-3**, and **DTE-4** displayed lower K_d^{app} values compared to **DTE-1** in both open and closed forms. This suggests that our structural modifications - incorporating additional alkynes,

extending π surfaces, and adding positive charges - successfully enhanced binding affinity between the DTEs and G4 structures, as hypothesized. The K_d^{app} values indicate stronger binding for the closed isomers of all DTEs compared to their open counterparts. However, these values for closed DTEs should be interpreted cautiously due to their characteristic absorption bands at ~650 nm, which overlap with the Cy5 fluorescence signal. This spectral overlap could potentially result in FRET between the Cy5 on the oligonucleotide and the closed DTE ligands if binding occurs in close proximity. This additional relaxation pathway for Cy5, not present in open DTE binding, could lead to artificially lower K_d^{app} values for closed DTEs. Although this fluorescence quenching assay has been cross validated with other assays for potential G4 ligand screening,[42] organic ligands with red-light absorption are not common, potentially limiting its applicability in this case. Moreover, it is crucial to note that the K_d^{app} may differ significantly from the true dissociation constant. The assay's reliance on binding to the same tetrad where the fluorophore is positioned means that different binding modes could result in overestimated K_d^{app} values. As reported by O'Hagan et al., open-form ligands interact with the outer tetrad, while closed-form ligands interact in a 2:1 stoichiometry on opposite tetrads. These different binding modes can significantly affect the dissociation constant calculation in this assay, further complicating the interpretation of the results.

4.2.6 Circular Dichroism Titration

To further elucidate the affinity of our ligands for G4 structures, we conducted circular dichroism (CD) spectroscopy titration experiments using hTELO G4-DNA. We monitored alterations in the CD signal at 290 nm, the CD λ_{max} corresponding to the DNA, as ligands were introduced. The resulting CD titration curves are presented in Figure 4.13, and the calculated dissociation constants (K_d) are summarized in Table 4.6. Ligand **DTE-1** is not included in the Table 4.6 because it failed to induce any significant changes in the CD spectrum of hTELO in either its open or closed form. Given that **DTE-1-c** induces quenching in the fluorescence quenching assay (Table 4.5), it is probable that **DTE-1-c** binds in a different mode compared to other DTEs and do not induce significant change in CD signal. As for **DTE-1-o**, this lack of CD spectral perturbation suggests weak binding interaction, as it does not induce and fluorescence quenching either (Table 4.5).

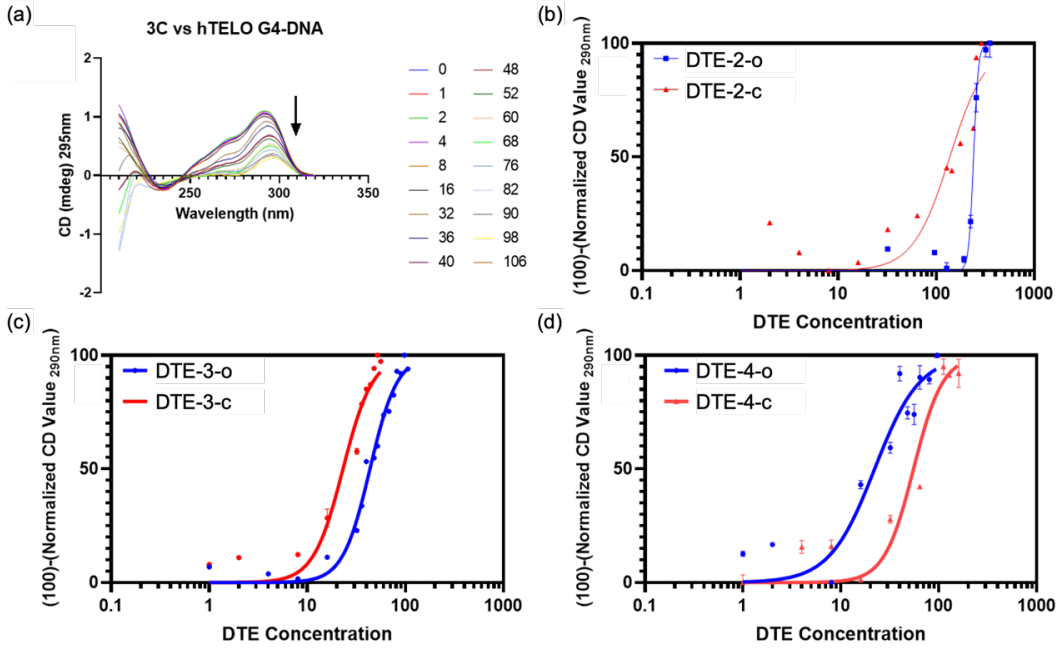


Figure 4.13 CD-titration experiment, performed in in 50 mM TrisHCl, pH 7.2 (50 mM KCl), at a concentration of 1 μM DNA. (a) Example of a CD titration experiment (hTELO in presence of increasing amounts of **DTE-3-c** 0-106 μM. Binding curve obtained upon titration of hTELO in presence of open (blue curves) and closed (red curves) ligands (b) **DTE-2**, (c) **DTE-3** and (d) **DTE-4**.

Table 4.6 K_d values of the DTEs against hTELO measured by CD titration.

	DTE-2-o	**DTE-2-c**	**DTE-3-o**	**DTE-3-c**	**DTE-4-o**	**DTE-4-c**
K_d (μM)	229	111	23.1	43.6	20.5	65.6
R^2	0.85	0.85	0.97	0.98	0.94	0.94

The CD titration experiments corroborated the findings from the fluorescence quenching assay, indicating that ligands **DTE-3** and **DTE-4**, in both open and closed forms, exhibit higher binding affinities for hTELO compared to **DTE-1** and **DTE-2**. This result supports our hypothesis that DTEs with larger π surfaces and additional positive charges engage in more favorable binding interactions with G-quadruplex structures. Intriguingly, the CD experiments revealed a stark contrast to the fluorescence quenching assay results regarding the relative binding strengths of open and closed isomers. For **DTE-3** and **DTE-4**, the CD data indicated that the open isomers bind more strongly to G4 than their closed counterparts. This discrepancy highlights the potential limitations of the fluorescence quenching assay, where the photophysical pathway for fluorescence quenching is not fully elucidated, and closed DTEs could potentially enhance fluorescence quenching through FRET mechanism. Given these considerations, the K_d values obtained from CD titration probably provide a more accurate description of ligand binding and allow for direct comparison between open and closed isomers. Specifically, the open isomers of **DTE-3** and **DTE-4** demonstrated two-fold and

three-fold stronger binding to G4 than their respective closed isomers. Interestingly, **DTE-2** deviated from this trend, with its closed isomer exhibiting stronger binding than the open form.

4.2.7 FRET Melting Assay

To further assess the stabilizing effects of our ligands on G4 structures, we employed a FRET melting assay, focusing on both hTELO and cKIT G4 structures. FRET melting assay not only provides information about ligand binding, but also shows the impact of the G4 stability due to the presence of the ligand. This experimental approach involves labeling the test oligonucleotide at both the 5' and 3' ends with distinct, FRET-paired fluorophores: carboxy-fluorescein (FAM) at the 5' end and carboxy-tetramethylrhodamine (TAMRA) at the 3' end. The principle behind this assay lies in the spatial relationship between the two fluorophores. When the G4 structure is folded, the fluorophores are in close proximity, resulting in fluorescence quenching. As the structure unfolds due to increasing temperature, the distance between the fluorophores increases, leading to a restoration of fluorescence. To determine the melting temperature of the G4 sequence, we plot the fluorescence intensity of FAM as a function of temperature. This approach provides a quantitative measure of G4 stability and allows us to evaluate the impact of our ligands on the thermal stability of these structures. The change in DNA melting temperature (ΔT_M) at different ligand concentrations is shown in Figure 4.14. The melting temperatures of hTELO and cKIT are shown in Table 4.7 and Table 4.8, respectively.

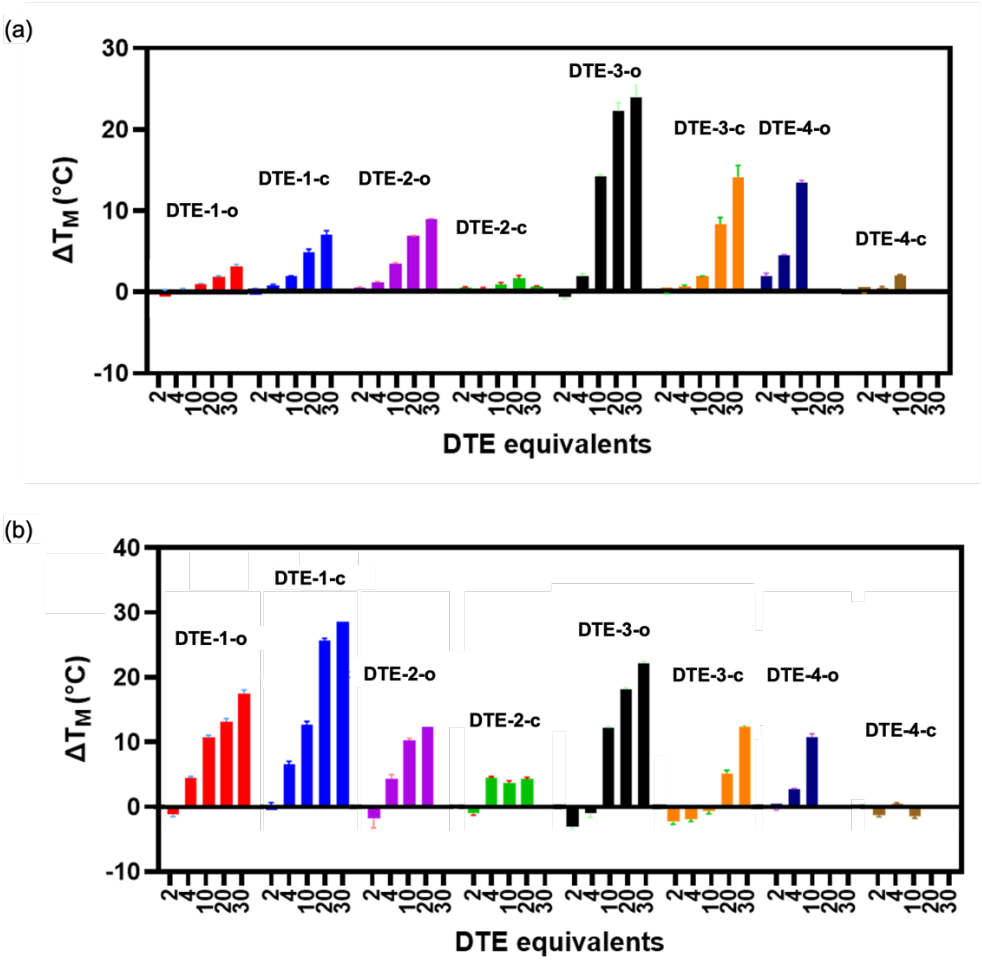


Figure 4.14 Change in DNA melting temperature of (a) hTELO and (b) cKIT at different equivalents of DTE ligands. The assay was performed in Tris HCl buffer (pH 7.4, 10 mM Tres) with 140 mM KCl (for hTELO) and 40 mM KCl (for cKIT).

Table 4.7 DNA melting temperatures (°C) obtained from the FRET melting assay for hTELO.

Equiv.	DTE-1-o	DTE-1-c	DTE-2-o	DTE-2-c	DTE-3-o	DTE-3-c	DTE-4-o	DTE-4-c
0	59.4	59.4	59.4	59.4	59.4	59.7	59.4	59.4
2	59.5	59.7	59.9	59.9	58.7	59.3	61.3	59.4
4	59.7	60.2	60.5	59.8	61.3	60.0	63.8	59.9
10	60.4	61.2	62.8	60.3	73.6	61.2	72.8	61.5
20	61.3	64.2	66.2	61.0	81.6	67.7	N.D.	N.D.
30	62.6	66.4	68.3	60.0	83.3	73.5	N.D.	N.D.

N.D.: not determined due to fluorescence quenching and/or DNA precipitation.

Table 4.8 DNA melting temperatures (°C) obtained from the FRET melting assay for cKIT.

Equiv.	DTE-1-o	DTE-1-c	DTE-2-o	DTE-2-c	DTE-3-o	DTE-3-c	DTE-4-o	DTE-4-c
0	61.4	61.4	61.4	61.4	61.4	61.4	61.4	61.4
2	60.2	61.7	59.6	60.4	58.3	59.1	61.2	60.1
4	65.9	68.0	65.8	65.9	60.4	59.5	64.1	61.9
10	72.1	74.1	71.7	65.1	73.6	60.8	72.1	60.0
20	74.6	87.1	73.9	65.7	79.6	66.6	N.D.	N.D.
30	78.9	<90	N.D.	N.D.	83.6	73.8	N.D.	N.D.

N.D.: not determined due to fluorescence quenching and/or DNA precipitation.

The DNA melting data revealed a ligand concentration-dependent stabilization of both G4 structures for all DTE derivatives, except for **DTE-4-c**. Generally, higher DTE concentrations resulted in increased G4 stabilization. The degree of G4 DNA stabilization varied significantly among different G4 structures, which can be attributed to the diverse and dynamic environments at the G-tetrad surface created by different backbones and end loops. This variability suggests that different ligands may be accommodated differently by various G4 structures. **DTE-1**, in both open and closed states, demonstrated only weak stabilization of hTELO (increasing melting temperature by 1.0 °C and 1.8 °C at 10 equivalents for open and closed isomers, respectively). However, its stabilization of cKIT was much more pronounced (increasing melting temperature by 10.7 °C and 12.7 °C for open and closed isomers, respectively). This preferential stabilization of cKIT by **DTE-1** aligns with the results from the fluorescence quenching assay, which indicated a lower K_d^{app} for **DTE-1** with cKIT compared to hTELO. **DTE-1-c** shows better G4 stabilization than **DTE-1-o**, in agreement with the stronger binding measured from the fluorescence quenching assay and the CD titration. Among all tested DTEs, **DTE-3-o** emerged as the most effective G4 stabilizer, increasing the melting temperature by over 20 °C for both cKIT and hTELO at 30 equivalents of DTE. At 10 equivalents of added DTE, a stark contrast in DNA stabilization was observed between the open and closed forms of **DTE-3**. While **DTE-3-o** stabilized both G4s by over 10 °C, **DTE-3-c** showed essentially no stabilization. This result corroborates the findings from the CD titration experiment, which also indicated stronger binding of **DTE-3-o** compared to **DTE-3-c**. Intriguingly, while both the fluorescence quenching assay and CD titration indicated moderate binding of **DTE-4-c**, the DNA melting assay showed essentially no G4 stabilization.

4.2.8 Cell Viability Assay

With these binding assay results, we set out to evaluate the toxicity of the ligands on two different cell lines: HEK293 (non-cancerous) and HeLa (cancerous), on a 96-well plate format. Approximately 5000 cells per well were treated with increasing concentrations of each ligand for 48 hours, in triplicate. The experiments demonstrated a dose-dependent activity of the ligands (Figure 4.15). The IC_{50} values of each DTE in the open and closed forms are shown in Table 4.9.

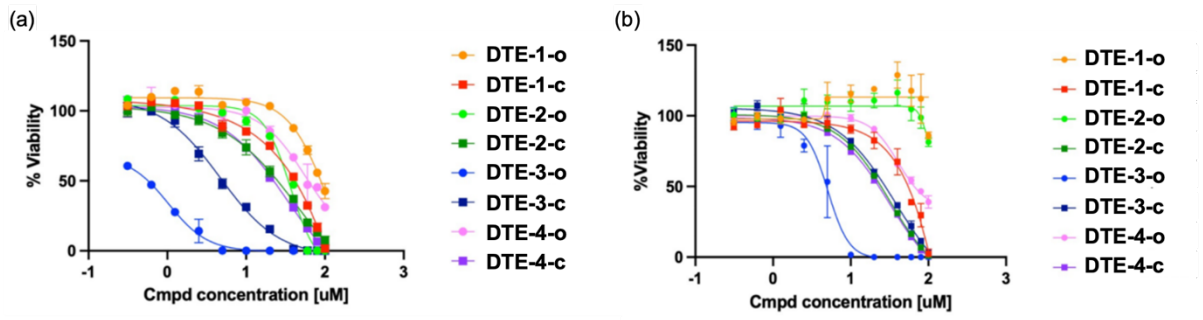


Figure 4.15 Cell viability assays performed on (a) HEK293 (non-cancerous) and (b) HeLa cells (cancerous).

Table 4.9 Inhibition of HEK293 and HeLa cell growth by photoswitchable DTE ligands.

Compound	IC_{50} (μM) HEK293	IC_{50} (μM) HeLa
DTE-1-o	>100	>100
DTE-1-c	>100	>100
DTE-2-o	36.7 ± 1.7	>100
DTE-2-c	47.4 ± 3.3	31.4 ± 2.7
DTE-3-o	1.03 ± 2.8	5.07 ± 8.4
DTE-3-c	4.68 ± 2.7	37.6 ± 2.4
DTE-4-o	55.6 ± 6.3	40.9 ± 2.1
DTE-4-c	32.6 ± 3.2	31.6 ± 1.5
PDS	4.81*	7.48*

Data are shown as average of three technical replicates from one biological assay ± SD values.
* PSD is a well-established G4 ligand used as a positive control.

The cytotoxicity assay results reveal that while **DTE-1** (in both open and closed forms) exhibits relatively low toxicity with IC_{50} values exceeding 100 μM for both HEK293 and HeLa cell lines, the other DTE derivatives demonstrate significantly higher cytotoxicity. The observed toxicity profiles of the studied DTEs correlate well with their ligand binding assay results. Compound **DTE-3-o** demonstrates particularly potent cytotoxicity, with IC_{50} values of 1.0 μM for HEK293 and 5.1 μM for HeLa cells, surpassing the toxicity of pyridostatin (PDS, a well-known G4 ligand), which served as a positive control. This pronounced cytotoxic effect aligns well with its K_d data from CD experiments and DNA melting assay results, suggesting that G4 stabilization may be a potential mechanism underlying its biological activity. The toxicity profile of **DTE-3-o** becomes especially noteworthy when compared to its closed form counterpart, **DTE-3-c**. The latter exhibits substantially lower toxicity, with IC_{50} values of 4.7 μM for HEK293 and 37.6 μM for HeLa cells, representing a 4–6-fold decrease in toxicity compared to **DTE-3-o**. This reduced toxicity of **DTE-3-c** is consistent with its weaker binding affinity and lower G4 stabilization potential, as evidenced by the CD and FRET melting data.

4.2.9 Conclusion

In this study, we expanded upon the foundational work conducted in Galan's research group, which had previously demonstrated differential binding of diarylethenes to G4s in their open and closed forms.[37] Our approach involved strategic structural modifications of DTEs, including the incorporation of additional alkynes, extended π surfaces, and additional positive charges. In agreement with O'Hagans study,[37] we found that all these DTEs preferentially bind to G4 structures over double-stranded DNAs. The structural modifications successfully enhanced the binding affinity of the DTE derivatives to G4 structures (both hTELO and cKIT). Notably, **DTE-3** and **DTE-4** exhibited superior binding properties compared to **DTE-1** and **DTE-2**, as evidenced by the fluorescence quenching assay, CD titration, and FRET melting experiments.

We observed discrepancies between different binding assays, particularly regarding the relative affinities of open and closed isomers. While the fluorescence quenching assay suggested stronger binding for closed isomers, both CD titration and DNA FRET melting experiments indicated that open isomers of **DTE-3** and **DTE-4** bind more strongly to G4 than their closed counterparts. The result is further supported by higher cytotoxicity of **DTE-3** and **DTE-4**. These findings suggest that the reliability of the fluorescence quenching assay may be compromised when additional quenching pathway such as FRET is available, potentially resulting in overestimated K_d^{app} values.

The FRET melting assay further revealed that **DTE-3-o** is the most effective G4 stabilizer among all tested compounds, significantly increasing the melting temperature of both cKIT and hTELO G4 structures. Both **DTE-3-o** and **DTE-4-o** stabilizes hTELO more than cKIT, emphasizing that the ligand-G4 binding critically depends on the target G4 structure. Different G4 surface and end loops could affect the ligand binding.

This potent stabilizing effect correlated well with the observed cytotoxicity of **DTE-3-o** in both HEK293 and HeLa cell lines, suggesting a possible G4-mediated mechanism of action. The marked difference in toxicity between the open and closed forms of **DTE-3** demonstrates the potential for using photoswitching to modulate the biological activity of these compounds. This photocontrol over G4 binding and cellular toxicity opens up exciting possibilities for the development of light-activated therapeutic agents in the field of photopharmacology.

4.3 Experimental

4.3.1 Fluorescence Quenching Assay

Before each experiment, in a 1.5 mL Eppendorf tube, a solution containing 20 μM DNA (IDT, Leuven), labelled at 5' with Cyanine5 dye, was freshly prepared in 50 mM TrisHCl, pH 7.2 (50 mM KCl, 0.5 w/v % CHAPS, 0.05 v/v % Triton X-100, assay buffer). The DNA solution was placed on an Eppendorf Thermomixer, annealed by heating at 95°C for 10 minutes, and left cooling down at 0.5°C/min. The DNA was distributed across a 96-well RT-PCR plate (Thermo Fischer Scientific), and supplemented with increasing equivalent amounts of each ligand, at a final oligonucleotide concentration of 10 nM. After the addition of the ligand, the solutions were incubated for 1 hour before the readings. Fluorescence readings were performed on a CLARIOStar Plate reader (BMG Labtech, Germany), in technical duplicate. The data points obtained were analyzed with GraphPad Prism 10, and the Kd App was calculated from a Hill binding slope curve (non-linear regression).

4.3.2 Circular Dichroism Titration

Before each experiment, in a 1.5 mL Eppendorf tube, a solution containing 1 μM DNA (IDT, Leuven), was freshly prepared in Tris HCl Buffer, pH 7.2, 10 mM Tris, 50 mM KCl. The DNA solution was placed on an Eppendorf Thermomixer, annealed by heating at 95°C for 10 minutes, and left cooling down at 0.5 °C/min. The obtained solution was transferred to a 200 μL quartz cuvette (1 mm optical pathlength), and the CD spectrum recorded from the range 320-200 nm on an Applied Photophysics ChiraScan V100, at a 2nm bandwidth, and 0.4 s equilibration time. Increasing amounts of each ligand were added to the solution, and CD spectra were recorded upon each addition, allowing the ligands to equilibrate with the DNA for 5 minutes after each addition. For the K_d calculation, the value of the CD maximum (290nm) was plotted in function of the ligand equivalents. The obtained values were normalized and subtracted from 100 to obtain the binding response. These data points were analyzed using GraphPad Prism 10, where the K_d value was extrapolated from a Hill-specific binding curve. Each experiment was performed in technical duplicate.

4.3.3 FRET Melting

Before each experiment, in a 1.5 mL Eppendorf tube, a solution containing 20 μM DNA (IDT, Leuven), labelled at 5' with FAM and at 3' with TAMRA, was freshly prepared in Tris HCl

Buffer, pH 7.4, 10 mM Tris (supplemented with KCl 50–140 mM, depending on the oligonucleotide sequence tested). The DNA solution was placed on an Eppendorf Thermomixer, annealed by heating at 95°C for 10 minutes, and left cooling down at 0.5 °C/min. The DNA was distributed across a 96-well RT-PCR plate (Thermo Fischer Scientific), and supplemented with increasing equivalent amounts of each ligand, at a final oligonucleotide concentration of 1 μM. Fluorescence readings were performed on an Agilent Stratagene MX3000P, in the range 25–95°C, in technical duplicate. The datapoints obtained were analyzed with GraphPad Prism 10, and the melting temperature was extrapolated from a Boltzmann Sigmoidal function.

4.3.4 Cell Viability Assay

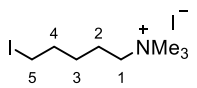
HEK-293 and HeLa cells were cultured in Dulbecco's Modified Eagle's Medium (DMEM) supplemented with 10% heat-inactivated fetal bovine serum. Cells were grown in T75 cell culture flasks maintained at 37 ℃ in 5% CO2 and sub-cultured when at 60–80% cell confluence.

The inhibition of HEK-293 and HeLa cell proliferation was determined using the CellTiter-Glo® reagent (Promega, Cat. No. G7572) according to the manufacturer's recommendation. Cells were diluted to 6×104 cells/ml in DMEM, plated in 96-well white polystyrene assay plates (90 μL/well), and allowed to adhere for 24 hrs. Twelve-point concentration-response assays were set up; test compounds were diluted in water and added to the 96-well assay plates (10 μL/well) to give final assay concentrations ranging from 100 μM to 0.31 nM. Assay plates were incubated at 37 °C and 5% CO2 for 48 h, followed by addition of 45 μL/well of CellTiter-Glo®. Luminescence was measured in CLARIOstar plus microplate reader (BMG LABTECH). The activity of test compounds was normalized to negative controls (i.e., no test compound) from the same plate. Dose–response curves and IC50 values, i.e., the concentration of compound required to inhibit cell growth by 50%, were calculated using GraphPad Prism. Assays were performed in triplicates for each test compound, and in duplicates for PDS (positive control). PDS was synthesised as previously described.1

4.3.5 Synthetic Procedures

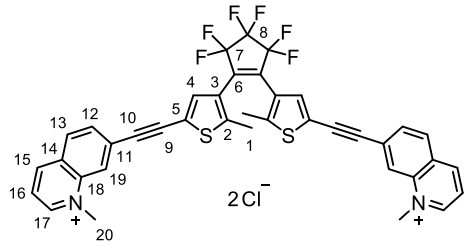
DTE-1 (**A-A**) and **DTE-2** (**Ay-yA**) were synthesized following the procedures described in Chapter 2 (Section 2.4.8).

5-Iodo-*N*,*N*,*N*-trimethylpentan-1-aminium iodide



The compound was prepared following a literature procedure for preparing the 4-iodo-*N*,*N*,*N*-trimethylbutan-1-aminium analogue.[41] To a solution of 1,5-diiodopentane (5.95 mL, 40.0 mmol, 5 equiv.) in Et_2O (100 mL) at 0 °C was dropwise added trimethylamine (1.89 mL, 33% in EtOH, 8.0 mmol, 1 equiv.). The reaction mixture was stirred at 0 °C for 1 h and then at 20 °C for 4 days in the dark. The precipitated product was filtered off and washed with excess Et_2O to afford the product as a white solid (2.96 g, 97%). δ_H (400 MHz, D_2O): 3.35–3.28 (4H, m, H^1 & H^5), 3.12 (9H, s, RN^+Me_3), 1.93–1.78 (4H, m, H^2 & H^4), 1.49 (2H, m, H^3); δ_C (101 MHz, D_2O, containing MeOH as an internal reference): 66.5 (t, 1:1:1, $^1J_{CN}$ 2.4), 53.0 (t, 1:1:1, $^1J_{CN}$ 4.1), 32.1, 26.5, 21.4, 7.5. HRMS (ESI+) m/z: $[M]^+$ calcd. for $C_8H_{19}IN$ 256.0557, found 256.0550.

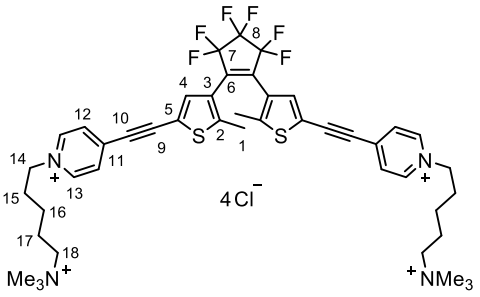
DTE-3 (chloride)



DTE-alkyne (**11** from Chapter 2, 600 mg, 1.44 mmol), 7-bromoquinoline (899 mg, 4.32 mmol, 3 equiv.), $Pd(PPh_3)_4$ (83.3 mg, 72.0 μmol, 0.05 equiv.) and copper(I) iodide (27.4 mg, 144 μmol, 0.1 equiv.) were dissolved in triethylamine (50 mL). The reaction mixture was stirred at 45 °C for 30 h and then concentrated in vacuo. The crude product was purified by flash column chromatography (PE 1:1 EtOAc) to yield a product contaminated with excess 7-bromoquinoline. Without further purification, the compound was dissolved in a mixture of CH_2Cl_2 (5 mL) and iodomethane (mL). The reaction mixture was stirred at 20 °C for 60 h and then concentrated in vacuo. The crude methylated product was purified by flash column chromatography (1–10% w/v KPF_6 in acetone). The resulting solid was dissolved in acetone (2 mL) and added to a solution of tetrabutylammonium chloride (500 mg) in acetone (30 mL). The ion exchange reaction mixture was stirred for 30 min and the precipitated solid was collected by filtration. The precipitate was further washed with THF and then diethyl ether to yield the final chloride salt of the product as a white solid (389 mg, 35%). δ_H (500 MHz, DMSO-d_6): 9.70 (2H, d, J_{HH} 5.7, H^{17}), 9.32 (2H, d, J_{HH} 8.2, H^{15}), 8.74 (2H, s, H^{19}), 8.54 (2H, d, J_{HH} 8.5, H^{13}), 8.19 (2H, dd, J_{HH} 5.7, J_{HH} 8.2, H^{16}), 8.14 (2H, d, J_{HH} 8.4, H^{12}), 7.67 (2H, s, H^4), 4.68 (6H, s, H^{20}), 2.06 (6H, s, H^1); δ_C (126 MHz, DMSO) 151.2, 146.7, 146.2, 138.3, 133.7, 131.5, 130.9,

128.9, 127.9, 124.4, 122.7, 121.8, 119.6, 92.9, 87.2, 45.4, 14.3. HRMS (ESI+) m/z: $[M]^{2+}$ calcd. for $C_{39}H_{26}F_6N_2S_2$ 350.0721, found 350.0725. UV-vis (water): λ_{max} = 398 nm (ε = 52300 M^{-1} cm^{-1}).

DTE-4 (chloride)



DTE-dipy (**Ay-yA(p)** from Chapter 2, 130 mg, 228 μmol) and 5-iodo-N,N,N-trimethylpentan-1-aminium iodide (262 mg, 684 μmol, 3 equiv.) were dissolved in DMF (2 mL) and stirred at 60 °C for 72 h. The crude mixture was concentrated in vacuo to yield a black oil. The black oil was dissolved methanol (5 mL) and added to an aqueous solution of potassium hexafluorophosphate (3.5 g in 50 mL) and stirred for 30 min. The precipitated black hexafluorophosphate salt was collected by filtration and then purified by flash column chromatography (3–15% w/v KPF_6 in acetone). After the fractions containing the photoswitch were combined and concentrated in vacuo, the hexafluorophosphate salt of the product was recovered from a salt mixture by dissolving the solid in water and filtering off the insoluble hexafluorophosphate salt of the product as a pale blue solid. The removal of excess starting material as confirmed by NMR, the solid was dissolved in acetone (2 mL) and added to a solution of tetrabutylammonium chloride (500 mg) in acetone (30 mL). The ion exchange reaction mixture was stirred for 30 min and the precipitated solid was collected by filtration. The precipitate was further washed with THF and then diethyl ether to yield the final chloride salt of the product as a pale blue solid (102 mg, 46%). δ_H (500 MHz, D_2O): 8.68 (4H, d, J_{HH} 6.4, H^{13}), 7.87 (4H, d, J_{HH} 6.4, H^{12}), 7.58 (2H, s, H^4), 4.47 (4H, t, J_{HH} 7.2, H^{14}), 3.21 (4H, m, H^{18}), 2.99 (18H, s, RN^+Me_3), 1.97 (4H, m, H^{15}), 1.85 (6H, s, H^1), 1.75 (4H, m, H^{17}), 1.31 (4H, m, H^{16}); δ_C (126 MHz, CD_3OD) 149.5, 144.0, 140.0, 136.1, 129.1, 125.1, 118.6, 96.1, 89.9, 66.2, 61.2, 53.0, 30.1, 22.4, 22.0, 14.1. HRMS (ESI+) m/z: $[M]^{4+}$ calcd. for $C_{29}H_{54}F_6N_4S_2$ 207.0918, found 207.0920. UV-vis (water): λ_{max} = 382 nm (ε = 62700 M^{-1} cm^{-1}).

4.4 Appendix

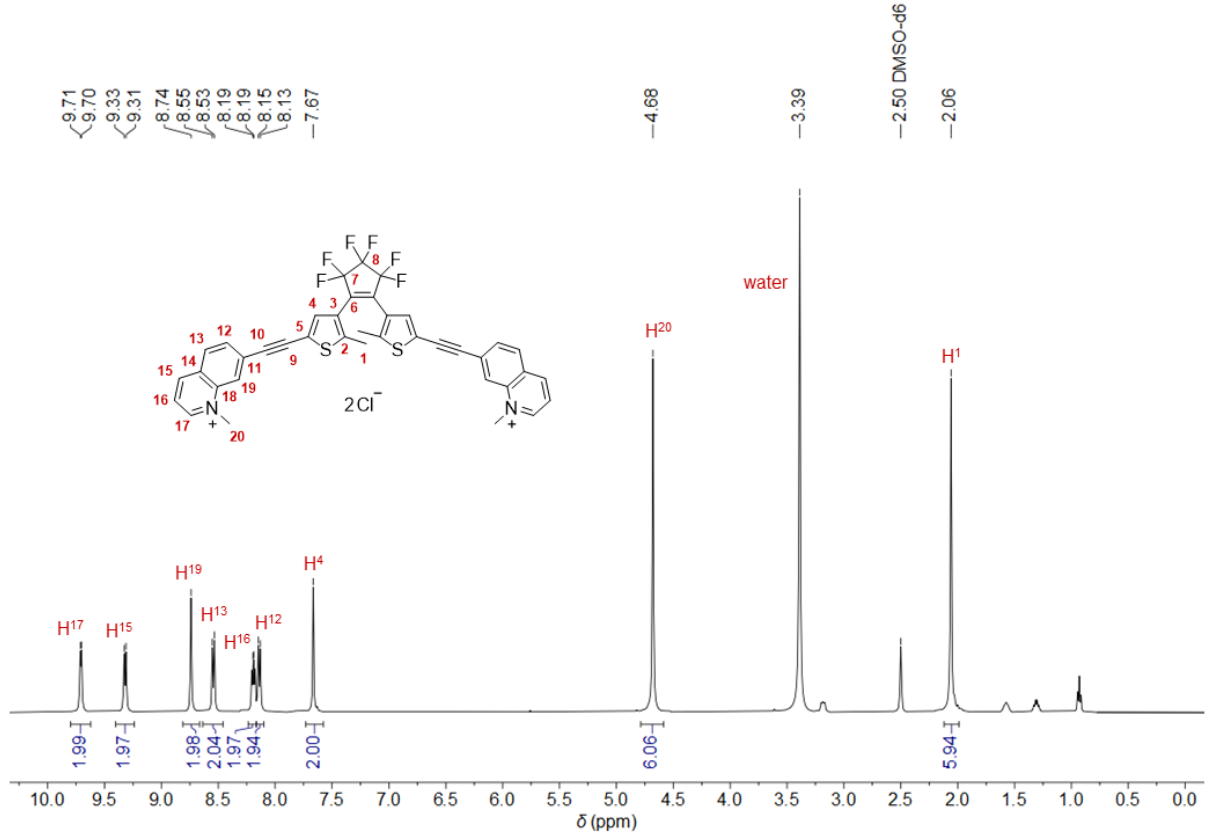


Figure 4.16 ^{1}H NMR spectrum (500 MHz, D_2O) of **DTE-3**.

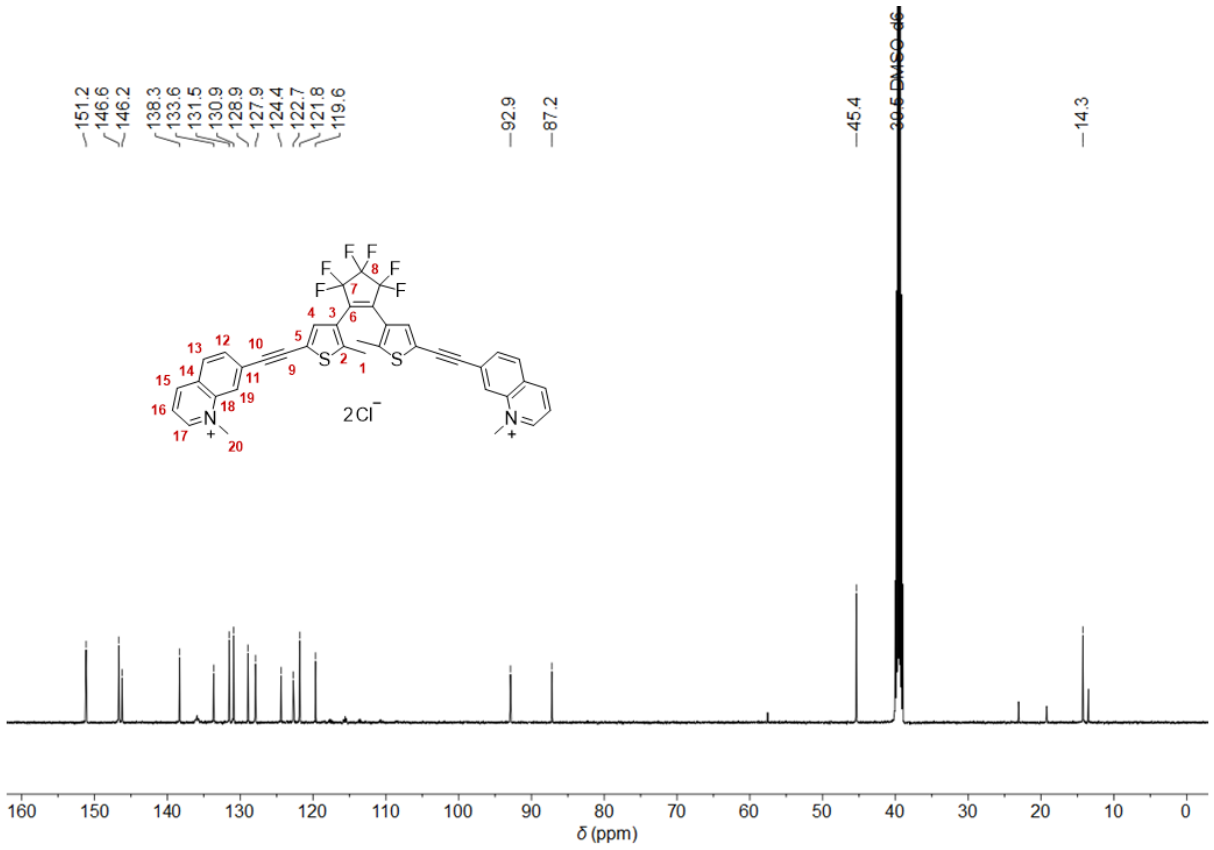


Figure 4.17 ^{13}C NMR spectrum (126 MHz, D_2O) of **DTE-3**.

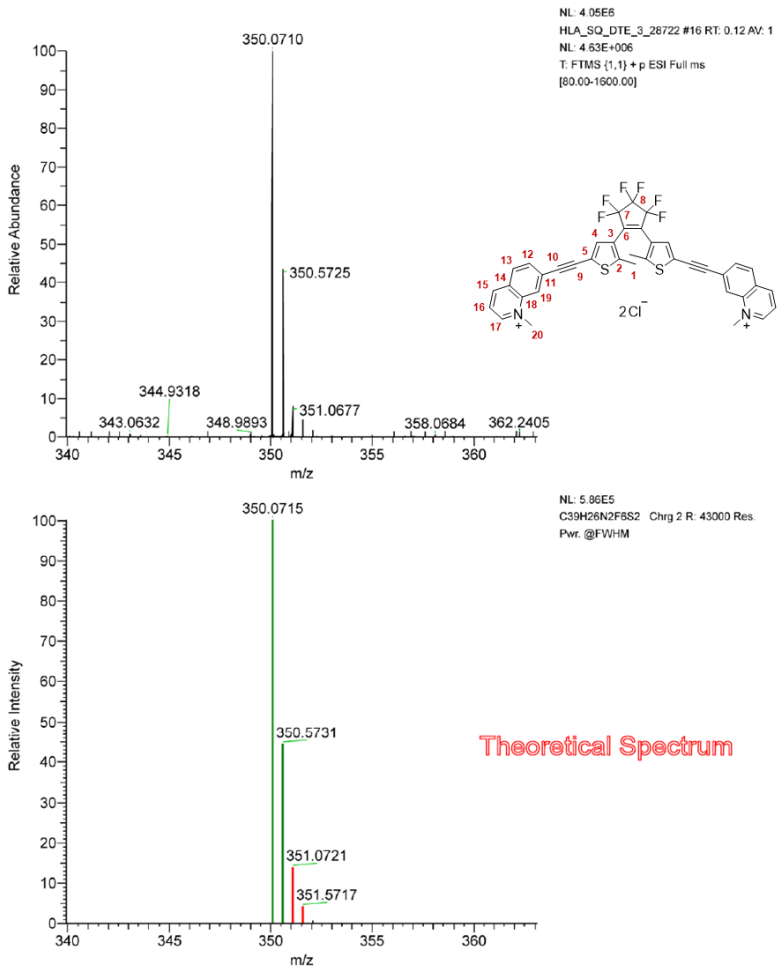


Figure 4.18 Experimental HRMS (ESI⁺) pattern of **DTE-3** and the theoretical pattern.

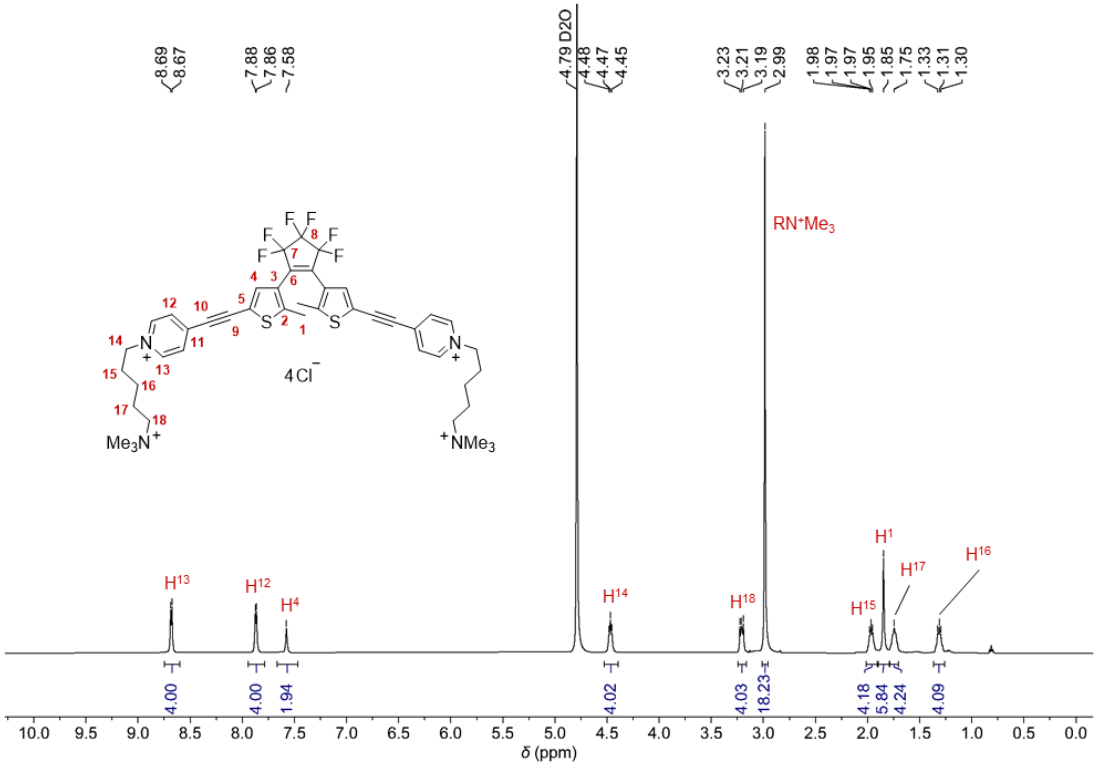


Figure 4.19 ^{1}H NMR spectrum (500 MHz, D_2O) of **DTE-4**.

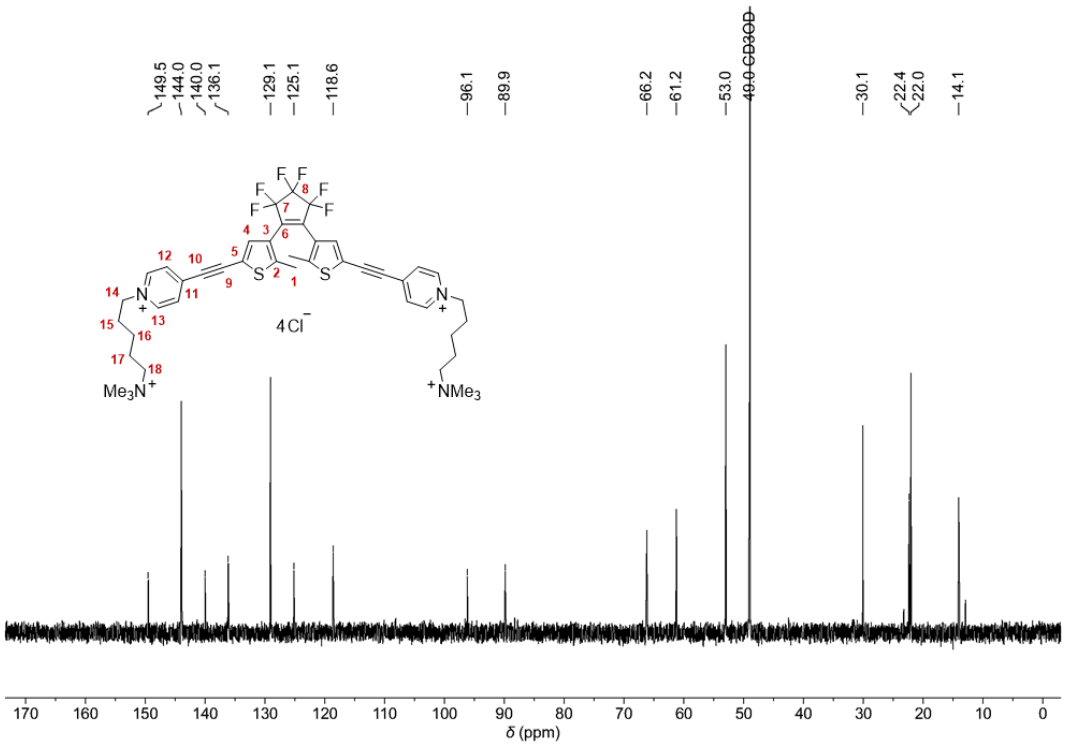


Figure 4.20 ^{13}C NMR spectrum (126 MHz, D_2O) of **DTE-4**.

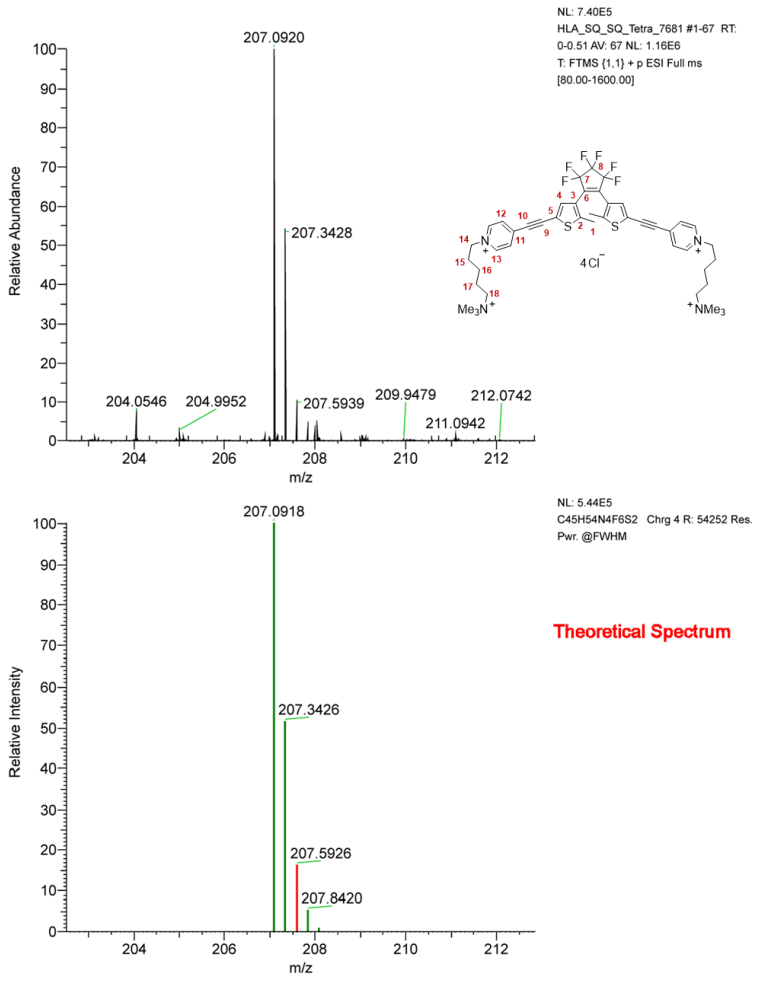


Figure 4.21 Experimental HRMS (ESI$^+$) pattern of **DTE-4** and the theoretical pattern.

References

1. J. A. DiMasi, H. G. Grabowski and R. W. Hansen, *J. Health Econ.*, 2016, **47**, 20–33.
2. M. J. Waring, J. Arrowsmith, A. R. Leach, P. D. Leeson, S. Mandrell, R. M. Owen, G. Pairaudeau, W. D. Pennie, S. D. Pickett, J. Wang, O. Wallace and A. Weir, *Nat. Rev. Drug Discovery*, 2015, **14**, 475–486.
3. R. W. Johnstone, A. A. Ruefli and S. W. Lowe, *Cell*, 2002, **108**, 153–164.
4. D. Hanahan and Robert A. Weinberg, *Cell*, 2011, **144**, 646–674.
5. M. Hay, D. W. Thomas, J. L. Craighead, C. Economides and J. Rosenthal, *Nat. Biotechnol.*, 2014, **32**, 40–51.
6. A. L. Hopkins, *Nat. Chem. Biol.*, 2008, **4**, 682–690.
7. J. M. A. Blair, M. A. Webber, A. J. Baylay, D. O. Ogbolu and L. J. V. Piddock, *Nat. Rev. Microbiol.*, 2014, **13**, 42–51.
8. W. A. Velema, W. Szymanski and B. L. Feringa, *J. Am. Chem. Soc.*, 2014, **136**, 2178–2191.
9. M. M. Lerch, M. J. Hansen, G. M. van Dam, W. Szymanski and B. L. Feringa, *Angew. Chem., Int. Ed.*, 2016, **55**, 10978–10999.
10. J. Broichhagen, J. A. Frank and D. Trauner, *Acc. Chem. Res.*, 2015, **48**, 1947–1960.
11. C. Brieke, F. Rohrbach, A. Gottschalk, G. Mayer and A. Heckel, *Angew. Chem., Int. Ed.*, 2012, **51**, 8446–8476.
12. R. Göstl, A. Senf and S. Hecht, *Chem. Soc. Rev.*, 2014, **43**, 1982–1996.
13. M. J. Fuchter, *J. Med. Chem.*, 2020, **63**, 11436–11447.
14. R. W. Redmond and I. E. Kochevar, *Photochem. Photobiol.*, 2006, **82**, 1178–1186.
15. Z. Huang, *Technol. Cancer. Res. Treat.*, 2016, **4**, 283–293.
16. M. Wainwright, *J. Antimicrob. Chemother.*, 1998, **42**, 13–28.
17. P. Klán, T. Šolomek, C. G. Bochet, A. Blanc, R. Givens, M. Rubina, V. Popik, A. Kostikov and J. Wirz, *Chem. Rev.*, 2012, **113**, 119–191.
18. K. Hüll, J. Morstein and D. Trauner, *Chem. Rev.*, 2018, **118**, 10710–10747.
19. P. Kobauri, F. J. Dekker, W. Szymanski and B. L. Feringa, *Angew. Chem., Int. Ed.*, 2023, **62**, e20230068.
20. H. Kaufman, S. M. Vratsanos and B. F. Erlanger, *Science*, 1968, **162**, 1487–1489.
21. A. Sailer, F. Ermer, Y. Kraus, F. H. Lutter, C. Donau, M. Bremerich, J. Ahlfeld and O. Thorn-Seshold, *ChemBioChem*, 2019, **20**, 1305–1314.
22. K. Fujimoto, M. Kajino, I. Sakaguchi and M. Inouye, *Chem. - Eur. J.*, 2012, **18**, 9834–9840.
23. O. Babii, S. Afonin, M. Berditsch, S. Reiβer, P. K. Mykhailiuk, V. S. Kubyshkin, T. Steinbrecher, A. S. Ulrich and I. V. Komarov, *Angew. Chem., Int. Ed.*, 2014, **53**, 3392–3395.
24. O. Babii, S. Afonin, L. V. Garmanchuk, V. V. Nikulina, T. V. Nikolaienko, O. V. Storozhuk, D. V. Shelest, O. I. Dasyukevich, L. I. Ostapchenko, V. Iurchenko, S. Zozulya, A. S. Ulrich and I. V. Komarov, *Angew. Chem., Int. Ed.*, 2016, **55**, 5493–5496.
25. O. Babii, S. Afonin, A. Y. Ishchenko, T. Schober, A. O. Negelia, G. M. Tolstanova, L. V. Garmanchuk, L. I. Ostapchenko, I. V. Komarov and A. S. Ulrich, *J. Med. Chem.*, 2018, **61**, 10793–10813.
26. U. Al-Atar, R. Fernandes, B. Johnsen, D. Baillie and N. R. Branda, *J. Am. Chem. Soc.*, 2009, **131**, 15966–15967.
27. S. Burge, G. N. Parkinson, P. Hazel, A. K. Todd and S. Neidle, *Nucleic Acids Res.*, 2006, **34**, 5402–5415.
28. A. B. Sahakyan, V. S. Chambers, G. Marsico, T. Santner, M. Di Antonio and S. Balasubramanian, *Sci. Rep.*, 2017, **7**, 14535.
29. I. Bang, *Biochemische Zeitschrift*, 1910, **26**, 293–311.
30. D. Rhodes and H. J. Lipps, *Nucleic Acids Res.*, 2015, **43**, 8627–8637.
31. J. L. Huppert and S. Balasubramanian, *Nucleic Acids Res.*, 2005, **33**, 2908–2916.

32. M. L. Bochman, K. Paeschke and V. A. Zakian, *Nat. Rev. Genet.*, 2012, **13**, 770–780.
33. G. Biffi, D. Tannahill, J. McCafferty and S. Balasubramanian, *Nat. Chem.*, 2013, **5**, 182 – 186.
34. A. Siddiqui-Jain, C. L. Grand, D. J. Bearss and L. H. Hurley, *Proc. Natl. Acad. Sci. U. S. A.*, 2002, **99**, 11593–11598.
35. S. Neidle, *Nat. Rev. Chem.*, 2017, **1**, 0041.
36. S. Balasubramanian, L. H. Hurley and S. Neidle, *Nat. Rev. Drug Discovery*, 2011, **10**, 261–275.
37. M. P. O'Hagan, J. Ramos-Soriano, S. Haldar, S. Sheikh, J. C. Morales, A. J. Mulholland and M. C. Galan, *Chem. Commun.*, 2020, **56**, 5186–5189.
38. M. Herder, B. M. Schmidt, L. Grubert, M. Patzel, J. Schwarz and S. Hecht, *J. Am. Chem. Soc.*, 2015, **137**, 2738–2747.
39. T. Santos, G. F. Salgado, E. J. Cabrita and C. Cruz, *Pharmaceuticals*, 2021, **14**, 769.
40. J. Ramos-Soriano and M. C. Galan, *JACS Au*, 2021, **1**, 1516–1526.
41. J. E. Reeve, H. A. Collins, K. D. Mey, M. M. Kohl, K. J. Thorley, O. Paulsen, K. Clays and H. L. Anderson, *J. Am. Chem. Soc.*, 2009, **131**, 2758–2759.
42. D. D. Le, M. Di Antonio, L. K. M. Chan and S. Balasubramanian, *Chem. Commun.*, 2015, **51**, 8048–8050.

5 Conclusions and Outlook

Contents

5.1 Conclusions 261
5.2 Outlook 262

Chapter 5 - Conclusions and Outlook

5.1 Conclusions

This thesis encompasses a comprehensive exploration of molecular photoswitches, beginning with a general introduction (Chapter 1), followed by the synthesis and optimization of dithienylethene-based molecular photoswitches (Chapter 2). The subsequent chapters focus on the application of the most effective DTE photoswitch in switchable fluorescence (Chapter 3) and photopharmacology targeting DNA G-quadruplex structures (Chapter 4).

Chapter 1 presented a thorough background analysis of key parameters governing molecular photoswitching ability and a systematic literature review of established molecular photoswitch classes. The conclusion from this analysis is that diazocines, diarylethenes, spiropyrans (specifically, spirooxazines and spironaphthoxazines), fulgimides, hemiindigos, and hemithioindigos are suitable for biological applications, particularly in switchable fluorescence and photopharmacology. These classes exhibit outstanding photoswitching parameters, while other photoswitches such as stilbenes, indigos, and thioindigos face critical limitations. Based on these findings, the thesis focuses on dithienylethenes.

Chapter 2 detailed the synthesis and characterization of eight push-push, pull-pull, and push-pull DTEs. Novel synthetic approaches were employed to functionalize the DTE arms with julolidine and *N*-methylpyridinium groups. To break the symmetry of DTEs, one-pot coupling reactions with two different partners and arm-to-core synthetic approaches were utilized, enabling access to DTEs with varied conjugation lengths and substitution patterns. Photochemical and photophysical characterizations revealed that the DTE bearing two *N*-methylpyridinium groups with an alkyne spacer exhibited optimal photoswitching properties, including visible light-triggered photocyclization and photoreversion, high PSD in both directions, and high photoswitching quantum yields. DFT and TD-DFT calculations indicated that molecular constructs forcing the DTE to adopt an anti-parallel conformation are crucial for achieving high photocyclization PSD.

Chapter 3 described the linkage of the best-performing DTE to two fluorescent dyes, Cy3 and Cy3B, to create switchable fluorophores based on a dyad design. These novel constructs demonstrate excellent photoswitching and fluorescence quenching properties. The chapter detailed the synthesis, characterization, and photophysical properties of these dyads. The dyads exhibit good water solubility, efficient fluorescence quenching in the closed form, and bright

fluorescence in the open form. Notably, they show superior fatigue resistance compared to previously reported switchable fluorophores, maintaining their switching ability over multiple cycles.

Chapter 4 explored the differential binding of open and closed DTE isomers to G4 DNA in the context of photopharmacology, focusing on four different DTE variants with varying sizes of hydrophobic surfaces and numbers of positive charges. Through a series of biophysical studies, including fluorescence quenching assays, CD titration, and FRET melting experiments, the binding affinities and stabilization effects of the DTE variants on G4 structures were determined. The results demonstrate that structural modifications of the DTEs, particularly the incorporation of extended π-surfaces and additional positive charges, resulted in stronger binding to G4 DNA. The chapter also presents cytotoxicity studies on cancer and non-cancer cell lines, revealing a correlation between G4 binding affinity and cellular toxicity. Importantly, the study shows differential activities between the open and closed forms of the DTEs.

5.2 Outlook

While our molecular design in Chapter 2 led to the discovery of a DTE with optimal photoswitching properties, the molecule still requires 405 nm blue light to trigger the photocyclization process. For biologically relevant applications, red and NIR light would be preferable due to their superior tissue penetration. However, developing a red-light-switchable DTE by simply extending π-conjugation is unlikely to be successful, as longer π-conjugation typically results in lower photocyclization quantum yields due to reduced frontier orbital contribution to the photoactive hexatriene unit. Therefore, to develop DTEs that can be switched with longer wavelength light, alternative strategies such as photosensitization, multi-photon absorption, upconversion nanoparticles, and plasmon-enhanced photoswitching need to be explored.

The outstanding switchable fluorophores developed in Chapter 3 warrant further investigation for their applications in advanced microscopy techniques such as RESOLFT microscopy and FRAP. For RESOLFT microscopy, these molecules could potentially target cell membranes and studied with model vesicles followed by live cells, as many previous dyads synthesized in our group selectively target membranes. By measuring the fluorescence intensity profile of a vesicle membrane, it would be possible to quantify the resolution enhancement due to the photoswitching capabilities. Currently, **DTE-Cy3** and **DTE-Cy3B** have limited applicability in FRAP or other microscopy experiments requiring specific labeling due to the

lack of necessary functional groups. However, the methyl-capped end of the DTE provides an opportunity to incorporate various labeling functionalities. By modifying these switchable fluorophores with functional groups such as alkynes, azides, HaloTag ligands, SNAP-tag ligands, or specific targeting substrates like folate groups, we could enable their use in super-resolution microscopy studies, single-molecule tracking, and cell kinetics measurements.

Regarding the photopharmacology study in Chapter 4, the results demonstrate interesting binding between DTEs and G4 structures, but the exact binding mode remains undetermined. To elucidate the precise binding mechanisms of both open and closed DTE forms, a combination of biological NMR studies, X-ray crystallography, and computational docking calculations should be employed. This structural information would be invaluable for the rational design of DTEs with even higher binding affinity and greater contrast in activity between open and closed forms. Furthermore, structure-activity relationship studies could be conducted to optimize the π-surface extensions, charge distribution, and G4-specific recognition elements of the DTEs, potentially leading to the development of more potent and selective G4-targeting photoswitchable ligands.